Physics of the Solid State, Vol. 43, No. 4, 2001, pp. 597–601. Translated from Fizika Tverdogo Tela, Vol. 43, No. 4, 2001, pp. 577–580.

METALS AND SUPERCONDUCTORS

Crystallization of a Eutectic Pb–Sn Melt in the Thermal Field of a Temperature Gradient

A. P. Belyaev*, S. A. Kukushkin, and V. P. Rubets***

** St. Petersburg Institute of Technology, Zagorodnyĭ pr. 49, St. Petersburg, 196013 Russia*

*** Institute for Problems in Mechanical Engineering, Russian Academy of Sciences, Bol'shoĭ pr. 61, Vasil'evskiĭ ostrov, St. Petersburg, 199178 Russia*

e-mail: belyaev@tu.spb.ru

Received September 7, 2000

Abstract—The crystallization of a eutectic Pb–Sn melt is investigated under nonuniform conditions in vacuum, in air, and in water. It is found that the structure of the solid-state systems formed depends on the cooling conditions. A structural inhomogeneity in volume and a correlation between the microstructure and the coordinate in a thermal field are revealed. Results of technological, electron-microscopic, and statistical investigations are reported. It is shown that the experiment is consistent with the crystallization theory of eutectic melts. *© 2001 MAIK "Nauka/Interperiodica".*

1. INTRODUCTION

The crystallization of eutectic melts has long been investigated. Interest in these melts is constantly stimulated by practical needs (metallurgy, microelectronics, and superconductor engineering). However, the specific features of the crystallization mechanisms in these systems have not yet been fully elucidated because of the complexity of the problem. In particular, this concerns processes of crystallization of eutectic melts in thermal fields of the temperature gradient, which were studied in the present work.

In recent years, a series of works devoted to the development of a general crystallization theory has appeared in the literature [1–4]. It is reasonable to attempt to apply the results of theoretical studies to the description of real systems. In this connection, the original data of an investigation into mechanisms of crystallization in the Pb–Sn system will be presented below and compared with the predictions of the current theory.

2. EXPERIMENTAL TECHNIQUE

The Pb–Sn system was investigated. The content of components in the system was chosen so that its composition was as close to eutectic as possible. For this purpose, a mechanical mixture was prepared from chemically pure lead and tin components. The composition of the mechanical mixture was determined according to the available data [5] (38.1 wt % Pb and 61.9 wt % Sn). The mixture was then heated under vacuum in a special quartz reactor. A thermocouple was placed inside the melt, and the kinetic crystallization curve was measured. A typical curve is shown in Fig. 1. The length of the plateau in the kinetic curve (the *bc* section) served as a parameter for determining the ultimate composition of samples. The composition was chosen so that the plateau length was maximum.

The melt obtained by the above technique was used to prepare samples in silica cells. Kinetic curves for each sample were recorded upon cooling in vacuum, in air, and in water.

After cooling, the cells were broken and the samples were cut from ingots. Then, the samples were polished and etched according to the standard preparation technique for investigations with a scanning microscope.

All the electron-microscopic investigations were conducted with a JSM-35 scanning electron microscope.

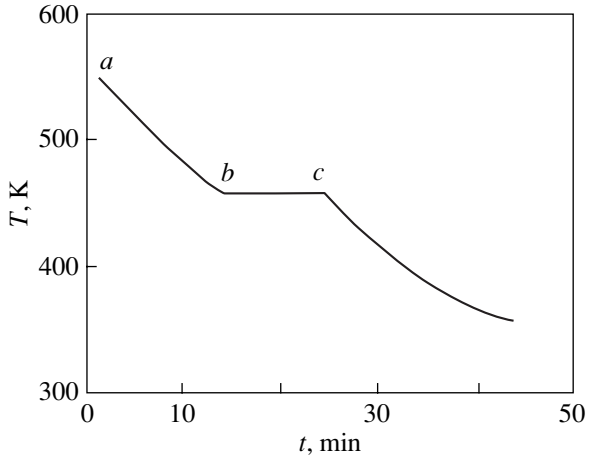

Fig. 1. Crystallization curve of the eutectic Pb–Sn melt.

1063-7834/01/4304-0597$21.00

3. MAIN RESULTS

The main experimental results are presented in Figs. 2–4.

Figure 2 demonstrates an electron microscope image of the surface of a sample section cut out parallel to the direction of the vector of the temperature gradient of the thermal field. The image was obtained in reflected electrons and positioned in the figure in such a way that its upper and lower parts correspond to the periphery (Fig. 2a) and the center (Fig. 2c) of the studied sample, respectively. Figure 2 displays the pattern observed upon vacuum cooling of a Pb–Sn melt with a close-to-eutectic composition.

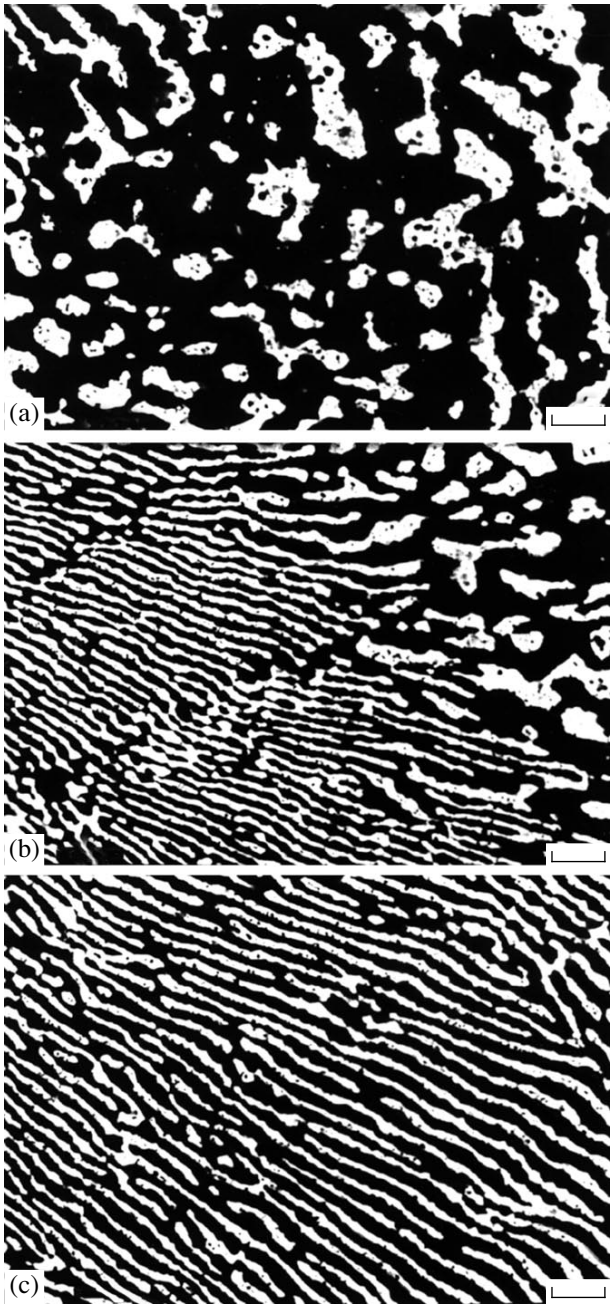

Fig. 2. Images of different surface regions of a specimen cut from the bulk of a sample prepared by crystallization of a close-to-eutectic Pb–Sn melt upon cooling under vacuum (×1000): (a) the peripheral region, (b) the region between the periphery and the center, and (c) the region corresponding to the center of the sample.

Figures 3 and 4 show the same image for the central region of the samples obtained upon cooling in air and in water, respectively. The black color corresponds to the Sn phase, and the white color designates the Pb phase in all the figures.

As is seen from these figures, the samples prepared by any one of the methods studied were structurally inhomogeneous in volume. The character and the degree of inhomogeneity of a particular region correlated with its distance from the sample periphery. Near the periphery, the samples predominantly contained the Sn phase with Pb inclusions of a complex shape in the matrix. The ratio between the phases changed with distance from the periphery.

The macrostructure of regions away from the periphery depended on the sample preparation technique. A pronounced lamellar structure with almost periodic alteration of the Pb and Sn phases was observed when the melt was cooled under vacuum (Fig. 2c). Cooling in air or in water disturbed the order. The structure of the regions became less ordered and more fine-grained (Figs. 3, 4).

4. DISCUSSION

The experiments discussed in the present work almost exactly correspond to the boundary conditions used in theoretical investigations into the mechanisms of the crystallization processes in multicomponent melts [2]. There are only two essential differences. First, the authors considered noneutectic melts. Second, the authors ignored the effect of the periphery temperature on crystallization. In order to interpret the experimental results, let us take these differences into account with the aid of theoretical studies of eutectic melts under uniform conditions [3, 4].

According to these works, we can consider Fig. 2 as a film on which the crystallization of a close-to-eutectic melt was recorded. Indeed, the upper part of this figure (Fig. 2a) corresponds to the sample periphery. Therefore, it is in this region of the sample that crystallization started. While a continuous crust of the new phase was formed here, crystallization did not necessarily start in the regions close to the sample center, because propagation of supercooling from the periphery to the center required a certain time.

As was shown in [2], the supercooling wave moves more quickly toward the center than the crust boundary. Hence, the formation time for each region in the solid sample depends on the distance between this region and the periphery. The larger the distance, the greater the time interval between the instant of supercooling and

the instant of the formation of a continuous crust. Thus, when viewing the figure from bottom to top, we can follow the course of the transformation in the macrostructure of a sample crystallizing from the eutectic melt at different crystallization times.

Let us return to the discussion of the structure of the sample periphery shown in Fig. 2a. It can be seen that this region predominantly contains one phase, namely, the Sn phase. This fully agrees with theoretical concepts. Upon crystallization of a close-to-eutectic melt, the supercooling wave primarily causes crystallization of the component that is excessive with respect to the eutectic composition. It follows from the figure that tin was such a component in the samples studied. The Sn crust, when moving to the center, pushed the liquid lead phase deeper, thus enriching the melt with lead and bringing the melt closer to a eutectic composition.

Crystallization of a eutectic melt is a self-consistent process. The same supercooling for both phases is established at the later stages of this process. Its value can be found from the kinetic crystallization curve. For the sample presented in Fig. 2, supercooling was ΔT = 2.3 K. Since the supercooling was the same for both phases, the critical radii of nuclei with different compositions met the similarity condition [3]

$$\bar{R}_{Sn} = \gamma \bar{R}_{Pb}, \quad (1)$$

which can be verified with the help of microphotographs. Here,

$$\gamma = \frac{\sigma_{Sn}\omega_{Sn}L_{Pb}}{L_{Sn}\sigma_{Pb}\omega_{Pb}}, \quad (2)$$

L_i is the latent crystallization heat per atom, ω_i is the volume per atom, and σ_i is the interfacial energy per unit area.

Statistical treatment of the images (Fig. 2) revealed that the experimental results are in close agreement with theoretical calculations. For example, the values $\gamma = 0.9$ and 1.1 were obtained for the images in Figs. 2b and 2c, respectively. The theoretical value $\gamma = 0.9$ was calculated from the following quantities [6]: σ_{Sn} = 673 erg/cm^2, $\omega_{Sn} = 3.37 \times 10^{-23}$ cm^3, $L_{Sn} = 1.20 \times 10^{-13}$ erg/atom, σ_{Pb} = 560 erg/cm^2, $\omega_{Pb} = 3.04 \times 10^{-23}$ cm^3, and $L_{Pb} = 7.92 \times 10^{-14}$ erg/atom.

Before statistically processing the electron microscope image, we verified the correspondence between the linear cluster dimensions $\bar{R}_i$ in microphotographs and the critical radius calculated by the formula [3]

$$\bar{R}'_{Pb} = \frac{2\sigma_{Pb}T_e\omega_{Pb}}{L_{Pb}\Delta T}. \quad (3)$$

Here, T_e is the eutectic temperature and ΔT is the supercooling.

The check revealed that these quantities are of the same order of magnitude (1 and 0.9 μm). One could hardly expect closer values in this case, at least, because of the technique used to determine the supersaturation. However, even if a larger difference existed between the cluster sizes $\bar{R}_i$ and $\bar{R}'_i$ in the microphotographs, in our opinion, this would not make the check of condition (1) useless. A large difference between $\bar{R}_i$ and R'_i would indicate that the phase clusters observed in the microphotographs were formed as a result of the coalescence of smaller clusters. Coalescence is a nonlinear process. The coalescence theory is still far from accurate. Hence, up to this point, it has been impossible to predict convincingly and unambiguously the relationship between the dimensions of the coalescing clusters and those already merged. However, the sizes of the clusters merged will most likely be proportional to

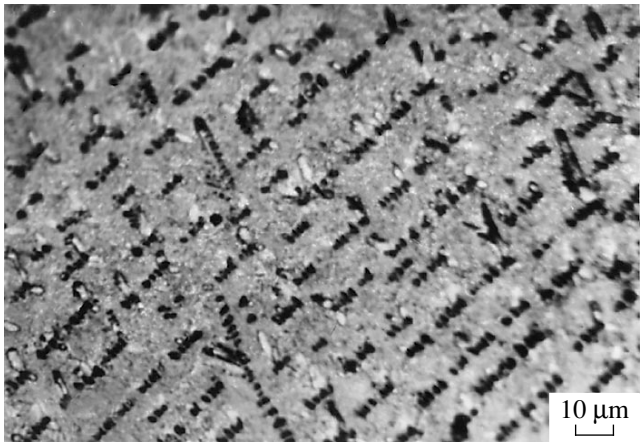

Fig. 3. Image of the surface of a specimen cut from the bulk of a sample prepared by crystallization of a close-to-eutectic Pb–Sn melt upon cooling in air.

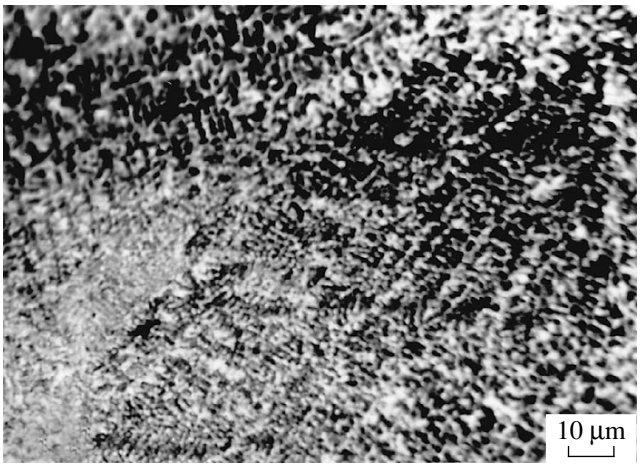

Fig. 4. Image of the surface of a specimen cut from the bulk of a sample prepared by crystallization of a close-to-eutectic Pb–Sn melt upon cooling in water.

the sizes of the coalescing clusters. Therefore, coalescence must not radically violate condition (1).

The close values of $\bar{R}_i$ and $\bar{R}_i'$ in the experiment on Pb–Sn indicate that the coalescence stage was almost by-passed in the formation of the samples under investigation and the merging of clusters into a solid crust took place immediately after the Ostwald ripening, which, as a rule, is the longest stage of the crystallization process. It is during this stage that a universal size distribution of nuclei of new phases is formed. The longer this stage, the more coarse-grained and homogeneous the structure formed. This correlates with the results under discussion. Figure 2 allows one to follow the increase in the cluster size when viewed from top to bottom, since the image of the sample is presented in such a way that the regions corresponding to the prolonged Ostwald ripening stage are at the bottom.

Let us now discuss the structure of the region of the sample in which the Pb phase starts to precipitate (the transition region). It is seen from Fig. 2 that Pb clusters have a more complex shape. It is reasonable to attribute such a behavior to the system composition, because, according to [4], noneutectic melts, unlike the eutectic melts, show a tendency to excitation of "dendrite"-type modes. The formation of complex-shaped clusters in the transition region, where the melt composition is far from eutectic, experimentally confirms the theoretical results obtained in [4].

In closing, let us consider how the cooling conditions affect the structure formed. First of all, we will formulate the important features of each of the cooling methods used.

The specific feature of cooling in air and under vacuum is that the temperature at the sample boundary is not constant during cooling, as is usually assumed in theoretical studies. By contrast, cooling in water is characterized by isothermal boundary conditions.

All the methods considered differ from one another by the power of heat removal from the system.

The influence of the heat removal rate on the formation of the ultimate structure of the material was theoretically treated in many works [1, 5], and a certain correlation between these parameters was noticed everywhere.

The experiments we performed with the Pb–Sn system also indicate a correlation between the cooling conditions and the structure. As is evident from a comparison of Figs. 2–4, the lower the power of the sources of heat removal, the more ordered the structures formed. The formation time certainly played an essential role. This is evidenced, above all, by the similarity of the electron microscope images of samples prepared under different conditions, which appears as if one pattern stipulated the other one but for a later crystallization stage. This agrees with the theory predicting that an increase in the duration of the Ostwald ripening favors the formation of a more homogeneous structure [1, 2]. According to the same theory, structural ordering is also favored by decaying heat outflows, whose occurrence, in turn, stipulates nonisothermal boundary conditions. The nonisothermal boundary conditions, as well as the large formation times, were characteristic of samples prepared upon vacuum cooling of the melt. In our opinion, this was the reason for the maximum order in the structure of these samples.

Let us now discuss the other extreme case of the most disordered systems. It is seen from Fig. 4 that apart from small sizes of grains of individual phases, the structure of samples formed upon cooling in water is characterized by a considerable disorder.

As was shown in [1], the Ostwald ripening is not realized and the supercooling remains practically unchanged when heat is removed from the eutectic melt with a time-independent constant rate, as was the case in water cooling of the Pb–Sn melt. In this situation, nucleation of two phases continuously proceeds in the melt (Pb and Sn crystals in this case). The crystal sizes were very small because the crystal growth rate was determined by diffusion and the rate of the supercooling withdrawal was controlled by thermal conduction. Since crystals of different sorts were formed simultaneously, crystals of a particular sort could serve as nucleation centers for crystals of another sort. The emergence of these centers substantially reduced the work of crystal formation and, thus, caused a drastic increase in the nucleation rate of small crystals. As a result, the structure of the sample formed acquired the form of a foam of interspersed nuclei of different compositions, as is shown in Fig. 4.

5. CONCLUSION

Thus, the following principal results have been obtained in the present work.

(1) The local microstructure of a particular region of the solid Pb–Sn sample prepared in a thermal field of the temperature gradient by crystallization of a close-to-eutectic melt depends on the temperature gradient and the coordinate of the region in the thermal field.

(2) The structure parameters of the Pb–Sn eutectic grown in the thermal field of the temperature gradient under nonisothermal boundary conditions, these latter providing decaying heat outflows, are adequately described by the current theory which accounts for generalized supercooling, the correlation between precipitates of different compositions, and their morphological stability.

(3) The distinctly nonuniform conditions of crystallization of eutectic melts favor the system disordering, the origin of which is satisfactorily explained by the kinetics of heat removal from the melt.

ACKNOWLEDGMENTS

The work was supported by the Russian Foundation for Basic Research, project nos. 99-03-32676 and 99-03-32768.

REFERENCES

1. S. A. Kukushkin and A. V. Osipov, Usp. Fiz. Nauk **168** (10), 1083 (1998) [Phys. Usp. **41**, 983 (1998)].
2. S. A. Kukushkin and D. A. Grigor'ev, Zh. Tekh. Fiz. **65** (10), 154 (1995) [Tech. Phys. **40**, 1059 (1995)].
3. S. A. Kukushkin and D. A. Grigor'ev, Fiz. Tverd. Tela (St. Petersburg) **38** (4), 1262 (1996) [Phys. Solid State **38**, 698 (1996)].
4. S. A. Kukushkin and A. V. Osipov, Fiz. Tverd. Tela (St. Petersburg) **39** (8), 1464 (1997) [Phys. Solid State **39**, 1299 (1997)].
5. A. I. Somov and M. A. Tikhonovskiĭ, *Eutectic Compositions* (Metallurgiya, Moscow, 1975).
6. W. Missol, *Energia powierzchni rozdzialu faz w metalach* (Slask, Katowice, 1975, Metallurgiya, Moscow, 1978), translated from Polish.

Translated by M. Lebedkin

Physics of the Solid State, Vol. 43, No. 4, 2001, pp. 602–608. Translated from Fizika Tverdogo Tela, Vol. 43, No. 4, 2001, pp. 581–586.

METALS AND SUPERCONDUCTORS

Symmetrical High-T_c Superconducting Bicrystal Josephson Junctions: Dependence of the Electrical Properties on the Misorientation Angle

Yu. V. Kislinskiĭ*, E. A. Stepantsov*, Z. G. Ivanov, and T. Claeson****

** Shubnikov Institute of Crystallography, Russian Academy of Sciences, Leninskiĭ pr. 59, Moscow, 117333 Russia*

*** Chalmers University of Technology, Göteborg, S-41296 Sweden*

e-mail: mechan@ns.crys.ras.ru

Received August 24, 2000

Abstract—The electrical properties of junctions at symmetrical bicrystal boundaries in high-T_c superconducting films are studied as functions of the misorientation angle in the range 8°–45°. The junctions are prepared by growing $YBa_2Cu_3O_7$ (YBCO) epitaxial films on Y–ZrO_2 (YSZ) bicrystal substrates. The proportional relationship between the characteristic voltages and the normal conductivities of junctions is derived from the dependences of the critical current and the normal resistance on the misorientation angle. The results are interpreted within the model of a superconductor–dielectric with defect levels in the band gap of the superconductor. The deviations from the proportional relationship are explained by the junction inhomogeneity. The thickness of the effective dielectric layer in the bicrystal junction and the Bohr radius of electrons on the defects are estimated. © *2001 MAIK "Nauka/Interperiodica".*

1. INTRODUCTION

Josephson junctions with critical currents I_c and normal resistances R_n which are as large as possible are necessary for high-T_c superconducting electronics. The grain boundaries in $YBa_2Cu_3O_7$ (YBCO) films on bicrystals with small misorientation angles θ possess a high characteristic voltage ($V_c = I_cR_n$), but these junctions are inhomogeneous [1]. At angles θ of about 30°, the boundaries are homogeneous [2], but the voltages V_c are small. The relation between the electrical properties and the structure of junctions has been studied by a number of research groups. The thickness of a dielectric $d \approx 2$ nm on Y–ZrO_2 (YSZ) at θ = 32° was calculated by Winkler *et al.* [2] from the junction capacitance.

The proportionality between V_c and the surface conductivity g_n follows from the model of direct pair tunneling through a dielectric [3]. The relationship $V_c \sim g_n^q$ (q = 1–1.5) was experimentally confirmed by Gross and Mayer [4]. However, Hilgenkamp and Manhart [5] found deviations from this relationship. The reasons for these deviations were studied in this work. Aslamazov and Fistul' [6] proposed a theory of Cooper pair tunneling through channels formed by periodically arranged defects in a semiconductor. This theory also leads to the relationship $V_c \sim g_n$ [7]. The tunneling of normal electrons through these channels was described by Glazman and Matveev [8]. In the present work, we estimated the parameters of electron tunneling through the YBCO grain boundary: the Bohr radius α_b of electrons on defects and the thickness d.

2. EXPERIMENTAL TECHNIQUE

YBCO films were grown by the pulsed laser deposition method on YSZ bicrystal substrates. The film thickness t was equal to about 250 nm. The films were grown in such a way that their principal axes C were perpendicular to the substrate surface and YBCO(110) ∥ YSZ(100), as was described in our previous work [9]. The YBCO grain boundary was formed during the film growth above the substrate boundary. Photolithography with subsequent ion milling were used for preparing Josephson junctions in the form of YBCO microbridges which cross the boundary in the same manner as was proposed in [10]. The junction width w was 1–8 μm. Contact pads were obtained by thermal evaporation of gold and ion milling. The bicrystal junctions thus produced had the following misorientation angles (deg): 8, 18, 26, 28, 34, 36, and 45. These angles were equal to twice the angle which was formed by the (100) and (010) directions with the grain boundary in the YBCO film.

The current–voltage characteristics were measured by the four-probe method. The accuracy of the measurement of I_c was about 20% because of the influence of magnetic fields. The values of R_n were determined from the tangents to current–voltage characteristics with an error of about 2%. The surface resistance ρ_n and

the surface conductivity g_n were calculated by the expression $\rho_n = 1/g_n = R_n wt$.

3. EXPERIMENTAL RESULTS

The current–voltage characteristics for the junctions are consistent with the resistively shunted junction (RSJ) model. As a rule, the current–voltage characteristics for junctions are described by the formula

$$i(v) = R_n^{-1}\sqrt{v^2 + (I_c R_n)^2} + I_{ex}. \quad (1)$$

The parameters obtained by the least-squares method for the current–voltage characteristic of a junction with $\theta = 18°$ and $w = 8$ μm at 77 K are as follows: $R_n = 1.85\ \Omega$, $I_c = 79$ μA, and the excess current $I_{ex} = 17$ μA (Fig. 1). The current–voltage characteristic for the boundary with $\theta = 34°$ and $w = 8$ μm at 77 K exhibits a small current $I_c \approx 8$ μA and, therefore, is rounded by the thermal noise. The characteristic of a junction with $\theta = 8°$ and $w = 6$ μm at 4 K is described by formula (1) in the range $v \geq V_c$ (inset in Fig. 1). The calculations with this formula give $R_n = 0.52\ \Omega$, $I_c = 4.30$ mA, and $I_{ex} = 2.30$ mA. The critical current measured with a 1 μV criterion is equal to 4.05 mA. The characteristic deviates from the RSJ model at $v < V_c$. The junction is "wide," because the ratio between the Josephson penetration depth λ_j and the width w is large ($w/\lambda_j \approx 7$). The magnetic field of the supply current induces the motion of current vortices along the boundary, which leads to a distortion of the current–voltage characteristic shape.

This current–voltage characteristic of a junction with $\theta = 8°$ changes under microwave radiation in accordance with the RSJ model. Figure 2 shows the dependences of the positions of edges of the first three Shapiro steps on the relative microwave current through the junction: $i_w = I_{rf}/I_c(0)$, where I_{rf} is the amplitude of the external microwave current and $I_c(0)$ is the critical current in the absence of microwave radiation. The dependence of the current that corresponds to the upper edge of the nth step on the current i_w is designated as $I_n^+(i_w)/I_c(0) = i_n^+$, the dependence of the current of the lower edge is denoted as $I_n^-(i_w)/I_c(0) = i_n^-$, and the critical currents at different microwave currents are symbolized as $I_c(i_w)/I_c(0) = i_0$. Let us introduce the relative frequency $\omega \approx V_1/V_c \approx 10^{-2}$, where $V_1 = 24.3$ μV is the voltage of the first Shapiro step and $V_c = 2.25$ mV. The RSJ characteristics at $\omega \ll 1$ and $i_w \ll 1/\omega$ are described by the formulas [11]

$$i_n^+ = 1 - i_w + (2n+1)\omega\sqrt{i_w}, \quad (2)$$

$$i_n^- = 1 - i_w + (2n-1)\omega\sqrt{i_w}. \quad (3)$$

The parameter $\omega = 0.037$ was determined numerically. At $i_w \leq 1$, the currents corresponding to the step edges

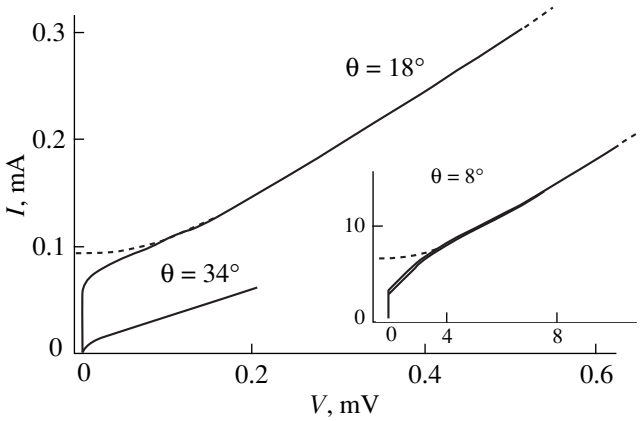

Fig. 1. Current–voltage characteristics for junctions with $w = 8$ μm at 77 K. The inset shows the current–voltage characteristic for a junction with $\theta = 8°$ and $w = 6$ μm at 4 K. Dashed lines are the current–voltage characteristics calculated by formula (1).

decrease with an increase in the microwave amplitude according to relationships (2) and (3) (Fig. 2a).

The parameters involved in formula (1) can be used to compare junctions with different angles θ (Table 1). A designation of the type 6 + 6 in the column w means a SQUID that consists of two bridges each 6 μm thick. An increase in θ results in a decrease in the I_c currents by two orders of magnitude and an increase in the R_n resistances by one order of magnitude. The excess current fraction I_{ex}/I_c decreases with an increase in the angle θ.

For junctions with $\theta \leq 36°$, R_n is temperature independent. At $\theta = 45°$, the normal conductivity G at $T > 40$ K increases with temperature (Fig. 3). The relative change in the conductivity $G(T)/G_1$ can be represented in the following form [8]:

$$\frac{G(T)}{G_1} = 1 + \frac{G_2}{G_1}(T - 35)^m. \quad (4)$$

Here, G_1 is the mean conductivity at $T \leq 30$ K. Two parameters $m = 1.1 \pm 0.5$ and $G_2/G_1 \approx 2 \times 10^{-3}$ were calculated by the least-squares method. The root-mean-square deviation σ_{G1} for G_1 is equal to 2%, which is considerably less than variations in the conductivity with temperature (Fig. 3).

The temperature dependences of V_c and the excess voltage $V_{ex} = I_{ex}R_n$ for a junction with angle $\theta = 18°$ are depicted in Fig. 4. At $T \geq 40$ K, V_c is given by the formula

$$V_c = V_0(1 - T/T_c)^M, \quad (5)$$

where T_c is the critical temperature of a given YBCO film. The parameters M and V_0 were found numerically from the experimental data. For junctions with $\theta = 8°$, 18°, 34°, and 45°, $M = 1.8$, 1.9, 1.8, and 2.0 and $V_0 = 7.0$, 3.8, 0.72, and 0.64 mV, respectively. At $T \lesssim T_c$, the

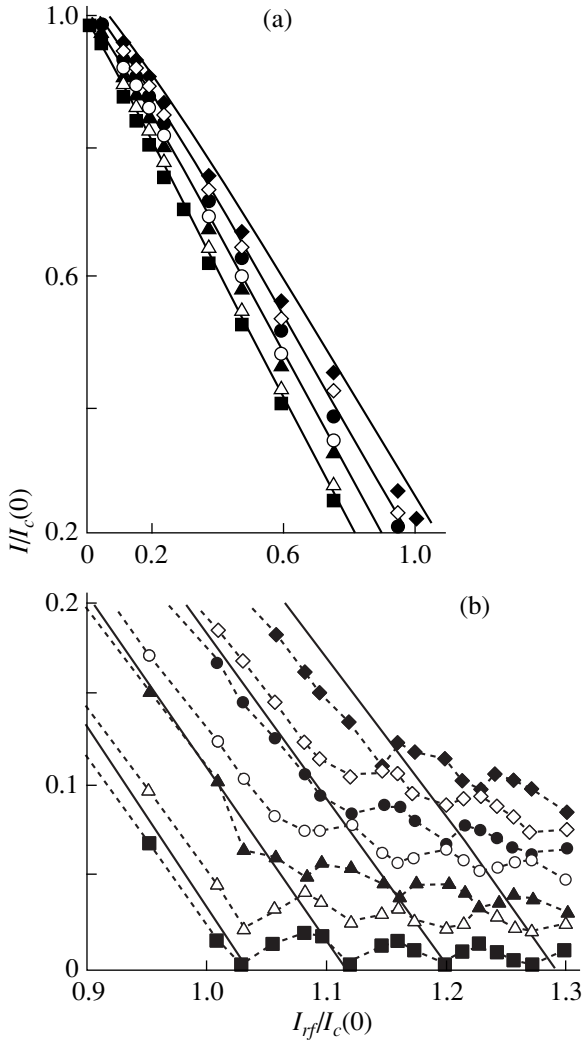

Fig. 2. Dependences of the current at edges of the Shapiro steps on the microwave current $i_w = I_{rf}/I_c(0)$ at i_w (a) ≤1 and (b) ≥1 for the junction with θ = 8° at T = 4 K. Critical currents are designated by squares. The edges of the first, second, and third steps are denoted by triangles, circles, and rhombuses, respectively. Closed and open symbols correspond to the upper and lower edges. Solid lines show the results of calculations for i_0, i_1^+, i_2^+, and i_3^+.

temperature dependence of V_c is similar to $(1 - T/T_c)^2$. At $T \lesssim T_c/2$ and θ < 30°, the characteristic voltage linearly decreases with a rise in temperature.

A decrease in the critical current density j_c and an increase in the resistance ρ_n with an increase in the misorientation angle can be described by the exponents (Fig. 5)

$$j_c(\theta, T) = j_c(0, T)\exp(-\beta\theta), \quad (6)$$

$$\rho_n(\theta, T) = \rho_n(0, T)\exp(\gamma\theta). \quad (7)$$

The coefficients β and γ were determined by the least-squares method. The ratio $\beta/\gamma \approx 2$ holds true over a wide

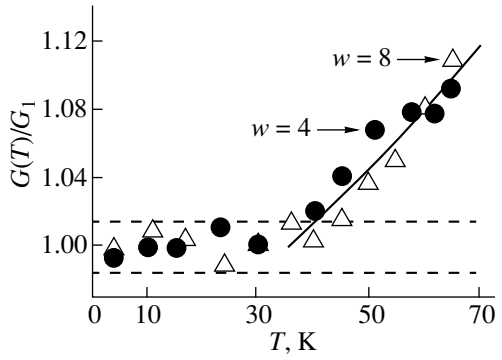

Fig. 3. Temperature dependence of the normal conductivity for junctions with θ = 45° at w = 8 (open symbols) and 4 μm (closed symbols). The solid line shows the results of calculation by formula (4). Dashed lines indicate the boundaries of the range $G_1 \pm \sigma_{G1}$.

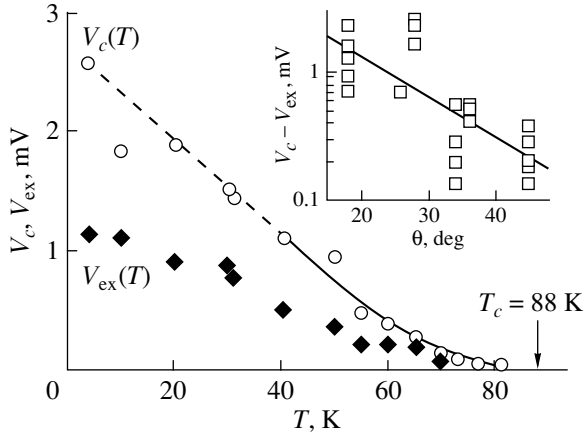

Fig. 4. Temperature dependences of the characteristic V_c (circles) and excess V_{ex} (rhombuses) voltages for a junction with θ = 18° and w = 8 μm. The results of calculations by formula (5) are depicted by the solid line. The dashed line corresponds to the linear dependence. The arrow indicates T_c for the YBCO film. The inset shows the dependence of $V_c - V_{ex}$ on the θ angle at 4 K. The straight line is the exp(–δθ) function.

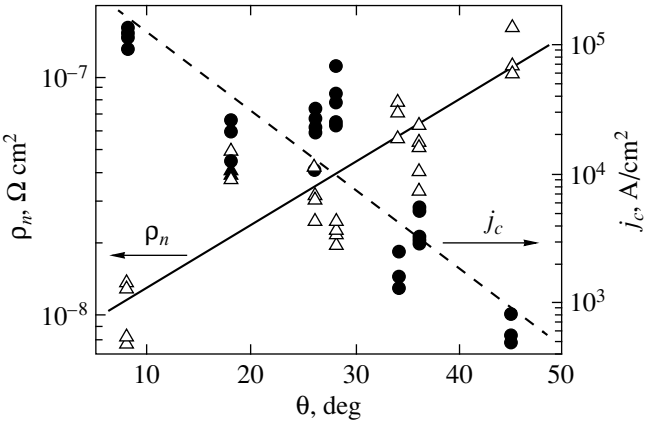

Fig. 5. Current densities j_c (circles) and resistivities ρ_n (triangles) for different misorientation angles θ at T = 50 K. Solid and dashed lines correspond to the exponential functions for $\rho_n(\theta)$ and $j_c(\theta)$, respectively.

Table 1. Electrical parameters of symmetrical Josephson junctions

θ, deg	*w*, μm	*T* = 77 K			*T* = 4 K		
		R_n, Ω	I_c, mA	I_{ex}/I_c	R_n, Ω	I_c, mA	I_{ex}/I_c
8	6	0.55	440	0.8	0.52	4.3	0.54
8	3	1.94	57	0.7	1.66	1.66	0.7
18	8	1.85	79	0.22	1.95	1.4	0.40
18	4	4.96	20	0.45	5.03	0.35	0.59
26	6 + 6	0.83	163	0.60	0.76	3.42	0.7
26	4	3.26	53	0.55	–	–	–
28	6 + 6	0.83	392	0.42	0.75	4.43	0.12
28	4	2.92	121	0.34	2.63	1.08	0.41
34	6 + 6	–	–	–	2.05	0.36	0.26
34	8	3.66	8	1	3.95	0.24	0.26
36	6 + 6	1.29	9	0.5	1.46	0.50	0.30
36	8	1.74	23	0.4	1.89	0.34	0.27
45	4	–	–	–	17.3	0.026	0.12
45	4 + 4	–	–	–	8.69	0.043	0.11

range of temperatures. As can be seen from Table 2, the differences between the values of 2γ and β do not exceed the sums of their root-mean-square deviations at temperatures from 4 to 60 K.

The voltage difference $V_c - V_{ex}$ decreases with an increase in the θ angle (see the inset in Fig. 4). This decrease at $T = 4$ K was approximated by the exponent: $V_c - V_{ex} = \exp(-\delta\theta)$. The coefficient $\delta = 0.074 \pm 0.014$ is close to the coefficient γ in the relationship describing an increase in ρ_n.

4. DISCUSSION

At present, techniques for producing Josephson junctions for low-temperature superconductors have been well developed. These junctions are based on three-layer structures that consist of thin-film low-temperature superconductor (S) elements separated by an insulator (I) layer serving as a barrier to the tunneling of electron pairs. The electrical characteristics of these junctions were studied in detail, which made it possible to develop physical models accounting for the mechanism of their operation. In the high-temperature superconductivity range, bicrystal Josephson junctions are produced on the basis of other principles and possess a different structure (in particular, they do not contain a barrier layer), but their electrical parameters are similar to those inherent, for example, in SIS low-temperature junctions. On this basis, as a first approximation, it is reasonable to consider the bicrystal junction as a SIS structure which involves a dielectric barrier layer with a certain effective thickness *d*.

The results of microwave measurements for junctions with a misorientation angle of 8° at large external microwave currents can be explained within the RSJ model. At $i_w \gtrsim 1$, the step amplitudes oscillate: the amplitudes of even steps are minimum at the same i_w currents at which the critical current exhibits minima, and the minima of odd step amplitudes coincide with the maxima of i_0 (Fig. 2b). At the same microwave current $i_w(r)$, the critical current has a minimum for the *r*th time ($r \geq 0$) and the function i_n^+ for a step with the number $n = r$ becomes zero. From relationship (2), we can obtain these i_w currents,

$$i_{w,0}(r) = 1 + (2r + 1)\omega \quad (8)$$

under the assumption that $\omega(r + 1) \ll 1$. In Section 3, formula (8) was used for the approximate calculation of the frequency ω from the experimental data on $i_0(i_w)$. Now, we introduce parameters $k_n = i_{w,n}(1)/i_{w,n}(0) - 1$,

Table 2. Coefficients β and γ and their root-mean-square deviations σ_β and σ_γ at different temperatures

T, K	β, deg^{-1}	σ_β	γ, deg^{-1}	σ_γ
4	0.120	0.013	0.061	0.008
10	0.118	0.020	0.061	0.012
20	0.118	0.025	0.062	0.014
30	0.125	0.022	0.060	0.012
40	0.129	0.018	0.062	0.011
50	0.139	0.013	0.060	0.007
60	0.137	0.019	0.058	0.011

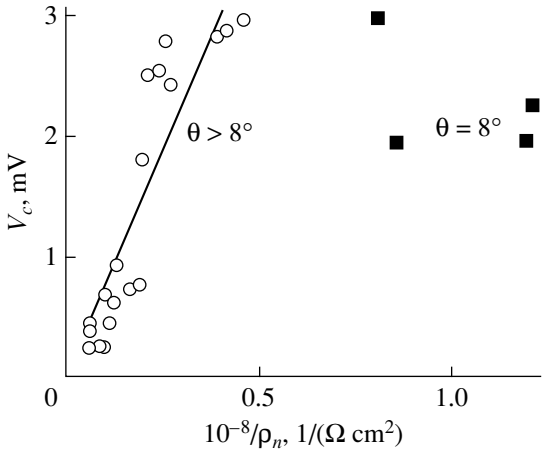

Fig. 6. Dependence of V_c on the resistivity ρ_n for junctions with angles $\theta > 8°$ (circles) and $\theta = 8°$ (squares). The straight line corresponds to the dependence $V_c = c/\rho_n$ for junctions with $\theta > 8°$.

where $i_{w,n}(r)$ is the relative microwave current at which the amplitude of the nth step becomes zero for the rth time [11]. It was found from the experimental data that $k_0 \approx 0.0866$ and $k_1 \approx k_2 \approx k_3 \approx 0.0715$. From expression (8), it follows that

$$\omega = \frac{k_n}{2 - k_n(n+1)}. \quad (9)$$

This relationship was derived using a qualitative pattern of oscillations, which is shown in Fig. 2b (see also [11]). Formula (9) is valid at $\omega(n+1) \ll 1$. The frequencies calculated from the oscillations of the critical current and the first three Shapiro steps turned out to be close in magnitude: $\omega(k_0) \approx 0.045$, $\omega(k_1) \approx 0.038$, $\omega(k_2) \approx 0.040$, and $\omega(k_3) \approx 0.042$.

The step amplitudes and the critical current at minima are virtually zero. This means that the relation between the current and the phase is close to $I = I_c \sin\varphi$ [12]. If the boundaries with $\theta = 8°$ would have *SS'S* superconducting short-circuits, the thickness of the *S'* layer should be of the order of 1 nm and the temperature of measurements (4 K) should be considerably lower than the critical temperature of *S'*. For example, $YBa_2Cu_3O_{6.5}$ single crystals are characterized by $T_c \approx$ 30–40 K. In this case, the relation between the current and the phase strongly differs from sinusoidal [13]. No indications of *SS'S* short-circuits were found for other misorientation angles. Junctions with different θ angles possess common properties: the step amplitudes and the critical currents oscillate at $i_w > 1$, the dependences $V_c(T)$ in the vicinity of T_c are similar to quadratic, and the normal resistances do not vary with temperature at $\theta \le 36°$. We assume that the band diagrams of insulator layers in junctions with different θ angles are qualitatively identical and the layer thickness increases with an increase in θ.

According to the SIS model [3], the Cooper pairs tunnel through a dielectric layer of thickness d. The critical current decreases with an increase in d as the exponent

$$j_c \propto n_S \exp(-2kd), \quad k = \sqrt{2mE_b\hbar^{-2}}, \quad (10)$$

where n_S is the density of states in the superconductor, $E_b \approx 1$ eV is the barrier height, and k is the constant describing a decrease in the wave function of pairs in the dielectric. The typical defect concentrations n_L in the dielectric are equal to $\approx 10^{20}$–10^{21} cm^{-3}. Defects form the levels in the band gap. The tunneling conductivity for single electrons through defects which are $d/2$ distant from both superconductors is maximum. The normal current varies as $j_n \propto n_S n_L \exp(-kd)$, and the resistance is determined as $\rho_n \sim 1/j_n$. Then,

$$\rho_n \propto n_S^{-1} n_L^{-1} \exp(kd). \quad (11)$$

In a dielectric, the pairs are broken under Coulomb repulsion. Hence, the barrier width for pairs is twice as large as that for electrons and the ratio $\beta/\gamma \approx 2$.

The proportionality between the voltage V_c and the quantity ρ_n^{-1} follows from this ratio. By multiplying relationship (10) into expression (11) and assuming that n_L varies only slightly with angle θ, we have

$$V_c = j_c\rho_n \propto \frac{\exp(-kd)}{n_L} \propto \frac{1}{n_S n_L \rho_n}. \quad (12)$$

The results of measurements at 4 K are shown in Fig. 6. The dependence of V_c on ρ_n was sought in the form of $V_c = c/\rho_n^q$. The exponent $q = 1.0 \pm 0.2$ and the coefficient $c = 7.7 \pm 1.5$ for the dependence of V_c (mV) on ρ_n (10^{-8} Ω cm^2) were determined by the least-squares method.

The characteristic voltages of the junctions with $\theta = 8°$ are substantially less than those predicted by the dependence $V_c = c/\rho_n$ (Fig. 6). In our case, these deviations are associated with an inhomogeneous distribution of j_c over the junction width.

The dependences of I_c on the magnetic field H were measured for junctions with a misorientation angle of 8° and the widths w = 1, 3, and 6 μm at 77 K (Fig. 7). No minima in the plots $I_c(H)$ are found up to fields of 46 mT. The Fraunhofer-like dependences $I_c(H)$ are observed for the sample *A* which involves asymmetric junctions with a misorientation angle of 32° (of the 0.32 type) and widths w = 2, 4, and 8 μm at 4 K. The half-widths of the main maximum are equal to 5.1, 1.0, and 0.21 mT, respectively (inset in Fig. 7). The maximum with double the width is not observed for the sample *B* with junctions on the substrate with the same misorientation but in YBCO films of a different quality. At an identical bridge width, the mean distance between the minima in the dependence $I_c(H)$ for junctions of the

B sample is close to H_0 for junctions of the A sample (inset in Fig. 7). A field period of larger than 46 mT indicates that the boundaries with $\theta = 8°$ have narrow regions with an increased current density j_c—filaments. The filament width w_f can be estimated from above. According to Rosenthal *et al.* [14], this period depends on the bridge width as $H_0 = c_0\Phi_0/w^2$, where $\Phi_0 = 2.07 \times 10^{-15}$ Wb is the magnetic flux quantum and w is measured in m. The constant $c_0 = 8.7$ was numerically determined from the data on $H_0(w)$ for the A sample. Then, we have

$$w_f \leq \sqrt{\frac{c_0\Phi_0}{H_0}} = 0.63\ \mu\text{m}. \qquad (13)$$

Let us compare the parameters of five homogeneous junctions on the A sample and five inhomogeneous junctions on the B sample. At 4 K, the mean parameters are as follows: $j_{cA} = (3.0 \pm 0.8) \times 10^3$ A/cm^2, $\rho_{nA} = (34.7 \pm 5.6) \times 10^{-8}\ \Omega\ \text{cm}^2$, $j_{cB} = (3.5 \pm 1.9) \times 10^3$ A/cm^2, and $\rho_{nB} = (17.5 \pm 4.7) \times 10^{-8}\ \Omega\ \text{cm}^2$. The error equal to $\pm\sigma$ is given for all the quantities. Compared to homogeneous junctions, the inhomogeneous junctions on the substrates with the same misorientation are characterized by identical critical currents and halved normal resistances. The same deviations toward the smaller voltages $j_c\rho_n$ and the larger conductivities $1/\rho_n$ are observed at a misorientation angle of 8°. The $V_c(\rho_n)$ dependences should be checked using samples with a Fraunhofer-like behavior of $I_c(H)$, which should be observed for junctions with a submicron width.

The resistance R_n does not depend on the temperature when normal electrons tunnel through one defect [8]. This process makes the contribution G_1 to the conductivity of the junctions with a misorientation angle $\theta = 45°$. The tunneling through a channel formed by several defects requires thermal activation, because the levels of defects have different energies. The conductivity through two levels is proportional to $T^{3/4}$, and the conductivity through three levels is proportional to $T^{5/2}$ [15]. The experimental dependence $G(T) = G_1 + G_2T^{1.1}$ indicates the presence of the conduction channels through both one and two levels.

On this basis, we can estimate the Bohr radius α_b of an electron on a defect. This quantity serves as a scale of an exponential decrease in G with the thickness of the dielectric: $G_1 \propto \exp(-d/\alpha_b)$. According to Glazman and Matveev [8], the presence of conduction channels through two levels and the absence of the channels through three levels implies that the thickness $d \approx n^3\alpha_b = 8\alpha_b$, where $n = 2$. The barrier width for the boundary with $\theta = 45°$ (d_{45}) and $\rho_n \approx 1.7 \times 10^{-7}\ \Omega\ \text{cm}^2$ can be estimated from the thickness of a dielectric in junctions of the A sample (d_{32}). These junctions are characterized by $\rho_n \approx 3 \times 10^{-7}\ \Omega\ \text{cm}^2$ and a considerable hysteresis: the ratio $I_c/I_{\text{cutoff}} \approx 0.9$, where I_c and I_{cutoff} are

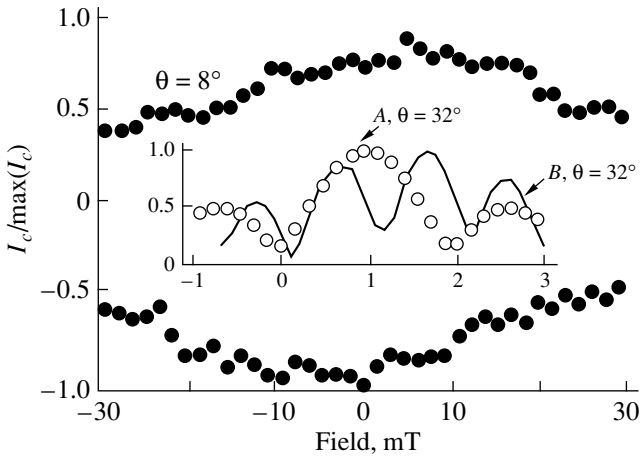

Fig. 7. Dependence $I_c(H)/\max(I_c)$ for junctions with $\theta = 8°$ and $w = 6$ μm at 77 K (closed circles). The inset shows the dependences $I_c(H)/\max(I_c)$ for junctions with $\theta = 32°$ and $w = 4$ μm in samples A (open circles) and B (solid line) at 4 K.

the maximum and cut off critical currents, respectively. Then, we have the McCamber parameter $\beta_c \approx 1.3$ [16]. From the definition of this parameter, we obtain the junction capacitance $C = \beta_c\hbar/(2eI_cR_n^2)$. The junctions on the YSZ substrate are parallel-plate capacitors, because w and $t \gg d$. Consequently,

$$d = \varepsilon\frac{\varepsilon_0 wt}{C}, \qquad (14)$$

where $\varepsilon \approx 4$–5 is the permittivity of YBCO with a deficit of oxygen [17]. For junctions with an angle $\theta = 32°$, the specific capacitance is equal to 15 fF/μm^2, the ratio d/ε is 0.58 nm, and the thickness d_{32} is 2.3–2.9 nm. Since $\ln(\rho_{32}/\rho_{45}) \approx 0.6$, $d_{32} \approx d_{45} + 0.6\alpha_b \approx 8.6\alpha_b$ and $\alpha_b \approx 0.27$–0.34 nm.

The description of the transport of normal electrons in the framework of the Glazman–Matveev [8] and Halbritter [3] models leads to the same results. The dependences of ρ_n on the thickness d in these models go over into each other by setting $k = \alpha_b^{-1}$. Our estimate $\alpha_b^{-1} \approx 3$ nm^{-1} coincides in the order of magnitude with the constant $k = 7$ nm^{-1} calculated in [3].

5. CONCLUSION

Thus, the characteristic voltage at $T \lesssim T_c$ quadratically depends on the temperature. The normal resistance of boundaries with angles $8° \leq \theta \leq 36°$ is independent of temperature. The normal conductivity of boundaries with $\theta = 45°$ increases with temperature by 10%.

The resistance R_n increases as $\exp(\gamma\theta)$ with an increase in the angle θ. The critical current decreases as $\exp(-2\gamma\theta)$ with an increase in the misorientation angle.

The characteristic voltage of homogeneous junctions is inversely proportional to the normal surface resistance. Compared to this dependence, the dependence $V_c(1/\rho_n)$ for junctions with an inhomogeneous distribution of j_c over the width deviates toward smaller V_c and larger normal conductivities. The Bohr radii of electrons on defects inside the grain boundaries are approximately equal to 0.3 nm.

The YBCO junctions on symmetrical bicrystals have characteristic voltages up to 0.3 mV at 77 K and 3 mV at 4 K. The resistivities ρ_n are as high as 1.7×10^{-7} Ω cm^2.

ACKNOWLEDGMENTS

We are grateful to K.I. Constantinian, V.P. Koshelets, G.A. Ovsyannikov, V. Roddatis, and A.Ya. Tsalenchuk for helpful discussions.

This work was supported in part by the Russian Foundation for Basic Research and the INTAS program of the European Union.

REFERENCES

1. J. A. Alarco and E. Olsson, Phys. Rev. B **52** (18), 13625 (1995).
2. D. Winkler, Y. M. Zhang, P. A. Nilsson, *et al.*, Phys. Rev. Lett. **72** (8), 1260 (1994).
3. J. Halbritter, Phys. Rev. B **48** (13), 9735 (1993).
4. R. Gross and B. Mayer, Physica C (Amsterdam) **180**, 235 (1991).
5. H. Hilgenkamp and J. Manhart, IEEE Trans. Appl. Supercond. **9** (2), 3405 (1999).
6. L. G. Aslamazov and M. V. Fistul', Zh. Éksp. Teor. Fiz. **86** (4), 1516 (1984) [Sov. Phys. JETP **59**, 887 (1984)].
7. I. A. Devyatov and M. Yu. Kupriyanov, Pis'ma Zh. Éksp. Teor. Fiz. **59** (3), 187 (1994) [JETP Lett. **59**, 200 (1994)].
8. L. I. Glazman and K. A. Matveev, Zh. Éksp. Teor. Fiz. **94** (6), 332 (1988) [Sov. Phys. JETP **67**, 1276 (1988)].
9. G. Brorsson, E. Olsson, Z. G. Ivanov, *et al.*, J. Appl. Phys. **75** (12), 7958 (1994).
10. P. A. Nilsson, Z. G. Ivanov, H. K. Olsson, *et al.*, J. Appl. Phys. **75** (12), 7972 (1994).
11. K. K. Likharev, in *Introduction to the Dynamics of Josephson Junctions* (Nauka, Moscow, 1985), p. 193.
12. A. N. Vystavkin, V. N. Gubankov, L. S. Kuzmin, *et al.*, Rev. Phys. Appl. **9**, 79 (1974).
13. K. K. Likharev, Rev. Mod. Phys. **51** (1), 101 (1979).
14. P. A. Rosenthal, M. R. Beasley, K. Char, *et al.*, Appl. Phys. Lett. **59** (26), 3482 (1991).
15. I. I. Vengrus, M. Yu. Kupriyanov, O. V. Snigirev, *et al.*, Pis'ma Zh. Éksp. Teor. Fiz. **60** (5), 372 (1994) [JETP Lett. **60**, 381 (1994)].
16. D. E. McCamber, J. Appl. Phys. **39** (7), 3113 (1968).
17. J. Humlicek, J. Kircher, H.-U. Habermeier, *et al.*, Physica C (Amsterdam) **190**, 383 (1992).

Translated by O. Borovik-Romanova

Physics of the Solid State, Vol. 43, No. 4, 2001, pp. 609–612. Translated from Fizika Tverdogo Tela, Vol. 43, No. 4, 2001, pp. 587–590.

METALS AND SUPERCONDUCTORS

Observation of Cooper Pairs in High-Temperature Superconductors by ^{67}Cu(^{67}Zn) Mössbauer Spectroscopy

N. P. Seregin, F. S. Nasredinov, and P. P. Seregin

St. Petersburg State Technical University, ul. Politekhnicheskaya 29, St. Petersburg, 195251 Russia

Received May 23, 2000; in final form, September 18, 2000

Abstract—A Mössbauer emission spectroscopy study on the ^{67}Cu(^{67}Zn) isotope showed that the superconducting transition in the $Nd_{1.85}Ce_{0.15}CuO_4$, $La_{1.85}Sr_{0.15}CuO_4$, and $Tl_2Ba_2CaCu_2O_8$ compounds is accompanied by an electron density redistribution in the crystal, which is considered evidence of Cooper-pair Bose condensation. *© 2001 MAIK "Nauka/Interperiodica".*

The phenomenon of superconductivity stems from Cooper pair generation and the formation of a Bose condensate described by a common coherent wave function [1]. This implies that the electron density distribution over the superconductor lattice sites should be different at temperatures above and below the transition to the superconducting state T_c.

Because the isomer shift IS of Mössbauer spectra is determined by the electron density at the nuclei under study, there is, in principle, a possibility of detecting the process of Cooper pair formation by measuring the temperature dependence of the centroid S of the Mössbauer spectra of a superconductor. The temperature dependence of S at a constant pressure P is given by three terms [2]:

$$(\delta S/\delta T)_P = (\delta \mathrm{IS}/\delta \ln V)_T(\delta \ln V/\delta T)_P + (\delta D/\delta T)_P + (\delta \mathrm{IS}/\delta T)_V. \quad (1)$$

The first term in Eq. (1) is the dependence of the isomer shift IS on volume V. The second term in Eq. (1) describes the effect of the second-order Doppler shift D and can be written in the Debye approximation in the form [2]

$$(\delta D/\delta T)_P = -(3k_B E_0/2Mc^2)F(T/\theta), \quad (2)$$

where k_B is the Boltzmann constant, E_0 is the isomer transition energy, M is the probe nucleus mass, c is the velocity of light in vacuum, θ is the Debye temperature, and $F(T/\theta)$ is the Debye function. Finally, the third term in Eq. (1) approximates the temperature dependence of the isomer shift IS at constant volume. The presence of this term is accounted for by the variation in the electron density at the Mössbauer nuclei, and this effect is expected to occur when the matrix transfers to the superconducting state. In other words, Mössbauer spectroscopy permits one to measure the electron density at lattice sites and its variation in the transition through T_c. A comparison of the experimental with theoretical values of the electron density may help in selecting the model which adequately describes the phenomenon of superconductivity. It is this consideration that accounts for the publication of numerous studies on the effect of superconducting transition on the parameters of Mössbauer spectra.

Attempts at detecting the formation of Cooper pairs and of the Bose condensate by measuring the temperature dependence of the centroid S of ^{119}Sn Mössbauer spectra for the Nb_3Sn classical superconductor failed; however [3], the observed dependence of S on temperature could be satisfactorily fitted by a second-order Doppler shift, and the behavior of $S(T)$ did not exhibit any features near T_c that could be assigned to a change in the isomer shift.

Later, after the discovery of high-temperature superconductivity, a theoretical model was proposed to account for the effect of Cooper pairs and Bose condensation on the isomer shift of ^{57}Fe Mössbauer spectra [4] and attempts were made to detect experimentally this effect for the ^{57}Fe impurity atoms in $YBa_2Cu_3O_7$ [5], $(BiPb)_2Sr_2Ca_2Cu_3O_{10}$ [6], and (Tl, Pb)(Sr, Ba)$_2$Cu$_2$O$_{10}$ [7]. However, no convincing evidence for the effect of the superconducting transition on the isomer shift of Mössbauer spectra was obtained in these cases either.

This can be accounted for by the small magnitude of $\Delta/2G$ (here, Δ is the maximum possible difference in the isomer shift of Mössbauer spectra between the normal and superconducting phases, $G = \hbar/\tau_0$ is the natural nuclear level width, and τ_0 is the mean nuclear level lifetime), which, for the case of Mössbauer spectroscopy on the ^{57}Fe and ^{119}Sn isotopes, does not exceed six.

The conditions for observation of Cooper pairs by Mössbauer spectroscopy should be more favorable for high-temperature superconductors (having a minimum Cooper correlation length) if one uses a probe for which $\Delta/2G \gg 10$. In choosing an object for the study, one should also take into account the necessity of placing the Mössbauer nucleus at lattice sites.

1063-7834/01/4304-0609$21.00 © 2001 MAIK "Nauka/Interperiodica"

All these conditions can be met if one uses the ^{67}Zn Mössbauer probe in cuprate lattices in the emission version of ^{67}Cu(^{67}Zn) Mössbauer spectroscopy; indeed, for ^{67}Zn, we have $\Delta/2G \sim 200$ and one can introduce the ^{67}Cu parent isotope into the lattice sites in the course of preparation so that the daughter isotope ^{67}Zn will likewise occupy the copper lattice site [8].

This paper reports on such a study made on the ^{67}Zn probe incorporated in the lattices of $Nd_{1.85}Ce_{0.15}CuO_4$, $La_{1.85}Sr_{0.15}CuO_4$, and $Tl_2Ba_2CaCu_2O_8$. Cu_2O, which does not undergo the superconducting transition, was chosen as a reference.

EXPERIMENTAL RESULTS AND THEIR DISCUSSION

The Mössbauer sources were prepared by diffusing carrier-free radioactive ^{67}Cu into polycrystalline samples of $Nd_{1.85}Ce_{0.15}CuO_4$ (T_c = 22 K), $La_{1.85}Sr_{0.15}CuO_4$ (T_c = 37 K), $Tl_2Ba_2CaCu_2O_8$ (T_c = 60 K), and Cu_2O in evacuated quartz ampoules at 550°C for two hours in an oxygen flow. No noticeable change of T_c was observed in the reference samples.

The ^{67}Cu(^{67}Zn) Mössbauer spectra were obtained with a ^{67}ZnS absorber. The temperature of the absorber was 10(2) K for all spectra, whereas that of the source could be varied from 10(1) to 80(1) K.

The Mössbauer spectra of all the ceramics represented in the temperature interval chosen are well-resolved quadrupole triplets, with isomer shifts corresponding to the $^{67}Zn^{2+}$ ions at copper sites. It was found that the quadrupole coupling constants C of all the ceramics are practically temperature independent. Because the electric field gradient at the ^{67}Zn nuclei acting on the Zn^{2+} probe is produced by the lattice ions only and the lattice constants change only by a negligible amount within the temperature interval of 4.2–80 K [9, 10], the independence of C from temperature does not come as a surprise.

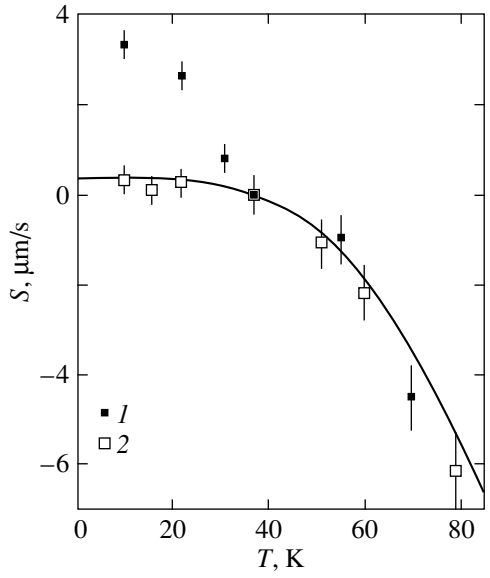

Fig. 1. Temperature dependence of the centroid S of the ^{67}Zn Mössbauer spectrum measured with respect to its value at 37 K for (*1*) $La_{1.85}Sr_{0.15}CuO_4$ and (*2*) Cu_2O. The solid line plots the theoretical temperature dependence of S for the case of the second-order Doppler shift for θ = 400 K.

The temperature dependences of the centroid S measured relative to its position at T_c differ substantially for the reference and superconducting samples (this is illustrated in Fig. 1 through the relation between $La_{1.85}Sr_{0.15}CuO_4$ and Cu_2O), although no sharp jumps are observed in the magnitude of S at the transition through T_c.

The temperature dependence of S is given by Eq. (1) and, as shown by calculations [11], the first term in Eq. (1) may be neglected in the case of ^{67}Zn, because for the temperature interval chosen, it does not exceed 0.03 μm/s and no structural phase transitions are observed within the 10- to 80-K region in any of the compounds studied [9, 10].

The second term in Eq. (1) relates to the effect of the second-order Doppler shift. As is seen from Fig. 1, the experimental data obtained on reference samples in the temperature interval chosen are fitted satisfactorily by Eq. (2) plotted for $\theta \approx 400$ K (Cu_2O). For the superconducting samples, the experimental data obtained for $T > T_c$ are also approximated by a relation of the type of Eq. (2) drawn for $\theta \approx 360$ K ($Nd_{1.85}Ce_{0.15}CuO_4$), 400 K ($La_{1.85}Sr_{0.15}CuO_4$), and 260 K ($Tl_2Ba_2CaCu_2O_8$) (for the Debye temperatures of Nd_2CuO_4, $La_{2-x}Sr_xCuO_4$, and $Tl_2Ba_2CaCu_2O_8$, heat capacity measurements yield 300 [12], 420 [13], and 270 K [13], respectively).

Finally, the third term in Eq. (1) describes the temperature dependence of the isomer shift. The value of the IS at a given temperature T can be found as the difference $[IS]_T = S_T - D_T$ (here, S_T and D_T are the centroid of the spectrum and the Doppler shift at the temperature T, respectively). The increase in the IS with decreasing temperature for $T < T_c$ indicates an increase in the electron density at the ^{67}Zn nuclei and, hence, localization of electron pairs at the Mössbauer probe. The limiting values of the IS for $T \longrightarrow 0$ K, $[IS]_0 = S_0 - D_0$, should depend on the size of the Cooper pairs, i.e., on the magnitude of T_c. The validity of this statement is illustrated by Fig. 2, which plots the dependence of $[IS]_0$ on T_c; one readily sees that $[IS]_0$ increases with increasing T_c (i.e., with decreasing Cooper correlation length), which signals an increase in the electron density at the ^{67}Zn nuclei.

We have thus established that the temperature dependence of S for the $Nd_{1.85}Ce_{0.15}CuO_4$, $La_{1.85}Sr_{0.15}CuO_4$, and $Tl_2Ba_2CaCu_2O_8$ superconductors at temperatures $T > T_c$ is governed by the second-order

Doppler shift, whereas for $T < T_c$, S is also affected by the process of Cooper pair localization at the Mössbauer probe nucleus. A decrease in the temperature amplifies the effect of this process on S, because the fraction of the Bose condensate grows with decreasing temperature. BCS theory yields the following relation for the temperature dependence of the effective density of superfluid electrons $\rho(T)$ [1]:

$$\rho(T) = 1 - (2\beta E_F/k_F^5) \times \int_0^\infty \{k^4 \exp(\beta E_k)/[\exp(\beta E_k) + 1]^2\} dk,$$

where $E_F = k_F^2/2m$ is the Fermi energy, m is the particle mass, k is the wave vector, k_F is the value of the wave vector at the Fermi surface, E_k is the energy of the k state, and β has the meaning of the binding energy of the superfluid component.

On the other hand, one could expect that $\rho(T) \sim [IS]_T/[IS]_0$. Figure 3 presents the theoretical dependence of ρ on the parameter $x = 1.76(k_B T/\Delta)$ (here, k_B is the Boltzmann constant and $\Delta = 3.06k_B[T_c(T_c - T)]^{1/2}$ is the energy gap in the spectrum of elementary superconductor excitations) taken from [1], together with our data on the dependence of $[IS]_T/[IS]_0$ on the x parameter. The experimental data are seen to be in satisfactory agreement with the calculations. In other words, Mössbauer spectroscopy using the ^{67}Zn isotope is an efficient tool to probe the formation of Cooper pairs and their Bose condensation in high-temperature superconductors.

Unfortunately, the problem of choosing a model which would adequately describe the increase in the electron density at the nuclei of the ^{67}Zn impurity center in a superconductor at temperatures below T_c remains to be solved. For instance, the increase in the electron density can be considered to result from the change in the charge state of the Zn probe. However, two problems arise here. First, the experimentally measured values of $[IS]_0$ (~2–5 μm/s) are substantially smaller than the magnitude of the isomer shift (~165 μm/s) expected for the charge exchange of the zinc center, $Zn^{2+} \longrightarrow Zn^0$ [11]. This difficulty can be overcome by assuming that the effective radius of electron-pair localization at the impurity center is considerably in excess of the Zn^{2+} ionic radius (for instance, one could accept, for the localization radius, a Cooper correlation length which is ~10^{-7} cm for the HTSCs). Second, the charge state of zinc is governed by the position of the zinc-impurity electronic energy level with respect to the Fermi level. Hence, one has to assume that for $T > T_c$, the zinc level lies considerably higher than the Fermi level and that the impurity charge state is temperature independent. By contrast, the observed

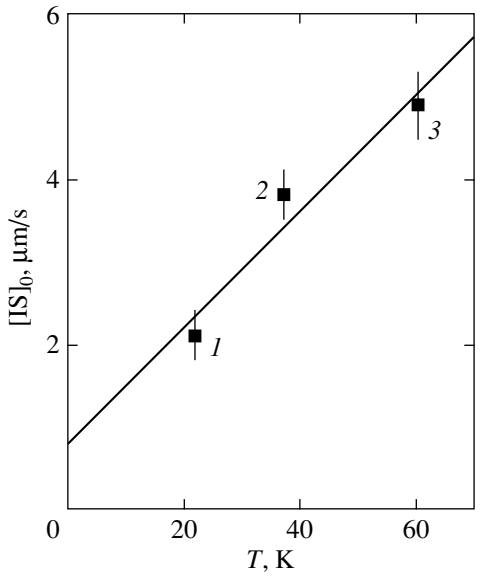

Fig. 2. Dependence of $[IS]_0$ on T_c for (*1*) $Nd_{1.85}Ce_{0.15}CuO_4$, (*2*) $La_{1.85}Sr_{0.15}CuO_4$, and (*3*) $Tl_2Ba_2CaCu_2O_8$.

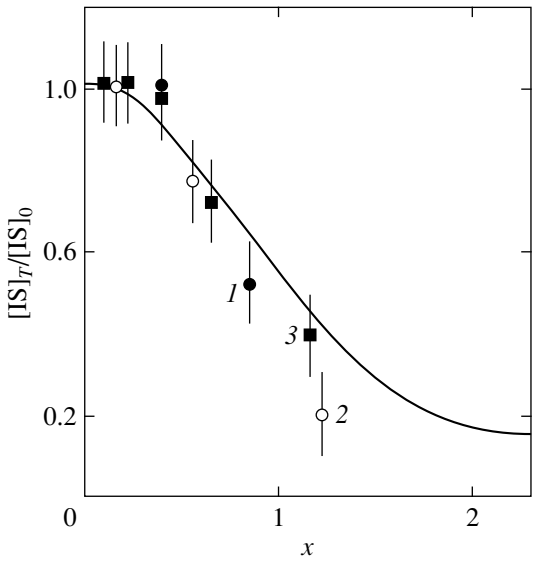

Fig. 3. Dependence of $[IS]_T/[IS]_0$ on the parameter $x = 1.76(k_B T/\Delta)$. The solid line is a plot of the theoretical dependence of the effective superfluid-electron density on the x parameter. The symbols identify (*1*) the $Nd_{1.85}Ce_{0.15}CuO_4$, (*2*) $La_{1.85}Sr_{0.15}CuO_4$, and (*3*) $Tl_2Ba_2CaCu_2O_8$ compounds.

temperature dependence of S implies that, for $T < T_c$, the zinc level lies close to the Fermi level to within $k_B T$.

Another explanation can be based on the assumption that the observed increase in the electron density at the ^{67}Zn nuclei is connected with the spatial redistribution of electrons produced by the Bose condensation. The problem arising with this model stems from the

real possibility of detecting such a redistribution of the electron density by means of an impurity probe. The ^{67}Zn probe is a two-electron center with a negative correlation energy [14]. For the *s*-electron pair localized at the zinc center, the total angular momentum, orbital angular momentum, and spin are zero. On the other hand, the BCS model assumes that the electrons pairing at $T < T_c$ have oppositely directed momenta, such that the total momentum, the orbital angular momentum, and the spin of a Cooper pair are likewise zero. It is the combination of these factors that is favorable for the observation of Bose condensation with the ^{67}Zn probe. It should, however, be borne in mind that the BCS theory assumes *s* pairing, whereas the pairing in HTSCs has the *d* symmetry [4]. Therefore, one should approach with caution the agreement found by us between the theoretical and experimental dependences of the effective superfluid-electron density on the *x* parameter (Fig. 3).

Thus, we have shown by ^{67}Cu(^{67}Zn) Mössbauer emission spectroscopy that the superconducting transition in the $Nd_{1.85}Ce_{0.15}CuO_4$, $La_{1.85}Sr_{0.15}CuO_4$, and $Tl_2Ba_2CaCu_2O_8$ compounds is accompanied by a redistribution of the electron density in the crystal and that ^{67}Cu(^{67}Zn) Mössbauer emission spectroscopy is an efficient tool for probing Cooper-pair Bose condensation.

REFERENCES

1. J. R. Schrieffer, *Theory of Superconductivity* (Benjamin, New York, 1964; Nauka, Moscow, 1970).
2. D. L. Nagy, in *Mössbauer Spectroscopy of Frozen Solutions*, Ed. by A. Vértes and D. L. Nagy (Akadémiai Kiadó, Budapest, 1990; Mir, Moscow, 1998).
3. J. S. Shier and R. D. Taylor, Phys. Rev. **174**, 346 (1968).
4. F. P. Marin and R. Iraldi, Phys. Rev. B **39**, 4273 (1989).
5. V. M. Cherepanov, M. A. Chuev, E. Yu. Tsymbal, *et al.*, Solid State Commun. **93**, 921 (1995).
6. Th. Sinnemann, R. Job, and M. Rosenberg, Phys. Rev. B **45**, 4941 (1992).
7. Yun-Bo Wang, Guo-Hui Cao, Yang Li, *et al.*, Physica C (Amsterdam) **282–287**, 1057 (1997).
8. F. S. Nasredinov, N. P. Seregin, and P. P. Seregin, Pis'ma Zh. Éksp. Teor. Fiz. **70**, 632 (1999) [JETP Lett. **70**, 641 (1999)].
9. W. Sadowski, H. Hagemann, M. Francois, *et al.*, Physica C (Amsterdam) **170**, 103 (1990).
10. M. Braden, P. Schweiss, G. Heger, *et al.*, Physica C (Amsterdam) **223**, 396 (1994).
11. M. Steiner, W. Potzel, C. Schafer, *et al.*, Phys. Rev. B **41**, 1750 (1990).
12. A. Tigheza, R. Kuentzler, G. Pourroy, *et al.*, Physica B (Amsterdam) **165–166**, 1331 (1990).
13. H. M. Ledbetter, S. A. Kim, and R. B. Goldfarb, Phys. Rev. B **39**, 9689 (1989).
14. F. S. Nasredinov, N. P. Seregin, and P. P. Seregin, Fiz. Tekh. Poluprovodn. (St. Petersburg) **34**, 275 (2000) [Semiconductors **34**, 269 (2000)].

Translated by G. Skrebtsov

Physics of the Solid State, Vol. 43, No. 4, 2001, pp. 613–615. Translated from Fizika Tverdogo Tela, Vol. 43, No. 4, 2001, pp. 591–593.

METALS AND SUPERCONDUCTORS

Superconductivity in the $Ba_{1-x}La_xPbO_3$ System

A. P. Menushenkov*, A. V. Tsvyashchenko, D. V. Eremenko*, K. V. Klementev*, A. V. Kuznetsov*, V. N. Trofimov***, and L. N. Fomicheva****

**Moscow Institute of Engineering Physics, Kashirskoe sh. 31, Moscow, 115409 Russia*

***Vereshchagin Institute of High-Pressure Physics, Russian Academy of Sciences, Troitsk, Moscow oblast, 142092 Russia*

****Joint Institute of Nuclear Research, Dubna, Moscow oblast, 141980 Russia*

e-mail: menushen@htsc.mephi.ru

Received July 12, 2000; in final form, October 2, 2000

Abstract—An analysis of the relationship between the local crystal and electronic structure of the $Ba_{1-x}K_xBiO_3$ and $BaPb_{1-x}Bi_xO_3$ perovskite systems, which was made in terms of an empirical model based on EXAFS spectroscopy studies of the above compounds, led to the conclusion that superconductivity is possible in the $Ba_{1-x}La_xPbO_3$ system. The $Ba_{1-x}La_xPbO_3$ multiphase compound synthesized at a pressure of 6.7 GPa was found to contain a superconducting phase with a critical temperature $T_c \simeq 11$ K. © *2001 MAIK "Nauka/Interperiodica".*

The $BaBiO_3$ compound belongs to the class of cubic perovskites with a common formula ABO_3, which are based on the BO_6 octahedral complexes. $BaBiO_3$ is an insulator, and the substitution of lead for a part of the bismuth ions in the *B* position or of potassium or rubidium for the barium ions in the *A* position forms the substitutional solid solutions $Ba_{1-x}K_xBiO_3$ (BKBO) and $BaPb_{1-x}Bi_xO_3$ (BPBO), which undergo a metal–insulator phase transition with increasing dopant concentrations. After the phase transition, these compounds become metallic superconductors with $T_c \simeq 13$ K for $BaPb_{0.75}Bi_{0.25}O_3$ [1] and $T_c \simeq 30$ K for $Ba_{0.6}K_{0.4}BiO_3$ [2]. To reveal the mechanisms by which doping in the *A* and *B* positions affects the properties of the bismuthates in the normal and superconducting states, attempts were made to prepare new $BaBiO_3$-based superconductors in a search for compounds with higher critical temperatures [3]. It was found that some chemical modifications not forming under normal conditions can be synthesized at a high pressure. Finally, a new superconducting phase, $(K_{1-x}Bi_x)BiO_3$ with $T_c \simeq 10.2$ K at $x = 0.1$, was synthesized [3].

Unlike layered high-temperature superconductors, $BaBiO_3$-based solid solutions have a weakly distorted cubic structure. They exhibit isotropic physical properties and zero magnetic coupling. The simpler structure of the 6*s*–2*p* valence band of the bismuthates compared with the 3*d*–2*p* band of the high-temperature superconductors, as well as the absence of charge reservoirs outside the BO_6 octahedral complexes, facilitates considerably an analysis of the electronic structure of the bismuthates. This analysis has led to an empirical model relating the specific features of the local crystalline to the local electronic structure of the bismuthates and an explanation for the appearance of the insulator–metal transition and the onset of superconductivity [4–6]. Based on this model, the conclusion is drawn below that superconductivity is possible in the $Ba_{1-x}La_xPbO_3$ compound, which does not contain bismuth ions.

$BaBiO_3$, the basic compound for the above systems, has a monoclinically distorted cubic lattice. This distortion is actually a combination of a static rotation of the BiO_6 octahedra about the [110]-type axes (rotational distortion) and alternation of the larger and smaller octahedra (breathing-mode distortion). The inequivalence of the octahedra was initially assigned to disproportionation of the bismuth valence, $2Bi^{4+} \longrightarrow Bi^{3+} + Bi^{5+}$, which gives rise to a charge density wave resulting in the unit-cell content doubling and the formation of an insulating band gap [7]. Doping with potassium or lead reduces both types of distortions and destroys the charge density wave. For instance, the metallic superconducting phase $Ba_{1-x}K_xBiO_3$ has an undistorted cubic structure for $x > 0.37$ [8]. It is believed on the basis of x-ray diffraction and neutron elastic scattering data [8, 9] that the inequivalence of the bismuth valence states typical of $BaBiO_3$ is destroyed by doping and that, in the superconducting phase of BKBO or BPBO, all bismuth ions are in the same state. As a result, it was maintained that the inequivalence of the bismuth states is responsible for the insulating properties of $BaBiO_3$ and is in no way connected with superconductivity [10].

Note that the above methods provide a pattern of the structure averaged over the sample volume. Structural studies of the BKBO–BPBO systems by the locally sensitive EXAFS method and high precision measurements of photoemission spectra revealed that the inequivalence of the bismuth states also persists in the superconducting BKBO compositions. This manifests

itself experimentally in the form of strongly anharmonic vibrations of the oxygen ion in the double-well potential along the Bi–O–Bi bonds [5, 11] and of a splitting of the Bi 4*f* lines of the photoemission spectra [12]. Therefore, a new model of the electronic structure and transport properties of the bismuthates was proposed based on experimental EXAFS data [4–6].

It was shown that the crystal structure of $BaBiO_3$ is described by an ordered alternation of the BiO_6 and $Bi\underline{L}^2O_6$ octahedral complexes, where $\underline{L}^2$ signifies the presence of a hole pair in the hybridized antibonding $6sBiO2p_{\sigma^*}$ orbital of the complex. The electronic structure of $BaBiO_3$ derives from a system of local electron and hole pairs separated by an insulating energy gap $2E_a = 0.48$ eV. The pairs are also separated spatially, because they belong to different complexes, namely, the electron pairs belong to BiO_6, and the hole pairs are in $Bi\underline{L}^2O_6$. The system does not have free charge carriers, and the conduction is effected by two-particle charge transport in the $Bi\underline{L}^2O_6 \longleftrightarrow BiO_6$ dynamic exchange.

Substitution of K^+ ions for a part of the Ba^{2+} ions reduces the number of electrons and transfers part of the BiO_6 complexes to the $Bi\underline{L}^2O_6$ state. As the number of the $Bi\underline{L}^2O_6$ complexes increases, they overlap spatially to produce a continuous $Bi\underline{L}^2O_6$ cluster, with its free L^2 levels forming the conduction band, which initiates the insulator–metal transition. The insulating gap now disappears, and the local electron pairs of the BiO_6 complexes move freely through the $Bi\underline{L}^2O_6$ clusters, thus making possible the superconducting transition at $T < T_c$.

Total substitution of the K for Ba ions produces $KBiO_3$, a compound consisting of only the $Bi\underline{L}^2O_6$ complexes, which should be a nonsuperconducting metal, because it does not contain the BiO_6 complexes with electron pairs. To make superconductivity possible, one should produce pairs by transforming part of the $Bi\underline{L}^2O_6$ complexes to BiO_6. This has recently been achieved by doping $KBiO_3$ in the *A* position with the trivalent Bi^{3+} ions [3].

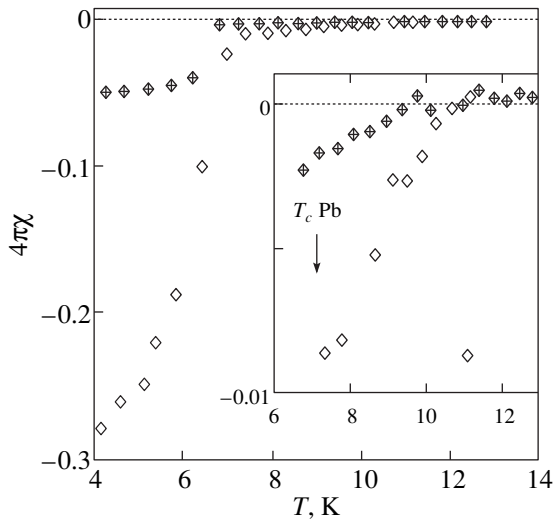

Fig. 1. Temperature dependence of the magnetization. The inset shows, in an expanded scale, the critical temperature interval. The arrow specifies the critical temperature of lead.

The $BaPbO_3$ compound is an electron analog of $KBiO_3$. It consists of equivalent $Pb\underline{L}^2O_6$ complexes [4–6] and exhibits metallic properties. While in $BaPbO_3$ there is no superconductivity, it appears when this compound is doped by bismuth to $BaPb_{1-x}Bi_xO_3$ and is observed within a fairly narrow doping interval of $0.05 < x < 0.35$ [1]. The onset of superconductivity is associated with the formation of local electron pairs at the BiO_6 complexes. The electronic structure of the $Pb\underline{L}^2O_6$ octahedra with lead ions at the center is identical to that of $Bi\underline{L}^2O_6$. Therefore, the metallic properties of $BaPb_{1-x}Bi_xO_3$ originate from the conduction band derived from free $\underline{L}^2$ levels in a continuous cluster consisting of both $Pb\underline{L}^2O_6$ and $Bi\underline{L}^2O_6$ complexes and the superconductivity is accounted for by coherent pair transport in the $BiL^2O_6 \longleftrightarrow BiO_6$ and $Pb\underline{L}^2O_6 \longleftrightarrow BiO_6$ dynamic exchange.

It thus follows that $BaPbO_3$ can be made superconducting by replacing a part of the $Pb\underline{L}^2O_6$ octahedra by PbO_6, which can be attained by electronic doping through substituting trivalent ions for a part of the Ba^{2+} ions, because such doping should favor the formation of local electron pairs in the PbO_6 complexes. We have made an attempt at checking this conjecture experimentally.

Among the trivalent ions, the ionic radius of La^{3+}, 1.17 Å, is the closest to that of Ba^{2+} (1.49 Å). Such a large difference between the ionic radii hampers the formation of $Ba_{1-x}La_xPbO_3$ at normal pressure. Our numerous attempts at obtaining this compound by solid-phase synthesis in an oxygen atmosphere or in air failed, thus leaving us the alternative of performing it at a high pressure.

Samples of a nominal composition $Ba_{0.9}La_{0.1}PbO_3$ were prepared of 99.9%-pure BaO_2, La_2O_3, PbO, and PbO_2 oxides. A stoichiometric sample of well-mixed oxides was pressed in an argon environment and placed into a cylindrical platinum ampoule 90 mm^3 in volume, which was mounted in a toroidal high-pressure chamber [13]. The ampoule was heated to 1000°C over 12 min at a pressure of 6.7 GPa, maintained at this temperature for 20 min, and then cooled in a few seconds to room temperature. The ceramic thus prepared was black, with a metallic luster seen at a fresh fracture. X-ray analysis showed that the compound obtained was multiphase. One of the phases had a perovskite structure with lattice parameters close to those of $BaPbO_3$. No attempts at identifying the other phases were made.

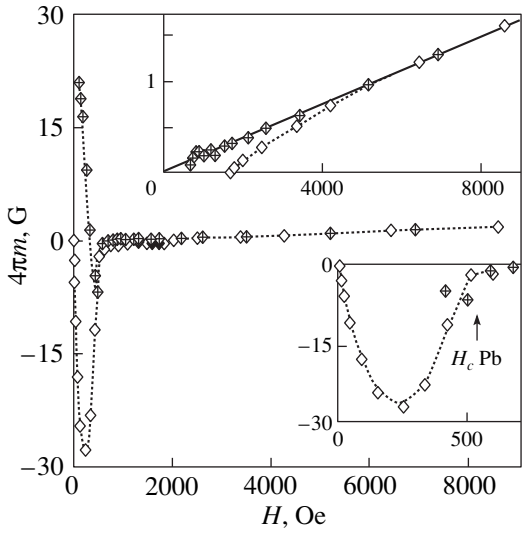

Fig. 2. Field dependence of the magnetization at the liquid helium temperature. The insets show, in an expanded scale, this dependence in weak and strong fields. The arrow identifies the critical field of lead.

The magnetization of this compound was measured with a SQUID magnetometer [14]. The temperature dependence of the magnetization presented in Fig. 1 indicates the existence of two superconducting phases in the sample. The phase with a larger volume, which does not exceed 28% at $T = 4.2$ K, has a critical temperature $T_c \simeq 7.2$ K; however, within a small, ~1%, fraction of the sample volume, superconductivity persists up to $T_c \simeq 11$ K.

The existence of two superconducting phases with different parameters is supported by the field dependence of the magnetization measured at $T = 4.2$ K (Fig. 2). In weak fields, $H \lesssim 520$ Oe, one observes a noticeable field hysteresis associated with flux pinning in the sample. In high fields, both the magnetization itself and its hysteresis are small. For $H \gtrsim 5000$ Oe, the superconductivity breaks down; the magnetization becomes reversible and grows linearly with the field. The slope of the reversible magnetization curve corresponds to the paramagnetic susceptibility $\chi = 1.14 \times 10^{-3}$ cm^3/mol.

The presence, in the sample, of a superconducting phase with a critical temperature close to T_c of metallic lead may be associated with the possible reduction of a part of the lead in the chemical reaction under high pressure. This conjecture is supported by the fact that the magnetization curve exhibits hysteresis in fields below the critical field of lead.

The very small volume fraction of the superconducting phase with $T_c \simeq 11$ K can be attributed to the fact that apparently, it forms only at grain boundaries of the ceramic, where the stressed state of the lattice produces more favorable conditions for the stabilization of phases with a large difference in the radii of the ions forming the lattice. It may be expected that, by optimizing the pressure and temperature of the synthesis, the cooling regime, and the batch composition, one would succeed in increasing the volume of the superconducting phase $Ba_{1-x}La_xPbO_3$ to the level permitting identification of its stoichiometry and crystal structure. In conclusion, it should be stressed that superconductivity has not been observed heretofore in the Ba–La–O and Ba–Pb–O systems.

ACKNOWLEDGMENT

This study was supported by the Russian Foundation for Basic Research (grant nos. 99-02-17343 and 99-02-17897) and the Ministry of Science Program "Fundamental Aspects of the Physics of the Condensed State" (grant no. 99010).

REFERENCES

1. A. W. Sleight, J. L. Gillson, and P. E. Bierstedt, Solid State Commun. **17**, 27 (1975).
2. R. J. Cava, B. Batlogg, J. J. Krajewski, *et al.*, Nature **332**, 814 (1988).
3. N. R. Khasanova, A. Yamamoto, S. Tajima, and X.-J. Wu, Physica C (Amsterdam) **305**, 275 (1998).
4. A. P. Menushenkov, Poverkhnost' **3**, 14 (1999); **12**, 58 (1999).
5. A. P. Menushenkov and K. V. Klementev, J. Phys.: Condens. Matter **12**, 3767 (2000).
6. M. Yu. Kagan, A. P. Menushenkov, K. V. Klementev, and A. V. Kuznetsov (in press).
7. D. E. Cox and A. W. Sleight, Acta Crystallogr., Sect. B: Struct. Sci. **35**, 1 (1989).
8. S. Pei, J. D. Jorgensen, B. Dabrowski, *et al.*, Phys. Rev. B **41**, 4126 (1990).
9. J. P. Wignacourt, J. S. Swinnea, H. Steinfink, and J. B. Goodenough, Appl. Phys. Lett. **53**, 1753 (1988).
10. M. Shirai, N. Suzuki, and K. Motizuki, J. Phys.: Condens. Matter **2**, 3553 (1990).
11. A. P. Menushenkov, K. V. Klement'ev, P. V. Konarev, and A. A. Meshkov, Pis'ma Zh. Éksp. Teor. Fiz. **67**, 977 (1998) [JETP Lett. **67**, 1034 (1998)].
12. M. Qvarford, V. G. Nazin, A. A. Zakharov, *et al.*, Phys. Rev. B **54**, 6700 (1996).
13. L. G. Khvostantsev, L. F. Vereshchagin, and A. P. Novikov, High Temp.–High Press. **9**, 637 (1977).
14. V. N. Trofimov, Cryogenics **32**, 513 (1992).

Translated by G. Skrebtsov

Physics of the Solid State, Vol. 43, No. 4, 2001, pp. 616–620. Translated from Fizika Tverdogo Tela, Vol. 43, No. 4, 2001, pp. 594–597.

SEMICONDUCTORS AND DIELECTRICS

Superstructure Ga_4InAs_5

A. A. Vaĭpolin, M. A. Sinitsyn, and A. A. Yakovenko

Ioffe Physicotechnical Institute, Russian Academy of Sciences, Politekhnicheskaya ul. 26, St. Petersburg, 194021 Russia

Received August 14, 2000

Abstract—An epitaxial layer of the $Ga_{0.82}In_{0.18}As$ solid solution is investigated. The coordination of arsenic atoms in the structure of this compound is determined by x-ray diffractometry. The ratio of arsenic atoms in the coordination 4Ga, 3Ga + In, and 2Ga + 2In corresponds to the superstructure in which an In atomic chain along the [110] direction alternates with four Ga chains. An ideal composition for this superstructure is Ga_4InAs_5. New specific features of the domain structure formed as a result of temperature-induced changes in the configuration of tetrahedral bonds are revealed. © *2001 MAIK "Nauka/Interperiodica".*

Despite the fact that A^3B^5 solid solutions have been investigated extensively and thoroughly, no reliable method exists for elucidating their atomic structure. Standard parameters determined by x-ray diffraction (unit cell parameters and root-mean-square displacements of atoms) do not provide an exhaustive characterization of the structure. Electron microscopy and electron diffraction are appropriate only in the case of microscopic volumes. For this reason, the possible inhomogeneity of the structure and the dependence of its properties on the growth conditions of a particular sample render generalization of the data obtained by these methods incorrect. This necessitates investigation of macroscopic samples of crystals and the epitaxial layers. For these samples, x-ray diffractometric measurements in the region of reflections with large indices are highly efficient [1–4]. In this respect, we performed x-ray measurements by the back-reflection technique in an asymmetric geometry with a double-crystal spectrometer (MoK_{α_1} radiation).

We studied a sample of the $Ga_{0.82}In_{0.18}As$ epitaxial layer (5.3 μm thick) grown by metalloorganic hydride deposition on a GaAs(001) substrate with a 5′ deviation. The required epitaxy was achieved with a vertical-type epitaxial reactor operating at atmospheric pressure and using high-frequency heating of a substrate holder. The deposition temperature was equal to 650°C, and the growth rate was 1 μm/h. The initial materials were gallium trimethyl, indium ethylenedimethyl, and arsine. No special doping of the layer was performed. The atomic composition of the layer was determined using an x-ray microanalyser.

X-ray diffraction determination of the unit cell parameters of the layer revealed a lattice distortion—the well-known phenomenon attributed to a translational mismatch between crystal lattices of the substrate and the layer. The substrate lattice was also characterized by an insignificant distortion. The unit cell parameters of the layer were as follows: $a_\parallel = 5.7127 \pm 0.0002$ Å and $a_\perp = 5.7278 \pm 0.0002$ Å.

Intensities of x-ray reflections of the layer were measured in the range $H^2 = h^2 + k^2 + l^2 = 200$–$248$ ($2\vartheta = 122°$–$155°$). As a result, we obtained an array of 105 unique absolute values of the experimental structure amplitudes $|F|_m$.

In the model of a sphalerite structure, the calculation with inclusion of atomic displacements in the harmonic approximation gives the following standard thermal parameters: $B_A = 0.870 \pm 0.007$ Å^2 for the "mean" atom 0.82Ga + 0.18In (the A-type atoms) and $B_B = 0.679 \pm 0.005$ Å^2 for As (the B-type atom). The correspondence between the structural model and the experimental data is characterized by the discrepancy factor $R = \Sigma||F_m| - |F_c||/\Sigma|F_m|$, where $|F_c|$ is the absolute structure amplitude calculated according to the accepted model and parameters. The found value of $|F_c|$ is equal to 5.48%; i.e., it is rather large. Therefore, the root-mean-square displacements of atoms from an ideal position roughly describe the structure.

The next step consists in calculating the displacements of atomic positions. In this step, it is expedient to ignore the lattice distortion and the lattice is assumed to be cubic with the lattice parameter $a = (2a_\parallel + a_\perp)/3 = 5.7171$ Å.

The atomic positions for the A atoms (Ga, In) are displaced as the result of temperature-induced changes in the configuration of bonds [5] from the intersection point of elements of the $\bar{4}3m$ symmetry to the position of the lower symmetry $3m$, 16 : (*e*)*xxx*. The positional parameter x can be estimated, as in [3, 4], from the structure parameters of the compounds, which gives $x_t = -0.0058$. Arsenic atoms (B) in a mixed environment are displaced because of the difference in lengths of the Ga–As and In–As bonds (in the initial compounds, these bond lengths are 2.448 and 2.623 Å, respectively). It is reasonable to assume that indium

atoms are uniformly distributed. In this case, the nearest environment of the arsenic atoms contains 3Ga + 1In and 4Ga. Each indium atom is bonded to four arsenic atoms. Therefore, the share of arsenic atoms in the coordination 3Ga + 1In accounts for 72%, which corresponds to a fourfold indium content, and twenty-eight percent is due to the 4Ga coordination. In the 3Ga + 1In environment, the As position is displaced along the threefold axis; i.e., these atoms occupy the 16 : (*e*) position. For the given unit-cell dimensions and positional parameter $x_g = 0.2635$, the bond lengths have a minimum deviation from the aforementioned values: 2.434 and 2.609 Å, respectively. In the 4Ga coordination, the Ga–As bond length is equal to 2.476 Å($\sqrt{3}\,a/4$).

Although the above displacements are not very large, it is necessary to evaluate their influence on the structure factors of x-ray reflections by adding the third-order term to the temperature factor. This term is determined by the difference in the mean products of the components of displacements from an ideal position $\overline{u_x u_y u_z}$ of the A and B atoms. In our case, we have $u_x/a = u_y/a = u_z/a = x$. Then, the corresponding dimensionless quantity should be equal to $x_{ef}^3 = x_t^3 - 0.72(x_g - 1/4)^3 = -1.97 \times 10^{-6}$. Experience has shown that a better estimate of this parameter from experimental data can be obtained using the relationship with structure factors of a pair of reflections $h_1k_1l_1$ and $h_2k_2l_2$ with odd indices for which $H_1^2 = H_2^2$, that is,

$$x_{ef}^3 = \frac{F^2(h_1k_1l_1) + F^2(\bar{h}_1\bar{k}_1\bar{l}_1) - F^2(h_2k_2l_2) - F^2(\bar{h}_2\bar{k}_2\bar{l}_2)}{512\pi^3(f'_A f'_B + \Delta f''_A \Delta f''_B)T_A T_B(h_1k_1l_1S_1 - h_2k_2l_2S_2)}.$$

Here, f'_A and f'_B are the atomic factors of A and B atoms with the real part of the dispersion correction that corresponds to the radiation used, $f + \Delta f'$; $\Delta f''_A$ and $\Delta f''_B$ are the imaginary parts of the dispersion correction; T_A and T_B are the temperature factors in the harmonic approximation; and $S = \sin 2\pi(h/4 + k/4 + l/4)$ The data of measurements yield the value $x_{ef}^3 = -(1.107 \pm 0.043) \times 10^{-6}$, which differs significantly from the value obtained above.

Now, we estimate the fraction of arsenic atoms in the 3Ga + 1In environment from the x_{ef}^3 value, which was obtained using the experimental data, as $-(x_{ef}^3 - x_t^3)/(x_g - 1/4)^3$. The calculation gives a value of 0.37. The remaining arsenic atoms should reside partly in the 4Ga coordination and partly in the 2Ga + 2In coordination. It can easily be shown that the former and latter atoms account for 45.5 and 17.5%, respectively. In the 2Ga + 2In coordination, the atoms should be displaced along one of the superlattice axes. The best suited positional parameter has the value $z_g = 0.2765$ when the bond lengths are equal to 2.566 and 2.391 Å, respectively. In the new statistical model of the structure at $B_A = 0.651 \pm 0.004$ Å^2 and $B_B = 0.551 \pm 0.005$ Å^2, the calculated *R* factor decreases to 3.78%.

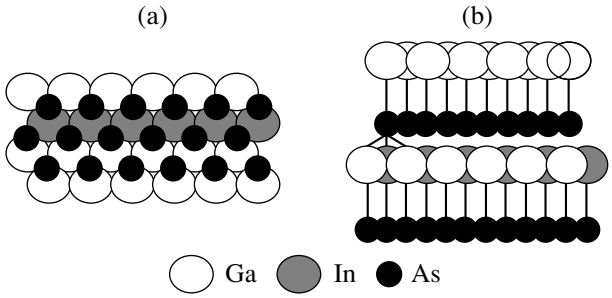

Fig. 1. Atomic packing in a layer parallel to the (111) planes in two projections (a) and (b).

The existence of the 2Ga + 2In coordination indicates an irregularity in the arrangement of indium atoms. It is reasonable first of all to consider a variant with atomic chains. Let us assume that a layer consisting of atoms A lies in the (111) plane with a chain of In atoms and adjacent chains of Ga atoms (Fig. 1). As can be seen from Fig. 1, the arsenic atoms nearest to the Ga atoms are bonded either to the 2Ga and In atoms or to the Ga and 2In atoms. These arsenic atoms should form the fourth bond with Ga atoms of the adjacent layer.

Let us now consider a chain of In atoms in the (001) plan that is extended along the [110] direction. Since the ratio between Ga and In atoms is close to 1 : 4, it is assumed that a chain of In atoms in the plane under consideration alternates with four Ga chains. Hence, a variant of chain arrangement in the adjacent (parallel) atomic layer suggests itself. Then, the third layer can repeat the first layer, i.e., can be related to it through translation (Fig. 2). In order to complete the model, it is necessary to arrange arsenic atoms in a known way. Thus, we obtain a variant of the superstructure with the smallest primitive cell (Fig. 3). It is seen from Fig. 3 that the ratio of arsenic atoms in the 2Ga + 2In, 3Ga + In, and 4Ga coordinations is equal to 1 : 2 : 2. This ratio corresponds to the above value with allowance made for the final accuracy of the estimate from the experimental data, "the deviation from the stoichiometric composition" of the solid solution, and the possible partial disordering of the superstructure.

The relationship for the experimental structure factors has another feature. The differences between $F_m^2(hkl)$ and $F_m^2(\bar{h}kl)$ obviously exceed the effect of anomalous dispersion, which implies a violation of the structural symmetry. These factors are well described by introducing the anisotropic thermal parameter $\exp(-\beta H^2 - 2\beta_{xy}hk)$. (In this form, its constants β and β_{xy} are dimensionless quantities; however, for conve-

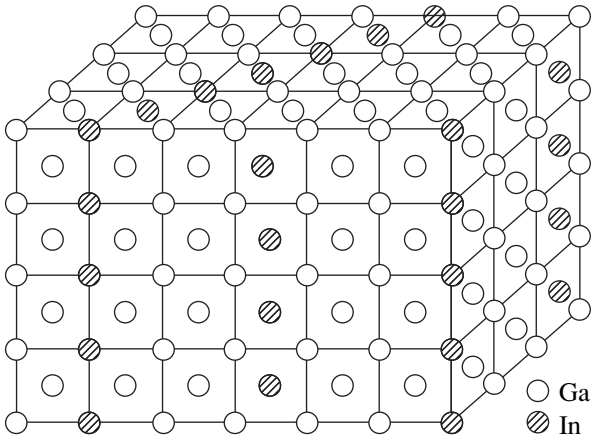

Fig. 2. Alternation of Ga and In atoms in the Ga_4InAs_5 superstructure. Boundaries of the substructure cells are shown.

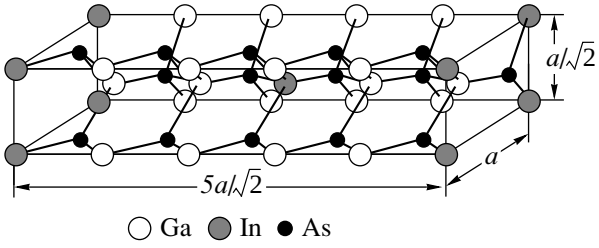

Fig. 3. A primitive cell of the Ga_4InAs_5 superstructure.

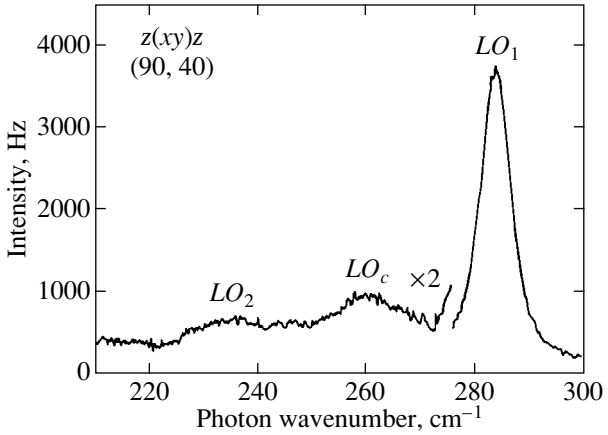

Fig. 4. Raman spectrum of the $Ga_{0.82}In_{0.18}As$ sample.

nience of comparison in the subsequent discussion, the particular values of these parameters will be given in conventional units, Å^2). The calculation with parameters $2\beta_{xy}$, which were separately refined for A and B atoms, leads to a decrease in the *R* factor to 3.54%.

Before elucidating the nature of the anisotropy, we consider the anomaly in the behavior of structure amplitudes, which is similar to that observed earlier in [4]. This behavior can be described more exactly either by introducing a normalizing factor of 0.63 for the experimental structure amplitudes (as if their values had been overestimated) or by using the thermal parameter expressed as $\exp(-\beta H^2 - 2\beta_{xy}hk)/0.63$ when calculating the structure amplitudes.

The calculation according to the above distribution of As atoms over the positions, the found values of x_t, x_g, and z_g, as well as the refined parameters B and $2B_{xy}$ (their values for A and B atoms are 0.923 ± 0.002, -0.042 ± 0.012 and 0.829 ± 0.003, -0.055 ± 0.017 Å^2, respectively) leads to a decrease in the *R* factor to 2.10%.

In attempting to elucidate the anomaly in the behavior of the structure amplitudes, we should note the following circumstances. As in our earlier work [4], where a similar situation took place, the experimental data suggest the formation of the superstructure with a rather large primitive cell. However, the superstructure reflections which would indicate the total ordering of the structure are not observed. In this case, we can see a partial ordering, which is typical of solid solutions prone to structural ordering. An inexact correspondence between the composition and the formula Ga_4InAs_5 leads to a certain disordering. In similar cases, there occurs a phenomenon such as the separation of the structure within the same substructure network into domains that are distinguished by the orientation of superlattice axes. A partial disordering in domains and the possible translational mismatch eventually transform the superstructure reflections into diffuse scattering.

For large periods of the superlattice, the most intense superstructure satellite reflections are observed near the main reflection. Let us now answer the question as to whether these satellites or the corresponding diffuse scattering can be captured in measurements of the intensity of the main reflections, thus increasing the experimental values of the structure amplitudes. In the superstructure described above, the period along one of the ⟨110⟩ directions of the substructure is increased by a factor of five. For convenience, we will use the nomenclature related to the substructure cubic cell, even though the fractional indices in this case should be assigned to the superstructure reflections. The satellites $h \pm 1/5\ h \pm 1/5\ 0$ should appear near the main reflections *hh*0. In the range of measurements, we observe the reflection 10 10 0, $2\vartheta = 122.78°$. For the satellite reflection 10.2 10.2 0, the scattering angle is 127.14°. With this difference, the satellite reflection cannot be recorded on a counter when measuring the intensity of the reflection 10 10 0.

However, thermal diffuse scattering is adjacent to the reflection. The formation of the superstructure changes the phonon spectrum. In particular, one should

Scheme for the formation of domain chains in the structure of atoms responsible for the anisotropy of room-mean-square displacements

Structural regions	Domain	Subdomain	Third link
Atom sort	A	B	A
Displacements	$\mathbf{r}_1(x_t\bar{x}_t\bar{x}_t)$	$\mathbf{r}_1 - \mathbf{r}_2(2x_t2\bar{x}_t0)$	$\mathbf{r}_1 - \mathbf{r}_2 + \mathbf{r}_1(3x_t3\bar{x}_t\bar{x}_t)$
	$\mathbf{r}_2(\bar{x}_tx_t\bar{x}_t)$	$\mathbf{r}_2 - \mathbf{r}_1(2\bar{x}_t2x_t0)$	$\mathbf{r}_2 - \mathbf{r}_1 + \mathbf{r}_2(3\bar{x}_t3x_tx_t)$

expect an increase in the weight of the longest wavelength vibrations of the acoustic branch. On the one hand, the temperature factor is sensitive to these vibrations (these modes correspond to the smallest frequencies and, consequently, the largest amplitude at a given temperature). On the other hand, the longest wavelength vibrations lead to thermal diffuse scattering which is most closely adjacent to reflections. In measurements, this part of thermal diffuse scattering is added to the integrated intensity of x-ray reflections, and thus, the structure factor turns out to be overestimated.

As could be expected from the results obtained in [3, 4], the anisotropy of root-mean-square displacements of the A atoms should be caused by the preferred orientation of domains formed upon displacements of atomic positions due to a temperature-induced change in the configuration of bonds. In this case, the superstructure domains with displacements $\bar{x}_tx_t\bar{x}_t$ and $x_t\bar{x}_t\bar{x}_t$ predominate. Similarly, the anisotropy in the displacements of the B atoms could be attributed to a predominance of superstructure domains in which chains of In atoms are aligned along the [110] direction, and the arsenic atoms in the 3Ga + 1In coordination are characterized by the displacements $\bar{x}_gx_g\bar{x}_g$ and $x_g\bar{x}_g\bar{x}_g$. However, calculations with a variation in the fraction of the A and B atoms thus displaced do not give the best fit of the calculated structure amplitudes to the experimental data. The *R* factor obtained in this case is tenths of a percent larger than the above value.

The specific feature of the structure of solid solutions is the capability of forming subdomains inside the domains or domain chains (see [1–4]). Therefore, the anisotropy in displacements of the B atoms can be due to the preferred orientation of subdomains. As regards the A atoms, they in turn should form the third link of a chain of temperature displacements of atomic positions inside subdomains. The table presents a scheme of combinations of the temperature displacement vectors $\mathbf{r}_j$ for atomic positions, which provide the required displacements.

In the case when 7% As atoms in subdomains and 3% A-type atoms in the third link of the chain are arranged in the aforementioned manner, $B_A = 0.920 \pm 0.002$ Å^2, $B_B = 0.821 \pm 0.003$ Å^2, and the normalizing factor is 0.625, the *R* factor is equal to 2.09%.

Earlier [6, 7], the epitaxial layers of similar compositions were investigated by the optical method. The features revealed in Raman and infrared spectra of the studied sample were attributed by these authors to the presence of the $GaInAs_2$ ordered phase (domains) which contained virtually all the indium. These inferences are in rather poor agreement with the results obtained in the present work. For this reason, we also investigated the Raman spectra of our sample at room temperature. The Raman spectra were excited with the 488-nm line of an argon laser, measured in a backscattering geometry (90, 40), and analyzed in a cross polarization $z(xy)\,\bar{z}$, where $x \parallel [001]$ and $y \parallel [010]$. According to the selection rules, the contribution to Raman scattering in this configuration is made only by longitudinal optical vibrations.

Figure 4 displays the Raman spectrum of our sample. The spectrum exhibits the LO_1 mode of GaAs (284 cm^{-1}) and the LO_2 mode of InAs (235 cm^{-1}). In addition, the spectrum contains the LO_c mode (260 cm^{-1}). A comparison of the spectra for the given sample and those studied in [6] shows their total identity.

In the sample studied in our work, the dimension of the unit cell in a layer corresponds to the given composition rather than to $Ga_{0.5}In_{0.5}As$. X-ray reflections of gallium arsenide are also observed: they are recorded from the substrate. As follows from measurements, these reflections are weakened by the shielding effect of the layer in complete agreement with the geometry of the x-ray path and the composition and thickness of the layer. Therefore, the epitaxial layer has neither a $GaInAs_2$ phase and nor ordering associated with this phase. In attempting to find any structural similarity between the $GaInAs_2$ and Ga_4InAs_5 superstructures, we can point only to the alternation of In and Ga atomic layers aligned parallel to the (110) plane of the substructure lattice, which was noted in [6] (in this respect, these authors introduced the term "monolayer superlattice $(InAs)_1(GaAs)_1$." In the proposed superstructure $GaInAs_2$, the Ga and In layers alternate with each other. In our superstructure, one In layer alternates with four Ga layers (Fig. 2). However, a similar alternation in the layers parallel to the $(1\bar{1}0)$ and (001) planes does not occur. Furthermore, the As atoms in layers which are aligned parallel to the (110) plane and located between

the Ga and In layers adopt different coordinations in two substructures. Therefore, we can conclude that the observed feature of the phonon spectrum is associated with the Ga_4InAs_5 superstructure.

In conclusion, it should be noted that, as far as we know, the Ga_4InAs_5 superstructure, which was identified from analysis of the x-ray measurements, has never been observed in A^3B^5 solid solutions.

ACKNOWLEDGMENTS

We are grateful to E.L. Portnoĭ and E.I. Terukov for their interest in this work and helpful discussions of the results and A.S. Vlasov for his assistance in optical measurements.

REFERENCES

1. A. A. Vaĭpolin and D. V. Pulyaevskiĭ, Fiz. Tverd. Tela (St. Petersburg) **34** (3), 732 (1992) [Sov. Phys. Solid State **34**, 392 (1992)].
2. A. A. Vaĭpolin, Fiz. Tverd. Tela (St. Petersburg) **35** (3), 789 (1993) [Phys. Solid State **35**, 404 (1993)].
3. A. A. Vaĭpolin and D. Melebaev, Fiz. Tverd. Tela (St. Petersburg) **36** (4), 1106 (1994) [Phys. Solid State **36**, 600 (1994)].
4. A. A. Vaĭpolin and D. Melebaev, Fiz. Tverd. Tela (St. Petersburg) **36** (7), 2107 (1994) [Phys. Solid State **36**, 1150 (1994)].
5. A. A. Vaĭpolin, Fiz. Tverd. Tela (Leningrad) **31** (12), 37 (1989) [Sov. Phys. Solid State **31**, 2045 (1989)].
6. A. M. Mintairov, D. M. Mazurenko, M. A. Sinitsyn, and B. S. Yavich, Fiz. Tekh. Poluprovodn. (St. Petersburg) **28** (9), 1550 (1994) [Semiconductors **28**, 866 (1994)].
7. A. S. Vlasov, V. G. Melehin, A. M. Mintairov, *et al.*, in *Proceedings of the 23rd International Symposium on Compound Semiconductor, St. Petersburg, 1996*, pp. 981–984.

Translated by O. Borovik-Romanova

Physics of the Solid State, Vol. 43, No. 4, 2001, pp. 621–624. Translated from Fizika Tverdogo Tela, Vol. 43, No. 4, 2001, pp. 598–600.

SEMICONDUCTORS AND DIELECTRICS

Fine Structure of the Valence Band Top in a 3*C* BN Crystal with a Nanopore

V. V. Ilyasov, I. Ya. Nikiforov, and Yu. V. Ilyasov

Don State Technical University, Rostov-on-Don, 344010 Russia

e-mail: victor.ilyasov@rost.ru

Received March 21, 2000; in final form, August 23, 2000

Abstract—The electronic band structure of a 3*C* BN boron nitride crystal with pores ($r \sim 0.3$ nm) statistically distributed over the crystal is calculated by the local coherent potential method within the multiple scattering approximation. The valence band tops of crystalline (stoichiometric) and porous boron nitride are compared to the x-ray photoelectron spectrum (XPS) of BN and the soft x-ray emission spectra (SXES) of nitrogen. The origin of a short-wavelength shoulder in XPS, N*K* XES, and N*K* SXES of binary nitrides is discussed.

1. INTRODUCTION

Progress in fine technologies of growing wide-gap semiconductor crystals, for example, chemical vapor deposition (CVD) or the sublimation sandwich method, has offered a variety of nanomaterials with unique properties for micro- and optoelectronics [1–3]. These materials exist in both amorphous and crystalline states. Porous crystalline materials whose electronic structure has been almost unexplored are of special interest. The traditional technique of investigating local densities of states (LDOS) in porous crystals is ultrasoft x-ray emission spectroscopy (USXES) [3]. However, this method does not provide comprehensive information on the specific features in the structure of valence band tops in a crystal. The application of band structure calculation methods to porous objects involves considerable difficulties. In this respect, it was of interest to demonstrate the possibilities of the cluster approximation of the local coherent potential by the example of a model object—a cluster of 235 atoms with a nanopore ($r \sim 0.3$ nm). Earlier [4, 5], this approach was developed for the class of nonstoichiometric compounds. The present work is a continuation of earlier works and is aimed at studying the fine structure of the valence band top in cubic boron nitride with a nanopore.

2. MODEL OBJECT

A single pore 0.6 nm in size in a 3*C* BN crystal was modeled according to the scheme presented in Fig. 1. This figure displays the part of the cluster centered at the pore in the projection onto the (000) plane. The values of fractions denote the height of the atoms above the basal plane (the edge of the cubic unit cell of boron nitride is taken to be a unit length). The sites unoccupied by boron and nitrogen atoms (distinguished by different sizes in the scheme) are hatched. The atomic sites which belong to the first, second, and third coordination spheres turn out to be free of atoms (29 vacancies). The next twelve coordination spheres are filled with boron and nitrogen atoms occupying standard positions: 6 nitrogen atoms reside in the fourth coordination sphere, 12 boron atoms are situated at the fifth sphere, and 24 nitrogen atoms are located in the sixth sphere. Thus, the space bounded by the fourth coordination sphere specifies the pore volume. The cluster

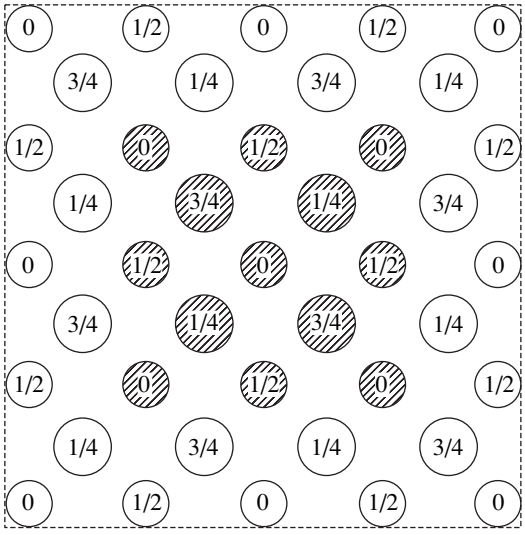

Fig. 1. Arrangement of atoms and vacancies (forming a nanopore) in the central part of a cluster centered at the pore (projection onto the cube base).

1063-7834/01/4304-0621$21.00

considered contains 206 atoms and 29 vacancies. It is assumed that these pores are uniformly distributed throughout the crystal. The pores occupy 20% of the entire volume of the crystal, and its density comprises 0.8 of the density of an ideal crystal.

3. METHOD AND DETAILS OF CALCULATION

The electronic band structure of the model object under consideration was calculated by the local coherent potential method within the framework of the multiple scattering theory. A remarkable feature of the method presented in [4] is its applicability to systems with crystal symmetry violation. The crystal potential was constructed in the muffin-tin (*MT*) approximation. The contributions of neighboring atoms to the electron density and the Coulomb potential of fifteen coordination spheres were taken into account. The exchange potential was constructed in the Slater X_α approximation with the exchange correction $\alpha = 2/3$. The effective crystal potential was determined as the sum of contributions of the Coulomb, exchange, and Madelung potentials. The Madelung potential was taken to be equal to the lattice potential of an ideal boron nitride 3*C* BN [6]. As was shown in [5, 7], the deficit of atoms in B and N sublattices can be accompanied by lattice "softening" because of the dangling bonds and can lead to relaxation of the crystal lattice and a decrease in the lattice parameter. In this work, the crystal potential was calculated for the equilibrium state with a lattice parameter of 5.69940 au in much the same way as in [5]. A decrease in the potential of boron and nitrogen atoms is observed in the presence of nanopores in 3*C* BN. The potential due to the nanopore remains constant inside the *MT*-sphere; the potentials of B and N atoms appear to be three orders of magnitude higher at the center, whereas in the vicinity of the *MT* sphere, they are close to the values of the potential at the pore. Multiple electron scattering was considered, including the eighth coordination sphere for each of the three clusters used in the calculations. The number of atoms in each of these clusters was equal to 99. Since scatterers in the fourth, fifth, and subsequent coordination spheres differed, the center of the calculated cluster was placed in each of them. The total number of atoms in each cluster was 235. The local partial densities of states (PDOS) at the pore and of B and N atoms can be calculated using the relationship [6]

$$n_l^A(E) = -\frac{\sqrt{E}}{\pi}\int_0^{r_{ws}} (rR_l^A(E,r))^2 dr \frac{\mathrm{Im}\,TrT^{00,A}_{lm,l'm'}(E)}{\mathrm{Im}\,t_l^A(E)}, \quad (1)$$

where *A* determines the sort of the atom in the cluster, *l* is the orbital quantum number, $R(E, r)$ are the radial wave functions, and *T* is the matrix element of the scattering operator. Since coordinations of B (N) atoms at the fourth and next coordination spheres differed, the clusters centered at the B (N) atom were considered for each coordination sphere. The local densities of states of B and N atoms were calculated with inclusion of the concentration of the *A*-type atoms at each coordination sphere. The total density of states (TDOS) of atoms in 3*C* BN was calculated by the formula

$$N(E) = c_j\sum_{l=0}^{2} n_l^{\mathrm{pore}}(E) + \sum_{k=4} c_{jk}\sum_{l=0}^{2} n_l^{\mathrm{B}}(E) + \sum_{k=4} c_{jk}\sum_{l=0}^{2} n_l^{\mathrm{N}}(E), \quad (2)$$

where c_{jk} is the concentration of the *A*-type atoms at the coordination sphere (k) and in the cluster (j). The pore concentration is taken equal to the concentration of the pore-forming atomic vacancies in the cluster.

4. RESULTS AND DISCUSSION

Figure 2 shows (a) the x-ray photoelectron spectrum (XPS) [8] and TDOS, (b) PDOS at the nanopore, and PDOS at the top of the valence band for (c) boron and (d) nitrogen atoms in the 3*C* BN crystal with a nanopore. A comparison of TDOS of the stoichiometric BN with the present calculation allows one to assert that the energy band structure of the boron nitride *c*-BN with a nanopore is determined equally by the *p* electron states of boron and nitrogen atoms. In earlier works [4, 6] dealing with a small number of atoms in the calculated cluster (up to four coordination spheres, which was specified by the low operation speed of PCs), it was found that the features of the valence band top in cubic boron nitride are governed primarily by the local partial 2*p* states of nitrogen. The valence band top of the 3*C* BN crystal with a nanopore is characterized by additional maxima E_2 and F_2, apart from all features of the TDOS curve, which are typical of the stoichiometric BN. The origin of the E_2 peak is explained by the occurrence of localized states at an energy of 0.96 Ry at the nanopore, and the F_2 peak results from boron *p* states (1.20 Ry). The singularity of the E_3 PDOS peak (0.96 Ry) suggests Mott localization of the *s* states at the nanopore; however, its impossibility of being in the energy band calculations was reported in [9]. Alyushin *et al.* [10] explained the *D* peak in the x-ray photoelectron spectrum by the presence of a B_xON_x-type oxide on the surface of the cubic boron nitride samples. The present calculation proved that the *D* peak can also be determined by contributions of the boron (D_4 peak) and nitrogen (D_5 peak) *p* states and the *s* states at the nanopore (E_3 peak). The state at an energy of 0.46 Ry (C_2 peak) proved to be the most stable and, in our opinion, correspond to the sp^3 configuration, which is characterized by a directed covalent bond between the boron and nitrogen atoms. The transformation of the energy spectrum of the valence band top in the BN–pore system leads to charge transfer in boron (0.65 *e*)

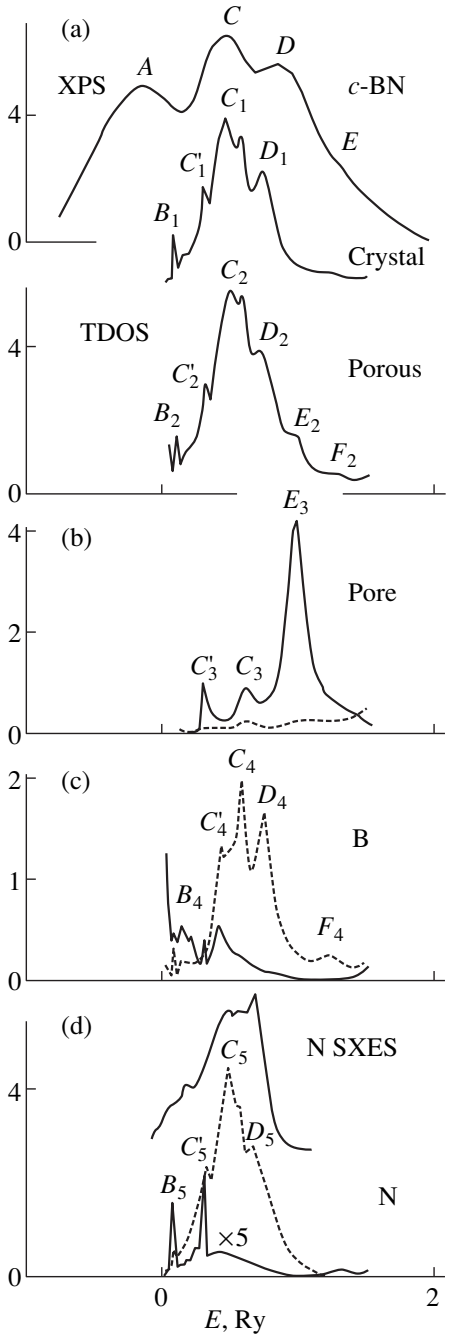

Fig. 2. (a) X-ray photo electron spectrum of the valence band [8] and the calculated total densities of states for porous and crystalline *c*-BN compounds. The local densities of *s* and *p* electron states at (b) the pore and the (c) boron and (d) nitrogen atoms. Dashed lines correspond to 2*p* electron states.

and nitrogen (0.11 *e*) toward the low-energy region (below the *MT* zero). This results in a decrease in the intensity of the maxima (except for B_1) in the TDOS curve. The decrease in the density of states at an energy of 0.70 Ry (D_1 peak) can be due to transformation of the sp^3 configuration of boron and nitrogen into the sp^2 configuration. A similar transformation of electronic configurations occurred in porous silicon carbide 3*C* Si_xC [3]. A comparison of N 2*p* states of porous B_xN_x with N SXES (Fig. 2d) allows certain assumptions to be made on the nature of specific features of the valence band top in cubic boron nitride. The E_2 peak can result from the occurrence of an "outer" collective band formed by electrons of the metal and nonmetal, as is the case in ultrasoft K_α emission bands of nitrogen [11]. However, the short-wavelength shoulder in the spectra of transition metal nitrides appears, according to [11], in the case when the concentration of valence electrons per MeN "quasi-molecule" exceeds eight. The authors of [11] suggested that the increase in the metal concentration can be responsible for the increase in the intensity of the aforementioned shoulder when the composition of zirconium nitride deviates from the stoichiometry with respect to nitrogen. The valence electron concentration in the BN quasi-molecule cannot exceed eight. Therefore, the short-wavelength shoulder in the curve of the density of nitrogen 2*p* states at an energy of 0.96 Ry (E_2 peak) can have a different nature. Since the present calculation treats a nanopore consisting of 29 vacancies of B and N atoms, it is reasonable to assume that the E_2 peak clearly appears and stems from a general regularity (characteristic of binary nitrides) which is associated with a decrease in the symmetry of nonstoichiometric and porous materials. The short-wavelength shoulder is also observed in the experimental x-ray photoelectron spectra XPS (*E* shoulder) [8, 10] and K_α emission bands of nitrogen (E_2 peak) [11, 12], which was probably given insufficient attention.

It follows from the above results that the model considered for a nanopore in cubic boron nitride does not contradict the published experimental data on the features of the electronic spectrum of real 3*C* BN crystals and provides a better insight into the nature of the short-wavelength shoulder in XPS, N*K* XES, and N*K* SXES of binary nitrides.

REFERENCES

1. Yu. A. Vodakov and E. N. Mokhov, Fiz. Tverd. Tela (St. Petersburg) **41** (5), 822 (1999) [Phys. Solid State **41**, 742 (1999)].
2. P. G. Baranov, I. V. Il'in, E. N. Mokhov, and V. A. Khramtsov, Fiz. Tverd. Tela (St. Petersburg) **40** (10), 1818 (1998) [Phys. Solid State **40**, 1648 (1998)].
3. V. A. Terekhov, V. A. Ligachev, N. S. Kovaleva, *et al.*, J. Adv. Mater. **3** (5), 370 (1996).
4. I. Ya. Nikiforov, V. V. Ilyasov, and N. Yu. Safontseva, J. Phys.: Condens. Matter **7**, 6035 (1995).
5. V. V. Ilyasov and I. Ya. Nikiforov, Fiz. Tverd. Tela (St. Petersburg) **39** (6), 1064 (1997) [Phys. Solid State **39**, 955 (1997)].

6. V. V. Ilyasov, N. Yu. Safontseva, and I. Ya. Nikiforov, Fiz. Tverd. Tela (St. Petersburg) **36** (2), 451 (1994) [Phys. Solid State **36**, 247 (1994)].
7. A. M. Zaĭtsev, A. G. Ul'yashin, and Hussein Ali Nur, Sverkhtverd. Mater. **70**, 18 (1991).
8. V. P. Elyutin, I. V. Blinkov, I. I. Goryunova, *et al.*, Izv. Akad. Nauk SSSR, Neorg. Mater. **26** (5), 978 (1990).
9. A. V. Kudinov, Fiz. Tverd. Tela (St. Petersburg) **41** (9), 1582 (1999) [Phys. Solid State **41**, 1450 (1999)].
10. V. G. Alyushin, A. N. Sokolov, and A. A. Shul'zhenko, Sverkhtverd. Mater. **5**, 12 (1985).
11. I. N. Frantsevich, E. A. Zhurakovskiĭ, and N. N. Vasilenko, Dokl. Akad. Nauk SSSR **198** (5), 1066 (1971) [Sov. Phys. Dokl. **16**, 481 (1971)].
12. A. Agui, S. Shin, M. Fujisawa, *et al.*, Phys. Rev. B **55** (4), 2073 (1997).

Translated by M. Lebedkin

Physics of the Solid State, Vol. 43, No. 4, 2001, pp. 625–628. Translated from Fizika Tverdogo Tela, Vol. 43, No. 4, 2001, pp. 601–604.

SEMICONDUCTORS AND DIELECTRICS

Effective Excitation Cross Section of Erbium in Amorphous Hydrogenated Silicon under Optical Pumping

M. S. Bresler, O. B. Gusev, P. E. Pak, E. I. Terukov, and I. N. Yassievich

Ioffe Physicotechnical Institute, Russian Academy of Sciences, Politekhnicheskaya ul. 26, St. Petersburg, 194021 Russia

Received September 5, 2000

Abstract—The effective excitation cross section of erbium embedded in an amorphous silicon matrix and the total lifetime of erbium ions in the excited state are determined by measuring the photoluminescence rise time of erbium ions under pulsed excitation of erbium-doped amorphous hydrogenated silicon. An analysis of the rate equations describing the excitation and deexcitation of erbium ions in a semiconducting matrix sheds light on the physical meaning of the effective excitation cross section. It is shown that measurement of the effective excitation cross section permits evaluation of the concentration of optically active erbium ions in the amorphous silicon matrix. © *2001 MAIK "Nauka/Interperiodica".*

Semiconducting matrices doped by rare-earth elements have a considerable application potential in optoelectronics. Particular interest has been recently focused on erbium embedded in crystalline and amorphous silicon, because light with the wavelength of 1.54 μm corresponding to the transition from the first excited state, $^4I_{13/2}$, to the ground state, $^4I_{15/2}$, of the inner 4*f* shell of the erbium ion Er^{3+} suffers minimum losses in quartz optical-fiber communication lines. In contrast to dielectric matrices, where the erbium ions are excited through direct absorption of photons, in a semiconducting host lattice erbium is excited primarily by free carriers via the Auger process [1], or by hot carriers, as is the case with erbium electroluminescence in a reverse-biased *p–n* junction [2]. The efficiency of erbium excitation in a semiconducting matrix can be characterized by the excitation cross section of the erbium ion in this matrix. The erbium excitation cross section was measured in crystalline silicon for various excitation mechanisms, and it was shown that it exceeds the erbium excitation cross section due to direct photon absorption in a dielectric matrix by several orders of magnitude [3, 4].

This paper reports on the first determination of the effective excitation cross section of erbium embedded in an amorphous silicon matrix under optical pumping. A comprehensive analysis of the excitation mechanism revealed the physical sense of the excitation cross section. The concept of the effective excitation cross section of optically pumped erbium is shown to extend to other semiconducting matrices as well. The concentration of optically active erbium in amorphous hydrogenated silicon and the excited-state lifetime of erbium ions are determined.

1. EXPERIMENTAL RESULTS

The samples of erbium-doped amorphous hydrogenated silicon, *a*-Si : H⟨Er⟩, studied in this work were grown by magnetron sputtering of erbium metal on a crystalline silicon substrate in an atmosphere of silane and argon. The erbium concentration in the film, as derived from SIMS data, was 10^{19} cm^{-3}, and the oxygen concentration was 10^{20} cm^{-3} (the residual oxygen in the magnetron chamber).

The erbium excitation source was an LED emitting at 0.64 μm, with the pulse length of 5 ms and the rise and decay times of 1 μs. The photoluminescence (PL) radiation was analyzed by a grating monochromator with a focal length of 820 mm and detected by a cooled germanium photoreceiver in a standard lock-in detection arrangement. The erbium PL kinetics was studied by a digital oscillograph and a cooled germanium photodetector. The time resolution of the measuring circuit, limited by the photodetector response, was 5 μs.

Figure 1 presents the PL spectrum of a Si : H⟨Er⟩ sample obtained in the 1- to 1.8-μm region. The line peaking at 1.54 μm is due to the transition from the first excited state $^4I_{13/2}$ to the ground state $^4I_{15/2}$ in the inner 4*f* shell of the erbium ion. The dependence of the erbium luminescence intensity at 1.54 μm on the pump power measured at 90 K is shown in Fig. 2.

An analysis of the oscillograms of the erbium PL signal at the wavelength of 1.54 μm permits one to derive the dependence of the erbium PL signal rise time, τ_{on}, on the pump power. Figure 3 displays the reciprocal rise time $1/\tau_{on}$ of the erbium PL intensity at 1.54 μm (circles) on the pump power.

1063-7834/01/4304-0625$21.00

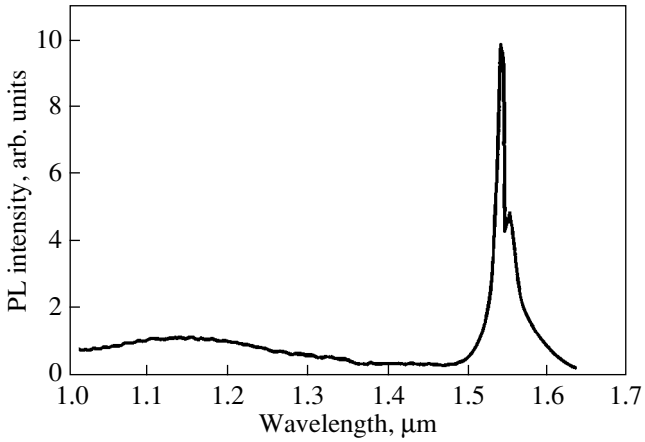

Fig. 1. Si : H⟨Er⟩ photoluminescence spectrum measured at $T = 90$ K.

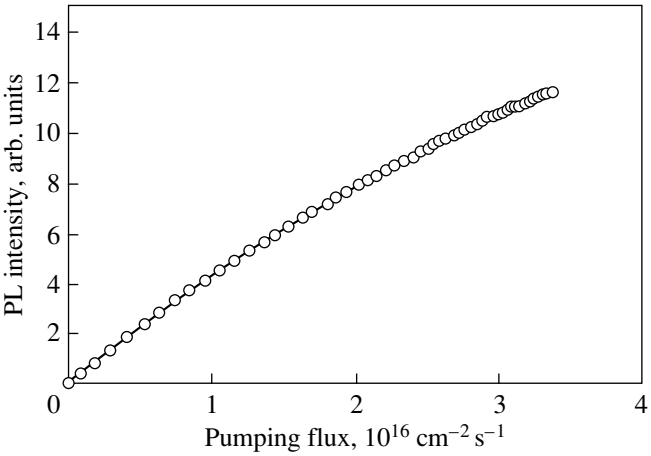

Fig. 2. Experimental (circles) and calculated (solid line) dependences of the erbium PL intensity on the pumping power for erbium embedded in an amorphous hydrogenated silicon matrix. $T = 90$ K.

2. DISCUSSION OF RESULTS

Similar to the case of erbium-doped crystalline silicon [2], the experimental data presented in Fig. 3 are well fitted by a solution to the rate equation taking into account the processes of excitation and deexcitation of erbium ions

$$\frac{dN^*}{dt} = \sigma\Phi(N_{\mathrm{Er}} - N^*) - \frac{N^*}{\tau}, \qquad (1)$$

where σ is the erbium excitation cross section, Φ is the pumping photon flux, τ is the total erbium-ion excited-state lifetime, and N_{Er} and N^* are the total and excited erbium-ion concentrations, respectively.

The solution to Eq. (1) describing the rise of the erbium PL intensity after the arrival of a square pump pulse can be written as

$$I_{\mathrm{Er}} = \frac{\sigma\tau\Phi}{\sigma\tau\Phi + 1}\frac{N_{\mathrm{Er}}}{\tau_{\mathrm{rad}}}\left\{1 - \exp\left[-\left(\sigma\Phi + \frac{1}{\tau}\right)t\right]\right\}, \qquad (2)$$

where τ_{rad} is the radiative lifetime of the erbium ion in the excited state. As follows from Eq. (2), on application of an LED pump pulse, the erbium luminescence intensity approaches the steady-state level with the characteristic time τ_{on} defined as

$$\frac{1}{\tau_{\mathrm{on}}} = \sigma\Phi + \frac{1}{\tau}. \qquad (3)$$

Figure 3 plots a calculated $1/\tau_{\mathrm{on}}$ relation fitted to experimental data with the parameters $\sigma = 1.4 \times 10^{-14}$ cm^2 and $\tau = 420$ μs.

The values of σ and τ thus obtained can be checked by describing the erbium PL intensity as a function of the pumping power in the steady state. Indeed, the stationary solution to Eq. (1) has the form

$$I_{\mathrm{Er}} = \frac{\sigma\tau\Phi}{\sigma\tau\Phi + 1}\frac{N_{\mathrm{Er}}}{\tau_{\mathrm{rad}}}. \qquad (4)$$

The dependence of the erbium PL intensity on the pumping level is determined by the same parameters σ and τ that enter Eq. (3). The relation calculated using these parameters fits the experimental curve well (Fig. 2).

The excitation cross section σ was introduced into Eq. (1) as a phenomenological parameter. To find the physical meaning of the excitation cross section σ, one has to analyze comprehensively the processes of excitation and deexcitation of erbium ions in an amorphous matrix.

It is known that introducing erbium into the amorphous silicon matrix initiates the formation of ruptured silicon bonds (defects), with either one electron (defect in the D^0 state) or two electrons (defect in the D^- state). These states create levels approximately at the midgap of the matrix and are separated by a correlation energy of ~0.1–0.2 eV. The $4f$ term of the erbium ion lies below the valence-band edge by about 10 eV. Therefore, the erbium-ion $4f$ shell can be excited only through the Coulomb interaction with the matrix carriers (the Auger process).

It is well known [5, 6] that doping crystalline silicon with erbium and oxygen leads to the formation of donor levels created by erbium–oxygen complexes, their binding energy lying in the 0.1- to 0.25-eV interval. One may therefore expect that similar doping of amorphous silicon is likewise accompanied by the formation of donor states. This suggestion is confirmed by the amorphous silicon doped by erbium and oxygen having *n*-type conduction. Measurements of the temperature behavior of electrical conductivity carried out on a

number of samples yield for the Fermi energy a value 0.5 eV below the mobility edge in the conduction band. Because the erbium concentration in amorphous silicon can reach 10^{20} cm^{-3} and the D defect concentration does not exceed 10^{18}–10^{19} cm^{-3} [7, 8], all the D defects in erbium-doped amorphous silicon are found in equilibrium to be in the D^- state.

The geminate radiative recombination of electron–hole pairs observed under interband excitation is efficient only at low enough temperatures, and, therefore, it appears natural to assume that, in our samples containing a large number of D defects [8], recombination occurs primarily nonradiatively via the D defects. This is supported by the absence of band-to-band radiative transitions in our samples at the temperature of the experiment T = 90 K (Fig. 1). Because the concentrations of electrons, holes, and D^0 centers are negligible at equilibrium while that of the D^- centers is practically equal to the total concentration of the D centers, $N_D^- \approx N_D$, the holes are captured in the first recombination stage by the D^- centers to convert them to the D^0 defects. This process is described by the rate equation

$$\frac{dp}{dt} = \alpha\Phi - c_p p N_D^-, \tag{5}$$

where Φ is the photon flux, α is the pump-radiation absorption coefficient, p is the free-hole concentration, and c_p is the hole capture coefficient by the D^- centers.

In the second stage of the recombination, the electrons transfer from the conduction-band tails to the D^0 centers and convert them to the D^- centers. The free-electron concentration is given by the equation

$$\frac{dn}{dt} = \alpha\Phi - c_n n N_D^0. \tag{6}$$

Here, n is the free electron concentration and c_n is the total trapping coefficient of electrons by the D^0 centers, which is actually the sum of the contributions due to two competing processes, more specifically, those of the electron capture with erbium excitation through the Auger process and those of the multiphonon nonradiative capture, $c_n = c_A + c_{mp}$ [8, 9].

Note that in our case the D^0 centers form only under excitation as a result of the hole capture by the D^- centers. Their concentration can be found from the relation

$$\frac{dN_D^0}{dt} = c_p p N_D^- - c_n n N_D^0. \tag{7}$$

The above coupled rate equations should be supplemented by the charge neutrality condition

$$n = p + N_D^0. \tag{8}$$

The processes of pumping, excitation, and radiation of erbium ions are displayed schematically in Fig. 4. Erbium ions in an amorphous silicon matrix are excited

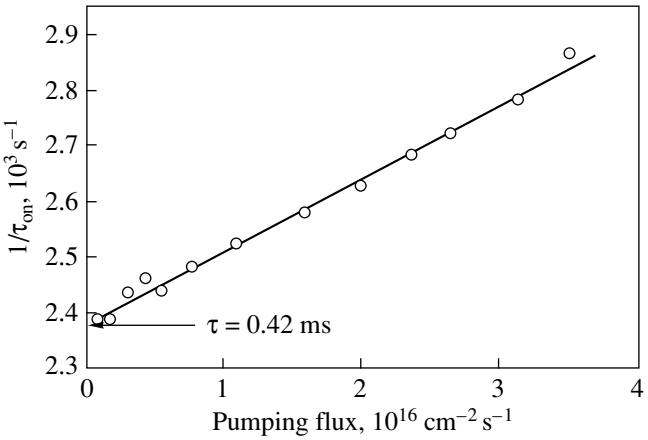

Fig. 3. Reciprocal characteristic erbium PL rise time vs. excitation level for erbium embedded in amorphous hydrogenated silicon. T = 90 K.

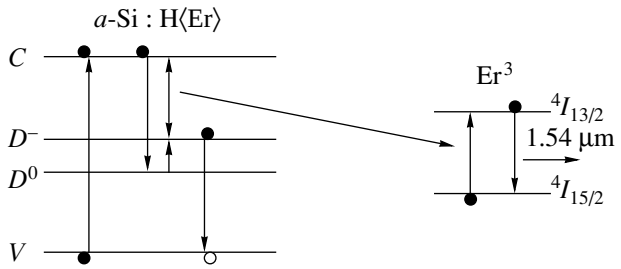

Fig. 4. Diagram of erbium excitation in amorphous hydrogenated silicon under interband optical pumping.

by the Auger process, whose probability is proportional to the product of the free-electron concentration by the concentration of the D^0 centers. The concentration of excited erbium ions is given by the rate equation

$$\frac{dN^*}{dt} = c_A n N_D^0 \left(1 - \frac{N^*}{N_{\mathrm{Er}}}\right) - \frac{N^*}{\tau}. \tag{9}$$

When analyzing the rate equations (5)–(9), one can make use of the fact that the system of the matrix and of the erbium ions is actually divided into two subsystems, namely, a "fast" one (matrix), in which the relaxation times of all electronic processes (recombination, free carrier capture by D centers) are not in excess of a few tens of microseconds, and a "slow" one (the erbium ions), where the characteristic time (excited-state lifetime of the erbium ions) is equal, in order of magnitude, to one millisecond. Therefore, the evolution of a system of ions acted upon by a pulsed pumping mechanism may be considered under the assumption that the subsystem of free carriers and defects is already in a steady state. In this case, Eq. (6) yields $nN_D^0 = \alpha\Phi/c_n$.

A comparison of Eq. (9) with Eq. (1) shows that the excitation of erbium ions in an amorphous silicon matrix can indeed be described by means of a phenomenological parameter σ, the erbium-ion excitation cross section, which has the meaning

$$\sigma = \frac{\alpha}{N_{\mathrm{Er}}}\frac{c_A}{c_A + c_{mp}}. \quad (10)$$

Note that by N_{Er} in Eqs. (1), (9), and (10) one should understand not the total concentration of the erbium ions, but rather the concentration of optically active ions, which, for instance, in crystalline silicon constitutes only a few percent of the total concentration.

Thus, as follows from Eq. (10), if pumping is effected via free carriers in an amorphous host matrix, the excitation cross section σ is inversely proportional to the concentration of optically active erbium. This is because in these conditions the absorption coefficient of the pumping radiation does not depend on the erbium concentration (as is the case with direct optical excitation of erbium in dielectric matrices) and is determined only by the joint density of states for the interband transition. In these conditions, the excitation probability of one ion is naturally higher, the smaller the number of ions acted upon by the given flux of exciting particles.

Obviously enough, the inverse proportionality of the excitation cross section to the erbium-ion concentration observed under optical pumping will be retained in all cases of pumping via free carriers; in other words, it will hold for all semiconducting matrices and for any excitation mechanism.

The probability of the Auger excitation of erbium ions when the electron is captured by a D^0 center (the DRAE process), as well as the probability of the competing process of multiphonon nonradiative capture, was calculated in [9], where it was shown that over a broad temperature region ranging from the liquid helium temperature to 200 K the DRAE probability is dominant and, hence, the c_A/c_n ratio is close to unity. As the temperature increases, the intensity of multiphonon transitions increases substantially and the c_A/c_n ratio drops noticeably.

Because at 90 K the ratio $c_A/(c_A + c_{mp}) \approx 1$ [9], one can use Eq. (10) to determine the concentration of optically active erbium ions in the amorphous matrix. Accepting 10^4 cm^{-1} for a typical absorption coefficient of amorphous silicon at the wavelength of 0.64 μm and the experimentally determined excitation cross section $\sigma = 1.4 \times 10^{-14}$ cm^2, we obtain 7×10^{17} cm^{-3} for the concentration of optically active erbium ions, i.e., a few percent of the total erbium-ion concentration, which in our samples reached about 10^{19} cm^{-3}.

Thus, we have measured for the first time the effective excitation cross section of erbium embedded in the amorphous silicon matrix. Its physical meaning is disclosed as applied to the excitation of erbium in this matrix under optical pumping. The good agreement between the experimental and calculated relations for the erbium PL intensity and the intensity rise time on the pump power supports the validity of the measured effective erbium excitation cross section and total erbium-ion excited-state lifetime. It is shown that by measuring the effective excitation cross section one can estimate the concentration of optically active erbium ions in amorphous silicon.

ACKNOWLEDGMENTS

The authors are indebted to B.P. Zakharchenya for support of the work and fruitful discussions.

This work was supported by the Russian Foundation for Basic Research (grant nos. 98-02-18246 and 99-02-18079), the Ministry of Science (grant no. 97-1036), INTAS (grant no. 99-01872), and COPERNICUS, grant no. 977048-SIER.

REFERENCES

1. I. N. Yassievich and L. C. Kimerling, Semicond. Sci. Technol. **8**, 718 (1993).
2. S. Coffa, G. Franzo, and F. Priolo, Appl. Phys. Lett. **69**, 2077 (1996).
3. J. Palm, F. Gan, B. Zheng, *et al.*, Phys. Rev. B **54**, 17 603 (1996).
4. F. Priolo, G. Franzo, S. Coffa, and A. Carnera, Phys. Rev. B **57**, 4443 (1998).
5. J. L. Benton, J. Michel, L. C. Kimerling, *et al.*, J. Appl. Phys. **70**, 2667 (1991).
6. S. Libertino, S. Coffa, G. Franzo, and F. Priolo, J. Appl. Phys. **78**, 3867 (1995).
7. K. Pierz, W. Fuhs, and H. Mell, Philos. Mag. B **63**, 123 (1991).
8. W. Fuhs, I. Ulber, G. Weiser, *et al.*, Phys. Rev. B **56**, 9545 (1997).
9. I. N. Yassievich, M. S. Bresler, and O. B. Gusev, J. Phys.: Condens. Matter **9**, 9415 (1977).

Translated by G. Skrebtsov

Physics of the Solid State, Vol. 43, No. 4, 2001, pp. 629–634. Translated from Fizika Tverdogo Tela, Vol. 43, No. 4, 2001, pp. 605–610.

SEMICONDUCTORS AND DIELECTRICS

Ordering of an Intercalated Impurity near the Temperature of Polaron Band Collapse in Ag_xTiTe_2

A. N. Titov* and S. G. Titova**

** Ural State University, pr. Lenina 51, Yekaterinburg, 620083 Russia*

*** Institute of Metallurgy, Ural Division, Russian Academy of Sciences, Yekaterinburg, 620016 Russia*

e-mail: alexander.titov@usu.ru

Received June 6, 2000; in final form, September 15, 2000

Abstract—The phase diagram of an Ag_xTiTe_2 intercalation compound near the temperature of polaron band collapse is studied by x-ray structure analysis. The results obtained confirm the assumption made earlier that, at temperatures close to the polaron band collapse point, a homogeneous state cannot exist in the charge carrier concentration range in which the Fermi level lies between the bottom and the center of an impurity band. The reversible transition accompanied by ordering of intercalated silver is revealed upon heating to a temperature close to the polaron band collapse point. This transition is explained by the enhancement of Coulomb repulsion between impurity atoms due to the localization of charge carriers. © *2001 MAIK "Nauka/Interperiodica"*.

1. INTRODUCTION

Intercalation of transition metals and silver into titanium diselenide and titanium ditelluride leads to localization of charge carriers in the form of polarons of a small radius [1]. This circumstance, as applied to the phase diagram, imposes certain limitations on the possibility of forming a single-phase state in the carrier concentration range in which the following condition is met: $E_L < E_F < E_d$, where E_L is the energy at the bottom of the polaron band, E_F is the Fermi energy, and E_d is the energy at the center of the polaron band [2]. This condition is important in the case when the polaron band lies above the Fermi level of the initial material and is fulfilled when silver serves as an intercalant [3]. The possibility of forming a single-phase state is restricted by the dominant contribution of the electronic subsystem to the thermodynamic functions of a material. However, the deviation from the temperature of polaron band collapse, for example, upon cooling, leads to a nearly exponential decrease in the density of states in the polaron band [4] and, hence, an equally rapid decrease in the contribution of the electronic subsystem to the total thermodynamic functions of a material. This suggests that, below the temperature of polaron band collapse, there is a certain temperature below which the criterion restricting the possibility of forming the single-phase state becomes invalid. Therefore, these materials should undergo a transition from a homogeneous (single-phase) state of the solid solution type (whose boundaries are determined by the interaction of intercalant ions) to an inhomogeneous (non-single-phase) state as the temperature of a maximum localization is approached. Moreover, it can be expected that the localization of electrons should provide an increase in the Coulomb repulsion between the centers of charge localization and, as a consequence, an ordering of these centers in approximately the same temperature range. It is clear that the above phenomena can be observed only in materials in which the mobility of the ionic subsystem is high enough for relaxation processes in the intercalant lattice to take a reasonable time.

In order to verify these assumptions, we undertook an x-ray structure investigation of the Ag_xTiTe_2 system (which satisfies the above criteria) in the range from room temperature to a temperature well above the polaron band collapse point.

According to the phase diagram, which was obtained using an electrochemical method in our earlier work [5] (Fig. 1), the Ag_xTiTe_2 system has no single-

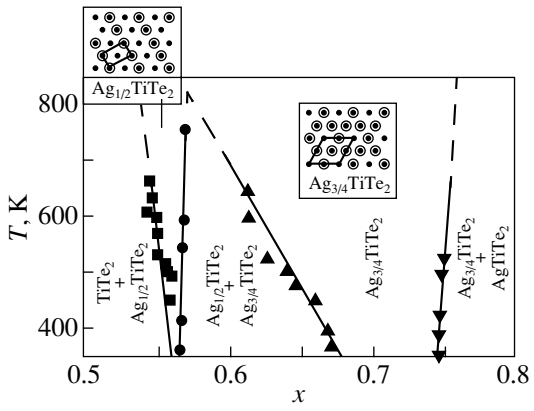

Fig. 1. High-temperature part of the phase diagram of the Ag_xTiTe_2 system. Insets show the ordering of silver in the corresponding phases.

1063-7834/01/4304-0629$21.00 © 2001 MAIK "Nauka/Interperiodica"

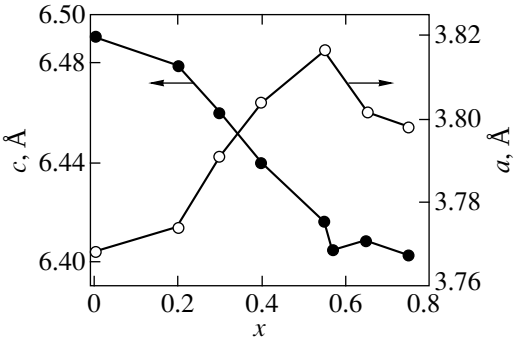

Fig. 2. Concentration dependences of the unit cell parameters of Ag_xTiTe_2 samples after slow cooling and prolonged storage at room temperature.

phase region at temperatures above 150°C at any silver concentrations as small as one likes. Upon intercalation, the conductivity decreases by almost a factor of 1000 and exhibits an activation character [5]. The host lattice layers approach each other due to intercalation [3], and a relative decrease in the conductivity as a function of the relative deformation is described by a relationship typical of other intercalation materials based on titanium dichalcogenides with a polar type of charge carrier localization [1]. The concentration dependence of the conductivity is well represented in the framework of the percolation theory by assuming the presence of Ti–Ag–Ti localized centers that form the sublattice in which polarons of a small radius can occur [6]. Taken together, these observations allow us to conclude that the intercalation of silver into titanium ditelluride brings about the formation of polarons. In this case, the polaron band lies somewhat higher than the Fermi level of the initial material and an increase in the intercalant concentration makes it possible to raise the Fermi level to energies above the top of the polaron band [3].

At the same time, as follows from the x-ray diffraction investigation of Ag_xTiTe_2 samples ($0 < x < 0.5$) which were slowly cooled and stored for a long time at room temperature and, according to [5], corresponded to a mixture of $TiTe_2$ and $Ag_{1/2}TiTe_2$ phases, their x-ray diffraction patterns at this temperature coincide with those of $TiTe_2$. Moreover, the unit cell parameters are found to be monotonic functions of the silver content at $x < 0.65$ (Fig. 2). These findings indicate that the material thus prepared involves only one phase and rule out the assumption made earlier that the second phase can exist in the form of inclusions undetectable by x-ray diffraction. Upon rapid cooling, the phases with ordered silver, which were found in [5] (see Fig. 1), are retained for a few days. Thus, it can be inferred that the polaron band collapse temperature near which the criterion restricting the possibility of forming a single-phase state becomes true [2] lies between room temperature and a temperature of 150°C above which the phase diagram was studied.

The aim of the present work was to elucidate the influence of the polaron band collapse on the possible ordering of polarons associated with impurity centers and on the phase diagram of Ag_xTiTe_2 at different positions of the Fermi level with respect to the polaron band. For this purpose, we investigated the structure of $Ag_{0.3}TiTe_2$, $Ag_{0.55}TiTe_2$, $Ag_{0.57}TiTe_2$, $Ag_{0.65}TiTe_2$, and $Ag_{0.75}TiTe_2$ samples in the temperature range 20–400°C. The location of the Fermi level with respect to the polaron band was evaluated from the following considerations. The $Ag_{0.3}TiTe_2$ composition at temperatures above 150°C falls in the two-phase region and, hence, should meet the condition $E_L < E_F < E_d$ [2]. Among single-phase compositions at temperatures above 150°C, the $Ag_{0.55}TiTe_2$ and $Ag_{0.57}TiTe_2$ samples are least enriched with silver and, as a consequence, should satisfy the condition $E_F \approx E_d$ [2]. For the $Ag_{0.75}TiTe_2$ sample at temperatures above the transition at 130–150°C, the conductivity remains metallic and the Seebeck coefficient retains the negative sign (*n*-type conductivity). In [3], these findings were interpreted by the filling of the impurity band and the shift of the Fermi level to the range of nonlocalized states. Therefore, the condition $E_F > E_h$ is satisfied for this sample. The $Ag_{0.65}TiTe_2$ composition is intermediate between $Ag_{0.57}TiTe_2$ and $Ag_{0.75}TiTe_2$, and, hence, should meet the condition $E_d < E_F < E_h$. Here, E_F is the Fermi level and E_L, E_h, and E_d are the energies at the bottom, top, and center of the polaron band, respectively.

2. EXPERIMENTAL TECHNIQUE

Samples used in this work were prepared by the standard pulse synthesis. The techniques of preparation and characterization were described in detail in [5]. The sample compositions lying in the single-phase region at temperatures above 150°C were electrochemically checked using the calibration curves obtained earlier in [3, 5]. X-ray powder diffraction analysis of the $Ag_{0.57}TiTe_2$ sample was performed on a STOE diffractometer ($CuK_{\alpha 1}$ radiation, Ge monochromator, transmission mode, 5°-linear-response position-sensitive detector, $2\theta = 2°–80°$). The sample was placed in an evacuated capillary 1 mm in diameter, and the measurements were carried out in a high-temperature chamber. The $Ag_{0.30}TiTe_2$ and $Ag_{0.55}TiTe_2$ samples were investigated with a DRON-3.0 x-ray instrument (CuK_α radiation, Ni filter, $2\theta = 22°–60°$) in a GPVT-1500 high-temperature chamber under vacuum (10^{-4} Torr). The high-temperature x-ray diffraction study of the $Ag_{0.65}TiTe_2$ and $Ag_{0.75}TiTe_2$ samples was performed using synchrotron radiation (position-sensitive detector, monochromator selecting a synchrotron radiation wavelength $\lambda = 1.9373$ Å, interplanar distances $d = 1.6–3.6$ Å) in a GPVT-1500 high-temperature chamber (VÉPP-3, Bud-

ker Institute of Nuclear Physics, Siberian Division, Russian Academy of Sciences). Prior to measurements, samples were allowed to stand at a specified temperature for 30 min. The data obtained for all the samples with the use of different instruments and radiation wavelengths demonstrate similar characteristic features in the temperature evolution, which suggests the comparability of these results.

3. RESULTS AND DISCUSSION

The x-ray diffraction patterns of the aforementioned samples at different temperatures and the temperature dependences of the unit cell volume are shown in Figs. 3 and 4, respectively.

For the $Ag_{0.3}TiTe_2$ sample, it is seen that heating leads to the appearance of additional lines which correspond to the superstructure $2a_0 \times 2a_0 \times c_0$ (the phase with a structure of the $Ag_{3/4}TiTe_2$ type [5]), are observed in the temperature range 50–130°C, and disappear upon further heating. The repetition of heating–cooling cycles demonstrated that the order–disorder transition is reversible but requires a prolonged holding (about a week) of the sample at room temperature. The temperature dependence of the unit cell parameters shows a wide scatter in the data in the range of ordering due to a drastic increase in the linewidths in this temperature range. As a consequence, because of the low accuracy of x-ray diffraction data, we could not answer the question as to whether the additional reflections correspond to the precipitation of another phase and the ordering of silver throughout the sample. However, the last assumption seems more probable, because the formation of the $2a_0 \times 2a_0$ superstructure in the case when intercalant atoms occupy an octahedral set of sites in the van der Walls gap becomes possible at a silver content $x = 0.25$, which is close to the silver content in the given sample. On the other hand, according to the electrochemical data, the material under investigation is two-phase when heated above 150°C. The localization of conduction electrons upon heating leads not only to an increase in the contribution of the electronic subsystem to the total thermodynamic functions but also to the enhancement of the Coulomb repulsion between the localization centers associated with intercalated silver. Therefore, it can be assumed that there is a temperature range in which the localization has already been sufficient for the ordering of these centers but insufficient for the phase decomposition through the mechanism proposed in [2].

In the case of $Ag_{0.55}TiTe_2$, the superstructure lines that correspond to the ordering of the $a_0 \times a_0\sqrt{3} \times c_0$ superstructure are observed even at room temperature. On the other hand, the data on the unit cell parameters of this sample fit well in the concentration dependence. This implies that the ordering stems most likely from an insufficient treatment of the sample at room temperature rather than from the stability of this superstructure. For this sample, as for $Ag_{0.3}TiTe_2$, the heating to temperatures in the range 100–110°C leads to a sudden appearance of the lines which are indexed in the $2a_0 \times 2a_0 \times c_0$ superstructure and disappear with further heating. Upon heating above 120°C, we can see only the lines of the $a_0 \times a_0\sqrt{3} \times c_0$ superstructure (the $Ag_{1/2}TiTe_2$ phase in Fig. 1) in complete agreement with the high-temperature part of the phase diagram.

For the $Ag_{0.57}TiTe_2$ sample, no lines differing from the lines of $TiTe_2$ are observed at room temperature. This agrees well with the data for $Ag_{0.3}TiTe_2$ and suggests that the presence of the superstructure in $Ag_{0.57}TiTe_2$ is, most likely, an artifact and that the ordering of silver at room temperature can be achieved only through the ion–ion interaction.

The superstructure lines attributed to $Ag_{0.57}TiTe_2$ appear upon heating to approximately the same temperature as for the other samples; however, the further structural evolution is much more complex. Upon heating to 150°C, we observe the lines of the $a_0 \times a_0\sqrt{3} \times c_0$ superstructure (the $Ag_{1/2}TiTe_2$ phase in Fig. 1) in complete agreement with the high-temperature part of the phase diagram. With further heating to temperatures above 300°C, apart from these lines, we can see the lines corresponding to the $2a_0 \times 2a_0 \times c_0$ superstructure (the $Ag_{3/4}TiTe_2$ phase in Fig. 1). In the phase diagram, this corresponds to the region of a mixture of the $Ag_{1/2}TiTe_2$ and $Ag_{3/4}TiTe_2$ phases. Then, upon heating to 400°C, the lines of the $Ag_{1/2}TiTe_2$ phase disappear, which is associated with the transition to the $Ag_{3/4}TiTe_2$ phase in the single-phase region. The lines of this phase remain stable up to the highest temperatures and exhibit only a gradual thermal broadening.

For the $Ag_{0.65}TiTe_2$ sample, the superstructure lines indexed under the assumption of the $2a_0 \times 2a_0 \times c_0$ superstructure are observed even at room temperature. However, the heating to 130°C leads to a structural transformation responsible for a weakening of the (002) reflection, which completely disappears at 200°C. This can indicate that the $2a_0 \times 2a_0 \times c_0$ ordering gives way to the $2a_0 \times 2a_0 \times 2c_0$ ordering with the same initial space group $P\bar{3}m1$. Apparently, this transition is associated with the orientational ordering of $2a_0 \times 2a_0 \times c_0$ planar networks in the sequence *ABABAB*, where *A* and *B* are one of the four possible sets of vacant octahedral sites ordered according to the $2a_0 \times 2a_0$ motif. The same tendency is observed for $Ag_{0.57}TiTe_2$ samples above 400°C and for the $Ag_{0.75}TiTe_2$ sample in a limited temperature range near 100°C (Fig. 3).

The temperature dependence of the unit cell volume for samples with silver contents $x = 0.65$ and 0.75 exhibits a small minimum at a temperature of ~120°C, which corresponds to the ordering with twice the *c* period. The unit cell volume of the sample with $x = 0.57$

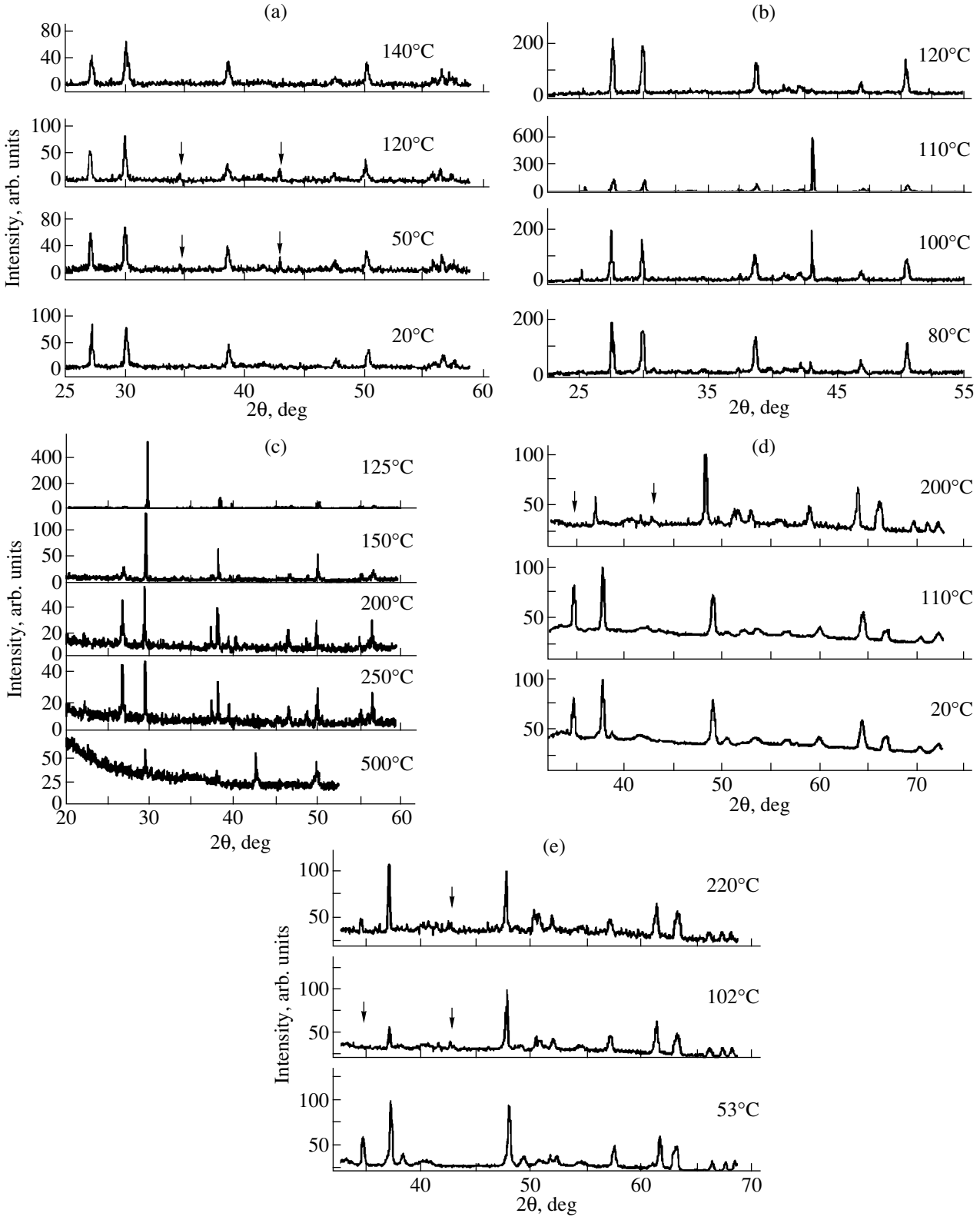

Fig. 3. Fragments of experimental x-ray diffraction patterns obtained at characteristic temperatures for (a) $Ag_{0.3}TiTe_2$, (b) $Ag_{0.55}TiTe_2$, (c) $Ag_{0.57}TiTe_2$, (d) $Ag_{0.65}TiTe_2$, and (e) $Ag_{0.75}TiTe_2$ samples. Arrows indicate the positions of additional reflections associated with the ordering of silver near the polaron band collapse temperature. Conditions: (a, b) Cu K_α radiation, (c) Cu K_{α_1} radiation, and (d, e) synchrotron radiation at the wavelength $\lambda = 1.9373$ Å.

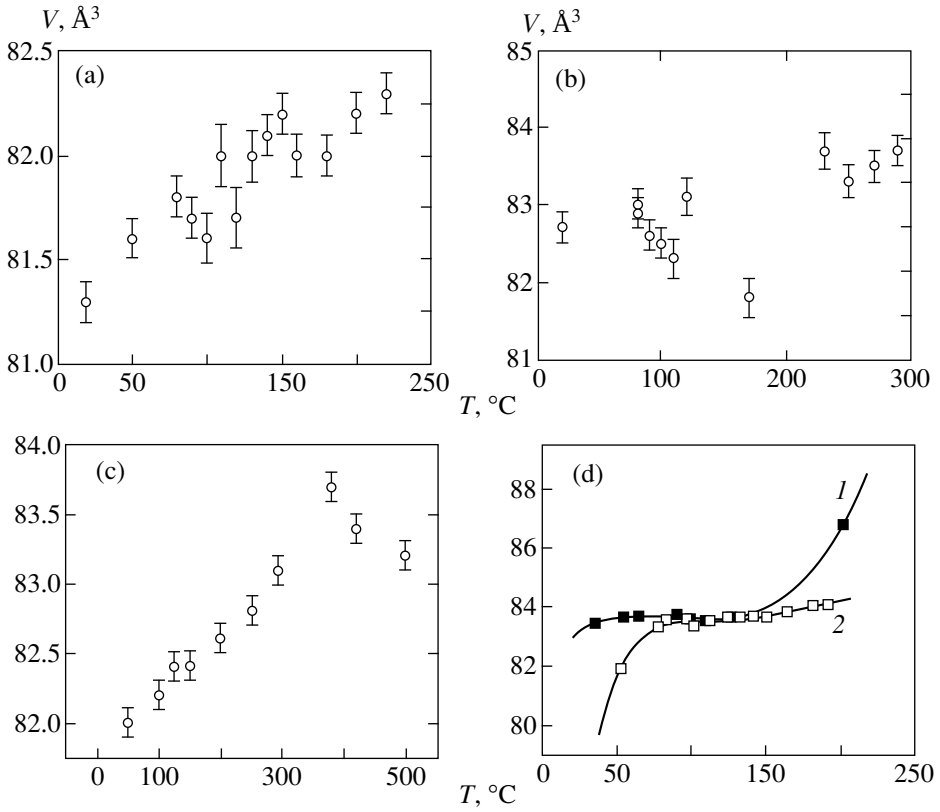

Fig. 4. Temperature dependences of the unit cell volume for Ag_xTiTe_2 without regard for a multiple increase in the parameters due to silver ordering: (a) $Ag_{0.3}TiTe_2$, (b) $Ag_{0.55}TiTe_2$, (c) $Ag_{0.57}TiTe_2$, and (d) (*1*) $Ag_{0.65}TiTe_2$ and (*2*) $Ag_{0.75}5TiTe_2$.

decreases with an increase in temperature above the ordering temperature. The temperature dependence of the unit cell volume for the sample with $x = 0.55$ has a minimum at $T \sim 170$°C. Since the formation of polarons in intercalation materials based on titanium dichalcogenides is usually accompanied by the lattice contraction, the coincidence of temperatures that correspond to the minimum volume and the onset of the ordering confirms the assumption made earlier about the polaron nature of the ordering. The absence of these anomalies in similar dependences for samples with a smaller silver content ($x = 0.33$) can be explained by the separation into phases with different silver contents, which results in a large width of x-ray lines and considerably decreases the accuracy in the determination of lattice parameters.

Therefore, the experimental data on the temperature evolution of the Ag_xTiTe_2 structure are in good agreement with the results of electrochemical investigations into the high-temperature part of the phase diagram for this material [5].

Note that the ordering temperature and the temperature of a minimum in the temperature dependence of the unit cell volume are close to the temperature of the metal–semiconductor transition found in [3] at which the material acquires semiconductor properties upon heating. This allows us to assume that these transitions have the same origin. The coincidence of the high-temperature parts of the phase diagrams obtained by electrochemical and x-ray diffraction methods with substantial differences in the low-temperature parts makes it possible to attribute this transition to the polaron band collapse. Then, the ordering can be ascribed to the localization of electrons on Ti–Ag–Ti centers and its attendant increase in the Coulomb repulsion between these centers. This assumption is in good agreement with the occurrence of an ordered state in a relatively narrow temperature range at low silver concentrations ($Ag_{0.3}TiTe_2$), because the deviation from the polaron band collapse point toward both the high-temperature and low-temperature ranges leads to a broadening of the polaron band and a decrease in the degree of localization of charge carriers. It should be noted that, for materials with $E_d < E_F$, the electronic contribution to the total entropy of the material upon polaron band collapse becomes positive and stabilizes the ordered state [2]. Thus, an increase in the stability of the ordered state with an increase in the silver concentration can be explained by the change in the contribution of the electronic subsystem to the total thermodynamic functions of the material and an increase in the strength of the conventional ion–ion interaction. For $Ag_{0.55}TiTe_2$ and $Ag_{0.57}TiTe_2$ ($E_F \approx E_d$), the contribution of the electronic subsystem to the total thermodynamic functions is

close to zero [2]. Therefore, the onset of the ordering upon heating can be explained only by the enhancement of Coulomb repulsion between Ti–Ag–Ti centers due to the localization of electrons, whereas the other structural transitions occur in accordance with the high-temperature phase diagram and can be interpreted in the framework of the purely ionic model. For samples with compositions lying in the homogeneity region of the $Ag_{3/4}TiTe_2$ phase, the ordering at room temperature can be associated with the usual interaction between intercalated silver ions. This explains its stability over the entire temperature range covered. However, an anomaly of the unit cell volume in the form of a minimum in its temperature dependence and an additional ordering toward the normal to the basal plane are observed in the range of the metal–semiconductor transition which is attributed to the polaron band collapse. It seems likely that this effect should be caused by the enhancement of the Coulomb repulsion between the Ti–Ag–Ti centers (polarons) of electron localization.

It is worth noting that the lattice contraction toward the normal to the basal plane, which is observed already at room temperature (Fig. 2), suggests that the phase diagram of Ag_xTiTe_2 even in its lowest-temperature part is determined not only by pure ionic interactions but is also due to a weak localization of conduction electrons.

4. CONCLUSION

Thus, the enhancement of the Coulomb repulsion at temperatures near the polaron band collapse point can impose certain limitations on the possibility of forming a single-phase state through the condition $E_d < E_F$ and leads to the ordering of polarons formed in this case and, hence, to the appearance of an additional gap in the density of states. In the case of Ag_xTiTe_2, the crossover to the activation conductivity is observed at the ordering temperature with a simultaneous increase in the magnitude of the Seebeck coefficient and the change in its sign [3], which can indicate the gap formation at the Fermi level. On the other hand, the difference between the relaxation time of the electronic properties and the decay time of the ordered state upon cooling to room temperature is very large: the conductivity and the thermopower reach their equilibrium values after holding at room temperature for several hours, whereas the time it takes for the ordering to break down completely is as much as several days. Thus, the problem of the band nature remains unresolved and calls for further investigation.

ACKNOWLEDGMENTS

We are grateful to J.T.S. Irvine and P. Lightfoot (Saint Andrews University, UK) for their assistance in x-ray diffraction measurements and B.P. Tolochko, who aided in performing synchrotron radiation experiments at the Budker Institute of Nuclear Physics, Siberian Division, Russian Academy of Sciences. S.G. Titova expresses her gratitude to the Royal Society for financial support, which made possible performing high-resolution high-temperature x-ray diffraction measurements at Saint Andrews University.

This work was supported by the Russian Foundation for Basic Research (project no. 98-03-32656a), the Ministry of General and Professional Education of the Russian Federation (grant no. 97-0-7.1-169), and in part by the grant REC-005 US CRDF.

REFERENCES

1. A. Titov, S. Titova, M. Neumann, *et al.*, Liq. Cryst. Mol. Cryst. **311**, 161 (1998).
2. A. N. Titov and A. V. Dolgoshein, Fiz. Tverd. Tela (St. Petersburg) **42**, 425 (2000) [Phys. Solid State **42**, 434 (2000)].
3. A. N. Titov, Neorg. Mater. **33**, 534 (1997).
4. A. S. Alexandrov and N. F. Mott, in *Polarons & Bipolarons* (World Scientific, Singapore, 1995), p. 191.
5. A. N. Titov and S. G. Titova, J. Alloys Compd. **256**, 13 (1997).
6. A. N. Titov, Fiz. Tverd. Tela (St. Petersburg) **38**, 3126 (1996) [Phys. Solid State **38**, 1709 (1996)].

Translated by O. Borovik-Romanova

Physics of the Solid State, Vol. 43, No. 4, 2001, pp. 635–639. Translated from Fizika Tverdogo Tela, Vol. 43, No. 4, 2001, pp. 611–615.

SEMICONDUCTORS AND DIELECTRICS

Spin Relaxation of Charged Centers in Silicon in the Presence of Photocarriers (Si : Cr^+, [Cr^+–B^-])

A. A. Konchits and B. D. Shanina

Institute of Semiconductor Physics, National Academy of Sciences of Ukraine, Kiev, 03028 Ukraine

e-mail: Konchits@spin.kiev.ua

Received June 29, 2000; in final form, September 29, 2000

Abstract—Spin relaxation of deep charged centers Cr^+ and of donor–acceptor pairs $(Cr^+–B^-)^0$ in silicon is studied by nonstationary EPR spectroscopy at liquid-helium temperatures. We observed the effect of an increase in the spin–lattice relaxation rate under band-to-band sample illumination; the magnitude of the effect is proportional to the photoelectron concentration. The spin-dependent carrier trapping is shown to play a dominant role in spin relaxation under illumination for centers of both types. Coupled rate equations describing the interaction of various subsystems with one another and with the bath are solved. A comparison of experimental data with theory yielded the electron trapping cross sections $\sigma_r(Cr^+) \cong 4.9 \times 10^{-12}$ cm^2 and $\sigma_r(Cr^+–B^-) \cong 1.6 \times 10^{-12}$ cm^2 at $T = 4.2$ K. The results obtained are discussed in terms of the theory of trapping by attractive centers.

Studies of spin system dynamics and spin-dependent carrier–impurity interactions in semiconductors reveal an intimate relation between the processes of relaxation in a system of local centers and those of electron–hole recombination and thermal ionization of donor (acceptor) centers (see, e.g., reviews [1–4]). The carrier–impurity interactions govern to a considerable extent the efficiency of the present-day optical [2] and electrical [1, 5, 6] detection of magnetic resonance. In particular, they give rise to new mechanisms (spin–lattice relaxation, SLR) involving exchange scattering (ES) of carriers by neutral paramagnetic centers (PC) [7, 8], as well as to the spin orientation of charged PCs through carrier trapping [3, 9].

This paper presents the first study of the effect of photoexcited current carriers on the SLR of charged centers in an elemental semiconductor in the specific example of Cr^+ interstitial centers and $(Cr^+–B^-)$ pairs in Si.

1. EXPERIMENTAL TECHNIQUE AND SAMPLES

The EPR and SLR measurements were conducted on a 3-cm-range superheterodyne spectrometer–relaxometer at liquid-helium temperatures. The Cr^+ PCs were introduced by chromium thermodiffusion at $T \cong 1520$ K to a concentration $N_0 \sim 3 \times 10^{15}$ cm^{-3} into Si samples containing a boron acceptor impurity in a concentration $\sim 7 \times 10^{15}$ cm^{-3}, which were subsequently quenched. Additional annealing of some of the samples at $T \cong 380$ K for 10–30 min produced Si : (Cr–B) pairs with a concentration $N_0 \sim 10^{15}$ cm^{-3}, high enough to allow SLR experiments. The conduction electrons (CE) were generated by illuminating the samples with an incandescent lamp. The light was supplied into the cryostat through a light guide. The free-carrier concentration in a sample was derived from Hall data under illumination.

The pulsed saturation method used here to study the effect of carriers on the SLR of local PCs was employed in two modifications: (i) burning a hole in an inhomogeneously broadened EPR line by a narrow microwave pulse, followed by observation of its subsequent disappearance, and (ii) saturation of the whole EPR line profile by sweeping it with a modulating H field ($f_{mod} = 100$ Hz) simultaneously with the application of a broad microwave pulse.

2. EXPERIMENTAL RESULTS

EPR spectra of single Cr^+ centers and $(Cr^+–B^-)^0$ pairs ($S = 5/2$) in Si were first studied in [10]. Their line intensities in the dark correspond to the equilibrium Boltzmann-distribution values.

When measured under band-to-band illumination, the EPR spectra of these centers change dramatically in shape, which is connected with their spin orientation [3, 9]. Figure 1 displays a simplified diagram of the spin-relaxation experiments and the shape of an EPR spectrum of a spin-oriented $(Cr^+–B^-)^0$ PC system measured in one of the samples studied in this work.

The SLR times τ_1 of single Cr^+ and $(Cr^+–B^-)^0$ pairs measured at $T = 4.2$ K in the dark were found to be similar, $\tau_1 \cong 0.9$ s. Band-to-band excitation was found to reduce the relaxation times of both types of centers strongly (by one to two orders of magnitude). It was established that the magnitude of the effect grows lin-

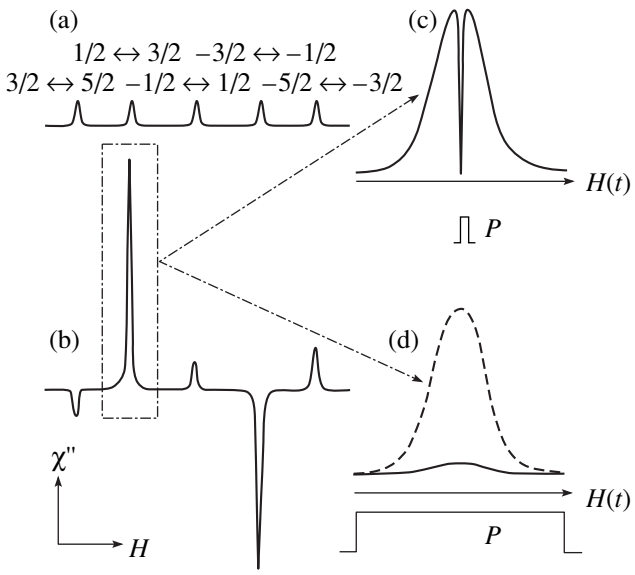

Fig. 1. Schematic of spin-relaxation experiments. Shown on the left is an EPR spectrum of $(Cr^+–B^-)$ pairs in Si obtained (a) in the dark and (b) under illumination. Shown on the right in a scale expanded in H is the result of the application of a microwave pulse: (c) narrow (hole burning) and (d) broad (saturation of the whole line). T = 4.2 K, $\mathbf{H} \parallel [1\bar{1}1]$, and $n \cong 10^8$ cm^{-3}.

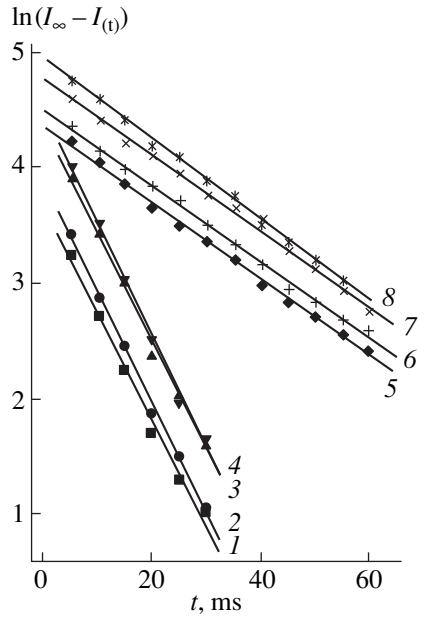

Fig. 2. Magnetization recovery after hole burning in the EPR lines of single Cr^+ PCs and $(Cr^+–B^-)^0$ pairs in Si [(*1*, *3*) and (*5*, *7*), respectively] and after the saturation of the whole line [(*2*, *4*) and (*6*, *8*), respectively]. (*1*, *2*, *7*, *8*, and *3*–*6*) relate to the 1/2 ⟷ 3/2 and –3/2 ⟷ –1/2 transitions, respectively. T = 4.2 K and $n \cong 8 \times 10^7$ cm^{-3}; continuous band-to-band illumination.

early with increasing n in the CE concentration range studied, $n \sim 10^7$–10^8 cm^{-3}.

Figure 2 shows the magnetization recovery in time following hole burning in the Cr^+ and $(Cr^+–B^-)^0$ EPR lines, as well as after saturation of the whole EPR line in the presence of the illumination. To achieve a good signal/noise ratio, the measurements were conducted at the strongest transitions, 1/2 ⟷ 3/2 and –3/2 ⟷ –1/2, in the EPR spectra observed under illumination (Fig. 1). One readily sees that the magnetization recovery rate of a given center does not depend on the transition within the experimental accuracy (±20%). Apart from this, the hole disappearance time τ_{1h}^* coincides with the time τ_1^* characterizing the relaxation following the saturation of the whole line. One also sees from Fig. 2 that the shortening of τ_{1h}^* and τ_1^* under illumination is three times larger for the Cr^+ PC than that for the $(Cr^+–B^-)^0$ donor–acceptor pair (DAP). For T = 4.2 K and $n \cong 8 \times 10^7$ cm^{-3}, the data in Fig. 2 yield the following values: $\tau_{1h}^* \cong \tau_1^* \cong 10$ ms for the Cr^+ centers and $\tau_{1h}^* \cong \tau_1^* \cong 30$ ms for the $(Cr^+–B^-)^0$ pairs.

At $T \cong 1.8$ K, the above relations between the quantities are retained, although the absolute shortening of τ_1 decreases by ~30%.

The data displayed in Fig. 2 were obtained for the $\mathbf{H} \parallel [001]$ and $\mathbf{H} \parallel [1\bar{1}1]$ orientations for the Cr^+ and $(Cr^+–B^-)^0$ PCs, respectively, which correspond to the maximum spin orientation effect of these centers [3, 11]. Measurements of the SLR rate in other **H** directions made under illumination did not reveal, within experimental error, an angular dependence of the τ_{lh}^* and τ_1^* quantities. It was also established that steady-state saturation of either transition in the allowed EPR spectrum of Cr^+ or $(Cr^+–B^-)^0$ under illumination does not produce even a partial saturation of other transitions, unlike the case of the neutral shallow phosphorus centers in Si, where the ES processes are dominant [3, 7].

3. THEORY

Unpolarized band-to-band light creates carriers in a semiconductor with a concentration n. When illuminated, the PCs present in a dark sample in a concentration N_0 become efficient centers of carrier trapping and exchange scattering. The number of CEs with a given spin orientation, $n_\uparrow$ or $n_\downarrow$, varies as a result of the following processes: (i) CEs are generated by light with an infinite spin temperature $\beta_e = (n_\downarrow - n_\uparrow)/(n_\downarrow + n_\uparrow)$ at a constant given generation rate G; (ii) they disappear with the recombination rate over the channels not associated with the given PCs; (iii) the CEs are trapped by PCs at a rate W^+ with formation of states with $j^+ = S + 1/2$, and at a rate W^- to form states with $j^- = S - 1/2$;

(iv) they undergo exchange scattering from PCs with a spin S at a rate W_u; and (v) they are created in the decay of a new center, formed after the trapping, at a thermal dissociation rate $b(T)$.

The PCs with spin S relax and take part in ES; they undergo charge exchange via electron trapping and transform to new PCs with a total angular momentum $j^{\pm} = S \pm 1/2$ and a trapping probability $W^{\pm}$. These new PCs with the concentration $N_{t,j}$ either thermally dissociate afterwards at a rate $b(T)$ or capture a hole, with subsequent electron–hole recombination and formation of PCs with spin S.

The coupled rate equations describing the above processes were derived by one of the present authors in [12]. The dynamics of the system is characterized by the following thermodynamic variables: the CEs are described by n and β_e and the PCs are characterized by macroscopic mean quantities

$$\beta_i = N_0^{-1}\sum_M (-1)^i M^i N_M, \tag{1}$$

which describe the spin orientation and polarization states:

$$\begin{aligned} &\beta_1 = \langle S_z\rangle, \quad \beta_2 = \langle S_z^2\rangle, \quad \beta_3 = \langle S_z^3\rangle, \\ &\beta_4 = \langle S_z^4\rangle, \quad \beta_5 = \langle S_z^5\rangle. \end{aligned} \tag{2}$$

The five variables in Eq. (2) are enough for PCs with a spin $S = 5/2$, and β_6 can be expressed through the above quantities: $\beta_6 = 3.516–16.1875\beta_2 + 8.75\beta_4$.

If the PC concentration does not change significantly in the course of the charge exchange, one may assume $\beta_0 \cong 1$. The equilibrium values are unambiguously defined by Eq. (1), and in the high-temperature approximation ($\varepsilon = \hbar\omega/kT \ll 1$), we have

$$\begin{aligned} &\beta_0 = 1, \quad \beta_{20} = S(S+1)/3 = 2.917, \\ &\beta_{40} = (-S(S+1) + 3S^2(S+1)^2)/15, \\ &\beta_{10} = \varepsilon\beta_2, \quad \beta_{30} = \varepsilon\beta_4, \quad \beta_{50} = \varepsilon\beta_0. \end{aligned}$$

Equation (1) permits one to express the population difference P_{ij} for any pair of levels through β. For instance, for the $P_{13} = N_{1/2} - N_{3/2}$ transition undergoing saturation we obtain

$$\begin{aligned} P_{13}(t) = {} & 175/256 - 73\beta_2(t)/96 + 5\beta_4(t)/48 \\ & - 475\beta_1(t)/384 + 47\beta_3(t)/48 + \beta_5(t)/8. \end{aligned} \tag{3}$$

As we established earlier from an analysis of stationary experiments on Cr^+ spin orientation in Si [3], the ratio of the probability of CE trapping, $W = W^+ + W^-$, to that of CE exchange scattering, W_u, is considerably in excess of unity and W greatly exceeds the PC SLR rate in the dark (at liquid-helium temperatures). For this reason, in the rate equations, we shall retain only the terms containing the spin-dependent CE trapping by the PCs.

In accordance with [11], we define the "weighted" probabilities of electron trapping by a PC with the formation of a new complex center in states with $j^{\pm} = S \pm 1/2$ as

$$W^+ = R^+(S+1)/(2S+1), \quad W^- = R^-S/(2S+1), \tag{4}$$

where $R^{\pm} = \sigma_r \bar{v} N$, σ_r is the trapping cross section and $\bar{v}$ is the thermal velocity.

In the final equations, one can conveniently use the total trapping probability W and the spin-dependent trapping coefficient α [1]

$$\alpha W = 0.5(R^- - R^+)/(2S+1). \tag{5}$$

If the spin-dependent trapping is considered a dominant process and if $S = 5/2$ is assumed, the coupled equations derived in [12] lead one to a system of rate equations for the thermodynamic variables β_e and β_i

$$\begin{aligned} \dot\beta_e &= -W\left[\beta_e - 2\alpha\beta_1 - \frac{1}{2}(1-2S\alpha)(x_5 + \beta_e y_5)\right], \\ \dot\beta_1 &= -W\frac{n}{2N}\left[-\beta_e + 2\alpha\beta_1 + \frac{1}{2}(1-2S\alpha)(x_5 + \beta_e y_5)\right] \\ &\quad - W_u\frac{n}{N}\left[\beta_1 - (S(S+1) - \beta_2)\beta_e - \frac{35}{6}\varepsilon\frac{\Delta g}{g}\right] - \frac{\beta_1 - \beta_{10}}{T_1}, \\ \dot\beta_3 &= -W\frac{n}{N}[3\alpha\beta_3 - 0.5(3-2\alpha)\beta_1 \\ &\quad - 0.5\beta_e(1 + 3(1-2\alpha)\beta_2) \\ &\quad + \frac{109}{16}(1-2S\alpha)(x_5 + \beta_e y_5)\Big], \\ \dot\beta_5 &= -W\frac{n}{N}\left[5\alpha\beta_5 - \frac{5}{4}(1-2\alpha)\beta_3 - \left(\frac{5}{2} - \alpha\right)\beta_1\right. \\ &\quad + \beta_e\left(-\frac{225}{16}\alpha + \left(5 - \frac{219}{8}\alpha\right)\beta_2\right. \\ &\quad \left.\left. + \frac{5}{2}(1-11\alpha)\beta_4 - 2\alpha\beta_6\right)\right], \\ \dot\beta_2 &= -W\frac{n}{N}[2\alpha\beta_2 - 0.5 + 1.5(1-2S_\alpha)y_5], \\ \dot\beta_4 &= -W\frac{n}{N}\left[4\alpha\beta_4 - (3-4\alpha)\beta_2 - 0.5\right. \\ &\quad \left. + \frac{111}{4}(1-2S\alpha)y_5\right]. \end{aligned} \tag{6}$$

Equations (6) make use of the notation $\Delta g = g - g_e$, where g and g_e are the PC and CE g factors, respectively; $x_5 = N_{-5/2} - N_{5/2} = 3\beta_1/320 - \beta_3/24 + \beta_5/60$; and $y_5 = N_{-5/2} + N_{5/2} = 3/128 - 5\beta_2/48 + \beta_4/24$.

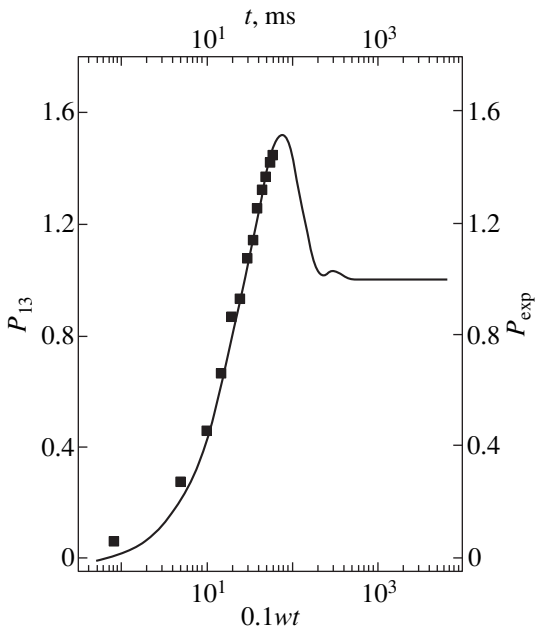

Fig. 3. Recovery of the 1/2 ⟷ 3/2 transition after its saturation by a microwave pulse under illumination. The solid line is theory (see text) and the symbols are experiment. T = 4.2 K.

Let us follow the evolution of the PC spin system for the experimentally realized case of cw excitation of the sample and total saturation of the 1/2 ⟶ 3/2 transition by a microwave pulse. These initial conditions correspond to the following population differences P_{ij} [P_{ij} are determined by the amplitude ratio of the observed transition to the transition corresponding to an equilibrium difference of the populations of the neighboring pair of levels, which is equal to (1/6)ε]:

$$P_{3,5}(t=0) = -(1/6)\varepsilon, \quad P_{1,3}(t=0) = 0,$$
$$P_{-1,1}(t=0) = (1/6)\varepsilon, \qquad (7)$$
$$P_{-3,-1}(t=0) = -(8/6)\varepsilon, \quad P_{-5,-3}(t=0) = (1/6)\varepsilon.$$

By definition in Eq. (1), the following initial values of β_i correspond to these conditions:

$$\beta_1(t=0) = 0.0172, \quad \beta_2(t=0) = 2.43,$$
$$\beta_3(t=0) = 0.1062, \quad \beta_4(t=0) = 11.9, \qquad (8)$$
$$\beta_5(t=0) = 1.3.$$

Equations (6), subject to the initial conditions (8), can be solved to yield

$$\beta_2 = 2.294 + 0.18\exp(-0.272wt) - 0.05\exp(-0.746wt),$$
$$\beta_4 = 11.5091 + 1.18\exp(-0.272wt) - 0.79\exp(-0.746wt), \qquad (9)$$

$$\beta_1(t) = 0.078 - 0.061\exp(-0.327uwt),$$
$$\beta_3(t) = 0.331(1 + 0.0674\exp(-0.272wt) - 0.0031\exp(-0.746wt)) - (0.225\cos(0.256wt) + 0.03\sin(0.256wt))\exp(-0.156wt), \qquad (10)$$
$$\beta_5(t) = 1.82(1 + 0.024\exp(-0.272wt) - 0.006\exp(-0.746wt)) - (0.52\cos(0.256wt) + 0.86\sin(0.256wt))\exp(-0.156wt).$$

Here, $u = W_u/W$ and $w = Wn/N$.

Substitution of Eqs. (9) and (10) into Eq. (3) yields the recovery function of the spectral transition $P_{13}(t)$ after saturation of this transition in the presence of unpolarized band-to-band illumination; this function is shown graphically in Fig. 3. The symbols in the plot are the data derived from the experiment.

4. DISCUSSION OF RESULTS

The results of our experiments, including the equality of τ_{1h}^* and τ_1^*, indicate that carrier trapping plays a dominant role in the spin relaxation of the Cr^+ and $(Cr^+–B^-)^0$ centers under band-to-band excitation. Indeed, if there is trapping, the burnt hole cannot relax through double exchange scattering [7, 8], where a carrier takes the spin energy from a PC in one ES event only to impart it in the next event to another PC, a process in which the energy is transferred from the "hot" (microwave pulse-saturated) part of the EPR line to its "cold" part, without it being absorbed by the lattice. In the absence of such CE-stimulated spectral diffusion, one may expect both the equality of τ_{1h}^* and τ_1^* and no saturation dissipation throughout the EPR spectrum under a stationary saturation of one of its components, which is exactly what is observed in our experiments. This conclusion is also in agreement with the results obtained in stationary experiments on the spin orientation of the Cr^+ centers in Si, whose analysis [3] suggests that $W_u/W \ll 1$.

The data obtained allow determination of the cross sections σ_r for low-temperature CE trapping by the Cr^+ and $(Cr^+–B^-)^0$ paramagnetic centers. As follows from definition (4), Eq. (6), and Fig. 3, $(\tau_1^*)^{-1} = 0.1W(n/N) = 0.1n\sigma_r\bar{v}$. Accepting $\bar{v} = 2.55 \times 10^6$ cm/s (for T = 4.2 K) and the measured values of $(\tau_1^*)^{-1}$ and n, we come to $\sigma_r(Cr^+) \cong 4.9 \times 10^{-12}$ cm^2 and $\sigma_r(Cr^+–B^-) \cong 1.6 \times 10^{-12}$ cm^2. These figures are quite large, exactly what should be expected in the case of trapping by attractive centers (see, e.g., review [13]); however, the value of $\sigma_r(Cr^+)$ is still less by an order of magnitude than that expected from theory for trapping by a single Coulomb center (see Eq. (5) in [13]). The reason for this lies in that the donor and acceptor concentrations in

our samples are high and the fluctuations of the trapping center potential E_0 play a substantial part. The conditions of our experiment correspond to the situation of $E_0 > kT > ms^2$ considered in [13]. In this case, the comparison should be performed in terms of the theory of trapping by a dipole potential [14]. Indeed, a quantitative estimation of $\sigma_r(Cr^+–B^-)$, made using Eqs. (A4) and (A5) in [14] with a $(Cr^+–B^-)$ DAP dipole length $d = 3 \times 10^{-8}$ cm, yields $\sigma_r(Cr^+–B^-) = 0.5 \times 10^{-12}$ cm^2, a figure close to our result. Because $\sigma_r(Cr^+)$ is of the same order of magnitude, this suggests that, in the case of Cr^+ centers, because of the donors and acceptors being present in high concentrations in our samples, the carriers are also trapped by a dipole potential with randomly distributed dipole lengths, while the real concentration of centers with a pure Coulomb potential is an order of magnitude lower. The decrease of the effect of illumination on the SLR observed to occur for both centers as the temperature is lowered to 1.8 K is due to the decrease of $\bar{v}$.

The absence of an angular dependence of τ_1^* within the experimental accuracy can be readily accounted for by the fact that this quantity is determined by the practically isotropic total trapping probability $W = W^+ + W^-$. At the same time, the spin orientation efficiency is dominated by the spin-dependent trapping coefficient $\alpha \propto W^+ - W^-$, which, because of its being governed by the local crystal field for the spin systems under study here [3, 9], depends substantially on the direction of **H**.

We note in conclusion that the magnitude of σ_r can be found by measuring the rate with which spin orientation sets in. However, the kinetics of these processes is complicated by the PC charge exchange occurring when the light is turned on or off, as well as by the presence of the corresponding long exponentials in the photocurrent rise. By contrast, our approach neglects only the change in the CE concentration when the microwave pulse is turned on or off, which is due to the spin-dependent recombination [1]. Indeed, this recombination channel may be created by the capture of carriers of the opposite sign, for instance, of holes on the $\{Cr^+ + e\}$ centers [15]. However, the relative change in the free carrier concentration observed to occur at the EPR transition saturation does not practically exceed 10^{-4}–10^{-3} [1, 5].

REFERENCES

1. I. Solomon, Top. Appl. Phys. **36**, 190 (1979).
2. S. Depinna, B. C. Cavenett, I. G. Austin, *et al.*, Philos. Mag. B **46** (5), 473 (1982).
3. A. A. Konchits and B. D. Shanina, in *Radiospectroscopy of Solid State* (Naukova Dumka, Kiev, 1992).
4. J.-M. Spaeth, in *Modern Application of EPR/ESR from Biophysics to Materials Science: Proceedings of the First Asia-Pacific EPR/ESR Symposium, Hong-Kong, 1997* (Springer, 1978), p. 587.
5. M. S. Brandt and M. Stutzman, Appl. Phys. Lett. **61** (21), 2569 (1992).
6. L. S. Vlasenko and M. P. Vlasenko, Mater. Sci. Forum **196–201** (3), 1537 (1995).
7. G. Feher and E. A. Gere, Phys. Rev. **114** (5), 1245 (1959).
8. M. F. Deĭgen, V. Ya. Bratus', B. E. Vugmeĭster, *et al.*, Zh. Éksp. Teor. Fiz. **69** (6), 2110 (1975) [Sov. Phys. JETP **42**, 1073 (1975)].
9. A. A. Konchits and B. D. Shanina, Fiz. Tverd. Tela (Leningrad) **28** (2), 399 (1986) [Sov. Phys. Solid State **28**, 221 (1986)].
10. G. W. Ludwig and H. H. Woodbury, Solid State Phys. **13**, 223 (1962).
11. L. D. Landau and E. M. Lifshitz, *Course of Theoretical Physics*, Vol. 3: *Quantum Mechanics: Non-Relativistic Theory* (Nauka, Moscow, 1989, 4th ed.; Pergamon, New York, 1977, 3rd ed.).
12. B. D. Shanina, Fiz. Tverd. Tela (Leningrad) **28** (1), 95 (1986) [Sov. Phys. Solid State **28**, 50 (1986)].
13. V. N. Abakumov, V. I. Perel', and I. N. Yassievich, Fiz. Tekh. Poluprovodn. (Leningrad) **12** (1), 3 (1978) [Sov. Phys. Semicond. **12**, 1 (1978)].
14. V. N. Abakumov, V. I. Perel', and I. N. Yassievich, Zh. Éksp. Teor. Fiz. **72** (2), 674 (1977) [Sov. Phys. JETP **45**, 354 (1977)].
15. H. Conzelmann, K. Graff, and E. R. Weber, Appl. Phys. A **30** (3), 169 (1983).

Translated by G. Skrebtsov

Physics of the Solid State, Vol. 43, No. 4, 2001, pp. 640–643. Translated from Fizika Tverdogo Tela, Vol. 43, No. 4, 2001, pp. 616–618.

SEMICONDUCTORS AND DIELECTRICS

Acoustic-Emission Probing of Line Defects in Silicon

A. A. Skvortsov, A. M. Orlov, and A. A. Solov'ev

Ul'yanovsk State University, ul. L'va Tolstogo 42, Ul'yanovsk, 432700 Russia

Received July 14, 2000; in final form, October 5, 2000

Abstract—The acoustic emission of donor silicon is studied. It is shown that the sound emission is due to the electric-current-stimulated motion of edge dislocations. When varying the current density flowing through a dislocated crystal, a correlation between the maximum of the acoustic-emission spectrum of the silicon and the velocity of the line-defect motion is revealed. By matching the theory with the experimental data, we estimate the diffusion constants of the atoms in the dislocation impurity atmosphere and the effective charge per atom in a dislocation line at different times (0.3–3 h) of the isothermal annealing (1273 K) of silicon samples. *© 2001 MAIK "Nauka/Interperiodica".*

INTRODUCTION

Acoustic emission, i.e., the emission of elastic waves which accompanies a rearrangement of the internal structure of condensed media, has been known beginning from the mid 1950s [1–3]. The physical mechanism explaining a number of specific features of the acoustic emission in dislocated crystals is the motion of dislocations and their clusters. The acoustic emission is of interest, because the dislocations themselves are the sources of sound waves and, therefore, it is easier to reveal and localize the defects in this case. Moreover, the acoustic emission signals contain information on the kinetics and mechanisms of the defect motion in this case [1, 3].

In spite of this, the number of works considering acoustic emission in semiconductors is extremely small. In addition, there has been almost no comparative analysis of the dislocation motion and spectral distribution of acoustic noise in semiconductors. The acoustic emission of a doped semiconductor subjected to thermal treatment has also not been considered. In this paper, we analyze acoustic emission in silicon and compare it with the electric-current-stimulated dynamics of line defects in dislocated silicon samples subjected to different thermal treatments.

1. EXPERIMENTAL

Dislocation-free single-crystal silicon laminas of the *n* type (phosphorus) and *p* type (boron) with a resistivity of 0.01–0.05 Ω cm were studied. The laminas were oriented along the [111] axis; their sizes were $15 \times 5 \times 0.4$ mm along the $[11\bar{2}]$, $[1\bar{1}0]$, and [111] axes, respectively. As in [4], the dislocations were introduced by applying a load to the laminas along the [111] axis. The defect density did not exceed $N_d \le 1 \times 10^7$ cm^{-2}. The dislocated samples were isothermally annealed in a resistance furnace at 1273 K for 0.3–3 h.

The acoustic emission was induced by the electric-current-stimulated motion of edge dislocations without applying an additional mechanical load. For this purpose, an electric current ($j < 5 \times 10^5$ A/m^2) was passed through the sample along the $[11\bar{2}]$ axis. The temperature was varied by the use of an external resistance heater ($T \le 430$ K). Following the method developed in [4], the acoustic emission signals $U(t)$ were detected by a piezoelectric sensor situated on the surface of the lamina investigated. The spectral distribution of the acoustic-emission signals $U(\omega)$ was determined by Fourier analysis of the initial oscillogram $U(t)$ [4, 5].

2. RESULTS AND DISCUSSION

The results of the investigation indicated a significant difference in the acoustic-emission signals between dislocation-free (curve *1* in Fig. 1) and dislocated silicon samples (curve 2 in Fig. 1). At the same electric-current parameters, an increase in the average density of dislocations in the sample, N_d, activates the processes of the acoustic emission (cf. curves *2–4* in Fig. 1), which obviously reveals the dislocation nature of the response observed.

To describe the motion of the defects, let us consider the radiation field V_i produced by a system of moving dislocations [6]

$$\rho \frac{\partial V_i(r, t)}{\partial t} - \frac{\partial \sigma_{ik}(r, t)}{\partial x_k} = f_i(r, t). \qquad (1)$$

Here, the vector f_i characterizes the bulk forces due to the motion of the crystal elements, σ_{ik} is the stress tensor produced by the system of the moving dislocations, and ρ is the crystal density. In the presence of moving

1063-7834/01/4304-0640$21.00 © 2001 MAIK "Nauka/Interperiodica"

dislocations, the radiation field is defined by the equation [6]

$$V_i(r, \tau) = -\frac{c_t}{2\pi r}\sum_{m=l,t}\frac{\Phi_{iks}^{(m)}}{c_m^3}\int\frac{\partial^2}{\partial t^2}j_{ks}dr. \quad (2)$$

Here, the index m stands for l and t which correspond to the longitudinal and transverse waves, respectively; c_m is the velocity of the corresponding acoustic waves; the quantities $\Phi_{iks}^{(m)}$ are functions of the wave normals n_i, n_k, and n_s; and j_{ks} is the dislocation flux density tensor. It is seen from Eq. (2) that the radiation emitted by the dislocation system (the acoustic field) $V_i(r, \tau)$ would be expected to occur only for their nonstationary motion, when the second derivative of the dislocation-flux density tensor j_{ks} is nonzero. This means that, in the process of the current-stimulated plasticization of the dislocated silicon, the acoustic emission signal appears only when dislocations move at varying velocities. In this case, the average velocity v of the ordered migration of the defects will be connected with the characteristic transition frequency of dislocations between two stable states, f_{max}, by the formula

$$v = af_{max}, \quad (3)$$

where a is the magnitude of a jump.

In order to test relationship (3), the acoustic-emission spectra were measured simultaneously with the monitoring of the dislocation migration rate in an electric field by the method of iterated selective etching [5]. Analysis of the paths of line defects performed over ~100 individual dislocations indicated that the edge dislocations move mainly to the positive electrode in *n*-Si and to the negative one in *p*-Si. The results of these investigations at a fixed current density are presented in Fig. 2. An increase in j gives rise to a regular growth in the velocity of motion of the edge dislocations in the silicon and a shift of the maximum of the acoustic-emission spectrum to the high-frequency region. The results of these studies are shown in Fig. 3. From this figure, the value $a = 0.13$ nm is found as the slope of the v versus f_{max} plot. This value corresponds to the interplanar spacing for the series of the (111) planes in silicon (0.134 nm).

Thus, the electric current passing through the sample expels the dislocations even at room temperature, which affects the acoustic-emission spectra. The current-stimulated influence on the ordered dislocation transport consists of the ion-drag and electron-(hole-) wind forces. Taking this into account, one can obtain a relation between j and f_{max} [5]:

$$j = \frac{1}{\Phi_1}\left(\frac{E_{p2}}{kT} + \ln(\Phi_2 f_{max}) + \Phi_3 f_{max}\left(\ln\frac{f_{max}}{\Phi_4}\right)\right), \quad (4)$$

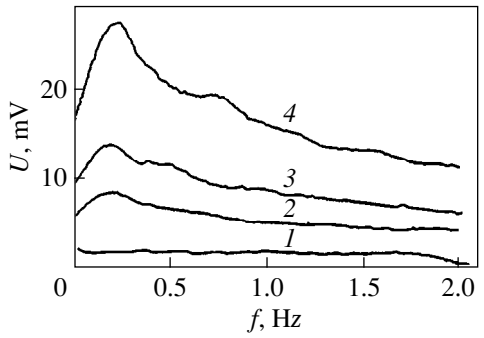

Fig. 1. Acoustic emission spectra of dislocated *n*-type silicon samples at a density current 4.5×10^5 A/m^2 flowing through them: (*1*) the dislocation-free sample and the dislocated sample with different dislocation density (cm^{-2}): (*2*) 8×10^5; (*3*) 2×10^6; and (*4*) 5×10^6.

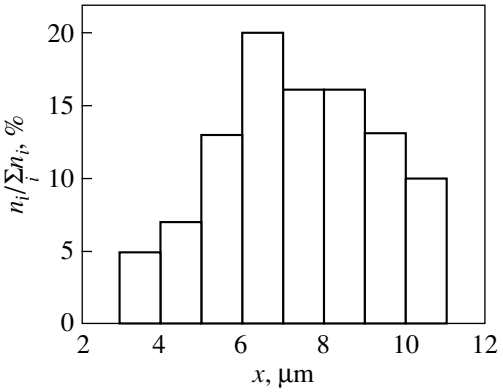

Fig. 2. The distribution of the dislocation free paths x in the *n*-type silicon ($\rho = 0.015$ Ω cm) at the electric current density $j = 3 \times 10^5$ A/m^2. The average density of dislocations in the sample is 5×10^8 cm^{-2}.

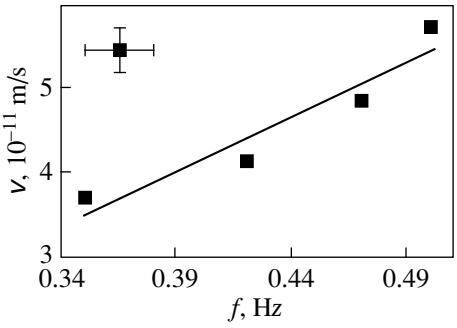

Fig. 3. Dependence of the dislocation expelling rate v by the electric current upon the acoustic emission maximum f_{max} at the same parameters of the electric current for the *n*-type silicon samples (0.015 Ω cm).

Characteristic parameters of the electron transfer in the dislocated (1×10^6 cm^{-2}) *n*-type silicon doped by phosphorus ($\rho = 1.5 \times 10^{-4}$ Ω m, $c_0 = 7 \times 10^{24}$ m^{-3})

Annealing time *t*, min	r_0, nm	$\Phi_1 \times 10^7$, m^2/A	$\Phi_2 \times 10^5$, s	Φ_3, s	Φ_4, s^{-1}	Z_{eff}, 1/atom	$V_0 \times 10^5$, m/s	$D_d \times 10^{18}$, m^2/s
20	5.8	3.5	0.723	4.23	1.75	0.012	1.8	1.3
70	7.2	3.3	1.070	6.53	1.11	0.011	1.2	1.0
115	8.9	3.1	1.357	8.35	0.86	0.011	0.96	1.0
175	9.9	1.7	1.305	8.32	0.85	0.006	0.96	1.0

where

$$\Phi_1 = \frac{eZ_{\text{eff}}N_{\text{at}}b\rho}{kT}, \quad \Phi_2 = \frac{a}{V_0},$$

$$\Phi_3 = \frac{\pi c_0 \gamma L b a}{2D_d(kT)^2}, \quad \Phi_4 = \frac{D_d}{ar_0},$$

are dimensional constants.

Here, N_{at} and Z_{eff} are the number of atoms and effective charge, respectively, per unit length of a dislocation in the presence of an impurity atmosphere; n, p, l_n, and l_p are the equilibrium concentrations and free paths of the electrons and holes; e is the elementary charge; L is the dislocation length; D_d is the diffusion constant of atoms within the defect region of the impurity atmosphere; c_0 is the equilibrium impurity concentration in a defect-free region of the crystal; γ is a dimensional constant; b is the Burgers vector; and V_0 is a constant having the dimension of the velocity [5].

It is seen that an increase in the current load should result in a shift of the maximum of the acoustic-emission spectrum along the frequency axis. Figure 4 (curve *1*) graphically illustrates this by the example of the *n*-type silicon. With the calculated values of Φ_i (see table) and the kind II Peierls barrier ($E_{p2} \approx 0.5$ eV) [4], there is a good agreement between the experiment and Eq. (2). This permits one to determine the effective charge Z_{eff} and diffusion constant D_d.

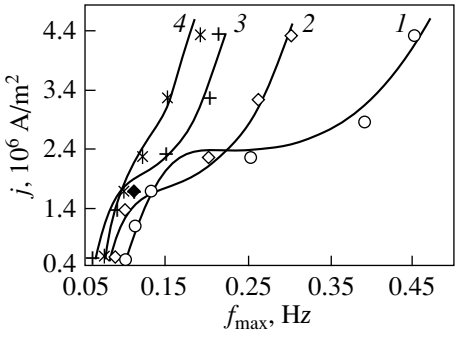

Fig. 4. Electric-current dependence of the maximum of the acoustic-emission spectra at different times of the isothermal annealing of the samples ($T_{\text{an}} = 1273$ K), t (min): (*1*) 20; (*2*) 70; (*3*) 115; and (*4*) 175.

As follows from Eq. (2), the acoustic emission in a semiconductor contains information about the transport processes involving the line defects. Therefore, a change in the state of the object "dislocation core–impurity cloud" should lead to a change in the dynamics of the emission spectra. To verify this prediction, we measured the current dependences of $f_{\max}$ after isothermal annealing.

According to these measurements, an increase in the duration of the thermal "load" leads to a change in the current dependence of $f_{\max}$ and, therefore, to a change in v. Indeed, according to the equation [7]

$$r_0^4 = 8\frac{DWb^2t}{kT}, \tag{5}$$

isothermal annealing of dislocated samples increases the size of the impurity atmosphere r_a around a dislocation. In Eq. (5), D is the bulk diffusion constant of the impurity atoms, W is the binding energy, kT is the thermal energy, and t is the duration of the thermal treatment. The change in the annealing time from 20 to 175 min leads to an increase in r_0 by 50% (see table). This certainly affects the defect mobility because of a "weighting" of the impurity atmosphere, which is revealed in the effective charge per unit dislocation length becoming twice as small in the presence of the impurity atmosphere (see table). Figure 4 illustrates these processes; it can be seen from Fig. 4 that the changes in the dislocation kinetics after the isothermal annealing affect the acoustic emission spectra. For example, the largest changes $\left.\frac{\partial f_{\max}}{\partial j}\right|_{t = 0.5\text{ h}} = 10^{-6}$ (Hz m^2)/A and $\left.\frac{\partial f_{\max}}{\partial j}\right|_{t = 3\text{ h}} = 4 \times 10^{-7}$ (Hz m^2)/A for different annealing times differ more than two times.

3. CONCLUSIONS

Thus, the acoustic emission caused by the electric-current-stimulated motion of edge dislocations in silicon is investigated in this paper. The influence of the isothermal annealing on the emission is also studied. When varying the current density flowing through the

sample, a distinct correlation between the maximum in the acoustic-emission spectra of the silicon and the velocity of the line defects is revealed. It is supposed that the mechanism of the dislocation motion is associated with the transition of the dislocation (or its fragment) into a neighboring quasi-equilibrium position, which is accompanied by the diffusive drag of the impurity atoms. It is shown that an increase in the annealing time of dislocated samples of the semiconductor leads to a decrease in the mobility of the line defects.

ACKNOWLEDGMENTS

This work was supported by the RF Ministry of Higher Education Program "Degradation Processes in Multilayer Thin-Film Structures" and by the Russian Foundation for Basic Research, project no. 98-02-03335.

REFERENCES

1. V. A. Greshnikov and Yu. B. Drobot, *Acoustical Emission* (Izd. Standartov, Moscow, 1976).
2. T. Suzuki, H. Yosinaga, and S. Takeucti, *Dislocation Dynamics and Plasticity* (Syokabo, Tokyo, 1986; Mir, Moscow, 1989).
3. A. M. Kosevich, *Dislocation in Theory of Plasticity* (Naukova Dumka, Kiev, 1978).
4. A. M. Orlov, A. A. Skvortsov, and V. A. Frolov, Pis'ma Zh. Tekh. Fiz. **25** (3), 28 (1999) [Tech. Phys. Lett. **25**, 95 (1999)].
5. A. A. Skvortsov, A. M. Orlov, V. A. Frolov, and A. A. Solov'ev, Fiz. Tverd. Tela (St. Petersburg) **42** (11), 1998 (2000) [Phys. Solid State **42**, 2054 (2000)].
6. V. D. Natsik and K. A. Chishko, Fiz. Tverd. Tela (Leningrad) **14** (11), 3126 (1972) [Sov. Phys. Solid State **14**, 2678 (1972)].
7. J. Friedel, *Dislocations* (Pergamon, Oxford, 1964; Mir, Moscow, 1967).

Translated by A. Poushnov

Physics of the Solid State, Vol. 43, No. 4, 2001, pp. 644–651. Translated from Fizika Tverdogo Tela, Vol. 43, No. 4, 2001, pp. 619–626.

SEMICONDUCTORS AND DIELECTRICS

Dispersive Characteristics of Diamond in the Range of Hard X-ray Waves

A. G. Tour'yanskiĭ, I. V. Pirshin, R. A. Khmel'nitskiĭ, and A. A. Gippius

Lebedev Physical Institute, Leninskiĭ pr. 53, Moscow, 117924 Russia

e-mail: tour@sci.lebedev.ru

Received July 6, 2000; in final form, August 17, 2000

Abstract—Dispersive properties of natural diamonds were studied for the first time in a range of x-ray wavelengths of 0.03–0.2 nm. The dispersion element represented an analog of a rectangular prism. A collimated beam of polychromatic radiation was directed onto the refracting face from inside under a small glancing angle ($\ll\pi/2$). The radiation was introduced into the prism through a side face oriented perpendicularly to the axis of the incident beam. In the range of energies near 8 keV, a resolution of 106 eV was achieved, which is about twice as good as the corresponding parameter for semiconductor detectors. Calculations show that under ideal conditions the limiting resolution for a diamond prism with a single refracting face can be reduced to 36–40 eV. This makes it possible to create a new type of analytical devices—dispersion x-ray spectrometers for the investigation of rapid processes involving generation and absorption of x-ray radiation. © *2001 MAIK "Nauka/Interperiodica".*

INTRODUCTION

For a detailed analysis of spectra of x-ray radiation propagating in a given direction in the range of $\lambda <$ 0.3 nm, monochromators made of perfect single crystals are used as a rule [1, 2]. For a fixed orientation of the unit vector $\mathbf{S}_0$ that characterizes the specified direction, reflection can occur only in narrow spectral intervals in accordance with the Bragg condition for diffraction. Therefore, in order to investigate the total spectrum in a wide spectral range, it is necessary to mechanically rotate the monochromator and multiply repeat measurements. It is obvious that such a method is inapplicable for the investigation of nonstationary fast processes, e.g., those occurring upon irradiation of a target with a power laser pulse [3]. Note that in practice the spectrum of the radiation that is reflected from a crystal monochromator is frequently detected using a photographic plate or other types of two-dimensional position detectors [4]. However, the condition of the constancy of $\mathbf{S}_0$ is violated in this case.

Pulsed radiation spectra also cannot be studied using cooled semiconductor detectors [5], since a fundamental condition for them to operate is a successive registration of isolated quanta in time intervals of $\geq$10 μs [6]. Diffraction gratings, which are widely used in the optical and soft x-ray spectral ranges, possess a low efficiency (~1%) at wavelengths less than 0.3 nm [7, 8]. In addition, uncontrolled distortions caused by the strong anisotropy of scattering are superimposed onto the spectrogram, since in the case of artificial periodic structures the radiation wavelength λ is much smaller than the grating period *p*.

Thus, at present, there is likely to be no suitable experimental means for the spectrometry of directional polychromatic beams of hard x-ray radiation generated during fast nonstationary processes.

In this work, we show for the first time that the dispersive properties of diamonds make it possible to decompose spectra of hard x-ray radiation with wavelengths down to 0.03 nm (E = 40 keV) and, owing to angular dispersion, to analyze the spectra of both stationary and pulsed sources without any limitations on the pulse duration.

1. EXPERIMENTAL

Figure 1 displays a schematic of an experimental setup we designed to perform dispersion measure-

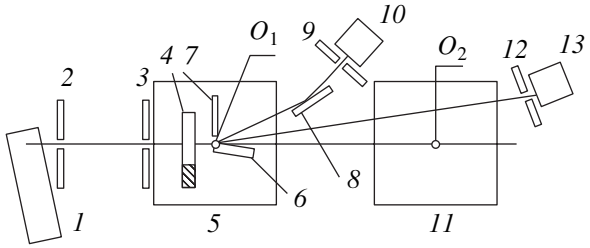

Fig. 1. Schematic of the experimental setup for measuring dispersion: (*1*) x-ray tube; (*2*, *3*, *9*, *12*) vertical collimating slits; (*4*) movable horizontal slit; (*5*, *11*) goniometers; (*6*) sample; (*7*) protecting absorbing shield; (*8*) monochromator; and (*10*, *13*) radiation detectors.

1063-7834/01/4304-0644$21.00 © 2001 MAIK "Nauka/Interperiodica"

ments. The source of radiation is a sharp-focus x-ray tube with a copper anode. The visible dimension of its focus in the measurement plane is 40 μm. Along the x-ray beam, two x-ray goniometers are mounted. The distances from the focus of the x-ray tube to the main axes O_1 and O_2 of goniometers *5* and *11* are 330 and 1161 mm, respectively, and those from the axes O_1 and O_2 to the entrance slits *9* and *12* are 225 and 192 mm, respectively. With an entrance slit of 30 μm wide, this scheme ensures an angular resolution of 0.0076° for the first (along the beam) goniometer *5* and 0.0017° for goniometer *11*.

As the samples, we used crystals of natural diamond (type Ia) with a density of 3.515 g/cm^3. The base (refracting) face was parallel to the (110) plane; perpendicularly to this base, two parallel side faces were prepared by lapping and polishing. The polishing of the surfaces was performed using an ASM28/20 diamond powder. The refracting face was additionally polished using a finer powder with an average grain size of ~1 μm. Three samples were prepared. The dimension of the refracting face (which has a minimum area of 12 mm^2) in the incidence plane of the beam was 2.2 mm. For comparison, we also used a single-crystal silicon plate cut from a standard optically polished wafer. In this case, the side surfaces perpendicular to the base face were obtained by cleaving on silicon cleavage planes.

The samples were mounted in such a manner that the edge formed by the base and the side surface facing the focus of the x-ray tube be coincident with the rotation axis O_1 of goniometer *5* (Figs. 1, 2). The typical angular divergence of the beam incident on the refracting face of the dispersive element was 24″. A graphite monochromator *8* and detector *10* mounted on a rotary arm were used to preliminarily adjust the x-ray scheme. All the results that are given below were obtained by angular scanning using detector *13* with an NaI(Tl) scintillator crystal with rotation about the O_2 axis. The program of controlling the data acquisition at a constant velocity of the detector made it possible to use an arbitrary time of data acquisition at each angular position. A typical angular interval between the readings was 0.0005°.

2. ANGULAR DISPERSION UPON REFRACTION OF X-RAYS

Let us consider (in terms of geometric optics) the passage of a parallel x-ray beam through a rectangular prism of a uniform material. We designate the refractive indices of the prism and the ambient medium $n_1(\lambda) = 1 - \delta_1(\lambda) - i\beta_1(\lambda)$ and $n_2(\lambda) = 1 - \delta_2(\lambda) - i\beta_2(\lambda)$, respectively. Let the *z* axis be perpendicular to and the *x* axis be parallel to the first interface and let them lie in the incidence plane (Fig. 2). Let the radiation be monochromatic ($\lambda \sim 0.1$ nm) and the angle φ of incidence onto the first interface be close to zero. Under the above

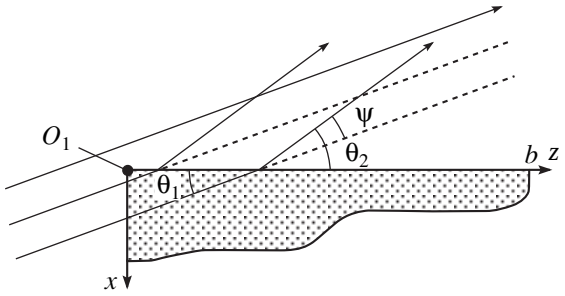

Fig. 2. Geometry of the x-ray radiation path for the case where a beam to be analyzed strikes from inside the refracting surface of a diamond crystal.

conditions, the following simplifications are possible. First, we can consider only refraction at the second interface, since the magnitudes of the coefficient of reflection and the changes in the refraction angle upon the intersection of the first interface are negligibly small. Second, we can ignore the state of polarization of the incident radiation, since, according to the Fresnel formulas, the coefficients of transmission for the *s* and *p* polarizations are virtually coincident at $\varphi \longrightarrow \pi/2$. Going from incidence angles φ to glancing angles $\theta = \pi/2 - \varphi$, we can transform the sine law [9] for the second interface to the form

$$\frac{1 - \delta_1 - i\beta_1}{1 - \delta_2 - i\beta_2} = \frac{\sqrt{1 - \sin^2\theta_2}}{\sqrt{1 - \sin^2\theta_1}}, \quad (1)$$

where θ_1 and θ_2 are the glancing angles for the incident and refracted radiations in the first and second media, respectively. The absolute magnitude of the decrement of the refractive index $|\delta + i\beta|$ for the wavelength used is less than 10^{-4} [10] ($\beta/\delta \ll 1$). This circumstance permits us to use, in the range of small glancing angles ($\theta_1 \ll \pi/2$), the expansion into a series and obtain the following expression for the glancing angle θ_2 of the refracted radiation in the second medium:

$$\theta_2 \cong \sqrt{\theta_1^2 - 2(\delta_2 - \delta_1)}. \quad (2)$$

Let us differentiate Eq. (2) with respect to θ_1. Then, for a beam with an angular divergence $\Delta\theta$, we obtain the following dependence of the coefficient of angular contraction C_a on θ_1 (here, θ_1 is the glancing angle of the central beam):

$$C_a = \frac{\Delta\theta_1}{\Delta\theta_2} = \frac{\sqrt{\theta_1^2 - 2(\delta_2 - \delta_1)}}{\theta_1}. \quad (3)$$

The decrement of the refraction index of air δ_2 can be neglected. As follows from Eq. (3), in the geometry that was chosen (Fig. 2), there occurs an angular contraction of the refracted beam ($C_a > 1$). Note that upon the reversion of the beam direction, i.e., upon the passage of the

radiation from air into the sample, the angular cone of the refracted beam will increase, since in this case $C_a < 1$. Consequently, in our case, a maximum angular resolution of the spectrum is observed.

Now, we take into account the spectral dependence of the refractive index. In the spectral range under consideration, the condition $\nu_0^2 \gg \nu_i^2$ for all electron shells of the C atom is fulfilled (here, ν_0 is the frequency of vibrations corresponding to an arbitrary line in the x-ray range under study and ν_i is the natural frequency of vibrations of an electron of the *i*th shell). Under the above condition, in accordance with the electron theory of dispersion [10], we have for any line λ of the x-ray spectrum

$$\delta\lambda = g\rho\lambda^2, \tag{4}$$

where g is a dimensional coefficient (which can be expressed through fundamental physical constants) and ρ is the physical density of the sample. Substituting Eq. (4) into Eq. (2) and differentiating with respect to λ, we obtain the following expression for the angular dispersion:

$$D(\rho, \lambda) = d\theta_2/d\lambda = \frac{2\lambda g\rho}{\sqrt{\theta_1^2 - 2g\rho\lambda^2}}. \tag{5}$$

It is obvious that at grazing angles ($\theta_1 \longrightarrow 0$) the angular dispersion is maximum. In this case, $D \propto \rho^{1/2}$ and is independent of λ. At $\theta_1^2 \gg 2g\rho\lambda^2$, the magnitude of $D(\rho, \lambda)$ changes approximately proportionally to ρ and λ. As is known from the theory of prism spectrometers [11], the spectral resolution $A = \lambda/\Delta\lambda$ is related to the diffraction limit. In the case under consideration, the effective cross section of the refracted beam in the plane of incidence can be restricted by two factors: first, the finite size of the elemental refracting area b and, second, the finite mean free path of photons in the sample, which is equal to the inverse linear coefficient of absorption $\mu(\lambda)$. More strictly, we can write the following expression for the diffraction angular width $\Delta\theta(\lambda)$ of the refracted beam:

$$\Delta\theta_d\lambda \cong \begin{cases} \lambda/b\theta_2, & b \le 2/\mu(\lambda) \\ \lambda\mu(\lambda)/2\theta_2, & b \ge 2/\mu(\lambda). \end{cases} \tag{6}$$

The introduction of the factor 2 is caused by the fact that, when estimating the diffraction broadening, we should take into account a decrease in the wave amplitude. For the regions of the x-ray spectrum near the CuK_α (0.154 nm) and CuK_β (0.139 nm) characteristic lines, the condition $b \ge 2/\mu(\lambda)$ is fulfilled. Substituting into Eq. (6) the value of $\mu(\lambda)$ for diamonds for the above-indicated wavelengths and the typical value of the angle $\theta_2 = 0.2°$ (3.5 mrad), we obtain $\Delta\theta_d(\text{Cu}K_\alpha) \approx 0.0019°$ (32 mrad) and $\Delta\theta_d(\text{Cu}K_\alpha) \approx 0.0012°$ (2.1 mrad). This permits us to estimate the spectral resolution $A(\lambda)$ of the dispersive element. Multiplying the left-hand and right-hand parts of Eq. (5) by $\Delta\lambda$ and substituting the values of the constants corresponding to the indicated parameters, we find $A_\alpha = 200$ and $A_\beta = 251$. By going from $\Delta\lambda$ to the energy resolution, we obtain $\Delta E = 40$ and 36 eV for the lines with the wavelengths 0.154 and 0.139 nm, respectively.

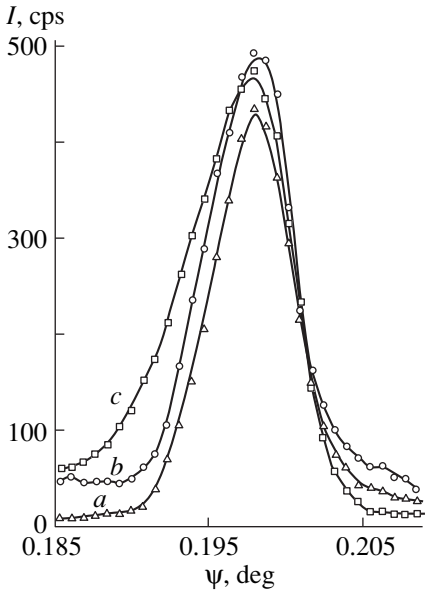

Fig. 3. Angular profiles of the refracted beam for the CuK_α line for three diamond samples (*a*–*c*). The beam strikes the refracting surface from inside the sample; the fixed glancing angle is $\theta_1 = 0.09°$.

3. MEASUREMENT RESULTS

Figure 3 displays the angular profiles of the refracted beam for three diamond samples (*a*, *b*, and *c*) measured under identical irradiation conditions. Hereafter, the abscissa axis corresponds to the deviation angle $\varphi = \theta_2 - \theta_1$ measured from the direction of the primary beam. The beam analyzed passed, in accordance with the geometry of the scheme shown in Fig. 2, through the side face and fell from inside on the base surface of the sample. The maintenance of a constant magnitude of the glancing angle θ_1 is a fundamental condition for obtaining maximum resolution. As can be seen from the comparison, the width at the half-height of the refraction peak is minimum for sample *a*. This indicates that the major part of its refracting surface meets the condition of maximum planeness. Therefore, we used just this sample for further measurements.

With decreasing glancing angle θ_1, the angular dispersion should increase according to Eq. (5). As was shown in [12], the effective width of the entrance aperture of a dispersion element for the spectral line with a wavelength λ in the geometry of Fig. 2 is equal to

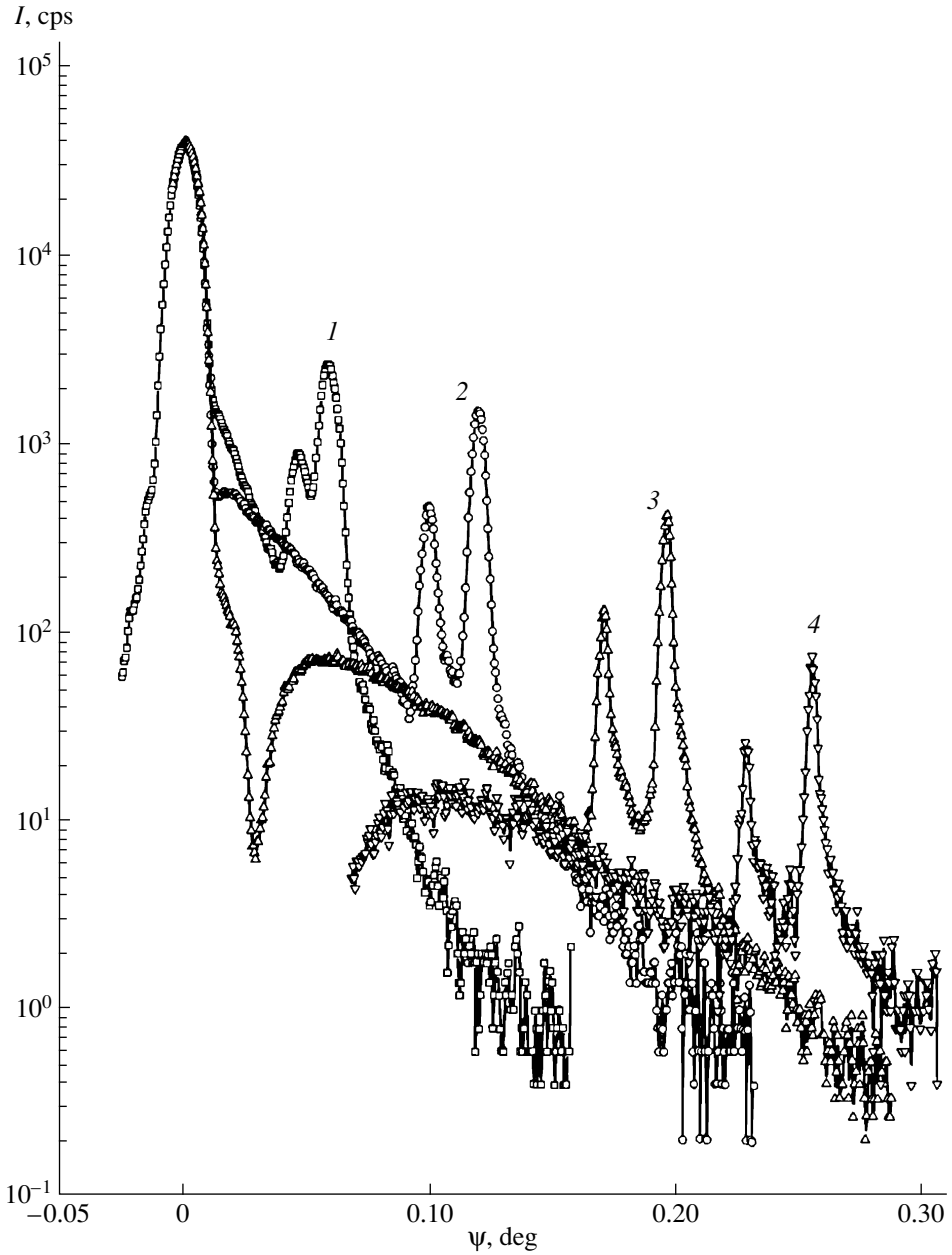

Fig. 4. Refraction patterns of diamonds at various glancing angles θ_1: (*1*) 0.60°, (*2*) 0.25°, (*3*) 0.09°, and (*4*) 0.01°.

$\theta_1/\mu(\lambda)$, and as θ_1 decreases, the intensity of the refracted beam decreases monotonically. The dependence is nonlinear, since the coefficient of reflection at the diamond–air interface tends to unity $R(\theta_1) \longrightarrow 1$ at $\theta_1 \longrightarrow 0$. The above regularities are confirmed by a series of refractograms obtained by angular scanning with detector *13* at several fixed grazing angles θ_1 (Fig. 4).

With going from the diamond to single-crystal silicon ($Z = 14$), the effective free path of x-ray photons $l_e = 1/\mu$ in the dispersive element decreases sharply for any wavelength in the spectral range considered. In particular, at $\lambda = 0.154$ nm (CuK_α line), we have μ(Si) = 145 cm^{-1} and μ(C) = 14.7 cm^{-1} [13–16]. According to Eq. (6), a decrease in $D(\rho, \lambda)$ should be observed for silicon in this case. As can be seen from Fig. 5, which displays the refractograms of Si (curve *1*) and C (curve *2*) for a grazing angle $\theta_1 = 0.08°$, the dispersive element made of silicon does not allow a complete resolution of the CuK_α and CuK_β spectral lines. At an acceleration voltage of 25 kV at the tube, the hardest part of the radiation spectrum in this case is not separated from the side wing of the primary beam that passes through the gap between the sample and shield *7* (Fig. 1).

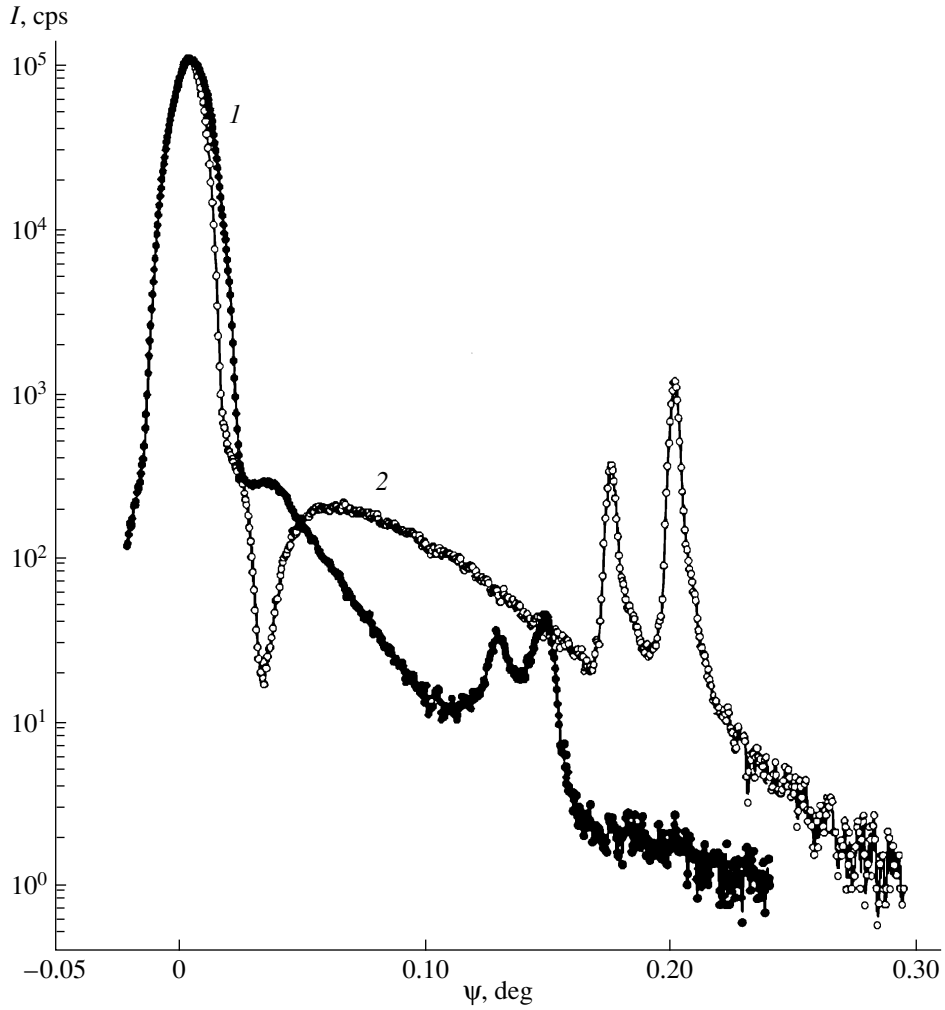

Fig. 5. Refraction patterns of (*1*) single-crystal silicon and (*2*) diamonds for a glancing angle $\theta_1 = 0.08°$ and a voltage at the x-ray tube $V = 25$ kV.

Figure 6 displays a series of refractograms of diamonds that were obtained at a fixed grazing angle $\theta_1 = 0.06°$ and various voltages at the x-ray tube in a range of 12 to 35 kV.

The spectral resolution of the diamond prism was determined using the refractogram (Fig. 7) that was obtained at $U_m = 40$ kV and $\theta_1 = 0.06°$. Measurements of the peak width at the half-height of the lines with the wavelengths of 0.154 and 0.139 nm with corrections for the instrumental function yield $\Delta\lambda = 19.7$ and 17.1 pm, respectively, or, on the energy scale, $\Delta E = 103$ and 110 eV, respectively. At smaller angles, as follows from Eq. (5), the spectral resolution should increase. No such an increase is observed in reality, since the radiation propagates along the surface through a distorted layer damaged by mechanical treatment, which increases the intensity of scattering by nonuniformities of the surface relief and leads to a smearing of the angular spectrum.

Thus, the investigations performed show the possibility of using a single-crystal diamond for practical measurements of hard x-ray radiation with wavelengths from 0.03 to 0.25 nm. This range includes the characteristic lines of the *K* and *L* series of virtually all elements with atomic numbers $Z > 25$. The range can be slightly extended to the long-wavelength region (to 0.3–0.5 nm) by fully or partially evacuating the working chamber in which the x-ray optical circuit is placed. With a further increase in λ, the absorption coefficient increases rapidly and the magnitude of *b* drops, which leads to a decrease in resolution due to diffraction effects related to the finite size of the effective refractive surface.

From the practical viewpoint, the most important result is that, owing to the angular dispersion of radiation, the full spectrum can be recorded using a single- or two-dimensional position detector, e.g., based on a linear or matrix CCD detector. This ensures the possi-

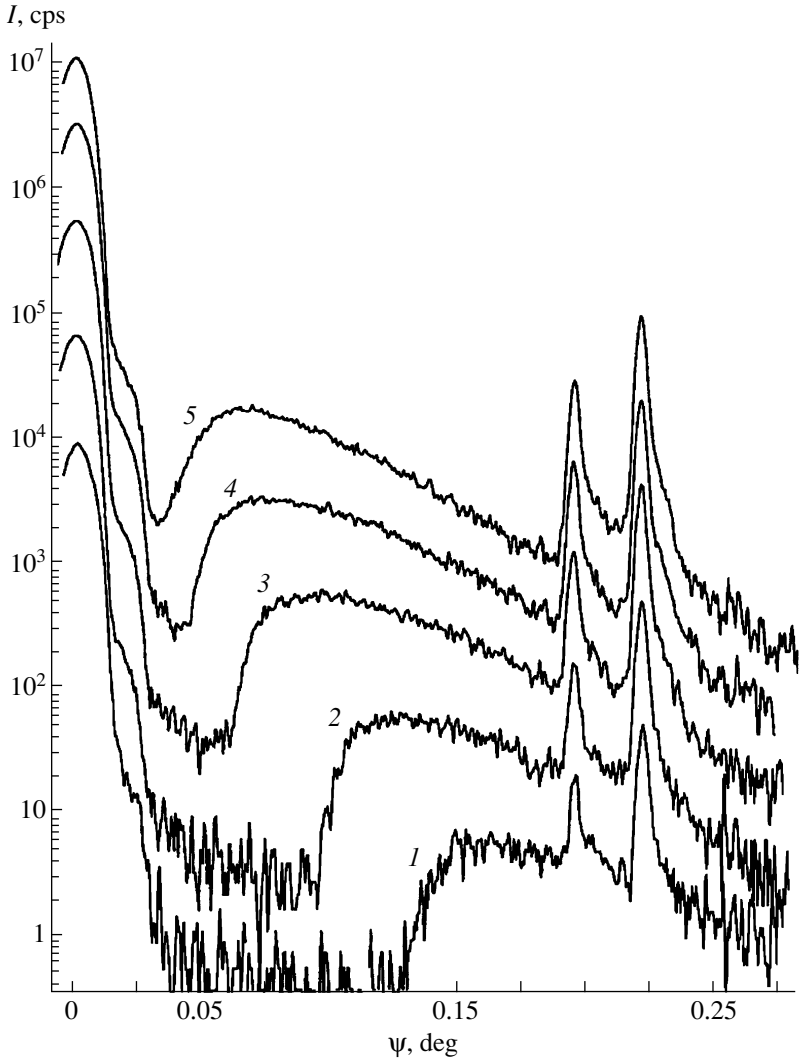

Fig. 6. Refraction patterns of a diamond at a glancing angle $\theta_1 = 0.06°$ and voltages at the x-ray tube equal to (*1*) 12, (*2*) 15, (*3*) 20, (*4*) 25, and (*5*) 35 kV.

bility of analyzing the spectrum without any restrictions on the magnitude of the time interval to be measured. Since the angular distribution is described well by Eq. (5) derived from the sine law and since the absorption properties of carbon have repeatedly been tabulated, we can calculate the spectral density of radiation $I^{\lambda}(\lambda)$ from the experimental dependence of $I(\varphi)$.

An alternative to diamonds as a material for dispersive elements is beryllium. In comparison with polycrystalline beryllium, the density of a natural diamond is greater by a factor of 1.9, which, according to Eq. (5), provides a higher angular dispersion. In addition, owing to the single-crystal structure, the scattering near the zero point of the reciprocal lattice is minimum. It is natural that, when using a polychromatic spectrum, some reciprocal-lattice points of single-crystal C (diamond) inevitably fall onto the Ewald sphere and part of energy flow will be dissipated into larger angles, in accordance with diffraction conditions. The diffraction scattering angles ϑ should be equal to or greater than $\geq \lambda/d$, where d is the maximum interplanar distance in the sample. In the spectral range under study, we have $\vartheta \gg \varphi$; i.e., the diffraction peaks cannot fall into the characteristic range of angles measured in refraction experiments. In addition, as was indicated above, the diffraction conditions are fulfilled only in narrow spectral bands for a finite set of reflections and, therefore, their presence virtually does not distort the monotonic distribution in the continuous part of the spectrum (Fig. 7). As to the characteristic lines, for a known crystallographic orientation of the diamond single crystal, we can always calculate in advance the angles between the refracting surface and atomic planes for which the

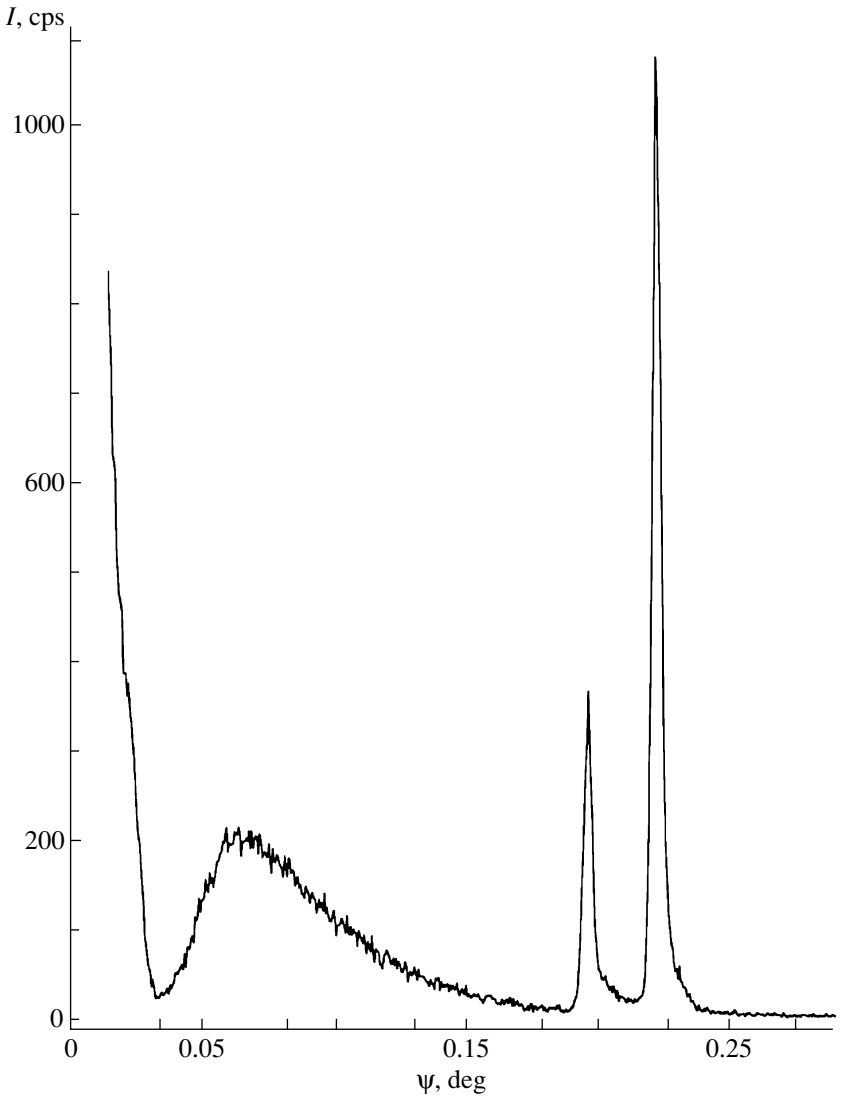

Fig. 7. Refraction pattern of a diamond at a glancing angle $\theta_1 = 0.06°$ and a voltage at the x-ray tube $V = 40$ kV.

diffraction conditions are not fulfilled for a given set of characteristic lines. Note that the samples of natural diamonds with an effective area of the refracting face of ~10 mm^2 that were used in our experiments are significantly cheaper than analogous synthetic crystals. In addition, in view of the mosaic structure of the latter, the spectral bands in which the intensity distribution in the angular spectrum can be distorted at the expense of Bragg reflections are wider in them than in natural crystals.

REFERENCES

1. *X-ray Techniques: A Handbook*, Ed. by V. V. Klyuev (Mashinostroenie, Moscow, 1980), Vol. 2, p. 60.
2. N. G. Volkov, V. A. Khristoforov, and N. P. Ushakov, in *Methods of Nuclear Spectrometry* (Énergoatomizdat, Moscow, 1990), p. 148.
3. J. A. Kyrala, J. Workman, S. Evans, *et al.*, in *Proceedings of the International Conference on High-Speed Photography and Photonics* (Moscow, 1998), p. 26.
4. K. N. Mukhin, in *Experimental Nuclear Physics* (Énergoatomizdat, Moscow, 1993), Vol. 1, Part 1.
5. L. S. Gorn and B. I. Khazanov, in *Modern Devices for Ionizing Radiation Measurements* (Énergoatomizdat, Moscow, 1989), p. 72.
6. R. Woldseth, *X-ray Energy Spectrometry* (Kevex Corporation, Burlingame, 1973; Atomizdat, Moscow, 1977).
7. A. Boscolo, L. Poletto, and G. Tondello, Pure Appl. Opt. **6** (1), L1 (1997).

8. A. V. Vinogradov, I. A. Brytov, A. Ya. Grudskiĭ, I. V. Kozhevnikov, M. T. Kogan, and V. A. Slemzin, *Mirror X-ray Optics* (Mashinostroenie, Leningrad, 1989).
9. M. Born and E. Wolf, *Principles of Optics* (Pergamon, Oxford, 1969; Nauka, Moscow 1973).
10. M. A. Blokhin, *Physics of X-rays* (GITTL, Moscow, 1957).
11. A. N. Zaĭdel', G. V. Ostrovskaya, and Yu. I. Ostrovskiĭ, *Techniques and Practice of Spectroscopy* (Nauka, Moscow, 1976).
12. A. G. Tour'yanskiĭ and I. V. Pirshin, Prib. Tekh. Éksp., No. 6, 104 (1999).
13. M. A. Blokhin and I. G. Shveĭtser, *A Handbook of X-ray Spectroscopy* (Nauka, Moscow, 1982).
14. B. L. Henke, E. M. Gullikson, and J. C. Davis, At. Data Nucl. Data Tables **54** (2), 181 (1993).
15. *Physical Quantities. Handbook*, Ed. by I. S. Grigor'ev and E. Z. Meĭlikhov (Énergoatomizdat, Moscow, 1991).
16. D. V. Fedoseev, N. V. Novikov, A. S. Vishnevskiĭ, and I. G. Teremetskaya, *Diamond: A Handbook* (Naukova Dumka, Kiev, 1981).

Translated by S. Gorin

Physics of the Solid State, Vol. 43, No. 4, 2001, pp. 652–654. Translated from Fizika Tverdogo Tela, Vol. 43, No. 4, 2001, pp. 627–629.

SEMICONDUCTORS AND DIELECTRICS

Electron Paramagnetic Resonance of the Eu^{2+} Ion in $SrCl_2$ at High Pressure

G. N. Neĭlo*, O. T. Antonyak, and A. D. Prokhorov***

** Donetsk Physicotechnical Institute, National Academy of Sciences of Ukraine, Donetsk, 340114 Ukraine*

*** Franko Lviv State University, Lviv, 290005 Ukraine*

e-mail: prohorov@pr.fti.ac.donetsk.ua

Received August 17, 2000

Abstract—This paper reports an EPR study of the effect of hydrostatic pressure (up to 10 kbar) and temperature (300, 77, and 4.2 K) on the spin Hamiltonian parameters of the Eu^{2+} ion in a $SrCl_2$ cubic crystal. It is found that the b_4 parameter is related by a power law to the distance from the Cl^{-1} ligand ($b_4 \sim R^{-13.5}$). The pressure and temperature are shown not to be equivalent thermodynamic parameters. Lattice vibrations contribute noticeably to the initial *S*-ion splitting. *© 2001 MAIK "Nauka/Interperiodica".*

1. INTRODUCTION

Since the resultant orbital momentum of electrons in ions in the *S* state, i.e., ions with the $3d^5$ configuration in the iron group (Mn^{2+}, Fe^{3+}) and $4f^7$ configuration in the rare-earth group (Eu^{2+}, Gd^{3+}), is zero, the crystal field should not split the ground levels of these ions. In actual fact, however, small splittings do exist, as evidenced by EPR measurements and adiabatic demagnetization experiments.

The phenomenon of *S*-state ions has attracted considerable attention of both experimenters and theorists [1–3]. Nevertheless, the main reasons for these splittings remain unclear, and, therefore, further steps in the theoretical justification and choice of the splitting mechanisms require correct determination of the dependence of the parameters characterizing the initial splitting of an *S* ion on the distance to the ligand.

The choice of Eu^{2+} in $SrCl_2$ as the subject of this study was based on the following considerations: (i) The cubic symmetry of the crystal corresponds to the simplest crystal field in which all distances from the paramagnetic ion to the eight ligands are equal, (ii) the isovalent substitution (Eu^{2+}–Sr^{2+}) and equal ionic radii of the divalent europium and strontium (1.12 Å) suggest the absence of any perturbations in the lattice under study, and (iii) the crystal is readily compressible and its elastic constants are known.

It is the choice of the crystal that determined the purpose of this work, which consists in studying EPR spectra of Eu^{2+} in $SrCl_2$ over a wide temperature range (4.2–300 K) and at a high hydrostatic pressure (up to 10 kbar) and establishing the dependence of the initial splitting on the distance to the ligand.

It should be pointed out that experimental studies of spectra of cubic crystals under hydrostatic pressure are extremely rare and we have been able to locate only two relevant publications [4, 5].

2. SAMPLES AND EXPERIMENTAL TECHNIQUES

The $SrCl_2$ crystal is the only chloride crystallizing in fluorite symmetry. The space group is O_h^1–$Fm3m$, and the lattice constant is a = 6.977 Å [6]. The crystal was grown at Franko Lviv State University. The data on the elastic constants, density [7, 8], and volume compressibility are listed in Table 1. The linear thermal expansion coefficient at 300 K is 17.7×10^{-6} K^{-1}. Faced with the lack of direct data on the thermal expansion coefficient below room temperature, we used the appropriate relations of this parameter available for other fluorites, which are given in [6, 9].

The EPR spectra were measured on a 3-cm-range radiospectrometer representing a classical superheterodyne arrangement with special leucosapphire resonators [10] allowing studies at high hydrostatic pressures over a wide temperature range. The pressures were produced in a self-contained double-layer high-pressure chamber [11], whose inner cylinder was made of the 40KhNYu-VI nonmagnetic alloy and outer cylinder, of beryllium bronze. The sample to be studied was mounted in the leucosapphire resonator, and the latter

Table 1. Mechanical properties of the $SrCl_2$ crystal [7, 8]: density ρ (g/cm^3); elastic constants c_{11}, c_{12}, and c_{44} (10^{11} dyn/cm^2); and volume compressibility σ_v (10^{-6} bar^{-1})

T, K	ρ	c_{11}	c_{12}	c_{44}	σ_v
300	3.052	6.8	1.6	0.945	3.0
195	3.065	7.02	1.64	0.972	2.91

was placed in the high-pressure chamber. The pressure transmitting medium was a dehydrated mixture of equal parts of transformer oil and kerosene. The resonator was coupled to the spectrometer waveguide through a thin coaxial cable. The pressure could be measured by the standard method (manganin resistance sensor) and a contactless technique. In the latter method, the pressure was deduced from the variation of the initial splitting parameter D of the Cr^{3+} ion in $AlCl_3$ ($P = \Delta D/k$, $k = 0.622 \times 10^{-2}$ cm^{-1}/kbar). This method has the following advantages: (a) the pressure is measured in the immediate vicinity of the sample and (b) the linewidth permits one to estimate the extent to which the medium is indeed hydrostatic. The temperature was measured with a copper resistance pickup.

3. RESULTS AND DISCUSSION

The electronic configuration of Eu^{2+} is $4f^7$, $L = 0$, $S = 7/2$. The spectrum containing contributions of the ^{151}Eu (47.77%) and ^{153}Eu (52.23%) isotopes has 84 lines. Line superposition causes difficulties in the treatment of spectra. The observed spectrum can be well fitted by the spin Hamiltonian

$$\hat{H} = g\beta\mathbf{B}\hat{\mathbf{S}} + 1/60 b_4(O_4^0 + 5O_4^4) + 1/1260 b_6(O_6^0 - 21O_6^4) + A\hat{\mathbf{S}}\hat{\mathbf{I}}. \quad (1)$$

Here, g is the factor of spectroscopic splitting, β is the Bohr magneton, $\mathbf{B}$ is the magnetic induction vector, $\hat{\mathbf{S}}$ and $\hat{\mathbf{I}}$ are the electron and nuclear spin operators, O_n^m are the Stevens operators, b_4 and b_6 are the fine structure parameters related to the notation accepted in [12] by the expressions $c = 4b_4$ and $s = 4b_6$, and A is the hyperfine structure (hfs) parameter. The spin Hamiltonian parameters derived from the EPR spectra of Eu^{2+} in $SrCl_2$ at temperatures of 300, 77, and 4.2 K and pressures of up to 10 kbar are listed in Table 2, and the figure shows the b_4 parameter as a function of the relative distance to the ligand. The variation in the b_4 parameter with temperature can be fitted by a linear relation with the coefficient $\Delta b_4/\Delta T = 7.23 \times 10^{-3}$ cm^{-1} K^{-1}. Note that the linear relation includes the point corresponding to the liquid-helium temperature. A similar linear relation in the range 4.2–300 K was observed for $KZnF_3 : Gd^{3+}$ [13].

The spin Hamiltonian parameters obtained at room temperature (300 K) are close in magnitude to those quoted in [12]. The sign of the parameter can be determined directly by comparing the intensities of the low- and high-field absorption lines at different temperatures [14]. A comparison of the intensities at 300 and 4.2 K shows that the b_4 parameter is negative. As is seen from the presented experimental data, the decrease in volume due to uniform compression or to a decrease in temperature affects the Hamiltonian parameters b_4 and A, whereas the g factor and the b_6 parameter do not change within experimental error.

Assuming the pressure-induced variation in the b_4 parameter to be inversely proportional to R^n, where R is the distance between the Eu^{2+} ion and the ligand, we obtain

$$n = \log[b_4(P)/b_4(0)]/\log[R(0)/R(P)] = 13.5,$$

where $R(0)$, $b_4(0)$ and $R(P)$, $b_4(P)$ are the lattice constants and the spin Hamiltonian parameters at atmospheric and external pressures, respectively.

Mn^{2+} EPR measurements made in MgO at high pressures yield $n = 21.34$ [5]. A comparison of the above values allows us to assume that the exponent in the case of $SrCl_2$ is more in line with the point-charge model, according to which the b_4 parameter is inversely proportional to R^{10} [15].

There were many attempts to estimate the dependence of the spin Hamiltonian parameters on the distance to the ligand. Among them are the aforementioned investigation [5] of the Mn^{2+} ion in MgO and studies where this relation was looked for with crystals of isomorphic series. For instance, Low and Rosenberg [12] estimated the $b_4(CaF_2)/b_4(SrCl_2)$ ratio for Gd^{3+}-doped CaF_2 and $SrCl_2$ crystals. The point-charge model yields 11.8 for this ratio. The experimental value is 4.7, which corresponds to the exponent $n = 4.5$.

Analysis of Eu^{2+} EPR spectra available for a number of fluorites, namely, CaF_2 ($b_4 = 57.9 \times 10^{-4}$ cm^{-1}), SrF_2 ($b_4 = 44.9 \times 10^{-4}$ cm^{-1}), and BaF_2 ($b_4 = 36.0 \times 10^{-4}$ cm^{-1}) [16], yields $n = 3.9$, if the distance from the paramagnetic ion to the ligand is assumed to be that of the impurity-free lattice.

This approach is apparently not fully justified, because the ion incorporated into the lattice has a valence and an ionic radius other than the replaced ion, which can change the distance to the ligand. It is known that introducing Gd^{3+} (with the ionic radius smaller than that of Sr^{2+}) into the $SrCl_2$ lattice reduces the b_4 parameter by a factor of 1.3 [12] compared to the case of Eu^{2+} in $SrCl_2$, whose valence state and ionic radius coincide with those of Sr^{2+}. Taking into account the dependence on R obtained by us, this corresponds to a change in the distance of 0.059 Å.

Table 2. Experimental parameters of spin Hamiltonian (1): spectroscopic splitting factor g, fine structure parameters b_4 and b_6 (10^{-4} cm^{-1}), hyperfine structure parameter A (10^{-4} cm^{-1}), and pressure P (kbar)

T, K	g	b_4	b_6	A
300	1.991(1)	–[14.7(3) + 0.218P]	0.4(2)	34.4(3)–0.145P
77	1.991(1)	–16.3	0.4(2)	33.5(3)
4.2	1.991(1)	–16.8	0.4(2)	33.8(3)

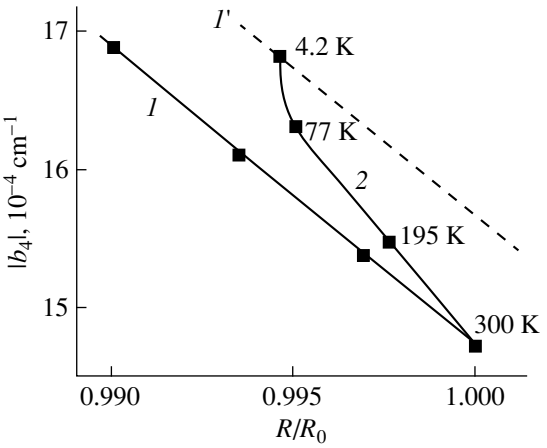

Dependence of the spin Hamiltonian parameter b_4 on the relative distance to the Cl^{1-} ligand. (*1*) Pressure dependence at 300 K, (*1*') the same dependence shifted vertically by the magnitude of the phonon contribution, and (*2*) temperature dependence. R_0 is the Sr–Cl distance at standard conditions (T = 300 K, P = 0).

As is evident from the character of variation in the b_4 parameter with an increase in the pressure or decrease in temperature (see figure), each new value of b_4 obtained by increasing the pressure can also be reproduced by lowering the temperature at atmospheric pressure. For instance, at a pressure of 6.5 kbar and a temperature T = 106 K, we have $b_4 = 16.1 \times 10^{-4}$ cm^{-1}. Using the data on compressibility and the variation in the $SrCl_2$ density with decreasing temperature listed in Table 1, we can readily show that V(6.5 kbar) = 0.981 V_0 and V(106 K) = 0.996V_0, where V_0 is the crystal volume at room temperature and atmospheric temperature. Similarly, the experimental data [11] for Mn^{2+} in MgO yield V(7.7 kbar) = 0.995V_0 and V(158 K) = 0.9955V_0.

Hence, it follows that the temperature and pressure are not equivalent thermodynamic parameters and that the effect of temperature cannot be reduced to a change of the volume only. There is an additional contribution to the parameter originating from lattice vibrations, the so-called phonon contribution. The figure demonstrates this inference in a most revealing way. Straight line *1* plots the dependence of b_4 on the ratio R/R_0 varied by the pressure, and curve *2* represents the same dependence but with the R/R_0 ratio changed by varying the temperature. Straight line *1*' is line *1* shifted along the ordinate axis by the magnitude of the phonon contribution. The difference between the ordinates of dependences *1*' and *2* is the phonon contribution increasing with temperature, which is opposite in sign to the static contribution to the b_4 parameter. The maximum phonon contribution at 300 K is $+0.92 \times 10^{-4}$ cm^{-1}, which is ~6% of the static value. A similar effect of lattice vibrations was observed in the case of Mn^{3+} in MgO [5, 17].

The pressure dependence of the hfs splitting constant permits one to obtain information on the contribution of the ion separation to the given spectral parameter. For the Eu^{2+} ion in $SrCl_2$, this relation has the form

$$A(P) = 34.4 \times 10^{-4}[R(P)/R(0)]^{0.047}\ \text{cm}^{-1}.$$

A comparison of this value with the magnitude of the hfs splitting constants of Mn^{2+} in MgO, $A(P) \sim [R(P)/R(0)]^{0.02}$, and in the covalent ZnS, $A(P) \sim [R(P)/R(0)]^{0.117}$, suggests that $SrCl_2$ is more likely an ionic than a covalent crystal.

In summary, we have found experimentally the dependence of the spin Hamiltonian parameters b_4 and A on the distance to the nearest ligand (Eu^{2+}–Cl^{1-}) in the undistorted lattice, demonstrated that the temperature dependence of the spin Hamiltonian parameter b_4 contains a substantial contribution of the lattice vibrations in addition to the contribution of the conventional thermal expansion, and shown the hfs constant to be only weakly dependent on pressure, which indicates the ionic character of bonding in $SrCl_2$.

REFERENCES

1. B. G. Wyborne, Phys. Rev. **148** (1), 317 (1966).
2. A. M. Leushin, Fiz. Tverd. Tela (Leningrad) **5**, 2332 (1965) [Sov. Phys. Solid State **5**, 1695 (1965)].
3. Wen-Cen Zheng, Phys. Status Solidi B **219** (1), 3 (2000).
4. I. Rimai, T. Deutsch, and S. D. Silverman, Phys. Rev. **133** (4a), A1123 (1964).
5. M. Walter and J. Walsh, Phys. Rev. **122** (3), 762 (1961).
6. M. Shand, R. C. Hanson, C. E. Derrington, and M. O'Keeffe, Solid State Commun. **18** (7), 769 (1976).
7. H. V. Lauer, Jr., K. A. Solberg, D. H. Kuhmer, and W. E. Bron, Phys. Lett. A **35** (4), 219 (1971).
8. Cao-Xuan An, Phys. Status Solidi A **43** (1), K69 (1977).
9. S. I. Novikova, in *Thermal Expansion of Solids* (Nauka, Moscow, 1974), p. 260.
10. G. N. Neĭlo, A. D. Prokhorov, and G. A. Tsintsadze, Zh. Éksp. Teor. Fiz. **72** (3), 1081 (1977) [Sov. Phys. JETP **45**, 565 (1977)].
11. I. M. Krygin, G. N. Neĭlo, and A. D. Prokhorov, Fiz. Tverd. Tela (Leningrad) **28** (4), 1136 (1986) [Sov. Phys. Solid State **28**, 634 (1986)].
12. W. Low and U. Rosenberg, Phys. Rev. **116** (1), 621 (1959).
13. M. Arakava, H. Aoki, H. Takeuchi, *et al.*, J. Phys. Soc. Jpn. **58** (8), 2459 (1982).
14. A. Abragam and B. Bleaney, *Electron Paramagnetic Resonance of Transition Ions* (Clarendon, Oxford, 1970; Mir, Moscow, 1972).
15. H. Watanabe, Phys. Rev. Lett. **4** (8), 410 (1960).
16. S. A. Altshuler and B. M. Kozyrev, *Electron Paramagnetic Resonance in Compounds of Transition Elements* (Nauka, Moscow, 1972; Halsted, New York, 1975).
17. Keshav N. Shrivastava, Phys. Rev. **187** (2), 446 (1969).

Translated by G. Skrebtsov

Physics of the Solid State, Vol. 43, No. 4, 2001, pp. 655–662. Translated from Fizika Tverdogo Tela, Vol. 43, No. 4, 2001, pp. 630–636.

SEMICONDUCTORS AND DIELECTRICS

Visualization of Conduction Channels and the Dynamics of Ion Transport in Superionic Conductors

V. I. Polyakov

OAO Giproniigaz, Saratov, 410600 Russia

Received September 15, 2000

Abstract—A method for visualizing conduction channels is proposed. This method is based on graphical analysis of conduction channel fragments which belong to a Voronoi–Dirichlet elementary polyhedron and lie outside the rigid sphere centered at a fixed-sublattice ion that is located at the geometric center of the elementary polyhedron under consideration. Taking into account the weak nonrigidity of spheres and root-mean-square displacements of ions in the fixed sublattice makes it possible to construct a channel as the surface of the mobile ion density. The most probable regions of mobile ion motion are quantum-mechanically interpreted as channel walls, which is confirmed by constructing the equipotential surfaces of interionic potential for α-AgI. It is found that the Andersson mathematical dynamics and the dynamics of ion transport in AgI lead to the same pattern of the motion. The symmetry rules are used for predicting the directions of motion along the allowed vibrational coordinates of tetrahedral and octahedral α-CuI fragments. *© 2001 MAIK "Nauka/Interperiodica".*

1. INTRODUCTION

The superionic state of solid electrolytes is a particular crystalline state of a material that exists in a certain temperature range and whose structure is characterized by a fixed sublattice built up of atoms of one sort inside which a set of mobile ions occupy a number of crystallographic positions or even appear as a "lattice liquid." The conduction channels are defined as crystal regions which involve positions of the highest stability of mobile ions and the most probable motion paths connecting these positions.

2. VISUALIZATION OF CONDUCTION CHANNELS

The method proposed for constructing the conduction channels is based on the excluded-volume model and the Voronoi–Dirichlet partition of a fixed sublattice. Within the excluded-volume model, the cation–anion interaction is approximated by the hard-sphere potential [1]

$$V_{ij}(r) = \begin{cases} 0, & r > r_i + r_j \\ \infty, & r \le r_i + r_j, \end{cases}$$

where r_i and r_j are the effective radii of hard spheres of the ith and jth atoms, respectively, and the parameter $r_{exc} = r_i + r_j$, to a rough approximation, is the sum of the effective ionic radii. The space appears to be partitioned into an allowed volume in which the motion is free and an excluded volume in which the motion is forbidden.

As was shown in [2], the Voronoi partition of a fixed sublattice is characterized by extreme points (minima, maxima, and saddles) of the potential energy in the path of moving a mobile ion. The most stable positions of mobile ions are located near vertices of a Voronoi–Dirichlet polyhedron. For a β-AgI electrolyte (with a wurtzite structure) that possesses a typical ionic conductivity with a hopping diffusion of silver ions, the most stable positions of mobile ions correspond to the centers of tetrahedral and octahedral holes in a hexagonal closest packing of anions (Fig. 1, drawing *1.1*). In the case of AgI, Ag_3SI, Ag_2S, and Ag_2Se silver-containing electrolytes with a body-centered cubic (bcc) structure, the Voronoi–Dirichlet polyhedron is a Fedorov cubooctahedron (Fig. 1, drawing *2.1*) whose vertices determine the equilibrium positions of Ag^+ ions. For a number of conductors with a face-centered cubic (fcc) lattice [an α-CuI electrolyte with the conductivity through Cu^+ ions and fluorides MF_2 (M = Ca, Sr, Ba, and Pb) with a fluorite structure and anionic conductivity], the Voronoi–Dirichlet polyhedron is a rhombododecahedron (Fig. 1, drawing *3.1*). However, the most stable positions of mobile ions correspond only to the rhombododecahedron vertices at the centers of tetrahedral holes. The transition states for bcc conductors do not coincide with the midpoints of edges, but are located in their vicinity. In the case of fcc conductors, as will be shown below, the transition states are realized in octahedral holes of a cubic closest packing.

The walls of conduction channels are formed by the boundary between the allowed and excluded volumes. The Voronoi–Dirichlet polyhedron part that lies outside the rigid sphere (with the radius r_{exc}) circumscribed about its center represents a conduction channel fragment corresponding to this polyhedron (Fig. 1, drawings *1.2–3.2, 1.3–3.3*). It is self-evident that the polyhe-

1063-7834/01/4304-0655$21.00 © 2001 MAIK "Nauka/Interperiodica"

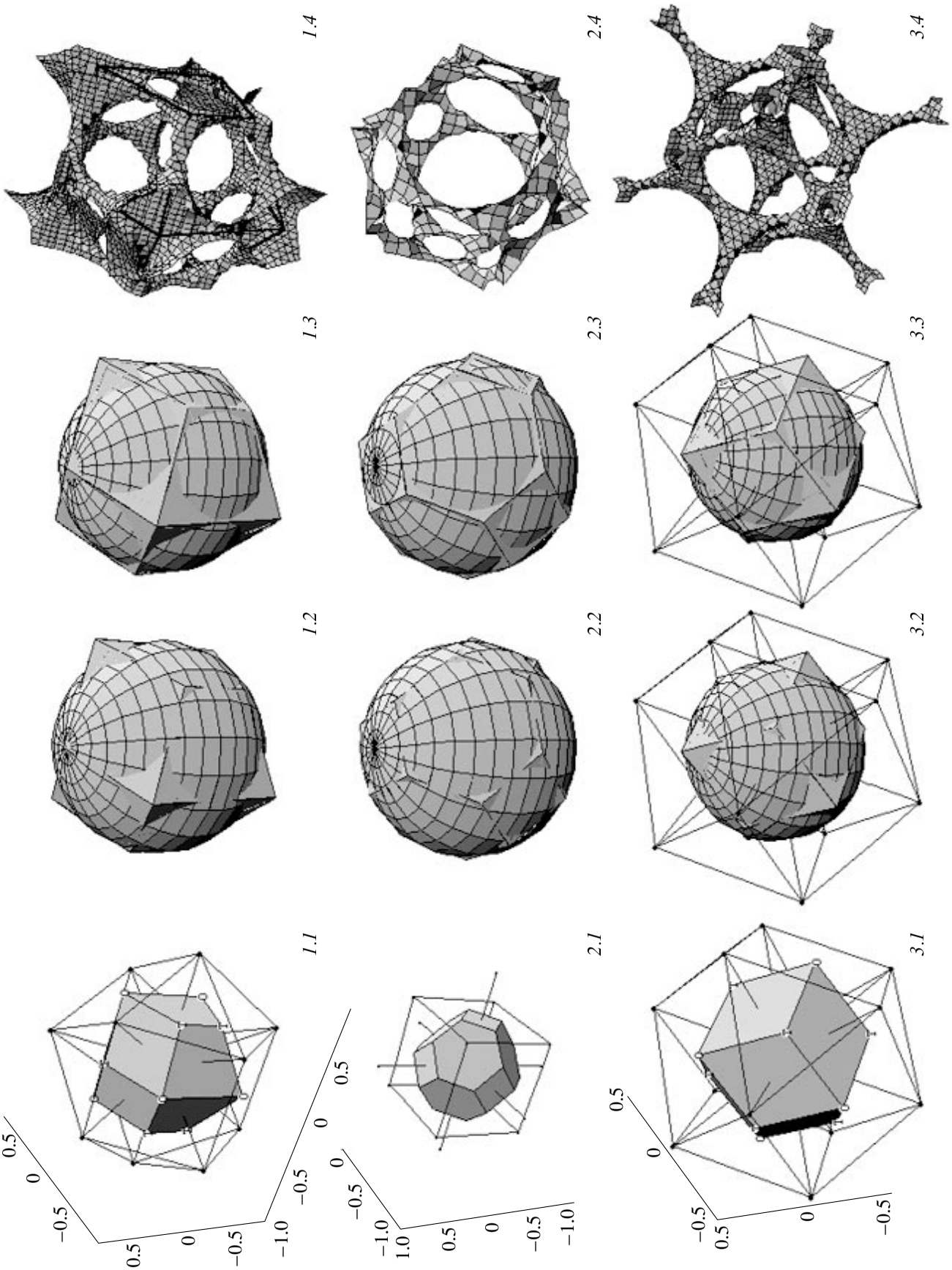
1.4
2.4
3.4
1.3
2.3
3.3
1.2
2.2
3.2
1.1
2.1
3.1
0.5
0
−0.5
0.5
0
−0.5
−1.0
0.5
0
−0.5
0
−0.5
−1.0
1.0
0.5
0
−0.5
−1.0
0.5
0
−0.5
0.5
0
−0.5

dron of this center is also intersected by other rigid spheres circumscribed about adjacent centers but just as much as its "own" sphere projects outside the polyhedron and the adjacent spheres penetrate into it. To put it differently, this makes it possible to visualize the entire allowed volume corresponding to the Voronoi–Dirichlet polyhedron. The form of the conduction channels provides a way of refining the r_{exc} and r_{face} parameters obtained by optimizing the EXAFS data with the use of the excluded-volume model. Here, r_{face} is the distance between the center of the tetrahedron face (trigonal position) (Fig. 1, drawings *1.1–3.1*) and the vertices of this face. In actual fact, at $r_{exc} \le r_{face}$, the allowed volume is connected. The optimization of the EXAFS data [1] for β-AgI at 20°C gives r_{exc} = 2.723 Å and r_{face} = 2.676 Å, and the allowed volume form isolated regions [these are the polyhedron corners projecting outside the sphere (Fig. 1, drawing *1.2*)]. In this case, the ionic conductivity is usual (at $r_{exc} = r_{face}$, the conduction channels should have the form shown in drawing *1.3* in Fig. 1). For α-AgI at 198°C, r_{exc} = 2.682 Å and r_{face} = 2.736 Å, and the conduction channels penetrate throughout the electrolyte bulk [the corners projecting outside the sphere are joined by the polyhedron edges (Fig. 1, drawing *2.3*)], which results in the superionic conductivity (at $r_{exc} = r_{face}$, the situation shown in drawing *2.2* in Fig. 1 should be realized).

The method proposed provides an explanation for the ionic conductivity in the low-temperature γ phase of AgI with a sphalerite structure, which is similar to the conductivity in β-AgI. In all three phases, the environment of silver ions is tetrahedral and the silver–iodine distances differ by no more than 0.02 Å. By using the same value of r_{exc} for the γ and β phases (stable at lower temperatures), we obtain the isolated regions—the polyhedron corners projecting outside the sphere (Fig. 1, drawings *1.2*, *3.2*). For anionic sublattice of the same fcc type in the case of the superionic α phase of CuI, the optimization of the EXAFS data [3] leads to a connected network of conduction channels (Fig. 1, drawing *3.3*): r_{exc} = 2.44 Å and r_{face} = 2.53 Å at 470°C.

Making allowance for the weak nonrigidity of spheres and root-mean-square displacements of ions in the rigid sublattice renders the excluded-volume model more realistic. The density of mobile ions is represented as the approximation of a step function by the error function [3].

Drawings *1.4–3.4* in Fig. 1 show the surfaces of the mobile ion density at such potentials V (1.0, 0.1, and 0.17 eV for β-AgI, α-AgI, and α-CuI, respectively) at which the connectivity arises throughout the electrolyte bulk; i.e., these surfaces are the conduction channel walls.

3. CONDUCTION CHANNEL WALLS AS REGIONS OF MOTION

In the framework of the excluded-volume model, ions as a gas move in allowed regions centered at tetrahedral sites in the anionic bcc sublattice of α-AgI. Mobile ions undergo a multiple scattering by walls of anionic rigid spheres until the direction of their motion coincides with the channel in the tetrahedron face near the trigonal position, which leads to the penetration of a cation into the adjacent tetrahedron and so on. According to [2], silver ions pass through a narrow part of conduction channels near the trigonal position with a higher probability when sliding over the channel wall as compared to the multiple scattering by walls in motion through the bulk of the allowed region.

Now, we apply the two-dimensional Schrödinger equation to quantum-mechanical consideration of the Ag^+ behavior within the excluded-volume model. The regions of the Ag^+ motion in the plane of the cubic unit cell face are bounded by the excluded volumes of I^- ions occupying vertices and center of a square (Fig. 1, drawing *2.4*). The silver ion resides in the potential well between the impenetrable inside circular wall of radius b' and the impenetrable outside wall formed by the arcs of four circumferences with the centers at the corners of the square. By replacing the composite outside wall by the circumference (concentric with the inside wall) of radius a, we change over to analysis of the two-dimensional Schrödinger equation in which the potential energy $V(x, y)$ is equal to zero at $b' < r < a$ ($x = r\cos\varphi$, $y = r\sin\varphi$) and infinity outside this interval (a ring infinite potential well). In the polar coordinates r and φ, substitution of the wave function $\Psi(r, \varphi) = R(r)\Phi(\varphi)$ into the Schrödinger equation leads to the separation of the variables to give the angular equation $\partial^2\Phi(\varphi)/\partial\varphi^2 = -m^2\Phi(\varphi)$ [where $\Phi(\varphi) = N\exp(im\varphi)$ and m is integer] and the dimensionless radial equation

$$\left(-\frac{\partial^2}{\partial\rho^2} - \frac{1}{\rho}\frac{\partial}{\partial\rho} + \frac{m^2}{\rho^2} - 1\right)R(\rho) = 0,$$

whose solutions are the Bessel functions. Here, we introduced the system of units in which the outside circumference radius a is the unit length and $\hbar/(2\mu a^2)$ is the unit energy (μ is the mass of a silver ion, $\rho = \sqrt{E}r =$

Fig. 1. Visualization of conduction channels in solid electrolytes with (*1.1–1.4*) hexagonal closest, (*2.1–2.4*) bcc, and (*3.1–3.4*) fcc closest packings of fixed ions in rigid subsystems. The unit length is taken equal to the cubic unit-cell parameter for cubic systems and the unit-cell parameter a for the hexagonal system ($a = b = 1$, $c = 2\sqrt{2/3}$). (*1.1–3.1*) Coordination polyhedra (a hexagonal analogue of a cubooctahedron, a cube, and a cubooctahedron), Voronoi–Dirichlet polyhedra, and their intersection with simplectic tetrahedra for the corresponding packings. The centers of tetrahedral and octahedral holes are designated by *T* and *O*.

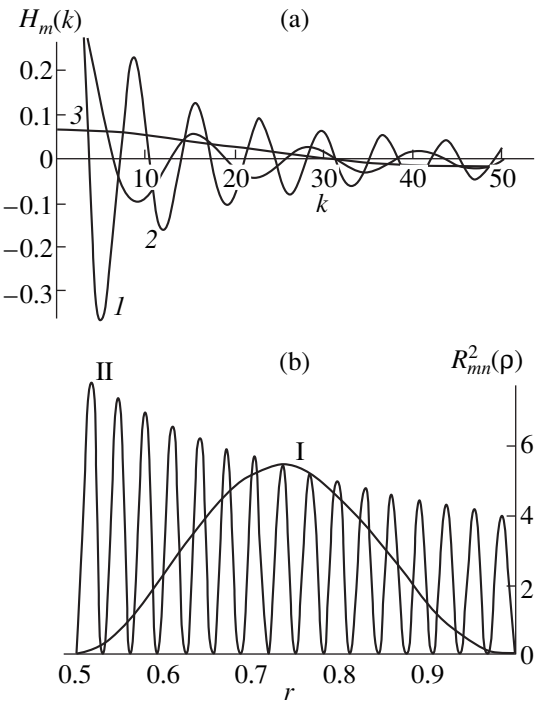

Fig. 2. The quantum-mechanical behavior of an Ag^+ ion in a ring infinite potential well. (a) Graphs of the $H_m(k)$ functions at $m = 0$ and $b = (1)$ 0.1, (2) 0.5, and (3) 0.9. (b) Graphs of the $R^2_{mn}(\rho)$ functions at $m = 0$, $b = 0.5$, and (I) $k_{0,1} = 6.24$ ($n = 1$) and (II) $k_{0,16} = 100.53$ ($n = 16$).

kr, and E is the energy of the silver ion). The wave function is sought as the general solution in the form of a linear combination $R(\rho) = AJ_m(\rho) + BY_m(\rho)$ [where $J_m(\rho)$ and $Y_m(\rho)$ are the m-integral-order Bessel cylindrical functions of the first and second kinds, respectively], which satisfies the boundary conditions $R(\rho) = 0$ at $r = b'/a = b$ and $r = 1$. As a result, we obtain a set of the homogeneous linear equations $AJ_m(bk) + BY_m(bk) = 0$ and $AJ_m(k) + BY_m(k) = 0$, which has a nontrivial solution at the condition $H_m(k) = Y_m(k)J_m(bk) - J_m(k)Y_m(bk) = 0$, i.e., at a discrete spectrum of the k_{mn} values (the second subscript refers to the nth root at the specified m) that are determined, for example, graphically at $m = 0$ (Fig. 2a). The ratio A/B obtained by solving the system at a given k_{mn} simultaneously with the normalizing condition determines the wave function $R_{mn}(\rho)$ whose square at $m = 0$ and $n = 1$ and 16 is depicted in Fig. 2b (curves I and II).

Instead of the consideration of a more realistic ion behavior in the well of variable width, we will treat the ion behavior as a function of the well width within the used simple model. The state of an ion in a narrow or wide part of the channel is approximately identical to that in a narrow or wide well of a constant width. As can be seen from Fig. 2b, the narrower the well, the larger the value of k_{mn}. If the ion moves from a wide part of the conduction channel to its narrow part with the activation energy E_a, the ion in the wide potential well should be in high-energy states with $k_{mn} \sim 100$ [the energy in the Schrödinger equation is converted to the usual system of units $E = k^2_{mn}\hbar^2/(2\mu a^2)$ and is equated to the activation energy $E_a = 0.1$ eV [1] at the a value taken equal to half the unit cell parameter]. However, it is seen from Fig. 2b that the larger the energy of state, the higher the probability of finding the ion near the channel wall (the "sliding" of the ion over the channel wall).

If the channel walls are actually the regions of mobile ion motion, the discrepancies between the aforementioned excluded-volume model (used for optimizing the EXAFS data) and the structural model with shifted equilibrium positions [4, 5] become clear. According to the latter model [4], each tetrahedral position in α-AgI is split into two positions in the directions ⟨100⟩. This corresponds to the motion region that closely encompasses tetrahedral positions and extends along the direction of the shift in equilibrium positions (Fig. 1, drawing *2.4*).

4. CONDUCTION CHANNELS AS EQUIPOTENTIAL SURFACES

The construction of conduction channels as equipotential surfaces is corroborated by calculations of the interionic potential for α-AgI [6]. Figure 3 shows the equipotential surfaces (drawings *1.1–1.4* at $V = 0.14$, 0.2, 0.4, and 1.15 eV, respectively) of the interionic potential for AgI in the field of which silver ions move. The interionic potential is constructed as a superposition (containing parameters) of the lattice sum of the iodine ion–silver ion pair Lennard-Jones potentials and the potential that describes the action of a uniform charge distribution of silver ions on an Ag^+ ion moving inside a unit cell. The parameters of the three-dimensional interionic potential are determined by the least-squares optimization in such a way as to approach the one-dimensional effective pair potential of the iodine ion–silver ion interaction in the EXAFS variant [7], which is independent of any structural models, including the excluded-volume model. The calculations of the interionic potential are described in detail in [6].

At energies less than the activation energy E_a, the regions of Ag^+ motion are anisotropic and are localized [1]. The motion regions at low energies are prolate ellipsoids centered at vertices of the Fedorov cubooctahedron [6]. At energies close to E_a, the ellipsoids first transform into isolated regions (Fig. 3, drawing *1.1*) and, with a further increase in the energy, they merge together (Fig. 3, drawing *1.2*) to form a connected network of conduction channels. The neckings in surface *1.2* coincide with trigonal positions. The centers of tetragonal faces of the cubooctahedron (octahedral posi-

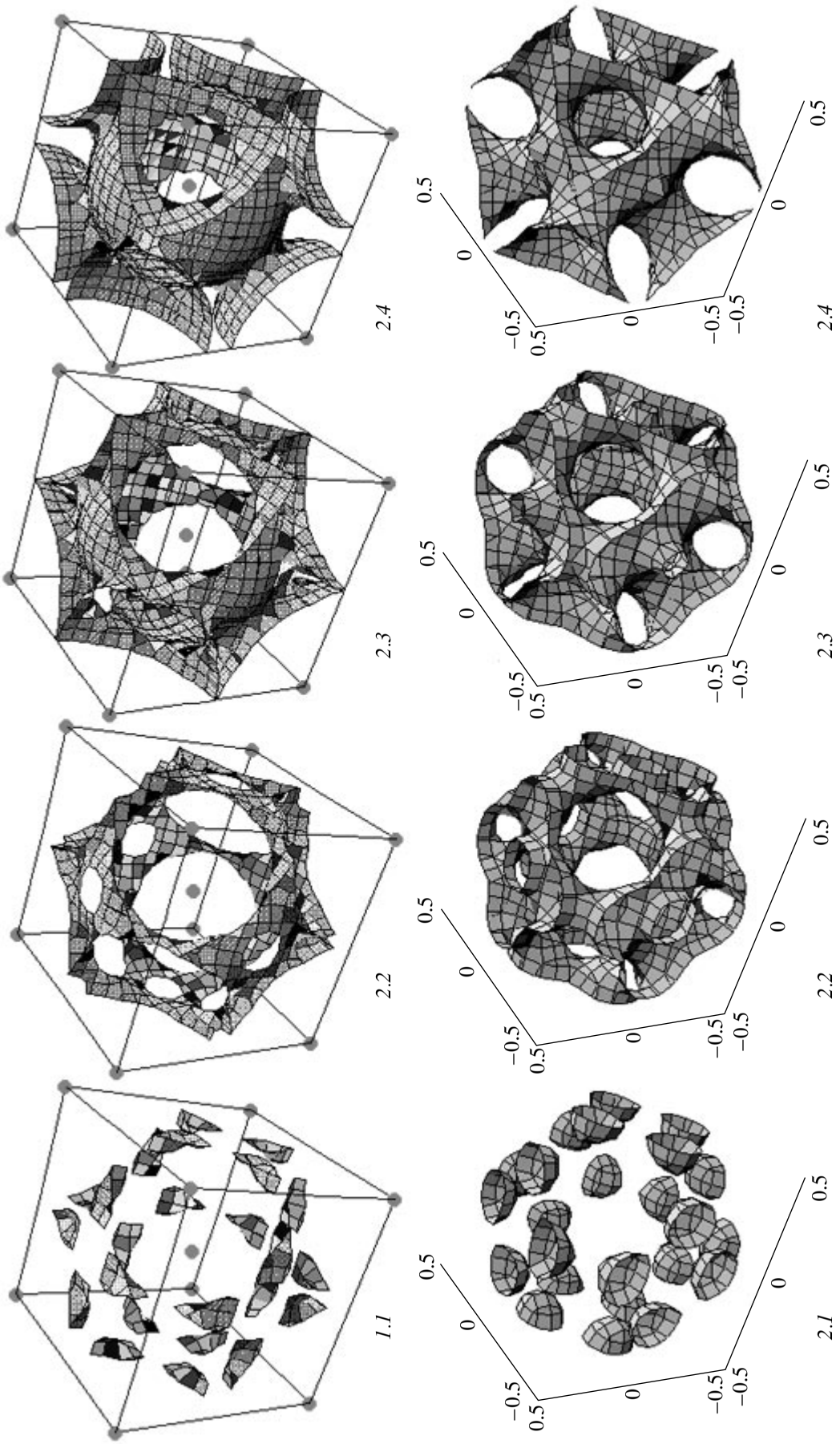

Fig. 3. (*1.1–1.4*) Equipotential surfaces of the Ag^+ ion motion in α-AgI and (*2.1–2.4*) mathematical dynamics. Energy (eV): (*1.1*) 0.14, (*1.2*) 0.2, (*1.3*) 0.4, and (*1.4*) 1.15. Parameter *C* in relationship (1): (*2.1*) 5.5, (*2.2*) 6, (*2.3*) 6.5, and (*2.4*) 7.

tions) are not occupied at first and then (with an increase in the energy) become accessible (Fig. 3, drawing *1.3*). At high energies, there are no particular positions of motion: surface *1.4* in Fig. 3 is composed of external parts of the bcc system of intersecting spheres. Since the density of mobile ions is related to the potential by the Boltzmann expression $\rho(r) = \rho_0 \exp[-V(r)/k_B T]$, drawings *1.1–1.4* in Fig. 3 also characterize the potential surfaces in order of decreasing density of the distribution of silver ions.

According to Andersson *et al.* [8], the rearrangement of the interionic potential surface can be described through the change in the parameter *C* defined by the following functional dependence:

$$\begin{aligned} F(x, y, z) \equiv \exp\{\cos[2\pi(x-y)]\} \\ + \exp\{\cos[2\pi(x+y)]\} + \exp\{\cos[2\pi(y-z)]\} \\ + \exp\{\cos[2\pi(z-x)]\} + \exp\{\cos[2\pi(x+z)]\} \\ + \exp\{\cos[2\pi(y+z)]\} = C \end{aligned} \quad (1)$$

(Fig. 3, drawings *2.1–2.4*). This rearrangement and the merging of isolated surface regions into a single surface depending on *C* are called mathematical dynamics [8]. Andersson *et al.* [8] derived simple mathematical functions that describe such important structures as primitive, bcc, and fcc packings and structures of the diamond, cristobalite, sphalerite, CsCl, CaF_2, ReO_3, and sodalite types. At smaller parameters *C*, the surface appears as isolated "bubbles" located at vertices of the Fedorov cubooctahedron (Fig. 3, drawing *2.1*). As the *C* parameter increases, isolated regions become larger, come close together, and their boundaries are merged with the formation of a periodic surface structure throughout the bulk (Fig. 3, drawings *2.2*, *2.3*). At large parameters *C*, the surface resembles the bcc system of touching spheres (Fig. 3, drawing *2.4*).

We assume that the interionic potential $V(x, y, z)$ is proportional to the function $F(x, y, z)$; i.e., $V(x, y, z) = V, F(x, y, z)$, and the activation energy E_a corresponds to the parameter $C = 6$, at which the connected surface is formed (Fig. 3, drawing *2.2*). Then, the *V* constant in the $v(x, y, z)$ function approximating the interionic potential is $V = E_a/C = 0.0167$ eV. The found potential $V(x, y, z)$ can be used in the solution of the quantum-mechanical problem on the behavior of silver ions at small energies.

5. SYMMETRY RULES AND REGIONS OF MOBILE ION MOTION FOR α-CUI

In the fcc phase of CuI, the tetrahedron and octahedron that involve atoms of the fixed lattice and form the corresponding holes in the structure share a common face. Even in the early diffraction investigations, Azaroff [9] revealed large thermal vibrations along the ⟨111⟩ direction and assumed that the diffusion occurs in this direction. This is quite natural, because an octahedral position is most crystallographically open and accessible.

Within the model of shifted equilibrium positions [5], it is supposed that positions of Cu^+ ions are shifted from tetrahedral centers (1/4, 1/4, 1/4) in four directions ⟨111⟩ toward tetrahedron faces. It was found by the fitting of diffraction data for the α phase at 445°C that copper ions are shifted to the (0.3, 0.3, 0.3) position.

By interpreting the EXAFS data in the framework of the excluded-volume model, Boyce *et al.* [3] obtained the best agreement ($T = 470$°C) when the occupancy of the octahedral position is approximately half as much as that of the tetrahedral position. The conductivity path in the ⟨100⟩ direction that directly connects the tetrahedral positions through the midpoint of the common edge of two tetrahedra is highly improbable due to the high energy barrier (~0.7 eV). The path in the direction ⟨111⟩ with a barrier of 0.16 eV through the face that, as follows from the contour map of ion density [3], can pass not exactly through the octahedral position (1/2, 1/2, 1/2) is more probable.

The recent structural study performed by Keen and Hull [10] proved that Cu^+ ions do not occupy the (1/2, 1/2, 1/2) positions at all and cast some doubt on the ⟨111⟩ direction as a diffusion direction, but did not give any alternative. The molecular-dynamics calculations carried out at approximately the same time by Zheng-Johansson *et al.* [11–13] showed that the ⟨100⟩ direction is the preferential conductivity path, even though thermal vibrations in the ⟨111⟩ direction are very large. According to Chahid and McGreevy [14], the interionic potential chosen so that the diffusion coefficients are best reproduced can, however, lead to local structural distortions that are actually absent, which calls into question the main conclusion made in [11–13]. That is partly why the distribution of mobile Cu^+ ions in the γ, β, and α phases of CuI was thoroughly investigated in [14]. The total structure factor (of Bragg and diffuse scatterings) measured by neutron diffraction was simulated by the reverse Monte Carlo method. This recent work confirmed that the conductivity path in the ⟨100⟩ direction immediately between the tetrahedral positions is preferential (Fig. 4a). The (1/2, 1/2, 1/2) positions are very insignificantly occupied at the highest temperatures when the diffusion proceeds through octahedral positions along the ⟨111⟩ direction.

Thus, it is seen that experimental and theoretical investigations into the conductivity paths of Cu^+ ions in α-CuI do not give a completely consistent and universally accepted pattern and do not provide conclusive answers to the question as to the direction (⟨111⟩ or ⟨100⟩) of the Cu^+ diffusion. However, it seems to be clear that the ion diffusion predominantly occurs in the periphery of octahedral holes. As is seen from Fig. 4b, this inference can be extended to superionic conductors of the fcc type not only with the cationic conductivity

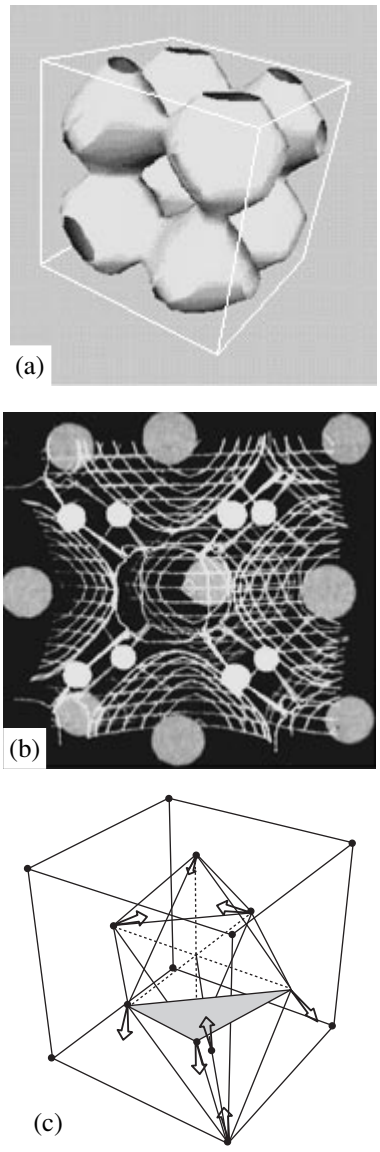

Fig. 4. (a) Density of distribution of Cu^+ ions at the 20% level. The maximum density of distribution in the unit cell is taken as 100% [14]. (b) Experimental paths of the F^- ion diffusion in PbF_2. (c) Symmetry rules for the allowed path of motion of a mobile Cu^+ ion in α-CuI.

but with the anionic conductivity as well: mobile F^- ions in PbF_2 migrate in the vicinity of the octahedral position and do not occupy it [15]. Our constructions (Fig. 1, drawing *3.4*) show that the mobile ion from the tetrahedral position moves first in the ⟨111⟩ direction, then along the periphery of the octahedral hole in the ⟨100⟩ direction, thereafter toward the empty tetrahedral position again in the ⟨111⟩ direction, etc.

Now we explain why the (1/2, 1/2, 1/2) position is not occupied. For this purpose, we invoke the second-order Jahn–Teller effect theory [16], which was successfully used in a similar case of α-AgI [2].

Let us consider tetrahedral and octahedral fragments with the common face in the fcc unit cell (Fig. 4c). In the motion of ion, the local clusters $[CuI_4]^{3-}$ and $[CuI_6]^{5-}$ are treated as Cu^+ fragments. From the ligand field theory for tetrahedral and octahedral complexes with π ligands [17], it is known that the highest filled (hf) and the lowest empty (le) levels exhibit the symmetry types $\Gamma_{hf} = t_2$ and $\Gamma_{le} = a_1$ for $[CuI_4]^{3-}$ and $\Gamma_{hf} = e_g$ and $\Gamma_{le} = t_{1u}$ for $[CuI_6]^{5-}$. The symmetry rules $\Gamma_{hf} \otimes \Gamma_{le} \supset \Gamma_Q$ [16] determine the symmetry types of the vibrational coordinate Γ_Q, along which the distortion of a tetrahedron ($t_2 \otimes a_1 = T_2$) and an octahedron ($e_g \otimes t_{1u} \supset T_{1u}$) is a spontaneous process. Figure 4c depicts the possible tetrahedron and octahedron distortions for the vibrational coordinates T_2 and T_{1u}, respectively. It is seen that the ion copper motion and iodine ion displacements are correlated and the common point symmetry group C_{3v} is retained upon distortion of local clusters.

By assuming that the transition state is realized exactly at the center of the octahedral hole, we immediately come to the following discrepancy. The degenerate vibration T_{1u} corresponds to several allowed motion paths from the initial tetrahedral position to empty positions, which is most pictorially seen in drawing *3.4* in Fig. 1. However, each transition state can correspond to only one path: "the saddle can connect only two valleys" [16]. Therefore, the transition state must necessarily conform to the octahedron distortion down to the C_{3v} symmetry. This state is realized in the periphery of the octahedral hole, and the (1/2, 1/2, 1/2) position remains unoccupied. The C_{3v} symmetry is exhibited by the local configuration of ions at nonextreme points along the motion path (Fig. 4c) and, according to the symmetry rules [16], this coordinate is totally symmetrical. As follows from the tables of correlations between the group representations, the T_{1u} representation in the C_{3v} point group transforms into totally symmetrical. This conclusion completes the consistent pattern of the allowed motion path.

REFERENCES

1. J. B. Boyce and T. M. Hayes, in *Physics of Superionic Conductors*, Ed. by M. B. Salamon (Springer-Verlag, New York, 1979; Zinatne, Riga, 1982).
2. V. I. Polyakov, Zh. Fiz. Khim. **71** (7), 1248 (1997); **72** (11), 1996 (1998); **72** (12), 2247 (1998).
3. J. B. Boyce, T. M. Hayes, J. C. Mikkelsen, and W. Stutius, Solid State Commun. **33** (2), 183 (1980).
4. W. Buhrer and W. Halg, Helv. Phys. Acta **47** (1), 27 (1974).
5. W. Buhrer and W. Halg, Electrochim. Acta **22** (7), 701 (1977).
6. V. I. Polyakov, Zh. Fiz. Khim. **73** (9), 1592 (1999).

7. G. Dalba, P. Fornasini, R. Gotter, and M. Grazioli, Philos. Mag. B **71** (4), 751 (1995).
8. S. Andersson, D. Lidin, and M. Jacob, Z. Kristallogr. **210** (11), 826 (1995).
9. L. V. Azaroff, J. Appl. Phys. **32** (9), 1658 (1961).
10. D. A. Keen and S. Hull, J. Phys.: Condens. Matter **7** (29), 5793 (1995).
11. J. X. M. Zheng-Johansson, I. Ebbsjo, and R. L. McGreevy, Solid State Ionics **82** (3/4), 115 (1995).
12. J. X. M. Zheng-Johansson and R. L. McGreevy, Solid State Ionics **83** (1/2), 35 (1996).
13. R. L. McGreevy and J. X. M. Zheng-Johansson, Solid State Ionics **95** (3/4), 215 (1997).
14. A. Chahid and R. L. McGreevy, J. Phys.: Condens. Matter **10** (12), 2597 (1998).
15. R. Bachmann and H. Schulz, Solid State Ionics **9/10** (1), 521 (1983).
16. R. Pearson, *Symmetry Rules for Chemical Reactions* (Academic, New York, 1976; Mir, Moscow, 1979).
17. I. B. Bersuker, *Electronic Structure and Properties of Coordination Compounds: Introduction to the Theory* (Khimiya, Leningrad, 1976, 2nd ed.).

Translated by O. Borovik-Romanova

Physics of the Solid State, Vol. 43, No. 4, 2001, pp. 663–664. Translated from Fizika Tverdogo Tela, Vol. 43, No. 4, 2001, pp. 637–638.

DEFECTS, DISLOCATIONS, AND PHYSICS OF STRENGTH

Screening of the Deformation Field in a Solid by Point Defects

V. I. Emel'yanov

Moscow State University, Vorob'evy gory, Moscow, 119899 Russia

Received July 19, 2000

Abstract—It is demonstrated that in an isotropic infinite solid body with a high concentration of point defects, the deformation produced by a test defect decreases with the distance from it according to a law similar to that of the decrease in the potential of a point charge with Debye screening. © *2001 MAIK "Nauka/Interperiodica".*

1. External effects (laser irradiation, irradiation with particle beams, action of shock waves, etc.) generate high concentrations of point defects (vacancies and interstices) in solids. The interaction of defects with a self-consistent deformation field brings about the formation of ordered defect-deformation (DD) structures, namely, clusters and periodic structures. The theory of the stationary DD nanostructures was elaborated in [1], and the nonlinear multimode dynamics of the formation of DD nanostructures was considered in [2].

This work deals with a new aspect of the theory of a self-organizing DD system. It is demonstrated that if the concentration of point defects is sufficiently high, the nature of the deformation field which is induced in an isotropic solid body by a point defect changes. Instead of a local deformation, which is typical of a point defect in an ideal isotropic solid body, a deformation emerges which decreases with distance r from the defect according to the law $\exp(-r/r_s)/r$ (similarly to the electrostatic potential of a point charge with Debye screening). The screening length r_s of the elastic interaction of defects is determined, which falls in the nanometer range.

The considered effect of the screening of the deformation field by point defects can be of interest in the theory of self-organization of defects, including the problem of the formation of ordered DD nanostructures, surface defect-induced melting, etc.

2. We assume that point defects are distributed with a mean concentration n_{d0} in an infinite isotropic solid body. Let a defect (dilatation center), which will be considered a test defect, be located at the origin of coordinates $\mathbf{r} = 0$. The defects interact with the deformation field $\xi(\mathbf{r}, t) = \mathrm{div}\mathbf{u}(\mathbf{r}, t)$, where $\mathbf{u}$ is the displacement vector of the medium and the energy of a single defect is equal to [3]

$$H_d = -\theta_d\xi. \tag{1}$$

Here, $\theta_d = K\Omega_d$, K is the elastic modulus, and Ω_d is the change in the crystal volume due to the generation of a single defect.

Let us determine the deformation field induced by a test defect located at the origin of coordinates under the assumption that there is a field of mobile point defects with a concentration n_d. Taking into account expression (1), the equation of this deformation can be written as

$$\frac{1}{c_l^2}\frac{\partial^2\xi}{\partial t^2} = \Delta\xi - \frac{\theta_d}{\rho c_l^2}\Delta(\delta(\mathbf{r}) + (n_d - n_{d0})), \tag{2}$$

where c_l is the longitudinal sound velocity, ρ is the medium density, Δ is the three-dimensional Laplace operator, and $\delta(\mathbf{r})$ is the three-dimensional Dirac function. We disregarded the sound dispersion in expression (1).

Taking into account expression (1), the equation for the defect concentration can be written as [1]

$$\frac{\partial n_d}{\partial t} = D_d\Delta n_d - \frac{D_d\theta_d}{k_B T}\mathrm{div}(n_d\mathrm{grad}(\xi + l_d^2\Delta\xi)), \tag{3}$$

where D_d is the diffusion coefficient of the defect and l_d is the length of the defect–atom interaction. The first term on the right-hand side of Eq. (3) represents the diffusion, and the second term describes the deformation induced drift of the defects. The second term in the parentheses accounts for the nonlocality of the interaction of the defect with an atom in the lattice (l_d is the length of defect–atom interaction in the lattice [1]). Equations (2) and (3) constitute a closed system of equations which describes a self-consistent DD system.

3. Let us consider the stationary state of a self-consistent DD system. The stationary distribution of the defect concentration in the field of the self-consistent deformation can be deduced from Eq. (3), where $\frac{\partial n_D}{\partial t} = 0$,

$$\begin{aligned} n_d &= n_{d0}\exp\left(\frac{\theta_d}{k_B T}(\xi + l_d^2\Delta\xi)\right) \\ &\approx n_{d0} + n_{d0}\left(\frac{\theta_d}{k_B T}(\xi + l_d^2\delta\xi)\right). \end{aligned} \tag{4}$$

1063-7834/01/4304-0663$21.00 © 2001 MAIK "Nauka/Interperiodica"

Here, an approximate equality holds with the proviso that $\theta_d(\xi + l_d^2 \Delta\xi)/k_B T \ll 1$. According to expression (4), when $r \longrightarrow \infty$ and $\xi \longrightarrow 0$, the concentration of defects tends to its spatially homogeneous value, $n_d \longrightarrow n_{d0}$.

Let us substitute expression (4) into Eq. (2), where we set $\frac{\partial^2 \xi}{\partial t^2} = 0$. After rearrangement, we obtain the following equation for the deformation produced by the test defect:

$$\Delta\xi - \frac{1}{r_s}\xi = -\frac{\theta_d}{\rho c_l^2 l_d^2 (n_{d0}/n_{dc})}\delta(\mathbf{r}), \tag{5}$$

where the screening length of the elastic interaction is given by

$$r_s = l_d \left(\frac{n_{d0}}{n_{dc}}\right)^{1/2} \Big/ \left(1 - \frac{n_{d0}}{n_{dc}}\right)^{1/2} \tag{6}$$

and the critical concentration of defects is

$$n_{dc} = \rho c_l^2 k_B T/\theta_d^2. \tag{7}$$

The solution to Eq. (5) with the constraint

$$n_{d0} < n_{dc} \tag{8}$$

has the form

$$\xi(\mathbf{r}) = \frac{\theta_d}{\rho c_l^2 4\pi l_d^2 (n_{d0}/n_{dc})}\frac{\exp(-r/r_s)}{r}. \tag{9}$$

When constraint (8) holds, in conformity with expression (9), the point defect located at the point $\mathbf{r} = 0$ generates a deformation field which decreases with distance similarly to the potential of a point charge screened by a self-consistent distribution of other charges (Debye screening). In this case, the analog of the Debye radius is the screening length of the elastic interaction which is defined by Eq. (6).

The change over to the case of a defect-free medium with a single test defect at the origin of coordinates $\mathbf{r} = 0$ is elaborated by a passage to the limit in formula (9), $n_{d0} \longrightarrow 0$. With due regard for the representation of δ-function

$$\delta(\mathbf{r}) = \lim_{r_s \to 0}\left(\frac{\exp(-r/r_s)}{4\pi r_s^2 r}\right)$$

and expression (6), from formula (9), we obtain

$$\lim_{n_{d0} \to 0} \xi(\mathbf{r}) = \frac{\theta_d}{\rho c_l^2}\delta(\mathbf{r}). \tag{10}$$

Formula (10) coincides with the standard expression for the deformation field of a point defect in an infinite isotropic solid body without defects [3].

4. If we take into account the sound dispersion in Eq. (2), condition (8), which determines the concentration of defects that corresponds to the screening of the deformation, is replaced by the condition

$$l_0^2 n_{dc}/l_d^2 < n_{d0} < n_{dc}, \tag{11}$$

where l_0 is the parameter of the sound dispersion (the length of the atom–atom interaction in the lattice). For metals, we have $l_d \gg l_0$ [4].

As can be seen from expression (11), the screening of the elastic interaction of point defects is observed when the concentration of the defects exceeds the first critical value $n_{dc1} = l_0^2 n_{dc}/l_s^2$, where $n_{dc} \sim 10^{19}$ cm^{-3} ($\rho c_l \sim$ K $\sim 10^{12}$ erg cm^{-3}, $T \sim 300$ K, $\theta_d \sim 10$ eV).

In [1, 2], it was shown that when condition (11) holds, the system of defects interacting through the elastic field exhibits an instability. This results in the formation of clusters of defects autolocalized in the deformation potential wells. The dimension of the DD cluster which was obtained in [1] with the proviso that $l_d \gg l_0$ coincides with the screening length of the elastic interaction r_s defined by formula (6).

Thus, assuming that $n_{d0} > n_{dc1}$, the solid body is partitioned into independent regions with dimensions of the order of the screening length r_s within which the elastic interaction between the defects causes the formation of DD nanoclusters.

If the second threshold related to the concentration of the defects is exceeded ($n_{d0} > n_{dc}$), periodic DD nanostructures are formed in the medium [1, 2]. In [1], it was demonstrated that their formation is described by the Landau–Ginzburg equation and occurs as a second-order phase transition. In this case, the screening length (6) fulfills the role of a correlation length in the region prior to the phase transition ($n_{d0} < n_{dc}$). As can be seen from expression (6), when the phase transition point is approached ($n_{d0} \longrightarrow n_{dc}$), the correlation length tends to infinity, $r_s \longrightarrow \infty$ in accordance with its usual behavior in second-order phase transitions [5].

REFERENCES

1. V. I. Emel'yanov and I. M. Panin, Fiz. Tverd. Tela (St. Petersburg) **39** (11), 2029 (1997) [Phys. Solid State **39**, 1815 (1997)].
2. V. I. Emel'yanov and I. M. Panin, Fiz. Tverd. Tela (St. Petersburg) **42** (6), 1026 (2000) [Phys. Solid State **42**, 1058 (2000)].
3. J. D. Eshelby, Solid State Phys. **3**, 79 (1956).
4. V. I. Emel'yanov and I. M. Panin, Proc. SPIE **3734**, 294 (1999).
5. L. D. Landau and E. M. Lifshitz, in *Statistical Physics* (Nauka, Moscow, 1976; Pergamon, Oxford, 1980), Part 1.

Translated by O. Moskalev

Physics of the Solid State, Vol. 43, No. 4, 2001, pp. 665–669. Translated from Fizika Tverdogo Tela, Vol. 43, No. 4, 2001, pp. 639–643.

DEFECTS, DISLOCATIONS, AND PHYSICS OF STRENGTH

Grain Boundaries and Elastic Properties of Aluminum-Oxide and Stainless-Steel-Based Cermets

S. N. Ivanov*, E. N. Khazanov*, A. V. Taranov*, I. S. Mikhaĭlova, V. M. Gropyanov**, and A. A. Abramovich****

**Institute of Radio Engineering and Electronics, Russian Academy of Sciences, Mokhovaya ul. 11, Moscow, 103907 Russia*
***St. Petersburg Technological University of Plant Polymers, ul. Ivana Chernykh 4, St. Petersburg, 198095 Russia*
e-mail: ivanov@mail.cplire.ru
e-mail: andrew@ns2740.spb.edu
Received July 25, 2000; in final form, September 11, 2000

Abstract—Elastic properties and thermal-phonon scattering are investigated in Al_2O_3 + 0.3% MgO ceramics and cermets of different porosities based on them. The cermets, reinforced with a metallic frame of the steel 12X18H9T, are obtained by dry compaction followed by sintering. It is shown that the elastic moduli of cermets are determined by their porosity and that the grain boundaries can be investigated in detail by a nonequilibrium-phonon propagation method. © *2001 MAIK "Nauka/Interperiodica".*

INTRODUCTION

New composites based on ceramics and metals (cermets) have been being developed since the 1960s, and unique materials have been produced which combine the virtues of both components, such as heat resistance, temperature stability, wear resistance, service reliability, and chemical stability [1]. At the present time, cermets are already in service in the machine-building industry (high-temperature elements of gas turbines, rolling bearings, high-precision temperature-stable tools), the medical and food industries (parts of pumps and devices for pumping over corrosive liquids), and other fields [2]. However, the development of cermets of new types and the prediction and investigation of their properties involve difficulties. Among these are the sophisticated high-temperature synthesis technology (often requiring a vacuum and high pressures), not entirely known mechanisms for the grain formation and for the grain-boundary influence on the strength and other properties of cermets, and the lack of methods providing reliable information about grain boundaries.

In this work, we investigate cermets based on Al_2O_3 and on the stainless steel 12X18H9T with the aim of (1) developing a comparatively simple and cheap technology for the fabrication of the cermets and (2) obtaining samples which have a high strength in combination with a low density. We synthesized a material which is characterized by large elastic moduli and high wear resistance and thermal stability and, therefore, has an application potential in machine building and other fields of engineering.

It is known that the mechanical properties of cermets depend heavily on their porosity and the quality of grain boundaries [3], which are determined by the synthesis technique of the original material, as well as by the fabrication technology of the samples and their finishing thermal treatment. To investigate the influence of these factors, we apply two different dynamic elastic-wave methods in this work. At room temperature, low-frequency ultrasound waves are used, while in the liquid-helium temperature range, we apply a nonequilibrium acoustic-phonon propagation method. The former method gives information about the elastic and, hence, strength properties of the materials. The data obtained by the latter method allowed us to construct a model for grain boundaries in the ceramic Al_2O_3 and cermets based on it.

1. EXPERIMENTAL TECHNIQUE

We investigated samples of the original ("basic") ceramic Al_2O_3, which contained a stabilizing addition MgO (0.3%), and cermets based on this ceramic in combination with 20% of the commercial-quality stainless steel 12X18H9T (18% Cr, 9% Ni, 1% Ti, 72% Fe).

The basic ceramic samples were prepared by dry compaction of the mixture under a pressure of 80–100 MPa followed by sintering in a vacuum at 1940°C. These samples and their characteristics will be called basic in what follows, because their preparation technology with adding small amounts of MgO is typical of the synthesis of Al_2O_3 ceramics. The samples thus obtained had a volume porosity lower than 1%, with the average grain diameter being 10^{-3} cm.

To fabricate a cermet, the initial fine-grained mixture was prepared by milling Al_2O_3 powder in a ball mill in the presence of balls 1–2 cm in diameter made from the stainless steel 12X18H9T. The milling was

Measured parameters of the Al_2O_3 ceramic and cermets based on it

Sample	Composition	Sintering temperature, K	Porosity, %	Elastic moduli, GPa			Strength σ, MPa	Poisson's ratio, ν	D_{eff}, cm^2/s (T = 3.8 K)
				G	*E*	*K*			
Basic	Al_2O_3 + 0.3% MgO	1920	≤1.0	144.0	358.0	234.5	900–1000	0.24	1.2×10^2
1	Al_2O_3 + 20% stainless steel	1920	9.1	71.4	170.3	238.7	560	0.35	1.2
2	Al_2O_3 + 0.5% Cr_2O_3 + 1% TiO_2 + 0.5% MnO_2 + 20% stainless steel	1640	19.0	58.5	153.1	151.1	425	0.33	0.82
3	Al_2O_3 + 20% stainless steel	1690	36.8	35.1	83.0	48.9	140	0.21	0.74

terminated when the steel content in the Al_2O_3 powder became equal to 20%. Then, the mixture obtained was doped with a plasticizer and subjected to dry compaction under a pressure of 80–100 MPa and then sintered in a vacuum at 1640–1920°C. Finally, the samples were cooled in the furnace at an average rate of 100°C/h and no further treatment was made. The cermets thus prepared (samples 1–3 in table) ranged in volume porosity from 9 to 37%, but had the same steel content (the composition of the basic ceramic in sample 2 differed insignificantly from that in the other samples). The cermet samples were then cut into smaller parts of the required dimensions, which were further ground and polished, depending on the measuring method.

To investigate the elastic properties of the cermets, we measured their density by the hydrostatic method and the velocities of longitudinal and transverse ultrasound waves of a frequency of 1.7 MHz. With the data obtained, we calculated Young's modulus *E*, the shear modulus *G*, the bulk modulus *K*, and Poisson's ratio from the well-known formulas of the elasticity theory for an isotropic medium [4]. We used the pulsed phase-interferometry method, which made it possible to determine the velocity of ultrasound within an accuracy of 1–2%, the elastic moduli within 5%, and Poisson's ratio within 10–20%.

The strength of samples was measured with an IP6011-500-1 hydraulic press. The ultimate compression strength was evaluated from the formula $\sigma = 4P/\pi d^2$, where P is the breaking load and d is the diameter of the sample; for each type of composite, the compression test was performed at a loading rate of 0.04–0.05 kg/s for ten samples and the results were averaged.

Examination of the surface structure (cleaved facet) of the Al_2O_3 ceramic samples was made with a JSM-840 scanning electron microscope (the Jeol company) and a P4-SPM-MTD scanning probe microscope (atomic-force microscopy regime) operating in the contact mode.

The kinetics of phonons at liquid-helium temperatures was investigated by the "heat pulse" method [5]. For this purpose, a gold film was sputtered on one face of a plate of the material under study; this film was heated by a short current pulse ($\cong 10^{-7}$ s) and served as an injector of nonequilibrium phonons into the sample. A meander-shaped bolometer with the dimensions 0.3×0.25 mm^2 was deposited on the opposite plate face. A weak bias magnetic field ($\sim 2 \times 10^2$ Oe) was applied to the bolometer in order to measure the temperature dependence of the scattered intensity of nonequilibrium phonons in the sample over the temperature range 1.7–3.8 K. The power dissipated in the heater was so low that the injected phonons could be characterized by a temperature equal to that of the thermostat (bath), and their frequency distribution was close to the Planck distribution.

2. EXPERIMENTAL RESULTS AND DISCUSSION

Micrographs of the surfaces of the Al_2O_3 ceramic and cermet samples obtained by scanning electron microscopy are presented in Fig. 1. It is seen that, for the most part, grains in the basic ceramic have isomeric hexagonal faces (Fig. 1a) and the grain faces meet at an angle close to 120° at interface junctions (see also [6]); the average grain diameter is about 10^{-3} cm. In the cermet samples (Fig. 1b), metal grains having a near-spherical shape are clearly visible against the background of faceted grains of the polycrystalline Al_2O_3. Examination of a fairly large area of cleaved facets of cermet samples revealed that the metal grains are distributed uniformly and do not form clusters or filament-like structures. This is supported by resistance measurements, according to which the cermets remained insulators and had no "junctions." A more detailed structure of the metal grains as obtained by atomic-force microscopy is presented in Fig. 1c; this allows one to estimate their minimum size with a reasonable accuracy. The dimensions of metal grains are strongly scattered and lie in a range of $R_m \approx$ 200–1000 nm (Figs. 1b and 1c).

The practically important room-temperature strength characteristics of the Al_2O_3 composites, their initial compositions, and the sintering temperatures are listed in the table. Note that the mechanical characteristics (elastic moduli and strength) of the cermets differ from their respective values for the basic ceramic and vary rather smoothly with increasing overall volume porosity. The measured elastic moduli correlate well with the data presented in [7], and their dynamics is

controlled only by the porosity of the material; that is, low-frequency measurements and strength data carry no information about the properties of grain boundaries in the Al_2O_3 and metal–α-Al_2O_3 interfaces.

The last column of the table lists the values of the effective phonon diffusion coefficient D_{eff} at a liquid-helium temperature. These values of D_{eff} are first invoked to characterize the ceramic materials; they allow one to infer the character of phonon scattering at grain boundaries in ceramics and to predict the mechanical characteristics of the material at room temperature.

Let us discuss the data on the propagation of weakly nonequilibrium phonons in the basic Al_2O_3 ceramic and cermet samples. The curves in Fig. 2 describe the propagation of a heat pulse in the basic Al_2O_3 sample at different temperatures. These bell-shaped bolometer signal curves are typical of diffusive pulse propagation and have a well-defined maximum. For phonons traveling the thickness L of the ceramic sample, the signal maximum will be observed at a time t_{max}, which characterizes the properties of grain boundaries and is given by the expression [8]

$$t_{max} \cong \frac{L^2}{D_{eff}} \cong \frac{L^2 S}{v_s R \Sigma f_\omega}. \quad (1)$$

Here, v_s is the velocity of sound in a ceramic grain, R is the average dimension of grains, S is the area of the grain surface, Σ is the total contacting area per grain, and f_ω is the probability that a phonon passes through the contact area.

The temperature dependence of t_{max} is determined by the temperature dependence of f_ω, which, in the model used [8], is a function of the wavelength (energy) of the phonon (i.e., of the temperature of the sample in our experiments) and determined by the mechanism of phonon scattering at the grain boundaries, which depends on the ceramic sintering process, the composition of the initial powder, and the other specific features of the ceramic fabrication. For the basic Al_2O_3 samples, the temperature dependence of t_{max} is closely approximated by the expression $t_{max} = A + BT^4$ (see inset in Fig. 2), where the first term is determined by the acoustic matching of the contacting ceramic grains for nonequilibrium phonons and the second is due to phonon scattering at the interface of the grains. In the range of the plateau, one can estimate the coefficient f_ω by putting $S/\Sigma \cong 1$, $v_s \cong 7 \times 10^5$ cm/s, and the grain diameter to be $\cong 10^{-3}$ cm for the dense basic ceramic with the result that f_ω is equal to 0.5–0.8, which is evidence that the grains matched fairly well in this material. In the most likely case of phonon scattering at grain boundaries, the temperature dependence $t_{max} \sim T^4$ will take place if the condition $ql_b \ll 1$ is met [9], where q is the phonon wave vector and l_b is the grain boundary thickness. In our experiments, $q = (1–2) \times 10^6$ cm^{-1}; therefore, l_b is estimated to be $l_b \cong 0.5–1.0$ nm, which supports the conclusion that grain boundaries are perfect in the dense α-Al_2O_3 ceramic.

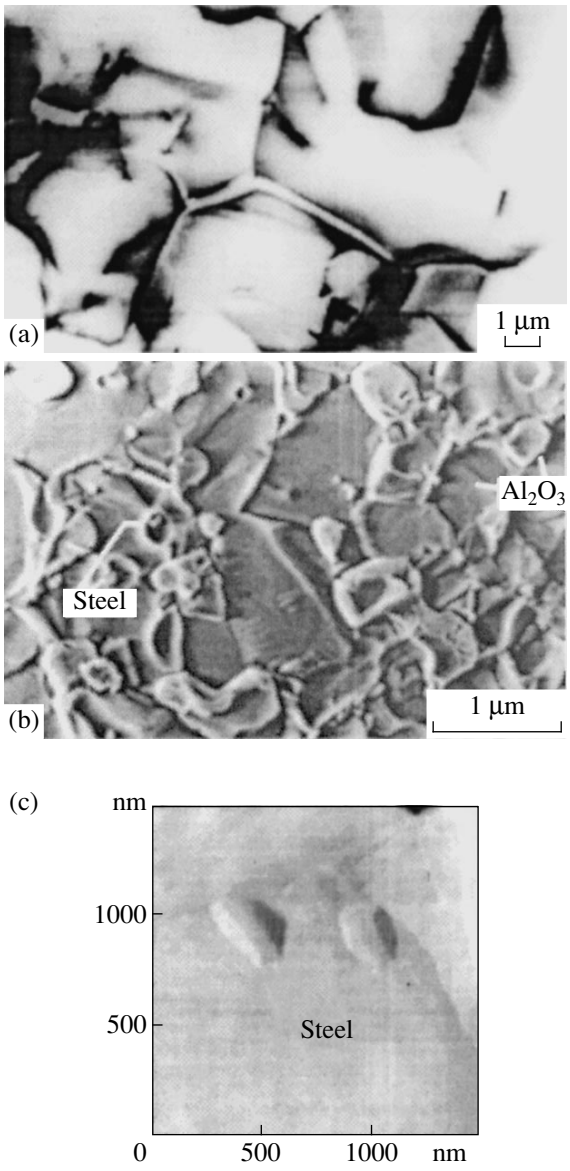

Fig. 1. Electron micrographs of cleaved facets of (a) ceramic Al_2O_3–0.3 wt % MgO (basic sample in table) and (b, c) cermet Al_2O_3 + 20 wt % stainless steel (sample 1 in table) differing in image scale.

In cermet samples, we have a completely different situation (Fig. 3). The time t_{max} is fully two orders of magnitude longer; that is, the effective phonon diffusion coefficient is smaller (see table). However, the most important result is that the temperature dependence of t_{max} is radically altered; namely, we have $\partial t_{max}/\partial T < 0$ in cermet samples. The slower phonon diffusion and negative $\partial t_{max}/\partial T$ in cermets cannot be due to metal grains, whose acoustic characteristics are different from those of α-Al_2O_3. Estimations of the possi-

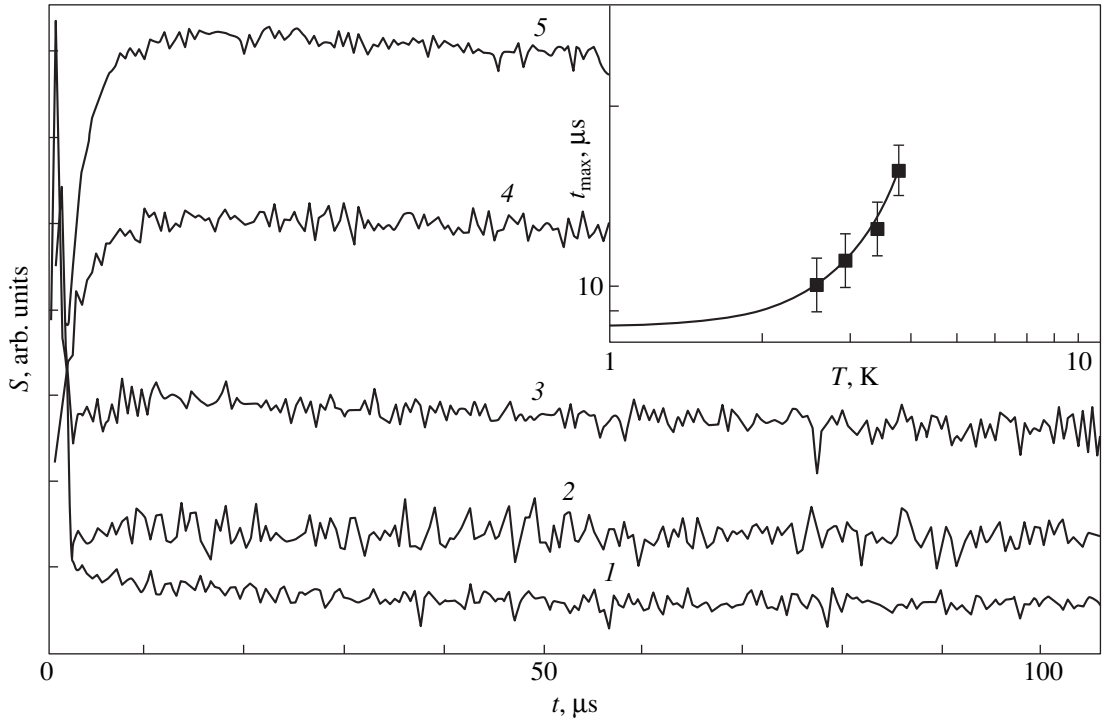

Fig. 2. Time dependence of the signal amplitude S of nonequilibrium phonons in the basic ceramic Al_2O_3 for L = 0.5 mm and different temperatures T (K): (*1*) 3.83, (*2*) 3.44, (*3*) 2.18, (*4*) 2.57, and (*5*) 2.28. The inset shows the temperature dependence of t_{max}, with the solid line being $t_{max} = A + BT^4$.

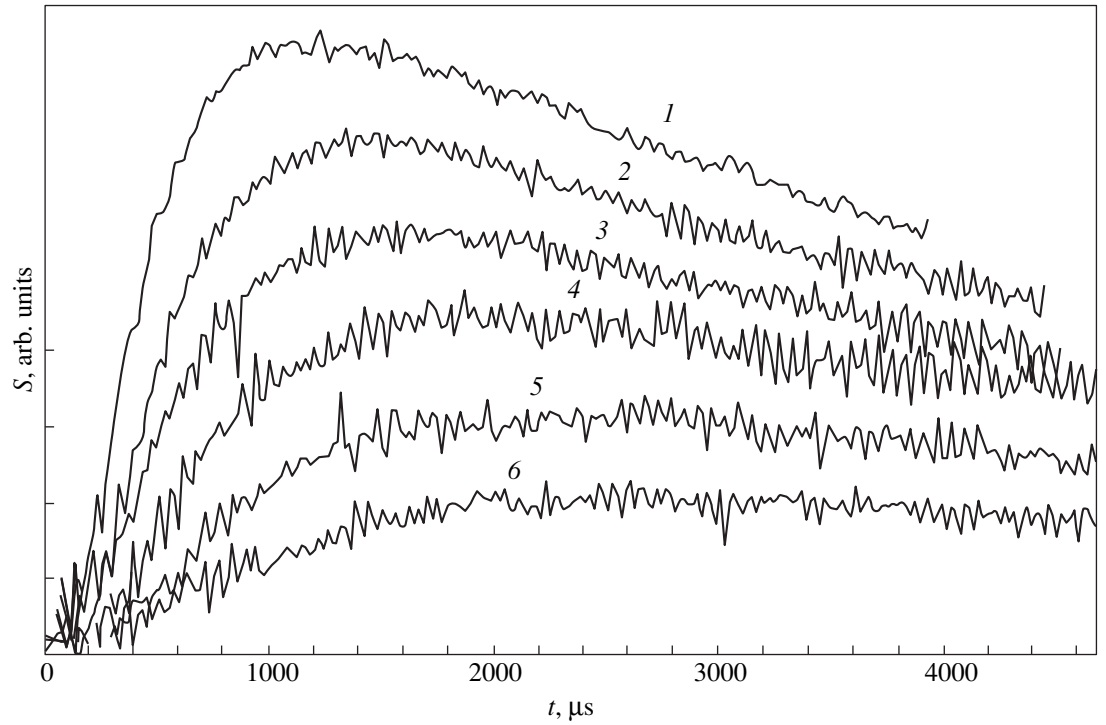

Fig. 3. Time dependence of the signal amplitude S of nonequilibrium phonons in a cermet sample with a porosity of 19% and L = 0.3 mm for different temperatures T (K): (*1*) 3.8, (*2*) 3.48, (*3*) 3.27, (*4*) 3.01, (*5*) 2.79, and (*6*) 2.61.

ble contribution from electron–phonon interaction to phonon scattering in the framework of classical papers [10] show that phonon scattering in the grains of a diameter less than 10^{-4} cm is insignificant and the direct contribution to the damping from the phonon–phonon interaction is also very small; therefore, it is most likely that phonon diffusion becomes slower because of phonon scattering by the metal–α-Al_2O_3 interfaces. According to [9], this can be true if there are many fine voids in these interfaces (for instance, because the metal–insulator wetting is poor [11, 12] and their contacts do not become close in the process of sintering). In this case, we have open interfaces with a noticeably lower density and elasticity. At $l_b \geq 1$ nm, such interfaces are significantly less transparent for phonons and can be the reason for the temperature dependence with $\partial t_{max}/\partial T < 0$. Estimations give reasonable values $l_b \geq 5.0$–10.0 nm for this case. For the cermet samples under study, the variation in D_{eff} correlates with the dynamics of the overall porosity P, which suggests that the porosity in the interfaces is proportional to P.

In closing, we note that the data obtained by the method of nonequilibrium phonon propagation (heat pulse method), proposed in this paper for investigating ceramic samples, allow one to construct a model of grain boundaries in the ceramic Al_2O_3 and cermets based on it. Analysis of the influence of grain boundaries on the mechanical properties of cermets at room temperature will be the objective of further investigation.

ACKNOWLEDGMENTS

The authors are grateful to O.V. Karban' for the examination of cleaved facets of ceramics by atomic-force microscopy.

This work was supported by the Russian Foundation for Basic Research, project no. 00-02-17426.

REFERENCES

1. S. M. Lang, NBS Monogr., No. 6, March 1, 45 (1960).
2. P. S. Kislykh, N. I. Bodnaruk, and M. S. Borovikova, *Cermets* (Naukova Dumka, Kiev, 1985).
3. W.-P. Tai and I. Watanache, J. Am. Ceram. Soc. **81** (6), 1673 (1998).
4. L. Bergmann, *Der Ultraschall und seine Anwendung in Wissenschaft und Technik* (S. Hirzel, Zürich, 1954; Inostrannaya Literatura, Moscow, 1957).
5. S. N. Ivanov, A. V. Taranov, and E. N. Khazanov, Zh. Éksp. Teor. Fiz. **99** (4), 1311 (1991) [Sov. Phys. JETP **72**, 731 (1991)].
6. S. N. Ivanov, E. N. Khazanov, and A. V. Taranov, Fiz. Tverd. Tela (St. Petersburg) **37** (10), 2902 (1995) [Phys. Solid State **37**, 1601 (1995)].
7. *Physical Acoustics: Principles and Methods*, Vol. 3, Part B: *Lattice Dynamics*, Ed. by W. P. Mason (Academic, New York, 1965; Mir, Moscow, 1968).
8. S. N. Ivanov, A. G. Kozorezov, A. V. Taranov, and E. N. Khazanov, Zh. Éksp. Teor. Fiz. **102** (2), 600 (1992) [Sov. Phys. JETP **75**, 319 (1992)].
9. L. M. Brekhovskikh and O. A. Godin, *Acoustics of Layered Media* (Nauka, Moscow, 1989; Springer-Verlag, New York, 1990).
10. *Physical Acoustics: Principles and Methods*, Ed. by W. P. Mason (Academic, New York, 1968–1970; Mir, Moscow, 1974), Vol. 7, Chap. 3.
11. V. N. Eremenko, Yu. V. Naĭdich, and A. A. Nosovich, Élektronika, No. 5, 136 (1959).
12. *Cermets*, Ed. by J. R. Tinklepaugh and W. B. Crandall (Reinhold, New York, 1960; Inostrannaya Literatura, Moscow, 1962).

Translated by Yu. Epifanov

Physics of the Solid State, Vol. 43, No. 4, 2001, pp. 670–676. Translated from Fizika Tverdogo Tela, Vol. 43, No. 4, 2001, pp. 644–650.

DEFECTS, DISLOCATIONS, AND PHYSICS OF STRENGTH

Computer Simulation of the Deformation and Fracture of Crystals

V. A. Lagunov and A. B. Sinani

Ioffe Physicotechnical Institute, Russian Academy of Sciences, Politekhnicheskaya ul. 26, St. Petersburg, 194021 Russia
e-mail: alfred@md1ab.ioffe.rssi.ru

Received June 14, 2000; in final form, September 5, 2000

Abstract—Methods for computer simulation of strength testing of crystals are proposed. The methods employed are similar to usual static methods, and they are used to investigate deformation and fracture of perfect fcc crystals having different orientations with respect to the tensile force. A strain-induced phase transition from the fcc to the hcp structure is detected, and the formation and displacement of crystal twins are observed. Plastoelastic deformation and fracture of crystals are investigated. © *2001 MAIK "Nauka/Interperiodica".*

INTRODUCTION

In [1, 2], we considered models of equilibrium crystals of a spherical shape and of a diameter of ten interatomic distances; the interaction of atoms in the model crystals was described by the Lennard–Jones potential. Such crystals have different structure, which can be the reason for their different behavior under a load. In this paper, we evaluate the strength of these crystals. For this purpose, a method for determining the strength of model crystals is developed, which is similar to the methods usually used under static conditions. By this method, we estimate the strength of perfect single crystals with fcc and hcp lattices, which form spontaneously in computer experiments. The bcc lattice, which was investigated in [3], does not form in the case of the Lennard–Jones interaction potential [1].

1. FORMULATION OF THE PROBLEM

Model crystals are represented in a computer by the coordinates of their atoms in tabulated form. We designate them as x_i, y_i, and z_i, with i running from 1 through n, where n is the number of atoms in the crystal. Cylindrical "samples" for tensile tests are "prepared" from crystals of spherical shape. They have the same cross section over the length of the cylinder; that is, the coordinates of atoms satisfy the condition

$$(y_i - y_0)^2 + (z_i - z_0)^2 < R^2, \tag{1}$$

where R is the radius of the cylinder and y_0 and z_0 are the coordinates of its axis. In computer experiments, the radius R is equal to a quarter of the diameter of the original spherical crystal. The cylindrical samples prepared are "cooled" using the same technique as in the case of the crystal for which relaxation of the surface layer was made [1].

The surface layers of the end faces of the cylinder are used as the "grips" for applying the external load. Therefore, all atoms are separated into three groups: internal atoms and atoms of the left-hand and right-hand grips.

In order to calculate the strength of the samples, one has to find the time dependence of a solution to the set of n differential equations (n is the number of atoms):

$$m\partial^2 u_i/\partial t^2 = \sum_{j=1}^{n} f_x(r_{ij}), \tag{2a}$$

$$m\partial^2 v_i/\partial t^2 = \sum_{j=1}^{n} f_y(r_{ij}), \tag{2b}$$

$$m\partial^2 w_i/\partial t^2 = \sum_{j=1}^{n} f_z(r_{ij}), \tag{2c}$$

where m is the atomic mass; u_i, v_i, and w_i are the displacements of the ith atom along the coordinate axes x, y, and z, respectively; and $f(r_{ij})$ is the modified Lennard–Jones interaction force between the ith and jth atoms [1]. Equations (2a)–(2c) are valid for the internal atoms.

In addition to the set (2), one should consider equations for the surface atoms in the grips to which external forces are applied. The forces are directed along the x axis and vary in time, e.g., according to a linear law. For the atoms of the left-hand grip, the tensile force is directed to the left and the following equations must be satisfied:

$$m\partial^2 u_i/\partial t^2 = \sum_{j=1}^{n} f_x(r_{ij}) - F(t)/n_1, \tag{3a}$$

where $F(t)$ is the time-dependent tensile force and n_1 is the number of atoms in the left-hand grip. For the atoms

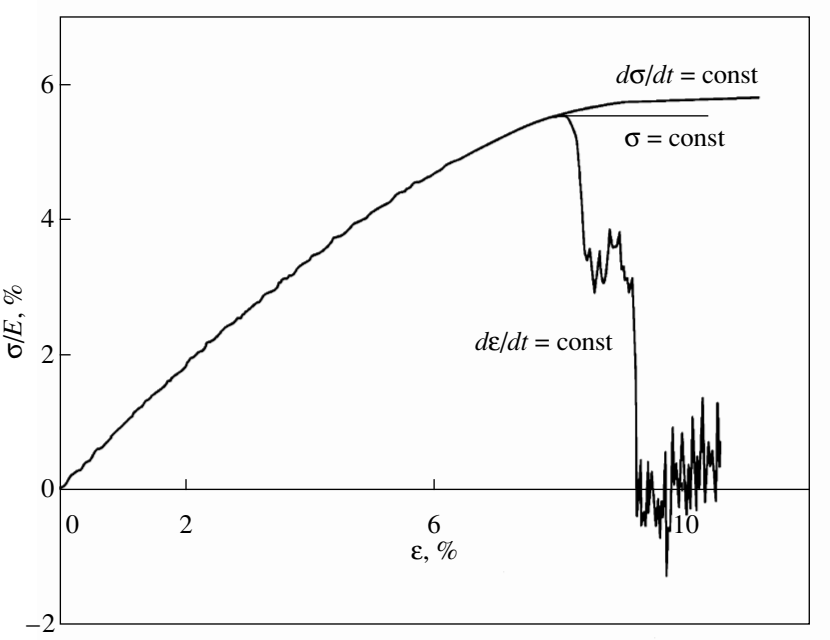

Fig. 1. Stress–strain curves in the initial range for the crystal identical to that in [1] as calculated in different computer-simulated tensile tests.

of the right-hand grip, the equations are similar and have the form

$$m\partial^2 u_i/\partial t^2 = \sum_{j=1}^{n} f_x(r_{ij}) + F(t)/n_2 . \qquad (3b)$$

In order to simplify the problem, we assume that the atoms of each grip are displaced as a unit. From Eqs. (2b), (2c), (3a), and (3b), we calculate the atomic displacements averaged over the grips to be the same for all atoms of each grip. The partition of the atoms of the sample into three groups, namely, the internal atoms subject to Eqs. (2) and the atoms of the left-hand and right-hand grips for which Eqs. (3) are satisfied, is made only once, at the beginning of the computer experiment. The surface atoms to which the external stresses are applied are chosen according to the calculated coordination number of atoms in the grips; an atom is considered to belong to the surface if its coordination number is less than ten.

Equations (2) and (3) are solved by the second-order finite difference method [4], which gives the stress–strain curve of the sample and a series of "snapshots" illustrating the process of stretching. The stress is measured in units of the Young's modulus, and the strain is averaged over the length of the cylinder.

2. CALCULATIONS

Equations (2) and (3) allow one to model the fracture of a sample at a constant loading rate, as well as at a constant load under creep conditions. The simulation program also made it possible to model the fracture at a constant strain rate. We used these three methods to investigate the fracture of a sample prepared from the crystal dealt with in [1]. The results are presented in Fig. 1.

From Fig. 1, it is seen that the different methods give the same result in the elastic-strain range. A fundamental difference is observed only when a critical strain is reached, which is equal to about 8% for the sample at hand. At this strain, the strength of the model single crystal is 5.5% of the Young's modulus, which is somewhat lower than the crystal strength predicted from the Orowan theory [5]. At a constant loading rate, after the critical strain is reached, the sample increases rapidly in length and ultimately tears, while at a constant strain rate, the stress drops because of structural changes and lattice vibrations occur.

It is seen from Fig. 1 that, without prior heating, creep tests can be conducted only at stresses close to their maximum value. For this reason, we chose the minimum stress at which the sample was torn after a reasonably long time.

First of all, we calculated the strength of samples prepared from perfect fcc crystals in an equilibrium state. Figure 2a shows the results of tensile tests for two differently oriented fcc crystals. The stresses were applied along the [100] or [110] axis of the crystal. Calculations show that, for the crystal tilted through 45° with respect to the direction of the applied force, the modulus of longitudinal elasticity is 3.4 times larger,

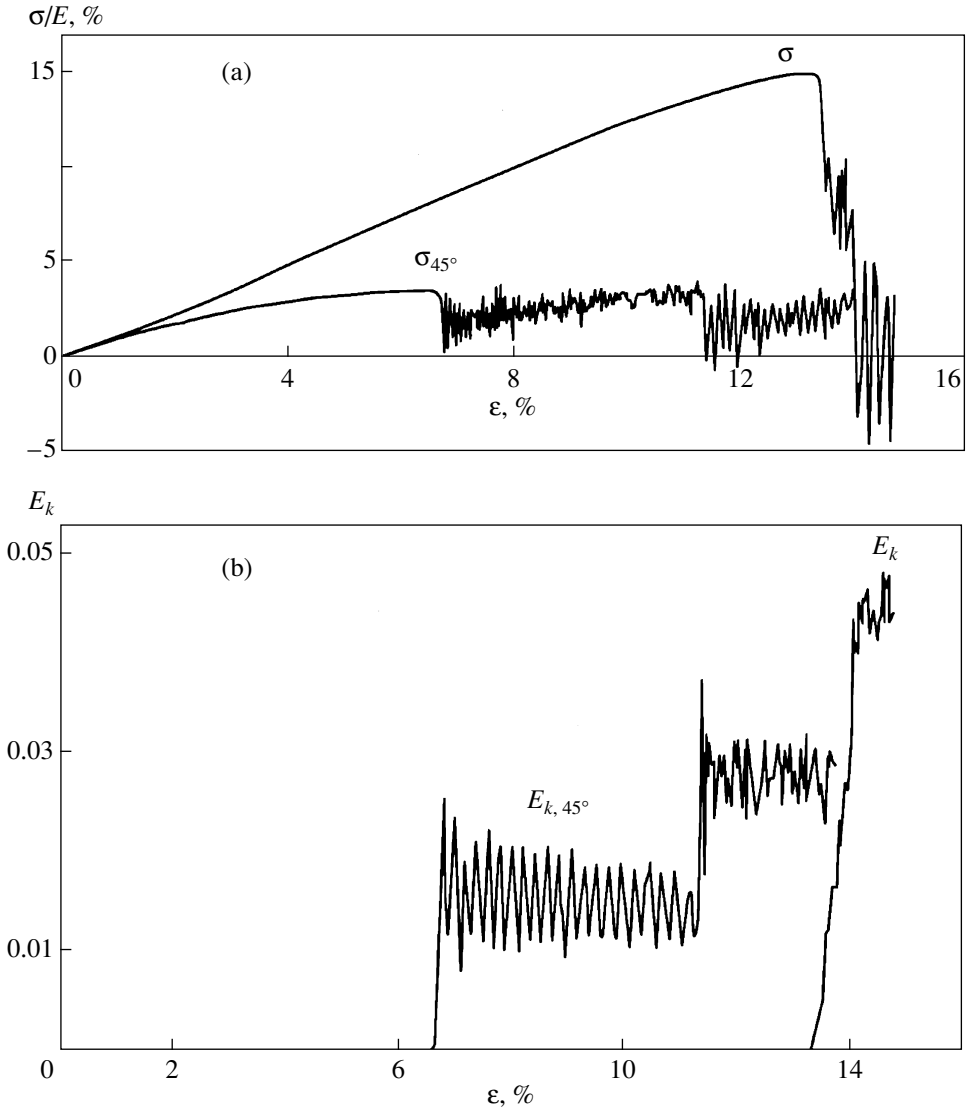

Fig. 2. (a) Stress–strain curve and (b) average kinetic energy of atoms of fcc crystals as calculated for adiabatic stretching at a constant strain rate $d\varepsilon/dt$.

while its strength is 20% lower and the elastic limit strain is smaller by more than half.

Figure 2b shows variations in the calculated average kinetic energy of atoms with increasing strain of fcc crystals. To find this energy, we calculated the kinetic energy of all atoms of the crystal. It is seen from Fig. 2b that the average thermal energy of atoms increases virtually instantaneously (within a time of the order of the period of lattice vibrations) at the instants the strength falls off steeply; the increase is $0.015D$ for a strain of 6.7%, while at a strain of 11.5%, it is $0.027D$ and $0.045D$ for the stresses applied along the [110] and [100] axes, respectively, where D is the dissociation energy of a pair of atoms.

The data presented in Fig. 2 correspond to computer simulation of adiabatic stretching (AS), where the atomic energy of the crystal is kept fixed. This is the reason why lattice vibrations occur when the crystal structure is rearranged suddenly and the strength of the crystal sharply decreases. In order to eliminate this effect, we consider quasi-isothermal stretching (QIS), where oscillations of atoms are significantly suppressed, as is the case with artificial damping introduced into the system [6].

A comparison of the stress–strain curves in the cases of SA (Fig. 3a) and QIS (Fig. 3b) in the whole range from the starting point to the instant the sample is torn shows that they are essentially different. In the former case, stretching is accompanied by stronger and more frequently occurring distortions of the sample structure and, furthermore, the fracture occurs at a larger strain.

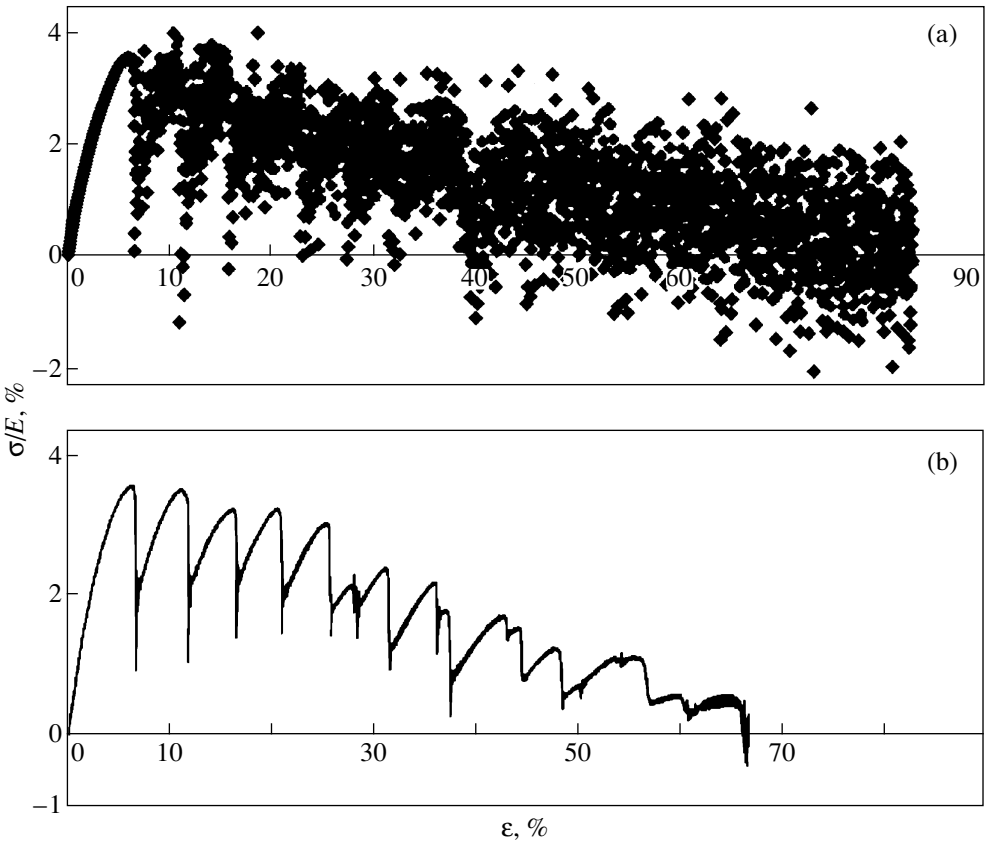

Fig. 3. Stress–strain curves for (a) adiabatic and (b) quasi-isothermal stretching of an fcc crystal along the [110] axis at a constant strain rate $d\varepsilon/dt$.

Figure 4 shows a sequence of snapshots of the arrangement of atoms in the initial stage of quasi-isothermal stretching along the [110] axis at a constant strain rate for the case where a plastic transformation occurs from one elastic state to another.[1] The shots correspond to the axial section of the sample at the instants the resistance to sample stretching reaches its first local minimum (Fig. 3b). According to Fig. 4, at a strain of 6.7% (shots *1* and *2*), over a period of time comparable to the period of lattice vibrations, sample narrowing ends with phase transformation of some fcc unit cells into hcp ones and with strain redistribution; there appear two atomic hcp sheets tilted at an angle of 45° to the direction of the external force.

In shot *3*, corresponding to $\varepsilon = 11.9\%$, the hcp double sheet of atoms is split into two single sheets and there appear two boundaries of a twin, each of which possesses mirror symmetry of fcc unit cells. One-half the unit cells undergo the reverse hcp $\longrightarrow$ fcc phase transformation, while in the adjacent sheet, the forward fcc $\longrightarrow$ hcp transformation occurs, with the result that one of the boundaries of the twin is displaced parallel to itself by one interatomic distance, thereby producing local elastic strain. On further stretching of the sample, a twin is nucleated with another orientation that is favorable to the formation of a kink band (Fig. 4, shots *4* and *5*).

The occurrence of the sudden phase transformation can easily be seen in Fig. 5, where the temporal variations in the angles that the two straight lines passing through the third and fifth central pairs of atoms in the excited zone, respectively, make with the external stress axis (during adiabatic stretching) are shown with a high temporal resolution, starting from the moment of time $t_0 = 80$. The atoms of these pairs are indicated by filled circles in panel *1* of Fig. 4. In the elastic-strain range, there was no reorientation of the lattice relative to the external-stress axis. According to Fig. 5, the variations in the orientation of the atomic pairs indicated above are described by the same curve to a high accuracy, especially over the initial portion of the strain range.

It is evident from Figs. 4 and 5 that the phase transformation of the lattice proceeds at a high rate and atoms in the excited zone are displaced synchronously; the duration of this transformation is comparable to the

[1] Time is measured in units of the period T of lattice vibrations, $t = \tau/T$, where τ is the running time.

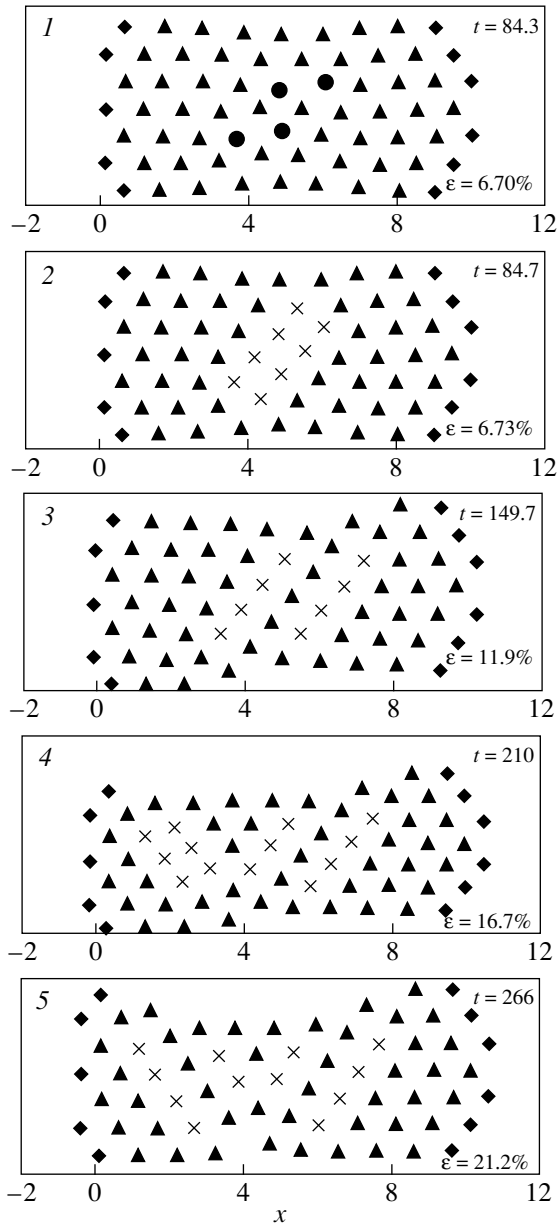

Fig. 4. Sequence of snapshots for the case of quasi-isothermal stretching of an fcc crystal along the [110] axis at a constant strain rate $d\varepsilon/dt$: (◆) atoms in the grips, (×) hcp unit-cell atoms, and (▲) fcc unit-cell and surface atoms.

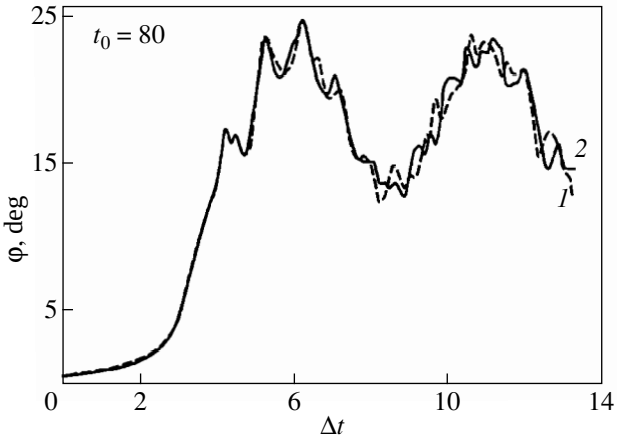

Fig. 5. Temporal variations in the orientation of pairs of atoms with respect to the externally applied force in the vicinity of a kink band as calculated with a high temporal resolution for adiabatic stretching: (*1*) central atoms of the third sheet and (*2*) atoms of the fifth sheet.

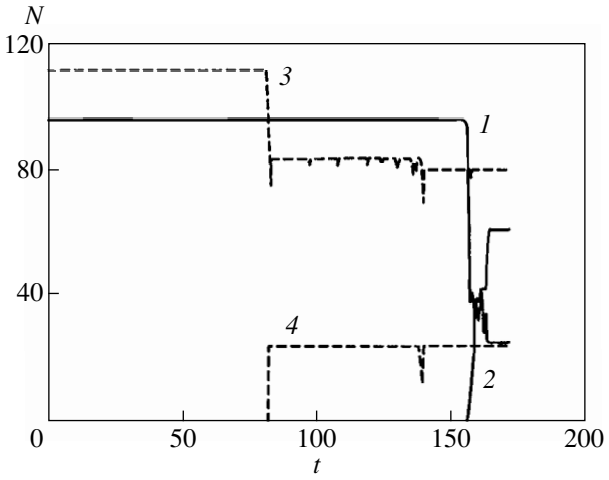

Fig. 6. Temporal variations in the numbers of (*1*, *3*) fcc and (*2*, *4*) hcp unit-cell atoms of fcc crystals being stretched at a constant strain rate $d\varepsilon/dt$ along (*1*, *2*) the [100] and (*3*, *4*) [110] axes.

period of fundamental lattice vibrations. The variations in the angle presented in Fig. 5 were calculated with the aim of revealing the formation of a dislocation. Instead of this, however, we observed the structural phase transformation of the fcc to an hcp lattice and, in addition, the formation and displacement of a twin. Note that the fcc and hcp lattices with the same number of atoms per unit cell differ only in symmetry; the hcp lattice possesses mirror symmetry, while the fcc lattice has inversion symmetry.

One can also see from Fig. 5 that there are high-frequency oscillations with a period of approximately 5, which are likely to be due to the flexural vibrations of the sample that accompany the formation of kink bands. These oscillations correlate with oscillations of the kinetic energy of atoms, which are observed in Fig. 2b and have a period that is twice as short.

Further information on the transformation of fcc to hcp unit cells which occurs during stretching of fcc crystals at a constant strain rate $d\varepsilon/dt$ is presented in Fig. 6. This figure also provides support for the occur-

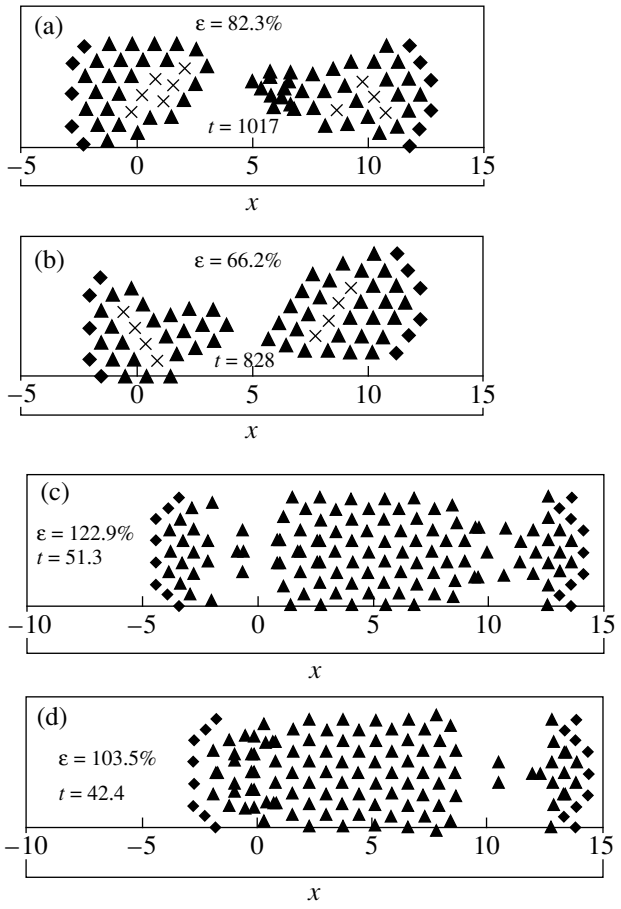

Fig. 7. Fracture of an fcc crystal being stretched along the [110] axis at constant (a, b) $d\varepsilon/dt$ and (c, d) $d\sigma/dt$ rates in the case of (a, c) adiabatic and (b, d) quasi-isothermal stretching: (◆) atoms of the grids, (×) central atoms of hcp unit cells, and (▲) fcc unit-cell and surface atoms.

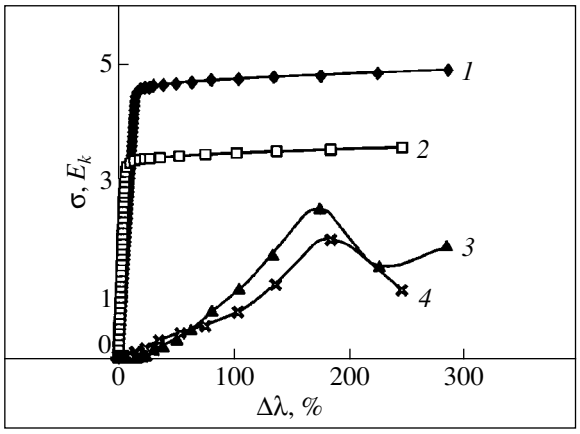

Fig. 8. (*1*, *2*) Stress–strain curves and (*3*, *4*) variations in the average kinetic energy of atoms of (*1*, *3*) fcc and (*2*, *4*) hcp crystals for the case of adiabatic stretching at a constant rate $d\sigma/dt$; $\Delta\lambda$ is the relative change in the distance between the grips (percentage of the initial sample length).

rence of the sudden strain-induced fcc ⟶ hcp phase transformation. It is notable that fcc unit cells are transformed not only into hcp cells, but also most likely into surface atoms, as indicated by the different amounts of discontinuous change in the numbers of fcc and hcp unit cells occurring upon this transformation.

Figures 7a and 7b illustrate the fracture of an fcc crystal during adiabatic and quasi-isothermal stretching, respectively. It is seen that, when stretched at a constant strain rate $d\varepsilon/dt$, the sample is divided into two parts at a strain of $\varepsilon = 82.3\%$ in the former case and at a strain of 66.2% in the latter. Therefore, the plasticity is higher in the former case, as judged from the higher limit deformation and the external appearance of the fractured sample. The forming twins are seen more clearly in Fig. 7b, which corresponds to the case of stretching with almost complete suppression of the kinetic energy of atoms. This figure shows the same section of the sample as that in Fig. 4. The onset of fracture is detected automatically in the computer experiments.

Figure 8 shows the data on the fracture of fcc and hcp crystals in tensile tests performed at a constant rate $d\sigma/dt$, with the increase in the applied force ΔF being equal to 0.01 at each time step of the integration procedure, which corresponds to approximately the same duration of elastic loading as that in the case of a constant rate $d\varepsilon/dt$. It is seen that the strength of the hcp crystals is significantly lower in absolute value (by about 25%) than that of the fcc crystals and that their homogeneous deformation ceases sooner. Perhaps this is due to the different initial orientation of the fcc and hcp crystals and their different deformability. Figure 8 also shows the variation in the average thermal energy of atoms in units of the dissociation energy D; the former energy is calculated with allowance for the kinetic energy of the fragments flying apart as the sample is disintegrated.

The peak in the energy variation curve in Fig. 8 is associated with the sample fracture, which occurs at a nearly doubled sample length. Figures 7c and 7d show the sections of the sample just before its fracture in AS and QIS tests, respectively, at a constant loading rate $d\sigma/dt$. In this case, as is seen from the figures, two necks are formed near the grips and the limit deformation is higher than that in the case of stretching at a constant strain rate $d\varepsilon/dt$; furthermore, the fcc ⟷ hcp phase transformation does not occur in quasi-isothermal stretching. In both cases, the fcc and hcp crystals behave as elastoplastic solids.

3. CONCLUSION

Thus, using the methods developed, we conducted computer experiments to determine the strength of perfect fcc and hcp crystals. The strength of a sample was found to depend heavily on its orientation with respect to the externally applied force. It was shown that,

before fracture, the crystal deformation becomes plastic because of the occurrence of the fcc ⟷ hcp phase transformation and, in addition, the crystal is deformed via the nucleation of twins and their motion.

REFERENCES

1. V. A. Lagunov and A. B. Sinani, Fiz. Tverd. Tela (St. Petersburg) **40** (10), 1919 (1998) [Phys. Solid State **40**, 1742 (1998)].
2. V. A. Lagunov and A. B. Sinani, Fiz. Tverd. Tela (St. Petersburg) **42** (6), 1087 (2000) [Phys. Solid State **42**, 1120 (2000)].
3. A. I. Lobastov, V. E. Shudegov, and V. G. Chudinov, Zh. Tekh. Fiz. **67** (12), 100 (1997) [Tech. Phys. **42**, 1460 (1997)].
4. L. Verlet, Phys. Rev. **159** (1), 98 (1967).
5. E. Orowan, in *Fatigue and Fracture of Metals* (Wiley, New York, 1952).
6. Yu. M. Plishkin, in *Defects in Crystals and Their Computer Simulation* (Nauka, Leningrad, 1980), p. 77.

Translated by Yu. Epifanov

Physics of the Solid State, Vol. 43, No. 4, 2001, pp. 677–681. Translated from Fizika Tverdogo Tela, Vol. 43, No. 4, 2001, pp. 651–655.

MAGNETISM AND FERROELECTRICITY

Magnetoresistance Effect in $A_2(FeMo)O_x$ Double Perovskites (A = Sr, Ca; $5.90 \le x \le 6.05$)

L. S. Lobanovskiĭ*, I. O. Troyanchuk*, N. V. Pushkarev*, and G. Szymczak**

**Institute of Solid-State and Semiconductor Physics, Belarussian Academy of Sciences, ul. Brovki 17, Minsk, 220072 Belarus*

e-mail: troyan@ifttp.bas-net.by

*** Institute of Physics, Poland Academy of Sciences, Warsaw, 02-668 Poland*

Received July 6, 2000

Abstract—The dependences of magnetic, electric, and magnetotransport properties on oxygen non stoichiometry were investigated in compounds of $Ca_2(FeMo)O_x$ and $Sr_2(FeMo)O_x$ ($5.90 \le x \le 6.05$). The regular trends in behavior of the magnetization, resistance, and magnetoresistance of samples of these series are determined. It is established that the magnetoresistance is composed of two parts that appear as a result of magnetic ordering in grain-boundary layers and of the intergrain transport of spin-polarized charge carriers. The electronic transport in the samples is assumed to be governed by percolation processes between grains which have a metallic type of conductivity and are separated by insulating spacers. *© 2001 MAIK "Nauka/Interperiodica".*

INTRODUCTION

The effect of "giant magnetoresistance" discovered in perovskites $Sr_2(FeMo)O_6$ and $Ba_2(FeMo)O_6$ has attracted considerable attention due to its possible applications [1–4]. Materials revealing a large magnetoresistance effect are necessarily involved in the operation of devices of information storage and processing and magnetic field sensors. It should be noted that the origin of the giant magnetoresistance effect in these compounds is poorly understood [5–8]. The magnetoresistance effect is assumed to be due to grain boundaries in these compounds and to strong spin polarization of charge carriers. This assumption is supported by the results obtained on thin epitaxial films [9]. The magnetoresistance effect was found to be positive in epitaxial films, whereas polycrystals exhibit the negative effect; that is, the electrical resistance of the samples reduces in a magnetic field. For manganites, a large magnetoresistance effect is observed, as a rule, in comparatively strong fields (higher than 1 T) [10, 11]. The grain-boundary magnetoresistance effect monotonically increases in manganites with reducing temperature, whereas in grains, this effect is the most pronounced near the phase transition temperatures.

At present, there are no data available on the magnetoresistance properties of $Ca_2(FeMo)O_6$ and $Sr_2(FeMo)O_6$ compounds in relation to oxygen content. It is well known that deviation from the stoichiometry strongly affects both magnetic and electric properties of $LaMnO_3$-type manganites.

The aim of the present work is to establish the dependences between the magnetic, electrical, and magnetic-transport properties and oxygen nonstoichiometry in compounds $A_2(FeMo)O_x$ (A = Ca, Sr; $5.90 \le x \le 6.05$).

1. EXPERIMENTAL METHOD

Samples of $A_2(FeMo)O_x$ (A = Ca, Sr) were prepared from oxides and carbonates of corresponding elements by the standard ceramic technique in the atmosphere of a noble gas. Compounds of $CaCO_3$, $SrCO_3$, MoO_3, Fe_2O_3, and MoO_2 taken in stoichiometric proportions were ground in an agate mortar. Then, the powders were pressed into pellets under a pressure of 6 kBar; these pellets were synthesized in an argon flow at a temperature of 1200°C for three hours. After synthesis, the samples were cooled at a rate of 100°C/h. X-ray diffraction analysis data, which were obtained using CoK_α radiation, confirmed the single-phase perovskite structure of the samples. The oxygen content in the compound prepared by this method was determined from the mass deficiency after reduction to calcium and strontium oxides, as well as to metallic iron and molybdenum, in a hydrogen flow.

The reduction of the samples was done in evacuated quartz ampules at a temperature of 900°C in the presence of ground metallic tantalum, which served as a getter of oxygen. For oxidation of the samples, ground $LaMnO_{3.1}$ was placed into the ampule. The oxygen content was determined from the mass deficiency of the sample after reduction or from the mass excess of the sample after oxidation. To determine the unit cell parameters and to control the single-phase conditions of the samples, x-ray analysis was performed after each treatment.

1063-7834/01/4304-0677$21.00 © 2001 MAIK "Nauka/Interperiodica"

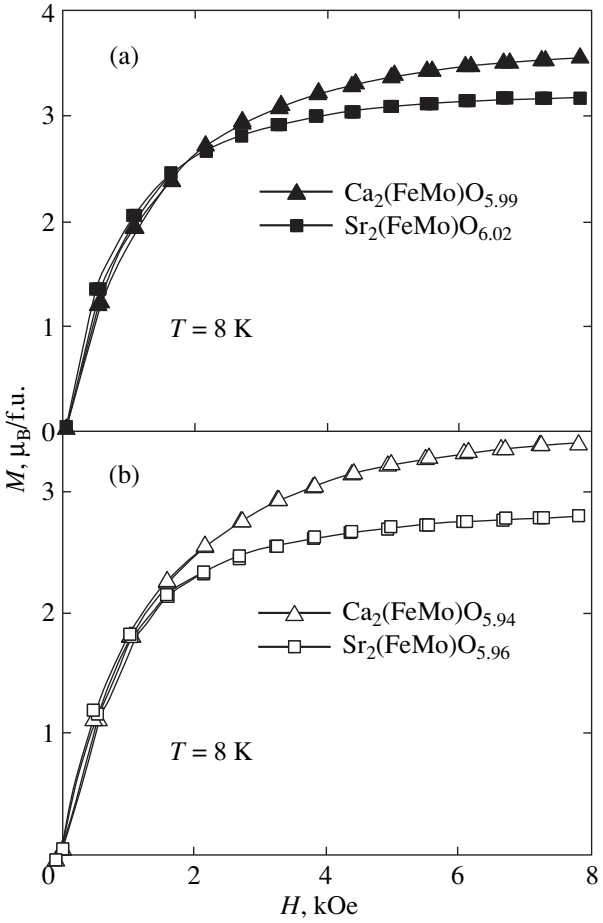

Fig. 1. Dependence of the magnetization of samples of the $Ca_2(FeMo)O_x$ and $Sr_2(FeMo)O_x$ series on the external magnetic field at 8 K: (a) as-synthesized and (b) the most reduced samples of each series.

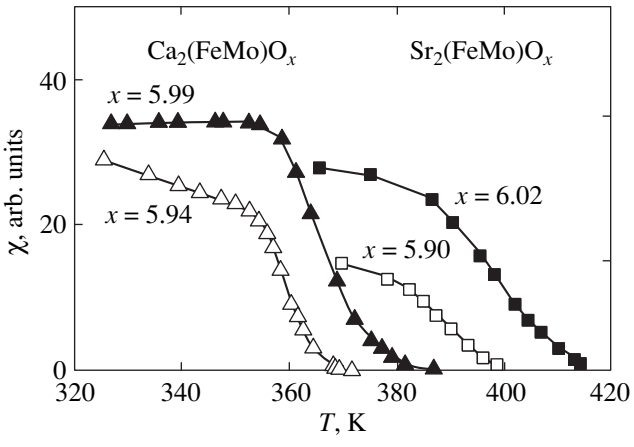

Fig. 2. Dependence of the dynamic magnetic susceptibility of $A_2(FeMo)O_x$ (A = Sr, Ca; $5.90 \le x \le 6.02$) on temperature (curves are shown near T_C).

The magnetic susceptibility was measured by the bridge technique, the resistance was measured by the standard four-probe method, and the magnetization was determined using a vibrating-sample magnetometer.

2. RESULTS AND DISCUSSION

The chemical formula of the samples synthesized was determined to be $Sr_2(FeMo)O_{6.02}$ and $Ca_2(FeMo)O_{5.99}$. According to x-ray analysis, the $Sr_2(FeMo)O_{6.02}$ sample had a cubic unit cell, with its parameter being equal to 7.873 Å, which corresponds to a unit-cell volume of 61.984 Å^3. The $Ca_2(FeMo)O_{5.99}$ compound was of *O*-orthorhombic symmetry with the parameters a = 5.384 Å, b = 5.522 Å, and c = 7.709 Å and a reduced unit cell volume of 57.225 Å^3. X-ray diffraction analysis of all compounds revealed weak superstructure peaks due to ordering of the iron and molybdenum ions in a NaCl-type structure. With increasing oxidation, the unit cell volume of all compounds decreased. The oxidized sample of $Sr_2(FeMo)O_{6.05}$ had a volume of 61.973 Å^3. The reduced volume of the oxidized $Ca_2(FeMo)O_{6.03}$ sample was 57.211 Å^3. With reduction, the unit cell volume of the compounds increased. The $Sr_2(FeMo)O_{5.90}$ compound had a unit cell volume of 62.247 Å^3. For the $Ca_2(FeMo)O_{5.94}$ composition, the reduced volume was 57.258 Å^3.

Earlier, Nakagawa measured the magnetization of $Sr_2(FeMo)O_6$ and $Ca_2(FeMo)O_6$ samples [12]. The magnetic moment value varied from 3.2 to 3.6 Bohr magnetons per formula unit (μ_B/f.u.) in these compounds.

Our measurements of magnetization performed at 8 K (Fig. 1a) showed that the $Ca_2(FeMo)O_{5.99}$ sample had a magnetic moment of 3.17 μ_B/f.u. and the magnetic moment of $Sr_2(FeMo)O_{6.02}$ was 2.9 μ_B/f.u. From the temperature dependences of the dynamic susceptibility (Fig. 2), the Curie temperatures T_C were determined for each composition. As can be seen from Fig. 2, the Curie temperatures of the as-synthesized $Ca_2(FeMo)O_{5.99}$ and $Sr_2(FeMo)O_{6.02}$ compounds are equal to 375 and 418 K, respectively. With reduction of the $Ca_2(FeMo)O_{5.99}$ and $Sr_2(FeMo)O_{6.02}$ samples, the magnetic moments (Fig. 1b) and the Curie temperatures (Fig. 2) were decreased. For the $Ca_2(FeMo)O_{5.94}$ composition, the magnetic moment was 3.07 μ_B/f.u. at 8 K and T_C decreased to 367 K. The magnetization of the $Sr_2(FeMo)O_{5.90}$ compound was 2.63 μ_B/f.u., and the Curie temperature was 399 K.

The resistivity (ρ) of the $Ca_2(FeMo)O_{5.99}$ sample was of the order of 10^{-4} Ω cm at the temperature of liquid nitrogen (Fig. 3b). For the $Sr_2(FeMo)O_{6.02}$ composition, $\rho \sim 1$ Ω cm at 77 K (Fig. 4b). With reduction, the resistivity ρ of the samples of both series decreased. The ρ temperature dependences of the as-synthesized

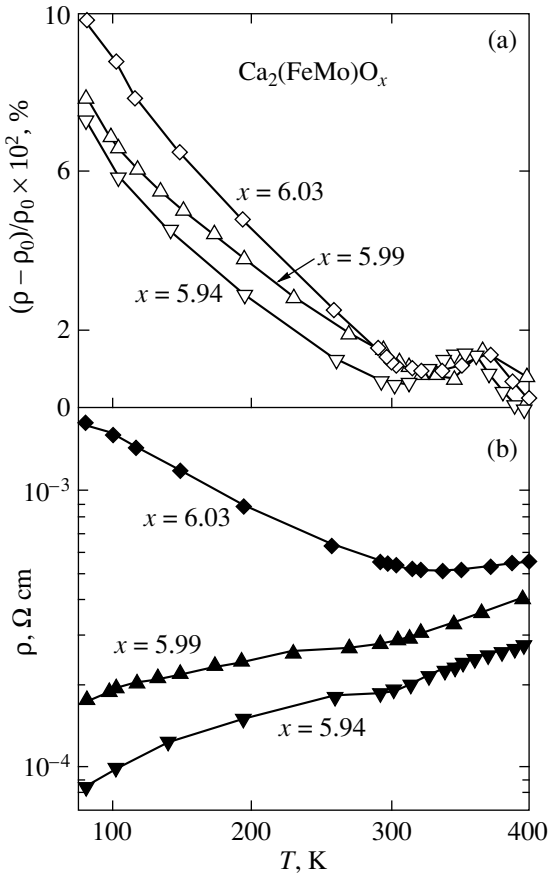

Fig. 3. Dependences of (a) the magnetoresistance and (b) electrical resistivity on temperature for $Ca_2(FeMo)O_x$ ($5.94 \le x \le 6.03$).

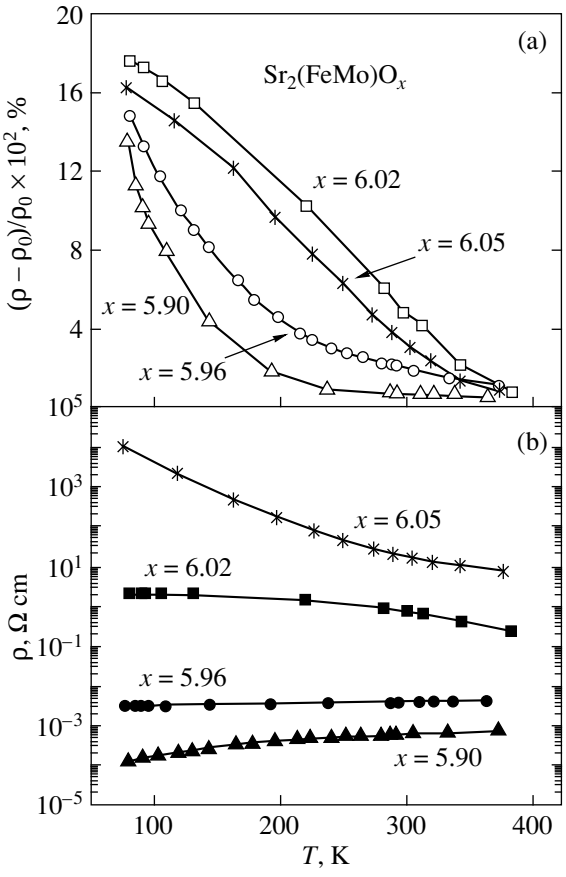

Fig. 4. Dependences of (a) the magnetoresistance and (b) electrical resistivity on temperature for $Sr_2(FeMo)O_x$ ($5.90 \le x \le 6.05$).

samples and those of the oxidized and reduced samples of each series are presented in Figs. 3b and 4b. One can see that the resistivity ρ of the reduced samples increased insignificantly with increasing temperature in the overall temperature interval measured, which is typical for metals. The compositions of the calcium series displayed a kink on the ρ(T) dependence near the Curie temperature.

With oxidation, the samples of all series exhibited an increase in the ρ. For the $Sr_2(FeMo)O_{6.05}$ composition with an oxygen content slightly changed from 6.02 to 6.05, the resistance increased by four orders of magnitude at the temperature of liquid nitrogen. The ρ temperature dependence of this sample also changed. The resistance of the $Sr_2(FeMo)O_{6.05}$ compound revealed the Arrhenius (activated) behavior in the overall temperature interval measured. For the oxidized sample of $Ca_2(FeMo)O_{6.03}$, a decrease in the ρ was observed with increasing temperature in the interval from 77 to 325 K. When further heated, the sample exhibited an increase in resistivity.

The magnetoresistance was calculated as $MR = \{[\rho(H = 0) - \rho(H = 5\ \text{kOe})]/\rho(H = 0)\} \times 100\%$. The temperature dependences of the magnetoresistance for the series of $Ca_2(FeMo)O_x$ ($5.94 \le x \le 6.03$) and $Sr_2(FeMo)O_x$ ($5.90 \le x \le 6.05$) are shown in Figs. 3a and 4a, respectively. The maximum value of the magnetoresistance effect was exhibited by the samples of the strontium series in a field of 5 kOe. The *MR* values ranged from 13 to 18% for all samples at the temperature of liquid nitrogen and decreased to ~1% with increasing temperature (Fig. 4).

At 77 K, the magnetoresistance of the $Ca_2(FeMo)O_x$ series ($5.94 \le x \le 6.03$) holds in the limits from 7 to 10%. As the temperature increases, the magnetoresistance effect decreases to ~0.5%. Then, at the Curie temperature, the magnetoresistance exhibits a peak not exceeding a value of 1.5%. The similar behavior of the magnetoresistance of a $Ba_2(FeMo)O_6$ composition near the Curie temperature was observed in [4]. At T_C, the *MR* of the samples of the $Ca_2(FeMo)O_x$ ($5.94 \le x \le 6.03$) series is weakly dependent on the oxygen nonstoichiometry of the composition.

Analyzing the temperature dependence of the magnetoresistance, one can see an interesting peculiarity in its behavior. As the oxygen content is reduced, the low-

temperature magnetoresistance effect decreases more rapidly with increasing temperature; that is, the smaller the oxygen index, the steeper the magnetoresistance curve slope for the compositions of each series. This tendency is the most pronounced for the samples of the strontium series.

According to the results of investigations of $Ba_2(FeMo)O_6$, $Sr_2(FeMo)O_6$, and $Ca_2(FeMo)O_6$ by the NMR method, the iron ions are in the trivalent state and the molybdenum ions are in the pentavalent state [13].

We suggest that, during the reduction process in the compounds, two contrary factors affect the unit cell volume, namely removal of the oxygen atoms and transition of the iron ions from the trivalent state to the divalent state. To conserve the electrical neutrality in the sample, as one oxygen atom is removed, two iron ions should pass to the divalent state. The former process results in a decrease in the unit cell parameter, whereas the latter process causes the parameter to increase, because the ionic radius of the Fe^{2+} is significantly greater than the ionic radius of the Fe^{3+}. As can be seen from the experimental data, the unit cell volume increases in the reduction process. This suggests that the unit cell parameter is more strongly affected by the decrease in the average oxidizing state of the iron ions.

It can be supposed that the oxidation process in the $A_2(FeMo)O_6$ (A = Ca, Sr) compounds is similar to the oxidation of $LaMnO_3$-type perovskites. In this case, with oxidation of the samples, the valence state of the molybdenum ions changes ($Mo^{5+} \longrightarrow Mo^{6}$) and cation vacancies appear. Both processes result in a decrease in the unit-cell volume. As was mentioned above, the unit cell parameter of our samples decreased with oxidation.

The spontaneous magnetic moment of the stoichiometric compounds of $A_2(FeMo)O_6$ (A = Ca, Sr) is determined by the antiparallel ordering of the magnetic moments of the iron Fe^{3+} ($3d^5$) and molybdenum Mo^{5+} ($4d^1$) ions. In this case, for the stoichiometric compound, the spontaneous magnetic moment should be expected to be of 4 μ_B/f.u. at 0 K. It seems likely that strong hybridization of the orbitals of the Fe and Mo ions with the 2p orbitals of the oxygen ions decreases the effective magnetic moment of these ions. In our case, the maximum value of magnetization was exhibited by the $Ca_2(FeMo)O_{5.99}$ composition; as mentioned above, its magnetic moment was 3.17 μ_B/f.u. at 8 K.

Reduction of the $Ca_2(FeMo)O_{5.99}$ and $Sr_2(FeMo)O_{6.02}$ samples results in a decrease in the spontaneous magnetic moment per formula unit in these compounds because of the change in the electronic configuration of a part of the iron ions from Fe^{3+} ($3d^5$) to Fe^{2+} ($3d^6$). The Fe^{2+} ($3d^6$) ions have a smaller magnetic moment than the Fe^{3+} ($3d^5$) ions. The hexavalent molybdenum ions are diamagnetic. Therefore, as a result of the oxidation of $A_2(FeMo)O_6$ (A = Ca, Sr), an increase in the spontaneous magnetic moment should be expected. The decrease in the Curie temperature in the reduction process of the samples seems to be due to the exchange interaction Fe^{2+}–O–Mo^{5+} being slightly weaker than the exchange interaction Fe^{3+}–O–Mo^{5+}.

As a result of the reduction of the samples, the electrical conductivity increased (Figs. 3b, 4b) in spite of the appearance of oxygen vacancies, which are structural defects and should restrict the mobility of charge carriers. It is possible that this tendency is associated with partial disordering of the Fe^{3+} and Mo^{5+} ions. In the strongly reduced samples, we observed a significant decrease in the intensity of the super structure peaks associated with the ordering of the iron and molybdenum ions. It is well known that the perovskites containing only Fe^{3+} ions are good insulators. When the oxygen content is greater than the stoichiometric value, a drastic increase in the resistance is observed. The resistivity temperature dependence (Figs. 3b, 4b) could be interpreted assuming that the conductivity of the strongly oxidized samples is due to percolation processes. It seems likely that the samples are composed of the bulk metallic phase and insulating interlayers. The insulating interlayers are weakened at some places, which results in percolation conductivity over the metallic phase. When the samples are oxidized, it is likely that the content of the grain-boundary layers radically changes first. This suggestion is indirectly supported by the strongly oxidized samples becoming brittle.

The magnetoresistance effect and magnetic properties correlate with each other. The weaker the exchange interaction in $A_2(FeMo)O_x$ (A = Sr, Ca), the faster the magnetoresistance decreases with increasing temperature. The maximum of the magnetoresistance effect in the vicinity of the Curie temperature seems to be due to the same processes as in the metallic $Tl_2Mn_2O_7$ with a pyrochlore structure [14]. In $Tl_2Mn_2O_7$ at the T_C temperature, the conductivity character also does not change, but the magnetoresistance effect is several times greater [14]. Possibly, it is in part due to the fact that the compounds of $A_2(FeMo)O_6$ (A = Sr, Ca) are ferrimagnetics, whereas $Tl_2Mn_2O_7$ is characterized by parallel ordering of the magnetic moments of all manganese ions. It is well known that the ferrimagnetic spinels of the $MnFe_2O_4$ type also exhibit a magnetoresistance peak near the Curie temperature, although its value is quite small.

ACKNOWLEDGMENTS

This work was supported by the Belarussian Foundation for Basic Research, project no. F99M-033.

REFERENCES

1. K.-I. Kobayashi, T. Kimura, H. Sawada, *et al.*, Nature (London) **395**, 677 (1998).
2. T. H. Kim, M. Uehara, S.-W. Cheong, and S. Lee, Appl. Phys. Lett. **74**, 1737 (1999).
3. K.-I. Kobayashi, T. Kimura, Y. Tomioka, *et al.*, Phys. Rev. B **59** (17), 11159 (1999).
4. A. Maignan, B. Raveau, C. Martin, and M. Hervieu, J. Solid State Chem. **144**, 224 (1999).
5. H. Asano, S. B. Ogale, and J. Garrison, Appl. Phys. Lett. **74** (24), 3696 (1999).
6. P. Raychaudhuri, K. Shechadri, and P. Taneja, Phys. Rev. B **59**, 13919 (1999).
7. M. Ziese, Phys. Rev. B **60**, R738 (1999).
8. S. Lee, H. Y. Hwang, and B. I. Shraiman, Phys. Rev. Lett. **82**, 4508 (1999).
9. H. Q. Yin, J.-S. Zhou, J.-P. Zhou, *et al.*, Appl. Phys. Lett. **75** (18), 2812 (1999).
10. H. Y. Hwang, S.-W. Gheong, and P. G. Radaely, Phys. Rev. Lett. **75** (5), 914 (1995).
11. S. Nakamura, K. Namba, and S. Iida, J. Magn. Magn. Mater. **177–181**, 884 (1998).
12. T. Nakagawa, J. Phys. Soc. Jpn. **24**, 806 (1970).
13. H. Yokoyama and T. Nakagawa, J. Phys. Soc. Jpn. **28** (5), 1197 (1970).
14. M. A. Subramanian, B. H. Toby, and A. P. Ramirez, Science **273**, 81 (1996).

Translated by N. Kovaleva

Physics of the Solid State, Vol. 43, No. 4, 2001, pp. 682–684. Translated from Fizika Tverdogo Tela, Vol. 43, No. 4, 2001, pp. 656–658.

MAGNETISM AND FERROELECTRICITY

Low-Frequency Behavior of Optical Spatial Dispersion Effects

V. N. Gridnev

Ioffe Physicotechnical Institute, Russian Academy of Sciences, Politekhnicheskaya ul. 26, St. Petersburg, 194021 Russia
e-mail: gridnev@pop.ioffe.rssi.ru

Received July 7, 2000

Abstract—A theoretical explanation is given for the frequency independence of the nonreciprocal birefringence of light, which was recently observed in the semiconductors $Cd_{1-x}Mn_xTe$, $Zn_{1-x}Mn_xTe$, and GaAs in the frequency range below the frequency corresponding to the interband absorption edge. It is shown that the symmetry of the effect becomes higher at such frequencies if the light-induced excitation energy $\hbar\omega_n(\mathbf{k})$ only slightly depends on the photon momentum $\mathbf{k}$. In this case, the nonreciprocal birefringence is completely determined by the second-rank magnetoelectric tensor. It is shown that the nonreciprocal birefringence of light can be observed in magnetic media with a tensor order parameter. © *2001 MAIK "Nauka/Interperiodica".*

In recently published works [1, 2], a number of unusual properties of light birefringence $\Delta n(\omega)$ induced by an external magnetic field in cubic semiconductors $Cd_{1-x}Mn_xTe$, $Zn_{1-x}Mn_xTe$, and GaAs were found experimentally. One of them is frequency-independent birefringence which is observed when the light quantum energy $\hbar\omega$ is less than the band gap E_g (except a small frequency range, ~0.2 eV near E_g). At first glance, there is nothing surprising in such a frequency independence of the birefringence, because the usual birefringence (in optically anisotropic crystals) also virtually does not depend on frequency in the transmission range. However, these two phenomena are essentially different, since magnetically induced birefringence is a linear spatial-dispersion effect; i.e., it is associated with the contribution to the optical permittivity tensor of the crystal, which depends on the wave vector of light $\mathbf{k}$ through the equation $\Delta\varepsilon_{ik}(\omega, \mathbf{k}, \eta) = \gamma^{(s)}_{ikl}(\omega, \eta)k_l$, where $\gamma^{(s)}_{ikl}$ is a *T*-odd tensor symmetric in indices *i* and *k*; and the symbol η denotes a *T*-odd quantity characterizing the medium (or the external magnetic field) and, generally, being a tensor with respect to spatial transformations. The odd parity of the tensor $\gamma^{(s)}_{ikl}$ with respect to the time reversal follows from the Onsager symmetry principle $\Delta\varepsilon_{ik}(\omega, \mathbf{k}, \eta) = \Delta\varepsilon_{ki}(\omega, -\mathbf{k}, -\eta)$. Similar to optical activity, which is described by a *T*-even tensor $\gamma^{(a)}_{ikl}$ antisymmetric in *i* and *k*, nonreciprocal birefringence can be observed only in noncentrosymmetric crystals. The distinction between the usual and the nonreciprocal birefringence at the phenomenological level reflects the essential differences in the microscopic nature of these two phenomena.

In addition to the frequency independence of $\Delta n(\omega)$ for $\hbar\omega < E_g$, another feature of nonreciprocal birefringence was revealed in [1, 2]. At these frequencies, the tensor $\gamma^{(s)}_{ikl}$ was found to have a higher symmetry in comparison with the symmetry admitted by the point group of the crystal. In other words, relations between some components of the tensor $\gamma^{(s)}_{ikl}$ arise for $\hbar\omega < E_g$, which lead to higher symmetry of the tensor and do not depend on the crystal under investigation.

In this paper, we give an explanation for the features of the nonreciprocal birefringence listed above. For this purpose, we consider the frequency dependence of the optical permittivity tensor of a crystal in the frequency range below the electron transition frequencies. The wave-vector-dependent contribution $\Delta\varepsilon_{ik}(\omega, \mathbf{k})$ to the real part of the permittivity tensor at zero temperature has the form [3]

$$\Delta\varepsilon_{ik}(\omega, \mathbf{k}) = \frac{4\pi}{\hbar\omega^2 V} \times \sum_n \left[\frac{J^i_{0,n-\mathbf{k}}(\mathbf{k}) J^k_{n-\mathbf{k},0}(-\mathbf{k})}{\omega_{n-\mathbf{k}} - \omega} + \frac{J^k_{0,n\mathbf{k}}(-\mathbf{k}) J^i_{n\mathbf{k},0}(\mathbf{k})}{\omega_{n\mathbf{k}} + \omega} \right], \quad (1)$$

where $\mathbf{J}(\mathbf{k})$ is the Fourier component of the current operator; $\mathbf{r}_\alpha$ and $\mathbf{v}_\alpha$ are the coordinate and velocity operators of αth particle, respectively; and $\hbar\omega_{n\mathbf{k}}$ is the transition energy from the ground state $|0\rangle$ to the exited state $|n\mathbf{k}\rangle$.

For small wave vectors $\mathbf{k}$, the matrix element $J^i_{n\mathbf{k},0}(\mathbf{k})$ can be expanded in a power series in $\mathbf{k}$. In the approximation linear in $\mathbf{k}$, we have

$$J^i_{n\mathbf{k},0}(\mathbf{k}) = i\omega_n(D^i_{n0} + Q^{il}_{n0}k_l) + ie_{ils}M^s_{n0}k_l, \quad (2)$$

where $\omega_n = \omega_{n0}$ and $|n\rangle = |n\mathbf{k} = 0\rangle$. This expansion is general; however, explicit calculation of the expansion parameters D^i_{n0}, Q^{il}_{n0}, and M^s_{n0} depends on the accepted model of electron states of the crystal.

1063-7834/01/4304-0682$21.00

Substituting Eq. (2) into Eq. (1) and retaining the terms linear in $\mathbf{k}$, we obtain the tensors $\gamma^{(a)}_{ikl}$ and $\gamma^{(s)}_{ikl}$, which determine the natural optical activity and the nonreciprocal birefringence, respectively. Since we are interested in $\Delta\varepsilon_{ik}(\omega, \mathbf{k})$ at frequencies which are low in comparison with the electron transition frequencies ω_n, we expand expression (1) in a power series in the parameter ω/ω_n and retain the first two terms of the expansion. It is a matter of direct calculation to prove that the first term of the expansion (containing the zeroth power of the parameter ω/ω_n) is antisymmetric in indices i and k. Since we consider the terms linear in $\mathbf{k}$, this term could give rise to optical activity. However, this term is exactly equal to zero by virtue of the sum rules, which are well known in the theory of optical activity [4]. A nonzero contribution to the optical activity arises only when the terms quadratic in the parameter ω/ω_n in expansion (1) are taken into account. The corresponding expressions are well known, and we do not present them here. We note only that the rotation of the polarization plane is proportional to ω^2 in the frequency range under investigation.

Let us now proceed to consideration of the nonreciprocal birefringence, which is described by the terms linear in the parameter ω/ω_n in expansion (1). Indeed, these terms are symmetric in indices i and k and, as a consequence of the Onsager relation, they have T-odd parity. Thus, we obtain the following expression for $\gamma^{(s)}_{ikl}$:

$$\gamma^{(s)}_{ikl} = e_{ils}\alpha_{ks} + e_{kls}\alpha_{is} + \sigma_{ikl}, \tag{3}$$

where

$$\alpha_{is} = \frac{4\pi}{\hbar\omega V}\sum_n \frac{D^i_{0,n}M^s_{n,0} + D^i_{n,0}M^s_{0,n}}{\omega_n}, \tag{4}$$

$$\alpha_{ikl} = \frac{4\pi}{\hbar\omega V}\sum_n \frac{D^i_{0n}D^k_{n0} + D^k_{n0}D^i_{0n}}{\omega_n}\frac{\partial\omega_{n\mathbf{k}}}{\partial k_l}\bigg|_{\mathbf{k}\to 0}. \tag{5}$$

As one can see from these formulas, the matrix elements of the electrical quadrupole moment operator Q^{il}_{n0} are not involved in expressions (3)–(5), which determine $\gamma^{(s)}_{ikl}$ at low frequencies. The last term in Eq. (3), i.e., the tensor σ_{ikl}, is responsible for the dependence of the excitation (electron–hole pair) energy upon $\mathbf{k}$ in a translation-invariant medium. This term is not equal to zero only if $\omega_{n\mathbf{k}} \neq \omega_{n-\mathbf{k}}$. The general expression for the tensor $\gamma^{(s)}_{ikl}$, which is correct for any frequency of light, was obtained in [5]. However, the consideration in [5] was applied to the antiferromagnetic–magnetoelectric Cr_2O_3, the symmetry properties of which dictate the equality $\omega_{n\mathbf{k}} = \omega_{n-\mathbf{k}}$. For this reason, the expression for the tensor $\gamma^{(s)}_{ikl}$ obtained in [5] does not include the contribution which contains the derivative $\partial\omega_n/\partial\mathbf{k}$. In semiconductors with the sphalerite structure, the dependence of ω_n on $\mathbf{k}$ in a magnetic field was investigated for the exciton spectrum range in [6,7].

In optical experiments on the propagation of light, $\mathbf{k}$ and ω are connected by the relation $ck(\omega)/\omega = n(\omega)$, where $n(\omega)$ is the refraction index; in the frequency range $\omega < \omega_n$ we have $n(\omega) \simeq$ const. Since the nonreciprocal birefringence $\Delta n \propto \gamma^{(s)}_{ikl}k_l$, it follows from Eqs. (3)–(5) that $\Delta n(\omega) \simeq$ const in the frequency range under investigation. Exactly the same behavior of $\Delta n(\omega)$ was revealed experimentally [1, 2] in the semiconductors $Cd_{1-x}Mn_xTe$, $Zn_{1-x}Mn_xTe$, and GaAs for $\hbar\omega < E_g$.

Let us now consider the symmetric properties of the tensor $\gamma^{(s)}_{ikl}$ given by Eq. (3). The first two terms in the right-hand side of Eq. (3) are defined by the second-rank tensor α_{is}. In the case of a homogeneous field, the contribution of these terms to the electromagnetic response of the medium is responsible for the magnetoelectric effect [8]. Therefore, the tensor α_{is} determined by Eq. (4) can be interpreted as a part of the complete magnetoelectric tensor, which is due to electron transitions, and the corresponding contribution to $\gamma^{(s)}_{ikl}$ will be designated as the magnetoelectric. The last term in Eq. (3), i.e., the tensor σ_{ikl}, cannot be reduced to a second-rank tensor in the general case; in other words, it contains a nonreducible third rank tensor, which we will refer to, following [5], as quadrupole. It is important that the quadrupole and the magnetoelectric contributions to the nonreciprocal birefringence can be separated experimentally [1, 2]. This separation is based on the various angular dependences of the nonreciprocal birefringence caused by the magnetoelectric and the quadrupole contributions to $\gamma^{(s)}_{ikl}$ upon orientation of the crystal. The analysis of this dependence for cubic semiconductors $Cd_{1-x}Mn_xTe$ and $Zn_{1-x}Mn_xTe$ ($x \simeq 0.4$) performed in [1, 2] has shown that the quadrupole contribution to $\Delta n(\omega)$ is much less than the magnetoelectric one in the transmission range for $\hbar\omega < E_g$, where $\Delta n(\omega) \simeq$ const. A similar behavior was revealed in the dielectrics Cr_2O_3 [9] and $Co_3B_7O_{13}I$ [10]. The first of them is a magnetoelectric antiferromagnet; therefore, its nonreciprocal birefringence is a spontaneous effect. The birefringence in the paramagnetic $Co_3B_7O_{13}I$ was induced by an external magnetic field.

It is easy to explain the absence of an appreciable quadrupole contribution in the dielectrics Cr_2O_3 and $Co_3B_7O_{13}I$ by taking into account that this contribution is proportional to $\partial\omega_n/\partial\mathbf{k}$, as can be seen from Eq. (5); i.e., it depends on the dispersion of electron excitations. However, in the wide-band-gap dielectrics to which these crystals belong, the dispersion is small (in Cr_2O_3,

by symmetry, $\partial\omega_n/\partial\mathbf{k} = 0$ at $\mathbf{k} = 0$); consequently, the quadrupole contribution to $\gamma_{ikl}^{(s)}$ is small.

It is more difficult to understand the reason why the quadrupole contribution is relatively small in the magnetic semiconductors $Cd_{1-x}Mn_xTe$ and $Zn_{1-x}Mn_xTe$, where the dispersion of electron excitations is substantial. Taking into account that the experiments were carried out on samples with a significant concentration of Mn^{2+} ions ($x \simeq 0.4$), one can assume that the essential contribution to the effect is due to the *d–d* transitions in the Mn^{2+} ion. Usually, the contribution of these transitions to the optical constants of solids is small, since the matrix elements of the electric dipole moment operator D_{0n} are nonzero in this case only owing to the relatively weak noncentrosymmetric part of the crystal field. However, this small contribution has an influence only for optical effects existing in the electric dipole approximation (in particular, without account of magnetic dipole transitions) and is insignificant in this case, since the product $D_{0,n}^{i} M_{n,0}^{s}$ of the matrix elements is always different from zero only because the crystal is noncentrosymmetric. Therefore, the contribution of *d–d* transitions in the Mn^{2+} to ion magnetoelectric tensor (4) can be comparable with the contribution of interband transitions to this tensor. At the same time, *d–d* transitions are well localized and, consequently, do not make any substantial contribution to the quadrupole tensor σ_{ikl}. The validity of this assumption can be tested by determining the relative value of the quadrupole contribution to the nonreciprocal birefringence in semiconductors which do not contain Mn^{2+} ions. Measurement of the frequency-independent nonreciprocal birefringence in CdTe, ZnTe, and GaAs was performed in [11]; however, reliable separation of the magnetoelectric and quadrupole contributions to Δn turned out to be impossible because of the smallness of Δn, which is due, among other factors, to the absence of exchange enhancement of interband transitions by Mn^{2+} ions. Nevertheless, the above consideration allows one to conclude that there is a substantial influence of the dispersion of electron excitations on the nonreciprocal birefringence despite the remaining uncertainty in the interpretation of these experiments. Such an influence is the characteristic feature of optical spatial-dispersion effects, and this influence manifests itself especially clearly in a given special case by defining not only the magnitude of the effect but also its symmetry.

In closing, we will point out the possible observation of nonreciprocal birefringence in a medium with a magnetic structure which is characterized by a tensor order parameter, namely, the three-point correlator of the microscopic magnetic moment density $\langle m_i(\mathbf{r}_1)m_k(\mathbf{r}_2)m_l(\mathbf{r}_3)\rangle$, provided that this correlator is odd with respect to spatial inversion; the average $\langle\mathbf{m}(\mathbf{r})\rangle$ can be equal to zero. Indeed the tensor σ_{ikl} in Eq. (3) has the same symmetry properties and can be different from zero in this case. Such a magnetic structure is difficult to reveal with the help of traditional resonant and x-ray diffraction methods. If the three-point correlator of the magnetic moment density is even with respect to spatial inversion, then the Faraday rotation which is quadratic in the wave vector of light $\mathbf{k}$ should be observed in the medium with such a magnetic structure [12]. Expanding Eq. (1) in a power series in $\mathbf{k}$ and ω/ω_n, it is easy to show the rotation of the polarization plane of light $\phi \propto \omega^2$ at low frequencies; i.e., it behaves like the usual Faraday rotation. At the same time, for the Faraday rotation which is quadratic in $\mathbf{k}$, we have $\phi(\omega) \simeq$ const at high frequencies [12].

ACKNOWLEDGMENTS

The author is grateful to B.B. Krichevtsov and R.V. Pisarev for their participation in discussing this paper.

This work was supported by the Russian Foundation for Basic Research, project no. 99-02-18028, and the program “Fundamental Spectroscopy.”

REFERENCES

1. B. B. Krichevtsov, R. V. Pisarev, A. A. Rzhevsky, *et al.*, Phys. Rev. B **57** (23), 14611 (1998).
2. B. B. Krichevtsov, R. V. Pisarev, A. A. Rzhevskiĭ, *et al.*, Zh. Éksp. Teor. Fiz. **114** (3), 1018 (1998) [JETP **87**, 553 (1998)].
3. V. M. Agranovich and V. L. Ginzburg, *Crystal Optics with Spatial Dispersion, and Excitons* (Nauka, Moscow, 1979; Springer-Verlag, New York, 1984).
4. A. M. Agranovich, *The Theory of Excitons* (Nauka, Moscow, 1968).
5. R. M. Hornreich and S. Shtrikman, Phys. Rev. **171** (3), 1065 (1968).
6. O. V. Gogolin, V. A. Tsvetkov, and E. G. Tsitsishvili, Zh. Éksp. Teor. Fiz. **87** (3), 1038 (1984) [Sov. Phys. JETP **60**, 593 (1984)].
7. E. G. Tsitsishvili, Fiz. Tekh. Poluprovodn. (Leningrad) **20** (2), 650 (1986) [Sov. Phys. Semicond. **20**, 412 (1986)].
8. L. D. Landau and E. M. Lifshitz, *Course of Theoretical Physics*, Vol. 8: *Electrodynamics of Continuous Media* (Nauka, Moscow, 1992; Pergamon, New York, 1984).
9. B. B. Krichevtsov, V. V. Pavlov, R. V. Pisarev, and V. N. Gridnev, Phys. Rev. Lett. **76** (26), 4628 (1996).
10. B. B. Krichevtsov, A. A. Rzhevsky, and H.-J. Weber, Phys. Rev. B **61** (15), 10084 (2000).
11. B. B. Krichevtsov, R. V. Pisarev, A. A. Rzhevskiĭ, and H.-J. Weber, Pis’ma Zh. Éksp. Teor. Fiz. **69** (7), 506 (1999) [JETP Lett. **69**, 551 (1999)].
12. V. N. Gridnev, Pis’ma Zh. Éksp. Teor. Fiz. **69** (7), 510 (1999) [JETP Lett. **69**, 546 (1999)].

Translated by O. Ivanov

Physics of the Solid State, Vol. 43, No. 4, 2001, pp. 685–691. Translated from Fizika Tverdogo Tela, Vol. 43, No. 4, 2001, pp. 659–665.

MAGNETISM AND FERROELECTRICITY

Statical Critical Properties of Gadolinium Models

A. K. Murtazaev, I. K. Kamilov, and K. Sh. Khizriev

Institute of Physics, Dagestan Scientific Center, Russian Academy of Sciences, ul. 26 Bakinskikh komissarov 94, Makhachkala, 367003 Dagestan, Russia

e-mail: kamilov@datacom.ru

Received July 10, 2000

Abstract—Microscopic models of real ferromagnetic gadolinium are proposed, and their critical properties are studied by the Monte Carlo method. The critical exponents α (heat capacity), γ (susceptibility), and β (magnetization) are calculated. The α, β, and γ exponents are determined by the approximation of the data on the basis of traditional power functions and in the framework of the finite-size scaling theory. It is revealed that the critical behavior of gadolinium is affected by the dipole–dipole interactions. It is shown that the Monte Carlo method is a powerful tool for investigations into the critical properties of complex models in which two types of weak relativistic interactions are jointly taken into account against the background of each of these interactions. © *2001 MAIK "Nauka/Interperiodica".*

1. INTRODUCTION

The ideas underlying the scaling and universality hypotheses and the renormalization-group theory appeared most fruitful in constructing a unified theory of phase transitions and critical phenomena [1, 2]. The most exact and reliable numerical values of critical exponents were obtained on the basis of the renormalization-group theory and the ε-expansion [3, 4]. Up to now, the renormalization-group theory remains one of the most efficient tools for quantitative investigations into the critical phenomena. However, this theory also involves serious problems in the study of complex models which require inclusion of numerous factors that are inherent in real systems but are ignored in first-approximation models (classical Ising, Heisenberg, and other models). Among these are anisotropy, impurities, multispin exchange, dipole–dipole interaction, lattice vibrations, and a number of other factors [2]. At the same time, the current state of the art in the investigation of phase transitions and critical phenomena is characterized by the study of more complex and realistic models [5, 6]. Moreover, the approach underlying the renormalization-group theory is not strictly microscopic [7].

For these reasons and others, phase transitions and critical phenomena have been extensively studied by Monte Carlo methods [5, 6, 8–10].

Quantitative analysis of the immediate critical region with the use of Monte Carlo methods became possible only in recent years. Nonetheless, the results obtained by these methods to date have been on a par in terms of accuracy with the most reliable data of other techniques and, sometimes, even surpass them [5–10]. The computational power of modern computers and the application of special algorithms in some cases make it possible to calculate critical parameters directly from the results of Monte Carlo calculations without invoking various tricks and technical procedures [5, 11].

Laboratory experiments thus far performed in the immediate vicinity of the critical point are too complicated, do not ensure the required accuracy for the theory, and do not provide answers to a number of important questions. Furthermore, the investigation into the critical behavior of some magnetic materials presents considerable difficulties. One of these materials is a rare-earth metal, viz., gadolinium. Despite a large number of experimental studies carried out with the aim of elucidating the character and specific features of the critical behavior of gadolinium, many important problems still remain to be solved.

In this work, we proposed microscopic models of real ferromagnetic gadolinium and studied their critical properties by the Monte Carlo method. The distinctive feature of the present study is that the models proposed account for weak relativistic interactions of different types against the background of each of these interactions, and their influence on the critical behavior has been the subject of investigation. This statement of the problem is of interest from the standpoint of the potentials of both the technique for analyzing critical phenomena and the Monte Carlo method in revealing the effect of weak factors on these phenomena.

2. CRITICAL PROPERTIES OF GADOLINIUM

Gadolinium is a rare-earth metal with a close-packed hexagonal structure. In the temperature range $232\ \text{K} < T < T_c \cong 293\ \text{K}$, gadolinium undergoes a simple ferromagnetic ordering. Magnetic and neutron diffraction investigations demonstrate that the one-ion and two-ion mechanisms are responsible for the anisotropy in gadolinium, whereas the anisotropy in the paramag-

1063-7834/01/4304-0685$21.00

netic phase is governed by the uniaxial anisotropy of a short-range magnetic order [12–14]. On the one hand, gadolinium is a uniaxial weakly anisotropic ferromagnet, and, hence, its critical behavior at temperatures sufficiently close to T_c can have an Ising character. On the other hand, a spherically symmetric distribution of the electron density and the absence of an orbital momentum lead to the isotropic exchange interaction, which suggests a Heisenberg character of the critical behavior.

The statistical critical behavior of gadolinium has been experimentally studied in a large number of works [14–24]. Investigations into thermal expansion [14, 15], heat capacity [16–18], and magnetic properties [19–23], as well as Mössbauer studies [24], which were performed with different single-crystal and polycrystalline samples, made it possible to determine a set of static critical exponents α, β, γ, and δ. The numeral values of these exponents are summarized in the tables given in [23–25]. A comparison of the experimental data with theoretical predictions within the Ising and Heisenberg three-dimensional models shows their discrepancy. As follows from the critical exponents α of the heat capacity and thermal expansion, gadolinium is either Heisenberg-type or isotropic dipole magnet. As regards the exponent β, which characterizes the temperature dependence of the spontaneous magnetization M_s, this dependence in all the studies also corresponds to either Heisenberg or isotropic dipole magnet. At the same time, the critical exponent γ of the susceptibility is closer to the characteristic values of the Ising model. Moreover, the exponent δ is consistent neither with microscopic theories nor with the molecular-field theory. This brings up the question of how the critical behavior of gadolinium can be explained when certain critical exponents correspond to one model and the other exponents follow another model.

According to analysis of the experimental data, the main reasons for these discrepancies are as follows.

(1) The reasons associated with the technique for determining particular critical exponents [23]. In the majority of works, the β, γ, and δ critical exponents were determined by the fitting of *M–H–T* experimental data to the scaling equation of state for the magnetization, which implies the fulfillment of the scaling law $\gamma = \beta(\delta - 1)$. In this definition, the critical exponents should obey the scaling laws which include the same exponents β, γ, and δ. However, their individual values can be inconsistent with the true asymptotic critical behavior.

(2) In real crystals, there occur additional interactions perturbing the initial critical behavior. For example, isotropic dipole interactions in Heisenberg magnets lead to the dependence of the γ exponent on the reduced temperature [23].

(3) As follows from recent experiments performed with different gadolinium samples, defects produce a considerable effect, which can change the character of the critical behavior [18].

(4) The critical properties of gadolinium, specifically the width and height of the heat capacity peak, depend on the conditions and the procedure of sample preparation [18].

(5) Theoretical estimates have been obtained for static models with fixed values of the geometric parameters of the lattice, angles, atomic positions, etc. At the same time, in the case when real samples are studied in laboratory experiments, these parameters can vary, which can lead to a change in the interaction parameters. In some cases, this can result in a disagreement between theoretical and experimental data.

Note that careful experimental investigations into the static critical properties of gadolinium were carried out by Aliev *et al.* [23], who determined the values of the β, γ, and δ exponents. The specific features in the behavior of the heat capacity were studied by Bednarz *et al.* [18]. The results of the latter work indicate that the critical behavior of the heat capacity is very sensitive to the procedure for preparing a sample, its purity, and chemical composition.

However, it should be noted that not all the above factors can be eliminated or taken into account in the course of laboratory experiments. For this purpose, it is necessary to carry out an experiment in which all the parameters involved are specified and rigidly controlled. These conditions can be provided only by a numerical experiment (the Monte Carlo method).

3. MICROSCOPIC MODELS OF GADOLINIUM

The following features of gadolinium should be taken into consideration when constructing the models of this material: (i) the electron density is distributed in a spherically symmetric way, and the orbital momentum is absent; (ii) the energy of the magnetic crystallographic anisotropy for gadolinium is substantially less than that for other rare-earth elements; and (iii) the isotropic dipole–dipole interactions in gadolinium can play a significant role in the critical region.

With due regard for these features, the Hamiltonian of a system can be represented in the form

$$H = -\frac{1}{2}\sum_{ij} J(\boldsymbol{\mu}_i\boldsymbol{\mu}_j) - D_A\sum_i (\mu_i)^2 - D_d\sum_i (\langle \mathbf{M}\rangle \cdot \boldsymbol{\mu}_i), \quad |\boldsymbol{\mu}_i| = 1, \tag{1}$$

where the first term accounts for the exchange interaction of each Gd^{3+} ion with all the nearest neighbors ($J > 0$), the second term describes the uniaxial anisotropy (D_A), and the third term represents the isotropic dipole–dipole interaction (D_d). According to the data obtained in terms of the molecular-field theory [12, 23, 26, 27], the parameters of the anisotropy D_A and the isotropic

dipole forces D_d are as follows: $D_A = 1.41 \times 10^{-4}$ and $D_d = 1.35 \times 10^{-3}$.

The calculations were performed by the Monte Carlo method for cubic samples of size $L \times L \times L$ (L = 8, 10, 12, 14, 16, 18, and 20) with periodic boundary conditions. The systems were simulated with allowance made for all magnetic and crystallographic features of real gadolinium. In order to bring the system to the equilibrium state, Markovian chain segments of a length up to 2.5×10^4 MCS/spin were cut off. Averaging was carried out over a Markovian chain of a length up to 1.2×10^5 MCS/spin.

In order to reveal the effect of dipole forces on the character of the critical behavior, we considered two gadolinium models. The model G1 takes into account the exchange interaction with the nearest neighbors and the uniaxial anisotropy. The model G2 additionally allows for the isotropic dipole–dipole interactions. It should be noted that, as far as we know, the influence of different-type weak interactions against the background of each of these interactions on the critical behavior has never been investigated by the Monte Carlo method, and, hence, the potentials and the "sensitivity" of the Monte Carlo method in this case remain unknown.

4. STATIC CRITICAL PROPERTIES OF GADOLINIUM MODELS

The temperature dependences of the heat capacity and the susceptibility were examined using the fluctuation relationships

$$C = (NK^2)(\langle U^2\rangle - \langle U\rangle^2), \quad (2)$$

$$\chi = (NK)(\langle m^2\rangle - \langle m\rangle^2), \quad (3)$$

where $K = |J|/k_BT$, U is the internal energy, and m is the magnetization. The temperature dependences of the heat capacity C and the susceptibility χ for the G1 model are shown in Figs. 1 and 2. Note that all the dependences exhibit clear maxima, which, within the limits of experimental error, correspond to the same temperature. Figure 3 depicts the temperature dependence of the magnetization m for the G1 model. The magnetization m monotonically decreases with an increase in temperature, and the high-temperature "tails" decrease with an increase in the number of spins N. The critical temperature was determined by the Binder cumulant method [5]. According to the finite-size scaling theory (see [5] and references therein), the cumulants $U_L = 1 - \langle M^4\rangle/3\langle M^2\rangle^2$ for systems with different sizes L intersect at the critical point T_c. The temperature thus determined $k_BT_c/|J| = 3.22(2)$ was taken

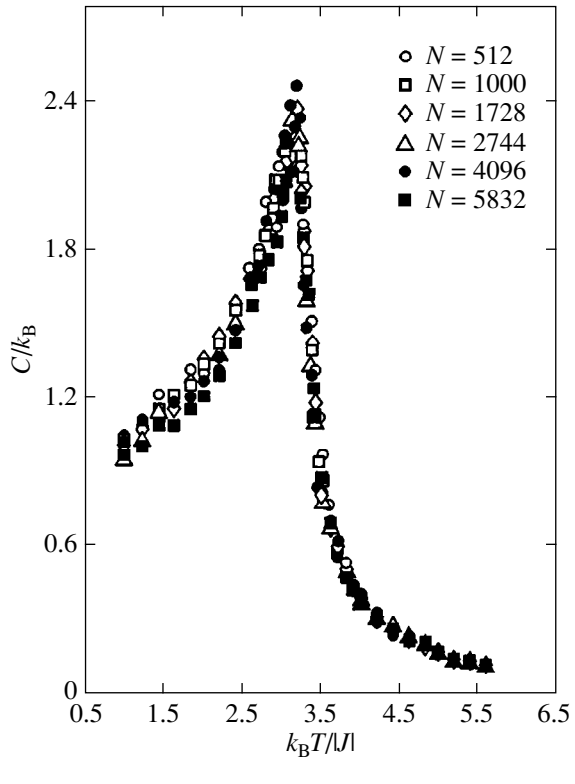

Fig. 1. Temperature dependence of the heat capacity for the G1 model.

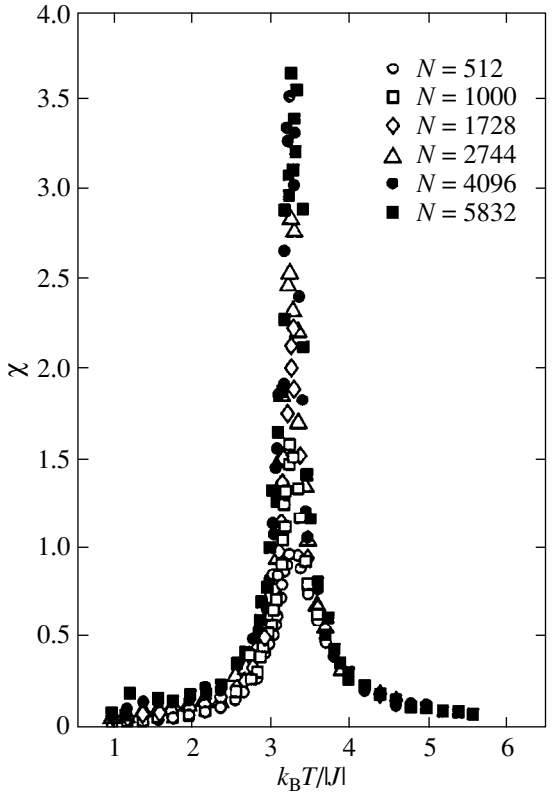

Fig. 2. Temperature dependence of the susceptibility for the G1 model.

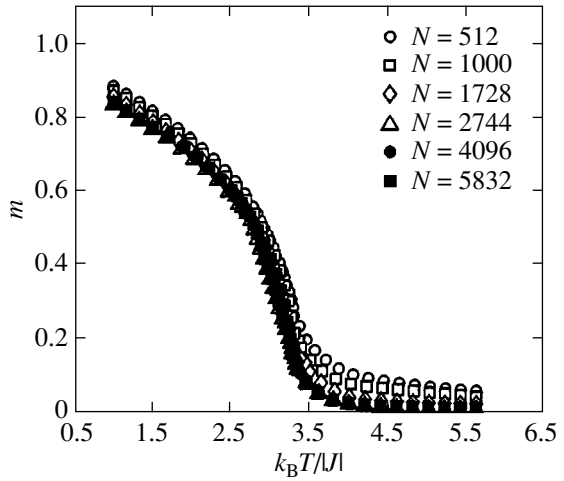

Fig. 3. Temperature dependence of the magnetization for the G1 model.

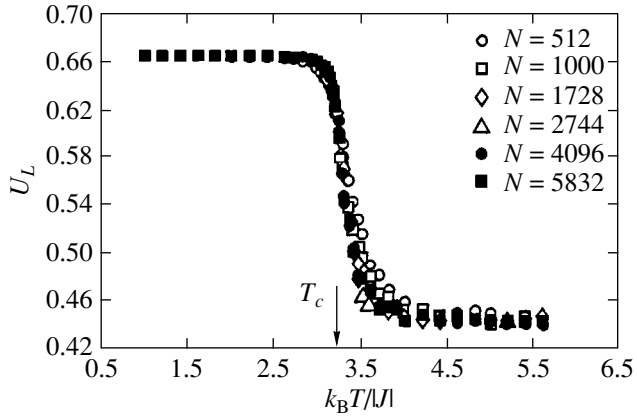

Fig. 4. Temperature dependence of the Binder cumulant U_L for the G1 model.

as the critical temperature. The temperature dependence of the Binder cumulant U_L for the G1 model at different N is displayed in Fig. 4.

Similar calculations were performed for the G2 model. Qualitatively, all the features characteristic of the G1 model (see Figs. 1–4) are also observed for the G2 model. The difference between the temperature dependences of C and χ for the models G1 and G2 lies in the fact that the height of the maxima for the G2 model is slightly less than that for the G1 model. The critical temperatures T_c for both models coincide within the limits of error.

The critical behavior of the heat capacity was approximated by the following relationships [18]:

$$C = \frac{A}{\alpha}|t|^{-\alpha}(1 + a_c|t|^x) + R|t| + E, \quad (4)$$

$$C = \frac{A}{\alpha}(|t|^{-\alpha} - 1) + a_c|t|^x + R|t| + E, \quad (5)$$

where $t = |T - T_c|/T_c$; α is the critical exponent of the heat capacity; and A, a_c, R, and E are the fitting parameters. The value of x was taken equal to 0.55 [3]. The data were processed using the nonlinear least-squares technique. For both gadolinium models, the critical parameters obtained from relationships (4) and (5) are equal to each other within the limits of error; however, expression (5) leads to a smaller error in their calculations.

Table 1 presents the critical exponents α, which were obtained by the approximation of the heat capacity in different temperature ranges with the use of relationship (5). As can be seen from Table 1, all the critical exponents in the temperature range $3 \times 10^{-3} \le t \le 5 \times 10^{-1}$ are negative (which is characteristic of the Heisenberg model) and fall in the range from –0.14 to –0.18. It is worth noting that, as the value of t_{max} decreases, the exponent α increases, approaches zero, and then becomes positive. This indicates the crossover from the Heisenberg to the Ising critical behavior.

The theoretical value of the crossover temperature t_{cr} can be calculated by the formula $t_{cr} = (D_A/|J|)^{1/f}$ [23], where $f = 1.25$ for the crossover from $n = 3$ to $n = 1$ (n is the number of order parameter components). In our case, $t_{cr} = 8.31 \times 10^{-4}$. As follows from the data presented in Table 1, the crossover range for the systems under consideration is sufficiently wide. Similar features are observed in the behavior of the heat capacity for the G2 model. The exponents α determined in a similar manner for the models G1 and G2 coincide within the limits of error.

For comparison, the theoretical values of the α, β, and γ exponents for three-dimensional systems are as follows: $\alpha = 0.108$, $\beta = 0.326$, and $\gamma = 1.24$ for the Ising model ($n = 1$) [3, 4]; $\alpha = -0.126$, $\beta = 0.368$, and $\gamma = 1.39$ for the Heisenberg model ($n = 3$) [3, 4]; and $\alpha = -0.135$, $\beta = 0.381$, and $\gamma = 1.37$ for the model with isotropic dipole–dipole interactions (see [23, 25] and references therein).

The effect of dipole forces, to some extent, manifests itself in the critical exponents γ of the susceptibility. The critical exponents γ and γ' were calculated using a simple power relationship

$$\chi = \Gamma|t|^{-\gamma}. \quad (6)$$

The exponents γ and γ' obtained for the models G1 and G2 are listed in Table 2. The susceptibility is a strongly fluctuating quantity, and the character of the critical behavior cannot be uniquely determined by traditional procedures of processing the Monte Carlo data. However, the data presented in Table 2 rather conclusively indicate a tendency for the exponents of the susceptibility to change when going from the G1 model to the G2 model. Note that there is a clear tendency for a

Table 1. Effective critical exponents α of the heat capacity for gadolinium (model G1, $t_{min} = 3.0 \times 10^{-3}$)

N	t_{max}							
	5×10^{-1}	4×10^{-1}	3×10^{-1}	2×10^{-1}	1×10^{-1}	0.9×10^{-1}	0.8×10^{-1}	0.7×10^{-1}
512	−0.18(2)	−0.16	−0.13	−0.08	−0.02	0.02	0.06	0.08
1000	−0.18	−0.15	−0.12	−0.09	−0.03	0.01	0.05	0.07
1728	−0.16	−0.14	−0.10	−0.06	−0.01	0.02	0.06	0.08
2744	−0.17	−0.15	−0.09	−0.07	−0.02	0.00	0.04	0.07
4096	−0.15	−0.13	−0.10	−0.04	−0.02	0.01	0.04	0.07
5832	−0.14	−0.12	−0.09	−0.04	−0.01	0.03	0.05	0.08

decrease in the magnitudes of the γ exponent in the G2 model as compared to those in the G1 model. At the same time, these features for the γ' exponent are considerably less pronounced.

The critical behavior of the magnetization was approximated by the expression

$$m = B|t|^{\beta}(1 + a_m|t|^{x}), \quad (7)$$

where B and a_m are the critical amplitude and the amplitude of the correction for scaling, respectively. The data of the Monte Carlo experiments were processed with correction for scaling ($a_m \neq 0$) and without regard for this correction ($a_m = 0$). The critical exponents β calculated for the models G1 and G2 are presented in Table 3.

The calculations were performed in the same temperature range as for the susceptibility. For the G1 model, the β exponents obtained from the data processed without correction for the scaling ($a_m = 0$) and those with this correction ($a_m \neq 0$) lie in the range 0.31–0.34. It is difficult to reveal the influence of the correction for the scaling from these data, because they coincide, to within the error, at $a_m \neq 0$ and $a_m = 0$. Making allowance for the dipole interactions in the G2 model leads to a small increase in the β exponents.

Note that the character of the critical behavior of the models under consideration cannot be uniquely determined using the critical exponents γ and β. In our opinion, this is explained by the fact that the susceptibility is a strongly fluctuating quantity and the magnetization exhibits high-temperature tails. Hence, the traditional procedures of processing these quantities lead to serious problems. As will be shown below, analysis of the same data in the framework of another approach gives a more clear pattern of the critical behavior.

5. A FINITE-SIZE SCALING

The basic principles of the finite-size scaling theory, which has been used extensively in recent years, are reduced to the inclusion of finite ($L \ll \infty$) sizes of the systems analyzed by the Monte Carlo method [5, 9, 28, 29]. According to this theory, the free energy of a sufficiently large system with periodic boundary conditions at a temperature close to the critical point T_c is scaled as follows:

$$F(T, L) = L^{-d}F(tL^{1/\nu}), \quad (8)$$

where d is the space dimension, $T_c = T_c(L = \infty)$, and ν is the statical critical exponent of the correlation length for an infinitely large system ($L = \infty$). Relationship (8) leads to similar dependences of the heat capacity, the

Table 2. Effective critical exponents γ (γ') of the susceptibility for gadolinium models G1 ($D_d = 0$) and G2 ($D_d \neq 0$) at $0.95 \times 10^{-3} \leq t \leq 7 \times 10^{-1}$

N	$D_d = 0$		$D_d \neq 0$	
	γ'	γ	γ'	γ
512	1.13(3)	1.29	1.11(2)	1.17
1000	1.14	1.24	1.11	1.18
1728	1.15	1.28	1.12	1.13
2744	1.14	1.23	1.13	1.14
4096	1.18	1.28	1.15	1.14
5832	1.19	1.27	1.14	1.13

Table 3. Effective critical exponents β of the magnetization for gadolinium models G1 ($D_d = 0$) and G2 ($D_d \neq 0$) at $0.95 \times 10^{-3} \leq t \leq 6 \times 10^{-1}$

N	$D_d = 0$		$D_d \neq 0$	
	$a_m = 0$	$a_m \neq 0$	$a_m = 0$	$a_m \neq 0$
512	0.30(2)	0.32	0.32	0.32
1000	0.31	0.33	0.33	0.34
1728	0.32	0.33	0.33	0.34
2744	0.32	0.34	0.34	0.36
4096	0.33	0.34	0.34	0.35
5832	0.33	0.34	0.34	0.36

magnetization, and the susceptibility per spin, that is,

$$C(T, L) \approx L^{\alpha/\nu} C_0(tL^{1/\nu}), \quad (9)$$

$$m(T, L) \approx L^{-\beta/\nu} m_0(tL^{1/\nu}), \quad (10)$$

$$\chi(T, L) \approx L^{\gamma/\nu} \chi(tL^{1/\nu}). \quad (11)$$

Relationships (9)–(11) describe well the critical behavior of infinitely large systems at $t \ll 1$ and $L \longrightarrow \infty$.

From this theory, it follows that the magnetization and susceptibility in the system of size $L \times L \times L$ at $T = T_c$ and sufficiently large L satisfy the following relationships:

$$m \propto L^{-\beta/\nu}, \quad (12)$$

$$\chi \propto L^{\gamma/\nu}. \quad (13)$$

Analysis of our data with the use of relationships (12) and (13) made it possible to determine the β and γ exponents. To accomplish this, the dependences of m and χ on the linear size L of the lattice were plotted on the log–log scale. For the G1 model, we obtained the ratios $\beta/\nu = 0.501$ and $\gamma/\nu = 1.987$. By assuming that the initial Hamiltonian is the Heisenberg one and setting $\nu = 0.706$ [3, 4], we have $\beta = 0.35(2)$ and $\gamma = 1.40(2)$. Note that these values are in good agreement with the exponents theoretically calculated within the Heisenberg model ($\beta = 0.368$ and $\gamma = 1.39$ [3, 4]). For the G2 model, $\beta/\nu = 0.569$ and $\gamma/\nu = 1.917$. Since this model allows for the dipole–dipole interactions in addition to the exchange interactions, let us determine the exponents at $\nu = 0.706$ (the Heisenberg model) and $\nu = 0.69$ (the dipole model [25]). As a result, we obtain $\beta = 0.40(2)$ and $\gamma = 1.35(2)$ at $\nu = 0.706$ and $\beta = 0.39(2)$ and $\gamma = 1.33(2)$ at $\nu = 0.69$. It is worth noting that the β and γ exponents for this model are shifted toward the values characteristic of three-dimensional dipole models ($\beta = 0.38$ and $\gamma = 1.37$ [25]). The exponent magnitudes obtained at $\nu = 0.706$ coincide with these theoretical values, to within the limits of error. It should be noted that the replacement of $\nu = 0.706$ by $\nu = 0.692$ leads to a decrease in the γ exponent, which is characteristic of the crossover from the critical behavior within the three-dimensional Heisenberg model with isotropic short-range forces to the behavior described by the three-dimensional dipole model.

In practice, the scaling of the heat capacity, as a rule, is performed with maximum values $C_{\max}$ and the expression [5, 28, 30],

$$C_{\max}(L) = C_{\max}(L = \infty) - aL^{\alpha/\nu}, \quad (14)$$

where a is a coefficient. The approximation of the data with the use of relationship (14) gives the critical exponents $\alpha = -0.15(2)$ for the G1 model and $\alpha = -0.17(2)$ for the G2 model at $\nu = 0.706$. The α value recalculated for the G2 model at $\nu = 0.69$ (the dipole model), to within the limits of error, coincides with the α exponent at $\nu = 0.706$. These data also agree well with theoretical predictions within the Heisenberg model and the results obtained in analysis of the Monte Carlo calculations on the basis of traditional power functions.

Our results obtained by the Monte Carlo method in the study of the models for real ferromagnetic gadolinium demonstrate that the G1 model exhibits a Heisenberg critical behavior. The critical exponents α of the heat capacity, which were determined by the approximation of the data with power functions and from the relationships of the finite-size scaling theory, agree well with each other and the theoretical values, as well as with the majority of the data obtained in laboratory experiments for gadolinium [18, 23–25].

The β and γ exponents determined by the traditional technique from relationships (6) and (7) have a specific feature typical of the Monte Carlo data: the character of the critical behavior is difficult to judge from these exponents. At the same time, the results obtained for β and γ by the processing of the same data in terms of the finite-size scaling theory unambiguously assign the G1 model to the Heisenberg universality class with exponents $\alpha = -0.15(2)$, $\beta = 0.35(2)$, and $\gamma = 1.40(2)$. A comparison of the critical parameters calculated for the G1 and G2 models shows that the inclusion of the isotropic dipole–dipole interactions in the G2 model leads to a certain shift in the critical parameters which is characteristic of the crossover from the Heisenberg model to the dipole model. Note also that the isotropic dipole–dipole interactions considered in the G2 model are only a weak perturbing factor on the background of strong exchange interactions. Since analysis of the effect of these forces on the critical behavior with the joint inclusion of another weak perturbing factor, namely, the uniaxial anisotropy, was not performed earlier, the resolution of the Monte Carlo method in this case remained unknown. For this reason, all the experiments and the data processing were carried out rigorously following the same procedure. The features that have manifested themselves in the G2 model indicate a high resolution of the Monte Carlo method.

It should be noted that, although the results of the data processing in the framework of the finite-size scaling theory are in better agreement with theoretical and experimental results, analysis of the same data by their approximation with power functions makes it possible to extract additional important information. In our opinion, in order to obtain a more comprehensive pattern of the critical behavior in these systems, the results of the Monte Carlo calculations should be analyzed within both approaches.

REFERENCES

1. A. Z. Patashinskiĭ and V. L. Pokrovskiĭ, *Fluctuation Theory of Phase Transitions* (Nauka, Moscow, 1982, 2nd ed.; Pergamon, Oxford, 1979).
2. S. Ma, *Modern Theory of Critical Phenomena* (Benjamin, Reading, 1976; Mir, Moscow, 1980).

3. J. J. C. Le Guillou and J. J. Zinn-Justin, Phys. Lett. **46**, L137 (1985).
4. S. A. Antonenko and A. I. Sokolov, Phys. Rev. E **51**, 1894 (1995).
5. I. K. Kamilov, A. K. Murtazaev, and Kh. A. Aliev, Usp. Fiz. Nauk **169**, 773 (1999).
6. A. K. Murtazaev, I. K. Kamilov, Kh. K. Aliev, and V. A. Mutaĭlamov, Zh. Éksp. Teor. Fiz. **117** (3), 559 (2000) [JETP **90**, 488 (2000)].
7. G. A. Martynov, Usp. Fiz. Nauk **169**, 600 (1999).
8. *Monte Carlo Methods in Statistical Physics*, Ed. by K. Binder (Springer-Verlag, Berlin, 1979; Mir, Moscow, 1982).
9. K. Binder and H. W. Heermann, *Monte Carlo Simulation in Statistical Physics: An Introduction* (Springer-Verlag, Berlin, 1988; Nauka, Moscow, 1995).
10. D. P. Landau, Physica A (Amsterdam) **205**, 41 (1994).
11. Ch. Holm and W. Janke, Phys. Rev. B **48**, 936 (1993).
12. K. P. Belov, M. A. Belyanchikova, R. Z. Levitin, and S. A. Nikitin, *Rare-Earth Ferromagnets and Antiferromagnets* (Nauka, Moscow, 1965).
13. V. M. Kuchin, V. A. Somenko, S. Sh. Shil'shteĭn, and Yu. B. Patrikiev, Zh. Éksp. Teor. Fiz. **55** (4), 1241 (1968) [Sov. Phys. JETP **28**, 649 (1969)].
14. R. H. Child, Phys. Rev. B **18**, 1247 (1978).
15. D. A. Doleisi and S. A. Swenson, Phys. Rev. B **24**, 6326 (1981).
16. E. A. Lewis, Phys. Rev. B **1**, 4368 (1970).
17. D. S. Simons and M. B. Salamon, Phys. Rev. B **10**, 4680 (1974).
18. G. Bednarz, D. J. W. Geldart, and M. A. White, Phys. Rev. B **47**, 14247 (1993).
19. G. H. J. Wantenaar, S. L. Campbell, and D. N. Chaplin, Phys. Rev. B **29**, 1419 (1984).
20. P. Molho and J. L. Portosseill, J. Magn. Magn. Mater. **31–34**, 1023 (1983).
21. A. J. Saleh and N. H. Saunders, J. Magn. Magn. Mater. **29**, 197 (1982).
22. P. Heller, Rep. Prog. Phys. **30**, 731 (1967).
23. Kh. A. Aliev, I. K. Kamilov, and O. M. Omarov, Zh. Éksp. Teor. Fiz. **94** (11), 153 (1988) [Sov. Phys. JETP **67**, 2262 (1988)].
24. A. R. Chowdhury, G. S. Collins, and Ch. Hohenemser, Phys. Rev. B **33**, 6231 (1986).
25. I. K. Kamilov and Kh. A. Aliev, *Statical Critical Phenomena in Magnetically Ordered Crystals* (Dagest. Nauchn. Tsentr Ross. Akad. Nauk, Makhachkala, 1993).
26. S. V. Vonsovskiĭ, *Magnetism* (Nauka, Moscow, 1971; Wiley, New York, 1974).
27. K. P. Belov, A. K. Zvezdin, A. M. Kadomtseva, and R. Z. Levitin, *Orientational Transitions in Rare-Earth Magnets* (Nauka, Moscow, 1979).
28. A. K. Murtazaev, Fiz. Nizk. Temp. **25**, 469 (1999) [Low Temp. Phys. **25**, 344 (1999)].
29. A. K. Murtazaev, I. K. Kamilov, and Kh. K. Aliev, J. Magn. Magn. Mater. **204** (1–2), 151 (1999).
30. P. Peczak, A. M. Ferrenberg, and D. P. Landau, Phys. Rev. B **43**, 6087 (1991).

Translated by O. Borovik-Romanova

Physics of the Solid State, Vol. 43, No. 4, 2001, pp. 692–697. Translated from Fizika Tverdogo Tela, Vol. 43, No. 4, 2001, pp. 666–671.

MAGNETISM AND FERROELECTRICITY

Diffraction of Light by Dynamic Elastic Deformations of a Moving Domain Wall in Orthoferrites on Breaking through the Sound Barrier

A. P. Kuz'menko, A. V. Kaminskiĭ, E. A. Zhukov, and V. N. Filatov

Khabarovsk State Technical University, Khabarovsk, 680035 Russia

e-mail: kap@tiis.khstu.ru

Received July 10, 2000

Abstract—Diffraction of light by dynamic deformations of a domain wall moving at the velocity of sound is observed in plates of rare-earth orthoferrites $TmFeO_3$ and $DyFeO_3$. In this case, the domain wall is shown to become bent across the thickness of the plate. The lifetime of the dynamic deformations is determined to be 20 ns, and their dimension is 2×10^{-4} cm. It is found that the polarization of light is altered and its change is comparable in magnitude to the Faraday rotation angle in the orthoferrites investigated. © *2001 MAIK "Nauka/Interperiodica".*

INTRODUCTION

In orthoferrites (weak ferromagnets) $RFeO_3$ (R^{3+} is a rare-earth or an yttrium ion), the crystalline and magnetic structure is such that the motion of domain walls (DWs) under a magnetic field is the dominant mechanism of magnetization reversal [1–6]. The mutual orientation of the easy magnetization axis and the optical axis in orthoferrites, as well as their high magnetooptical quality factor in the visible spectral region, is favorable for study of the DW dynamics in these materials. The maximum DW velocity in $YFeO_3$ is higher than that in all other magnets studied to date. The experimental value of this velocity is the same as the minimum phase velocity of spin waves corresponding to the linear portion of the spin-wave dispersion curve and equals 19.74×10^3 m/s [1], which is significantly higher than the velocities of transverse (v_t) and longitudinal sound (v_l) in this material. The dependence of the DW velocity on the amplitude of the driving magnetic field $v(H)$ is nonlinear in $YFeO_3$ and earlier investigated rare-earth orthoferrites. It has been shown [1] that the DW ceases to be one-dimensional in $YFeO_3$ when its velocity exceeds the velocity of sound. The $v(H)$ curve has a number of "shelves," i.e., magnetic-field ranges ΔH over which the DW velocity varies only insignificantly. The ranges ΔH over which the DW velocity is equal to v_t or v_l were theoretically shown [1, 4] to be due to magnetoelastic coupling. Some shelves corresponding to DW motion at a supersonic velocity are due to DW interaction with magnons, which are created near a DW under parametric-resonance conditions [1, 2]. The number of shelves on the $v(H)$ curve and their width ΔH increase as the DW velocity approaches the limiting velocity C. These features were observed in plates of $YFeO_3$, no matter what the synthesis method, the DW type (Bloch, Néel, or intermediate one), the plate thickness, the boundary conditions at the plate surfaces, or the temperature in the range of 4.2–460 K [1, 2].

The DW motion at a supersonic velocity, which is characteristic of orthoferrites, was investigated theoretically in a model which allows for strong dissipation [1, 4] and magnetoelastic interaction of the DW with bulk acoustic waves. By simultaneously solving the magnetodynamics and elasticity equations, the effect of the external magnetic field on the time dependence of the DW magnetization was calculated with allowance for the magnetoelastic coupling and energy dissipation in the elastic subsystem. The $v(H)$ dependence found correlates well with the experimental dependence. The dynamic elastic deformations U_t' and U_l' associated with the moving DW were calculated [1, 4] to be

$$U_t' = -\delta_t \sin\vartheta\cos\vartheta / C(1 - v^2/v_t^2),$$
$$U_l' = -\delta_l \sin^2\vartheta / C(1 - v^2/v_l^2), \quad (1)$$

where δ_t and δ_l are the magnetoelastic coupling constants and ϑ is the angle between the easy axis and the direction of the DW motion. It follows from Eq. (1) that the magnitude of the dynamic elastic deformation tends to infinity as the DW velocity approaches v_t or v_l. Because of this, the magnetic anisotropy constants are significantly renormalized and can even change their sign, which, in turn, leads to a change in the DW structure and dimensions and affects the DW dynamics, as was observed in [1, 5].

In [3], the parameters of the dynamic deformations produced by a moving DW were found from the spectra of inelastic light scattering by the DW; the Brillouin scattering spectra, which were formed during the DW

passing 10^6 times across the beam spot of a He–Ne laser, were used to determine the frequency and wave vector of excited phonons; they were found to be 10 GHz and 3×10^5 cm^{-1}, respectively (at liquid-helium and room temperatures). It was also confirmed in [3] that the magnitude of the dynamic deformation depends on the direction of the DW motion; when this direction does not coincide with the crystallographic *a*, *b*, and *c* axes of the crystal, the DW interacts with all three phonon modes. The dynamic deformations of a moving DW increase significantly when it breaks through the sound barrier, as was found experimentally and substantiated theoretically in [1, 4].

Chetkin *et al.* [5] showed that, when the DW velocity equals the transverse sound velocity, the DW width becomes almost an order of magnitude smaller and then, at supersonic velocities, again increases sharply almost to its initial value. It was proposed that the DW tilts through an angle as large as approximately 50° when it breaks through the sound barrier.

Fraunhofer diffraction from a single fixed DW in orthoferrites was investigated in [7]. The sample was a 100 μm thick plate of orthoferrite $YFeO_3$, and diffraction from a DW between two domains magnetized in opposite directions was observed; in passing through them, the polarization of light was changed.

In contrast to $YFeO_3$, rare-earth orthoferrites (REOs) are characterized by an additional magnetic ordering in the sublattice formed by rare-earth ions. Because of this, the magnetoelastic coupling constants in $RFeO_3$ are larger than those in $YFeO_3$ and the coupling of the magnon and phonon subsystems is strengthened when DWs move at a near-sonic velocity.

The objective of this paper is to investigate the behavior of a DW breaking through the sound barrier during pulsed magnetization reversal in plates of REOs, such as $TmFeO_3$ and $DyFeO_3$. Earlier investigations of the DW dynamics in REOs [1, 2] were conducted using a magnetooptical analog of the Sixtus–Tonks induction method, which does not allow one to measure high velocities with satisfactory accuracy and investigate the shape of the DW. The DW dynamics at supersonic velocities in the yttrium orthoferrite was investigated in [1, 2] by a method that yielded a high spatial (less than 1 μm) and temporal resolution (less than 1 ns), but this method has not yet been applied to investigate the DW dynamics in REOs.

1. EXPERIMENTAL RESULTS

We investigated $TmFeO_3$ and $DyFeO_3$ samples which had been grown by the crucibleless melting method with optical heating at the Moscow Power Institute. The samples had the shape of plates and were cut out perpendicular to the optical axis. The thickness of the plates was about 60 μm, which ensured the highest magnetooptical contrast and allowed one to visualize dynamic DWs without using an image interferometer. The plate surfaces were preliminarily treated by immersing the plates in overheated orthophosphoric acid, which relieved internal stresses and increased the mobility of the DWs.

The investigation was made by a double-exposure high-speed photography method [6]. A dynamic DW was illuminated synchronously with the pulsed magnetic field by two subnanosecond pulses of an oxazine 17 dye laser pumped by a nitrogen transverse discharge laser. The emission wavelength 630 nm fell within the optical transparency window of the samples investigated. The method allows one to conduct an investigation in real time. Improvements in the method reduced the error to 2% for a velocity of 20×10^3 m/s; this error was fundamentally determined by the light pulse length alone [2]. The time separation between the two illuminating pulses was 15 ns. The distance traveled by the DW over this time interval was used to calculate the DW velocity, which allowed the $v(H)$ dependence to be determined very accurately in the $TmFeO_3$ and $DyFeO_3$ samples.

The temperature dependence of the DW mobility in orthoferrites is known to follow the $1/T^2$ law [1]. At room temperature, the DW mobility in REOs is an order of magnitude lower than that in $YFeO_3$; therefore, in order to investigate the DW dynamics in these materials, strong magnetic fields must be applied. For this reason, we measured the temperature dependence of the DW mobility in $TmFeO_3$. It was found that the maximum DW mobility in the $TmFeO_3$ samples studied was reached at 168 K and equaled 860 cm/(s Oe). In the temperature range 94–98 K, weakly ferromagnetic thulium orthoferrite exhibits reorientation of its magnetization from the [001] to [100] direction, which is likely the reason for the decrease in the DW mobility at temperatures below 168 K. Our investigations of the DW dynamics in $TmFeO_3$ were all conducted at 168 K in an optical liquid-nitrogen cryostat. The sample was fixed to a cooling copper lead, which allowed the temperature to be kept constant.

We also investigated the temperature dependence of the DW mobility in $DyFeO_3$ plates of different thicknesses. The maximum mobility was found to be equal to 340 cm/(s Oe), and it was reached at room temperature. Because of the low DW mobility, the velocity of the DW motion in this orthoferrite can only slightly exceed the longitudinal sound velocity 7.2×10^3 m/s. In $DyFeO_3$, as well as in $TmFeO_3$, the $v(H)$ dependence exhibited shelves ΔH at velocities equal to v_t and v_l.

Figure 1a shows a photomicrograph of two superimposed dynamic domain structures with alternate light and dark stripes. As in $YFeO_3$ [1], the moving DW in the $TmFeO_3$ samples investigated ceases to be planar when it breaks through the sound barrier. A leading portion occurs on the DW, as is seen from the photomicrograph in Fig. 1a. On the left and on the right of this portion, the DW velocity remains equal to the trans-

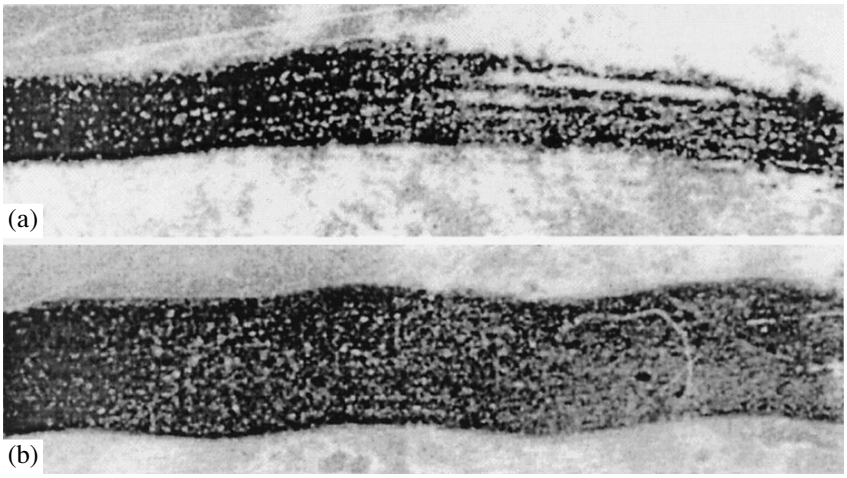

Fig. 1. Photomicrographs of two superimposed dynamic domain structures in $TmFeO_3$ at 168 K (the time separation between the two illuminating pulses is equal to 15 ns). (a) Diffraction pattern from a portion of the DW at the instant it breaks away from a dynamically deformed region and (b) a non-one-dimensional DW moving at a supersonic velocity equal to 8×10^3 m/s.

verse sound velocity in $TmFeO_3$, 3.6×10^3 m/s, while the velocity of the leading portion exceeds this value and is as high as 5×10^3 m/s. (All measurements of the dynamic DW parameters were made by processing the original photomicrographs with a computer.) As is seen from Fig. 1a, the brightness of the light stripes decreases with their distance from the leading portion of the DW. This variation in brightness is more pronounced in the dark region, where the DW has already broken through the sound barrier. Microphotometric measurements showed that stripes are also observed in the light region, but they are feebly marked. The overall width of the part of the dark region in which light stripes are observed is 67.5 μm. It should be noted that, during a time of 15 ns, the DW travels a distance of 54 μm when moving at a velocity of $v_t = 3.6 \times 10^3$ m/s, while in the region where the DW moves at a supersonic velocity 5×10^3 m/s, the distance traveled by the DW is 75 μm. Therefore, the width of the just mentioned region, containing four light stripes, is smaller than the distance traveled by the DW with supersonic velocity during the time elapsed between two laser pulses. The distances of the centers of the four light stripes from the leading portion of the DW are 35, 50, 60, and 67.5 μm, respectively. According to microphotometric measurements, the relative brightnesses of these light stripes with respect to that of the first light stripe of the leading DW portion are 76, 64, 50, and 35%, respectively.

Similar modulation of the brightness was also observed in a $DyFeO_3$ plate when the DW velocity became equal to the velocity of sound. It should be stressed that this modulation takes place only at the instant the DW breaks through the sound barrier, as can be seen from the photomicrographs for $TmFeO_3$ presented in Fig. 1. Indeed, Fig. 1b shows the dynamic domain structure in the case where the DW velocity is 8×10^3 m/s and there are three leading DW portions with the radius of curvature approximately 180 μm, but no modulation of brightness is observed.

2. DISCUSSION

It has been shown both theoretically [1, 4] and experimentally [3] that, when the DW velocity is near the velocity of sound, a region of localized dynamic deformation (elastic soliton) as large as several DW widths can break away from the DW. In order to interpret the observed modulation of the light intensity transmitted through $TmFeO_3$ and $DyFeO_3$ plates, let us analyze the diffraction of light by the phase inhomogeneities [8] associated with dynamic deformations of the DW breaking through the sound barrier.

The characteristic size of a dynamically deformed region breaking away from a moving DW must be comparable to the DW width and can be as large as several micrometers. We will assume that the shape of the dynamically deformed region separating from the DW is identical to the shape of the DW before it breaks through the sound barrier. Under these conditions, the observed amplitude modulation of light can be due to diffraction by phase inhomogeneities associated with variations in the refractive index in the deformed region.

The double-exposure pulsed photomicrography method allowed us to immediately record the diffraction pattern (Fig. 1a) that occurs when the moving DW breaks through the sound barrier. A diffraction pattern similar to that in Fig. 1a was also observed for the DW moving at the velocity of sound in rare-earth orthoferrite $DyFeO_3$ at room temperature. It should be noted

that this phenomenon does not occur in $YFeO_3$ [1, 2], which suggests that the effect of the magnetic ordering of rare-earth ions on moving DWs becomes more significant at transonic velocities.

Let us analyze the conditions under which diffraction of light is observed in this situation. Our investigation of the $v(H)$ dependence in $TmFeO_3$ revealed that the magnetic field range ΔH_t over which damping of DW motion occurs at $v = v_t$ is several times larger than that observed earlier in $YFeO_3$ plates of the same thickness. These ranges are 350 and 75 Oe, respectively. In fact, ΔH_t in $TmFeO_3$ is closer to its value in a thin (10 μm thick) $YFeO_3$ plate, where $\Delta H_t = 500$ Oe [1, 2]. In this case, one might expect a noticeably larger dynamic DW deformation if one assumes that the power that is expected for producing this deformation is increased with increasing ΔH_t. This power can be calculated from ΔH_t, velocity v_t, the duration of the DW motion, and the saturation magnetization M_0 which is equal to 140 G for $TmFeO_3$ and, according to our estimates, is as large as several microwatts. Under these conditions, the shape and dynamic behavior of the DW can be significantly changed, as indicated in [1, 3–5]. In addition, the higher coercitivity of the surface layers of the samples investigated can be favorable to bending of the initially planar DW not only over the plane of the plate, as in Fig. 1, but also across the plate thickness. Furthermore, according to [1, 3], when the moving DW breaks through the sound barrier, a dynamically deformed region can separate from the DW and, at $v > v_t$, it will lag behind the DW and retain a shape similar to that of the DW for some time. This conclusion is supported by the data obtained in [3, 4], according to which the leading edge of a dynamically deformed region is sharp, while its trailing edge is diffuse.

In the case of light incident normal to the surface of the plate, the formation of the diffraction pattern is determined by the phase modulation of the light wave passing through different portions of the DW bent over the plate thickness. The different spacing between the light stripes observed does not correspond to the usual diffracted intensity distribution, where the spacing between principal maxima is approximately the same [8]. To account for this fact, we assume that each of the light stripes observed is the resultant distribution of the diffracted intensity from different portions of the dynamically deformed region breaking away from the non-one-dimensional DW. The usual diffracted intensity distribution over the maxima of different orders does not take place because, perhaps, there is no regularity in the structure of the dynamic DW deformations [4]. The fact that several maxima of the diffracted intensity are observed will be interpreted below in terms of the specific features of DW dynamics.

In our experiments, the light incident on an orthoferrite plate is linearly polarized and the diffraction pattern observed is formed by the light transmitted through the analyzer. When there are no dynamic deformations, a dark region is observed through which the DW passes during the time separation between the two laser pulses (this region is seen in Fig. 1b and at the left of Fig. 1a, where the DW is not curved). The appearance of dynamic deformations leads to a change in the polarization of light in this region, and light stripes corresponding to diffraction maxima of the type indicated above are observed against a dark background. The change in the polarization is due, perhaps, to a change in the elastooptical coefficients and/or in the Verdet magnetooptical constant of the orthoferrite plate, and it is comparable to the effect produced by the Faraday rotation, judging from the change in the contrast observed. The Faraday rotation angle is approximately 20° for a $TmFeO_3$ plate 60 μm thick.

Let us discuss the features of the dynamic DW behavior when it breaks through the sound barrier. As is seen from Fig. 2, the $v(H)$ dependence is strongly nonlinear in a $TmFeO_3$ sample. Note that it is analogous to the $v(H)$ dependence for orthoferrite $DyFeO_3$. As in the case of $YFeO_3$, there is a range ΔH_t over which the DW velocity v is virtually constant and equal to v_t. Discussion of other features of the $v(H)$ dependence is beyond the purpose of this paper. Figure 2 also shows a predicted $v(H)$ dependence calculated by simultaneously solving magnetodynamics and elasticity equations [1, 4]; the curve in Fig. 2 has portions on which the differential DW mobility is negative at DW velocities close to the velocity of sound. According to a model based on a probabilistic approach to describing DW dynamics, the DW motion becomes unstable at $v = v_t$. In this case, the DW behavior is significantly affected by fluctuations, such as inhomogeneities of the crystalline and magnetic structure, the magnetic field, and elastic strains, leading to phase transformations of

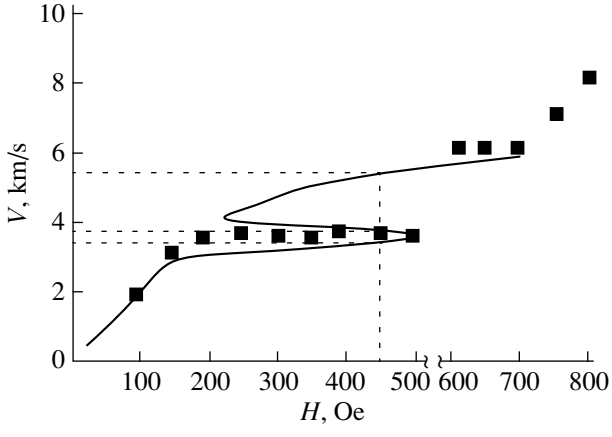

Fig. 2. Experimental and calculated magnetic-field dependences of the DW velocity in a thulium orthoferrite plate 60 μm thick at 168 K.

the first order. As follows from theory and experimental data [1–4] and as is seen from Fig. 2, the critical behavior of the DW moving at a transonic velocity manifests itself in the fact that there are three values of the velocity at which the DW can move at the same value of the magnetic field, which is typical of the first-order phase transformations. According to the Maxwell rule, which applies to this dynamic system [1, 4], the DW moves at the transverse sound velocity over a longer period of time, which is due to an increase in the amplitude of dynamic deformations caused by its motion.

In order to produce a stable two-domain structure in REO, one should apply gradient fields several times higher than those applied to $YFeO_3$. In the specific case of $TmFeO_3$ and $DyFeO_3$, the field gradient is as large as 2500 Oe/cm. In the beginning, the DW is situated in the region where this field is zero. As the DW is displaced from its equilibrium position under the action of the magnetic pulse field, the resultant magnetic field decreases uniformly at the expense of the gradient field. When the DW velocity is not close to the velocities of sound, the field gradient has only a marginal effect on the resultant field if the pulse field has a large amplitude. However, near the sound velocities, the dynamic DW is in an unstable state and any fluctuation can have a dramatic effect on it.

The appearance of several light stripes in the diffraction pattern from dynamic DW deformations can be understood if one takes into account that the driving field decreases because of the gradient field. The first diffraction stripe appears at a distance of about 250 μm from the starting position of the DW. At this point, the resultant field is decreased by 62.5 Oe. Note that, under the conditions indicated above, the field magnitude at which the DW velocity becomes equal to the velocity of sound is of the order of 500 Oe in $TmFeO_3$. Because of the decrease in the amplitude of the driving magnetic field, when accelerated to a velocity $v \geq v_t$, the DW is brought into the field of a magnitude which is not large enough for the DW to move at a supersonic velocity. Nevertheless, the DW has already broken away from the dynamically deformed region, which resulted in the formation of the first (in time) of the diffraction stripes observed. The appearance of the other light diffraction stripes can be interpreted in the same way. Since the gradient component of the resultant field increases with the increasing DW distance from its starting position (64.5, 66.5, and 70.25 Oe), the time it takes for the DW to accelerate to a velocity higher than v_t also increases, which is the reason why the diffraction stripes are not equidistant.

Analysis of the photomicrograph in Fig. 1a revealed that the brightness of the diffraction stripes decreased linearly with time. At the instant the DW breaks away from the deformed region, the maximum DW velocity is 5×10^3 m/s. Using this value, we found that the four diffraction stripes appeared at 9, 10, 12, and 15 ns, respectively, after the DW velocity became higher than the velocity of sound v_t. By extrapolating our data on the decrease in the brightness of the diffraction stripes with time, we evaluated the lifetime of the dynamic deformations produced by the moving DW in $TmFeO_3$ to be 20 ns.

The widths of the diffraction stripes were measured to be 14, 8.5, and 3.25 μm. The brightness of the stripe that was the fourth to appear is likely to be determined by unrelaxed deformation; therefore, we can evaluate the characteristic size of this deformation from the width of the fourth stripe L. The image was formed in the specimen surface closer to the observation point. We assume that the dominant contribution to this diffraction maximum comes from the central region of the DW curved across the plate thickness. Therefore, the distance S of the observed diffraction pattern from this region is equal to half the plate thickness, i.e., 30 μm. The diffraction angle can be taken to be roughly equal to L/S. On the other hand, this angle can be expressed in terms of the ratio λ/d, where λ is the wavelength of light and d is the characteristic size of the dynamic deformation. With the numerical data indicated above, the value of d is thus found to be about 2 μm, which is close to the apparent DW thickness in orthoferrites. At the same time, diffraction of light by static DWs of much smaller widths (about 40 nm [7]) was observed in these materials. Thus, analysis of our experimental data and that obtained in [7] revealed that DWs are curved across the thickness of the samples.

The widths of the diffraction stripes indicated above allow one to conclude that the dynamic deformations are not changed in shape, but only decrease in magnitude. According to [4], the dynamic deformations of the transverse and longitudinal types evolve in radically different ways. Transverse deformations decay rapidly and become diffuse in shape, while longitudinal deformations have a longer lifetime and hold their shape. The evolution of dynamic deformations of DWs moving at a velocity close to v_t as described above suggests that, in the case considered, transverse and longitudinal deformations occur simultaneously. It can also be concluded that, when the moving DW breaks through the sound barrier, its profile across the plate thickness is changed.

ACKNOWLEDGMENTS

The authors are grateful to M.V. Chetkin for his continued interest in this work; to A.K. Zvezdin, A.F. Popkov, and A.A. Mukhin for useful discussions of the results obtained; and to A.M. Balbashov for the single crystals of rare-earth orthoferrites.

This work was supported by the Ministry of Higher Education of the Russian Federation (Fundamental Natural Science Program, grant no. 97-0-7.0-29).

REFERENCES

1. V. G. Bar'yakhtar, M. V. Chetkin, B. A. Ivanov, and S. N. Gadetskiĭ, *Dynamics of Topological Magnetic Solitons. Experiment and Theory* (Springer-Verlag, Berlin, 1994); Springer Tracts Mod. Phys. **129** (1994).
2. M. V. Chetkin, A. P. Kuz'menko, A. V. Kaminskiĭ, and V. N. Filatov, Fiz. Tverd. Tela (St. Petersburg) **40** (9), 1656 (1998) [Phys. Solid State **40**, 1506 (1998)].
3. S. D. Demokritov, A. I. Kirilyuk, N. M. Kreines, *et al.*, J. Magn. Magn. Mater. **104** (1), 663 (1992).
4. M. V. Zvezdin and A. M. Mukhin, Zh. Éksp. Teor. Fiz. **102** (8), 577 (1992) [Sov. Phys. JETP **75**, 306 (1992)].
5. M. V. Chetkin, Yu. N. Kurbatova, and A. I. Akhutkina, Phys. Lett. A **215**, 211 (1996).
6. M. V. Chetkin, A. P. Kuz'menko, S. N. Gadetskiĭ, and V. N. Filatov, Prib. Tekh. Éksp. **3**, 196 (1984).
7. Y. S. Didosyan, H. Hauser, J. Nicolics, and I. R. Yavorsky, J. Magn. Magn. Mater. **203** (1–3), 247 (1999).
8. M. Born and E. Wolf, *Principles of Optics* (Pergamon, Oxford, 1969; Nauka, Moscow 1970).

Translated by Yu. Epifanov

Physics of the Solid State, Vol. 43, No. 4, 2001, pp. 698–704. Translated from Fizika Tverdogo Tela, Vol. 43, No. 4, 2001, pp. 672–677.

MAGNETISM AND FERROELECTRICITY

Structural and Magnetic Phase Transformations in Multilayer Gadolinium Films

V. O. Vas'kovskiĭ*, A. V. Svalov*, A. V. Gorbunov*, N. N. Shchegoleva, and S. M. Zadvorkin*****

**Ural State University, pr. Lenina 51, Yekaterinburg, 620083 Russia*

***Institute of Metal Physics, Ural Division, Russian Academy of Sciences, ul. S. Kovalevskoĭ 18, Yekaterinburg, 620219 Russia*

****Institute of Mechanical Engineering, Ural Division, Russian Academy of Sciences, Yekaterinburg, 620219 Russia*

Received July 18, 2000

Abstract—A study was made of the effect of thickness and thermal treatment on the microstructure and magnetic properties of Gd/Cu and Gd/Si multilayer films obtained by rf ion sputtering. It was found that the magnetic layers have an amorphous–crystalline structure, with the component ratio depending on the thickness of the magnetic layers and nonmagnetic spacers and on the annealing temperature. An analysis of the temperature dependences of the torque, which was made within the molecular field approximation, yielded a quantitative description of the changes in the film phase composition. The correlation between the exchange coupling parameter and the structural state of gadolinium was established. © *2001 MAIK "Nauka/Interperiodica".*

INTRODUCTION

The properties of thin films of rare-earth elements, as well as of other magnetically ordered substances, are subject to a strong size effect [1]. The specific features of this influence were studied primarily on single layers and multilayer films of Gd. In particular, one found a direct connection between the Gd layer thickness and such characteristics as the magnetic moment [2], the Curie temperature [3, 4], and magnetic anisotropy [5]. Thickness was also found to indirectly affect the magnetic properties through the variation in the structural imperfection of films [6]. Although the above studies dealt with single-crystal Gd films, the latter variation may underlie a certain quantitative disagreement between the results quoted by various authors.

The structural state may reveal still more noticeable variations in nonepitaxially grown thin films. Among such objects are multilayer films containing, in addition to the rare-earth metals, intervening 3*d* metal layers. In such conditions, rare-earth metals (Tb, Dy, Gd) exhibit a tendency to amorphization [7, 8]. In magnets with indirect exchange interaction, a group to which rare-earth metals belong, such a phase transition should strongly affect the magnetic ordering parameters. The present study deals with this effect in the specific example of Gd/Cu and Gd/Si multilayer films.

1. EXPERIMENTAL

The film samples were prepared on silicon substrates by rf ion sputtering. The base and the argon gas pressures were 2×10^{-6} and 2×10^{-4} mm Hg, respectively. Each film deposition was preceded by one-hour sputtering of Gd, which served as a getter. All materials were deposited at a rate of ~1 Å/s. The samples differed in the thickness of the Gd layers (75–400 Å) or of the nonmagnetic Cu or Si spacers (2–20 Å). The total thickness of the magnetic component in the multilayer samples was practically constant (≈4000 Å). In addition, we used several thicker Gd single-layer films in the experiment. Each sample had a buffer underlayer and an insulating cap layer of a nonmagnetic material not less than 100 Å thick. After preparation, some films were subjected to thermal treatment in a vacuum at temperatures of up to 450°C.

The magnetic properties of the films were measured on a torque magnetometer. The structure was characterized with an x-ray diffractometer and an electron microscope. In the latter case, we studied thinner samples (down to 500 Å) deposited on cleaved surfaces of NaCl crystals.

2. RESULTS AND DISCUSSION

Figure 1 shows (with symbols) the experimental dependences of the torque P on temperature T obtained on a one-layer Gd film 7200 Å thick (curve *2*) and on multilayer Gd/Cu films (curves *3*, *4*) with magnetic layers differing in thickness (L_{Gd}) and spacers of a fixed thickness (L_{Cu} = 10 Å). The measurements were carried out in a magnetic field of 1 kOe applied at 45° to the sample plane. Also shown for comparison is the $P(T)$ relation (curve *1*), which was obtained in a weak magnetic field on a bulk Gd sample prepared directly from the target material. A comparison of curves *1* and *2* reveals that even a thick film is characterized by a con-

siderably lower Curie temperature (~250 K) and a smoother course of the $P(T)$ relation than those of the bulk material. This is probably associated with the specific features of the rf ion sputtering. The Gd films deposited by this technology exhibit substantial microstrains, which may account for the observed decrease in the exchange coupling. Reducing the Gd layer thickness by introducing nonmagnetic spacers also gives rise to a variation of the magnetic properties, and it is this variation that was the main subject of this investigation.

As can be seen from Fig. 1 (curves *3*, *4*), the transition to the thin-film state is accompanied by a further decrease in the Curie temperature and the appearance of a more or less pronounced break in the $P(T)$ curves at temperatures of ~160 K. This behavior of the torque, which actually reflects the variation of spontaneous magnetization with temperature, indicates that the Gd layers are magnetically not single-phase. Moreover, these data suggest that the parameters characterizing the deviation from the single-phase state are dependent on the value of L_{Gd}. The Gd/Si films, close in thickness to the ones discussed, yielded very similar results, both qualitatively and quantitatively. This reflects the passive role of the nonmagnetic spacer and, thus, argues for the existence of a relation between the phase composition and the thickness of the magnetic layers.

The x-ray diffraction measurements made with CrK_α radiation lend a certain support to this conjecture. This is seen from a comparison of the diffractograms presented in Fig. 2 for the substrate coated by a Si buffer layer (curve *1*) and the Gd(L_{Gd})/Si(10 Å) films with L_{Gd} = 75 (curve *2*) and 150 Å (curve *3*). These diffraction patterns indicate that the insulating Si layers and the thin Gd layers are amorphous for the x-rays, while the thicker Gd layers contain a crystalline phase. Viewed in the given angular interval, this phase produces only one strongly broadened line. It can be identified with the (002) Gd reflection, which, nevertheless, is shifted relative to its position for bulk Gd (46.68°). These features support the conclusion that the crystalline Gd phase is textured and that its lattice is strongly distorted. The hexagonal axis of the crystallites is predominantly perpendicular to the film plane, and the corresponding interplanar spacing is, on average, substantially larger compared with its equilibrium value.

The structural state of the films was analyzed in more detail with an electron microscope. Figure 3 displays electron diffraction patterns and photomicrographs of Gd/Si(10 Å) samples with Gd layers of different thicknesses. The absence of distinct lines in the pattern and the presence of the characteristic ripple in the electron microscope image in Fig. 3a, when combined with the x-ray diffractograms, indicate that the thin Gd layers are amorphous. At the same time, the electron diffraction patterns exhibit two rather than one halo, thus evidencing the existence of two systematic interatomic distances. Their estimation based on the average halo diameter yields 2.8 and 1.8 Å. The fact that these figures are incommensurate suggests that the second halo is not associated in any way with second-order diffraction. This second halo is probably a precursor of crystallization, because there are intense diffraction lines of crystalline Gd at the corresponding angles.

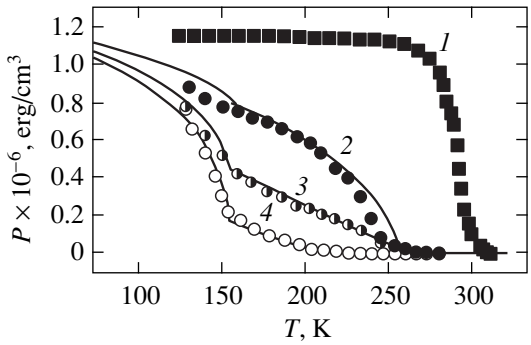

Fig. 1. Experimental (symbols) and theoretical (lines) dependences of the torque on temperature for (*1*) a bulk sample and (*2–4*) Gd(L_{Gd})/Cu(10 Å) films with different magnetic-layer thicknesses (Å): (*2*) 7800, (*3*) 225, and (*4*) 75.

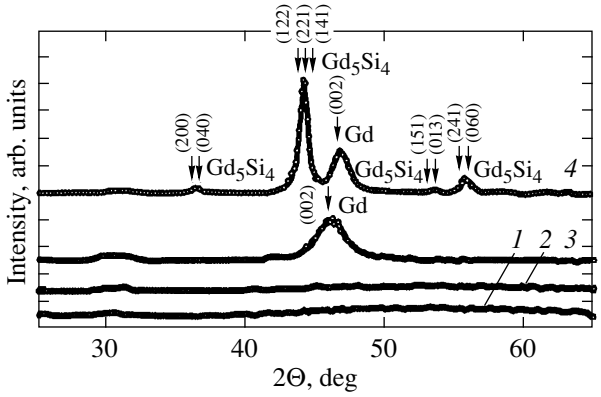

Fig. 2. Diffractograms of (*1*) the substrate and (*2–4*) Gd(L_{Gd})/Si(10 Å) films with different magnetic-layer thicknesses (Å): (*2*) 75 and (*3*, *4*) 150 in (*2*, *3*) the initial state and (*4*) after annealing at 400°C. Arrows identify the positions of some calculated lines for the Gd_5Si_4 compound and of the line assigned to (002) Gd.

The phase state of the samples with L_{Gd} = 150 Å (Fig. 3b) may be characterized as amorphous–crystalline; indeed, one clearly sees both diffuse diffraction lines and a halo in the electron diffractogram, and the photomicrograph includes elements of an amorphous ripple and crystallites with an average diameter not above 50 Å. An analysis of the diffraction lines present assigns them to the crystalline α-Gd. The *c* axis of the corresponding crystallites tends to align normal to the film. In some places, one also observes a texture in the sample plane. On the whole, these films exhibit strong

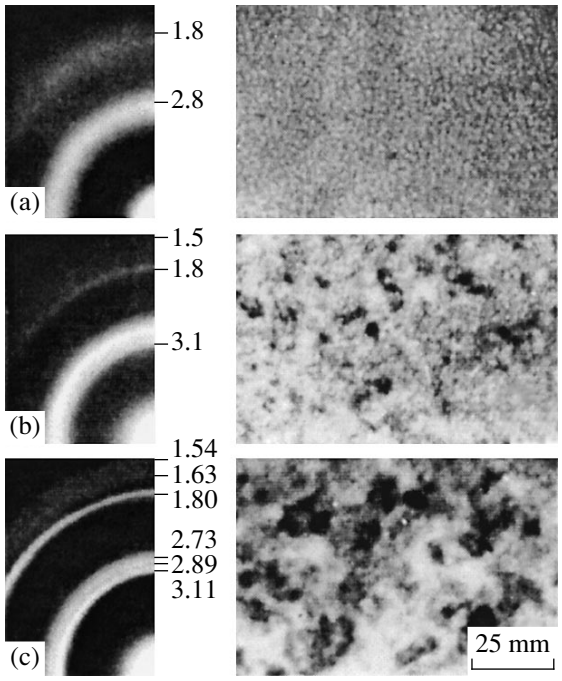

Fig. 3. Electron diffraction patterns and photomicrographs of Gd(L_{Gd})/Si(10 Å) films with different magnetic-layer thicknesses (Å): (a) 75, (b) 150, and (c) 400. The figures specify the interplanar distances d corresponding to the diffraction lines under study.

phase nonuniformity over their area. There are regions where either the crystalline or the amorphous phase dominates. Nevertheless, visual estimates show the content of the latter phase to be higher. Samples with the thickest (L_{Gd} = 400 Å) Gd layers (Fig. 3c) are also in the amorphous–crystalline state. However, the crystalline α phase is more clearly pronounced in them and is quantitatively dominant. The average crystallite size is as high as 100 Å.

The above results show convincingly that, as the layer thickness decreases, Gd is observed to transfer from the crystalline to the amorphous state. This transition comes practically to a close at L_{Gd} = 100 Å. It appears natural to assume that it is the phase transformations that underlie the above-mentioned changes in the magnetic properties of the films. We employed the molecular field approximation for a phenomenological description of this relationship. It was assumed that the magnetic moment of the atoms and the Gd density in the amorphous and crystalline states are the same, while the molecular-field parameters (λ_a and λ_c, respectively) are different and correspond to different Curie temperatures of the amorphous, T_C^a, and the crystalline, T_C^c, phases, whose concentrations are n_a and n_c.

A subsequent analysis revealed that the two-phase model does not provide an adequate description of the experimental data. To attain it, we had to introduce into the model a third component, which we call conventionally the transition phase. It is nonuniform and consists of elements whose Curie temperatures range from T_C^a to T_C^c. For the sake of simplicity, we assume that the Curie temperature distribution law is such that the molecular field parameter is characterized by a distribution function constant over the range from λ_a to λ_c. Then, the magnetization of the transition phase will be given by the expression

$$M_{ac}(T, \lambda_a, \lambda_c) = M(0)\frac{1}{\lambda_c - \lambda_a}\int_{\lambda_a}^{\lambda_c} B\left(\frac{\mu\lambda M_{ac}}{kT}\right)d\lambda, \quad (1)$$

where $B(x)$ is the Brillouin function, μ is the magnetic moment of the Gd atom, and $M(0)$ is the bulk Gd magnetization at $T = 0$. The last assumption implies that the film and bulk densities are equal. Thus, the film magnetization contains three components:

$$M(T) = n_a M_a(T) + n_c M_c(T) + n_{ac} M_{ac}(T), \quad (2)$$

where M_a, M_c, and M_{ac} are the magnetizations and n_a, n_c, and n_{ac} are the concentrations of the amorphous, crystalline, and transition phases, respectively. The magnetizations of the amorphous and crystalline phases were calculated in terms of the molecular field theory, as in the case of the transition phase, but with constant molecular field parameters λ_a and λ_c.

Equation (2) was used in calculating the torque component necessary for comparison with the experiment:

$$P = P_z = H_x M_y - H_y M_x. \quad (3)$$

In Eq. (3), the components of the external magnetic field H_x and H_y were set by the actual experimental conditions, while the magnetization components M_x and M_y were derived by minimizing the free energy. This was done under the assumption that the magnetization in the film bulk is uniform and the magnetic anisotropy of the films is due only to the shape anisotropy.

Figure 1 shows the theoretical $P(T)$ relations (solid lines) fitted to the corresponding experimental plots by varying the concentration of the three phases properly. The values of T_C^a and T_C^c were estimated preliminarily in every case from the experiment by linearly extrapolating the low- and high-temperature parts of the $P(T)$ graphs to zero. These temperatures were used subsequently to determine the molecular field parameters λ_a and λ_c. The fairly good agreement between the theoretical and experimental $P(T)$ curves testifies to the validity of the model used and offers the possibility of quantitatively characterizing the multiphase state of the films.

It was found that the T_C^a temperature depends only weakly on the thickness and is close to 160 K. The T_C^c

temperature shows a tendency to increase from 240 to 260 K with increasing layer thickness. However, for all film samples, its magnitude remains smaller than the Curie temperature of bulk Gd. This probably reflects the strong lattice distortions observed by us. Figure 4 plots the concentrations of the various magnetic phases vs. the Gd layer thickness. The symbols relate to the multilayer films, the Gd(L_{Gd})/Cu(10 Å) film, and the thick (3800 and 7200 Å) single Gd layers. It should be pointed out that the absolute error in the determination of n_a, n_c, and n_{ac} by fitting reaches 5%. Nevertheless, the course of the relationships is fully in accord with the above qualitative reasoning. As L_{Gd} increases, the content of the crystalline phase grows and that of the amorphous phase decreases. The transition phase exhibits an indistinct maximum in the thickness region where n_a and n_c approach each other.

The above results relate to Gd layers in multilayer films with nonmagnetic spacers 10 Å thick. This figure was found to be the lowest thickness ensuring a practically complete break of any structural coupling between the magnetic layers. The corresponding investigation was performed on a number of samples with a fixed total thickness of the magnetic layers (3800 Å) and nonmagnetic Si and Cu spacers of different thicknesses. The latter thicknesses were chosen such that L_{Gd} = 75 Å.

The $P(T)$ curves measured on samples with different L_{Si} and L_{Cu} showed that their magnetic properties vary with the spacer thickness. Note that this variation is qualitatively similar to that observed when varying L_{Gd}. This is indicated, in particular, by the dependence of the concentrations n_a, n_c, and n_{ac} on the Si spacer thickness L_{Si} (Fig. 5). As can be seen from the figure, introducing even the thinnest spacer layer used (2 Å) changes the magnetic phase composition of the samples dramatically. The crystalline phase transforms practically completely to the transition phase, which, in turn, transfers to the amorphous phase for L_{Si} > 5 Å. Thus, the $n_{ac}(L_{Si})$ relation follows a nonmonotonic pattern. Note that the maximum in this curve is more clearly pronounced than that in the $n_{ac}(L_{Gd})$ dependence. Figure 5 also shows that for L_{Si} > 10 Å, the phase composition varies very little. Similar results were obtained for samples with copper spacers.

Thermal treatment is known to affect the phase composition of nonequilibrium structural systems. We performed accumulating vacuum annealing of the Gd/Cu and Gd/Si samples. It was found that the effect of annealing on the film properties depends primarily on the material of the spacers, as well as on the thicknesses of the spacer and magnetic layers. The films containing copper spacers revealed sharp degradation of their magnetic properties (a decrease in the Curie temperature and a transition to the paramagnetic state) already under low–temperature annealing ($T_{an} \leq$ 200°C). This degradation was higher in films with a

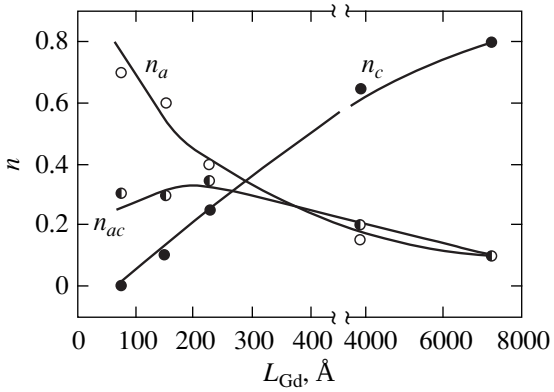

Fig. 4. Dependences of the calculated concentrations of the amorphous (n_a), crystalline (n_c), and transition (n_{ac}) magnetic phases on the layer thickness in Gd(L_{Gd})/Cu(10 Å) films.

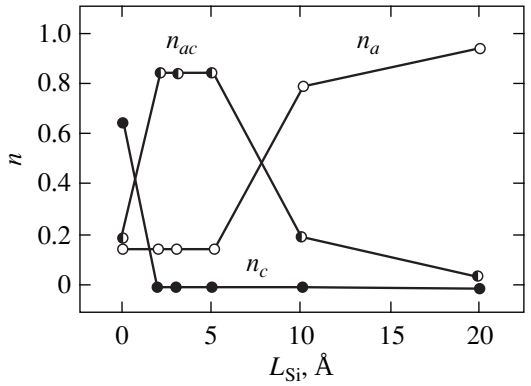

Fig. 5. Dependences of the calculated concentrations of the amorphous (n_a), crystalline (n_c), and transition (n_{ac}) magnetic phases on the Si spacer thickness.

smaller L_{Gd} and larger L_{Cu}. This suggests that in this case, the annealing not so much affects the structural state of Gd, as stimulates the formation of the Gd–Cu intermetallic compounds, which possess substantially lower magnetic ordering temperatures than Gd [9].

The situation observed in the thermal treatment of the Gd/Si samples was totally different. The annealing regime used ($T_{an} \leq$ 450°C, the anneal time equaled one hour in each stage) did not bring about a noticeable degradation of the magnetic properties of films, thus permitting a fairly comprehensive phase analysis. The torque curves revealed that the Gd(75 Å)/Si(10 Å) films are not very sensitive to annealing in the T_{an} interval indicated above. This is also supported by the electron microscope images. Figure 6a presents an electron diffraction pattern and a photomicrograph of the sample structure after annealing at 380°C. A comparison of

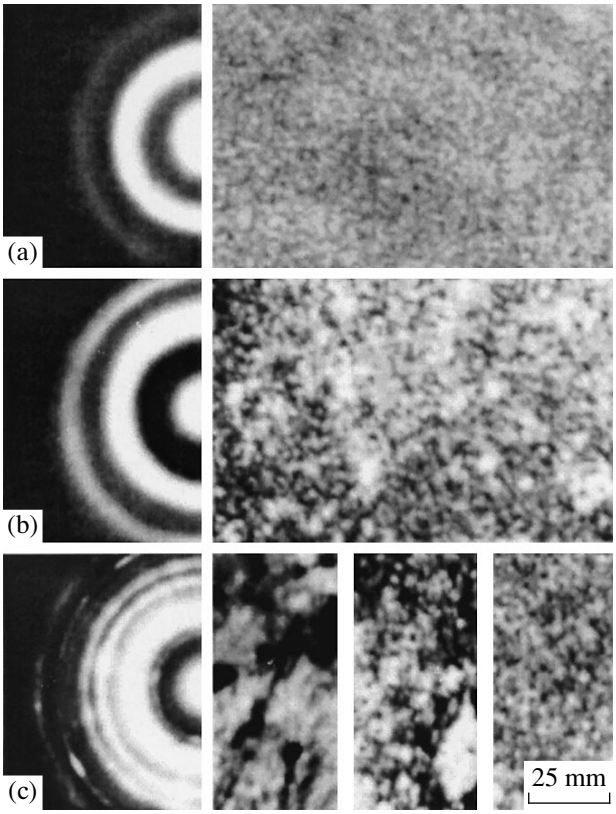

Fig. 6. Electron diffraction patterns and photomicrographs of (a) Gd(75 Å)/Si(10 Å) and (b, c) Gd(150 Å)/Si(10 Å) samples after annealing at different temperatures (°C): (a) 380, (b) 250, and (c) 380.

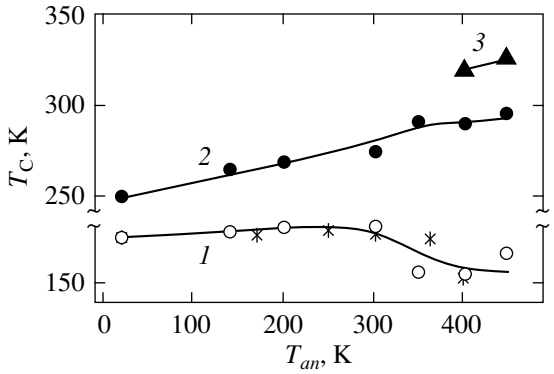

Fig. 7. Dependences of the Curie temperatures of various magnetic phases on the annealing temperature: (*1*, stars) T_C^a of the Gd(75 Å)/Si(10 Å) sample; (*1*, circles) T_C^a of the Gd(150 Å)/Si(10 Å) sample; (*2*) T_C^c of the Gd(150 Å)/Si(10 Å) sample; and (*3*) T_C of the Gd_5Si_4 phase.

these data with the corresponding initial-state measurements (Fig. 3a) does not reveal any noticeable differences; the clearly defined amorphous phase and indications of the onset of crystallization are observed as before.

Phase composition calculations likewise revealed the presence of only an amorphous and a transition phase in the sample in all stages of the annealing. The concentrations of these phases remain practically constant, $n_a = 0.7$ and $n_{ac} = 0.3$. By contrast, the Curie temperatures undergo some changes. In particular, T_C^c drops sharply (from 240 to 200 K) in the initial anneal stage. However, because of the transition phase being in a low concentration, this affects the overall pattern of the $P(T)$ relations only weakly. The variation of the Curie temperature of the amorphous phase is more clearly pronounced in the experiment. The $T_C^a(T_a)$ relation is shown graphically in Fig. 7 (curve *1*). As T_{an} increases, a slight growth followed by a decrease in T_C^a down to ~130 K is observed. It can be conjectured that annealing brings about some short-range changes in the amorphous structure. However, their direct detection would require more detailed structural studies.

Annealing affects the properties of films with thicker Gd layers much more dramatically. This is seen, in particular, from Fig. 8, in which the circles relate to the $P(T)$ dependences for the Gd(150 Å)/Si(10 Å) sample measured in different stages of the annealing. These data permit dividing the annealing into two stages, with the boundary passing within the 300–350°C region. Low-temperature thermal treatment influences the shape of the $P(T)$ curves only weakly. The quantitative characteristics of the phase composition practically do not change as well. As in the preceding cases, they were derived from the fitting $P(T)$ curves shown by lines in Fig. 8 and found to be $n_a = 0.6$, $n_c = 0.15$, and $n_{ac} = 0.25$.

Thus, magnetometric measurements performed at $T_{an} < 350$°C suggest that the amorphous phase remains dominant. Similar information is provided by electron microscopy. Figure 6b shows an electron diffraction pattern and a photomicrograph of a Gd(150 Å)/Si(10 Å) sample annealed at $T_{an} = 250$°C. They are seen to differ very little from the corresponding patterns characterizing the initial state of such films (Fig. 6b). The changes observed relate only to the Curie temperatures of the amorphous and crystalline phases. The dependences of these characteristics on the annealing temperature are shown in Fig. 7 (curves *1*, *2*). Both T_C^a and T_C^c are seen to exhibit a trend to growth within the T_{an} region under study.

Annealing at $T_{an} = 350$°C (curve *3* in Fig. 8) transforms the $P(T)$ relation markedly. It results in a change in the curve from a concave to a convex shape, an increased Curie temperature T_C^c close to the magnetic ordering temperature of bulk Gd, and a decrease in the torque at low temperatures. The last effect is apparently a result of the decrease in the Curie temperature of the amorphous phase, as is the case with the

Gd(75 Å)/Si(10 Å) films. The fitting $P(T)$ curve drawn for T_C^a = 130°C and T_C^c = 290°C yields the following calculated concentrations of the magnetic phases: n_a = 0.4, n_c = 0.4, and n_{ac} = 0.2. It follows that this annealing brings about a substantial growth in the volume of the crystalline phase, which occurs at the expense of both the amorphous and the transition phase. It should be noted that, if the crystalline phase is textured, it can give rise to a systematic error in the quantitative analysis of the phase composition proposed here. This error arises from the disregarded crystalline magnetic anisotropy.

As can be seen from Fig. 8, the thermal treatment carried out at higher temperatures also affects the properties of multilayer films. The most essential point here is that magnetic ordering persists to temperatures substantially in excess of the Curie point of bulk Gd. This could possibly be due to the thermally induced formation of new chemical compounds in the film. There is only one compound in the system of elements under study here, Gd_5Si_4 [9], whose Curie point (345 K) is above room temperature. The slight bend in the $P(T)$ relation at room temperature (curve *4* in Fig. 8) may indicate the formation of a new magnetic phase in the films. Taking into account this factor yields the Curie temperatures of the crystalline Gd and of the Gd_5Si_4 phase shown by curves *2* and *3* in Fig. 7.

Figure 2 presents the x-ray diffraction pattern (diffractogram *4*) of the Gd(150 Å)/Si(10 Å) sample annealed at T_{an} = 400°C. It contains a distinct line of crystalline Gd. This line is narrower than the corresponding line of the original sample (diffractogram *3*). Additionally, it lies close to the tabulated position. Both these observations evidence an annealing-induced reduction of Gd lattice distortions, which, in turn, can account for the observed changes in the Curie temperature of the crystalline phase. The other lines probably belong to Gd silicides, in particular, to the Gd_5Si_4 compound. The latter has a very rich structure of diffraction lines, some of which fit well into the diffraction pattern obtained (Fig. 2).

Figure 6c also presents electron microscopy data obtained on the Gd(150 Å)/Si(10 Å) sample after annealing at T_{an} = 380°C. The high-temperature annealing is seen to extremely complicate the electron diffraction pattern. It exhibits a large number of diffraction lines and traces of the original halos. Unambiguous interpretation of this pattern would be difficult. Nevertheless, there are grounds to assume that the films contain an amorphous and a crystalline Gd phase, as well as silicides, the most probable of them being Gd_5Si_4 and $GdSi_2$. It should also be stressed that the electron diffractograms did not reveal any traces of contaminating phases like oxides or carbides. Moreover, the nonuniformity of the diffraction ring intensity suggests the presence of a crystalline texture both in the Gd itself and in the derivative crystalline phases.

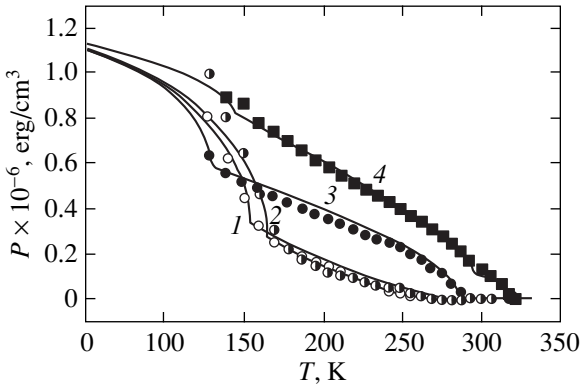

Fig. 8. Experimental (symbols) and calculated (lines) dependences of the torque of the Gd(150 Å)/Si(10 Å) films on the annealing temperature (°C): (*1*) initial state, (*2*) 200, (*3*) 350, and (*4*) 450.

A visual analysis of the microstructure shows it to be strongly nonuniform in the samples subjected to high-temperature treatment. Figure 6c displays the most typical fragments of these patterns. The films exhibit regions of an amorphous and of a crystalline phase with a large dispersion of the grains in size and shape. A more detailed analysis revealed that grains of the new crystalline phases occur only in close proximity to Gd grains. At the same time, one observes a large number of islands of crystalline Gd with no other crystalline phases present nearby. This suggests that the above phase transformations take place in a certain sequence.

3. CONCLUSION

On the whole, our study permits the following conclusion. Gd films obtained by rf ion sputtering are multiphase. The main phase components are crystalline and amorphous gadolinium modifications, which possess substantially different magnetic-ordering temperatures. However, there are apparently a number of intermediate states inbetween, which account for a continuous variation in the magnetic properties. One can also conceive of a variation of the exchange coupling parameters within the main structural states, which would give rise to changes in the Curie temperatures of the amorphous and crystalline phases within 130–160 K and 250–290 K, respectively. The film phase composition depends on the thickness of the magnetic layers, the thermal treatment temperature, and the properties of the intervening nonmagnetic materials. Being highly neutral, silicon provides a good protection of Gd films against the deleterious effects of external factors.

ACKNOWLEDGMENT

The authors express gratitude to V.S. Gaviko for assistance in the structural studies.

REFERENCES

1. Z. S. Shan and D. J. Sellmyer, in *Handbook on the Physics and Chemistry of Rare Earths* (North-Holland, Amsterdam, 1996), Vol. 22, p. 81.
2. C. F. Majkrzak, J. W. Cable, J. Kwo, *et al.*, J. Appl. Phys. **61** (8), 4055 (1987).
3. J. Samuel Jiang and C. L. Chien, J. Appl. Phys. **79** (10), 5615 (1996).
4. M. Farle, A. Berghaus, and K. Baberschke, Phys. Rev. B **39** (7), 4838 (1989).
5. M. Farle, Rep. Prog. Phys. **61**, 755 (1998).
6. M. Farle and W. A. Lewis, J. Appl. Phys. **75** (10), 5604 (1994).
7. N. Sato and K. Habu, J. Appl. Phys. **61** (8), 4287 (1987).
8. S. Honda, M. Nawate, and I. Sakamoto, J. Appl. Phys. **79** (1), 365 (1996).
9. K. N. R. Taylor and M. Darby, *Physics of Rare-Earth Solids* (Chapman and Hall, London, 1972; Mir, Moscow, 1974).

Translated by G. Skrebtsov

Physics of the Solid State, Vol. 43, No. 4, 2001, pp. 705–709. Translated from Fizika Tverdogo Tela, Vol. 43, No. 4, 2001, pp. 678–682.

MAGNETISM AND FERROELECTRICITY

Crossover of Polaron Conductivity and the Inhomogeneous State of Lanthanum Manganites in the Magnetic Phase Transition Region

V. N. Krivoruchko

Galkin Physicotechnical Institute, National Academy of Sciences of Ukraine, Donetsk, 83114 Ukraine
e-mail: krivoruc@host.dipt.donetsk.ua

Received September 5, 2000

Abstract—The transport properties of lanthanum manganites over a wide range of temperatures below the magnetic phase transition point are discussed within the model of a two-phase composite whose phases differ in the magnetic order and charge carrier concentration. The volume ratio of the phases depends on the temperature and the magnetic field. The magnetoelastic polarons are charge carriers in both phases, and the metal–dielectric transition occurs as a percolation transition accompanied by the crossover of the polaron conductivity. The results obtained by numerical simulation of the resistivity, magnetoresistance, and thermopower are compared with the experimental data for $La_{0.7}Mn_{1.3}O_{3-\delta}$ thin films. The theoretical and experimental data are in good agreement. © *2001 MAIK "Nauka/Interperiodica".*

1. INTRODUCTION

A superposition of ferromagnetic and antiferromagnetic peaks of neutron scattering for a number of samples doped with lanthanum manganites was already observed many years ago by Wollan and Koehler [1] and lent impetus to a considerable discussion (see, for example, review [2] and references therein). However, it seems likely that only recent experimental investigations [3–6] uniquely confirmed the magnetic and electric inhomogeneities of lanthanum manganites in the magnetic phase transition region. The results obtained conclusively demonstrated that ferromagnetic and antiferromagnetic regions are spatially separated and form charge-carrier–enriched (metallic) and charge-carrier–depleted (semiconducting) domains. Magnetization vectors of different ferromagnetic regions are disordered. The application of an external magnetic field leads to the percolation transition to a metallic phase, which is accompanied by the giant magnetoresistance effect. It is interesting that a sample does not undergo complete transformation into the ferromagnetic state even in a strong magnetic field [4].

Although the results obtained in [3–6] revealed the phase separation, a number of questions essential to the understanding of the physics of the giant magnetoresistance effect in manganites remain unclear. In particular, it remains to be seen whether the conductivity mechanism in charge-enriched (metallic) domains radically differs from that in charge-depleted domains. To put it differently, whether these regions should be considered to be separated by a true metal–dielectric phase transition or the conductivity in domains changes according to a scenario of the conductivity-crossover type. A variant of the answer to this problem determines the type of Ginzburg–Landau functional and, hence, the results of the application of the phenomenological theory of phase transitions to lanthanum manganites.

In the present work, the transport properties of lanthanum manganites over a wide range of temperatures below the magnetic phase transition point T_C were discussed within the model of a composite (efficient medium) formed by long ferromagnetic domains with a metallic conductivity which were embedded in a semiconducting paramagnetic matrix (Fig. 1). It was assumed that the magnetization $m(T, H)$ is an order parameter, and the fraction $C(T, H)$ of charge carriers

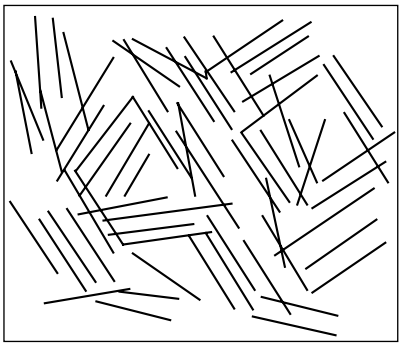

Fig. 1. A composite with phases differing only in the charge carrier concentration and the magnetic order. The volume ratio of phases depends on the temperature and the magnetic field. Near T_C, the composite consists of strongly oblong ferromagnetic ellipsoids with a metallic conductivity (*FMm*) (solid lines) which are embedded in a paramagnetic semiconducting matrix (*PMs*) (bright field of the drawing).

1063-7834/01/4304-0705$21.00 © 2001 MAIK "Nauka/Interperiodica"

contained in metallic domains is a secondary order parameter. The metal–dielectric transition occurs as a percolation transition. Note that this transition in the case of strongly oblong ferromagnetic domains is very sharp and exhibits a low percolation threshold [7]. The obtained theoretical dependences of the electrical resistivity and the thermopower of a composite on the temperature and magnetic field were compared with the experimental data taken from [8, 9] for $La_{0.7}Mn_{1.3}O_{3-\delta}$ thin films grown by magnetron sputtering. An excellent agreement between the experimental and theoretical results shows that the effective medium model adequately reflects the physics of the phenomenon under consideration.

It should be noted that a model similar to that discussed in the present work was considered recently by Jiame *et al*. [10]. The obtained theoretical dependences well represented the experimental data for Ca systems. It was reasonable to analyze a generalization of the model proposed in [10]. In particular, by assuming the internal inhomogeneity and the percolation transition to the metallic phase, we introduced two essential changes as compared to [10]. First, we supposed that magnetoelastic polarons are charge carriers in the metallic and semiconducting phases, so that the metal–dielectric transition occurs as a percolation transition attended by the crossover of the polaron conductivity. Second, the relation between the order parameters was taken into account through an interaction of the m^2C type rather than m^2C^2, as was proposed in [10] (see discussion below).

2. THE GINZBURG–LANDAU FUNCTIONAL

In the magnetic phase transition region, we assume that the magnetization $m(T, H)$ is the primary order parameter and the fraction of charge carriers $C(T, H)$ contained in metallic domains is the secondary order parameter. The interaction between the order parameters is considered within the lowest symmetry-allowed approximation (see, for example, [10, 11]), viz., $\sim m^2C$. Note that a similar term in the expansion of the free energy for cubic crystals appears, for example, when the interaction of macroscopic strains with the primary order parameter is taken into account (see [12]). It is this situation that occurs in lanthanum manganites under the assumption of their phase separation: the formation of charge-inhomogeneous regions leads to the aggregation of Jahn–Teller Mn^{3+} ions into clusters and the collectivization of the corresponding lattice strains.

The free energy functional has the form

$$F = \frac{1}{2}\alpha_m\tau m^2 + \frac{1}{4}bm^4 + \frac{1}{2}aC^2 + \frac{1}{4}\beta C^4 - dm^2C. \quad (1)$$

Here, $\tau = (T - T_{cm})/T_{cm}$, T_{cm} is a bare temperature of the magnetic phase transition. All the coefficients in expansion (1) are assumed to be positive. We do not seek to develop the phenomenological theory of phase transitions in lanthanum manganites. Hence, we will restrict our consideration to the situation when the paramagnet–ferromagnet phase transition is a second-order transition. This implies introduction of an additional condition $ab > 2d^2$ for the parameters of expansion (1). From the set of equations of state

$$\partial F/\partial m = -(\alpha_m\tau + 2dC)m + bm^3 = 0,$$

$$\partial F/\partial C = aC + \beta C^3 - dm^2 = 0,$$

it follows that $C(T, H) \sim m^2(T, H)$ and the phase transition temperature is determined as $T_C = (1 + 2d\bar{C})/T_{cm}$. Therefore, the phase separation process and a nonzero concentration $\bar{C}$ below the T_{cm} temperature bring about an increase in the "effective" critical temperature of the phase transition.

3. TRANSPORT PROPERTIES OF A COMPOSITE

Let us consider a composite whose phases are crystallographically (chemically) homogeneous but differ in the concentration of charge carriers. The volume ratio of the phases depends on the temperature and the magnetic field. Our aim is to reconstruct the transport properties of the composite from the known characteristics of its components. These characteristics can be found from the experimental data for La-deficient thin films of $La_{0.7}Mn_{1.3}O_{3-\delta}$ in the range of low (metallic phase) and high (semiconducting phase) temperatures.

Details of the film preparation and the data on their magnetic, magnetoresistive, thermoelectric, and magnetoresonant properties were described in [8, 9, 13]. Note that the $La_{0.7}Mn_{1.3}O_{3-\delta}$ films ~3500 Å thick were grown by reactive magnetron sputtering on the (001)-oriented $SrLaAlO_4$ substrates. According to x-ray structure analysis, the films are homogeneous and have a perovskite structure.

3.1. Magnetoresistance. The properties of a composite made up of long metallic wires embedded in a semiconducting matrix (Fig. 1) were studied earlier by Lágarkov and Sarychev [7]. Specifically, the effective resistivity $\rho \equiv \rho(H, T)$ of a sample whose components are characterized by the resistivities $\rho_m \equiv \rho_m(H, T)$ and $\rho_s \equiv \rho_s(H, T)$ is represented by the relationship (see expression (9) in [7])

$$\frac{1}{3}C(\rho - \rho_m)\{1/[\rho_m + G_\parallel(\rho - \rho_m)] + 4/(\rho_m - \rho)\} + 3(1 - C)(\rho - \rho_s)/(2\rho_s + \rho) = 0. \quad (2)$$

Here, the depolarization factor $G_\parallel = (b^2\rho_s/a^2\rho)\ln[1 + (a\rho/b\rho_s)]$ is introduced according to the composite model [7] and $C \equiv C(H, T)$ is the mixing factor (the fraction of charge carriers in the metallic region).

As follows from the preceding section, $C(H, T) \sim m^2(T, H)$. In numerical calculations, we will use the relationship

$$C(H, T) = 1 - \left(\frac{T - T_0}{T_m - T_0}\right)^2 \Theta(T - T_0), \qquad (3)$$

where T_0 is the temperature of a transition to the homogeneous ferromagnetic state ($T_0 \ll T_C$); T_m is the temperature of metallic domain nucleation; in the absence of a magnetic field, $T_m = T_C$; and $\Theta(x)$ is a theta function.

The experimental temperature dependence of the electrical resistivity of $La_{0.7}Mn_{1.3}O_{3-\delta}$ films in a zero magnetic field is shown by points in Fig. 2. The behavior of the reduced resistivity of the sample $\rho(H, T) \equiv R(T, H)/R(77\text{ K}, 0)$ in the metallic region ($T < 200$ K) is approximated by the phenomenological dependence

$$\rho_m(T, H) = 10^{-2.8} K^{-3/2} T^{3/2} + 10^{-2} \exp\{\alpha N(\varepsilon + g\mu_B S_C H)\}. \qquad (4)$$

Here, the first term corresponds to band carriers and describes the asymptotic behavior of $\rho_m(T)$ at low temperatures $T < 70$ K. The second term—the basic term in the temperature range under consideration—reflects the fact that a carrier in the crystal becomes a charged magnetoelastic polaron which is covered with a "phonon and magnon coat" (see, for example, [14, 15] and references therein). By generalizing in this way the physical meaning of the second term as compared to [16], we assume that $N(\varepsilon + g\mu_B S_C H) = \{\exp((\varepsilon + g\mu_B S_C H)/T) - 1\}^{-1}$ is the mean number of magnetoelastic polarons with an energy $\varepsilon \approx 950$ K, S_C is the effective number of spins participating in the formation of a "magnon coat" of the polaron, and $\alpha \approx 550$ is the structure factor [16]. The numerical values of the parameters involved in relationship (4) and formulas (5)–(7) given below were obtained from analysis of the experimental data and were taken from [8, 9].

The resistivity of films in the semiconducting phase ($T > 220$ K) is approximated by a dependence of the type

$$\rho_s(T, H) = 10^{-2.3} K^{-1} T \exp(E_\rho/T), \qquad (5)$$

which corresponds to inelastic processes of charge carrier hoppings with an activation energy $E_\rho \approx 1220$ K, which differs from that in a ferromagnetic domain. It is assumed that, in the paramagnetic phase, the "magnetic" component of a polaron is small so that its energy is virtually independent of the magnetic field.

The calculated temperature dependences of the resistivity of a composite at different axial ratios a/b for a ferromagnetic ellipse are depicted by solids lines in Fig. 2. The calculations were performed using formula (2) in the case when $\rho_m(H, T)$ and $\rho_s(H, T)$ were defined by relationships (4) and (5), respectively. As can be seen from this figure, the theory satisfactorily describes the experimental dependences only for very oblong ferromagnetic ellipsoids ($a/b > 10$). In other words, metallic regions in $La_{0.7}Mn_{1.3}O_{3-\delta}$ films are formed as strip domains rather than as compact clusters.

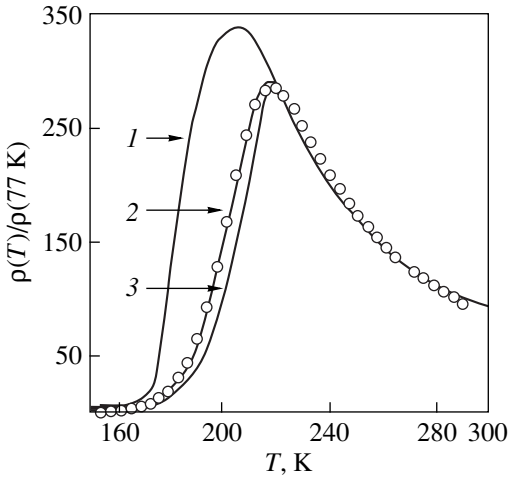

Fig. 2. Temperature dependences of the resistivity of the composite at different axial ratios for metallic ellipses a/b = (*1*) 1, (*2*) 10, and (*3*) 50. Points are the experimental data for $La_{0.7}Mn_{1.3}O_{3-\delta}$ films in the absence of a magnetic field.

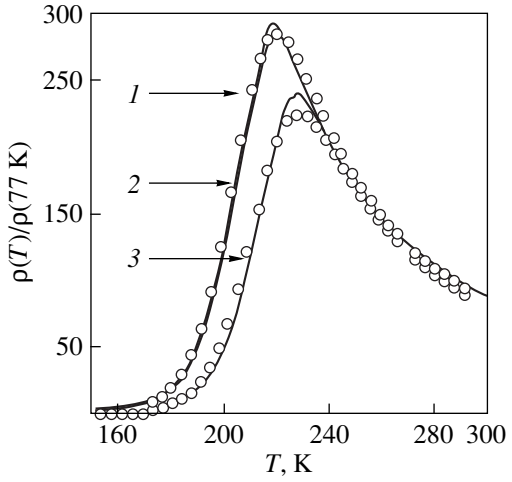

Fig. 3. Temperature dependences of the resistivity of the composite at different temperatures of the formation of metallic domains. $a/b = 10$. Conditions: (*1*) $T_0 = 120$ K, $T_m = 220$ K $= T_C$, and $H = 0$ kOe; (*2*) $T_0 = 120$ K, $T_m = 220$ K $= T_C$, and $g\mu_B S_C H = 50$ K; and (*3*) $T_0 = 130$ K, $T_m = 235$ K, and $g\mu_B S_C H = 0$. Points are the experimental data for $La_{0.7}Mn_{1.3}O_{3-\delta}$ films without magnetic field and at $H = 10$ kOe.

The temperature dependences of the resistivity, which were numerically simulated using expressions (2), (4), and (5) at $a/b = 10$ and the magnetic fields $H = 0$ and 10 kOe, are displayed by solid lines in Fig. 3. The

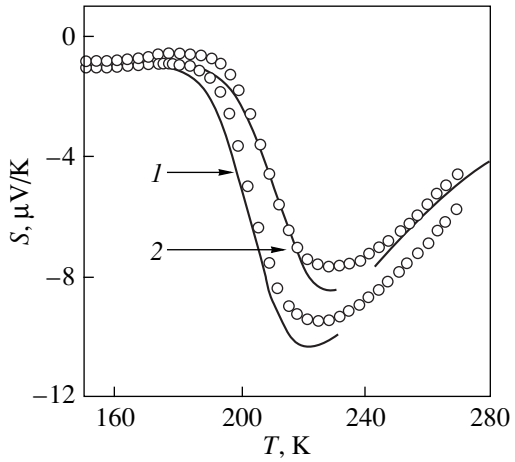

Fig. 4. Temperature dependences of the Seebeck coefficient for a thin composite film on a bulk substrate. $a/b = 10$, $T_0 = 120$ K, and $T_m = 220$ K = T_C. Points are the experimental data for $La_{0.7}Mn_{1.3}O_{3-\delta}$ films (*1*) without magnetic field and (*2*) at $H = 5$ kOe.

relevant experimental data for $La_{0.7}Mn_{1.3}O_{3-\delta}$ films are also shown by points in this figure. Allowance should be made for the fact that the magnetic field leads to (i) a change in the energy of a magnetoelastic polaron, (ii) a shift in the temperature of metallic domain nucleation and, correspondingly, the temperature of percolation transition, and (iii) the orientation of magnetic moments of ferromagnetic domains. Let us evaluate the relative contribution of each effect.

The last term in formula (4) accounts for the first factor. Curve *2* in Fig. 3 corresponds to the situation when the energy of a magnetoelastic polaron is changed by 50 K in a field of 10 kOe, i.e., when the number of spins per charge carrier is of the order of $20S_{Mn}$. In this case, the temperature of metallic domain nucleation remains unchanged, i.e., $T_m = T_C$. It is seen from this figure that the effect of magnetic field on the resistivity through this mechanism is extremely weak even at a large number of spins of manganese ions S_{Mn}, which form the magnon component of the polaron coat.

Relationship (3) makes it possible to elucidate the role of the second factor. Curve *3* in Fig. 3 illustrates how the change in the temperature of metallic domain nucleation T_m in a magnetic field affects the composite resistivity. A shift in T_m and T_0 by approximately 10 K toward the high-temperature range allows us to describe adequately the experimental dependence for $La_{0.7}Mn_{1.3}O_{3-\delta}$ films.

The change in the composite resistivity at a given temperature due to a change in the orientation of magnetic moments of ferromagnetic domains in a magnetic field can be accounted for with the use of the models proposed earlier for granular systems (see, for example, [17]). This mechanism of the magnetoresistivity for lanthanum manganites was discussed in my earlier work [18]. Consideration was given to the situation in which metallic ferromagnetic domains in the semiconducting matrix are spherical in shape and their relative fraction (the filling factor *f*) is small ($f \ll 1$). In this case, the magnetoresistivity effect associated with the reorientation of magnetic moments is proportional to the factor *f*. The case of strongly oblong ferromagnetic ellipsoids calls for separate analysis. At the same time, there are grounds to believe that this mechanism of the magnetoresistivity in lanthanum manganites at the temperatures of interest is insignificant [2, 15].

3.2. Seebeck coefficient. The temperature and field dependences of the thermopower for the composite can be determined from the results of the preceding section and from the relationships for the thermopower of composite components.

The experimental temperature dependence of the Seebeck coefficient for $La_{0.7}Mn_{1.3}O_{3-\delta}$ films in a zero magnetic field and a field of 5 kOe [9] are shown by points in Fig. 4. The behavior of the thermopower in the metallic phase ($T < 180$ K) is represented as

$$S_m(T) = (10^{-2}K^{-1}T - 3 \times 10^{-4}K^{-2}T^2)\ \mu V/K. \quad (6)$$

In the paramagnetic phase ($T > 220$ K), we have

$$S_s(T) = (7000\ K/T - 22)\ \mu V/K. \quad (7)$$

Now, we take into account that the thermal conductivity of a thin-film sample is predominantly determined by the thermal conductivity of the substrate. Then, the Seebeck coefficient for the film on the substrate is defined as [10, 19]

$$S(T, H) = \frac{\rho_s S_m - \rho_m S_s + \rho_{exp}(T, H)(S_s - S_m)}{(\rho_s - \rho_m)}. \quad (8)$$

It should be emphasized that the dependence $S(T, H)$ in the entire field range is determined only by the experimental dependence of the resistivity $\rho_{exp}(T, H)$, because the asymptotics for the low-temperature and high-temperature thermopower components are independent of the magnetic field.

The simulated temperature dependences of the Seebeck coefficient are shown by solid lines in Fig. 4. The Seebeck coefficients were calculated by formula (8) at the ratio $a/b = 10$ and magnetic fields $H = 0$ and 5 kOe. The experimental data for $La_{0.7}Mn_{1.3}O_{3-\delta}$ films are depicted by points in this figure. The coincidence of the theoretical and experimental data indicates that the effective medium model correctly reflects the physics of the phenomenon under investigation.

4. DISCUSSION

In our earlier works [8, 9], we attempted to describe the properties of La-deficient systems in the framework of a two-liquid model. According to this model, above and below the magnetic transition temperature, the system involves two types of charge carriers that differ in their character of interaction with a magnetic sub-

system (two conduction channels). Band charge carriers elastically interact with the magnetic subsystem, and charge carriers of the other group are characterized by the activation motion attended by the emission and absorption of magnons. The temperature dependences of the resistivity for carriers of these two groups are quite different: in the former case, the resistivity increases with an increase in the temperature, whereas the resistivity for inelastic processes decreases with an increase in the temperature. It turns out that, in the case when the properties of the system meet certain conditions, the crossover from one conductivity mechanism to another mechanism occurs rather abruptly and is sufficiently sensitive to the magnetic field for providing the giant magnetoresistance effect. (A description of the properties of lanthanum manganites in terms of the two-liquid model is also available in [16, 20, 21].)

The two-liquid model satisfactorily reproduced the magnetoresistive properties of $La_{0.7}Mn_{1.3}O_{3-\delta}$ thin films but was inapplicable to the description of the thermoelectric characteristics, which was also noted by other researchers (see, for example, [20]). The results obtained allowed us to argue for the magnetic and electric internal inhomogeneity of the system [9]. With due regard for recent experimental data [3–6], it is quite reasonable to use the aforementioned effective medium model for the phenomenological description of the magnetotransport properties of La-deficient manganites in the temperature range below the T_C temperature.

In this work, we studied the transport properties of a two-phase composite whose phases are crystallographically homogeneous but differ in the charge carrier concentration and the magnetic order. The volume ratio of the phases depends on the temperature and the magnetic field strength. It was assumed that it is this electrical and magnetic structure which is characteristic of lanthanum manganites over a wide range of temperatures below the magnetic phase transition point T_C.

The results obtained were discussed within the model in which the concentration of the metallic ferromagnetic phase in the semiconducting paramagnetic matrix is the secondary order parameter and the magnetization is the primary order parameter. The basic assumption of the theory lies in the fact that magnetoelastic polarons are charge carriers in both metallic and semiconducting phases, so that the metal–dielectric transition occurs as a percolation transition attended by the crossover of the polaron conductivity.

It was demonstrated that the phenomenological description of electrical and magnetic internal inhomogeneities of $La_{0.7}Mn_{1.3}O_{3-\delta}$ films leads to a qualitatively correct representation of the field and temperature dependences of their transport properties over a wide range of temperatures below T_C. As in [10], we revealed that metallic domains are formed in the form of very oblong ellipsoids rather than "drops" compact in shape. This form of domains ensures a sufficiently sharp metal–dielectric transition, which is characteristic of high-quality samples.

REFERENCES

1. E. O. Wollan and W. C. Koehler, Phys. Rev. **100** (2), 545 (1955).
2. É. L. Nagaev, Usp. Fiz. Nauk **166** (8), 833 (1996) [Phys. Usp. **39**, 781 (1996)].
3. M. Uehara, S. Mori, C. H. Chen, and S.-W. Cheong, Nature **399**, 560 (1999).
4. M. Fath, S. Freisem, A. A. Menovsky, *et al.*, Science **285** (5433), 1540 (1999).
5. M. Hennion, F. Moussa, G. Biotteau, *et al.*, Phys. Rev. Lett. **81** (9), 1957 (1998).
6. G. A. Petrakovskiĭ, N. V. Volkov, V. N. Vasil'ev, and K. A. Sablina, Pis'ma Zh. Éksp. Teor. Fiz. **71** (4), 210 (2000) [JETP Lett. **71**, 144 (2000)].
7. A. N. Lágarkov and A. K. Sarychev, Phys. Rev. B **53** (10), 6318 (1996).
8. V. N. Krivoruchko and S. I. Khartsev, Fiz. Nizk. Temp. **24** (11), 1070 (1998) [Low Temp. Phys. **24**, 803 (1998)].
9. V. N. Krivoruchko, S. I. Kharzev, A. D. Prokhorov, *et al.*, J. Magn. Magn. Mater. **207** (1–3), 168 (1999).
10. M. Jiame, P. Lin, S. H. Chun, *et al.*, Phys. Rev. B **60** (2), 1028 (1999).
11. F. Zhong and Z. D. Wang, Phys. Rev. B **61** (5), 3192 (2000).
12. Yu. A. Izyumov and V. N. Syromyatnikov, *Phase Transitions and Symmetry of Crystals* (Nauka, Moscow, 1984).
13. V. Dyakonov, A. Prohorov, V. Shapovalov, *et al.*, Phys. Lett. A **268** (3), 202 (2000).
14. L. J. Zou, H. Q. Lin, and Q. Q. Zeng, J. Appl. Phys. **83** (11), 7363 (1998).
15. V. M. Loktev and Yu. G. Pogorelov, Fiz. Nizk. Temp. **26** (3), 231 (2000) [Low Temp. Phys. **26**, 171 (2000)].
16. S. Zhang, J. Appl. Phys. **79** (8), 4542 (1996).
17. M. Rubinstein, Phys. Rev. B **50** (6), 3830 (1994).
18. V. N. Krivoruchko, Fiz. Nizk. Temp. **22** (9), 1047 (1996) [Low Temp. Phys. **22**, 798 (1996)].
19. D. Bergman and D. Stroud, in *Solid State Physics*, Ed. by H. Ehrenreich and D. Turnbull (Academic, New York, 1992), Vol. 46, p. 147.
20. M. Rubinstein, D. J. Gillespie, J. E. Snyder, and T. Tritt, Phys. Rev. B **56** (9), 5412 (1997).
21. M. Rubinstein, J. Appl. Phys. **87** (9), 5019 (2000).

Translated by O. Borovik-Romanova

Physics of the Solid State, Vol. 43, No. 4, 2001, pp. 710–714. Translated from Fizika Tverdogo Tela, Vol. 43, No. 4, 2001, pp. 683–686.

MAGNETISM AND FERROELECTRICITY

Magnetic Properties and Structure of the Nanocrystalline Gd–Ti–Ge Intermetallic Compound

G. F. Korznikova*, Kh. Ya. Mulyukov*, S. A. Nikitin, and Yu. A. Ovchenkova****

**Institute of Problems of Metal Superplasticity, Russian Academy of Sciences, ul. Khalturina 39, Ufa, 450001 Bashkortostan, Russia*

e-mail: korznikova@anrb.ru

***Department of Physics, Moscow State University, Vorob'evy gory, Moscow, 119899 Russia*

Received September 18, 2000

Abstract—This paper reports an experimental study of the magnetization processes and structure of the Gd–Ti–Ge compound in the initial coarse-grained state and a nanostructured state obtained under torsion at a high quasihydrostatic pressure. It is established that in a nanocrystalline sample, the magnetic ordering temperature is 30 K lower, the coercive force is eight times higher, and the magnetization is 3.7 times lower than their respective values in a coarse-grained sample. The observed changes in the magnetic properties are shown to be related primarily with the conversion of a part of the initial phase with the CeScSi-type lattice to a CeFeSi-type weakly magnetic phase. The effect of structural defects and of partial disorder on the magnetic characteristics of the compound are also discussed. © *2001 MAIK "Nauka/Interperiodica".*

The ternary silicides and germanides of rare-earth and transition metals make up a new class of magnetically ordered substances. Investigation of magnetism in these compositions revealed a number of new compounds of the types *R*Sc*X* [1] [here, *R* stands for a rare-earth (RE) metal, and *X*, for Si or Ge] and *R*TiGe [2] possessing high magnetic-ordering temperatures. For instance, the magnetic ordering temperature of the *R*TiGe compounds considerably exceeds those of pure RE metals, although only the RE ions have a magnetic moment in this series.

GdTiGe was found to undergo a polymorphic transformation [3]; more specifically, this composition can crystallize, depending on the actual preparation conditions, in a number of lattice types: CeFeSi (space group *P*4/*nmm*) and CeScSi (space group *I*4/*mmm*). Note that a change in the structural type affects the magnetic properties of a given composition considerably.

The available data relate to single-crystal samples. At the same time, it is known that the magnetic characteristics of RE ferromagnets are determined to a considerable extent by their structural state. This becomes particularly noticeable in samples with a nanocrystalline structure. In particular, in a nanocrystalline state, the coercive force of pure Dy and Tb increases by thousands of times [4, 5]; the magnetization of Dy [4, 6], Tb [5], and Gd [7] decreases by a few times; the magnetic transformation points change [5, 6]; and the magnetic ordering changes its character [4, 6].

In this connection, we carried out an experimental study of the magnetization processes and structure of a GdTiGe alloy in the nanocrystalline and coarse-grained states, the results of which are presented here. The choice of the method of severe plastic deformation to produce a nanocrystalline structure was motivated by the fact that this method precludes contamination and permits obtaining bulk nonporous samples which do not need subsequent compacting before performing structural and magnetic measurements.

1. MATERIAL AND EXPERIMENTAL TECHNIQUE

For this study, we used the ternary compound GdTiGe (35 at. % Gd–33 at. % Ti–32 at. % Ge) with the initial structure of the CeScSi type (see table) prepared by rf melting.

The nanocrystalline structure was attained by intense plastic deformation, more specifically, by room-temperature torsion on Bridgman anvils through an angle of 10π at a pressure of 8 GPa.

The magnetization curves were measured on a vibrating sample magnetometer in a field of 1.6×10^3 kA/m. The temperature dependence of the magnetization was studied with a magnetic balance [6] in a vacuum of 1.3×10^{-2} Pa and a field of 250 kA/m within the temperature range from 290 to 1070 K.

The microstructure of the samples was investigated with a JEM 2000EX transmission electron microscope. The sample chemical composition was measured on a JSM-840 scanning electron microscope equipped with a Link attachment. The phase composition was determined by the standard technique on a DRON 3M x-ray diffractometer.

1063-7834/01/4304-0710$21.00

Structural and magnetic data for GdTiGe samples with different lattice types

Structure	Space group	*a*, nm	*c*, nm	Type of ordering	$T_{C,N}$, K	θ_p, K	μ_{eff}, μ_B
CeFeSi	*P*4/*mmm*	0.4065(1)	0.7716(2)	Weak FM	412	317	8.3
CeScSi	*I*4/*mmm*	0.4065(1)	1.5454(1)	FM	377	413	8.6

2. RESULTS OF THE STUDY

2.1. Magnetic Properties

The measurements of the coercive force showed that H_c does not exceed 0.64 kA/m in the initial nondeformed, coarse-grained (CG) sample with the CeScSi structure and it increases to 5.2 kA/m in the nanocrystalline (NC) sample.

Figure 1 displays the magnetization curves $\sigma(H)$. One readily sees that the magnetization curves for the CG (curve *1*) and NC (curve *2*) structures follow practically the same pattern; namely, in fields of up to 160 kA/m, the magnetization grows rapidly to subsequently reach a linear portion. However, the magnetization of the NC sample remains substantially lower than that of the CG sample throughout the range of the fields applied. For instance, at $H = 10^3$ kA/m, the magnetization of the CG sample is 3.7 times that of the NC sample. The magnetization curve of a sample having the CeFeSi structure, which is a weak ferromagnet (curve *3*), is also shown for comparison.

Figure 2 presents the temperature dependences of the magnetization, $\sigma(T)$, for the structural states studied. The room-temperature magnetization of the initial CG sample (*1*) with the CeScSi structure is substantially higher than that of the NC sample (*2*). These curves also differ slightly in character; indeed, in the CG sample, the $\sigma(T)$ dependence follows a pattern typical of ferromagnets, while in the NC sample, the magnetization decreases more slowly. The ferromagnetic Curie point determined by extrapolation of the steepest part of the $\sigma(T)$ curve to the temperature axis was found to be 375 K for the NC state, which is lower by 30 K than that for the CG state.

The direct and reverse runs of the temperature dependence of the magnetization measured on the CG sample coincide completely. Heating the NC sample to 1070 K and maintaining it at this temperature for 30 min increases the magnetization slightly, as is evident from the reverse course of the $\sigma(T)$ curve; however, this does not affect the ferromagnetic Curie point. Note that the magnetization of the NC sample remains higher than that of the sample with the CeFeSi structure throughout the temperature range studied (curve *3*).

2.2. Structural Studies

Figure 3 displays an electron microscope image of the microstructure of the NC sample. The crystallite size estimated from bright-field electron micrographs is 10–20 nm. Inside the crystallites, one observes a high dislocation density. The crystallite boundaries are broad and diffuse.

The x-ray diffractograms of the samples are shown in Fig. 4. A comparison of the diffraction patterns of the initial CG sample with the CeScSi structure (*1*) with the NC sample (*2*) reveals that the deformation resulted in the disappearance of most of the lines present in the initial phase. The figure also shows a diffractogram of the sample with the CeFeSi structure (*3*). The intense reflections in the diffractogram of the NC sample are seen to be due to the CeFeSi phase. However, these lines are broadened to the extent where one cannot make a quantitative analysis of the phase composition of the NC sample. The line broadening is apparently associated with the small size of the crystallites and the high level of internal stresses. Taking into account the complex character of the Gd–Ti–Ge lattice, the quantitative separation of the contributions due to these factors to the broadening cannot be done because the line intensity is too weak.

3. DISCUSSION

The above results show that the NC and CG structural states of the Gd–Ti–Ge compound differ considerably in magnetic properties. In the NC sample, the coercive force increases eight times, while the magne-

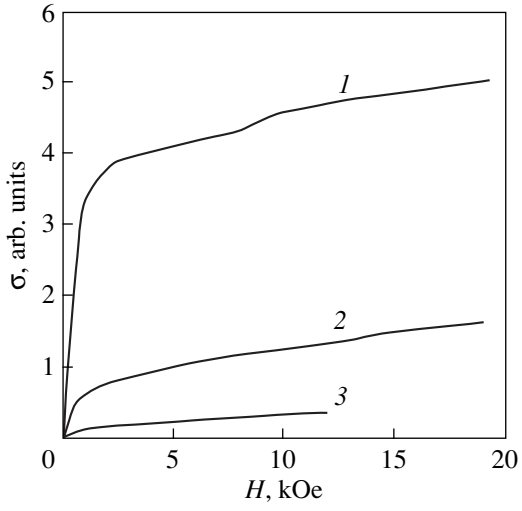

Fig. 1. Magnetization curves of (*1*) Gd–Ti–Ge samples in the initial state (CeScSi-type structure) and (*2*) in the nanocrystalline state and (*3*) a sample with a CeFeSi-type structure.

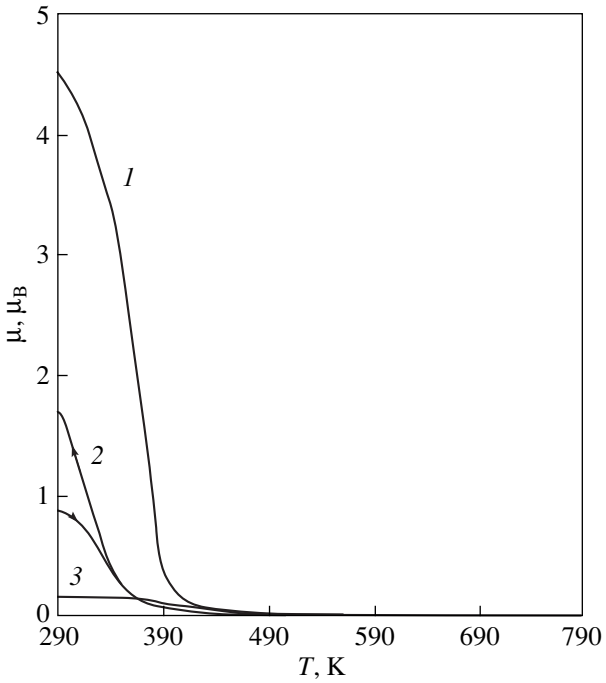

Fig. 2. Temperature dependence of the magnetization of (*1*) Gd–Ti–Ge samples in the initial state (CeScSi-type structure) and (*2*) in the nanocrystalline state under heating and cooling and (*3*) a sample with a CeFeSi-type structure.

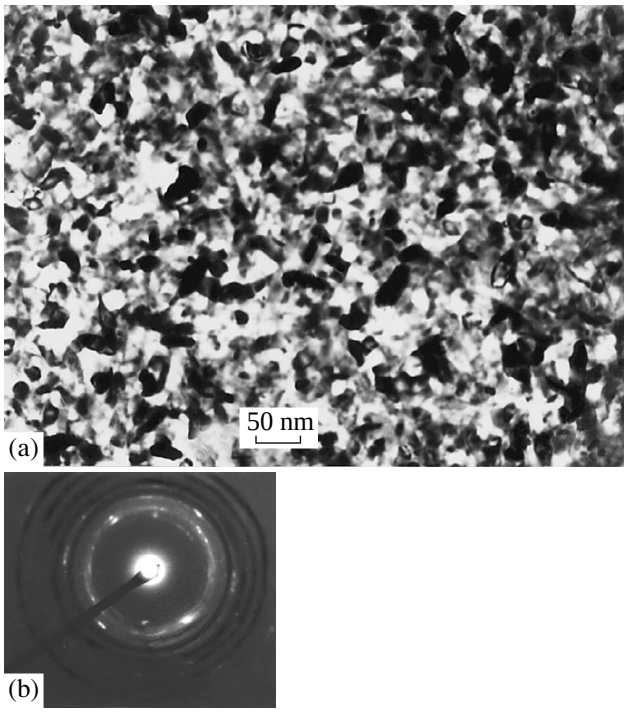

Fig. 3. Fine structure and electron microscope image of a nanocrystalline Gd–Ti–Ge sample.

tization decreases by a few times. The ferromagnetic Curie temperature deduced from the temperature dependence of the magnetization is lower by 30 K than that of the CG sample. Because all magnetic measurements on the NC and CG samples were conducted in identical conditions, the observed differences may be attributed obviously both to the different phase compositions of the samples and to specific features of the NC structure which formed in the course of intense plastic deformation.

As was already pointed out, annealing at 1070 K does not result in a substantial change in the character of the temperature dependence of the magnetization, although annealing at such a high temperature is known to reduce the density of structural defects by several orders of magnitude. This point argues for the suggestion that the difference between the magnetic properties of the NC and CG samples is primarily due to a part of the initial phase with the CeScSi structure transforming to a weakly magnetic phase with a CeFeSi-type lattice. The substantial decrease in the magnetization of a sample as it converts to the NC state is also obviously associated with the phase transformation, with the magnetization of the NC sample following practically a linear course (curve *2* in Fig. 1). Because the magnetization of the NC sample exceeds that of the sample consisting only of the CeFeSi-type phase, this suggests that severe plastic deformation produces a mixture of the two phases.

The phase transformation stimulated by deformation was also observed to occur in pure Gd with a nanocrystalline structure, which was likewise produced on Bridgman anvils [6].

The noticeable decrease in the Curie point in the NC sample cannot be associated with the presence of a weakly magnetic phase, because its magnetic ordering temperature is higher than that of the initial strongly magnetic phase. At the same time, it is known that a decrease in the crystallite size and the presence of defects break up the long-range order, which in turn entails a decrease in both the magnetization and the magnetic ordering temperature via exchange interaction.

As was already mentioned, pure RE ferromagnets subjected to severe plastic deformation exhibit similar changes in magnetic properties. These changes, as illustrated by Tb [8], are connected primarily with a certain change in the lattice parameters, large lattice microdistortions, and a small crystallite size, which destroy the periodicity and weaken the exchange interaction, particularly, close to the crystallite boundaries [6, 7, 9, 10]. Unlike pure RE metals, the Gd–Ti–Ge compound has a very complex ordered lattice consisting of layers alternately containing and free of RE elements. Interlayer coupling is responsible for the high magnetic transition temperature [1–3]. At the same time, as is shown by recent studies of the ordered intermetallic compounds Ni_3Al [11] and TiAl [12], severe

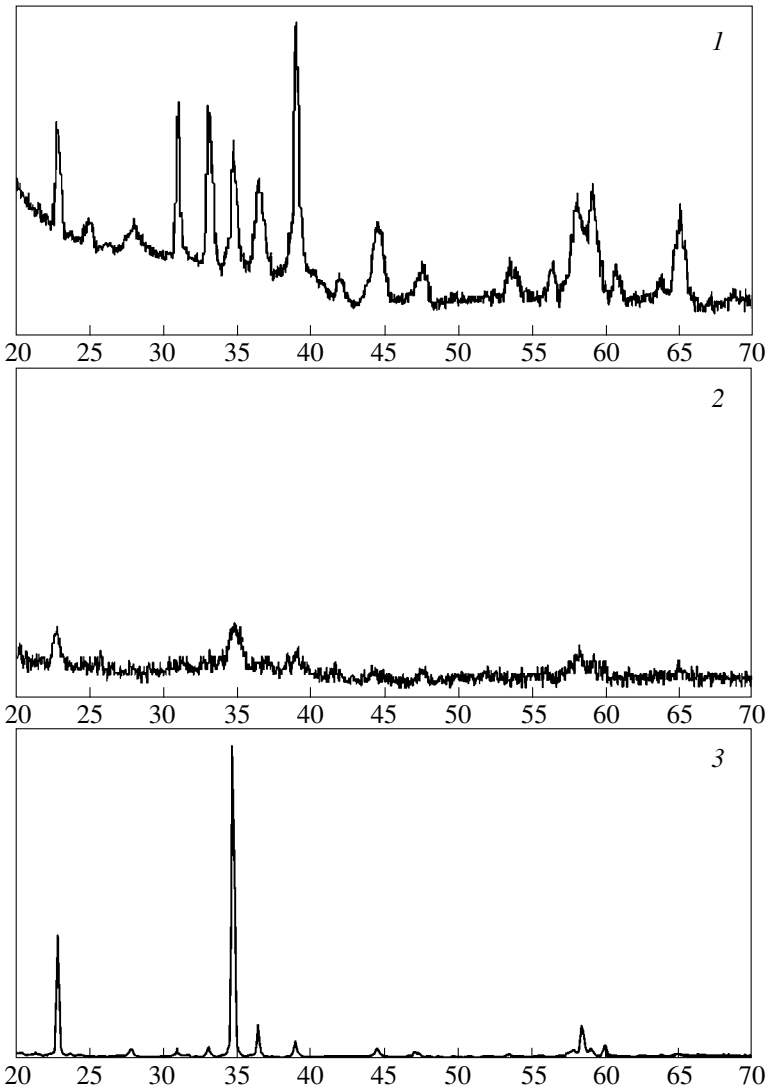

Fig. 4. X-ray diffraction patterns of (*1*) Gd–Ti–Ge samples in the initial state (CeScSi-type structure) and (*2*) in the nanocrystalline state and (*3*) a sample with a CeFeSi-type structure.

plastic deformation by torsion may bring about both a partial and complete structural disorder and the formation of a solid solution. Note that the structure undergoes a substantial disordering even with the anvils turned through an angle $\sim\pi/2$. One may therefore suggest that deformation of the Gd–Ti–Ge samples on the Bridgman anvils also resulted in a partial structural disorder. Because the lattice distortions are maximum near the boundaries of crystallites and at defect pileups, the disordering associated with deformation starts to develop apparently near the crystallite boundaries and dislocation pileups. It is in these regions that the phase with a CeFeSi-type lattice, which exhibits the properties of a weak ferromagnet, is formed.

On the other hand, such a composite NC sample structure, consisting of an ordered, weakly distorted lattice in the bulk of the crystallites and a disordered lattice with large microdistortions near the boundaries, interferes with the domain wall displacement and gives rise to an increase in H_c. Moreover, the structural disorder reduces, on the whole, the magnetization and lowers the magnetic transformation temperature slightly.

ACKNOWLEDGMENTS

This work was supported by the Russian Foundation for Basic Research, project nos. 00-02-17723 and 00-02-17862.

REFERENCES

1. S. A. Nikitin, I. A. Tskhadadze, and A. V. Morozkin, in *Proceedings of Moscow International Symposium on Magnetism, Moscow, 1999*, Part 2, p. 368.

2. S. A. Nikitin, I. A. Tskhadadze, I. V. Telegina, *et al.*, J. Magn. Magn. Mater. **183**, 375 (1998).
3. I. A. Tskhadadze, V. V. Chernyshev, A. N. Streletskii, *et al.*, Mater. Res. Bull. **34** (10–11), 1773 (1999).
4. Kh. Ya. Mulyukov, G. F. Korznikova, and S. A. Nikitin, J. Appl. Phys. **79** (11), 8584 (1996).
5. Kh. Ya. Mulyukov, G. F. Korznikova, R. Z. Sharipov, and S. A. Nikitin, Nanostruct. Mater. **8** (7), 953 (1997).
6. Kh. Ya. Mulyukov, G. F. Korznikova, and S. A. Nikitin, Fiz. Tverd. Tela (St. Petersburg) **37** (8), 2481 (1995) [Phys. Solid State **37**, 1359 (1995)].
7. Kh. Ya. Mulyukov, G. F. Korznikova, and S. A. Nikitin, J. Magn. Magn. Mater. **153**, 241 (1996).
8. G. F. Korznikova, Kh. Ya. Mulyukov, I. Z. Sharipov, and L. A. Syutina, J. Magn. Magn. Mater. **196–197**, 207 (1999).
9. Kh. Ya. Mulyukov, I. Z. Sharipov, and S. S. Absalyamov, Prib. Tekh. Éksp., No. 3, 149 (1998).
10. S. A. Nikitin, *Magnetic Properties of Rare-Earth Metals* (Mosk. Gos. Univ., Moscow, 1989).
11. O. Dimitrov, A. V. Korznikov, G. F. Korznikova, and G. Tram, J. Phys. IV **10**, Pr6-33 (2000).
12. A. V. Korznikov, O. Dimitrov, G. F. Korznikova, *et al.*, Nanostruct. Mater. **11** (1), 17 (1999).

Translated by G. Skrebtsov

Physics of the Solid State, Vol. 43, No. 4, 2001, pp. 715–717. Translated from Fizika Tverdogo Tela, Vol. 43, No. 4, 2001, pp. 687–689.

MAGNETISM AND FERROELECTRICITY

Giant Magnetocaloric Effect near the Curie Temperature in the $Sm_{0.6}Sr_{0.4}MnO_3$ Manganite

A. I. Abramovich, A. V. Michurin, O. Yu. Gorbenko, and A. R. Kaul'

Moscow State University, Vorob'evy gory, Moscow, 119899 Russia

e-mail: abramovich@ofef343.phys.msu.su

Received September 19, 2000

Abstract—A method is proposed for the calculation of the magnetocaloric effect from simultaneous measurements of thermal expansion and magnetostriction made in different regimes (adiabatic and isothermal). The magnitude of the magnetocaloric effect for $Sm_{0.6}Sr_{0.4}MnO_3$ is estimated. It is found that near the Curie temperature T_C it passes through a maximum to reach a giant value $\Delta T = 4.6$ K for $\Delta B = 0.84$ T. In addition, in the neighborhood of T_C, we observed colossal magnetoresistance $\Delta\rho/\rho = [\rho(H) - \rho(0)]/\rho(0) = 72\%$ in a weak magnetic field of 0.84 T, a giant negative volume magnetostriction $\omega = -5 \times 10^{-4}$ in a field of the same strength, and a large change in the sample volume $\Delta V/V \approx 0.1\%$. © *2001 MAIK "Nauka/Interperiodica".*

Rare-earth manganites with perovskite structure exhibit typically strong coupling of the electron and spin subsystems with the lattice, which gives rise to anomalies in their magnetic, electrical, optical, and elastic properties. Theoretically and from the practical standpoint, the most interesting effects are undoubtedly the colossal magnetoresistance (CMR) and giant magnetostriction, which are observed in some of these compounds near the Curie temperature T_C. While the CMR has been dealt with in a large number of publications (see reviews [1–3] and references therein), the magnetostriction of rare-earth manganites remains much less studied [4–6]. Materials possessing a large magnetostriction can be employed in a variety of devices converting electrical to mechanical energy. As for the magnetocaloric effect (MCE) in manganites, it has practically not been investigated at all [7–9]. It was pointed out in [10] that the MCE in manganites is comparable in magnitude with that in Gd, which makes these materials promising for application in magnetic coolers. For instance, calculation of the MCE from heat capacity measurements in $La_{0.6}Ca_{0.4}MnO_3$ yields $\Delta T = 2$ K for $\Delta B = 3$ T near $T_C = 260$ K [11]. This illustrates the need to search for materials exhibiting a high magnitude of the above effects at room temperature and in weak magnetic fields. This paper reports a study of thermal expansion, magnetostriction, MCE, electrical resistivity, magnetoresistance, and ac initial magnetic and paramagnetic susceptibility of $Sm_{0.6}Sr_{0.4}MnO_3$.

The initial magnetic susceptibility in an ac magnetic field of 0.8 to 8 kHz was measured with an F-5063 ferrometer, and the paramagnetic susceptibility was found by weighing with electromagnetic compensation. The electrical resistivity was determined by the four-probe technique. The longitudinal and transverse magnetostriction and thermal expansion were measured by means of strain gauges with a resistance of $92.30 \pm 0.01\ \Omega$ and a strain sensitivity coefficient of 2.26. One gauge was pasted onto the sample; the other, on the quartz plate. When taking a measurement, the gauges on the sample and the quartz plate were oriented in the same way relative to the magnetic field.

$Sm_{0.6}Sr_{0.4}MnO_3$ was prepared using standard ceramic technology. The phase composition and lattice parameters were checked with a Siemens D5000 diffractometer. The ceramic prepared was established to be a single-phase perovskite with orthorhombic structure (*Pnma* group). The single-phase state of the ceramic was also confirmed by Raman spectroscopy using a Jobin–Yvon T64000 triple-grating spectrometer; indeed, we detected only those phonon modes characteristic of orthorhombic manganites with *Pnma* symmetry.

Figure 1 plots the temperature dependence of the initial magnetic (left-hand scale) and the paramagnetic (right-hand scale) susceptibility of the compound under study. The $\chi(T)$ temperature dependence exhibits a sharp maximum at $T_N = 32$ K and an abrupt decay at $T_C = 110$ K (T_C was determined as the position of the minimum in the $\{d\chi/dT\}(T)$ curve). Within the 230- to 300-K interval, the paramagnetic susceptibility obeys the Curie–Weiss law with a paramagnetic Curie temperature $\Theta = 124$ K. At $T \le 230$ K and a deviation from the Curie–Weiss law is observed, which indicates that the magnetic state in this temperature region is not homogeneous. The electrical resistivity ρ is seen to increase sharply (by several orders of magnitude) near T_C (Fig. 2). Application of an external magnetic field brings about a decrease in ρ in the region of T_C and, hence, a negative MR (Fig. 2). Note the very large magnitude of MR, $\Delta\rho/\rho = [\rho(H) - \rho(0)]/\rho(0) = 72\%$, in a

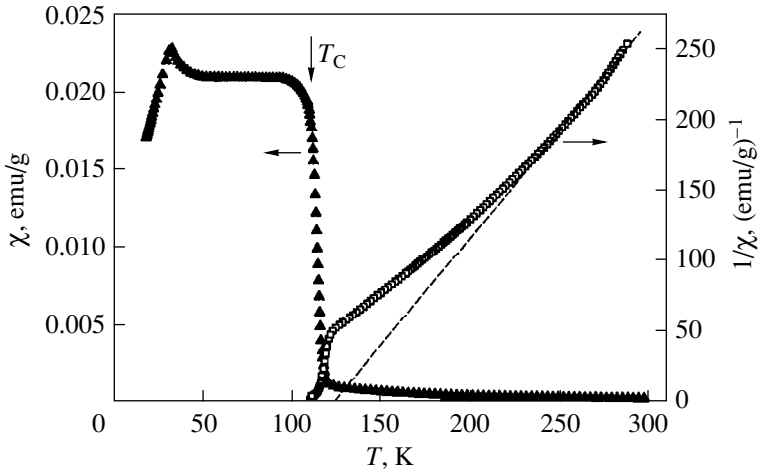

Fig. 1. Temperature dependence of the ac initial magnetic susceptibility in a field of 10^{-4} T and a frequency of 8 kHz (left-hand scale) and of the paramagnetic susceptibility (right-hand scale).

weak magnetic field of 0.84 T. Figure 3 presents the temperature dependence of the thermal expansion $\Delta l/l(T)$ measured under heating and cooling of the sample. As the temperature drops below T_C, one observes a strong decrease in $\Delta l/l$ corresponding to a volume compression $\Delta V/V = 3\Delta l/l = 0.1\%$. As seen from Figs. 2 and 3, the electrical resistivity and thermal expansion undergo a temperature hysteresis below T_C, which indicates a first-order phase transition at T_C. It is known that first-order phase transitions occur at a constant temperature T and, hence, $|(dM/dT)_H|$ should, theoretically, be infinite. In this case, one should observe a large MCE, because

$$\Delta T = -(T/C_{P,H})(dM/dT)_H \Delta H,$$

where $C_{P,H}$ is the heat capacity at a constant pressure in a constant magnetic field and M is the magnetization.

The MCE is usually either measured directly or estimated from the experimental heat capacity or magnetization data. We propose a method for estimating the magnitude of the MCE which is based on simultaneous measurement of thermal expansion and magnetostriction in different regimes, namely, adiabatic and isothermal. The fact is that when studying magnetostriction, one usually measures the adiabatic change in the volume or length, i.e., immediately after the application of a magnetic field, where all the heat generated by the MCE has not yet dissipated and remains inside the sample. In this case, the total change in the length or volume is the sum of the magnetostriction and thermal expansion due to the MCE. Assuming the relative elongation $\lambda = \Delta l/l$ to be a function of H and T, we can write [12]

$$d\lambda = (d\lambda/dH)_T dH + (d\lambda/dT)_H dT.$$

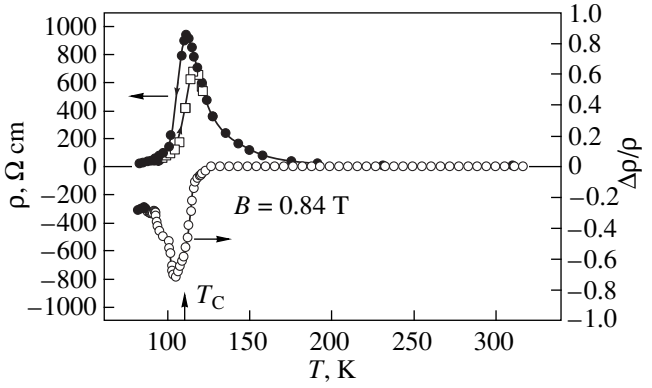

Fig. 2. Temperature dependence of the electrical resistivity (left-hand upper scale) and of magnetoresistance in a field of 0.84 T (right-hand lower scale).

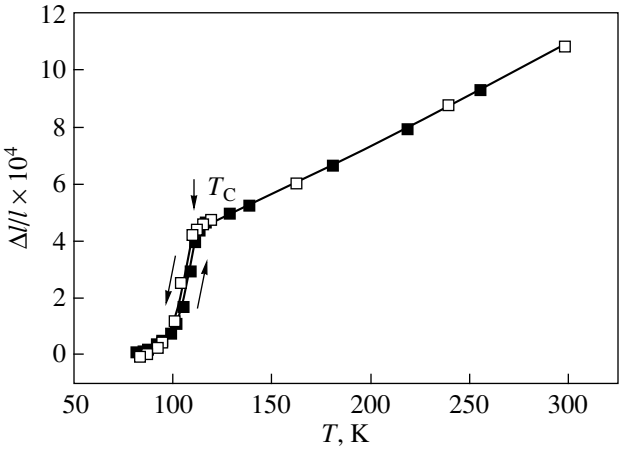

Fig. 3. Temperature dependence of the thermal expansion measured in a heating and a cooling run.

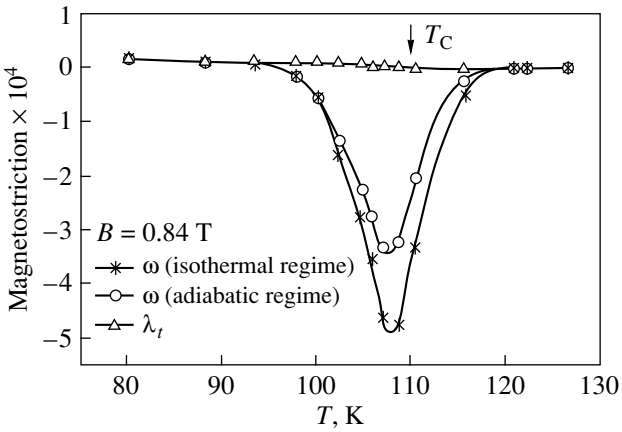

Fig. 4. Temperature dependence of the volume magnetostriction measured in the adiabatic and isothermal regimes, and of the anisotropic magnetostriction in a magnetic field of 0.84 T.

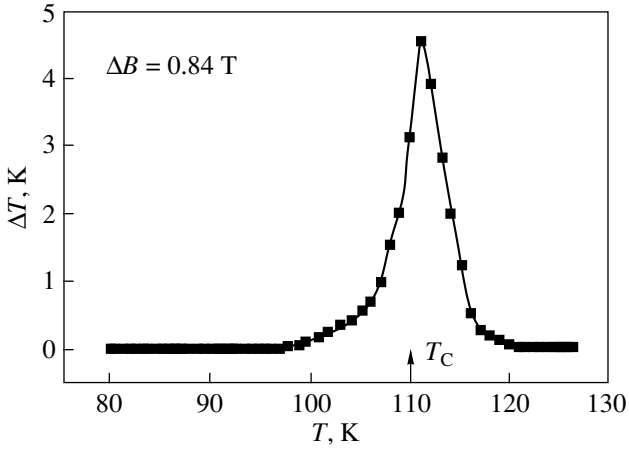

Fig. 5. Temperature dependence of the magnetocaloric effect.

Whence for the magnetostriction measured in the adiabatic regime, one obtains

$$(d\lambda/dH)_{ad} = (d\lambda/dH)_T + \alpha(dT/dH)_{ad},$$

where $\alpha = (d\lambda/dT)_H$ is the coefficient of thermal linear expansion and $(dT/dH)_{ad}$ is the MCE. In accordance with the above expression, we measured the temperature dependence of the magnetostriction in the adiabatic regime $(d\lambda/dH)_{ad}$ and of that in the isothermal regime $(d\lambda/dH)_T$ (Fig. 4) and derived the coefficient of linear thermal expansion from the $\Delta l/l(T)$ relation (Fig. 3). (Note that we measured the longitudinal $\lambda_\parallel$ and transverse $\lambda_\perp$ magnetostriction components, while the volume ω and the anisotropic λ_t magnetostriction were calculated from the expressions $\omega = \lambda_\parallel + 2\lambda_\perp$ and $\lambda_t = \lambda_\parallel - \lambda_\perp$.) The temperature dependence of the MCE $\Delta T(T)$, obtained for $\Delta B = 0.84$ T, is shown in Fig. 5. One readily sees a sharp MCE maximum near T_C with a giant amplitude $\Delta T = 4.6$ K, which yields an extremely high field dependence of the MCE of 5.5 K/T. We also note the giant volume magnetostriction of -5×10^{-4} in a weak magnetic field of 0.84 T. The anisotropic component of the magnetostriction is very small throughout the temperature range studied (Fig. 4).

Thus, we report on the first observation, in the $Sm_{0.6}Sr_{0.4}MnO_3$ manganite near the Curie temperature, of a giant magnetocaloric effect, a giant negative volume magnetostriction, and a large volume change, which are accompanied by a colossal magnetoresistance.

ACKNOWLEDGMENT

The authors are indebted to L. I. Koroleva for fruitful discussions.

The work was supported by the Russian Foundation for Basic Research, project nos. 00-02-17810 and 00-15-96695, and INTAS-97-open-30253.

REFERENCES

1. É. L. Nagaev, Usp. Fiz. Nauk **166** (8), 833 (1996) [Phys. Usp. **39**, 781 (1996)].
2. A. P. Ramirez, J. Phys.: Condens. Mater. **9** (7), 8171 (1997).
3. Y. Tokura and Y. Tomioka, J. Magn. Magn. Mater. **200** (1), 1 (1999).
4. L. I. Koroleva, R. V. Demin, and A. M. Balbashov, Pis'ma Zh. Éksp. Teor. Fiz. **65** (6), 449 (1997) [JETP Lett. **65**, 474 (1997)].
5. M. R. Ibarra, P. A. Algarabel, and C. Marquina, Phys. Rev. Lett. **75** (19), 3541 (1995).
6. R. Mahendiran, M. R. Ibarra, A. Maignan, *et al.*, Phys. Rev. Lett. **82** (10), 2191 (1999).
7. X. X. Zhang, J. Tajada, Y. Xin, *et al.*, Appl. Phys. Lett. **69** (18), 3596 (1996).
8. W. Chen, W. Zhong, D. Hou, *et al.*, Phys. Lett. **15** (1), 134 (1998).
9. X. Bohigas, J. Tejada, E. Del Barco, *et al.*, Appl. Phys. Lett. **73** (2), 390 (1998).
10. V. K. Pecharsky and K. A. Gschneidner, Jr., J. Magn. Magn. Mater. **200** (1), 44 (1999).
11. X. Bohigas, J. Tejada, M. L. Marinez-Sarrion, *et al.*, J. Magn. Magn. Mater. **208** (1), 85 (2000).
12. K. P. Belov, *Elastic, Thermal, and Electrical Phenomena in Ferromagnetic Metals* (GITTL, Moscow, 1951).

Translated by G. Skrebtsov

Physics of the Solid State, Vol. 43, No. 4, 2001, pp. 718–721. Translated from Fizika Tverdogo Tela, Vol. 43, No. 4, 2001, pp. 690–692.

MAGNETISM AND FERROELECTRICITY

Nonlinear Waves in a Chain of Plane-Parallel Domain Walls in Ferromagnets

M. A. Shamsutdinov, S. É. Rakhimov, and A. T. Kharisov

Bashkortostan State University, ul. Frunze 32, Ufa, 450074 Russia

e-mail: KharisovAT@ic.bashedu.ru

Received September 29, 2000

Abstract—Taking into account the nonlinear interaction between plain domain walls (DWs) in a chain of DWs, one- and two-parameter solitons are obtained. These solitons are solitary shear waves propagating along the DW chain. © *2001 MAIK "Nauka/Interperiodica".*

INTRODUCTION

In a stripe domain structure, along with volume spin waves, there are excitations localized in a domain wall (DW) associated with coupled oscillations of DWs [1]. A chain of plane-parallel DWs can exhibit wave properties similar to those of an atomic crystal lattice [2–5]. The long-range magnetostatic interaction forces between the DWs play the role of elastic forces. The waves of deformation of both the flexture and shear types can propagate in the chain of a DW. The dispersion characteristics of the DW shear waves in a plane-parallel domain structure are similar to the wave characteristics in the one-dimensional chain of masses [6]. In this case, the linear waves of both acoustic and optical modes of the DW oscillations can exist [4]. The forced nonlinear oscillations in the chain of plane-parallel DWs have many special features [7]. In such a chain, nonlinear DW-shear waves of the acoustic and optical modes of excitations can also occur.

BASIC EQUATIONS AND DISCUSSION OF RESULTS

In this work, the nonlinear DW shear waves of the acoustic mode are considered in a ferromagnet plate with uniaxial anisotropy (its axis is perpendicular to the plate plane) and with a plane-parallel domain structure (PDS). If the domain width D is considerably larger than the DW width, one can obtain the following expression for the DW interaction energy [7] by using the procedure of calculation of the magnetostatic energy for a plate with PDS [8]:

$$W = \sum_n w_n,$$

$$w_n = \frac{2\pi M_0^2}{D^2} Q_n^2 + \frac{16 M_0^2 D}{\pi^2 h} \times \sum_{p=1}^{\infty} \frac{1}{p^3}\left[1 - \exp\left(-\frac{\pi h}{D} p\right)\right] \sin^2\left[\frac{\pi p}{2}\left(1 + \frac{Q_n}{D}\right)\right], \quad (1)$$

$$Q_n = j_{n+1} - j_n,$$

where h is the plate thickness, M_0 is the component of the magnetization vector along the normal to the plate plane, and j_n is the displacement of the nth DW from its equilibrium position. In deriving Eq. (1), we ignored the DW interaction with distant neighbors, which is justified for the waves corresponding to acoustic modes with small wave vectors. The kinetic energy of the system is defined by the expression

$$T = \frac{1}{2}\sum_n \frac{m_w}{D}\left(\frac{d}{dt} j_n\right)^2,$$

where

$$m_w = \frac{1}{2\pi\gamma^2\Delta_0}$$

is the DW mass per unit area [9], γ is the gyromagnetic ratio, $\Delta_0 = \sqrt{A/K_u}$, A is the nonhomogeneous-exchange constant, and K_u is the uniaxial anisotropy constant. Introducing a new variable $q = \pi j/D$, we write the equation of motion in the form

$$\frac{d^2}{dt^2} q_n = \omega_0^2 [f(q_{n+1} - q_n) - f(q_n - q_{n-1})], \quad (2)$$

where

$$\omega_0^2 = 4\pi M_0^2/(D m_w), \quad (3)$$

1063-7834/01/4304-0718$21.00

$$f(q) = q + \frac{2}{b}\sum_{p=1}^{\infty}\frac{(-1)^p}{p^2}(1-e^{-bp})\sin(qp), \qquad b = \frac{\pi h}{D}. \tag{4}$$

Using the relation

$$\sum_{p=1}^{\infty}\frac{(-1)^p}{p^2}(1-e^{-bp})\sin(qp) = -\int_0^b \arctan\frac{\sin q}{\cos q + e^a}da$$

and representing the integral in the form of a power series in q, we obtain the following expression correct to the fifth order:

$$f(q) = \alpha q + \beta q^3 + \delta q^5, \tag{5}$$

where

$$\alpha = \frac{2}{b}\ln\cosh\frac{b}{2}, \quad \beta = \frac{1}{12b}\tanh^2\frac{b}{2},$$

$$\delta = \frac{1}{120b}\tanh^2\frac{b}{2}\left(1-\frac{3}{4}\tanh^2\frac{b}{2}\right).$$

The dependence of α and β/α on the ratio $\pi h/D$ is presented in the figure. Since $\beta/\delta \sim 10$–40, we limit ourselves to the first two terms in Eq. (5). At $\delta = 0$, Eq. (2) is known as the Fermi–Pasta–Ulam equation [10]. Introducing a continuous space variable $x = nD$ and denoting $u = q_x$, we obtain

$$u_{tt} = s^2\partial_x^2\left[u + \frac{D^2}{12}u_{xx} + \frac{\beta D^2}{\alpha}u^3\right], \tag{6}$$

$$s = \omega_0 D\sqrt{\alpha}. \tag{7}$$

Equation (6) is the modified Boussinesq equation. The corresponding linearized equation ($\beta = 0$) has a wave solution $u = u_0\cos(kx - \omega t)$ with the dispersion law

$$\omega^2 = s^2k^2\left(1-\frac{D^2}{12}k^2\right),$$

where $k \ll 2\pi/D$ and s is the velocity of the linear DW shear waves.

Using the reductive perturbation theory [10] with

$$\vartheta = \varepsilon(x \pm st), \quad \tau = \varepsilon^3 t, \quad u = \sum_{n=1}^{\infty}\varepsilon^n u^{(n)}(\vartheta, \tau), \tag{8}$$

we obtain the modified Korteweg–de Vries (MKdV) equation

$$\pm 2\partial_\tau u^{(1)} + r\partial_\vartheta^3 u^{(1)} + \rho\partial_\vartheta (u^{(1)})^3 = 0,$$

where

$$r = \frac{sD^2}{12}, \quad \rho = \frac{sD^2\beta}{\alpha}.$$

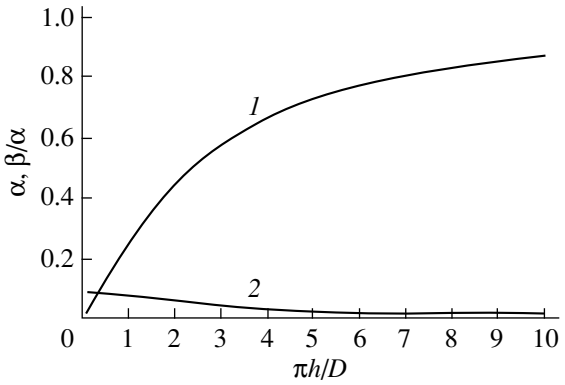

Dependences of α and β/α (curves *1* and *2*, respectively) on the ratio of the specimen thickness h to the domain width D.

By passing from the slow variables ϑ and τ to the usual variables $\zeta = x \pm st$ and t in accordance with (8) and introducing $U \equiv \varepsilon u^{(1)}$, we obtain

$$\pm 2\partial_t U + r\partial_\zeta^3 U + \rho\partial_\zeta U^3 = 0. \tag{9}$$

In Eq. (8), the small parameter ε is the quantity $(V_g - s)/s \ll 1$, where V_g is the velocity of the nonlinear wave of deformation. This means that Eqs. (8) and (9) are applicable if the velocity of nonlinear waves is close to that of a linear wave.

Equation (6) is of the second order in time. It describes the waves which propagate in either of the two directions along the coordinate axis. The sign alternative appears in the scale transformation and, hence, in Eq. (9), because Eq. (9) is of the first order in time and describes a wave that propagates only in one direction. Therefore, the choice of sign determines the direction of the wave propagation (forward or backward) along the coordinate axis.

A one-soliton solution to the MKdV equation has the form [11]

$$U = \pm U_0\cosh^{-1}\left(\frac{\eta}{\Delta_1}\right), \qquad q = \pm q_0\arctan\left[\sinh\left(\frac{\eta}{\Delta_1}\right)\right], \tag{10}$$

$$U_0 = 2\sqrt{\frac{v}{\rho}}, \quad \Delta_1 = \sqrt{\frac{r}{2v}}, \quad q_0 = \sqrt{\frac{2r}{\rho}} = \sqrt{\frac{\alpha}{6\beta}}, \tag{11}$$

where $\eta = x \pm (s + v)t$ and $v > 0$. Note that Eq. (9), with each sign, has solutions of both signs in Eq. (10).

The velocity of nonlinear longitudinal DW shear waves V_g is higher than the velocity of linear waves s; i.e., $V_g = s + v$, $s \gg v$ (because $v > 0$). Let us compare

the velocity of the nonlinear wave with Walker's DW limit velocity V_w [9]

$$V_w = \frac{M_0}{\gamma m_w}.$$

One can obtain the following expression for the velocity ratio:

$$\frac{W_g}{V_w} \approx \frac{s}{V_w} = \sqrt{\frac{2\alpha D}{\Delta_0}}.$$

At usual bubble-domain film thicknesses $h \sim 8Q\Delta_0$ ($Q = K_u/2\pi M_0^2$ is the quality factor), the domain width is $D \sim 8Q\Delta_0$ [9]. Then, we have $V_g/V_w \sim 4\sqrt{\alpha Q}$ and at $Q = 10$–10^3, we have $V_g/V_w \sim 10$–10^2.

One can go from the discrete model to the continuous one if the soliton width exceeds the domain width considerably; i.e., if

$$\frac{\Delta_1}{D} = \frac{1}{2\sqrt{6}}\sqrt{\frac{s}{v}} \gg 1.$$

This condition is fulfilled at least at $\Delta_1/D > 10$, which imposes additional limits on the soliton velocity: $v/s < 4 \times 10^{-4}$. The maximal value of the relative domain deformation in the region of the soliton localization can be found to be

$$\sigma = \frac{DU_0}{P\pi} = \frac{2}{\pi}\sqrt{\frac{\alpha}{\beta}\frac{v}{s}}.$$

At $\alpha/\beta \sim 10^2$ and $v/s \sim 10^{-4}$, we have $\sigma < 0.1$. At $v = 100$ cm/s, $D \approx h = 0.01$ cm, $m_w = 3 \times 10^{-10}$ g/cm^3, and $M_0 = 100$ G, the value of the relative deformation is $\sigma \approx 0.03$.

A two-parametrical solution of Eq. (9) has the form [12]

$$U = 2\sqrt{\frac{2r}{\rho}}\frac{\partial}{\partial\xi}\arctan\left\{\frac{\sin(k_0\xi \pm \Omega t)}{\Delta_2 k_0 \cosh(\xi/\Delta_2)}\right\}, \quad (12)$$

$$k_0 = \frac{1}{\Delta_2}\sqrt{\frac{2v_1\Delta_2^2 + r}{3r}}, \quad \Omega = \frac{2}{3}\left(v_1 + \frac{2r}{\Delta_2^2}\right)k_0, \quad (13)$$

where $\xi = x \pm (s - v_1)t$. We can choose the soliton velocity v_1 (which is measured from the velocity of the of linear wave s) and the characteristic size of the localized excitation Δ_2 to be independent parameters. It is clear from Eq. (13) that the range of the parameters v_1 and Δ_2 where the soliton exists is defined by the inequality

$$v_1\Delta_2^2 > -r/2. \quad (14)$$

In the case where condition (14) is fulfilled, k_0 in Eq. (13) is a real quantity. Let us analyze two limiting cases of Eq. (12) [12]. In the first case, the amplitude is small; i.e., $\Delta_2 k_0 \gg 1$. The solution in Eq. (12) is a weakly localized small-amplitude wave. In the second, extremely nonlinear case, we have $k_0\Delta_2 \ll 1$ and solution (12) represents a breather, that is, a system of two solitons with opposite signs, oscillating with the frequency Ω around the common center of gravity, which moves with the velocity $s - v_1$. The maximum distance that can separate two solitons is equal to

$$\Delta = 2\Delta_2 \ln\frac{2}{k_0\Delta_2}. \quad (15)$$

In contrast to Eq. (11), where v is strictly positive, the quantity v_1 in the breather solution (12) can be negative [see Eq. (14)]. Let the velocity v_1 be close to its critical value [which corresponds to the equality in Eq. (14)], $v_1 = -r(1 - \mu)/(2\Delta_2^2)$, $0 < \mu \ll 1$. Then, we have $k_0\Delta_2 = \sqrt{\mu/3} \ll 1$ and $\Omega \approx 2|v_1|k_0$ and Eq. (15) can be rewritten in the form $\Delta = \Delta_2 \ln(12/\mu)$. At $\mu \approx 0.05$, we have $\Delta \approx 5\Delta_2$.

If the relation between v_1 and Δ_2 is similar to that between v_1 and Δ_1 for the soliton solution in Eq. (11), viz., $\Delta_2 = \sqrt{r/v_1}$, we have

$$k_0 = 1/\Delta_2, \quad \Omega = 2v_1k_0, \quad (16)$$

and the two-parametrical solution in Eq. (12) takes the simplest form

$$U = 2\sqrt{\frac{2r}{\rho}}\frac{\partial}{\partial\xi}a\arctan\left\{\frac{\sin[\sqrt{v_1/r}(\zeta \pm v_1t)]}{\cosh[\sqrt{v_1/r}(\zeta \mp v_1t)]}\right\}.$$

It is seen from Eq. (16) that the wave number k_0 is inversely proportional to the width Δ_2, while the frequency Ω is directly proportional to the velocity v_1 and the wave number k_0.

As was indicated above, all the calculations were carried out ignoring the interaction with far-spaced neighbors. For this reason, as is evident from a comparison of Eq. (2) with the equations of the linear wave theory as applied to the chain of plane-parallel DWs [4, 5], the results obtained at $b \geq 1$ are qualitative in character, while, at $b \ll 1$ (when the domain width D far exceeds the plate thickness h), they are of a quantitative character. A domain structure with the domain width D being considerably larger than the plate thickness h can exist in both ferromagnets (see, e.g., [13]) and rare-earth orthoferrites.

CONCLUSIONS

Thus, under certain conditions, the nonlinear waves of DW deformation, which are similar to solitons in an anharmonic chain of atoms, can exist in the chain of plane-parallel DWs. Physically, such waves are localized waves of compression and dilatation, i.e., of the

longitudinal deformation of the DW chain with possible additional internal degrees of freedom. The velocity of DW shear solitons exceeds Walker's limit velocity by an order of magnitude and more, which can be of certain practical importance. Such nonlinear waves of deformation can be excited with a pulsed or a high-frequency magnetic field inhomogeneous over the plate plane, as is the case with linear deformation waves of the acoustic type [14].

ACKNOWLEDGMENTS

The authors are grateful to B.N. Filippov for his insightful remarks.

REFERENCES

1. M. M. Farztdinov, *Theory of Spin Waves in Ferro- and Antiferromagnets with Domain Structure* (Nauka, Moscow, 1988).
2. V. G. Bar'yakhtar and B. A. Ivanov, Fiz. Met. Metalloved. **36** (4), 690 (1973).
3. Yu. I. Gorobets, Ukr. Fiz. Zh. **19** (6), 1025 (1974).
4. L. É. Gurevich and É. V. Liverts, Zh. Éksp. Teor. Fiz. **82** (1), 220 (1982) [Sov. Phys. JETP **55**, 132 (1982)].
5. E. S. Denisova, Fiz. Tverd. Tela (St. Petersburg) **42** (3), 503 (2000) [Phys. Solid State **42**, 514 (2000)].
6. C. Kittel, *Introduction to Solid State Physics* (Wiley, New York, 1976; Nauka, Moscow, 1978).
7. B. N. Filippov and M. M. Solov'ev, Fiz. Met. Metalloved. **80** (2), 20 (1995).
8. C. Kooy and V. Enz, Philips Res. Rep. **15**, 7 (1960).
9. A. P. Malozemoff and J. C. Slonczewski, *Magnetic Domain Walls in Bubble Materials* (Academic, New York, 1979; Mir, Moscow, 1982).
10. R. K. Dodd, J. C. Eilbeck, J. Gibbon, and H. C. Morris, *Solitons and Nonlinear Wave Equations* (Academic, New York, 1982; Mir, Moscow, 1988).
11. G. L. Lamb, Jr., *Elements of Soliton Theory* (Wiley, New York, 1980; Mir, Moscow, 1983).
12. A. M. Kosevich and A. S. Kovalev, *Introduction in Nonlinear Physical Mechanics* (Naukova Dumka, Kiev, 1989).
13. A. Hubert and R. Schäfer, *Magnetic Domains: The Analysis of Magnetic Microstructures* (Springer-Verlag, Berlin, 1988).
14. *Elements and Devices on Cylindrical Magnetic Domains: Handbook* (Radio i Svyaz', Moscow, 1987).

Translated by N. Ostrovskaya

Physics of the Solid State, Vol. 43, No. 4, 2001, pp. 722–726. Translated from Fizika Tverdogo Tela, Vol. 43, No. 4, 2001, pp. 693–696.

MAGNETISM AND FERROELECTRICITY

Unusual Spontaneous Twisting of an $(NH_4)_2SO_4$ Crystal in a Torsion Pendulum below the Curie Point

S. A. Gridnev*, O. N. Ivanov*, L. P. Mikhaĭlova*, T. N. Davydova**

**Voronezh State Technical University, Moskovskiĭ pr. 14, Voronezh, 394026 Russia*

***Kirenskiĭ Institute of Physics, Siberian Division, Russian Academy of Sciences, Akademgorodok, Krasnoyarsk, 660036 Russia*

e-mail: gridnev@nsl.vstu.ac.ru

Received September 19, 2000

Abstract—It is found that the ferroelectric phase transition in the ammonium sulphate crystal $(NH_4)_2SO_4$ at $T_C = 223$ K is accompanied by spontaneous twisting of samples around the *a*, *b*, and *c* crystallographic axes in the ferroelectric phase. This twisting, observed with a torsion pendulum, cannot be explained solely by the change in symmetry $mmm \longrightarrow mm2$ at the Curie point. It is supposed that the twisting is connected with a complex rearrangement of the structural elements of the crystalline lattice below the Curie temperature. © *2001 MAIK "Nauka/Interperiodica".*

INTRODUCTION

The effect of spontaneous twisting of a sample in a torsion pendulum at temperatures lower than the Curie point (T_C) was first observed in pure proper ferroelastics $KH_3(SeO_3)_2$ and $KD_3(SeO_3)_2$ [1]. Later, this twisting was observed in other ferroelastics, for example, in K_2ZnCl_4 [2], in crystals of the KH_2PO_4 family [3], in $KLiSO_4$ [4], and in some other materials. In all these cases, crystals undergo displacive phase transitions (PTs) which are accompanied by the appearance of new components of the shear deformation in the ferroelectric phase. Such components are absent in the high-symmetry phase. If no new components of the shear deformation appear at T_C, as, for instance, in a $Ba_2NaNb_5O_{15}$ crystal at the ferroelectric phase transition ($T_C = 858$ K) from the tetragonal phase (4*mm* point symmetry group) to another tetragonal phase (4/*mmm*), then the twisting effect is not observed [5].

In this connection, it is of interest to clarify if a ferroelectric ammonium sulfate $(NH_4)_2SO_4$ sample will be twisted as a result of a rhombic–rhombic PT when the temperature is changed. It is known [6] that this crystal has three components of shear deformation in the ferroelectric and paraelectric phases. In addition, none of these components is a new shear component, but all of them undergo an abrupt change at T_C [7, 8]. Moreover, an anomalous behavior of the elastic and nonelastic properties of the crystal subjected to twist deformations was detected in the vicinity of T_C. This behavior is likely to be due to jumplike changes in the shear components of the elastic rigidity at T_C [9].

Ammonium sulfate crystals undergo the ferroelectric PT from the high-temperature rhombic phase with D_{2h}^{16} (*Pnam*) symmetry into the low-temperature rhombic phase with C_{2v}^{9} (*Pna*2) symmetry at the Curie temperature $T_C = 223$ K [10, 11]. This transition is accompanied by the appearance of a spontaneous polarization P_s along the *c* axis. The P_s changes its sign at a temperature of about 85 K [12]. Some characteristic features (such as a small value of the Curie–Weiss constant ($C_{CW} = 33.8$ K), an anomalous behavior of the spontaneous polarization in the vicinity of the 85-K temperature, etc.) allow one to classify $(NH_4)_2SO_4$ as a weak ferroelectric [13]. The mechanism of the ferroelectric PT in this crystal is quite complex and is still not completely understood in detail. The $(NH_4)_2SO_4$ crystal unit cell contains 60 atoms or four formula units. It is fairly difficult to describe the structural rearrangement of this crystal at T_C. According to the idea formulated in [14], one can suppose that two ferroelectric sublattices are formed in $(NH_4)_2SO_4$, as well as in some other weak ferroelectrics, at the temperature of the ferroelectric PT. These sublattices have oppositely directed spontaneous polarizations P_{s1} and P_{s2} (subscripts 1 and 2 indicate the corresponding ferroelectric sublattices) with different temperature dependences. The spontaneous polarizations P_{s1} and P_{s2} are due to displacements of the tetrahedrons $(NH_4)_1$ and $(NH_4)_2$ along the *c* axis. Twisting of these tetrahedrons is caused by a rearrangement inside the $(SO_4)_1$ and $(SO_4)_2$ groups. It is assumed that the distortion of the $(SO_4)_1$ and $(SO_4)_2$ groups and their rotation at some angle take place at the Curie temperature. Their rotation angle depends on the temperature of the sample (below the Curie point).

It is obvious that the rearrangement of different structural elements of a crystal at $T = T_C$ can lead to a

complex deformation of ammonium sulfate samples in the ferroelectric phase. The main purpose of this work was to measure the spontaneous twist of ammonium sulfate crystal samples under a change in temperature in the vicinity of T_C and in the range corresponding to the ferroelectric phase. We also investigated the mechanism of this phenomenon by analyzing the macroscopic deformation of a sample in a torsion pendulum.

1. EXPERIMENTAL

The $(NH_4)_2SO_4$ crystals were grown by the isothermal evaporation method at $T = 303$ K from a saturated water solution with pH = 4. To prepare the ammonium sulfate solution, a twice-recrystallized substance was used. Samples for measurements were cut out in the form of bars with the rectangular cross section having a size of $2 \times 2 \times 18$ mm. The length of these bars was oriented along the *a*, *b*, or *c* crystallographic axes. We will refer to these samples as *x*-, *y*-, and *z*-oriented samples, respectively.

The amount of the twist deformation was measured by means of a setup, based on an inverse torsion pendulum [15], with the relative error not exceeding $\pm 5 \times 10^{-5}$. The twist deformation created in the sample led to the rotation of the disk of the pendulum torsion system at some angle. The rotation angle φ was measured by capacitive sensors in the case of considerable twist deformations and by photoelectric sensors in the case of small deformations. The experimental curves $\varphi(T)$ were automatically recorded by an *XY*-coordinate recorder. The sample temperature was measured with an error of ±0.5 K.

2. RESULTS AND DISCUSSION

The results of measurements of twist deformations *X* obtained in the cooling regime with a cooling rate of about 0.2 K/min for samples with *x*, *y*, and *z* orientations are shown in Fig. 1. It is clear that the twist deformations are absent in the paraelectric phase at $T > T_C = 223$ K. However, the samples of all three orientations are spontaneously twisted in the ferroelectric phase. The X_x, X_y, and X_z deformations are initially changed in a jump at T_C, and then a gradually increasing twist deformation is observed in the $X_x(T)$, $X_y(T)$, and $X_z(T)$ dependences in the course of cooling in the ferroelectric phase. The maximal value of the *X* deformation is observed for samples of the *z* orientation, while the minimal one is observed for samples of the *x* orientation. For samples of the *z* and *y* orientations, the jumps in deformation ΔX at T_C were found to be $\Delta X_z = 3 \times 10^{-3}$ and $\Delta X_y = 1.2 \times 10^{-3}$, respectively. The temperature dependence of the spontaneous twist of the $(NH_4)_2SO_4$ samples, recorded in the heating and cooling regimes, demonstrates a qualitatively similar behavior (Fig. 2). Since the dependences of $\ln(X - \Delta X)$ upon $\ln(T_C - T)$ shown in Fig. 3 are linear over the interval $\Delta T = T_C - T \approx 20$ K, the experimental $X(T)$ curves were approximated over this interval by a power-law function:

$$(X - \Delta X) = A(T_C - T)^n, \quad (1)$$

where *A* is a temperature-independent factor and *n* is the exponent.

The slope of the linear parts of the $\ln(X - \Delta X) = f\{\ln(T_C - T)\}$ plots is the same for samples of the *y* and *z* orientations. From this slope, the exponent *n* in Eq. (1) was found to be ≈0.5.

To understand the reason for the sample twisting in the torsion pendulum, let us first find the relation between the twisting angle and the characteristics of the crystal in the case where a torque *M* is applied to the sample. Since one of the sample ends is fixed in the pendulum and the torque *M* is applied to the other end, a nonuniform deformation will be produced in the sample in torsion oscillations. It is obvious that this defor-

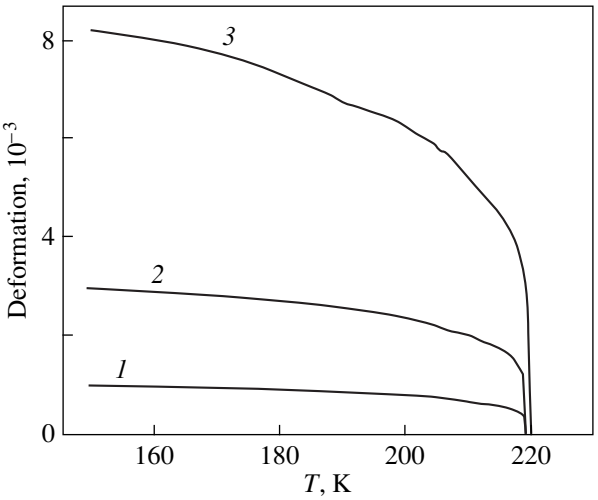

Fig. 1. Temperature dependences of the *X* twist deformations for samples of (*1*) *x*, (*2*) *y*, and (*3*) *z* orientations.

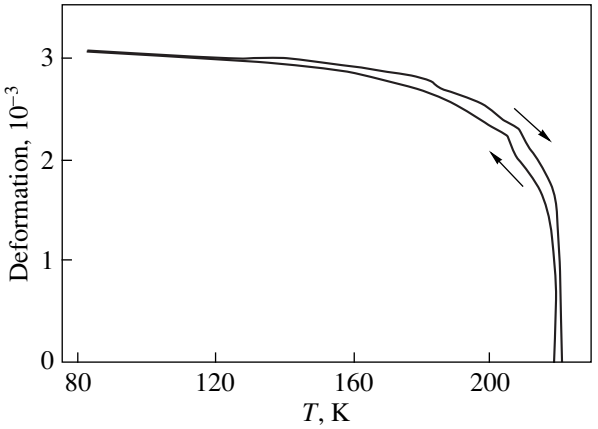

Fig. 2. Temperature dependences of the twist deformation *X* for the *z*-oriented sample in the heating and cooling runs. Arrows indicate the directions of the temperature change.

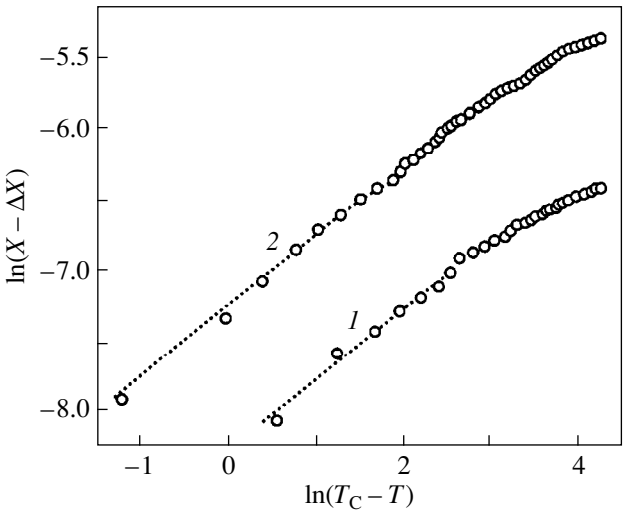

Fig. 3. Dependences of $\ln(X - \Delta X)$ upon $\ln(T_C - T)$ for samples of (*1*) *y* and (*2*) *z* orientations.

mation is varied both along the sample length and over any of its cross sections as one moves away from the torsion axis. In any cross section of the sample, the shear deformation is maximal at the periphery, i.e., in the exterior layers, while the deformation of the central part of the sample along the torsion axis is absent.

Note that, in the torsion pendulum, the elastic torsional rigidities C_x, C_y, and C_z are functions of different components of the shear rigidity for samples of the *x*, *y*, and *z* orientations, namely, $C_x = f(C_{55}; C_{66})$, $C_y = f(C_{44}; C_{66})$, and $C_z = f(C_{44}; C_{55})$.

For an anisotropic sample (for instance, of the *z* orientation) of a rectangular cross section, in the case of a linear relation between the stress σ and the deformation *X*, the twisting angle is

$$\varphi_z = Ml/C_z, \tag{2}$$

where *l* is the sample length and C_z is the torsional rigidity.

Suppose, for simplicity, that we deal with a pure ferroelastic crystal having a novel shear deformation component X_5, which appears spontaneously at T_C. In this case, the shear component σ_5 of the external stress is related to the deformation X_5 as

$$\sigma_5 = C_{55}X_5. \tag{3}$$

Then, one can write down the torque causing the sample to twist around the *z* axis in the form

$$M = 2\int \sigma z dS = 2a\int_0^{a/2} C_{55}X_5 z dz = C_{55}X_5\frac{a^3}{4}, \tag{4}$$

where *a* is the transverse dimension of the sample.

The torsional rigidity C_z for samples of the *z* orientation can be written, according to [16], as

$$C_z = \frac{64a^2}{\pi^4}\sum_k\sum_n \frac{1}{kn}\frac{\int_0^a \sin\frac{kx\pi}{a}dx\int_0^a \sin\frac{ny\pi}{a}dy}{\frac{k^2}{C_{44}} + \frac{n^2}{C_{55}}} = \frac{256a^2}{\pi^6 l}\sum_k\sum_n \frac{1}{kn}\frac{1}{\frac{k^2}{C_{44}} + \frac{n^2}{C_{55}}}, \tag{5}$$

where the coefficients *n* and *k* take the values $n = 1, 3, 5, \ldots$; and $k = 1, 3, 5, \ldots$ in the temperature interval near T_C. If, for example, the C_{55} component becomes "soft" ($C_{55} \ll C_{44}$) when the temperature approaches T_C, then Eq. (5) will have the form

$$C_z = \frac{256a^2}{\pi^6}C_{55}\sum_1\sum_2, \tag{6}$$

where

$$\sum_1 = \sum_{n=1}^{\infty}\frac{1}{n^2} = \frac{\pi^2}{8}, \quad \sum_2 = \sum_{k=1}^{\infty}\frac{1}{k^4} = \frac{\pi^4}{96}. \tag{7}$$

Thus, we have

$$C_z = C_{55}a^4/3. \tag{8}$$

Substituting Eqs. (4) and (8) into Eq. (2), we get

$$\varphi_z = \frac{3l}{4a}X_5. \tag{9}$$

It is seen that, in the vicinity of the Curie point, the twisting angle φ of the sample in the torsion pendulum is proportional to the shear deformation *X* of the proper ferroelectric crystal. The coefficient of proportionality in Eq. (9) depends only on the sample geometry and does not depend on the elastic properties of the crystal. One can assume that this relation is also valid for the case of spontaneous deformation of the samples in the absence of external forces. Then, according to Eq. (9), the sample will twist if some component of the shear deformation *X* appears as a result of the PT, as is the case with the ferroelectric PT. However, $(NH_4)_2SO_4$ is not a proper ferroelastic, and a spontaneous twisting of $(NH_4)_2SO_4$ crystals in a torsion pendulum at $T \leq T_C$ is quite an unexpected phenomenon. It cannot be solely due to the change in symmetry *mmm* ⟶ *mm*2 at the PT.

However, we should take into account that, in spite of the fact that no softening of the elastic rigidity components of the crystal takes place at the Curie point, an abrupt change in both the longitudinal and the shear components of the elastic compliance matrix was detected [8]. The latter can serve as the reason for the

sample twisting in the torsion pendulum with changing temperature.

The complex stressed state of a sample realized under the experimental conditions is characterized by the torsional shear modulus G. This modulus is determined by both the corresponding shear components of the elastic compliance tensor and the longitudinal compliance component along the twisting axis [17], which are mutually related. This can be verified by comparing the temperature dependences of the twist deformation of a z-oriented sample in the vicinity of T_C in two cases, namely, in the presence and in the absence of an external tensile stress σ_t applied to the sample along the c axis (Fig. 4). It is clearly visible that, in the presence of the tensile stress $\sigma_t = 3 \times 10^5$ Pa, the deformation X_z is changed more sharply in the vicinity of T_C; that is, the twist and stretching deformations of the $(NH_4)_2SO_4$ monocrystal are tightly connected with each other.

Since the rotation of the SO_4 tetrahedrons takes place in the $(NH_4)_2SO_4$ structure when it is cooled from the paraelectric phase through T_C and their rotation angle has a pronounced temperature dependence in the ferroelectric phase, one can assume that the SO_4 tetrahedron rotation is connected with the twist deformation and the spontaneous twisting of the sample. At the same time, the displacement of the SO_4 groups in the course of the PT contributes to the tensile and compressive deformation (longitudinal deformations). In other words, the twist deformations of $(NH_4)_2SO_4$ are connected with the microscopic mechanism of the ferroelectric PT, while the spontaneous twisting of samples is due to the spontaneous polarization of the crystal.

It is obvious that, in the case of torsional oscillations, a nonuniform deformation appears in the sample along its radius. This deformation is characterized by the gradient terms $\partial X_{12}/\partial y$ and $\partial X_{13}/\partial z$ for x-oriented samples, $\partial X_{21}/\partial x$ and $\partial X_{23}/\partial z$ for y-oriented samples, and $\partial X_{31}/\partial x$ and $\partial X_{32}/\partial y$ for z-oriented samples.

It is known that the nth-rank tensor is transformed according to the same irreducible representation as the product of its n coordinates does. In particular, the P_3 polarization, which is the first-rank tensor, is transformed as its z coordinate. The X_{31} deformation (the second-rank tensor) is transformed according to the same irreducible representation as the product of its coordinates zx. Therefore, in the case of samples of the z orientation, the nonuniform deformations $\partial X_5/\partial x$ and $\partial X_4/\partial y$ are transformed as the polarization P_3. For this reason, if in samples of the z orientation the spontaneous polarization P_3 appears in a jump at T_C, then the nonuniform deformations $\partial X_5/\partial x$ and $\partial X_4/\partial y$, which initiate the rotation, also appear in a jump simultaneously with this polarization. Due to the inverse piezoeffect, the jump of the polarization P_3 at T_C should lead to an abrupt change in the X_1, X_2, and X_3 deformations, which are related to P_3 by the piezoelectric moduli d_{31}, d_{32}, and d_{33} [6]. Note that the abrupt change in the longitudinal and shear components of the elastic compliance was experimentally observed in $(NH_4)_2SO_4$ at the first-order ferroelectric PT [8].

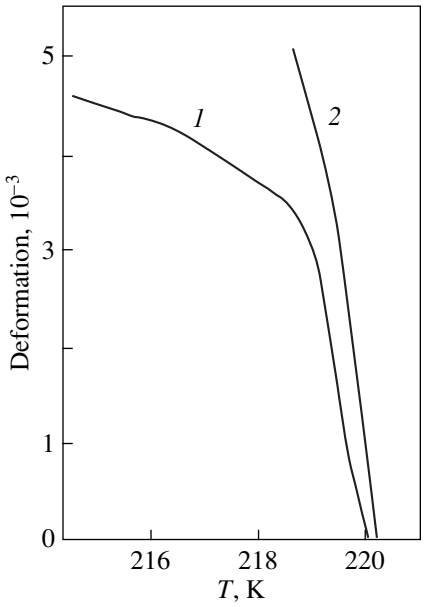

Fig. 4. Temperature dependences of the twist deformation X for a sample of z orientation in the vicinity of T_C: (*1*) for zero external stress and (*2*) for external tensile stress $\sigma = 3 \times 10^5$ Pa applied along the twisting axis.

ACKNOWLEDGMENTS

This work was supported by the Russian Foundation for Basic Research, project no. 98-02-16055.

REFERENCES

1. S. A. Gridnev, V. I. Kudrjash, B. N. Prasolov, and L. A. Shuvalov, Ferroelectrics **26**, 669 (1980).
2. L. A. Shuvalov, S. A. Gridnev, B. N. Prasolov, and V. G. Sannikov, Ferroelectr. Lett. Sect. **1**, 85 (1983).
3. S. A. Gridnev and S. A. Kravchenko, Ferroelectrics **186**, 313 (1996).
4. S. A. Gridnev and A. A. Khodorov, Ferroelectrics **199**, 279 (1997).
5. S. A. Gridnev, A. V. Biryukov, and O. N. Ivanov, Fiz. Tverd. Tela (St. Petersburg) **41** (10), 1848 (1999) [Phys. Solid State **41**, 1697 (1999)].
6. J. F. Nye, *Physical Properties of Crystals: Their Representation by Tensors and Matrices* (Clarendon Press, Oxford, 1964; Mir, Moscow, 1967).
7. N. A. Romanyuk, V. M. Gaba, and Z. M. Ursul, Ukr. Fiz. Zh. **33** (9), 1381 (1988).
8. T. Ikeda, K. Fujibayashi, T. Nagai, and J. Kobayashi, Phys. Status Solidi A **16**, 279 (1973).

9. S. A. Gridnev, L. P. Safonova, O. N. Ivanov, and T. N. Davydova, Fiz. Tverd. Tela (St. Petersburg) **40** (12), 2202 (1998) [Phys. Solid State **40**, 1998 (1998)].
10. T. Yamaguchi, T. Tomita, and N. Ikarashi, Ferroelectrics **169**, 173 (1995).
11. M. V. Belousov, V. A. Kamyshev, and A. A. Shultin, Izv. Akad. Nauk SSSR, Ser. Fiz. **39**, 744 (1975).
12. H. G. Unruh, Solid State Commun. **8** (23), 1951 (1970).
13. A. K. Tagantsev, I. G. Siniĭ, and S. D. Prokhorova, Izv. Akad. Nauk SSSR, Ser. Fiz. **1** (12), 2082 (1985).
14. V. Dvorak and Y. Ishibashi, J. Phys. Soc. Jpn. **41** (2), 548 (1976).
15. S. A. Gridnev, V. I. Kudryash, and L. A. Shuvalov, Izv. Akad. Nauk SSSR, Ser. Fiz. **43**, 1718 (1979).
16. S. G. Lekhnitskiĭ, *Torsion of Anisotropic and Heterogeneous Bars* (Nauka, Moscow, 1971).
17. Yu. I. Sirotin and M. P. Shaskol'skaya, *Fundamentals of Crystal Physics* (Nauka, Moscow, 1975; Mir, Moscow, 1982).

Translated by A. Sonin

Physics of the Solid State, Vol. 43, No. 4, 2001, pp. 727–731. Translated from Fizika Tverdogo Tela, Vol. 43, No. 4, 2001, pp. 697–700.

LATTICE DYNAMICS AND PHASE TRANSITIONS

Grüneisen Parameters for Layered Crystals

N. A. Abdullaev

Institute of Physics, Academy of Sciences of Azerbaijan, pr. Dzhavida 33, Baku, 370143 Azerbaijan

Received July 25, 2000

Abstract—The temperature dependences of Grüneisen parameters for layered crystals of the hexagonal crystal system are constructed. It is demonstrated that the Grüneisen parameters calculated in the framework of the model proposed by I.M. Lifshits for a strongly anisotropic crystal agree satisfactorily with those obtained from the experimental data for graphite, the most typical layered crystal. It is found that the effect of bending vibrations on the Grüneisen parameters decreases with a decrease in the anisotropy of the elastic properties. © *2001 MAIK "Nauka/Interperiodica".*

1. INTRODUCTION

Grüneisen parameters γ belong to the most important characteristics of crystal lattice dynamics. They enter into the equation of state, represent a measure of the anharmonicity of the forces acting in a crystal, and reflect the features and character of the distribution of the frequencies of the phonon spectrum and their variations under pressure. Using the Grüneisen parameters, it is possible to relate various thermodynamic quantities. The magnitudes of these parameters determine physical processes such as thermal expansion, heat conduction, sound absorption, etc. This high information content stimulates interest in the investigation of the Grüneisen parameters.

2. THEORY

Two methods of theoretical treatment of thermal expansion of crystals exist, namely, the microscopic and phenomenological (thermodynamic) approaches. According to the thermodynamic method, the tensor of thermal expansion coefficients is related to the free energy F by the thermodynamic relationship

$$\alpha_{ik} = -\frac{1}{V}\frac{\partial^2 F}{\partial p_{ik}\partial T}. \quad (1)$$

Since the calculation of the thermal expansion coefficients is rather complicated in the framework of the anharmonic model, the quasi-harmonic model is widely used [1]. In the quasi-harmonic model, atomic vibrations are considered harmonic. However, it is assumed that the frequencies ω_j for each mode depend on the pressure applied. Because the amplitudes of atomic vibrations in solid-state lattice sites are actually always small, the supposition that the vibrations are of an "almost harmonic" character is substantiated well. The free energy of the crystal in the framework of the quasi-harmonic model can be treated as the sum of free energies of independent oscillators, each of which corresponds to a single normal mode. In this case, the free energy (without regard for the energy of zero-point vibrations) can be written as [2]

$$F = kT\sum_j \mathrm{Ln}(1 - \exp(\hbar\omega_j/kT)). \quad (2)$$

Then, according to Eq. (1), we have

$$a_{ik} = -\frac{1}{V}\frac{\partial}{\partial T}\left(\sum_j \frac{\hbar\partial\omega_j/\partial p}{\exp(\hbar\omega_j/kT)-1}\right). \quad (3)$$

In terms of Eq. (3) for layered crystals with the axial symmetry (specifically in the hexagonal crystal system), the linear thermal expansion coefficients take the form

$$\begin{aligned} a_\parallel &= \frac{C_V}{V}\left[\frac{C_{33}\gamma_\parallel}{(C_{11}+C_{12})C_{33}-2C_{13}^2}\right. \\ &\quad \left. -\frac{C_{13}\gamma_\perp}{(C_{11}+C_{12})C_{33}-2C_{13}^2}\right], \\ a_\perp &= \frac{C_V}{V}\left[\frac{(C_{11}+C_{12})\gamma_\perp}{(C_{11}+C_{12})C_{33}-2C_{13}^2}\right. \\ &\quad \left. -\frac{2C_{13}\gamma_\parallel}{(C_{11}+C_{12})C_{33}-2C_{13}^2}\right]. \end{aligned} \quad (4)$$

Here, $\alpha_\parallel$ and $\alpha_\perp$ are the linear thermal expansion coefficients in the layer planes and normal to layers, respectively; C_{ik} are the elastic constants; and $\gamma_\parallel$ and $\gamma_\perp$ are the weighted mean Grüneisen parameters in the layer planes and normal to layers, respectively,

$$\gamma_\parallel = \sum_j \gamma_{\parallel,j}C_j/\sum_j C_j, \quad \gamma_\perp = \sum_j \gamma_{\perp,j}C_j/\sum_j C_j,$$

where

$$\gamma_{\parallel,j} = -\frac{\partial \mathrm{Ln}\omega_j}{\partial \mathrm{Ln}a} \quad \gamma_{\perp,j} = -\frac{\partial \mathrm{Ln}\omega_j}{\partial \mathrm{Ln}c}.$$

Here, a and c are the lattice parameters in the layer planes and normal to layers, respectively; $\gamma_{\parallel,\perp,j}$ are the Grüneisen parameters for the jth mode; and C_j is the contribution of the jth mode to the heat capacity.

The C_{ik}, γ, and V parameters, as a rule, are weak functions of temperature. Hence, it follows from relationship (4) that the temperature dependence of the thermal expansion coefficients should be determined by the temperature behavior of the heat capacity. In fact, numerous experimental data indicate that $\alpha(T) \sim T^3$ at low temperatures, while $\alpha \sim$ const at high temperatures (above the Debye temperature θ). On the other hand, the features in the temperature behavior of the thermal expansion coefficients can be governed by the specific features of the temperature dependence of the Grüneisen parameters $\gamma(T)$, because C_{ik} and V, as a rule, vary monotonically with the temperature.

It also follows from relationship (4) that, for example, the linear thermal expansion coefficient in the layer planes $\alpha_\parallel$ can be negative for two reasons. First, the second term has a dominant role: a strong expansion normal to the layers causes the lateral compression (the so-called Poisson's compression). Second, the Grüneisen parameter $\gamma_\parallel$ itself is negative.

As a rule, the mode Grüneisen parameters $\gamma_{\parallel,j} = -\partial \mathrm{Ln}\omega_j/\partial \mathrm{Ln}a$ are positive [2]. As the pressure increases, atoms in a solid approach each other, the amplitudes of their vibrations at the same energy decrease, and the frequency increases. However, it was pointed out for the first time in [3] that, under specific conditions, $\gamma_\parallel$ can be negative in the layered crystals. The matter is that the layer subjected to the uniaxial tension should be considered a membrane. The membrane tension leads to an increase in the frequency of transverse vibrations; i.e., $\partial \mathrm{Ln}\omega_j/\partial \mathrm{Ln}a > 0$. The so-called membrane effect results in the negative mode parameters $\gamma_{\parallel,j}$. For layered crystals, the density of states of the acoustic vibrations that are transverse with respect to the layer plane (the so-called bending vibrations) is rather large at low temperatures, which corresponds to a large statistical weight of C_j/C. Since this vibrational mode corresponds to the negative values of the mode Grüneisen parameter $\gamma_{\parallel,j}$, we can expect that the weighted mean parameter $\gamma_\parallel$ will be negative.

Relationship (4) can be rewritten as [4]

$$\gamma_\parallel = \frac{V}{C_p}[(C_{11} + C_{12})\alpha_\parallel + C_{13}\sigma_\perp],$$
$$\gamma_\perp = \frac{V}{C_p}[C_{33}\sigma_\perp + 2C_{13}\alpha_\parallel]. \quad (5)$$

We take into account the quasi-continuity of the spectrum and change over from summation in relationships (2) and (3) to integration with allowance made for the dispersion laws of the spectrum of acoustic vibrations in the layered crystal and their variations under pressure, which are given in [3]. In the limiting cases, we can obtain the analytical form of the temperature dependences of the heat capacity $C(T)$ and the thermal expansion coefficients $\alpha_\parallel(\mathrm{T})$ and $\alpha_\perp(\mathrm{T})$. Specifically, for an intermediate temperature range $\eta^2\Theta \ll T \ll \xi\Theta$ (designations are the same as in [3, 5]), by retaining only the largest terms with respect to ξ and T/Θ, we can derive the following temperature dependences:

$$\alpha_\parallel(T) = -\frac{\pi^3 N_0 k}{48\zeta\nu^2\rho v^2}\left(\frac{T}{\Theta}\right),$$
$$\alpha_\perp(T) = \frac{7.2\pi^2 N_0 k\varphi_1}{32\zeta^3\nu\rho v^2}\left(\frac{T}{\Theta}\right)^2, \quad (6)$$
$$C(T) = \frac{\pi^5 Nk}{40\zeta\nu}\left(\frac{c}{a}\right)\left(\frac{T}{\Theta}\right)^2,$$

where N and N_0 are the numbers of unit cells in the crystal and unit volume, respectively;

$$\eta^2 = C_{44}/\rho v^2; \quad \zeta^2 = C_{33}/\rho v^2;$$
$$2/\rho v^2 = 1/C_{11} + 1/C_{66}; \quad \Theta = \hbar v\pi/ka;$$

ν is the dimensionless parameter characterizing the flexural rigidity of the layer ($\nu < 1$); and $\varphi_1 = dC_{33}/dp$.

The inclusion of dependences (6) in expressions (5) allows one to determine the form of the temperature dependences of the Grüneisen parameters

$$\gamma(T) = -\frac{A}{T} + B, \quad (7)$$

where A and B are the positive numbers. Using the numerical values of the parameters taken from [5] ($dC_{33}/dp = 16$, $\nu = 0.47$), the quantitative estimations from relationship (7) can be made for graphite, one of the typical layered crystals. In the case of graphite in the temperature range $0.7 \ll T \ll 390$ K [5], the following relationships are valid:

$$\gamma_\parallel(T) = -400\ \mathrm{K}/T + 1.5, \quad \gamma_\perp(T) = 3.5 - 10\ \mathrm{K}/T.$$

3. RESULTS AND DISCUSSION

Let us consider the thermal behavior of the Grüneisen parameters $\gamma_\perp(T)$ and $\gamma_\parallel(T)$, which were calculated from relationships (5) for layered crystals of the hexagonal crystal system.

The temperature dependences of the Grüneisen parameters $\gamma_\perp(T)$ and $\gamma_\parallel(T)$ for graphite single crystals with due regard for the temperature dependence of the elastic constants $C_{ik}(T)$ and without regard for it are shown in Fig. 1. In order to calculate the required dependences, we used the experimental data on the heat capacity [6], thermal expansion [7], and elastic constants [8].

It is seen from Fig. 1a that the temperature dependences $\gamma_\perp(T)$ and $\gamma_\parallel(T)$ differ substantially. The $\gamma_\perp(T)$ quantity is positive over the entire temperature range

under consideration, whereas $\gamma_{\parallel}(T)$ is negative. The common feature is a monotonic decrease in the absolute values of $\gamma_{\perp}(T)$ and $\gamma_{\parallel}(T)$ with an increase in temperature. This indicates that the anharmonicity of interatomic bonding forces for graphite in the layer planes and normal to them decreases with an increase in temperature. It is evident from comparison of the curves that the inclusion of $C_{ik}(T)$ has little or no effect on the character of the $\gamma_{\parallel,\perp}(T)$ dependence. The $\gamma_{\parallel}(T)$ quantity decreases by 30%.

The theoretical dependences of the Grüneisen parameter calculated from relationship (7) are shown in Fig. 1b. A good agreement is observed with the data obtained for $\gamma_{\parallel}(T)$.

Figure 2 shows the temperature dependences of the Grüneisen parameters for the GaS, GaSe, and InSe layered crystals, which were calculated from the data on the heat capacity [9], thermal expansion [5], and elastic constants [10]. It is easy to see that, for all these crystals, there is a temperature range near 30–50 K in which the Grüneisen parameter $\gamma_{\parallel}$ is negative. As for graphite, this can be explained by the dominant contribution of transverse acoustic vibrations, which are caused by atomic displacements normal to layers and propagate in the layer planes. In other words, the membrane effect, which is specific to layered crystals, manifests itself. At temperatures above 50 K, the $\gamma_{\parallel}$ parameter increases rapidly due to an increase in the contribution of the modes with positive values of the mode Grüneisen parameter $\gamma_{\parallel,j}$ and flattens out at temperatures close to the Debye temperature. The quantitative estimations with relationship (7) cannot be applied to these crystals because of the lower anisotropy of the elastic properties [5] and the invalidity of the assumptions made when deriving relationship (7). However, the quantitative reasoning holds.

For comparison, let us consider the known experimental data for zinc and cadmium [11]. Elemental zinc and cadmium, as well as the crystals investigated above, crystallize in the hexagonal crystal system. The interaction of the atoms located in planes normal to the sixfold axis is stronger than the interaction between the planes. The strong anisotropy of the forces acting in the crystal is also evidenced by a considerable anisotropy of the thermal expansion ($\alpha_{\perp}/\alpha_{\parallel} \sim 6$ at $T \sim \theta$) and by the temperature range in which $\alpha_{\parallel}$ is negative.

The temperature dependences of the Grüneisen parameters $\gamma_{\perp}(T)$ and $\gamma_{\parallel}(T)$ for zinc and cadmium [11] are shown in Fig. 3. It is evident that the contribution of the modes with the negative parameter $\gamma_{\parallel,j}$ manifests itself in these crystals as a small decrease in the values in the temperature range where $\alpha_{\parallel}$ is negative. The parameter $\gamma_{\parallel}$ itself remains positive over the entire temperature range. The nature of the negative thermal expansion for zinc and cadmium crystals is apparently determined by the dominant part of the second term in relationship (4), i.e., by Poisson's compression, all the more that the functions $f_1(T) = 6\alpha_{\parallel}/T^3$ and $f_2(T) = \alpha_{\perp}/T^3$ constructed for these elements represent a mutual mirror image.

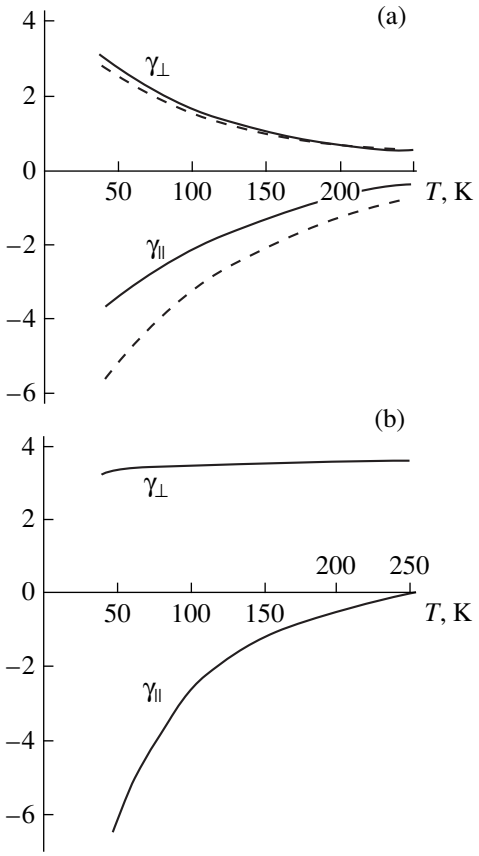

Fig. 1. Temperature dependences of the Grüneisen parameter for graphite: (a) with due regard for $C_{ik}(T)$ (solid lines) and without regard for $C_{ik}(T)$ (dashed lines) and (b) theoretical calculations from relationship (7).

Thus, the transverse acoustic vibrations in layered crystals, which propagate in the layer planes and at which the atomic displacements are normal to the layer planes, play the dominant role in the temperature behavior of the Grüneisen parameters. These vibrations (modes) correspond to negative values of the mode Grüneisen parameters $\gamma_{\parallel,j}$ because of the manifestation of the specific membrane effect. For a strongly anisotropic layered crystal, this can lead to negative values of the weighted mean Grüneisen parameter $\gamma_{\parallel}$. It follows from the above figures that if all of the modes are involved in motion (at temperatures close to the Debye temperature), $\gamma_{\parallel} > \gamma_{\perp}$ for layered crystals. In other words, the anharmonicity of interatomic bonding forces is stronger toward the stronger bond (in the layer planes). This trend is clearly observed for graphite, because the Debye temperature is approximately equal to 1600 K.

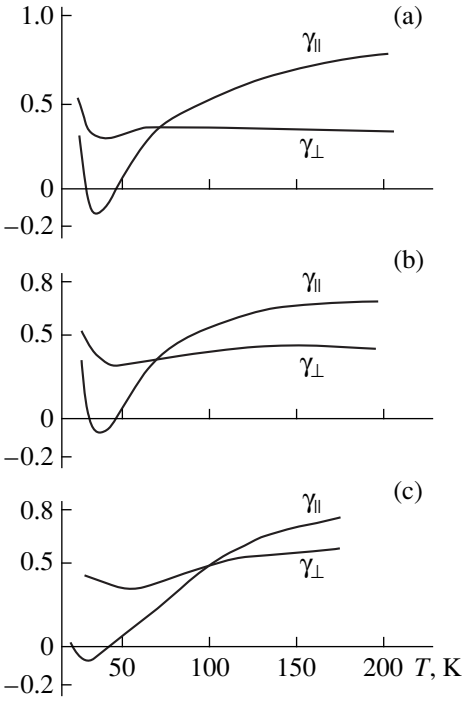

Fig. 2. Temperature dependences of the Grüneisen parameters for layered crystals: (a) GaS, (b) GaSe, and (c) InSe.

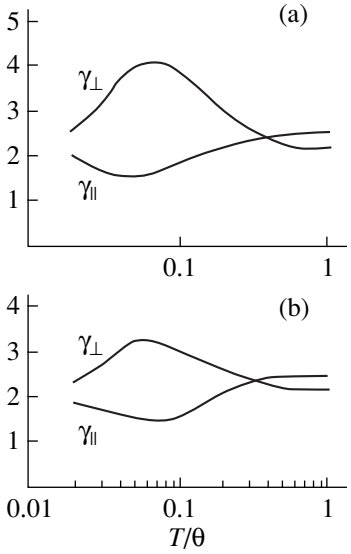

Fig. 3. Temperature dependences of the Grüneisen parameters for (a) cadmium (θ = 210 K) and (b) zinc (θ = 320 K).

Another mechanism, which is known from the literature, leads to negative Grüneisen parameters [12]. It is known that Group IV elements of the periodic table crystallize in the cubic crystal system of the diamond type (for example, germanium, silicon, and α-tin), whereas compounds of the germanium isoelectronic series crystallize in the cubic crystal system of the sphalerite type (for example, InSb, InAs, GaAs, GaSb, and AlSb). All these semiconductors are characterized by the negative values of the low-temperature thermal expansion coefficients due to negative Grüneisen parameters [11]. As was shown in [12], the specific features of the phonon spectrum of germanium, which was constructed using the neutron diffraction data, can lead to a negative thermal expansion. The reason is that the branch of the transverse acoustic vibrations for germanium has a horizontal portion in the vicinity of the Brillouin zone boundary (a similar phenomenon was also observed for silicon and α-tin). Therefore, this branch in calculations can be considered as consisting of two parts, namely, a Debye's part at the beginning of the spectrum and an Einstein's part at the end. According to [12], the Einstein's part of transverse acoustic vibrations is responsible for negative values of the Grüneisen parameter.

The phonon spectra of layered crystals also exhibit specific features. However, in these spectra, unlike the phonon spectra of the aforementioned materials, the acoustic branch of transverse vibrations with the displacement vector directed normally to the layer is characterized by the dispersion dependence $\omega^2 \sim Aq^2 + Bq^4$ [3], where q is the wave vector projection onto the layer plane, A is the quantity determined by the elastic constant of the interlayer shear C_{44}, and B is the quantity characterizing the flexural rigidity of the layers. A similar quadratic dispersion dependence was experimentally found for graphite [13], GaS [14], and other layered crystals.

In conclusion, it should be emphasized that the direct measurements of the mode Grüneisen parameters $\gamma(T)$, which usually involve considerable experimental difficulties, could provide important information on the character of phonon spectra in these crystals and their variations under deformation.

ACKNOWLEDGMENTS

I am grateful to R.A. Suleĭmanov for helpful discussions.

REFERENCES

1. G. Leibfried and W. Ludwig, Solid State Phys. **12**, 276 (1961).
2. L. D. Landau and E. M. Lifshitz, *Statistical Physics* (Nauka, Moscow, 1976; Pergamon, Oxford, 1980).
3. I. M. Lifshits, Zh. Éksp. Teor. Fiz. **22** (4), 475 (1952).
4. T. H. K. Barron and R. W. Munn, Philos. Mag. **15** (133), 85 (1967).
5. W. de Sorbo and W. Tyler, J. Chem. Phys. **21** (5), 1660 (1953).
6. A. C. Bailey and B. Yates, J. Appl. Phys. **41** (13), 5088 (1970).

7. M. B. Gauster and I. J. Fritz, J. Appl. Phys. **45** (8), 3309 (1974).
8. K. K. Mamedov, M. A. Aldzhanov, I. G. Kerimov, and M. I. Mekhtiev, Fiz. Tverd. Tela (Leningrad) **20** (1), 42 (1978) [Sov. Phys. Solid State **20**, 22 (1978)].
9. G. L. Belen'kiĭ, R. A. Suleĭmanov, N. A. Abdullaev, and V. Ya. Shteĭnshraĭber, Fiz. Tverd. Tela (Leningrad) **26** (12), 3560 (1984) [Sov. Phys. Solid State **26**, 2142 (1984)]; R. A. Suleymanov and N. A. Abdullaev, Carbon **31** (7), 1011 (1993).
10. M. Gatulle, M. Fischer, and A. Chevy, Phys. Status Solidi B **119** (1), 327 (1983).
11. S. I. Novikova, *Thermal Expansion of Solids* (Nauka, Moscow, 1974).
12. V. S. Oskotskiĭ, Fiz. Tverd. Tela (Leningrad) **6** (5), 1294 (1964) [Sov. Phys. Solid State **6**, 1011 (1964)].
13. R. Nicklow, N. Wakabayashi, and H. G. Smith, Phys. Rev. B **5** (12), 4951 (1972).
14. B. M. Powell, S. Iandl, I. L. Brebner, and F. Levy, J. Phys. C **10** (16), 3039 (1977).

Translated by N. Korovin

Physics of the Solid State, Vol. 43, No. 4, 2001, pp. 732–736. Translated from Fizika Tverdogo Tela, Vol. 43, No. 4, 2001, pp. 701–705.

LATTICE DYNAMICS AND PHASE TRANSITIONS

Acoustic Study of the Ferroelastic Phase Transition in $LiCsSO_4$ Crystal

A. K. Radzhabov and E. V. Charnaya

Institute of Physics (Petrodvorets Branch), St. Petersburg State University, ul. Pervogo maya 100, Petrodvorets, St. Petersburg, 198904 Russia

e-mail: charnaya@paloma.spbu.ru

e-mail: ali.radzhabov@pobox.spbu.ru

Received September 25, 2000

Abstract—The paper reports on an acoustic study of the temperature dependences of the ultrasonic-wave velocity and attenuation in a $LiCsSO_4$ crystal within the 190–295 K temperature region, which includes the interval of the pseudoproper second-order ferroelastic phase transition (202 K). The velocity of the transverse *xy* acoustic mode is found to decrease by more than six times at the phase transition. The possibility of performing ultrasonic studies both in the region of the ferroelastic phase transition temperature and below it is demonstrated. The results are treated in terms of Landau's theory. Waves not associated with the soft mode are shown to exhibit anomalies which are supposedly due to an intermediate phase, whose existence was suggested in a number of publications. © *2001 MAIK "Nauka/Interperiodica".*

The lithium–cesium sulfate $LiCsSO_4$ is of interest as a material undergoing a phase transformation and having a ferroelastic domain structure at low temperatures (see, e.g., [1] and references therein). There are also reports of its good optical characteristics [1] and unusual thermal properties [2], which makes $LiCsSO_4$ a promising crystal for device applications. This accounts for its having become the subject of numerous studies performed by various methods.

$LiCsSO_4$ belongs to a family of $ACBX_4$-type compounds (the potassium sulfate family), where *A* and *C* stand for alkali metals or the NH_4 ion and BX_4 is SO_4, SeO_4, or some other tetrahedral ion [3]. According to [4–8], $LiCsSO_4$ undergoes a structural phase transition at a temperature of about 202 K from the paraelastic phase with an *mmm* rhombic point group to the ferroelastic monoclinic structure of the class 2/*m*, without a change of the unit cell content. A polarizing microscope study suggests that the transition to the 2/*m* group occurs through an intermediate phase with an unidentified, supposedly monoclinic symmetry within a temperature interval from 206 to 199 K [7]. Subsequent x-ray diffraction and calorimetric studies [4, 8, 9] did not confirm the existence of such an intermediate phase, and the transformation itself was considered to be a typical second-order phase transition. However, later EPR studies of the phase transition in $LiCsSO_4$ again reported observation of an intermediate structure in the above-mentioned temperature region [2, 10]. Thus, the problem of the mechanism of the transition in $LiCsSO_4$ from the para- to the ferroelastic phase remains unclear.

The properties of $LiCsSO_4$ were also investigated by Raman scattering [11], NMR [1, 12], and other methods. It was established that the transition to the ferroelastic phase involves a strong softening of the acoustic phonon mode associated with the shear component ε_{xy} of the strain tensor. At the same time, the primary (microscopic) order parameter characterizes the ordering of the sulfate tetrahedra [7], and, by the terminology of [13], this phase transition is a pseudoproper ferroelastic transformation in which the primary parameter η and the strain shear component ε_{xy} are linearly related. In connection with the ferroelastic nature of the phase transition in $LiCsSO_4$, the elastic properties of the crystal were studied. The temperature dependences of the dynamic elastic moduli $c_{\alpha\beta}$ (α and β are the Voigt indices) were investigated primarily by Brillouin light scattering [5] and ultrasonic [14–16] methods. A strong decrease in the c_{66} elastic constant and weak anomalies of other elasticity tensor components in the region of the phase transition were observed. The most complete information on all independent moduli $c_{\alpha\beta}$ of the *mmm* group can be found in [5] for a broad temperature region including the Curie point T_C. Attempts to measure the sound velocity directly in the region of the phase transition and below it were unsuccessful in all of the chosen directions [14, 15] because of the strong attenuation of the ultrasonic wave caused by the ferroelastic domain structure [17]. Note that the measurements reported in [15] were made only for the wave associated with the c_{66} elastic constant, while in [14], seven independent $c_{\alpha\beta}$ components were studied. The first measurements of the velocity of the transverse ultrasonic wave corresponding to the soft acoustic

mode were made in the ferroelastic phase in [16]. No anomalies in the elastic moduli which would indicate the existence of an intermediate phase were observed in [5, 14–16].

Here, we report a comprehensive ultrasonic study of crystalline $LiCsSO_4$ within the 190–295 K range including the Curie point. We measured the temperature dependences of the relative variations in the velocity and attenuation of a *y*-polarized transverse sonic wave propagating along the rhombic crystallographic axis *x* and of longitudinal waves launched along the [100], [101], and [011] directions of the rhombic phase. There are no reports of earlier studies of the temperature dependence of sound absorption in $LiCsSO_4$.

1. EXPERIMENT

Colorless transparent $LiCsSO_4$ crystals were grown from water solutions at a constant temperature of 315 K. The crystals thus grown had a pseudohexagonal symmetry with twins, which could be observed in polarized light. The crystals were characterized by chemical and x-ray diffraction analysis. The samples for the study, cut of twin-free parts, were parallelepiped-shaped and measured $5 \times 5 \times 5$ mm, with sides parallel to the rhombic axes and at 45° to them. The samples for measurements of the velocity and attenuation of the *xy* mode associated with the c_{66} elastic constant measured $1 \times 5 \times 5$ mm. The error of aligning with the crystallographic axes was not above 1°, and the faces were plane-parallel to within 5 μm.

The measurements were conducted by several versions of the echo-pulse method [18] at a frequency of 5.5 MHz. Because of the strong sound attenuation in the ferroelastic phase, the *xy* acoustic mode was studied by a technique specially developed for strongly absorbing media, by which one observed the interference of a pulse transmitted through the sample with that reflected from its front face [19]. In the region of the strongest attenuation, the sound velocity was determined by measuring the pulse transit time through the sample.

All the measurements were conducted under slow cooling and heating of the sample at a rate lower than 0.1 K min^{-1}. Prior to each measurement, the sample was thermally stabilized for 5 min, and below 260 K, for 15 min. This time was long enough for the acoustic parameters to reach a stable level. The temperature was stabilized to within 0.05 K, and the temperature gradient in the sample did not exceed 0.02 K cm^{-1}. The relative measurement error in the paraelastic phase was 10^{-2}% for the velocity and 10% for the attenuation. In the region of the ferroelastic transition and below it, the measurement errors of acoustic parameters for the *xy* mode could increase up to 1% and 50%, respectively.

The results obtained for the *xy* mode under cooling from room temperature are shown in Fig. 1. The velocity of the *xy* wave is seen to decrease strongly near the Curie point. Such a temperature behavior is characteristic of the inverse susceptibility associated with the order parameter or with a macroscopic quantity related linearly with the primary order parameter in the vicinity of proper (pseudoproper) ferroelastic transitions (see, e.g., [20]). Note that the minimum velocity of the *xy* wave was found to be 380 m s^{-1}, which coincides, within experimental error, with the minimum value of 340 m s^{-1} obtained [5] by the Brillouin scattering method. The minimum velocity corresponds to a softening of the elastic modulus c_{66} to 5.0×10^8 N m^{-2} at room temperature (the elastic modulus was calculated assuming the crystal density to be 3.442 g cm^{-3} [5]). Figure 1 also shows the temperature dependence of the sound wave attenuation coefficient. The attenuation increases strongly as one approaches the Curie point from the high-temperature side and continues to grow as the temperature decreases below T_C. At T = 190 K, the sound attenuation became so strong that the signal was completely corrupted by noise and further measurements were impossible. When heated subsequently from low temperatures up, the measurements could be resumed only for $T > 210$ K because of the attendant difficulties of detecting and identifying the signals. The data obtained in heating runs are also shown in Fig. 1. The velocity of the *xy* mode measured under heating is seen to coincide, within experimental error, with that in the cooling run. The attenuation of the sound under heating was slightly higher than that measured under cooling, which is apparently associated with acoustic contact degradation at low temperatures.

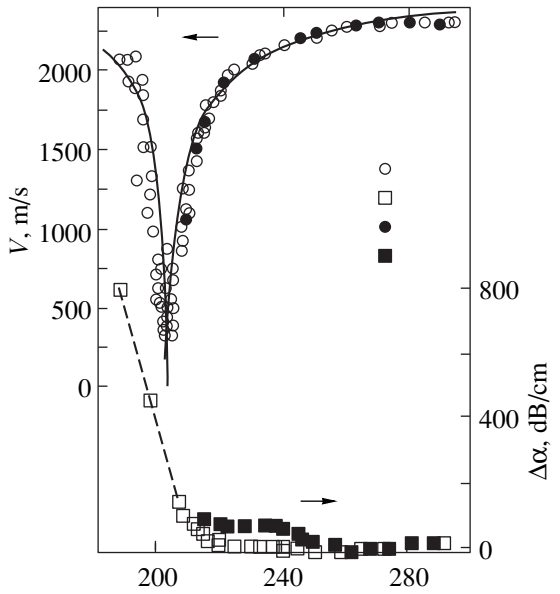

Fig. 1. Temperature dependences of the velocity v and relative attenuation coefficient $\Delta\alpha$ for a *y*-polarized transverse ultrasonic wave propagating along the *x* axis in the $LiCsSO_4$ crystal for (*1*, *2*) cooling and (*3*, *4*) heating. The solid line plots the theoretical relation for the velocity derived from Eqs. (4) and (5). The dashed line is drawn to aid the eye.

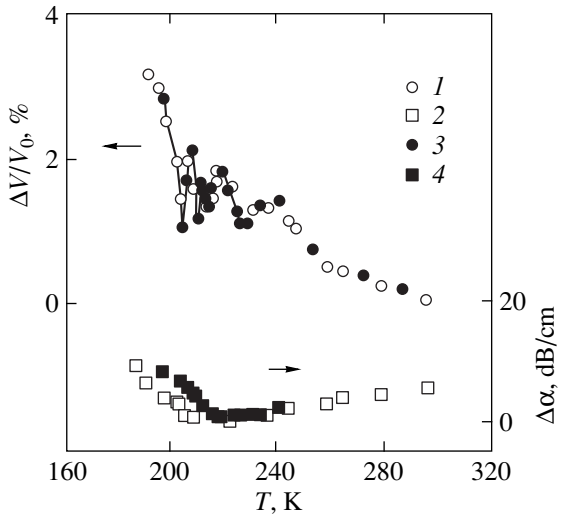

Fig. 2. Temperature dependences of the relative velocity variation $\Delta v/v_0$ and of the relative attenuation coefficient $\Delta\alpha$ for a longitudinal ultrasonic wave propagating along the [011] direction in the $LiCsSO_4$ crystal for (*1*, *2*) cooling and (*3*, *4*) heating. The solid line is drawn to aid the eye.

Figures 2–4 display the temperature dependences of the sound velocity and attenuation obtained for the other acoustic modes studied by us. The longitudinal ultrasonic waves propagating along the [011], [100], and [101] directions of the rhombic phase exhibit substantially smaller velocity changes near the phase transition than is the case with the *xy* mode, and a relatively weak increase in their attenuation near T_C and below it is observed, which implies weak coupling of the primary order parameter with deformations produced by these waves. Using the ultrasonic technique (which offers a higher accuracy than the Brillouin scattering method does) has permitted us to reveal a number of anomalies undetected heretofore. In particular, the wave propagating along [011] exhibited a nonmonotonic variation of the velocity with temperature near the phase transition; this variation was not accompanied by noticeable changes in the attenuation coefficient (Fig. 2). For the *xx* mode, we observed small maxima in the velocity and attenuation when approaching the Curie temperature (Fig. 3). As in [5], the ultrasonic wave propagating along the [101] direction (Fig. 4) was found to suffer a slight decrease in velocity near T_C, which was accompanied by an increase in the attenuation. The results presented in Figs. 2–4 were repeatedly reproduced, within experimental error, in subsequent cooling–heating runs.

2. DISCUSSION OF RESULTS

The anomalies observed in the *xy* mode velocity at the phase transition can be described by Landau's thermodynamic theory. Taking into account that the phase transition in $LiCsSO_4$ is pseudoproper in character, the principal terms in Landau's expansion in powers of the order parameter and strain can be written, following the general approach outlined in [13], as

$$\Phi = \Phi_0 + \alpha_0(T - T_0)\eta^2 + \beta\eta^4 + \gamma\eta\varepsilon_{xy} + \frac{1}{2}c_{66}^0\varepsilon_{xy}^2 + \frac{1}{2}\sum{}'c_{ijkl}^0\varepsilon_{ij}\varepsilon_{kl} + \ldots, \quad (1)$$

where Φ_0 is the value of the thermodynamic potential of the paraelastic phase in the absence of strains; T_0 is

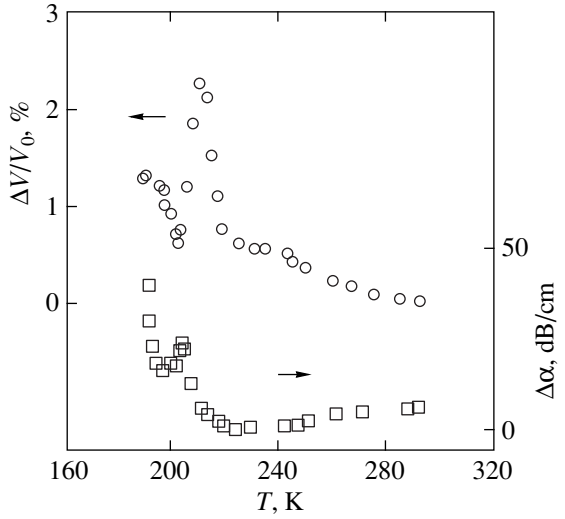

Fig. 3. Temperature dependences of the relative velocity variation $\Delta v/v_0$ and of the relative attenuation coefficient $\Delta\alpha$ for a longitudinal ultrasonic wave propagating along the [100] direction in the $LiCsSO_4$ crystal. Cooling run.

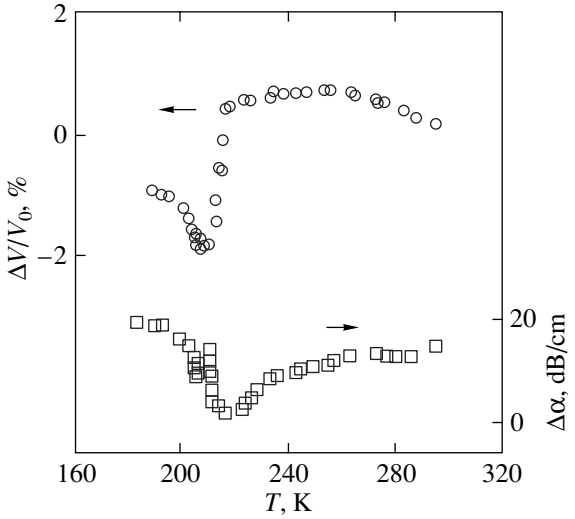

Fig. 4. Temperature dependences of the relative velocity variation $\Delta v/v_0$ and of the relative attenuation coefficient $\Delta\alpha$ for a longitudinal ultrasonic wave propagating along the [101] direction in the $LiCsSO_4$ crystal. Cooling run.

the phase-transition temperature for a clamped crystal ($T_0 = T_C - \gamma^2/(\alpha_0 c_{66}^0)$); η is the order parameter; ε_{ij} are the strain tensor components; c_{ijkl}^0 are the elastic moduli in the paraelastic phase; and $i, j, k, l = x, y, z$. The prime on the sum indicates that it does not contain a term with c_{66}^0. Combining Eq. (1) with the order-parameter relaxation equation [21]

$$\Gamma\frac{d\eta}{dt} = -\frac{\partial\Phi}{\partial\eta}$$

(Γ is a rate coefficient) and generalized Hooke's law,

$$\sigma_{ij} = \frac{\partial\Phi}{\partial\varepsilon_{kl}} = c_{ijkl}\varepsilon_{kl},$$

one can derive general expressions for the velocity v and additional attenuation $\Delta\alpha$ of an elastic wave coupled with the soft mode above and below the phase-transition temperature:

$$v = \sqrt{\frac{2}{\rho}}\frac{c_{66}}{\sqrt{c_{66} + c_{66}'}}, \quad (2)$$

$$\Delta\alpha = \omega\sqrt{\frac{\rho}{2}}\frac{\sqrt{c_{66} - c_{66}'}}{c_{66}}, \quad (3)$$

where

$$c_{66} = c_{66}^0\sqrt{\frac{((T - T_C)/(T - T_0))^2 + \omega^2\tau^2}{1 + \omega^2\tau^2}},$$

$$c_{66}' = c_{66}^0\frac{1 + \omega^2\tau^2 - ((T_C - T_0)/(T - T_0))}{1 + \omega^2\tau^2}$$

for $T > T_C$ and

$$c_{66} = c_{66}^0\sqrt{\frac{1 + (\omega\tau/2)^2}{\left[\frac{T_C - T_0}{2(T_C - T)} + 1\right]^2 + (\omega\tau/2)^2}},$$

$$c_{66}' = c_{66}^0\frac{1 + (\omega\tau/2)^2 + \frac{T_C - T_0}{2(T_C - T)}}{\left[\frac{T_C - T_0}{2(T_C - T)} + 1\right]^2 + (\omega\tau/2)^2}$$

for $T < T_C$. In Eqs. (2) and (3), ω is the sound velocity, $\tau = \Gamma/[\alpha_0(T - T_0)]$ is the order-parameter relaxation time in the paraelastic phase, c_{66} is the effective elastic modulus, and c_{66}' is the real part of this modulus. Within model (1), the velocities of the other acoustic modes do not change at the phase transition and the additional sound attenuation for them is zero.

A comparison of our experimental results with the data obtained near T_C in [5] does not show any velocity dispersion within the frequency interval from a few megahertz to about ten gigahertz. Thus, a theoretical analysis of the temperature dependences of the *xy* wave velocity can be done using the low-frequency relations derived from Eqs. (2) and (3), which coincide with the corresponding expressions presented in [20]:

$$v = \sqrt{\frac{c_{66}^0}{\rho}}\left(\frac{T - T_C}{T - T_0}\right)^{1/2} \quad (4)$$

for $T > T_C$ and

$$v = \sqrt{\frac{c_{66}^0}{\rho}}\left(\frac{T_C - T}{T_C - T + \frac{T_C - T_0}{2}}\right)^{1/2} \quad (5)$$

for $T < T_C$. The best fit of the theoretical $v(T)$ relation obtained from Eqs. (4) and (5) to the experiment is reached for $T_C - T_0 = 15$ K and $c_{66}^0 = 2.2 \times 10^{10}$ N m^{-2}, which corresponds to a room-temperature velocity of the *xy* mode of $v_{xy}^0 = 2530$ m s^{-1} (Fig. 1). The value of v_{xy}^0 accepted to reconcile the theory with the experiment differs somewhat from that measured at room temperature (Fig. 1), which is possibly due to our having neglected higher order terms in ε_{xy} and η in Landau's expansion (1). The difference $T_C - T_0 = 15$ K determined by us indicates a fairly strong coupling between the order parameter η and strain ε_{xy}.

Consider the variation of the elastic constants near T_C for the other modes studied. For a longitudinal wave propagating along the [101] crystallographic direction (Fig. 4), one observed a certain decrease in the sound velocity near T_C in a cooling run. Note the peak near the velocity minimum, which is weakly pronounced against the general sound attenuation background apparently caused primarily by scattering. The most probable explanation of this behavior of the acoustic parameters lies in a weak "admixing" of the soft mode to the effective elastic modulus corresponding to the given longitudinal wave because of a slight misorientation of the samples under study.

The longitudinal acoustic wave propagating along [100] revealed a maximum in the velocity slightly above T_C, which was accompanied by a attenuation peak (Fig. 3). As can be seen from Fig. 2, the velocity of the [011] longitudinal wave undergoes nonmonotonic variations above T_C. These variations are, on the whole, reproduced in the cooling–heating runs. The observed velocity changes do not exceed 1% in magnitude and could not be seen in [5], because the sensitivity of the Brillouin scattering method is not high enough for that. As can also be seen from Fig. 2, the anomalies observed for this mode in the temperature behavior of the sound velocity are not accompanied, within experimental accuracy, by any anomalies in the attenuation coefficient.

The nonmonotonic velocity variation of the ultrasound propagating along the [011] crystallographic direction, as well as the behavior of the elastic characteristics of the [100] wave, does not find explanation within Landau's theory for a pseudoproper second-order ferroelastic transition. The anomalies revealed can supposedly be associated with the presence of an intermediate phase in the $LiCsSO_4$ crystal, whose existence was suggested in [2, 7, 10].

3. CONCLUSIONS

Thus, we have performed measurements of the sound velocity and attenuation in $LiCsSO_4$ for the transverse *xy* mode and longitudinal waves propagating along [011], [100], and [101] within the temperature interval of 190–295 K, which includes the region of the ferroelastic phase transition. A softening of the elastic modulus c_{66} and an increase in the *xy* wave attenuation were found to occur near T_C. The temperature behavior of the velocities and attenuation coefficients of the longitudinal ultrasonic waves were observed to have anomalies, which provide supportive evidence for the assumption of the presence of an intermediate phase at the transition to the ferroelastic state. The possibility of performing acoustic measurements in the region of proper (pseudoproper) second-order ferroelastic phase transitions has been demonstrated.

ACKNOWLEDGMENTS

The authors are grateful to T. Krajewski for providing the crystals for this study.

REFERENCES

1. A. R. Lim and S. Y. Jeong, Solid State Commun. **113** (9), 513 (2000).
2. S. K. Misra and L. E. Misiak, Phys. Rev. B **48** (18), 13579 (1993).
3. K. S. Aleksandrov and B. V. Beznosikov, *Structural Phase Transitions in Crystals (Family of Potassium Sulfate)* (Nauka, Novosibirsk, 1993).
4. K. S. Aleksandrov, L. I. Zherebtsova, I. M. Iskornev, *et al.*, Fiz. Tverd. Tela (Leningrad) **22** (12), 3673 (1980) [Sov. Phys. Solid State **22**, 2150 (1980)].
5. B. Mroz, H. Kiefte, M. J. Clouter, and J. A. Tuszynski, Phys. Rev. B **36** (7), 3745 (1987).
6. T. Hidaka, Phys. Rev. B **45** (1), 440 (1992).
7. A. I. Kruglik, M. A. Simonov, E. P. Zhelezin, and N. V. Belov, Dokl. Akad. Nauk SSSR **247** (6), 1384 (1979) [Sov. Phys. Dokl. **24**, 596 (1979)].
8. T. Asahi and K. Hasebe, J. Phys. Soc. Jpn. **57** (12), 4184 (1988).
9. A. Pietraszko, P. E. Tomaszevski, and K. Lukaszewicz, Phase Transit. **2** (2), 141 (1981).
10. Jiang-Tsu Yu, Shen-Yuan Chou, and Shu-Jeu Huang, J. Phys. Chem. Solids **49** (3), 289 (1988).
11. M. N. Shashikala, N. Chandrabhas, K. Jayaram, *et al.*, J. Phys. Chem. Solids **55** (2), 107 (1994).
12. A. R. Lim and S. Y. Jeong, J. Phys. Chem. Solids **60** (11), 1773 (1999).
13. P. Toledano, M. M. Fejer, and B. A. Auld, Phys. Rev. B **27** (9), 5717 (1983).
14. K. S. Aleksandrov, M. P. Zaĭtseva, L. A. Shabanova, and O. V. Shimanskaya, Fiz. Tverd. Tela (Leningrad) **23** (8), 2440 (1981) [Sov. Phys. Solid State **23**, 1426 (1981)].
15. H. Ozeki and A. Sawada, J. Phys. Soc. Jpn. **51** (7), 2047 (1982).
16. E. V. Charnaya and A. K. Radzhabov, Ferroelectrics **158**, 7 (1994).
17. B. Litov and C. W. Garland, Phys. Rev. B **2** (11), 4597 (1970).
18. J. Williams and J. Lamb, J. Acoust. Soc. Am. **30**, 308 (1958).
19. B. F. Borisov, E. V. Charnaya, and A. K. Radzhabov, Phys. Status Solidi B **181**, 337 (1994).
20. T. V. Quinh, G. Schmidt, N. R. Ivanov, and L. A. Shuvalov, Phys. Status Solidi A **36** (1), K85 (1976).
21. L. D. Landau and I. M. Khalatnikov, Dokl. Akad. Nauk SSSR **96** (3), 472 (1954).

Translated by G. Skrebtsov

Physics of the Solid State, Vol. 43, No. 4, 2001, pp. 737–745. Translated from Fizika Tverdogo Tela, Vol. 43, No. 4, 2001, pp. 706–713.

LATTICE DYNAMICS AND PHASE TRANSITIONS

Changes in the Electronic Structure upon the *B*2–*B*19' Martensitic Transformation in Titanium–Nickel

S. E. Kulkova, D. V. Valujsky, and I. Yu. Smolin

Institute of Strength Physics and Materials Science, Siberian Division, Russian Academy of Sciences, Akademicheskiĭ pr. 2/1, Tomsk, 634021 Russia

e-mail: kulkova@ispms.tsc.ru

Received April 17, 2000; in final form, September 26, 2000

Abstract—The self-consistent band structure of a TiNi intermetallic compound in two phases is calculated by the full-potential linearized augmented-plane-wave (FLAPW) method. The features of changes in the density of states upon *B*2–*B*19' martensitic transformation are discussed. The influence of atomic positions on the electronic structure of the martensitic monoclinic phase is examined. The frequency dependence of the optical conductivity and the emission, absorption, and the characteristic electron-energy-loss spectra are calculated with due regard for the transition probability matrix element. The results of calculations are in reasonable agreement with the available experimental data. © *2001 MAIK "Nauka/Interperiodica".*

1. INTRODUCTION

Considerable interest in the TiNi intermetallic compound is motivated by its unique properties and, primarily, the so-called "shape-memory effect," which accompanies martensitic transformations [1]. Titanium–nickel materials have widespread technological application and, in the last decade, have been extensively used as biomaterials. The crystal structure and properties of TiNi have been studied in detail in numerous experimental and theoretical works (see, for example, [1–16]). It is known that the mechanical behavior of an alloy strongly depends on the doping with a third element and on precipitates formed in a TiNi matrix. The phase transformations in TiNi are attributed to the features of its electronic structure. Upon cooling, the high-temperature phase becomes unstable to the formation of charge density waves, which is explained by geometric features of the Fermi surface [10, 13, 17]. The electronic structure of the austenitic phase of TiNi was first calculated by Papaconstantopoulos and Nagel [9] and was then investigated repeatedly (see, for example, [10–17]). Despite discrepancies between the results of the first calculations performed in the framework of non-self-consistent methods, at present, the electronic structure of this phase is beyond question. The electronic structure of the *B*19' martensitic monoclinic phase is not clearly understood by researchers. The crystallographic structure of this phase was investigated in a number of works [2–5]. Note that the obtained lattice parameters differ from each other, but even a larger scatter was observed in atomic positions in a unit cell. According to [12, 13, 16], the differences in the electronic structures are most pronounced in the range of the Fermi energy E_F. The rhombohedral "premartensitic" *R* phase was not explored for the lack of crystallographic data, which were published only recently by Hara *et al.* [18]. Experimental data on the electronic properties of different phases, which can be used for a comparison with calculations of the electronic energy spectrum, are very limited. In particular, Shabolovskaya *et al.* [7, 8] measured the dispersion of the optical conductivity $\sigma(\omega)$. A considerable change in the spectral curve $\sigma(\omega)$ in the low-frequency range was observed upon *B*2–*B*19' transition. An intense asymmetric absorption peak appeared at 0.52–0.80 eV. At the same time, upon *B*2–*R* transformation, Sasovskaya and Pushin [19] did not find similar features in the optical conductivity curve, which only slightly differed from that obtained for the *B*2 phase. The calculations performed by Fukuda *et al.* [20] for the rhombohedral phase confirmed the assumption made in [19] that its electronic structure only insignificantly changes upon *B*2–*R* transformation. According to calculations carried out in [12, 13], the optical conductivity in the energy range 0.5–1.0 eV exhibits only a very low-intensity peak. Bihlmayer *et al.* [13] drew the conclusion that the use of the constant transition probability matrix element approximation led to underestimating the intensity of this peak.

The aim of the present work was to investigate thoroughly the electronic structure of the *B*19' martensitic phase as a function of lattice parameters and atomic positions, to calculate a number of electronic properties (the emission, absorption, and characteristic electron-energy-loss spectra and the optical conductivity) in two phases, and to analyze changes in the electronic structure upon structural transformation.

1063-7834/01/4304-0737$21.00 © 2001 MAIK "Nauka/Interperiodica"

2. COMPUTATIONAL TECHNIQUE

The band structure was investigated by the full-potential linearized augmented-plane-wave (FLAPW) method [21]. The approximation proposed by Perdew *et al.* [22] was used for the exchange–correlation potential. The scalar–relativistic calculations included not only the valence bands (3*d*, 4*s*, and 4*p*) but also the 3*s* and 3*p* states. These states should be taken into account, because they are located sufficiently close to the valence bands. The expansion of the wave function for valence electrons in terms of spherical functions involved more than 120 augmented plane waves for the RKM parameters (the product of the largest reciprocal lattice vector into the mean muffin-tin radius), which are equal to 8 and 9 in the case of the *B*2 phase, and more than 250 plane waves for the *B*19' phase. The potential in the intersphere region for the *B*2 phase was described using 80–100 Fourier coefficients. The expansion in l was limited by $l_{max} = 10$. The self-consistency was performed for 165 **k** vectors in the irreducible part of the Brillouin zone for a cubic lattice and 128 **k** vectors for a monoclinic lattice and was considered achieved when the change in the total energy did not exceed 10^{-5} Ry. The radii of muffin-tin spheres for titanium and nickel were taken equal to 2.3 au and kept constant in the calculations of two phases for correct analysis of the electronic characteristics. The test calculations at different ratios between the muffin-tin radii demonstrated that the density of states is virtually unchanged, even though the charge inside spheres depends on the chosen radius. The x-ray and electron-energy-loss spectra were calculated with due regard for the transition probability matrix element. The theoretically calculated spectra were smeared taking into consideration instrumental resolution and widths of the core and valence levels.

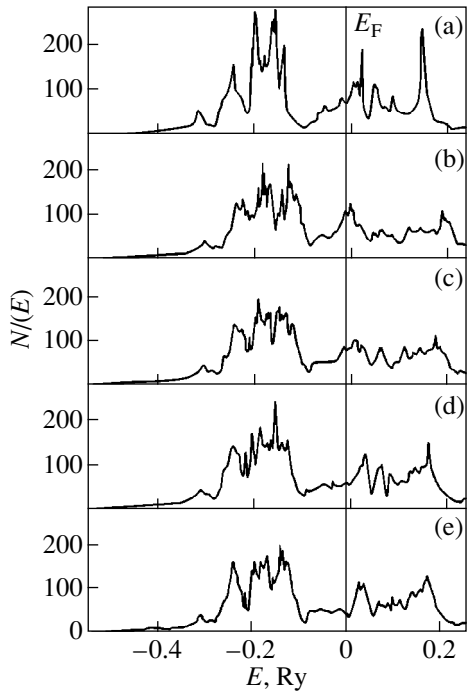

Fig. 1. Total densities of states (electrons/cell Ry) for (a) *B*2-TiNi and (b–e) *B*19'-TiNi at lattice parameters and atomic positions taken from [2–5], respectively.

3. RESULTS AND DISCUSSION

Figure 1 shows the calculated total density of states for the austenitic and martensitic phases of TiNi. As a whole, the results obtained are in reasonable agreement with our data calculated by the linear muffin-tin orbital (LMTO) method within the atomic-sphere approximation [12]. Let us dwell in more detail on analysis of the density of states for the monoclinic lattice. Four calculations with parameters taken from [2–5] (variants 1–4) were carried out for the *B*19' phase. Note that the data of different authors on the lattice parameters for the TiNi martensitic phase differ insignificantly, whereas the scatter in the positions of titanium and nickel atoms in the unit cell is considerably larger. The unit cell parameters obtained in [4, 5] most adequately describe the experimental diffraction data. Therefore, for the most part, these parameters were used in previous calculations [12, 13, 16, 20]. Actually, the densities of states $N(E_F)$ at the Fermi level that were calculated with the use of the parameters taken from [2, 3] (Figs. 1b, 1c) are larger than or virtually identical to those for the *B*2 phase (see table). The total energies are also larger than the total energy of the *B*2 phase, which does not count in favor of this structural transformation. It seems likely that the lattice parameters of the *B*19' monoclinic phase in these works were determined insufficiently correctly and, moreover, the measurements were carried out with polycrystalline samples. The total and partial densities of states for the *B*2 phase and all the variants (1–4) of calculations for the *B*19' phase are given in the table. The density of states for variant 3 (Fig. 1d) virtually coincides with that obtained by Bihlmayer *et al.* [13], who used the LAPW method. The LMTO method applied in [12, 16] at the same lattice parameters taken from [4] gave a more distorted density of states with a dip to the right of the Fermi level. Note that the fine structure of the density of states for the monoclinic phase stems from the lowering in the lattice symmetry, which leads to the splitting of degenerate energy terms. In spite of small differences near the Fermi level in calculations performed by different band theory methods, there is a general tendency to smearing of the valley (characteristic of the *B*2 structure) between the two groups of bands that are related to the alloy components. The effect of the anisotropy of the crystal potential in the intersphere region, which was ignored in earlier calculations, is most pronounced in the E_F range. The fact that this dip in the density of

states near the Fermi level is primarily associated with atomic displacements upon structural transformation is evident from the calculation according to variant 4 (the maximum displacements of atoms from the positions that correspond to those in the *B*2 phase) (Fig. 1e). The same effect is observed in calculations by using the lattice parameters taken from [4] or [5] and varying only the atomic displacements. The dispersion curves along the symmetric direction in the Brillouin zone are shown in Fig. 2a (variant 4). The coordinates of the Brillouin zone points are as follows: Γ, $\pi/a(0, 0, 0)$; X_C, $\pi/a(1, 0, 0)$; M_c, $\pi/a(1, 0, a/c)$; and Z, $\pi/a(0, 0, a/c)$.

Thus, analysis of the calculated density of states for the monoclinic martensitic phase shows that there is the characteristic redistribution of the density of states in the range of the Fermi level: the splitting of the high-energy peak, the shift in a number of unoccupied titanium states away from E_F, and the appearance of states between two main peaks of the density of states, which brings about a decrease in $N(E_F)$ and the total energy E_{tot}. The change in E_{tot} is 0.005 Ry for variant 4 and even smaller for variant 3. All these facts demonstrate that the stability of the martensitic phase at low temperatures is higher than that of the cubic phase.

Examination of changes in the partial charges in titanium and nickel spheres upon structural transition indicates the tendency for the localization of a metal charge inside its sphere; i.e., the "antibonding" states of the metal upon martensitic transformation become occupied, whereas the titanium states are, as if, displaced beyond the Fermi level. It is of interest that the nickel and titanium states with the de_s symmetry predominantly appear between the main peaks. Upon phase transformation, the value of $N(E_F)$ decreases by 35%. As a whole, the $N(E_F)$ value for nickel changes insignificantly, while the $N(E_F)$ value for titanium is virtually halved as compared to that in the *B*2 phase.

Note that data obtained by different authors for the contributions of the components to the density of states at the Fermi level in the *B*2 phase differ substantially; however, a small predominance of $N(E_F)$ for titanium was noted in recent works. Why does this question attract so much attention of researchers? If we consider *B*2 titanium compounds with Group VIII 3*d*–5*d* metals, the stability of TiFe, TiRu, and TiOs compounds can be explained in the framework of the Yamashita criterion [23]. In terms of bonding and antibonding states, the stability depends on the position of the Fermi level in the valley separating these states. An increase in the mean number of valence electrons per atom (from 6 to 7) results in the occupation of the metal and titanium antibonding states. According to Shabolovskaya [8], the Ti *d* states that dominate at the Fermi level are responsible for the instability of the *B*2 lattice. On the other hand, the portion in the slope of the second high-energy peak in the density of states (at which the Fermi level arrives when passing along the series) is predominantly formed by the metal *d* states, which are present as an admixture to the dominant titanium states in this spectral range. Therefore, the situation near the Fermi level turns out to be much more complex than that proposed in [8], and the metal can play an important role

Densities of states at the Fermi level (electrons/cell Ry) for Ti and Ni in *B*2-TiNi (2 atoms per cell) and *B*19'-TiNi (4 atoms per cell)

Alloy	$N(E_F)$-total	$N(E_F)$ Ti	$N(E_F)$ Ni
*B*2-TiNi	35.38	16.76	12.40
*B*2-TiNi [12]	39.61	22.46	17.15
*B*2-TiNi [13]	38.34	19.48	14.60
*B*2-TiPd	43.56	24.62	10.74
*B*19'-TiNi (1)	101.05	54.17	30.02
*B*19'-TiNi (2)	75.24	37.61	24.00
*B*19'-TiNi (3)	57.30	25.42	21.21
*B*19'-TiNi (4)	42.78	16.52	16.12
*B*19'-TiNi [12]	40.82	19.86	20.96
*B*19'-TiNi [13]	60.64	30.52	10.46
*B*19-TiNi	51.98	29.12	15.88
*B*19-TiPd	74.84	49.88	17.00
*B*19-TiPd [13]	77.50	50.26	17.02

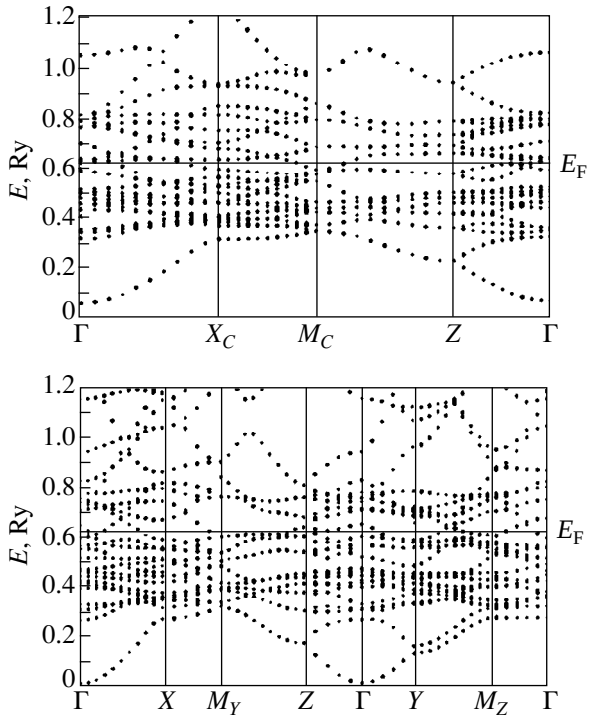

Fig. 2. Calculated electronic energy spectra of (a) *B*19'-TiNi (variant 4) and (b) hypothetical *B*19 structure.

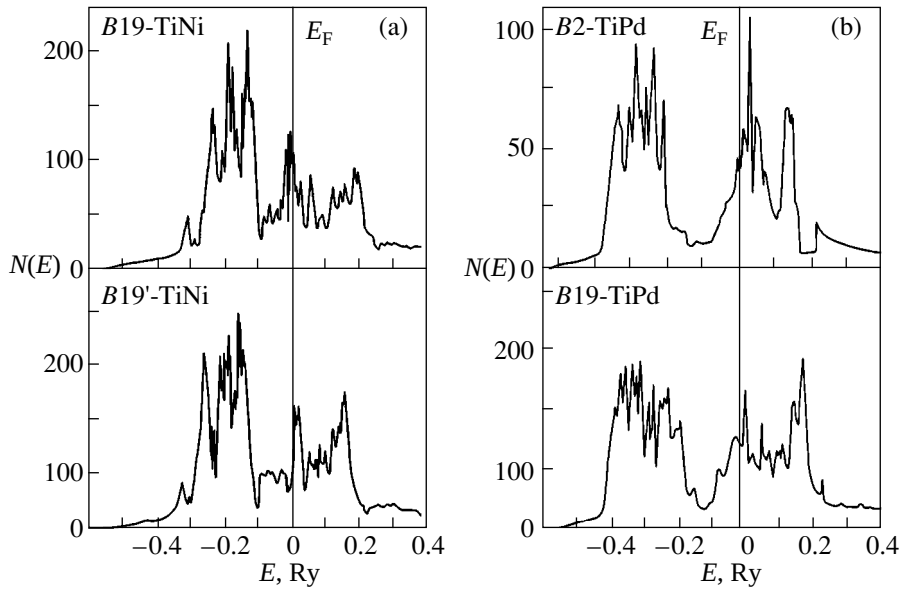

Fig. 3. Total densities of states for (a) TiNi and (b) TiPd in two phases.

in the explanation of structural transformations in titanium alloys. At the same time, the Shabolovskaya statements [8] hold some validity. Furthermore, our calculations and those performed by Zhang and Guo [16] for TiCu in a hypothetical *B*2 phase showed that $N(E_F)$ for titanium is substantially larger than $N(E_F)$ for copper. In this case, the Fermi level coincides with a sharp peak in the density of states, which explains the instability of the given lattice.

According to the calculations of the present work and the results obtained in [12, 13], the *B*2–*B*19' transformation is accompanied only by an insignificant lowering in the Fermi level (the distance between E_F and the bottom of conduction band changes by 0.2 eV). This results agrees with the conclusion regarding a small shift in the Fermi level, which was made in [7, 8] reasoning from the absence of noticeable changes in the location of the absorption edge and absorption band maxima at 1–5 eV. The experimental data on the temperature dependence of the magnetic susceptibility for an alloy with an almost equiatomic composition suggest a qualitative change in the position of the Fermi level upon martensitic transformation, which is also in agreement with the calculated density of states (Fig. 1e).

By using the band calculations, it was interesting to consider why TiNi undergoes a transformation into the *B*19' phase rather than into the *B*19 phase as in TiPd. For this purpose, we carried out the calculations for the hypothetical *B*19 orthorhombic phase in TiNi. The lattice parameters were taken from [24] (these parameters were actually obtained by the extrapolation of the crystallographic data for the Ti–Ni–Cu alloys in which this phase is observed). The total density of states for *B*19-TiNi is displayed in Fig. 3. In this case, the Fermi level coincides with a peak in the density of states and the value of $N(E_F)$ = 25.98 electrons/(cell Ry spin) is larger than the values of $N(E_F)$ for both the *B*19' and *B*2 phases of TiNi. Moreover, the structure of the density of states itself indicates the presence of flat portions near the Fermi level, which is corroborated by the corresponding calculations (Fig. 2b, direction Γ–*Y*). Therefore, we deal with the structural instability, and any distortion (in our case, a monoclinic distortion of the lattice) leads to a more stable structure. This feature is absent in the spectrum of TiPd. As can be seen from Fig. 3b, the Fermi level in the *B*2 phase of TiPd, as in the *B*2 phase of TiNi, is located in a small local minimum at the slope of the high-energy peak; however, E_F upon structural transformation remains in the range of the local minimum of the high-energy peak in the density of states. Unlike *B*2-TiNi, in which the titanium contribution at the Fermi level somewhat exceeds the nickel contribution (see table), the titanium contribution in *B*2-TiPd is virtually twice as large as the palladium contribution (12.31 and 5.37 electrons/(atom Ry)). In *B*19-TiPd, the palladium contribution decreases, whereas the titanium contribution remains almost unchanged. Note that the localization of palladium in its sphere is stronger than that of nickel in both *B*2 and *B*19 phases (8.04–8.60 and 7.97–8.20 electrons in TiPd and TiNi, respectively).

The electronic structure obtained for two TiNi phases was used for the calculation and analysis of x-ray spectra. It should be noted that, although the electronic properties of the *B*19' phase were calculated using the electronic structure determined for variants 3 and 4, we present the results only for variant 4, because the observed differences in the structure of the density of states in this case are more pronounced. A large

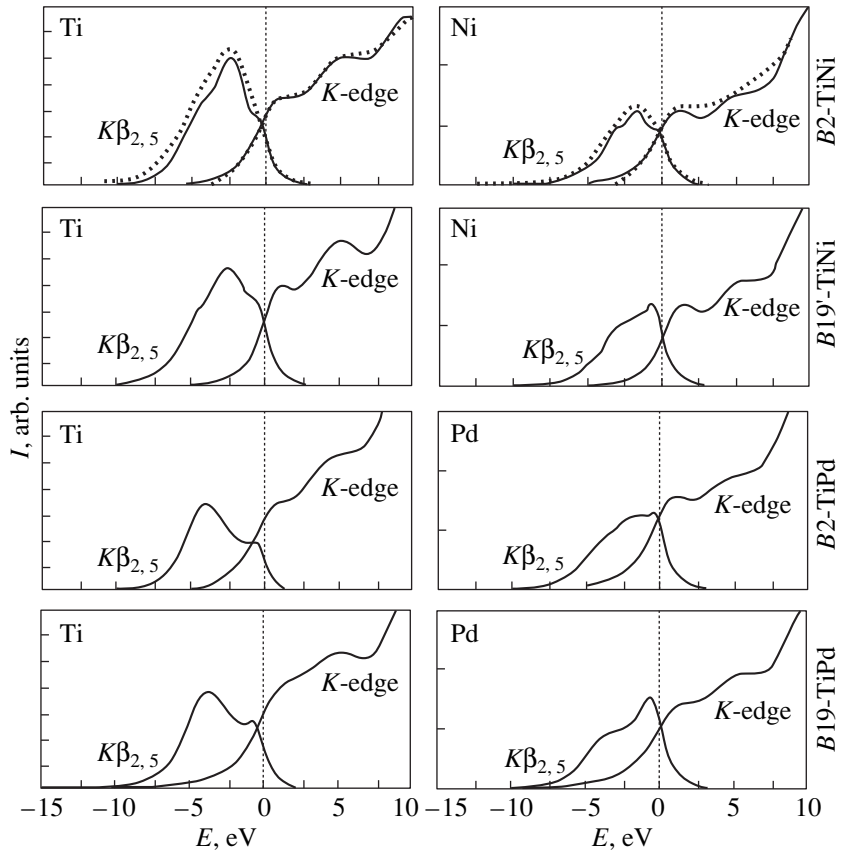

Fig. 4. *K* x-ray emission and absorption spectra of TiNi and TiPd in two phases. Solid lines correspond to the theoretical spectra, and points are the experimental spectra taken from [25].

number of works have been devoted to the x-ray spectrum investigation of TiNi whose *K* and *L* emission and absorption spectra and x-ray photoelectron spectra are of particular interest. Figure 4 shows the calculated *K* x-ray emission and absorption spectra and the experimental spectra (points) taken from [25]. A comparison between the calculated and experimental spectra demonstrates that the positions and intensities of the main peaks are in satisfactory agreement. There are several possible mechanisms responsible for the formation of the $K\beta_{2,5}$ line for transition metals and alloys [25, 26]. It is believed that the line shape as a whole reflects the distribution of the *d* states in the valence band, and the main features coincide with the centers of gravity of the de_g and dt_{2g} bands. An increase in the valence charge of components in the series TiFe–TiCo–TiNi leads to the atomization and lowering not of the *d* band as a whole but only its triplet dt_{2g} component, because a further filling of the *d* shell occurs at the expense of this band. The main features in the $K\beta_{2,5}$ lines of the compounds begin to come close together, which is consistent with the behavior of the partial densities of states. At the same time, the shift in the Fermi level toward the titanium peak in the density of states and the filling of the de_g antibonding states bring about the appearance of a shoulder near the Fermi level in the titanium and nickel $K\beta_{2,5}$ lines. (In order to save space, we do not present the results for TiFe and TiCo.) This shoulder becomes more pronounced in the titanium spectra when passing to TiPd and TiPt, in which $N(E_F)$ for titanium increases as compared to that in TiNi. Moreover, the low-energy shoulder for TiPd virtually disappears (Fig. 4). The linewidth also increases when going along the isoelectronic TiNi series. Upon structural transformation, the Ni and Pd $K\beta_{2,5}$ lines change more strongly than the corresponding titanium lines of the two compounds. In this case, the intensity is maximum directly near the Fermi level. It is interesting to note that this maximum is already observed for *B*2-TiPd and its intensity virtually does not decrease up to 3 eV.

Analysis of the absorption edge of titanium alloys revealed the following features. The selective absorption line is isolated, which manifests itself more clearly in the spectra of nickel or palladium as compared to the spectra of titanium. A small disagreement with the experimental data can be associated with the smearing parameters used in the calculations. However, a decrease in these parameters results not only in the formation of the more pronounced so-called *m* substructure but in a disagreement with the experimental data at

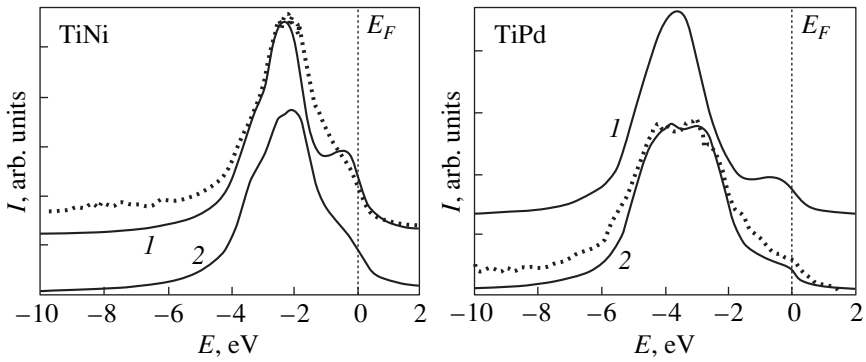

Fig. 5. *L* x-ray emission spectra of TiNi and TiPd in (*1*) *B*2 and (*2*) *B*19' and *B*19 phases. Points are the experimental data taken from [7].

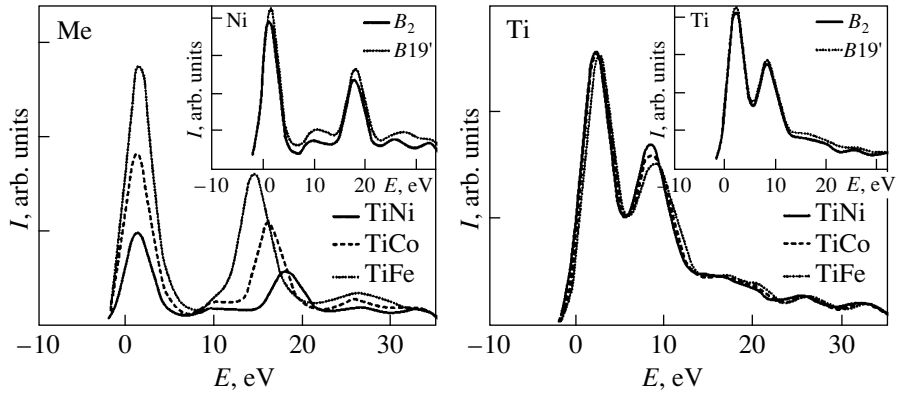

Fig. 6. $L_{2,3}$ electron-energy-loss spectra of a metal (Me = Fe, Co, and Ni) and titanium in 3*d* titanium compounds. Insets show the spectra of Ni and Ti for the austenitic and martensitic TiNi phases.

energies higher than 5 eV (the well-defined second dip). Upon *B*2–*B*19' transformation in TiNi, the selective line also becomes more pronounced in the titanium spectrum. By contrast, upon *B*2–*B*19 transformation in TiPd, the *m* substructure becomes less pronounced in the spectra of both titanium and palladium. Since the absorption spectra reflect the states that lie above the Fermi level and the crystal field has a stronger effect on outer orbitals, the difference in the splitting of the *d* band into two subbands with different symmetries primarily manifests itself in the width of the selective absorption lines. This width increases in the series TiFe–TiCo–TiNi and decreases in the series of titanium compounds with nickel, palladium, and platinum.

It is known that the shape of the L_3 emission line also well reflects the state with the *d* symmetry. For transition metal alloys, the L_3 line exhibits a rather simple shape (virtually without fine structure). Furthermore, this line is shifted toward the high-energy range and is somewhat narrower than the $K\beta_{2,5}$ line. As a rule, the change in the intensity of lines and their shift with respect to the *K* spectra are discussed in the literature. The calculated L_3 spectra of TiNi and TiPd in two phases and the experimental x-ray photoelectron spectra are depicted in Fig. 5. The locations of the main peak are in good agreement, and the appearance of a shoulder near the Fermi level reflects the shift in E_F toward the range of the second peak in the density of states for TiNi and TiPd. The shoulder in the low-energy part of the spectrum is associated with the de_g bounding states of the metal. Upon structural transformation, the change in the valence band of TiNi is less than that of TiPd whose valence band exhibits a doublet. Reasonable agreement is observed between the results of calculations and the experimental data for *B*2-TiNi and *B*19-TiPd. A small difference in the location of the theoretical maxima for the *B*19' and *B*2 phases (0.2 eV) confirms the conclusion that the low-energy part of the density of states for TiNi weakly changes upon martensitic transformation. It should be noted that the intensity of the Pd L_3 line for the *B*19 phase considerably decreases as compared to that of the corresponding line for the *B*2 phase, whereas the intensity of the Ni L_3 spectra of both phases remains virtually constant

and the intensity of the Pt L_3 spectrum of $B19$-TiPt decreases only slightly.

In recent years, the characteristic electron-energy-loss spectra of intermetallic compounds have been studied in a large number of experimental works [27–29]. This spectroscopic technique is sufficiently precise, and its results can serve as an excellent test for theoretical calculations of electronic structure. The results of our calculations are displayed in Fig. 6. The L absorption spectra of transition metals and their alloys in the range of the main edge exhibit a characteristic feature known as the "white line"—a sharp maximum of the absorption coefficient. The martensitic transformation in TiNi is attended by a small increase in the white-line intensity for both components (Ni and Ti), which reflects an insignificant change in the width of the unoccupied part of the d band. Note that this change is one order of magnitude less than that observed, for example, in the series TiFe–TiCo–TiNi. The intensity of the Co white line increases almost by a factor of two as compared to the intensity of the Ni line, and the intensity of the Fe line for the TiFe alloy increases even greater. A similar tendency to a change in the intensity of the L spectra of metals is also observed in a series of their compounds with Al [27], even though the structure of the line differs from that found for transition metal alloys. The lines obtained for the 3d titanium alloys are virtually identical in shape to the corresponding experimental spectra of metals. For the early elements of the first long period, the wave functions of d electrons considerably differ from the corresponding atomic functions, which are characterized by a substantial localization near their atoms. The screening conditions becomes less rigid, which, in particular, leads to a broadening of the line with a decrease in the charge of the element. At the same time, the theoretical calculations of the titanium line do not reproduce the experimental ratio of peaks. In the framework of the one-electron model, the ratio $L_3 : L_2$ should be equal to 2 : 1, whereas the inverse ratio is found from the experimental spectrum of titanium. This is explained by many-electron effects, which cannot be taken into account in the calculations at present.

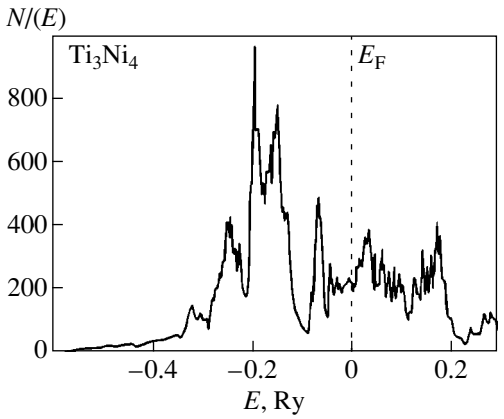

Fig. 7. Total density of states for Ti_3Ni_4.

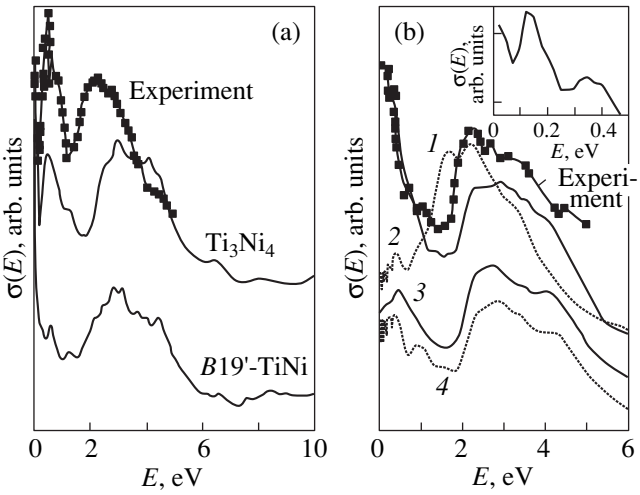

Fig. 8. Optical conductivities for (a) $B19'$-TiNi and Ti_3Ni_4 bulk alloys and (b) the $B2$-TiNi(100) surface: (*1*) titanium- and (*2*) nickel-terminated surfaces and (*3*, *4*) bulk calculations for two surface models, respectively. Points are the experimental data taken from [7]. The inset shows the theoretical dependence $\sigma(E)$ at energies up to 0.5 eV.

The optical absorption spectra were also calculated with due regard for the transition probability matrix element. However, as expected, the experimental intense absorption peak at 0.52–0.80 eV [7] manifests itself in the calculations of the $B19'$ phase only as a peak with a very low relative intensity, which agrees well with our earlier LMTO calculations [12]. The presence of this intense peak in the optical conductivity curve $\sigma(\omega)$ in the aforementioned energy range cannot be considered reliably revealed reasoning from the sole experimental work [7]. At the same time, it would be of interest to establish its possible origin on the basis of theoretical calculations. The probability of the Ti_3Ni_4 precipitation in the TiNi alloy is sufficiently high. Therefore, it was instructive to calculate the optical conductivity of this compound. The crystallographic data for Ti_3Ni_4 were taken from [24]. Figure 7 shows the calculated density of states for Ti_3Ni_4, which is in reasonable agreement with the results of the LMTO calculations carried out by Fukuda *et al.* [20]. The optical conductivities $\sigma(\omega)$, which were calculated for $B19'$-TiNi and Ti_3Ni_4, and the experimental dependence taken from [7] are displayed in Fig. 8a. The interband and intraband contributions are shown. The orientation dependence of the optical conductivity was included in the calculations. Note that the calculation of the optical conductivity in the IR range requires a high computational accuracy and integration over a large number of **k** vectors in the Brillouin zone. The shift in the theoret-

ical curves toward the high-energy range is associated with the use of the local-electron-density approximation. As can be seen from Fig. 8a, the $\sigma(\omega)$ curve for Ti_3Ni_4 well represents all the features of the experimental dependence for the martensitic phase and also the structure of the sharp peak in the range 0.52–0.80 eV. Unfortunately, as far as we know, the chemical composition of the samples was not controlled at all experimental stages. It would be tempting to attribute the peak at 0.52–0.80 eV to the Ti_3Ni_4 rhombohedral precipitate in the TiNi matrix and to argue that the experimental data in [7] were obtained for the sample that was not a pure *B*19' phase. Another possible explanation can be connected with the surface effect. The calculation of the electronic structure for the surface of the *B*19' martensitic phase is a sufficiently complex problem, which requires a large computational power. It is much easier to perform similar calculations for the *B*2 structure and to estimate the possible surface effect in this case. The results of calculations of the electronic structures of the (001) and (110) seven-layer surfaces will be reported in a separate work. The (001) surface can be terminated either with titanium atoms or with nickel atoms. Figure 8b shows the optical conductivity curves for these two variants (curves *1* and *2* correspond to the titanium- and nickel-terminated surfaces, respectively). It turns out that the first variant well reproduces the structure of the experimental dependence in the visible and IR ranges, namely, the experimental peaks at 0.085, 0.113, 0.17, 0.24, and 0.35 eV, which are not reproduced by the bulk calculations. Furthermore, an increase in the intensity in the IR range is determined only by the intraband contributions. The theoretical curve $\sigma(\omega)$ (interband contributions) in the IR range for the titanium-terminated surface (001) is depicted in the inset. The sharp peak at 0.17 eV is noteworthy. As follows from the calculated density of states, an increase in the number of titanium states near the Fermi surface is observed when passing from the bulk to the surface. It is possible that an even larger transformation of titanium states at the surface can occur in the martensitic phase, which can result in the formation of a sharp peak near 0.5 eV. On the other hand, according to Shabolovskaya [30], the surface composition very strongly depends on the procedure of treating a sample. The composition of surface layers can be changed and shifted toward the region enriched with nickel. Our calculations demonstrate that the titanium-terminated surface (001) in TiNi possesses a high chemical activity and reconstruction ability. It should be noted that a better insight into the electronic structure of the monoclinic martensitic phase calls for reliable experiments and new experimental data on the optical and x-ray spectra. At the same time, the results obtained make it possible to conclude that the general features in the electronic structure of the *B*19' martensitic phase are revealed. The rearrangement observed in the structure of the density of states in the range of the Fermi level and the changes in the electronic characteristics of the alloy are governed by the transformation of titanium states at the Fermi level. It is clear that the transition to the structure, which is described by the lattice parameters and the atomic positions determined in [4, 5], turns out to be reasonable from the standpoint of the band theory.

ACKNOWLEDGMENTS

We are grateful to K. Schwartz and P. Blaha (University of Technology, Vienna, Austria) for supplying the WIEN97 software package, which was used for performing the present calculations.

REFERENCES

1. F. E. Wang, W. J. Buehler, and S. J. Pickart, J. Appl. Phys. **36**, 3232 (1965).
2. K. Otsuka, T. Sawamura, and K. Shimizu, Phys. Status Solidi A **5**, 457 (1971).
3. R. F. Hehemann and G. D. Sandrock, Scr. Metall. **5**, 801 (1971).
4. G. M. Michal and R. Sinclair, Acta Crystallogr., Sect. B: Struct. Crystallogr. Cryst. Chem. **B37**, 1803 (1981).
5. Y. Kudoh, M. Tokonami, S. Miyazaki, and K. Otsuka, Acta Metall. **33**, 2049 (1985).
6. V. N. Khachin, Yu. I. Paskal', V. É. Gyunter, *et al.*, Fiz. Met. Metalloved. **46**, 511 (1978).
7. I. I. Sasovskaya, S. A. Shabolovskaya, and A. I. Lotkov, Zh. Éksp. Teor. Fiz. **77**, 3241 (1979) [Sov. Phys. JETP **50**, 1128 (1979)].
8. S. A. Shabolovskaya, Phys. Status Solidi B **132**, 327 (1985).
9. D. A. Papaconstantopoulos and D. J. Nagel, Int. J. Quantum Chem. **5**, 515 (1971).
10. V. E. Egorushkin and S. E. Kulkova, J. Phys. F **12**, 2823 (1982).
11. V. V. Nemoshkalenko, M. L. Miller, V. N. Antonov, and A. V. Zhalko-Titarenko, Metallofizika **9** (3), 119 (1987).
12. S. E. Kulkova, V. E. Egorushkin, and V. V. Kal'chikhin, Fiz. Tverd. Tela (Leningrad) **33**, 2828 (1991) [Sov. Phys. Solid State **33**, 1198 (1991)].
13. G. Bihlmayer, R. Eibler, and A. Neckel, J. Phys.: Condens. Matter **5**, 5083 (1993).
14. G. Bihlmayer, R. Eibler, and A. Neckel, Phys. Rev. B **50**, 13113 (1994).
15. G. Bihlmayer, R. Eibler, and A. Neckel, Phys. Mag. **73**, 511 (1996).
16. J. M. Zhang and G. Y. Guo, J. Phys.: Condens. Matter **7**, 6001 (1995).
17. G. L. Zhao, T. C. Leung, and B. N. Harmon, Phys. Rev. B **40**, 7999 (1989).
18. T. Hara, T. Ohba, and K. Otsuka, J. Phys. IV **5**, C8-641 (1995).
19. I. I. Sasovskaya and V. G. Pushin, Fiz. Met. Metalloved. **60** (5), 879 (1985).
20. T. Fukuda, T. Kakeshita, H. Houjoh, *et al.*, Mater. Sci. Eng. A **273–275**, 166 (1999).

21. P. Blaha, K. Schwartz, and J. Luits, *WIEN97* (Vienna Univ. of Technology, 1997). [Improved and updated Unix version of the origin copyrighted WIEN-code, which was published by P. Plaha, K. Schwartz, P. Sorantin, and S. B. Trickey; Comput. Phys. Commun. **59**, 399 (1990)].
22. J. P. Perdew, S. Burke, and M. Ernzerhof, Phys. Rev. Lett. **77**, 3865 (1996).
23. J. Yamashita and S. Asano, Prog. Theor. Phys. **48**, 2119 (1972).
24. T. Suburi, S. Nenno, and T. Fukuda, J. Less-Common Met. **125**, 92 (1986).
25. V. V. Nemoshkalenko, *X-ray Emission Spectroscopy of Metals and Alloys* (Naukova Dumka, Kiev, 1972).
26. V. A. Trofimova, K. M. Kolobova, and S. A. Nemnonov, in *Electronic Structure of Transition Metals, Their Alloys, and Intermetallic Compounds*, Ed. by V. V. Nemoshkalenko (Naukova Dumka, Kiev, 1979), p. 178.
27. G. Botton, G. Guo, W. Temmerman, and C. Humphreys, Phys. Rev. B **54** (3), 1682 (1996).
28. Y. Murakami, D. Shindo, K. Otsuka, and T. Oikawa, J. Electron Microsc. **47** (4), 301 (1998).
29. D. Pearson, C. Ahn, and B. Fultz, Phys. Rev. B **47** (14), 8471 (1993).
30. S. A. Shabolovskaya, J. Phys. IV **5**, C8-1199 (1995).

Translated by O. Borovik-Romanova

Physics of the Solid State, Vol. 43, No. 4, 2001, pp. 746–751. Translated from Fizika Tverdogo Tela, Vol. 43, No. 4, 2001, pp. 714–718.

LOW-DIMENSIONAL SYSTEMS AND SURFACE PHYSICS

Ground-State Energy of X^- and X^+ Trions in a Two-Dimensional Quantum Well at an Arbitrary Mass Ratio

R. A. Sergeev and R. A. Suris

Ioffe Physicotechnical Institute, Russian Academy of Sciences, Politekhnicheskaya ul. 26, St. Petersburg, 194021 Russia
e-mail: rinat@theory.ioffe.rssi.ru

Received July 27, 2000

Abstract—A simple model variational function is proposed for an adequate unified description of X^+ and X^- two-dimensional trions over the entire range of electron-to-hole mass ratios with the use of a minimum number of variable parameters. © *2001 MAIK "Nauka/Interperiodica".*

1. INTRODUCTION

The bound electron–hole complexes which involve either two electrons and a hole (trion X^-) or two holes and one electron (trion X^+) are referred to as trions. X^- and X^+ trions represent formations composed of two identical Fermi particles bound by Coulomb forces on a third particle that possesses a charge equal in magnitude but opposite in sign. The mass of the third particle does not necessarily coincide with masses of the two other particles. The dependence of the energy of a trion complex on the mass ratio of its constituent particles is the subject of our investigation. An adequate model of a trion should describe the complex at any mass ratio of its constituent particles and, in the limit, lead to the known objects, such as a hydrogen ion H^-, a hydrogen molecule H_2^+, a D^- center in a semiconductor (two electrons bound on a positively charged center), a positronium ion (two electron + positron), etc.

The practical necessity of investigating similar objects first arose in chemistry in the late 1920s for the description of lithium hydride, in particular, the interaction between Li^- and H^- ions (Hylleraas [1]). In 1929, Bethe [2] performed the first theoretical calculation of an H^- ion by using a variational method with three variable parameters.

In the forties, the properties of a negative hydrogen ion were invoked for explaining the solar and solar-type atmospheric opacities. This required an essential refinement of the results obtained earlier by Bethe. For the most part, attempts were reduced to a simple increase in the number of variational parameters [3–5]. However, more exact variational functions were also sought by researchers. In 1944, a certain success in this field was achieved by Chandrasekhar [6].

Three-particle electron–hole complexes (trions) in semiconductors were predicted in 1958 by Lampert [7]. The experimental investigation of trions involved considerable difficulties due to the low characteristic binding energy of this complex (tenths of meV), which imposed rigid restrictions on the temperature of their possible observation (~1 K).

More recently, interest in trions was rekindled with advances in the field of heterostructures and the advent of molecular engineering—the creation of artificial objects or the control over parameters of the existing objects by using quantum-well structures (wells, wires, and dots). In particular, theoretical calculations performed in the 1980s demonstrated that the binding energy of a trion in a semiconductor structure with a quantum well can increase substantially (by the order of magnitude) [8–10]. This opened up fresh opportunities for experimental observations of trions in these structures, which was realized in 1992 by Kheng *et al.* [11].

Since that time, trions of both types have been repeatedly observed in different heterostructures at low temperatures. The possibility of investigating these objects in practice has stimulated theoretical interest in them.

The difference between a trion and an H^- ion (or H_2^+ molecule) resides in the fact that the ratio of the effective masses of the electron and the hole constituting the complex is not a small quantity and the wave functions of electrons and holes cannot be separated. It is interesting that different electron-to-hole mass ratios can be realized in different semiconductors. As a result, the X^- and X^+ complexes can qualitatively change in their structures and properties from the positronium ion in one limit (at equal masses of the electron and the hole) to the H^- ion or the H_2^+ molecule in the other limit (at electron mass $\ll$ hole mass). Trions are in fact natural intermediate objects between H^- and H_2^+. When studying the X^- and X^+ complexes at different electron-to-hole mass ratios, we can gradually change over from the negative ion to the positively charged molecule, which, taking into account the large difference between

these two objects, is of great theoretical and experimental interest.

A considerable number of works concerned with calculations of the energy and wave functions of trions at different mass ratios have been published in recent years [12–15]. The parameters of these complexes have also been investigated as functions of the well width [16, 17] and the magnetic field strength [18–21].

The present paper is devoted to the study of the X^- and X^+ trions in an infinitely deep quantum well (within the two-dimensional approximation) at all mass ratios in the absence of an external magnetic field. One of the problems in present-day calculations of trions is a poor behavior of trial variational functions of the X^+ trion in the case when the electron-to-hole mass ratio tends to zero, i.e., in the limit of the H_2^+ molecule. The problem lies in the fact that the complex in this limit involves two infinitely heavy particles, and, hence, the wave function of this system should take the form of a δ function of the distance between these particles. Therefore, it is at a small mass ratio that the wave function and the energy of the X^+ trion begin to change drastically. It is known that the formation energy for an H_2^+ molecule (H + p) is almost four times higher than that for the H^- ion (H + e). As follows from calculations [8, 10, 12], the characteristic binding energy ratio for a trion and the corresponding exciton is virtually independent of the electron-to-hole mass ratio μ for the X^- complex and slowly increases for the X^+ complex with a change in the mass ratio μ from the positronium ion ($\mu = 1$) to the H_2^+ molecule ($\mu = 0$). In this case, the binding energy of the X^+ trion predominantly changes at small mass ratios ($\mu < 0.1$). In this range of mass ratios, the binding energy of the trion changes by almost a factor of two. In actual fact, at the mass ratio in the range $\mu \in 0.1 - 0.3$, the structure of a wave function similar to that of the H^- ion qualitatively transforms into the structure of a wave function similar to that of the H_2^+ molecule.

All the previous calculations were performed using trial functions which were based on the structure of an H^- ion and gave no way of describing two infinitely heavy particles in the H_2^+ molecule. In the limit of an H_2^+ molecule, these trial functions either led to inadequate results or required the use of a large number of variable parameters in order to ensure the aforementioned δ-functional dependence. For this reason, the use of these trial functions became, at least, inefficient.

In this work, we proposed a relatively simple variational function which depends on a small number of parameters and adequately describes both X^- and X^+ complexes at any electron-to-hole effective mass ratios in the rigorously two-dimensional case.

2. MODELS AND THE WAVE FUNCTION

Two models of a trion can be considered qualitatively.

(1) In the limit H^-, there is the model of a heavy nucleus with two light electrons which are localized in its vicinity and strongly screen each other. Within this model, the trion is well described by a two-dimensional analog of the variational function proposed by Chandrasekhar [6]:

$$\psi(\mathbf{r}_1, \mathbf{r}_2) = (\exp(-ar_1 - br_2) + \exp(-br_1 - ar_2))(1 + c|\mathbf{r}_1 - \mathbf{r}_2|). \quad (1)$$

This function consists of the symmetrized exciton-like part with different electron orbit radii and the polarization factor. The quantities $\mathbf{r}_1$ and $\mathbf{r}_2$ are the two-dimensional vectors from the nucleus to electrons. The variational parameters a and b have the meaning of orbit radii of two electrons, and the parameter c ensures an increase in the wave function with an increase in the distance between electrons; i.e., it accounts for the polarization effects. This wave function adequately represents the singlet state of trions over the entire range of mass ratios, except for trions similar in structure to the H_2^+ molecule, i.e., the X^+ complexes with the mass ratio $\mu < 0.1$. Despite a small number of variational parameters (only three), it is known that this function for three measurements reproduces the energy of the H^- ion with an accuracy of 10% [22].

(2) In the limit H_2^+, there is the model of a molecule, i.e., the model of two heavy nuclei and an electron residing on a bonding orbital. In the ground state, this system is well described by the following function:

$$\psi(\mathbf{r}_1, \mathbf{r}_2) = (\exp(-ar_1) + \exp(-ar_2))\Re(|\mathbf{r}_1 - \mathbf{r}_2|). \quad (2)$$

This function is composed of the sum of two hydrogen-like wave functions [23], which is multiplied by the wave function of the relative motion of nuclei $\Re(R)$, where $R = |\mathbf{r}_1 - \mathbf{r}_2|$.

In the limit of an infinite nucleus mass, the $\Re(R)$ function should transform into a δ-like function of $R - R_0$ (where R_0 is the minimum of the binding potential). In the case when the nucleus masses are large but not infinite, the $\Re(R)$ function at large R should decrease as $\exp(-sR)$, where $s = \sqrt{-2m_hE/\hbar^2}$, E is the binding energy of the given trion with respect to the decay into a free exciton and a hole, and m_h is the hole mass. In the vicinity of R_0, the $\Re(R)$ function should follow the relationship $\Re(R) \sim \exp(-d(R - R_0)^2)$; in this case, if the electron-to-nucleus mass ratio tends to zero, the parameter d should tend to infinity.

3. THE GROUND STATE OF X^+ AND X^- TRIONS

In the absence of a magnetic field, the ground state of the X^+ and X^- complexes is their singlet state, i.e.,

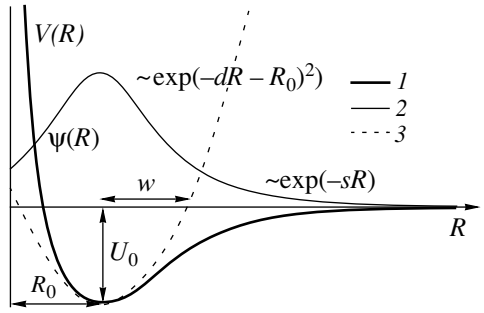

Fig. 1. Structure of an H_2^+ molecule: (*1*) the qualitative form of the potential binding nuclei in H_2^+, (*2*) the parabolic approximation of the binding potential near the potential well bottom, and (*3*) the qualitative dependence of the wave function for H_2^+ on the internuclear separation.

the state with the antiparallel spin orientation of two identical Fermi particles (electrons for X^- and holes for X^+). At present, it is believed that this ground state of the X^- trion is the sole state. In any case, there is no theoretical or experimental evidence for excited states of this complex. A different situation occurs in the X^+ complex, because the H_2^+ molecule obtained in the limit $\mu \longrightarrow 0$ at an infinite mass of nuclei possesses an infinite discrete spectrum of vibrational and rotational levels.

A "good" function for describing the ground state of both trions at any masses of their constituent particles will be constructed as follows.

(i) The entire range of mass ratios is divided into two ranges, in each of which the trion can be described by the aforementioned, relatively simple models. To put it differently, we assume that the trion at any electron-to-hole mass ratio is described by a wave function similar in structure to the wave function either for the H^- ion (two particles "rotate" about one particle) or for the H_2^+ molecule (one particle binds the two other particles). The conventional division into these two ranges does not correspond to the division of trions into the X^- and X^+ trions. As was noted above, the conventional boundary corresponds to the mass ratio $\mu \sim 0.1$–0.3 for the X^+ complex.

(ii) In the framework of each model, we choose the simplest (with a minimum number of variable parameters) wave function which adequately describes the trion in this approximation. In this case, the trion wave functions that correspond to different models should be as closely similar in structure as possible, and the maximum number of variational parameters of one wave function should be used in the other function. Functions (1) and (2) considered above meet these requirements. It is easy to see that the polarization-free term $(\exp(-ar_1 - br_2) + \exp(-br_1 - ar_2))$ in the wave function (1) structurally corresponds to the electronic term $(\exp(-ar_1) + \exp(-ar_2))$ in function (2). Moreover, the term $(\Re(|\mathbf{r}_1 - \mathbf{r}_2|))$, which is responsible for the relative motion of nuclei in function (2), corresponds to the polarization term $(1 + c|\mathbf{r}_1 - \mathbf{r}_2|)$ in function (1).

(iii) The sought trial function is constructed as a combination of the two wave functions chosen in the preceding item. The structural similarity of the chosen wave functions allows us to reduce the total number of variable parameters in the final function.

The sought trial variational function obtained by combining the above functions (1) and (2) is represented as

$$\psi(\mathbf{r}_1, \mathbf{r}_2) = (\exp(-ar_1 - br_2) + \exp(-br_1 - ar_2)) \times \frac{1 + cR}{1 + d(R - R_0)^2}\exp(-sR), \quad (3)$$

where $R = |\mathbf{r}_1 - \mathbf{r}_2|$ and a, b, c, d, R_0, and s are the variational parameters.

These parameters have the following physical meaning: a and b are the reciprocals of the radii of two identical particles localized on the third particle with allowance made for their mutual screening, the parameter c accounts for the polarization effects, the parameter d describes the longitudinal vibrations of two identical particles with respect to each other, R_0 is the mean interparticle distance, and the parameter s optimizes the wave function at infinity.

It is obvious that the above wave function involves the wave function (1) of the negative ion H^- (at $d, s = 0$) and the wave function (2) of the positive molecule H_2^+ (at $b, c = 0$), and the additional parameters only lead to a better result in both limiting cases. It is also easy to justify the choice of the factor $(1 + d(R - R_0)^2)^{-1}$ in function (3), which is responsible for longitudinal vibrations of the complex.

It should be noted that, in the case when the binding between two identical particles of the trion can be described by a parabolic potential (Fig. 1), the wave function (3) should exhibit a Gaussian dependence on R (the distance between these two particles), $\psi(R) \sim \exp(-d(R - R_0)^2)$. However, a strictly parabolic potential can describe only very small vibrations of the X^+ complex and only in the limit of the H_2^+ molecule. In reality, the potential binding two identical particles in a trion at large distances is considerably weaker than the parabolic one and the Gaussian approximation of the trion wave function leads to its substantially faster decrease with distance as compared to the actual dependence. Hence, we used a weaker dependence $\psi(R) \sim 1/(1 + d(R - R_0)^2)$, which, to a first approximation, adequately describes the trion vibrations near $R = R_0$, and the behavior of the $\psi(R)$ function at infinity was specified by a weaker factor $\exp(-sR)$ as compared to the Gaussian function.

As a consequence, we derive the wave function (3), which, in both limits, should lead to the results not worse than those obtained with functions (1) and (2) and shows promise of obtaining a good approximation for the trion energy over the entire range of electron-to-hole mass ratios with a minimum number of variational parameters.

4. RESULTS AND DISCUSSION

Figure 2 shows the dependence of the trion binding energy normalized to the energy of the corresponding two-dimensional exciton (hereafter, this energy will be considered to mean the trion binding energy) on the electron-to-hole mass ratio, which was calculated with our variational function (3). For comparison, the dependence (converted in terms of the same variables) obtained by Stebe and Ainane [10] with the use of the variational method including 22 parameters is also depicted in Fig. 2.

Despite the considerable difference in the numbers of fitting parameters (6 and 22), these dependences are in good agreement. Our results reproduce the data obtained in [10] with an accuracy of better than 5% over the entire range of mass ratios, except for the limit H_2^+ (at $\mu < 0.1$). Note that the error obtained turned out to be even smaller than the error (~10%) of the calculation with the use of the Chandrasekhar wave function (1) in the limit of the H^- ion. This illustrates the fact that functions (1) and (2) combined above into function (3) noticeably improve and complement each other. It is worth noting that the error (<5%) in the determination of the trion energy is approximately the same for all the mass ratios. This gives grounds to conclude that our variational function (3), which is constructed from the wave functions of the H^- ion and the H_2^+ molecule, makes it possible to describe equally well the entire range of mass ratios rather than only these limiting cases.

Of special interest is the limit H_2^+ ($\mu < 0.1$). As was already mentioned, the problem lies in the fact that the X^+ trion at these masses acquires a pronounced molecular structure. Therefore, the wave functions based only on the structure of the H^- ion (among them was the function used in [10]) cease to give good results even with a large number of variational parameters. For this reason, the dependence calculated in [10] terminates at the mass ratio $\mu = 0.1$ in Fig. 2. In our opinion, even in this case, the accuracy of the results obtained with our function (3) is no less than before. For comparison, we note that the trion energy (0.41) calculated in the present work at $\mu = 0$ completely coincides with that obtained by Varga [24].

The results of our calculations and the theoretical dependence obtained by Thilagam [12] with the use of the averaged binding potential of a trion are also compared in Fig. 2. It should be noted that, unlike the

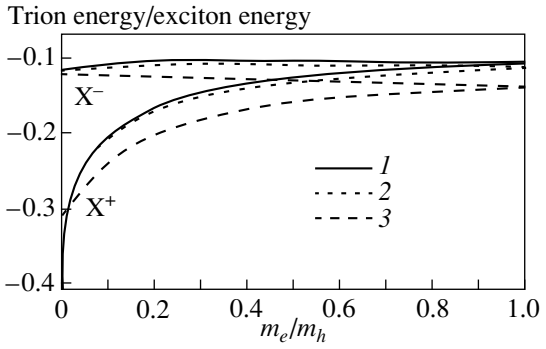

Fig. 2. Dependences of the trion binding energy on the electron-to-hole mass ratio: (*1*) this work, (*2*) variational calculations with 22 variable parameters [10], and (*3*) the approximation of model trion potential [12].

results obtained by variational methods, the trion binding energy reported in [12] is not of necessity less than the exact energy of the complex. However, a qualitative comparison between our dependence and that obtained in [12] enables us to draw the same inference: the dependences qualitatively agree over the entire range of mass ratios, except for the aforementioned H_2^+ limit ($\mu < 0.1$). In this limit, the trion energy calculated within the model proposed in [12] is almost a quarter less than that in our case. This is explained by the fact that the trion model used in [12] for calculating the dependence under consideration is well applied to the complexes with a structure similar to that of the H^- ion but leads to failures when changing over to the H_2^+ structure (see also [24, 25]). This is another example of how models and approximations well describing the X^- and X^+ trions over a wide range of masses are inapplicable in the limit of the H_2^+ molecule. This is the reason why the inclusion of the H_2^+ model is so important in the construction of the general trion model.

It should be emphasized that the trion energy (normalized to the exciton energy) for X^- is virtually constant (≈0.12) and does not depend on the electron-to-hole mass ratio, whereas the trion energy for X^+ increases as the limit H_2^+ is approached and the main increase is observed in the least studied range $\mu \le 0.1$. In this range, the trion energy increases from 0.22 (at $\mu = 0.1$) to 0.41 (at $\mu = 0.0$) by almost a factor of two.

Let us now interpret this fact in the framework of our models. Note that the mass ratio range $\mu \le 0.1$ corresponds to the case of two heavy holes and a nucleus that are bound through an electron into a molecule. It can be assumed that the electron wave function has had time to adapt adiabatically to the slow motion of holes for which the binding interatomic potential approximation [23] becomes applicable. In this case, the problem is reduced to the motion of a hole with the reduced mass $m_h/2$ in the two-dimensional potential $V(R)$,

which is the sum of the electron binding potential and the Coulomb repulsion potential of holes. A qualitative form of the $V(R)$ potential is depicted in Fig. 1. At large hole masses, it is believed that the hole wave function is localized in the vicinity of R_0, i.e., the minimum of the $V(R)$ potential. Then, within the parabolic-potential approximation, we have

$$V(R) \approx V(R_0) + \frac{\kappa}{2}(R - R_0)^2. \quad (4)$$

In this approximation, the trion binding energy is given by

$$E_{tr}(\mu) \approx V(R_0) + \frac{\hbar\omega}{2} \quad (5)$$

and the quantity $\hbar\omega$ is written as

$$\hbar\omega = \hbar\sqrt{\frac{\kappa}{m_h}} = \sqrt{\frac{\hbar^2}{m_h}\left.\frac{\partial^2 V(R)}{(\partial R)^2}\right|_{R = R_0}}. \quad (6)$$

The quantity $\partial^2 V(R)/(\partial R)^2|_{R = R_0}$ can be evaluated from the depth U_0 and the half-width w of the potential well formed by the potential $V(R)$, that is,

$$\left.\frac{\partial^2 V(R)}{(\partial R)^2}\right|_{R = R_0} \sim 2\frac{U_0}{w^2}. \quad (7)$$

It is clear that the well depth can be estimated as $U_0 = V(R_0) = E_{tr0}$ (the trion binding energy at $\mu = 0$). In order to evaluate the well half-width, we note that $w < 2R_0$ since the potential $V(R) \longrightarrow +\infty$ at $R \longrightarrow 0$ due to the Coulomb repulsion of holes. On the other hand, we can assume that $w > R_0/2$, because both the hole Coulomb repulsion potential and the electron binding potential substantially decrease only at distances $R > 2R_0$. Hence, it follows that

$$\frac{1}{2}\frac{E_{tr0}}{R_0^2} < \left.\frac{\partial^2 V(R)}{(\partial R)^2}\right|_{R = R_0} < \frac{8E_{tr0}}{R_0^2}. \quad (8)$$

As an estimate, we set

$$\left.\frac{\partial^2 V(R)}{(\partial R)^2}\right|_{R = R_0} \approx \frac{2E_{tr0}}{R_0^2}. \quad (9)$$

The optimum interatomic distance R_0 in a two-dimensional molecule H_2^+ is as follows:

$$R_0 \approx 0.5a_0, \quad (10)$$

where a_0 is the three-dimensional Bohr radius. Then, taking into account the dependence of the exciton binding energy on the mass ratio, that is,

$$E_{ex}(\mu) = -\frac{2}{1+\mu}\frac{\hbar^2}{m_e a_0^2}, \quad (11)$$

from formulas (5)–(11), we obtain

$$\frac{E_{tr}(\mu)}{E_{ex}(\mu)} = (1+\mu)\frac{E_{tr}(0)}{E_{ex}(0)} + \sqrt{\mu}(1+\mu)\sqrt{\frac{E_{tr}(0)}{E_{ex}(0)}} \quad (12)$$
$$\approx 0.41(1+\mu) - 0.64\sqrt{\mu}(1+\mu).$$

As can be seen, the trion energy in the limit of the H_2^+ molecule (at small μ) depends on the mass ratio as a square root. For the electron-to-hole mass ratio $\mu = 0$, the trion-to-exciton energy ratio is represented as

$$\frac{E_{tr}(0.0)}{E_{ex}(0.0)} \approx 0.41,$$

whereas relationship (12) even at the mass ratio $\mu = 0.1$ leads to an almost twofold decrease in the trion-to-exciton binding energy ratio, that is,

$$\frac{E_{tr}(0.1)}{E_{ex}(0.1)} \approx 0.23.$$

With due regard for the approximate character of the estimates performed, this result is in excellent agreement with the calculated ratio of 0.22.

In conclusion, it can be noted that simple qualitative considerations on the basis of the wave functions for the H^- ion and the H_2^+ molecule allowed us to construct the trial function which makes it possible to describe adequately both trions over the entire range of mass ratios with the use of a not very large number of variable parameters. Recall that the results reported in [10] were obtained with 22 variable parameters, whereas we used only six parameters. This provides a means of applying the proposed models to the construction of trial functions for variational calculations in more complex cases, specifically for the trion in a well of a finite width or in the presence of a magnetic field.

ACKNOWLEDGMENTS

This work was supported in part by the Russian Foundation for Basic Research (project no. 99-02-16796) and the "Scientific School" (project no. 00-15-96812).

REFERENCES

1. E. A. Hylleraas, Z. Phys. **63**, 771 (1930).
2. H. A. Bethe, Z. Phys. **57**, 815 (1929).
3. E. A. Hylleraas, Z. Phys. **63**, 291 (1930).
4. L. R. Henrich, Astrophys. J. **99**, 59 (1944).
5. E. A. Hylleraas and J. Midtdal, Phys. Rev. **103**, 829 (1956).
6. S. Chandrasekhar, Astrophys. J. **100**, 176 (1944).
7. M. A. Lampert, Phys. Rev. Lett. **1** (12), 450 (1958).
8. B. Stebe and C. Comte, Phys. Rev. B **15** (8), 3967 (1977).

9. R. Schilling and D. C. Mattis, Phys. Rev. Lett. **49** (11), 808 (1982).
10. B. Stebe and A. Ainane, Superlattices Microstruct. **5** (4), 545 (1989).
11. K. Kheng, R.T. Cox, Y. M. d'Aubigne, *et al.*, Phys. Rev. Lett. **71** (11), 1752 (1993).
12. A. Thilagam, Phys. Rev. B **55** (12), 7804 (1997).
13. K. Varga and Y. Suzuki, Phys. Rev. A **53** (3), 1907 (1996).
14. Y. K. Ho, Phys. Rev. A **48** (6), 4780 (1993).
15. N. P. Sandler and C. R. Proetto, Phys. Rev. B **46** (12), 7707 (1992).
16. B. Stebe, G. Munschy, L. Stauffer, *et al.*, Phys. Rev. B **56** (19), 12454 (1997).
17. C. Riva, F. M. Peeters, and K. Varga, Phys. Status Solidi A **178** (1), 513 (2000).
18. B. Stebe, E. Feddi, and G. Munschy, Phys. Rev. B **35** (9), 4331 (1987).
19. B. Stebe, A. Ainane, and F. Dujardin, J. Phys.: Condens. Matter **8** (29), 5383 (1996).
20. J. J. Quinn, A. Wojs, I. Szlufarska, and K. S. Yi, Phys. Rev. B **60** (16), 11273 (1999).
21. A. B. Dzyubenko, Solid State Commun. **113** (12), 683 (2000).
22. H. A. Berhe and E. E. Salpeter, *Quantum Mechanics of One- and Two-Electron Atoms* (Springer-Verlag, Berlin, 1957).
23. L. D. Landau and E. M. Lifshitz, *Course of Theoretical Physics*, Vol. 3: *Quantum Mechanics: Non-Relativistic Theory* (Nauka, Moscow, 1974; Pergamon, New York, 1977), Problems of Paragraphs 81, 82.
24. K. Varga, Phys. Rev. B **57** (20), 13305 (1998).
25. A. Thilagam, Phys. Rev. B **57** (20), 13307 (1998).

Translated by O. Borovik-Romanova

Physics of the Solid State, Vol. 43, No. 4, 2001, pp. 752–762. Translated from Fizika Tverdogo Tela, Vol. 43, No. 4, 2001, pp. 719–729.

LOW-DIMENSIONAL SYSTEMS AND SURFACE PHYSICS

Exciton Energy Relaxation on Acoustic Phonons in Double-Quantum-Well Structures

D. A. Mazurenko and A. V. Akimov

Ioffe Physicotechnical Institute, Russian Academy of Sciences, Politekhnicheskaya ul. 26, St. Petersburg, 194021 Russia
e-mail: akimov@os.ioffe.rssi.ru

Received May 12, 2000; in final form, September 5, 2000

Abstract—The paper analyzes the rate of energy relaxation involving acoustic phonon emission between exciton states in a double quantum well. A theoretical study is made of the part played by two mechanisms, one of which is a one-step transition with emission of an acoustic phonon and the other is a two-step transition, which includes elastic exciton scattering from interface nonuniformities followed by energy relaxation within an exciton subband. The rate of the two-step transition in real double quantum wells is shown to be higher than that of the one-step transition. As follows from calculations, the fast energy relaxation between exciton states is determined by the elastic scattering of phonons from the interface.

INTRODUCTION

The double quantum well (DQW) is one of the simplest model objects to study tunneling through a potential barrier [1]. The interest in this object stems primarily from the fact that present-day technologies are capable of creating structures with predetermined parameters (layer thickness, barrier height) whose scatter introduced in the course of manufacture is extremely small. This substantially reduces the interaction of carriers and excitons with nonuniformities (heterojunction defects, composition nonuniformities, impurities).

The DQW consists of two quantum wells separated by a thin barrier transparent to tunneling. At low temperatures, the carriers become bound rapidly to form excitons [2]; therefore, exciton effects play an essential role in the optical properties of DQWs [3]. A DQW may have excitons of two types, direct and indirect (Fig. 1). The indirect exciton (IX) is formed by an electron and a hole which reside in different quantum wells and are bound by Coulomb interaction; the direct exciton (DX) is made up by an electron and a hole located in the same quantum well. The indirect exciton has a very large radiative lifetime ($>10^{-6}$ s [4, 5]), which exceeds that of the direct exciton by several orders of magnitude ($\sim 10^{-9}$ s [6]). Since the electron and the hole in an indirect exciton state are spatially separated, the binding energy of the IX is less than that of the DX (for instance, the IX binding energy in a DQW with quantum well widths of 10 nm and a barrier a few nm thick is ~3–4 meV [3, 7, 8], whereas the binding energy of a DX is 8 meV [3]).

The energy position of an IX with respect to a DX can be varied by properly varying the electric field applied to the DQW. Because the IX is a dipole, its recombination energy depends linearly on the electric field [3, 9], whereas in weak fields (<10 kV/cm), it is practically electric-field independent. Figure 1b shows schematically the exciton-state recombination energy as a function of the electric field perpendicular to the DQW plane. At certain values of the electric field, the energies of some exciton states become equal and energy resonance sets in. Two of such resonances presented in Fig. 1b involve pairs of exciton states whose electronic parts of the wave functions are localized in different quantum wells (they are identified in the scheme by dashed circles). The other two (shown by dotted triangles) involve the pairs of the exciton states whose electronic wave-function parts coincide, but the hole parts are localized in different quantum wells. One more resonance, specified by a dashed square, corresponds to a pair of the exciton states in which both hole and electronic parts of the wave functions are different. Tunneling interaction between these pairs of states near the resonance gives rise to the repulsion of exciton levels, a phenomenon well known in quantum mechanics. In this case, the wave functions of exciton states represent linear combinations of the unperturbed DX and IX wave functions. The repulsion of exciton energy states near resonance is experimentally observed only for the pair of exciton states which differ in the electronic part of the wave function [3, 7–10]. The exciton splitting between exciton states at resonance for the other pairs turns out to be too small to be detected experimentally because the hole component of the exciton wave function penetrates only weakly into the barrier.

Investigation of the rate of exciton energy relaxation in a DQW is an essential problem, which is currently attracting the attention of researchers. If the energy separation Δ between the first-size-quantized exciton states in two quantum wells exceeds the optical phonon energy [2, 11–14], the corresponding transition time, determined by the interaction of excitons with optical

1063-7834/01/4304-0752$21.00

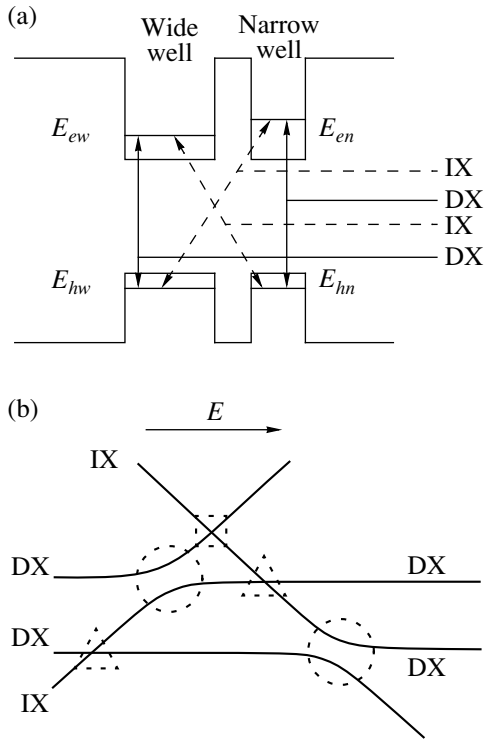

Fig. 1. (a) DQW band diagram and exciton states; (b) schematic relating the exciton-state recombination energy to the electric field applied perpendicular to the DQW plane. The circles identify the region of resonance between exciton states differing in the wave-function electron component; the triangles show the resonance of the IX and DX differing in the wave-function hole component; and the square specifies the region where the two states differing in electronic and hole components of the wave function are at resonance.

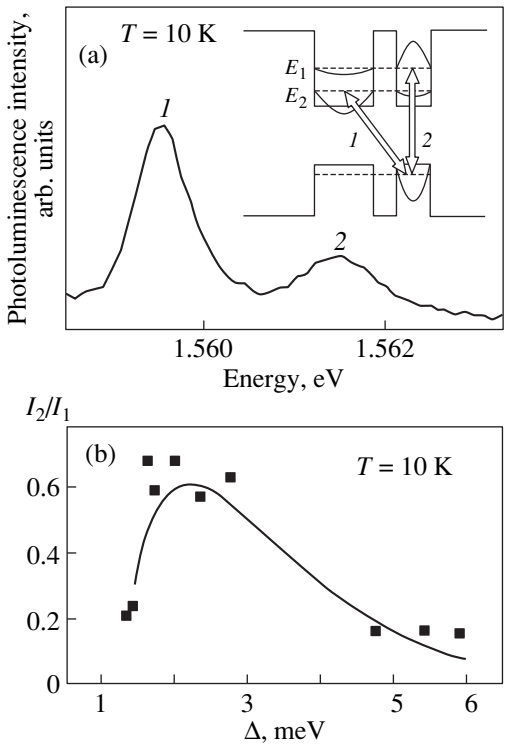

Fig. 2. (a) DQW photoluminescence spectrum measured at $T = 10$ K with an electric field $U = 0.2$ V applied perpendicular to the DQW plane. The inset shows the diagram of exciton transitions *1* and *2*; (b) experimental (symbols) and theoretical (solid line) ratios I_2/I_1 of the photoluminescence line intensities of exciton states *2* and *1* plotted vs. the energy spacing between exciton levels Δ for $T = 10$ K.

phonons, is ~10–100 ps, depending on the actual DQW parameters.

In the case where the difference between the energy levels in two quantum wells is less than the optical phonon energy, the transition time between exciton states differing in the electronic component of the wave function is determined by the coupling with acoustic phonons and, accordingly, should increase substantially compared with the exciton–phonon transitions involving an optical phonon.

Data on the rate of energy relaxation between exciton states, which is determined by interaction with acoustic phonons, have been recently obtained from an experimental study of stationary photoluminescence (PL) in a slightly asymmetric DQW [7, 8]. The structure under study was a $CaAs/Al_{0.33}Ca_{0.67}As$ DQW with quantum wells 9.6 and 10.2 nm thick separated by a 3.8-nm thick barrier. The PL spectrum of this DQW measured at $T = 10$ K is shown in Fig. 2a. One readily sees two narrow, well-resolved exciton lines. The energy splitting between the exciton levels at the DX–IX resonance (which is governed by the electron coherent tunneling) is $\delta = 1.3$ meV. The inset to Fig. 2a shows schematically the wave functions of the exciton states (*1* and *2*) and the radiative transitions corresponding to these states. The solid line in Fig. 2b plots the PL intensity ratio I_2/I_1 for $T = 10$ K, which was calculated under the assumption of the exciton states *1* and *2* being in thermodynamic equilibrium by means of the relation [7]

$$\frac{I_2}{I_1} = \frac{\Delta \pm (\Delta^2 - \delta^2)^{1/2}}{\Delta \mp (\Delta^2 - \delta^2)^{1/2}} \exp\left(-\frac{\Delta}{k_B T}\right), \qquad (1)$$

where δ is the energy splitting between the exciton levels at resonance ($\delta = 1.3$ meV) and Δ is the energy spacing between exciton states *1* and *2*. The squares are experimental data [7]. The good agreement between the experimental data and the I_2/I_1 ratio calculated from Eq. (1) permits the conclusion that the exciton states coupled by the transition of the "exciton" electron are in thermodynamic equilibrium. This means that the rates $w_{2\to1}$ and $w_{1\to2}$ of the exciton–phonon transitions involving the emission and absorption of phonons, respectively, far exceed the DX radiative

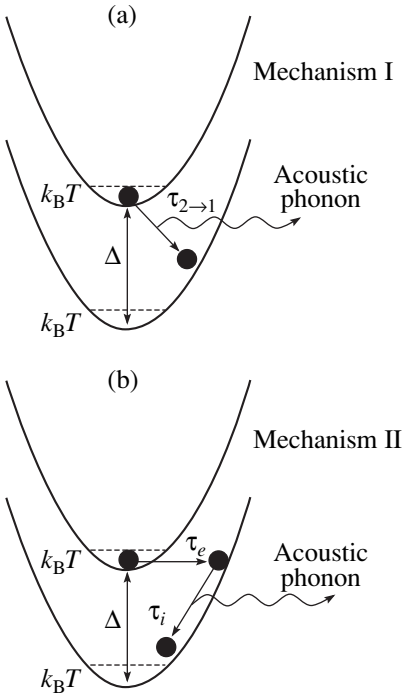

Fig. 3. Two mechanisms of transition between exciton states: (a) one-step transition with emission of an acoustic phonon and (b) two-step transition involving elastic exciton scattering from an impurity with subsequent relaxation within an exciton subband.

recombination rate $w_R \sim 10^9$ s^{-1} for $T \geq 10$ K and $\Delta \sim k_BT$.

This work is aimed primarily at theoretical calculation of the transition rate between exciton states in the case where acoustic phonons are involved in the process. For the sake of definiteness, we are going to consider only the $2 \longrightarrow 1$ transitions involving phonon emission at $T = 0$ (Fig. 3). In a real DQW, this energy relaxation can proceed in two ways.

(I) One-step transition I (Fig. 3a). This transition transfers an exciton from one exciton subband to the other while changing the exciton energy and wave vector. The acoustic phonon emitted in this transition provides preservation of the energy and momentum conservation laws.

(II) Two-step transition II (Fig. 3b). This transition can take place in a real DQW with quantum-well thickness fluctuations, which act as exciton scattering centers. The transition proceeds in two stages. In the first stage, the exciton is scattered elastically from an impurity or interface nonuniformity to transfer to the other subband, a process in which the momentum of the exciton is changed, but its total energy is preserved. In the second stage, the interaction with a phonon changes the exciton energy within the exciton subband.

The question of which, the one- or two-step, transition mechanism is responsible for the energy relaxation between the exciton states presently remains open. Experiments with nonequilibrium phonons also did not provide a definite answer to this question [15]. The interest in this problem is also connected with the possibility of using tunnel structures as a frequency-tunable acoustic-phonon detector (phonon spectroscopy) [16–19].

In this work, we shall calculate the probability $w_{2\to1}$ of an electron transition from a higher- to a lower-energy exciton state in a symmetric DQW, proceeding at $T = 0$ and involving the emission of an acoustic phonon, for different Δ. We assume that, at low temperatures, $k_BT \leq \Delta$, the $w_{2\to1}$ is affected primarily by spontaneous acoustic-phonon emission. In these conditions, one can also neglect the exciton distribution in k in the high-energy state. Thus, the $T = 0$ approximation will adequately describe the experimental situation considered above. The calculation of $w_{2\to1}$ will be carried out separately for the inelastic (one-step) transition mechanism I (Fig. 3a) and mechanism II (the two-step one), in which the exciton electron scatters elastically from interface nonuniformities, following which exciton energy relaxation occurs (Fig. 3b). We shall show the differences in the dependence of $w_{2\to1}$ on Δ between the transitions proceeding in mechanisms I and II. We shall also construct angular dependences of the emitted acoustic phonons in the case where DX and IX are in resonance ($\Delta = \delta = 1.3$ meV), as well as far from resonance for the one-step transition mechanism I. Section 1 will present analytical expressions for the transition probability between the exciton states $w_{2\to1}$ for mechanisms I and II. In Section II, we shall give the results of a numerical calculation of the one-step-transition probability $w_{2\to1}$ and estimate the probabilities of the two-step transition by mechanism II. We are also going to construct the angular dependences of the flux of acoustic phonons generated in the transition by mechanism I between the exciton states. In Section 3, we shall use the results of the calculation to compare the parts played by mechanisms I and II in the fast energy relaxation between the DQW exciton states, which accounts for the experimentally observed thermodynamic equilibrium, and draw the corresponding conclusions.

1. EXCITON–PHONON COUPLING

We are going to present here the main relations governing the rate of energy relaxation between the exciton states, which involves acoustic phonons. We shall assume the DQW to consist of two identical quantum wells separated by a barrier transparent to tunneling. Our problem consists in determining the transition probability between exciton states *1* and *2* with different electronic components of the wave functions (see inset to Fig. 2a). We shall also assume for definiteness that the high-energy state *2* corresponds to a direct exci-

ton and the low-energy state *1* is an indirect-exciton-type state. Our calculation of the energy relaxation will take into account only the transitions from the high- to the low-energy exciton state at $T = 0$ which are accompanied by phonon emission.

1.1. Energy Relaxation between Exciton States in an Ideal DQW

In an ideal DQW, a transition between exciton states is possible only through exciton–phonon coupling, which makes possible the one-step transition (inset to Fig. 2a) from high-energy state *2* (with wave vector $k_2 \sim 0$) to low-energy exciton state *1*.

For definiteness, we assume the hole to be localized in the right-hand quantum well (see inset in Fig. 2a). We shall also assume subsequently that the energy spacing Δ between the exciton states does not exceed the binding energy of the indirect exciton. Otherwise, transitions involving ionization of the indirect exciton, i.e., transitions in which a "free" electron and a "free" hole arise in the final state in different quantum wells, would be possible. The transition probability per unit time from state *2* with wave vector $k_2 = 0$ to state *1* with an arbitrary wave vector k_1 can be written as

$$w_{2\to 1} = \frac{2\pi}{\hbar}\sum_{\mathbf{k}_1,\,\mathbf{q}} \left|M_{2\to 1}^{\mathbf{q},\,\nu}\right|^2 \delta\left(\frac{\hbar^2 k_1^2}{2m} - \Delta + \hbar\omega_\nu(q)\right), \quad (2)$$

where $\mathbf{q}$ is the three-dimensional wave vector of an acoustic phonon with dispersion $\omega_\nu(q) = sq$, where s_ν is the sound velocity; $\mathbf{k}_1$ is the two-dimensional exciton wave vector in the final state; $M_{2\to 1}^{\mathbf{q},\,\nu}$ is the transition matrix element from state *2* with the exciton wave vector $k_2 = 0$ to state *1* with the exciton wave vector k_1, involving the emission of an acoustic phonon with polarization ν = LA, TA; and $m = m_e + m_h$ is the exciton mass, with m_e and m_h being the electron and hole masses, respectively.

The matrix element $M_{2\to 1}^{\mathbf{q},\,\nu}$ is determined by the overlap integral of the exciton wave functions Ψ_i with the phonon:

$$M_{2\to 1}^{\mathbf{q},\,\nu} = \langle \Psi_2 | H | \Psi_1 \rangle \delta_{0,\,\mathbf{k}_1 + \mathbf{q}_{xy}}, \quad (3)$$

where H is the Hamiltonian describing the exciton coupling with acoustic phonons, $\delta_{0,\,\mathbf{k}_1+\mathbf{q}_{xy}}$ is the Kronecker symbol accounting for momentum conservation in the DQW plane, and $\mathbf{q}_{xy}$ is the projection of $\mathbf{q}$ on the DQW plane.

In the case where the exciton level spacing is small ($\Delta \ll E$, where E is the size quantization energy reckoned from the quantum-well bottom), the exciton wave functions in the DQW, Ψ_1 and Ψ_2, can be presented as a linear combination of the direct and indirect exciton wave functions $\Psi_{\mathrm{DX}}(k_i)$ and $\Psi_{\mathrm{IX}}(k_i)$[20]:

$$\Psi_1 = \alpha\Psi_{\mathrm{DX}}(k_1) + \beta\Psi_{\mathrm{IX}}(k_1), \quad (4a)$$

$$\Psi_2 = -\beta\Psi_{\mathrm{DX}}(k_2) + \alpha\Psi_{\mathrm{IX}}(k_2), \quad (4b)$$

$$\alpha^2 + \beta^2 = 1, \quad \alpha = \frac{\delta}{\sqrt{\left(\sqrt{\Delta^2 - \delta^2} + \Delta\right)^2 + \delta^2}}.$$

In the simplest approximation, the wave functions of the direct and the indirect exciton with a wave vector k_i can be written as

$$\Psi_{\mathrm{IX(DX)}}(k_i) = \sqrt{\frac{2}{\pi\lambda_{\mathrm{IX(DX)}}^2}}\exp(ik_iR)\exp\left[-\frac{\rho}{\lambda_{\mathrm{IX(DX)}}}\right] \times \varphi_{e1(2)}(z_e)\varphi_h(z_h), \quad (5)$$

where $\varphi_{e1}(z_e)$ and $\varphi_{e2}(z_e)$ are the electron wave functions of the size-quantized ground level in the isolated left- and right-hand quantum wells, respectively; $\varphi_h(z_h)$ is the hole wave function of the size-quantized ground level in the isolated left-hand and right-hand quantum wells; R is the position of the exciton center of mass in the quantum well plane; ρ is the distance between the electron and the hole in the quantum well plane; λ_{DX} and λ_{IX} are the diameters of the direct and indirect excitons, respectively; and z_e and z_h are the electron and hole coordinates in the direction perpendicular to the quantum well plane.

Denoting the widths of the quantum well and of the barrier by a and b, respectively, we can write the electron wave functions in a single quantum well (SQW) in the form

$$\varphi_{e1(2)}(z) = \begin{cases} N\cos(\eta a/2)\exp[\eta_{\mathrm{B}}(z - z_{1(2)} + (a/2))] \\ z < z_{1(2)} - (a/2) \\ N\cos(\eta z - \eta z_{1(2)}), \quad |z - z_{1(2)}| < a/2 \\ N\cos(\eta a/2)\exp[-\eta_{\mathrm{B}}(z - z_{1(2)} - (a/2))] \\ z > z_{1(2)} + (a/2). \end{cases} \quad (6)$$

Here, the following notation has been introduced: $\eta_{\mathrm{B}} = \sqrt{2m_e(U-E)}/\hbar$ and $\eta = \sqrt{2m_eE}/\hbar$, with U being the barrier height and E, the electron size-quantized energy; N is the normalization factor; and z_1 and z_2 are the positions of the left- and right-hand quantum wells, respectively.

For high enough barriers, $U \gg E$, the electron wave functions penetrate only weakly into the barrier, so that $\eta a \approx \pi$.

Two kinds of the interaction governing the exciton–phonon transitions in GaAs/AlGaAs quantum wells are possible: (i) the interaction determined by the deformation potential (DP) and (ii) the piezoacoustic (PA) interaction. The interaction of an exciton with an acoustic phonon is actually a sum of the phonon interactions

with the electron and the hole, $H = H_e + H_h$. However, because the electronic components of the exciton-state wave functions are orthogonal, the matrix element of the electron interaction with the hole is zero, $\langle\Psi_2|H_h|\Psi_1\rangle = 0$. Viewed from the physical standpoint, this means that transitions between exciton states are possible only because they are mediated by the phonon coupling with the exciton electron.

The Hamiltonian of the exciton interaction with an acoustic phonon having a wave vector $\mathbf{q}$ and polarization ν can be presented in the form

$$H_e^{\mathrm{DP}} = \sqrt{\frac{\hbar}{2\rho_0 V s_\nu q}}\, iq\Xi_e \exp(\pm i\mathbf{q}\mathbf{r}_e) A_{\mathbf{q},\nu}^{\mathrm{DP}}, \qquad (7)$$

where Ξ_e is the deformation potential constant, ρ_0 is the density of the medium, $\mathbf{r}_e$ is the electron position vector, and V is the total volume. For a GaAs(100) quantum well, $A_{\mathbf{q}}^{\mathrm{DP}} = 1$ for the LA and $A_{\mathbf{q}}^{\mathrm{DP}} = 0$ for the TA phonons [21].

The Hamiltonian of the PA interaction has the form

$$H_e^{\mathrm{PA}} = \sqrt{\frac{\hbar}{2\rho_0 V s_\nu q}}\, (eh_{14}) \exp(\pm i\mathbf{q}\mathbf{r}_e) A_{\mathbf{q},\nu}^{\mathrm{PA}}, \qquad (8)$$

where h_{14} is the piezoacoustic constant and e is the electronic charge. The squared coefficient $A_{\mathbf{q},\nu}^{\mathrm{PA}}$, which determines the angular dependence of $\left|M_{2\to1}^{\mathbf{q},\nu}\right|^2$, can be written for a GaAs(100) layer as [22]

$$\begin{aligned} (A_{\mathbf{q},\mathrm{TA}}^{\mathrm{PA}})^2 &= \sin^2(2\theta) + (1/2)\sin^6\theta, \\ (A_{\mathbf{q},\mathrm{LA}}^{\mathrm{PA}})^2 &= \frac{9}{2}\sin^4\theta\cos^2\theta. \end{aligned} \qquad (9)$$

The transition probabilities between exciton states can be found by calculating the matrix element in Eq. (3) and substituting the expression thus obtained into Eq. (2). For the DP interaction with an LA phonon, we have

$$w_{2\to1}^{\mathrm{DP}} = \frac{\Xi_e^2}{2\pi\hbar\rho_0 s_\nu^2}\int_0^{\pi/2} d\theta \sin\theta \frac{q^3}{\sqrt{1+4\gamma\sin^2\theta}} |Y(q)|^2, \qquad (10)$$

where θ is the angle between the phonon propagation vector and the z direction.

There is no DP interaction with the TA phonon. The transition probability for the PA interaction with a phonon of polarization ν is

$$\begin{aligned} w_{2\to1}^{\mathrm{PA}} = \frac{(eh_{14})^2}{2\pi\hbar\rho_0 s_\nu^2}\int_0^{\pi/2} d\theta \sin\theta \frac{q}{\sqrt{1+4\gamma\sin^2\theta}} \\ \times |Y(q)|^2 (A_{\mathbf{q},\nu}^{\mathrm{PA}})^2. \end{aligned} \qquad (11)$$

In the last two expressions, we introduced the notation

$$q = \frac{2}{1+\sqrt{1+4\gamma\sin^2\theta}}\frac{\Delta}{\hbar s_\nu},$$

where $\gamma = \Delta/2ms_\nu^2$ is the ratio of the energy spacing between the exciton levels to the characteristic exciton–phonon coupling energy.

The overlap integral $Y(q)$ of the exciton wave functions with the phonon can be presented in the form

$$\begin{aligned} |Y(q)|^2 = \xi^2 \Big\{ 4P(\lambda_{\mathrm{DX}})P(\lambda_{\mathrm{IX}})\sin^2\frac{a+b}{2}q_z \\ + [P_e(\lambda_{\mathrm{DX}}) - P_e(\lambda_{\mathrm{IX}})]^2 \Big\} Z_e(q_z)^2, \end{aligned} \qquad (12)$$

where

$$\xi = \alpha\beta = \delta/2\Delta \qquad (13)$$

is the exciton-state wave-function mixing coefficient; $q_z = q\cos\theta$ is the perpendicular component of vector $\mathbf{q}$; $P_e(\lambda)$ is the overlap integral of the phonon wave functions with the exciton electron in the DQW plane,

$$P_e(\lambda) = \left[1 + \left(\frac{m_h}{2m}\lambda_q \sin\theta\right)^2\right]^{-3/2}, \qquad (14)$$

and $Z_e(q_z) = \int_{-\infty}^{\infty} dz\, \varphi_e^2(z)\exp(iq_z z)$ is the overlap integral (in the z direction) of the phonon wave function with the electron wave-function component of the exciton in an isolated quantum well.

For infinitely high barriers, we have

$$Z_e(q_z) = \frac{\sin q_z a/2}{q_z a/2[1-(q_z a/2\pi)^2]}. \qquad (15)$$

1.2. Energy Relaxation between Exciton States in Real DQWs

The relaxation between exciton states in a real DQW can proceed in two stages (Fig. 3b). First, the exciton electron is scattered with a probability w_e from interface nonuniformities and transfers to the other exciton subband (an intermediate state). This transition conserves the total energy of the exciton while changing its momentum. Next, with the probability w_i, the exciton transfers to the final state by emitting an acoustic phonon, and the exciton energy is changed. The rate of relaxation between the exciton states will be deter-

Table 1. Time of the 2 ⟶ 1 two-step transition from a high- to a low-energy exciton state with emission of an acoustic phonon, calculated for different Δ and phonon polarizations

Δ, (meV)	Time of phonon emission by an exciton with energy Δ				Elastic-transition time τ_e (ns)	Total transition time $\tau_{2\to 1}$ (ns)
	DP interaction with a LA phonon τ (ns)	PA interaction with a TA phonon τ (ns)	PA interaction with a LA phonon τ (ns)	Total time τ_i (ns)		
1.3	0.065	0.12	0.52	0.039	0.012–0.060	0.051–0.099
2.0	0.14	0.59	2.3	0.11	0.028–0.14	0.14–0.25
3.5	0.18	1.1	4.6	0.15	0.086–0.44	0.24–0.59

mined by the rate equations

$$\frac{dn_2}{dt} = G + w_e^b n_i - w_e n_2,$$
$$\frac{dn_i}{dt} = w_e n_2 - w_e^b n_i - w_i n_i, \tag{16}$$

where w_e is the probability of a direct elastic transition from state *2* to state *1*; w_e^b is the probability of the reverse elastic transition from state *1* to state *2*; n_2 and n_i are the exciton concentrations in the initial (at level *2*) and intermediate states, respectively; G is the exciton generation rate; and w_i is the probability of an inelastic transition from the intermediate to the final state.

The probabilities w_e^b and w_e are determined by the matrix element of the elastic transition connecting the exciton states and by the density of the initial and intermediate states, respectively. In a two-dimensional system, the density of exciton states does not depend on exciton energy, and, therefore, the densities of the initial and intermediate exciton states are equal. Thus, one can assume the probabilities of the direct and reverse elastic transitions to be equal: $w_e^b = w_e$.

In a steady state, the total transition probability between exciton states determines the exciton transition rate from the initial state: $w_{2\to 1} n_2 = G$. For a steady state, Eq. (16) yields

$$w_{2\to 1}^{-1} = w_e^{-1} + w_i^{-1}. \tag{17}$$

1.2.1. Scattering from impurities or interface defects. We shall assume that excitons interact with interface nonuniformities and impurities at the interface. Then, the matrix element of an elastic transition between exciton states will be proportional to the overlap of the wave functions of exciton states at the interfaces, $\Psi_1(z_i)\Psi_2(z_i)$, where z_i is the coordinate of the ith interface. Neglecting the tunneling penetration of the wave function through the barrier and summing over all interfaces yields

$$w_e \sim \sum_{i=1}^{N} \left|\Psi_1(z_i)\Psi_2(z_i)\right|^2 \approx \frac{\delta^2 N}{4\Delta^2}\left|\Psi_{\mathrm{DX}}^2(z_i)\right|^2, \tag{18}$$

where $N = 4$ is the number of interfaces in the DQW.

At the same time, the probability of elastic exciton scattering in SQW is $w_{\mathrm{SQW}} \sim N\left|\Psi_{\mathrm{DX}}^2(z_i)\right|^2$, where $N = 2$. When the exciton states are at resonance, the amplitudes of the wave functions $\Psi_1(z_i)$ and $\Psi_2(z_i)$ are equal. Hence, in this case, the transition probability w_e is one half that of the elastic exciton scattering in a SQW:

$$w_e = \frac{\delta^2}{2\Delta^2} w_{\mathrm{SQW}}. \tag{19}$$

The probability of elastic exciton scattering in a SQW was studied both theoretically [23–25] and experimentally [26, 27]. This probability depends on the exciton gas temperature, the quantum-well thickness, and the quality of the quantum-well interfaces: $w_{\mathrm{SQW}} = R\sqrt{T}/a^2$, where R is a constant depending on the interface properties. We assume that the structures on which our experiments were performed (see Introduction) have a high interface quality [7, 8], which is evidenced by the small inhomogeneous broadening of the exciton PL line (less than 1 meV). As an upper estimate of the probability of exciton scattering in our quantum wells we shall use the value $R = 4.79\ \mathrm{m^2/(K^{1/2}\ s)}$ obtained from the experimentally measured diffusion coefficient [26]. On the other hand, we believe that the interface quality in our samples is certainly poorer than that in samples with quantum wells grown by the growth interruption method. The probability of elastic scattering from interface nonuniformities in the latter samples is substantially lower and comparable with that of inelastic scattering from acoustic phonons [28]. We believe that $(w_{\mathrm{SQW}})^{-1}$ lies in our structure from 6 to 30 ps. Thus, at exciton level resonance, we have $12 < w_e^{-1} < 60$ ps. As the spacing between the exciton energy levels increases, the wave-function overlap decreases, as does the transition probability, $w_e \sim \Delta^{-2}$ (Table 1).

1.2.2. Energy relaxation. Probability w_i can be readily found by straightforward calculation. Let the exciton have a kinetic energy Δ and wave vector $k_2 = \sqrt{2m\Delta}/\hbar$. The probability for such an exciton to change its energy when transferring, with emission of

an acoustic phonon, to a state with a wave vector $\mathbf{k}_1$ is determined by the interaction matrix element:

$$M^{\mathbf{q},\nu}_{\mathbf{k}_2\to\mathbf{k}_1} = \langle\Psi_1(k_2)|H|\Psi_1(k_1)\rangle\delta_{\mathbf{k}_2,\,\mathbf{k}_1+\mathbf{q}_{xy}}, \quad (20)$$

where the exciton wave function $\Psi_1(k_{1(2)})$ is given by Eq. (4.1); the Kronecker symbol $\delta_{\mathbf{k}_2,\,\mathbf{k}_1+\mathbf{q}_{xy}}$ accounts for momentum conservation in the DQW plane; that is, $|\mathbf{k}_1 - \mathbf{k}_2| = q\sin\theta$.

The total transition probability to all lower lying states is obtained by summing over all acoustic-phonon wave vectors $\mathbf{q}$:

$$w_i = \frac{2\pi}{\hbar}\sum_{\mathbf{k}_1,\,\mathbf{q}}\left|M^{\mathbf{q},\nu}_{\mathbf{k}_2\to\mathbf{k}_1}\right|^2\delta\left(\frac{\hbar^2k_2^2}{2m} - \frac{\hbar^2k_1^2}{2m} - \hbar\omega_\nu(q)\right). \quad (21)$$

Note that in this case, where the exciton–phonon coupling, rather than causing a transition to the other exciton state, changes only the energy and momentum of the exciton, the acoustic phonon interacts with both the electron and the hole: $\langle\Psi_1(k_2)|H_h|\Psi_1(k_1)\rangle \neq 0$.

The deformation potential of the interaction of an acoustic phonon with a hole can be written as [29]

$$H_h^{\mathrm{DP}} = \sqrt{\frac{\hbar}{2\rho_0 V s_\nu q}}iq\Theta_h(\mathbf{q})\exp(\pm i\mathbf{q}\mathbf{r}_h), \quad (22)$$

where

$$\Xi_h(\mathbf{q}) = \begin{cases} -A - \dfrac{B}{2} + \dfrac{3}{2}B\cos^2\theta, & \text{(LA phonons)} \\ \dfrac{3}{4}B\sin 2\theta, & \text{(TA phonons)} \end{cases} \quad (23)$$

and A and B are the deformation potential constants.

For the PA interaction, we have

$$H_h^{\mathrm{PA}} = \sqrt{\frac{\hbar}{2\rho_0 V s_\nu q}}(eh_{14})\exp(\pm i\mathbf{q}\mathbf{r}_h)A^{\mathrm{PA}}_{\mathbf{q},\nu}. \quad (24)$$

By calculating the matrix element in Eq. (20) and substituting the result into Eq. (21), we find the probability w_i:

$$w_i^{\mathrm{DP}} = \frac{\Xi_e^2}{2\pi^2\hbar\rho_0 s_\nu^2}\int_0^{k_2}dk_1\int_0^{\pi}d\varphi\frac{|k_2\cos\varphi - k_1|}{q_z}q^2 \times X_{\mathrm{DP}}\Theta(q - q_{xy}), \quad (25.1)$$

$$w_i^{\mathrm{PA}} = \frac{(eh_{14})^2}{2\pi^2\hbar\rho_0 s_\nu^2}\int_0^{k_2}dk_1\int_0^{\pi}d\varphi\frac{|k_2\cos\varphi - k_1|}{q_z} \times X_{\mathrm{PA}}\Theta(q - q_{xy}), \quad (25.2)$$

where φ is the angle between the $\mathbf{k}_1$ and $\mathbf{k}_2$ vectors, $q = (2ms_\nu/\hbar)(k_2^2 - k_1^2)$, $q_{xy} = |\mathbf{k}_1 - \mathbf{k}_2|$, $q_z = \sqrt{q^2 - q_{xy}^2}$, $\Theta(x)$ is the Heaviside step function

$$\Theta(x) = \begin{cases} 1, & x \geq 0 \\ 0, & x < 0, \end{cases}$$

and X_{DP} and X_{PA} are integrals which characterize the DP and PA interactions of the acoustic phonon with the exciton and are defined as

$$X_{\mathrm{DP}} = \left|A^{\mathrm{DP}}_{\mathbf{q},\nu}\alpha^2P_e(\lambda_{\mathrm{DX}}) + \beta^2\exp[iq_z(a+b)]P_e(\lambda_{\mathrm{IX}})\} + \frac{\Xi_h(\mathbf{q})}{\Xi_e}[\alpha^2P_h(\lambda_{\mathrm{DX}}) + \beta^2P_h(\lambda_{\mathrm{IX}})]\right|^2,$$

$$X_{\mathrm{PA}} = \left|\alpha^2P_e(\lambda_{\mathrm{DX}}) + \beta^2\exp[iq_z(a+b)]P_e(\lambda_{\mathrm{IX}}) - \alpha^2P_h(\lambda_{\mathrm{DX}}) - \beta^2P_h(\lambda_{\mathrm{IX}})\right|^2(A^{\mathrm{PA}}_{\mathbf{q},\nu})^2, \quad (26)$$

$$P_e(\lambda) = Z_e(q_z)\left[1 + \left(\frac{m_h}{2m}\lambda q_{xy}\right)^2\right]^{-3/2},$$

$$P_h(\lambda) = Z_h(q_z)\left[1 + \left(\frac{m_e}{2m}\lambda q_{xy}\right)^2\right]^{-3/2}.$$

For high enough barriers, one can assume that the wave functions of the electron and the hole in a SQW coincide, $Z_e(q_z) = Z_h(q_z)$.

2. RESULTS OF NUMERICAL CALCULATION

2.1. Energy Relaxation Rates

In our calculation of the transition probability $w_{2\to1}$ between exciton states involving the emission of an acoustic phonon due to the PA or DP potential, we used the following parameters of the exciton in a GaAs/AlGaAs quantum well: $m_e = 0.067m_0$, $m_h = 0.15m_0$ (where m_0 is the free electron mass), $a = 10$ nm, $b = 3.8$ nm, $\lambda_{\mathrm{DX}} = 14$ nm, $\lambda_{\mathrm{IX}} = 26$ nm (the data are taken from a theoretical calculation in [3]), $\Xi_e = 7.3$ eV, $h_{14} = 1.45 \times 10^7$ V/cm, $s_{\mathrm{LA}} = 5 \times 10^5$ cm/s, $s_{\mathrm{TA}} = 3 \times 10^5$ cm/s, $\delta = 1.3$ meV, $\rho_0 = 5.3$ g/cm^3, $A = -6.7$ eV, and $B = -2$ eV. The results of the calculation of the time $\tau_{2\to1}$ for the one-step mechanism of energy relaxation (Fig. 3a) are given in Table 2 for various values of Δ. At resonance ($\Delta = \delta$), the transition time between the exciton states involving emission of an acoustic LA phonon in the case of DP interaction is $\tau_{2\to1} = 0.29$ ns. The transition time increases strongly with increasing Δ and is as long as $\tau_{2\to1} = 2.4$ ns for $\Delta = 3.5$ meV.

For small Δ ($\Delta \sim \delta$), the PA interaction plays a substantial role in exciton–phonon transitions. Indeed, the transition time under the PA interaction of excitons

Table 2. Time of the elastic one-step transition 2 ⟶ 1 from a high- to a low-energy exciton state with emission of an acoustic phonon, calculated for different Δ and phonon polarizations

Δ, (meV)	DP interaction with a LA phonon τ (ns)	PA interaction with a TA phonon τ (ns)	PA interaction with a LA phonon τ (ns)	Total time $\tau_{2\to1}$ (ns)
1.3	0.29	0.30	2.7	0.14
2.0	0.71	0.80	6.0	0.35
3.5	2.38	4.0	29	1.4

with TA phonons was found to be $\tau_{2\to1} = 0.30$ ns at resonance and $\tau_{2\to1} = 4$ ns for $\Delta = 3.5$ meV. However, the PA interaction with LA phonons is considerably less efficient. This is connected with the specific selection rules for the PA interaction in Eq. (9), as well as with the TA and LA phonons having different sound velocities. Note that the dependences of the phonon-assisted exciton transition probabilities on Δ for the DP and PA interactions are different. Indeed, the deformation potential is directly proportional to $q^{1/2}$, whereas the PA interaction potential is inversely proportional to $q^{1/2}$. Therefore, in contrast to the DP interaction, the transition probability due to the PA interaction is affected more strongly by phonons with a small q. As Δ increases, phonons with large q, which play a more important part in the DP interaction, become involved in the phonon-assisted exciton transitions. Therefore, as Δ increases, the PA interaction grows progressively less efficient and the transition time due to the PA interaction grows faster than that due to the DP interaction.

The results of calculation of the time $\tau_{2\to1}$ for the two-step mechanism of energy relaxation between exciton states is presented in Table 1 for different values of Δ. The time of the exciton DP interaction with a TA phonon was found to be negligible compared with the total relaxation time, and, therefore, it is not given in Table 1. At resonance ($\Delta = \delta$), the relaxation time within an exciton subband is $\tau_i = 0.04$ ns and is close to the exciton energy-relaxation time in a SQW, $\tau_{SQW} = 0.022$ ns at $T = 10$ K, given by the relation $(1/\tau_{ac}) = A_{ac}T/a$ (where a is the quantum-well width and $A_{ac} = 45$ m/(K s) [26]). The time τ_i increases with increasing Δ to reach 0.14 ns.

2.2. Angular Dependences of the Generated Phonon Flux

The probability of exciton interaction with phonons propagating at an angle θ to the z direction is determined by the integrand in Eqs. (10) and (11). Figures 4a and 4b display the angular dependences of the flux density of acoustic phonons emitted in the DP and PA interactions, respectively, into a unit solid angle in the one-step transition. The dashed lines correspond to the region near the resonance ($\Delta = 1.3$ meV), and the solid lines are far from the resonance ($\Delta = 3.5$ meV). In contrast to the case of a SQW, the transitions between exciton states in the DQW are due primarily to the interaction of excitons with acoustic phonons emitted mainly perpendicular to the DQW plane. The distribution is characterized by several phonon propagation directions (shown by lobes in the figures) in which the interaction of phonons with the excitons is particularly strong. As Δ increases, the lobes displace toward larger angles and a new lobe forms in the $\theta = 0$ direction. Thus, as Δ increases, phonons with progressively larger θ angles begin to participate in the transitions.

Interestingly, the probability of DP interaction with a phonon propagating exactly perpendicular to the DQW plane oscillates with increasing Δ. Thus, the interaction with phonons moving along the z axis is maximum at a certain value of Δ different from δ.

A distinctive feature of the PA interaction is the existence of additional selection rules, which forbid exciton interaction with phonons propagating in the z direction. Therefore, the angular dependences of the acoustic phonon energy in a PA interaction, which are presented in Fig. 4b, always have at least one full lobe. A comparison of this distribution with the angular distribution in the DP interaction reveals that the lobes corresponding to the PA interaction are turned through a larger angle θ. The reason for this lies in that the PA interaction potential decreases with increasing q, i.e., with decreasing angle θ (unlike the DP interaction, which grows with decreasing angle θ).

Because the PA interaction is more efficient for excitons with small q, the maximum of the phonon flux density due to the PA interaction falls always on the first lobe. In contrast to the PA potential, the deformation potential increases with increasing q, but the wave-function overlap of the exciton and phonon decreases with growing q. Therefore, the maximum in the flux density due to the DP interaction occurs at some medium values of q; for the parameters chosen above, these values correspond to the second lobe.

3. DISCUSSION OF RESULTS

In the case of the inelastic (one-step) mechanism, the probability of one-step transitions between exciton states with emission of acoustic phonons exhibits a strong dependence on Δ. The value of $w_{2\to1}$ decreases rapidly with increasing Δ, primarily as a result of the decreasing exciton wave-function overlap between the

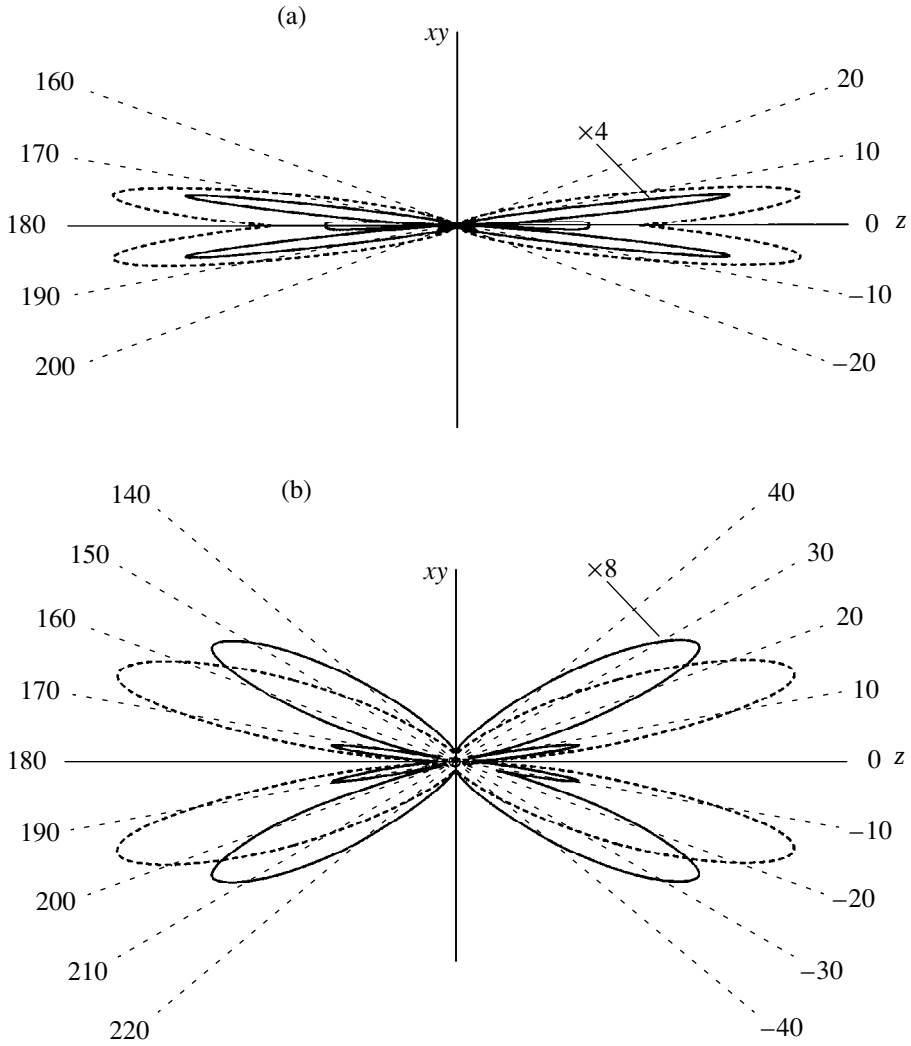

Fig. 4. Angular dependence of the flux density of acoustic phonons emitted in the transition between exciton states (mechanism I) for: (a) DP interaction (LA phonons) and (b) PA interaction (TA phonons). The dashed and solid lines show the relations calculated for $\Delta = 1.3$ and 3.5 meV, respectively. The horizontal axis is along the direction perpendicular to the DQW plane.

quantum wells. The increase in the wave-vector range $q_{\max}$–$q_{\min}$ of phonons involved in the exciton–phonon coupling with increasing Δ is compensated by the decrease of the exciton and phonon wave-function overlap in the DQW plane because of the increasing longitudinal component of the exciton wave vector q_{xy} (see below). Thus, in a first approximation, we have $w_{2\to 1} \sim \xi^2$, where ξ is the exciton-state mixing coefficient defined by Eq. (13), or, in view of Eq. (13), $w_{2\to 1} \sim \Delta^{-2}$. For $\Delta = 3.5$ meV, the transition probability becomes less than one reciprocal nanosecond, which is less than the DX emission probability at $T = 10$ K, $w_R \sim 4$ ns^{-1} [6]. However, the thermodynamic equilibrium, experimentally observed to exist between the exciton states at $\Delta = 3.5$ meV and $T = 10$ K, indicates that the transition probability between exciton states should actually be higher. Hence, the transition probability is governed by another mechanism.

We believe the two-step transition to be such a mechanism. While the rate of transitions between exciton states in this mechanism also decreases with increasing Δ, the probability of these transitions lies between 1.7 and 4.2 ns^{-1} even for $\Delta = 3.5$ meV. We thus come to the conclusion that the energy relaxation in transitions between exciton states occurs primarily by the two-step mechanism.

Consider now with what phonons excitons predominantly interact in the one-step transition. We note first of all that the interaction is possible only with phonons whose energy is less than $\hbar q_{\max} s_v = \Delta$, while being at the same time above a certain value $\hbar q_{\min} s_v \sim \gamma^{-1/2}\Delta$. The contribution of each phonon satisfying this selection rule to the total exciton–phonon coupling responsible for the transition between exciton states is deter-

mined by its wave vector **q**. As follows from Eq. (12), phonons whose half-wavelength in the *z* direction, perpendicular to the DQW plane, fits an even number of times into the separation $a + b$ between the quantum wells should weakly interact with the excitons. By contrast, the exciton–phonon transition probability between exciton states should be affected most of all by phonons whose half-wavelength along the *z* direction fits an odd number of times into the DQW width. Note also that the overlap integral of the exciton and phonon wave functions drops sharply with increasing q_z if several phonon half-wavelengths fit into the quantum well width in the *z* direction. Thus, the interaction will have the highest efficiency if the following two conditions are satisfied:

$$q_z < \frac{\pi}{a} \quad \text{and} \quad q_z \approx \frac{\pi}{a+b}(2n+1), \tag{27}$$

where n is an integer.

There is also a condition for efficient interaction of excitons with phonons which imposes a constraint on the magnitude of the longitudinal (along the DQW plane) component of the phonon wave vector. It consists in that the phonon wavelength in the DQW plane is not substantially smaller than the exciton diameter. Therefore, the longitudinal component of the phonon wave vector q more strongly affects the indirect exciton, which has larger linear dimensions.

The exciton–phonon coupling in the case of the two-step relaxation mechanism exhibits essential differences from the interaction involved in the one-step mechanism (Fig. 3b). First, in the two-step relaxation, the phonon can interact not only with the electronic component of the exciton wave function but also with the hole component. This factor substantially increases the transition probability $w_{2\to 1}$. Second, the overlap between the exciton and phonon wave functions does not depend on Δ. For this reason, w_i no longer depends strongly on Δ. Third, in this relaxation, the interaction with phonons propagating primarily along the DQW layer is not weak. As the energy spacing Δ increases, the lower exciton state becomes progressively more indirect. Phonons with a large $\mathbf{q}_{xy}$ couple more weakly to the indirect exciton, because the latter has a larger diameter. This is what primarily determines the dependence of $w_{2\to 1}$ on Δ.

The calculations made in Section 2 show that the interaction of excitons with acoustic phonons in the inelastic (one-step) transition between exciton states is frequency-dependent. This implies the possibility, in principle, of using DQWs and other tunnel structures as narrow-band subterahertz and terahertz generators and detectors of phonons [15–19, 30]. Several groups of experimenters are presently working on the realization of this idea to develop a new instrument which would permit one to probe the phonon spectrum and to study phonon dynamics in semiconducting nanostructures. The results of our calculations can be used in analyzing some experimental data obtained in experiments with nonequilibrium phonons. In such an analysis, one should take into account the two-step transitions by mechanism II (Fig. 3b). The angular dependences (Fig. 4) demonstrate the need of using a narrow enough phonon beam in order to exclude the effect of two-step relaxation processes, which considerably reduce the spectral resolution of a DQW as a phonon spectrometer. In this case, phonon generation will be determined by the one-step exciton relaxation mechanism and the energy of the generated phonons will be $\hbar\omega \approx \Delta$.

Phonon absorption also follows an anisotropic pattern and can be analyzed in a similar manner. For instance, at temperature $T < 5$ K and $\Delta = 3.5$ meV, the one-step transition between exciton states will be accompanied by absorption of only the phonons incident at angles $\theta < 8°$. At the same time, such phonons will not, in any way, influence the transitions involving elastic processes (two-step transitions). Indeed, absorption of phonons propagating at small angles θ in single quantum wells is forbidden by the selection rules. Thus, by creating a beam of nonequilibrium phonons propagating perpendicular to the DQW plane and by studying the changes in the exciton PL spectra induced by such a beam, one can exclude the effect of the two-step transition mechanism. In these conditions, the effect of nonequilibrium phonons on the PL spectrum will reflect the spectrum of nonequilibrium phonons.

4. CONCLUSIONS

Thus, we have calculated the times of exciton energy relaxation due to acoustic phonons in a DQW as functions of Δ. The energy relaxation between exciton states in a DQW is governed by two mechanisms, namely, the inelastic one-step transition involving an acoustic phonon (mechanism I) and elastic scattering from interface defects, followed by energy relaxation within an exciton subband (mechanism II). We have studied the influence of both mechanisms on the transition probabilities between the exciton states and drawn the conclusion that the energy relaxation between the exciton states is dominated by two-step transitions with participation of elastic processes.

The exciton–phonon coupling has different angular dependences in the one- and two-step mechanisms. Therefore, the phonons propagating in a direction close to *z* interact with exciton states by the one-step mechanism only.

ACKNOWLEDGMENTS

The authors are indebted to L.E. Golub for fruitful discussions.

The support of the Russian Foundation for Basic Research, grant no. 99-02-18276, and of the Young Scientists' Support Program, Presidium RAS, is gratefully acknowledged.

REFERENCES

1. J. Shah, in *Optics of Semiconductor Nanostructures*, Ed. by F. Henneberger, S. Schmitt-Rink, and E. O. Gobel (Akademie Verlag, Berlin, 1993), p. 149.
2. R. Strobel, R. Eccleston, J. Kuhl, and K. Koehler, Phys. Rev. B **43** (15), 12564 (1991).
3. A. M. Fox, D. A. B. Miller, G. Livescu, *et al.*, Phys. Rev. B **44** (12), 6231 (1991).
4. J. E. Golub, K. Kash, J. P. Harbison, and L. T. Florez, Phys. Rev. B **41** (12), 8564 (1990).
5. M. R. Reshotko, L. D. Shvartsman, and J. E. Golub, Phys. Rev. B **50** (7), 4692 (1994).
6. J. Martinez-Pastor, A. Vinattieri, L. Carraresi, *et al.*, Phys. Rev. B **47** (16), 10456 (1993).
7. A. V. Akimov, E. S. Moskalenko, A. L. Zhmodikov, *et al.*, Acta Phys. Pol. A **90** (5), 895 (1996).
8. A. V. Akimov, E. S. Moskalenko, A. L. Zhmodikov, *et al.*, Fiz. Tverd. Tela (St. Petersburg) **39** (4), 735 (1997) [Phys. Solid State **39**, 649 (1997)].
9. O. Brandt, K. Kanamoto, Y. Tokuda, *et al.*, J. Appl. Phys. **75** (4), 2105 (1994).
10. K. Leo, J. Shah, E. O. Gobel, *et al.*, Phys. Rev. Lett. **66** (2), 201 (1991).
11. D. Y. Oberli, J. Shah, T. C. Damen, *et al.*, Phys. Rev. B **40** (5), 3028 (1989).
12. T. B. Norris, N. Vodjdani, B. Vinter, *et al.*, Phys. Rev. B **40** (2), 1392 (1989).
13. A. P. Heberle, W. W. Ruehle, M. G. W. Alexander, and K. Koehler, Semicond. Sci. Technol. **7**, B421 (1992).
14. R. Ferreira, C. Delalande, H. W. Liu, *et al.*, Phys. Rev. B **42** (14), 9170 (1990).
15. A. V. Akimov, A. A. Kaplyanskii, D. A. Mazurenko, *et al.*, Phys. Status Solidi B **204**, 400 (1997).
16. S. A. Cavill, A. V. Akimov, F. F. Ouali, *et al.*, Physica B (Amsterdam) **263–264**, 537 (1999).
17. F. F. Ouali, N. N. Zinov'ev, L. J. Challis, *et al.*, Phys. Rev. Lett. **75** (2), 308 (1995).
18. D. N. Hill, S. A. Cavill, A. V. Akimov, *et al.*, Phys. Status Solidi B **204**, 431 (1997).
19. S. A. Cavill, A. V. Akimov, F. F. Ouali, *et al.*, Superlattices Microstruct. **25**, 459 (1999).
20. A. S. Davydov, in *Quantum Mechanics* (Nauka, Moscow, 1973; Pergamon, Oxford, 1976), p. 217.
21. V. Karpus, Fiz. Tekh. Poluprovodn. (Leningrad) **20** (1), 12 (1986) [Sov. Phys. Semicond. **20**, 6 (1986)].
22. V. Karpus, Fiz. Tekh. Poluprovodn. (Leningrad) **22** (3), 439 (1988) [Sov. Phys. Semicond. **22**, 268 (1988)].
23. T. Matsusue, H. Akiyama, and H. Sakaki, Superlattices Microstruct. **13**, 41 (1993).
24. T. Takagahara, Phys. Rev. B **31** (10), 6552 (1985).
25. P. K. Basu and P. Ray, Phys. Rev. B **44** (4), 1844 (1991).
26. K. T. Tsend, O. F. Sankey, and H. Morkoc, Appl. Phys. Lett. **57** (16), 1666 (1990).
27. H. Hillmer, S. Hansmann, A. Forchel, *et al.*, Appl. Phys. Lett. **53** (20), 1937 (1988).
28. H. Hillmer, A. Forchel, R. Sauer, and C. W. Tu, Phys. Rev. B **42** (15), 3220 (1990).
29. L. E. Golub, A. V. Scherbakov, and A. V. Akimov, J. Phys.: Condens. Matter **8**, 2163 (1996).
30. F. T. Vasko, O. G. Balev, and P. Vasilopoulos, Phys. Rev. B **47** (24), 16433 (1993).

Translated by G. Skrebtsov

Physics of the Solid State, Vol. 43, No. 4, 2001, pp. 763–765. Translated from Fizika Tverdogo Tela, Vol. 43, No. 4, 2001, pp. 730–732.

LOW-DIMENSIONAL SYSTEMS AND SURFACE PHYSICS

Optical and Structural Properties of Thallium Halide Microcrystals in a Porous Matrix

V. F. Agekyan and Yu. A. Stepanov

Institute of Physics Petrodvorets Branch, St. Petersburg State University, ul. Pervogo maya 100, Petrodvorets, 198904 Russia

Received September 8, 2000

Abstract—Thallium halide microcrystals were grown from water solutions in a porous matrix obtained from alkali borosilicate glass by etching, and their absorption and luminescence spectra were studied. Constraining the crystal size was found to affect the stability of some crystal modifications. The exciton radii were determined, and the dimensions of microcrystals in which size quantization effects become observable were estimated from the absorption spectra of bulk TlBr and TlCl crystals. © *2001 MAIK "Nauka/Interperiodica".*

A remarkable property of thallium halide crystals is their high dielectric permittivity. The static values are 30 and 32 for the cubic TlBr and TlCl and 15 for the cubic and 21 for the orthorhombic TlI. In standard conditions, TlBr and TlCl have a CsCl-type cubic structure, while TlI crystallizes in an orthorhombic structure with the *Cmcm* (D_{2h}^{17}) space group and transforms to a CsCl-type structure (the red TlI modification) at room temperature and at a pressure of 5 kbar, or at atmospheric pressure when heated to 170°C. Thin films of the $TlBr_{1-x}I_x$ solid solutions retain the CsCl-type structure throughout the x range from 0 to 1; however for $x > 0.3$, bulk crystals of these solid solutions are orthorhombic. At $x = 0.3$, bulk $TlBr_{1-x}I_x$ crystals transfer from the cubic to orthorhombic phase when cooled to the liquid nitrogen temperature. Cubic $TlBr_{1-x}Cl_x$ (KRS-5) and $TlBr_{1-x}I_x$ (KRS-6) crystals find application in acoustics and electronics.

Cubic thallium halides are indirect-gap crystals. The extremum of their valence band lies at the X point of the Brillouin zone (X_6^+), while the extremum of the conduction band lies at the R point (R_6^+); the direct transitions $X_6^+ \longrightarrow X_6^-$ are higher in energy [1, 2]. At low temperatures, the energies of the indirect (E_g^i) and direct (E_g^d) transitions are 3.22 and 3.42 eV (TlCl), 2.66 and 3.02 eV (TlBr), and 2.75 and 2.86 eV (TlI), respectively. The values of $[E_g^d/(E_g^d - E_g^i)]^2$, which govern the relative magnitude of the oscillator strengths of the indirect and direct transitions, are approximately 300 (TlCl), 80 (TlBr), and 550 (orthorhombic TlI). As a result, the absorption coefficient for the indirect transitions in thallium halides is comparatively high. The absorption and luminescence spectra of thallium halides reveal, at the fundamental edges, clearly pronounced exciton effects, namely, series of narrow exciton lines, which imply the existence of bound exciton–phonon states [1]. Under strong optical excitation, bands appear at the indirect edges, which are assigned to the electron–hole liquid [3].

Investigation of the microcrystals of the halides of many metals, in particular, of the copper, mercury, bismuth, and lead iodates, revealed structural features and size quantization effects [4–10]. The properties of the thallium halides (structural transformations, two easily observable types of band-to-band transitions, a strong excitonic effect) make the preparation and study of the characteristics of the microcrystals of these compounds a problem of considerable interest. This relates to both small microcrystals, in which quantum confinement effects become manifest, and comparatively large ones. We report here on the first experiments on the growth of thallium-halide microcrystals in a host matrix and on a study of their properties.

1. EXPERIMENTAL

The porous matrix was prepared of alkali borosilicate glass (ABSG) etched at 50–100°C in a 3 M solution of hydrochloric acid. Etching produces pores with an average diameter of about 7 nm, which have a fairly narrow size distribution, in the ABSG. Porous glass matrices were immersed into a saturated aqueous solution of TlI at 100°C, after which the samples were dried at various temperatures. To obtain matrices with different TlI densities, the samples were subjected to such cycles from one to seven times. The solubility of TlCl in water at 100°C exceeds 20 times that of TlI, and therefore, in the case of TlCl, the matrix was dipped only once into a saturated or unsaturated solution. The number of crystallization cycles for TlBr, whose solubility in water at 100°C is twice that of TlI, varied from one to a few times. Water solutions of TlBr and TlI were

1063-7834/01/4304-0763$21.00

used to grow mixed $TlBr_xI_{1-x}$ microcrystals with a high bromine content ($x > 0.7$) in the ABSG pores.

We studied the absorption and luminescence spectra of the matrices containing thallium halide microcrystals, which were pumped by a nitrogen laser with a photon energy of 3.68 eV, a pulse length of 5 ns, and pulse repetition frequency of 100 Hz. The luminescence spectra were measured at 80 and 300 K in the cw mode and with time resolution.

2. RESULTS AND THEIR DISCUSSION

2.1. Thallium Iodate

The time-resolved, zero-delay emission spectrum of a TlI sample subjected to three crystallization cycles does not differ much from that of the empty matrix; however, when studied in the cw mode, the luminescence spectrum exhibits a band peaking at 2.74 eV, which belongs to the TlI microcrystals. The reason for the difference between the spectra obtained in the two modes consists in that the TlI luminescence band builds up more slowly than the matrix radiation and has a longer decay time. In an optically denser sample (seven crystallization cycles), this band becomes noticeable against the matrix radiation background already at room temperature and it is dominant at 80 K (Fig. 1). This emission band of TlI microcrystals overlaps the direct and indirect band-to-band transition regions in a bulk crystal. The absorption spectrum of the matrix with embedded TlI microcrystals exhibits a structure coinciding in energy with the direct transition in bulk TlI crystals [1] (Fig. 1). As follows from this absorption spectrum, the TlI microcrystals grown in a porous ABSG matrix from a saturated aqueous solution are not small enough to allow reliable observation of the quantum-confined level shift in them. The position of the fundamental transition edge indicates that the TlI phase growing in the matrix pores is orthorhombic. We established that, in contrast to bulk crystals which transfer to the cubic phase at 170°C, TlI microcrystals remain orthorhombic at substantially higher temperatures, close to the melting point of bulk crystals (440°C). This stability of microcrystals in the low-symmetry phase is in agreement with the structural properties of the "large" microcrystals of CuI [4] and HgI_2 [5, 6] observed earlier.

2.2. Thallium Chloride

The luminescence spectrum of the matrix with TlCl microcrystals obtained by slow dehydration exhibits a band peaking at 2.59 eV at 80 K and a weaker band at a lower energy. As in the case of TlI, these bands grow in intensity more slowly than the matrix radiation does and decay with a characteristic time of a few μs (Fig. 2). If the sample was dehydrated rapidly at 100°C, the emission band maximum measured with the same delay lies at a lower energy of 2.54 eV. This may be due to large Stokes losses, because rapidly formed microcrystals are usually of a poorer quality (and smaller in size). We did not observe any sharp features in the absorption spectrum of TlCl microcrystals within the energy region from 3.0 to 3.6 eV. The diffuse character of the fundamental absorption edges may be caused by a strong size dispersion of the microcrystals. The dynamics of TlI and TlCl growth in a porous matrix are different because of the much higher solubility of TlCl in water and of the larger temperature gradient of the solubility. Moreover, when grown in spatially confined

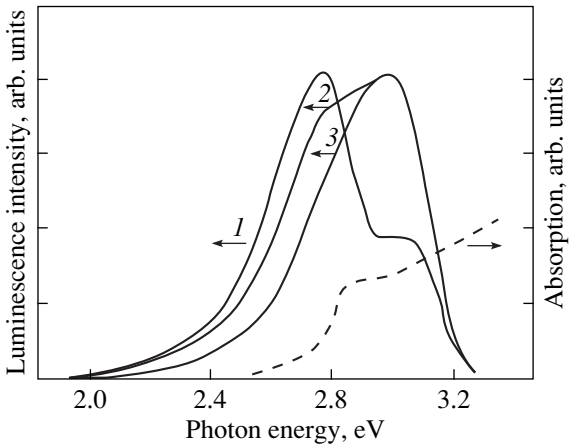

Fig. 1. Normalized integral luminescence spectra and the absorption spectrum of a porous matrix with embedded TlI microcrystals (six cycles of growth from saturated solution). T = (*1*) 80 K, (*2*) 300 K, and (*3*) empty matrix at 80 K. The dashed line is the absorption spectrum.

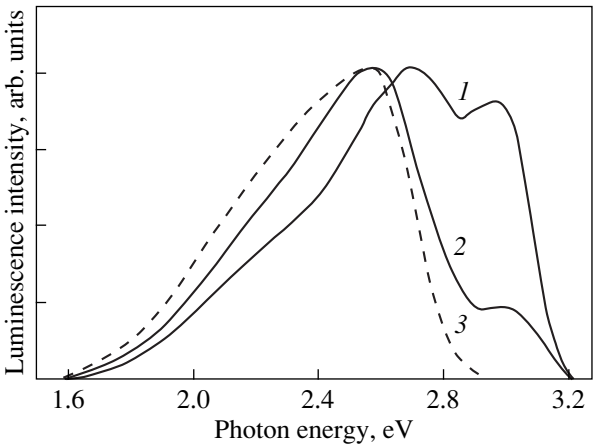

Fig. 2. Normalized luminescence spectra of a porous matrix with embedded TlCl microcrystals (saturated solution, one growth cycle), measured with the following time delays relative to the exciting pulse (μs): (*1*) 0, (*2*) 5, and (*3*) 8. The high energy band corresponds to the glass matrix emission. T = 80 K.

conditions, TlCl may form in the orthorhombic phase rather than in the cubic one, which is likely to be stable only for bulk crystals; this point requires further study.

2.3. Thallium Bromide and Mixed $TlBr_{1-x}I_x$ Crystals

No luminescence corresponding to the spectral regions of the direct and indirect transitions in cubic TlBr is observed in a matrix filled by TlBr. At high TlBr concentrations, the diffuse absorption edge of the matrix lies in the 3.4-eV region. In a matrix containing mixed $TlBr_{1-x}I_x$ crystals with a high bromine concentration, we observed luminescence excited below the fundamental transitions in cubic $TlBr_{1-x}I_x$.

Matrices with embedded $TlBr_{1-x}I_x$ and TlCl exhibited sharp emission peaks near 3.360 and 3.315 eV at 80 K; the peaks weakened strongly on heating to room temperature (Fig. 3). While it would be difficult to identify the origin of this structure, it is most likely associated with the luminescence of the thallium ions.

2.4. Exciton Parameters of Thallium Halides

The energy separations between the narrow lines of the $n = 1$ and $n = 2$ excitonic series observed for direct transitions in TlBr and TlCl show that their Rydberg energies are approximately the same and equal to 0.011 eV. Accepting the well-known low-temperature values of 30 and 35 for the low-frequency permittivity of TlBr and TlCl, respectively, we estimate the reduced effective masses μ^d for direct transitions at the X point as $0.72m_0$ (TlBr) and $0.95m_0$ (TlCl), where m_0 is the free electron mass. It thus follows that the radius of the direct exciton is not much larger than 2 nm for these compounds. Article [3] gives the following values of the effective masses of the electron at the R point and the hole at the X point: $m_e^i = 0.525m_0$ and $m_h = 0.66m_0$ (TlBr) and $m_e^i = 0.56m_0$ and $m_h = 0.797m_0$ (TlCl). Our estimates of μ^d are seen to be at odds with these data (μ^d should be less than m_h). The reasons for this disagreement may lie either in the inaccuracy of the data presented in [3] or in the fact that the low-frequency value of the permittivity is inapplicable to the lower states of the direct excitons. Our estimates place the radii of the indirect exciton states in TlBr and TlCl in the 4- to 6-nm interval. These values are the upper bounds on the size of the TlBr and TlCl microcrystals in which exciton quantum confinement should be observable. Similar values of the exciton radii are apparently typical of the orthorhombic TlI as well (we did not succeed in finding information on the carrier masses for this crystal), because TlI microcrystals embedded in matrix pores of sizes up to 7 nm do not exhibit size quantization effects.

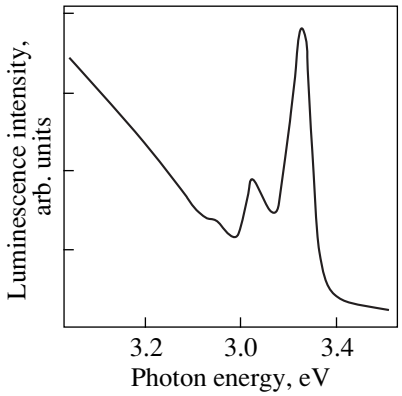

Fig. 3. Spectral structure at the high energy radiation edge of the porous matrix containing $TlBr_{1-x}I_x$ (two growth cycles, saturated solution). $T = 80$ K (see text).

Thus, we have grown thallium halide microcrystals from aqueous solutions in pores of a glass matrix and investigated their structural and optical properties. The most reliable results were obtained for the thallium iodate; the interpretation of some experimental data requires further studies: improvements in the technology of thallium halide microcrystal growth, and extension of this technology to other matrices, in particular, to polymer matrices.

REFERENCES

1. J. Nakahara, K. Kobayashi, and A. Fujii, J. Phys. Soc. Jpn. **37**, 1319 (1974).
2. J. Nakahara and K. Kobayashi, J. Lumin. **12/13**, 297 (1976).
3. K. Takiyama, J. Nakahara, H. Takenaka, *et al.*, J. Phys. Soc. Jpn. **65**, 307 (1995).
4. A. Tanji, I. Akai, K. Kojima, *et al.*, J. Lumin. **87–89**, 516 (2000).
5. I. Kh. Akopyan, O. N. Volkova, B. V. Novikov, and B. I. Venzel', Fiz. Tverd. Tela (St. Petersburg) **39**, 468 (1997) [Phys. Solid State **39**, 407 (1997)].
6. V. F. Agekyan, A. Yu. Serov, and Yu. A. Stepanov, Fiz. Tverd. Tela (St. Petersburg) **42**, 1786 (2000) [Phys. Solid State **42**, 1832 (2000)].
7. T. Komatsu, D. Kim, T. Kobayashi, *et al.*, Surf. Rev. Lett. **3**, 1127 (1996).
8. T. Goto, M. Tanaka, M. Y. Chen, *et al.*, Solid State Commun. **97**, 587 (1996).
9. E. Lifshitz, M. Yassen, L. Bykov, and I. Dag, J. Lumin. **70**, 421 (1996).
10. V. F. Agekyan, Fiz. Tverd. Tela (St. Petersburg) **40**, 1724 (1998) [Phys. Solid State **40**, 1568 (1998)].

Translated by G. Skrebtsov

Physics of the Solid State, Vol. 43, No. 4, 2001, pp. 766–771. Translated from Fizika Tverdogo Tela, Vol. 43, No. 4, 2001, pp. 733–738.

LOW-DIMENSIONAL SYSTEMS AND SURFACE PHYSICS

Depth Profiles of Metal Ions Implanted in Dielectrics at Low Energies

A. L. Stepanov*, V. A. Zhikharev, and I. B. Khaĭbullin****

** I Physikalisches Institut, Aachen Technical University RWTH, Aachen, D-52056 Germany*

*** Kazan Physicotechnical Institute, Russian Academy of Sciences, Kazan, 420029 Tatarstan, Russia*

e-mail: stepanov@physik.rwth-aachen.de

Received August 11, 2000

Abstract—The depth profiles of Cu^+, Ag^+, and Au^+ ions implanted into amorphous dielectric SiO_2, Al_2O_3, and soda–lime silicate glass (SLSG) are simulated by the DYNA program. The algorithm follows projectile-ion–substrate-atom pair collisions giving rise to a dynamic variation in the phase composition in the surface layer of the irradiated material and takes into account surface sputtering. Ion implantation up to doses of $\leq 10^{16}$ ion/cm^2 at low ion energies of 30, 60, and 100 keV is considered. The measured dynamic variation of the depth profiles of implanted ions as a function of the dose is compared with the standard statistical distribution calculated by the TRIM algorithm. © *2001 MAIK "Nauka/Interperiodica".*

Ion implantation (II) as a method of producing metallic nanoparticles embedded in a dielectric matrix has recently been gaining ever increasing recognition in the preparation of composite materials with nonlinear optical [1, 2] or magnetic [3–5] properties. Of particular interest in this respect is the implantation of low-energy (10–100 keV) noble-metal ions into silicate glasses with the aim of forming optical composites, which allows easy integration into a silicon substrate in order to produce combined optoelectronic devices [6]. The specific features of the optical properties of glasses with metallic nanoparticles originate from inhomogeneities in the depth profiles of the implanted metal ions [1, 7]. This is illustrated in Fig. 1 by a depth profile of silver ions implanted at an energy of 60 keV into the near-surface region of a silicate glass, which was obtained from Rutherford backscattering measurements [8]. This profile differs noticeably from the Gaussian statistical distribution of implanted ions over the sample depth, which was obtained by Monte Carlo simulation, for instance, by means of the TRIM (Transport of Ions in Matter) or SRIS (Stopping and Range of Ions in Solids) codes [9]. It was suggested earlier [10] that one of the reasons for the asymmetric distributions of implanted metal ions may lie in the efficient sputtering of the glass substrate in the course of ion implantation [11]. In order to take this effect into account, it was proposed [10] to determine the depth profile of impurities by standard TRIM calculations of the spectra, with subsequent exclusion of a certain region determined by the thickness of the sputtered substrate layer. To illustrate this approach, Fig. 2 presents calculated silver depth profiles obtained after implanting silver ions of energies 30, 60, 100, and 150 keV into a soda–lime silicate glass (SLSG) substrate. The sputtered glass layer thickness parameters calculated for ion implantation with doses of 4×10^{16} ion/cm^2 at different ion energies can be found in [10]. The data presented provide qualitative evidence for the conclusion that as the energy of ion implantation decreases, the sputtering factor becomes dominant in the final distribution of implanted ions over the sample depth, which no longer follows a symmetric Gaussian profile. However, TRIM calculations within this approach disregard the change in the phase composition in the surface layer of the irradiated substrate due to the penetrating metal ions and, consequently, the corresponding change in the depth of the implanted ions in various stages of ion implantation.

This paper reports the results of a new simulation using the DYNA program [12] following pair collisions of implanted ions with substrate atoms, which give rise

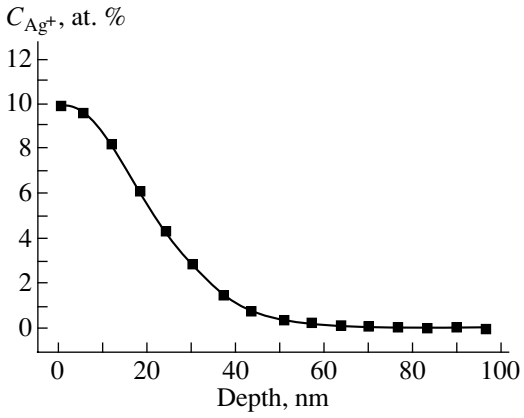

Fig. 1. Depth profile of silver ions implanted into silicate glass, obtained from Rutherford backscattering measurements. Conditions: implantation energy, 60 keV; dose, 7×10^{16} ion/cm^2 [8].

to dynamic variation in the phase composition in the surface layer of an irradiated amorphous substrate, and taking into account surface sputtering. In the DYNA program, the elastic scattering of a projectile ion from the target atoms is described using the results obtained in [13]. The DYNA program has already demonstrated a good agreement between calculated and experimental depth profiles of impurities in the cases of ion implantation with energies > 200 keV into monatomic metal and semiconductor substrates [11, 14]. We present the results of a profile simulation for heavier ions Cu^+, Ag^+, and Au^+ implanted at energies of 30, 60, and 100 keV into amorphous polyatomic dielectric SiO_2, Al_2O_3, and SLSG.

To simulate the dynamic variation of the phase composition in a surface layer of an irradiated material upon cascade pair collisions and mixing of atoms, one has to preset the volumes and/or size of the atoms participating in the events under consideration [13]. These values were found by us from known densities of the corresponding solid materials and, for the oxygen atoms, from the interatomic distances in the dielectrics under study. The sputtering coefficients of the dielectric substrates, which are required for the DYNA program, were calculated by the SRIM-2000 code [9] for the case of normal incidence of the projectile ions as a function of their energy, with due regard for the surface energy parameters and atomic bonding energies in the SiO_2, Al_2O_3, and SLSG amorphous structures. The densities used for these materials were 2.25, 4.0, and 2.47 g/cm^2, respectively. The sputtering coefficients thus obtained are shown in Fig. 3.

DYNA simulation treats the near-surface region of an irradiated sample as a set of thin (in our case, ~2 nm thick) plane-parallel layers containing a preset number of atoms of specific elements. The total thickness of the multilayer model structure exceeds the maximum penetration depth of ions into the material for the corresponding energies of ion implantation. In each stage of the depth profile calculations, the atom concentration in every layer was recalculated after the entrapment of the chosen ion dose fraction, so that the target used in the subsequent steps of ion implantation had a new atomic composition. The variation in the composition and concentration of atoms in each layer was calculated for approximately 25 cascade collisions of each incident ion with the substrate atoms. The step in the dose dependence after which the target composition was recalculated was approximately 5×10^{14} ion/cm^2 for all the situations considered.

The results of the depth profile simulation for the Cu^+, Ag^+, and Au^+ ions incident on various dielectric matrices upon ion implantation are displayed graphically in Figs. 4–6. For comparison, the profiles calculated with the TRIM code are also shown. One readily sees that the concentration maximum in the DYNA profiles is always closer to the irradiated sample surface than that in the TRIM distributions, and the DYNA profile becomes asymmetric for doses in excess of a certain critical value. For instance, at an implantation energy of 30 keV, this critical level lies between

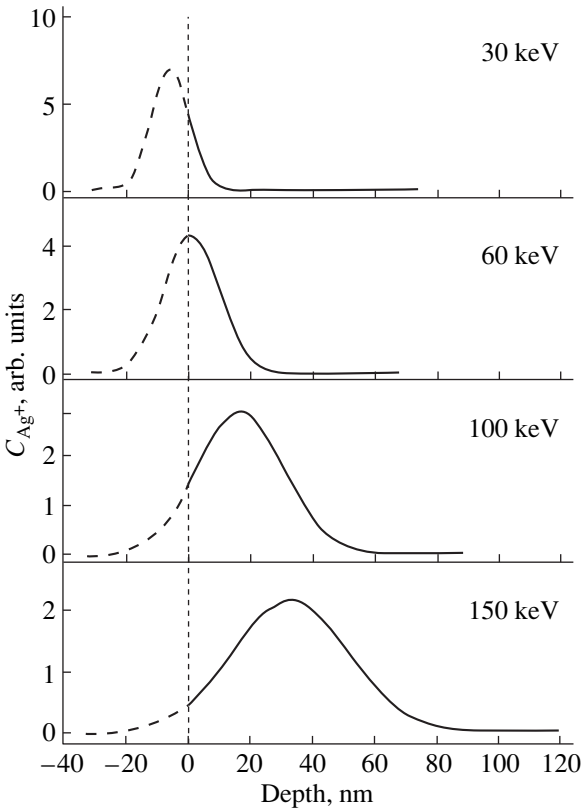

Fig. 2. Calculated depth profiles of Ag^+ ions implanted at different energies with statistical inclusion of the sputtering effect. The thickness of the sputtered surface layer is given for a dose of 4×10^{16} ion/cm^2. The vertical dashed line indicates the surface position after the sputtering, and the left-hand part of the profile relates to the sputtered fraction of the Ag^+ ions.

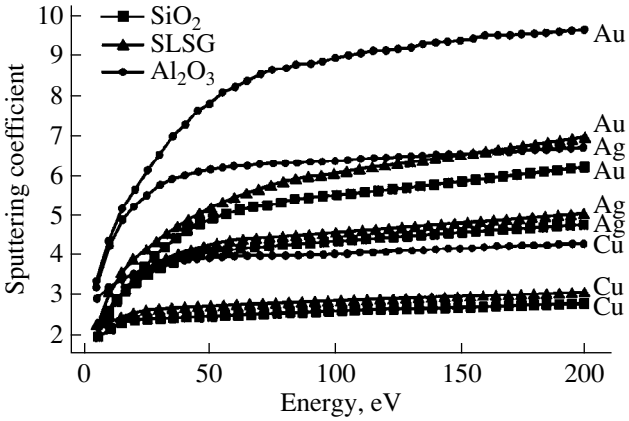

Fig. 3. Calculated sputtering coefficients of the dielectrics SiO_2, Al_2O_3, and SLSG as functions of the energy for the Cu^+, Ag^+, and Au^+ implants.

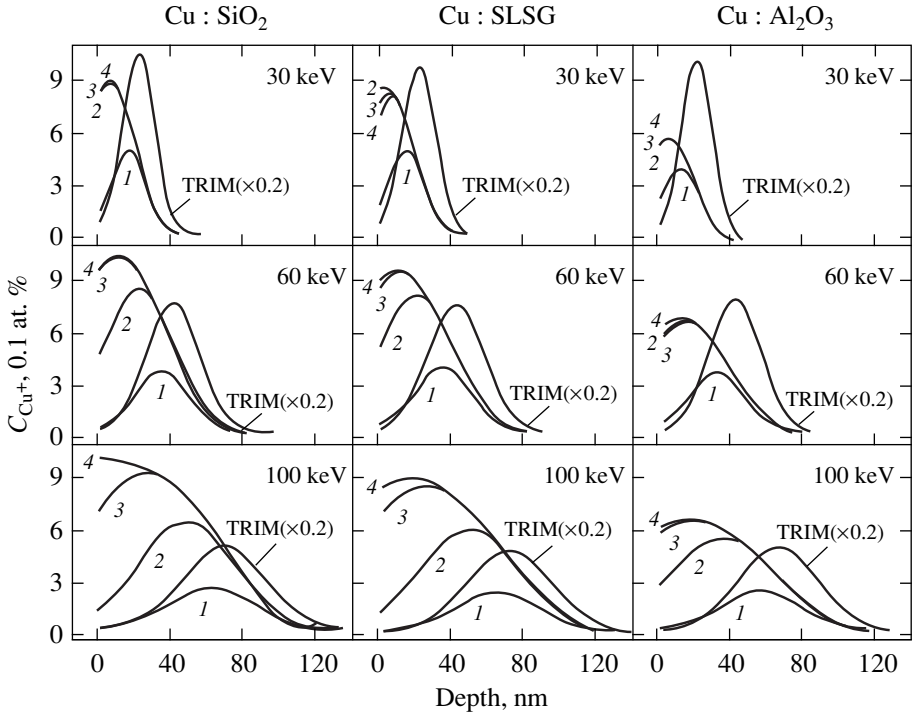

Fig. 4. DYNA depth profiles of Cu^+ ions implanted into amorphous dielectric SiO_2, Al_2O_3, and SLSG for different ion energies and doses (ion/cm^2): (*1*) 0.1×10^{16}, (*2*) 0.3×10^{16}, (*3*) 0.6×10^{16}, and (*4*) 1×10^{16}. The ion depth profiles calculated with the TRIM code are shown for comparison.

0.1×10^{16} ion/cm^2 for the heavy Ag^+ and Au^+ ions and 0.3×10^{16} ion/cm^2 for the lighter Cu^+ ions.

Figures 4–6 show the dynamic variation in the depth profiles, which is particularly clearly pronounced at higher energies (60 and 100 keV), with time, i.e., with the buildup of implanted ions in the irradiated materials (curves *1–4*). In the early stages of ion implantation (i.e., for small doses), the DYNA distribution of the implanted ions coincides with the TRIM profile. As the exposure is increased, i.e., the dose grows, the ion implantation gives rise to sputtering both of the target atoms and of a fraction of the embedded impurity atoms from the surface layer of the sample. Moreover, it is known [15] that the competing processes of surface sputtering and variation in the atomic composition of the matrix and its density, which affect the projective range and the character of the incident ion collisions with the target atoms, begin to play a substantial role at high doses of ion implantation. These processes are particularly important for the implantation of heavy ions into matrices consisting of lighter atoms, which is exactly our case. As a result, the maximum in the impurity concentration distribution shifts toward the surface as compared to the TRIM profiles. While it is presently difficult to say which of the two processes responsible for the variation in the depth profile shape is dominant, both of them should be included in the profile simulation. On the other hand, one can readily conceive a situation where in certain "equilibrium" conditions of ion implantation, the fraction of the implanted ions sputtered out of the near-surface region would be replenished with newly implanted ions. Eventually, the profile would stabilize at a certain depth. In this case, the competing processes are governed by the rate of ion supply and the magnitude of the sputtering coefficient. In this simulation, we were not interested in determining the dependence of the distribution profiles on the rate of ion supply, although the DYNA code permits variation of this parameter.

The data presented in Figs. 4–6 reveal another interesting feature, namely, that despite the noticeable difference between the densities of SiO_2 and Al_2O_3, the profile depths of the implanted ions are virtually the same for the two materials. There is, naturally, a difference in the absolute atomic concentration between these profiles. Nevertheless, their similarity clearly indicates that the competing processes and the scatter of their parameters (sputtering coefficients, atomic masses, etc.) may bring about unexpected impurity distributions and, in particular, coincidence of profiles for totally different materials.

An additional example of how the depth profiles vary depending on the dose of the implantation of 40-keV Cu^+ ions into an amorphous Al_2O_3 matrix is illustrated by Fig. 7. The three-dimensional plot covering the dose range 10^{15}–10^{16} ion/cm^2 clearly reveals the depth profile evolution from a Gaussian at low doses to

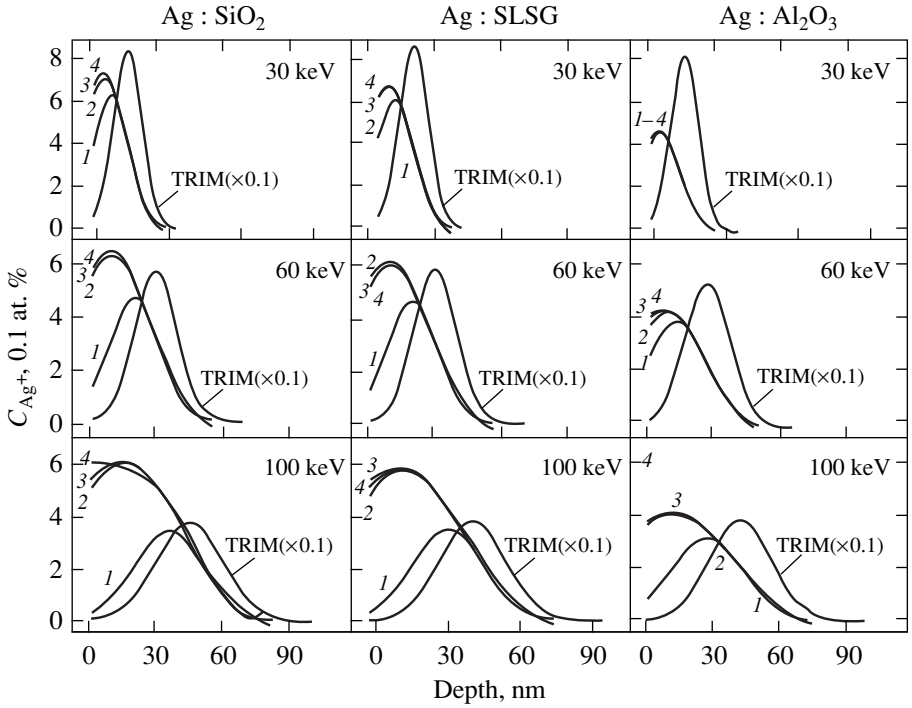

Fig. 5. DYNA depth profiles of Ag^+ ions implanted into amorphous dielectric SiO_2, Al_2O_3, and SLSG for different ion energies and doses (ion/cm^2): (*1*) 0.1×10^{16}, (*2*) 0.3×10^{16}, (*3*) 0.6×10^{16}, and (*4*) 1×10^{16}. The depth profiles calculated with the TRIM code are shown for comparison.

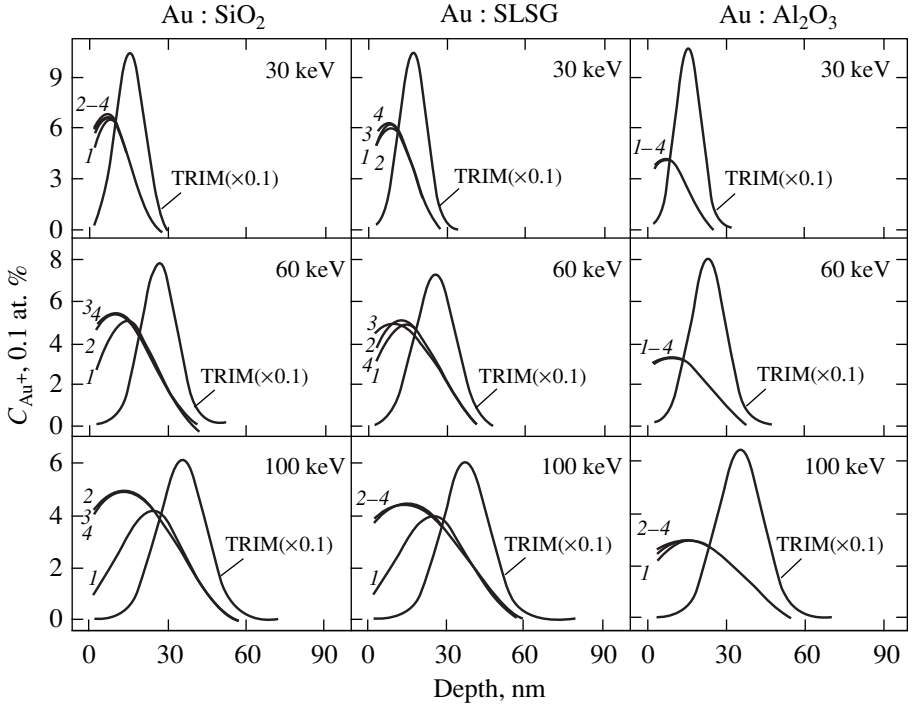

Fig. 6. DYNA depth profiles of Au^+ ions implanted into amorphous dielectric SiO_2, Al_2O_3, and SLSG for different ion energies and doses (ion/cm^2): (*1*) 0.1×10^{16}, (*2*) 0.3×10^{16}, (*3*) 0.6×10^{16}, and (*4*) 1×10^{16}. The depth profiles calculated with the TRIM code are shown for comparison.

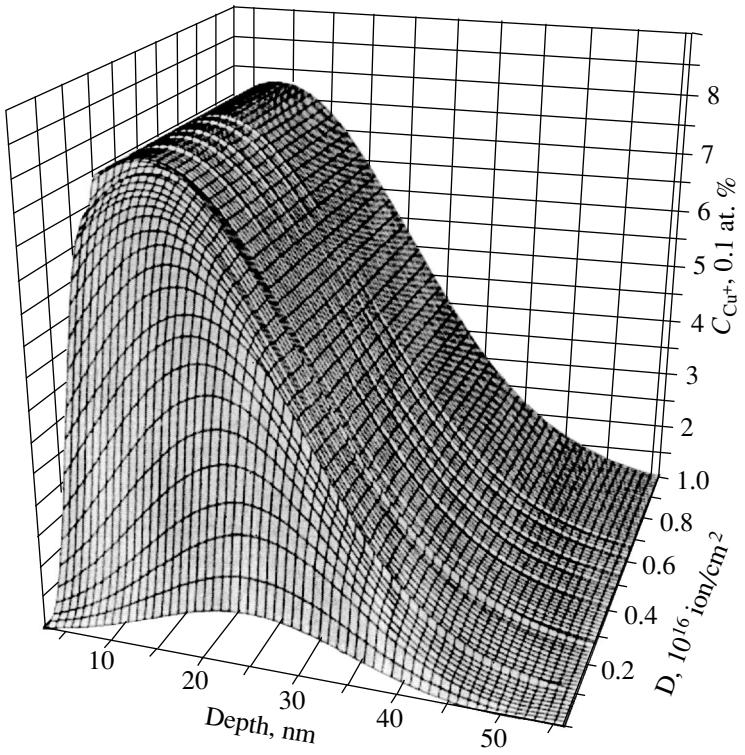

Fig. 7. Dose dependence of the DYNA depth profiles calculated for 40-keV Cu^+ ions implanted into amorphous Al_2O_3.

an asymmetric one, with the concentration maximum shifting toward the surface. On reaching a dose of $\approx 0.3 \times 10^{16}$ ion/cm^2, the depth profile stabilizes and no longer changes with further increase in the dose.

The DYNA calculations performed for all the simulations discussed in this work were made for doses not in excess of 10^{16} ion/cm^2, because, at higher doses and low energies of ion implantation, the impurity ion concentration accumulated in the near-surface region exceeds the metal solubility limit in dielectrics [1, 2]. This gives rise to the nucleation and growth of nanoparticles, which immediately changes the phase composition of the irradiated material and affects the ion range and the atomic collision mechanisms. In this case, the approach which is based on pair collisions of atoms in a homogeneous amorphous medium and realized in the DYNA program becomes no longer applicable. Nevertheless, the depth distribution of metallic nanoparticles in the case of high doses can also be predicted from the calculated data shown in Figs. 4–7. Because the increase in the absolute concentration of implanted metal ions in the depth profiles and the sputtering coefficient depend on the implantation time (or on the built-up dose), the nucleation and growth of metallic nanoparticles will also be functions of time. Obviously enough, the size of forming metallic particles at different depths will be "proportional" to the metal filling factor in the dielectric at the same depth, because both these quantities are governed by the concentration profile of the implanted ions. Therefore, the asymmetric depth profiles of the metal ions, which are calculated for ion doses of $\sim 10^{16}$ ion/cm^2 (Figs. 4–7), permit the conclusion that, in the cases of ion implantation with doses in excess of this value and resulting in a similar profile, the larger synthesized metallic nanoparticles (and/or higher filling factors) should lie closer to the irradiated surface, whereas smaller particles should tail off into the bulk of the sample. This suggestion of the size distribution of metallic nanoparticles over the sample depth is supported by electron microscope observations of sample sections [1, 16] and optical reflectance studies of silicate glasses irradiated by 60-keV Ag^+ ions to a dose of 2×10^{16} ion/cm^2 [7].

The model examples considered above represent a simplification as compared with real implantation conditions. In particular, in addition to the difficulties encountered in calculations for high doses, there are additional competing processes which considerably affect the redistribution of impurities. Among them are effects originating from radiation and thermally stimulated diffusion in materials subjected to implantation, segregation, the effect of crystallinity of real dielectrics, associated ion channeling, etc. Nevertheless, the above approach and the use of the DYNA program permit one to simulate the depth profiles of the implanted impurity, which are closer to the experimental distributions than those obtained by the standard TRIM program. Thus, we have demonstrated the possibility of

efficiently taking into account the modification of the atomic composition of an irradiated target and the surface sputtering, which is particularly important at low implantation energies and when incorporating heavy ions into a matrix made up of lighter chemical elements, as well as of obtaining a correct account of the changes in the composition of the bombarded layer.

ACKNOWLEDGMENTS

One of the authors (A. L. S.) expresses his warm gratitude to the Alexander Humboldt Foundation (Germany) for financial support, which made possible his visit to the Institute of Physics 1, Technical University of Aachen (Germany), as well as to D. Hole and P. Townsend from Sussex University (Great Britain) and V.N. Popok from the Belorussian State University for fruitful discussions.

This work was supported by the Russian Foundation for Basic Research, project no. 99-02-17767.

REFERENCES

1. P. D. Townsend, P. J. Chandler, and L. Zhang, *Optical Effects of Ion Implantation* (Cambridge Univ. Press, Cambridge, 1994).
2. A. L. Stepanov, I. B. Khaĭbullin, P. Townsend, D. Hole, and A. A. Bukharaev, RF Patent No. 99106057/28 (006367) (1999).
3. S. N. Abdullin, A. L. Stepanov, R. I. Khaĭbullin, *et al.*, Fiz. Tverd. Tela (St. Petersburg) **38** (8), 2574 (1996) [Phys. Solid State **38**, 1412 (1996)].
4. S. N. Abdullin, A. L. Stepanov, R. I. Khaĭbullin, and I. B. Khaĭbullin, RF Patent No. 2096835 (1996).
5. I. Sakamoto, S. Honda, H. Tanoue, *et al.*, Nucl. Instrum. Methods Phys. Res., Sect. B **148**, 1039 (1999).
6. A. A. Bukharev, A. V. Kazakov, R. V. Manapov, and I. B. Khaĭbullin, Fiz. Tverd. Tela (Leningrad) **33** (4), 1018 (1991) [Sov. Phys. Solid State **33**, 578 (1991)].
7. A. L. Stepanov, Opt. Spektrosk. **89** (3), 444 (2000) [Opt. Spectrosc. **89**, 408 (2000)].
8. A. L. Stepanov, D. E. Hole, and P. D. Townsend, J. Non-Cryst. Solids **244**, 275 (1999).
9. J. F. Ziegler, J. P. Biersak, and U. Littmark, *The Stopping and Range of Ions in Solids* (Pergamon, New York, 1996).
10. D. E. Hole, A. L. Stepanov, and P. D. Townsend, Nucl. Instrum. Methods Phys. Res., Sect. B **148**, 1054 (1999).
11. P. Sigmund, in *Sputtering by Particle Bombardment*, Ed. by R. Behrisch (Springer-Verlag, New York, 1981; Mir, Moscow, 1984).
12. V. M. Konoplev, Poverkhnost, No. 2, 207 (1986).
13. V. M. Konoplev, Radiat. Eff. Lett. Sect. **87**, 207 (1986).
14. V. M. Konoplev, M. Vicanek, and A. Gras-Marti, Nucl. Instrum. Methods Phys. Res., Sect. B **67**, 574 (1992).
15. M. Nastasi, J. W. Mayer, and J. K. Hirvonen, *Ion–Solid Interactions: Fundamentals and Applications* (Cambridge Univ. Press, Cambridge, 1996).
16. Hideo Hosono, Phys. Rev. Lett. **74**, 110 (1995).

Physics of the Solid State, Vol. 43, No. 4, 2001, pp. 772–777. Translated from Fizika Tverdogo Tela, Vol. 43, No. 4, 2001, pp. 739–744.

LOW-DIMENSIONAL SYSTEMS AND SURFACE PHYSICS

Europium Adsorption on a Tungsten Surface with Various Degrees of Oxidation

V. N. Ageev and E. Yu. Afanas'eva

Ioffe Physicotechnical Institute, Russian Academy of Sciences, Politekhnicheskaya ul. 26, St. Petersburg, 194021 Russia
e-mail: Afanaseva@ms.ioffe.rssi.ru

Received August 21, 2000

Abstract—The kinetics of europium adsorption on a W(100) face with various degrees of oxidation were studied by thermal desorption and Auger electron spectroscopy. The spectrum of Eu atoms desorbed thermally from the W(100) face consists of three successively filling desorption phases whose desorption activation energy decreases from 3 to 2.1 eV with an increase in the surface coverage. The thermodesorption spectrum of Eu atoms from the W(100) face coated with a monatomic oxygen film contains five successively forming desorption phases, with the desorption activation energy increasing to 4 eV for the high-temperature phase. The oxidized W is reduced by europium, and the desorption of the W oxides is replaced by that of EuO. After a monolayer film has formed, the Eu film adsorbed on tungsten starts to grow in the form of three-dimensional crystallites. As the degree of W oxidation increases, the Eu film becomes less nonuniform, until a solid Eu film starts to grow on bulk W oxides and completely screens the tungsten Auger signal. © *2001 MAIK "Nauka/Interperiodica".*

1. INTRODUCTION

Rare-earth metals are widely used in electronics, electrical engineering, oil refining, and the car industry, as well as in space technology, for manufacture of electron emitters, permanent magnets, and construction and HTSC ceramics [1]. However, information on the characteristics of their adsorption on the surface of refractory metals is scarce [2–7] and on the surface of their oxides, it is completely lacking. In this work, we studied europium adsorption on the surface of oxidized tungsten by thermodesorption spectroscopy (TDS) and Auger electron spectroscopy (AES). Our earlier study dealt with electron-stimulated desorption (ESD) of Eu atoms from an Eu layer adsorbed on oxidized tungsten [8].

2. EXPERIMENTAL TECHNIQUE

The measurements were conducted by TDS and AES methods, which were described in detail in [9, 10]. The thermodesorption products were identified by a pulsed time-of-flight mass spectrometer. The Eu atom flux was derived from the Eu^+ ion current which corresponded to the 152 line in the mass spectrum, and the flux of the EuO molecules was deduced from the EuO^+ ion current (the 168 mass line in the mass spectrum).

The Auger spectra were recorded with a 120° quasi-spherical retarding field energy analyzer. Quantitative determination of Eu was based on the intensity of the $N_{45}O_{23}N_{67}$ Auger line at an energy of 109 eV, and the intensity of the $4d$–$4f$ direct recombination peak at 139 eV was used to determine the extent of Eu oxidation [11]. The screening of tungsten by europium was found from the change of the N_5N_6V tungsten Auger line at 169 eV. The primary electron energy was 1.3 keV, and the current density did not exceed 1.3×10^{-3} A/cm^2. Textured tungsten ribbons $0.01 \times 1.0 \times 30$ mm in size with a predominantly (100)-oriented surface served as substrates. The ribbons were freed of carbon by the standard technique, namely, by annealing in oxygen at a pressure of 10^{-6} Torr and a ribbon temperature of ~1600 K for several hours.

The W ribbons were oxidized in two regimes: (i) the ribbons were exposed to oxygen at a pressure of $\sim 3 \times 10^{-7}$ Torr and $T = 1600$ K for 10 min (the conditions in which a monatomic oxygen film forms on the W surface [12] together with a small amount of surface W oxides) and (ii) the oxidation was conducted at an oxygen pressure of $\sim 3 \times 10^{-7}$ Torr and $T = 1000$ K for different times (the conditions favoring growth of bulk W oxides [12]).

The source of europium atoms was made of a 30-mm-long tantalum tube 3 mm in diameter with a wall thickness of 0.05 mm, which was sealed on both ends and into which europium was placed directly before instrument evacuation. Seven holes 0.3 mm in diameter were drilled along the tube length to ensure a uniform flux of Eu atoms onto the surface of the W ribbon. The source was heated by passing a direct current. The source heating time to the establishment of a steady-state Eu atom flux was about 10 min. Two regimes of Eu deposition were employed: (i) the source was heated for 10 min, after which the W ribbon was cleaned by heating to $T = 2400$ K and its temperature was lowered to the temperature of Eu adsorption; after the adsorption, the ribbon temperature was

1063-7834/01/4304-0772$21.00

increased and the desorption products were identified; (ii) the tungsten ribbon was cleaned by high-temperature heating, after which the Eu source was turned on, the deposition was carried out, the source of europium atoms was turned off, and one either recorded the Auger spectrum or produced a high-temperature flash with measurement of the flux of the desorbing particles. In the first regime, the amount of deposited Eu was a linear function of deposition time and, in the second, it was nonlinear, with the deposition rate increasing with the Eu source temperature.

The W ribbon and the Eu source were mounted on a manipulator, which permitted positional adjustment of the sample between the entrance to the mass-spectrometer source and the energy analyzer. The ribbon heating rate could be varied from 20 to 2000 K/s, with a close-to-linear dependence of the temperature on time. The deviation from linearity within the temperature range 600–2000 K did not exceed 50 K. In the high-temperature range, the ribbon temperature was measured with an optical micropyrometer and at low temperatures, by linear extrapolation of the dependence of the ribbon temperature on the heater current to room temperature. The base pressure in the instrument was about 10^{-10} Torr.

3. RESULTS

(a) Thermodesorption of Eu from W(100). Figure 1 shows thermodesorption spectra of Eu atoms from W(100) for various coverages. The coverage is expressed in units of $\theta_s = N_{ads}/N_s$, where N_{ads} is the number of Eu adatoms and N_s is the surface concentration of W atoms on the (100) face (~10^{15} atoms/cm^2). It is seen that, as the coverage increases, three maxima appear in the desorption curves, which indicate the presence of three phases of Eu desorption from the W(100) face. The two high-temperature desorption phases reach saturation with an increase in the coverage, whereas the low-temperature phase shows no saturation. A similar behavior of the spectra of the Eu thermodesorption from the W(100) face was earlier reported in [3], where the Eu atom flux was derived from measurements of the surface ionization current. The Eu concentration which corresponded to the saturation of the first high-temperature phase was found to be 5×10^{14} atoms/cm^2 and was due to monolayer formation. The filling of the low-temperature phase starts, accordingly, at coverages $\theta_s > 0.75$. Because the slope of the desorption curve of this phase does not depend on the coverage and the europium content in it increases without limit with increasing exposure, it can be assumed to have zero-order desorption kinetics [13, 14] and to be due to europium desorption from three-dimensional formations. Figure 2 shows the dependence of $\ln(dN/dt)$ on T^{-1} for this phase of desorption. The plot is well fitted by a straight line whose slope yields the Eu desorption activation energy in this phase, $E = 2.1 \pm 0.2$ eV, which is slightly higher than the heat

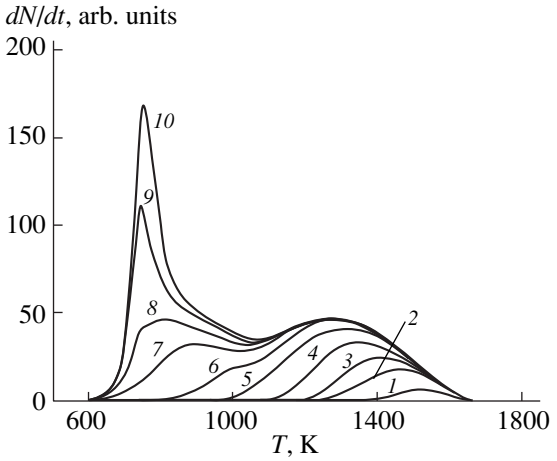

Fig. 1. Thermodesorption spectra of Eu atoms from W for different initial coverages θ_s: (*1*) 0.03, (*2*) 0.1, (*3*) 0.15, (*4*) 0.25, (*5*) 0.4, (*6*) 0.5, (*7*) 0.7, (*8*) 0.82, (*9*) 1.0, and (*10*) 1.1. The adsorption temperature T is 300 K, and the heating rate is 200 K s^{-1}.

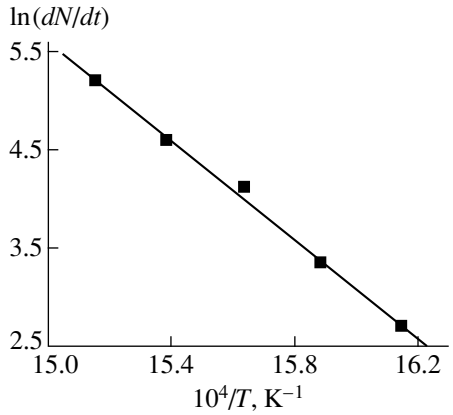

Fig. 2. Dependence of $\ln(dN/dt)$ on T^{-1} for the initial coverage of W by europium, $\theta_s = 1.3$.

of europium sublimation, 1.84 eV [15]. As follows from Fig. 1, the first high-temperature phase contains twice the number of Eu atoms in the second phase, which is at variance with the data obtained in [3]. This is possibly due to the europium adsorption in [3] having been performed at temperatures above 700 K.

Figure 3 plots $\ln((dN/dt)/N)$ as a function of T^{-1} for thermodesorption of Eu atoms from W(100) for various surface europium coverages θ_s. For $\theta_s \le 0.03$, the plot can be approximated by a straight line whose slope yields the desorption activation energy $E = 3.0 \pm 0.2$ eV. This value coincides with that found by the temperature modulation technique [2] and the activation energy calculated under the assumption of trivalent Eu on W [16], as well as with the TDS result for the W(110) face [17]. On the other hand, it lies substantially below the value $E = 4.42$ eV obtained by the adsorption isobar method [3].

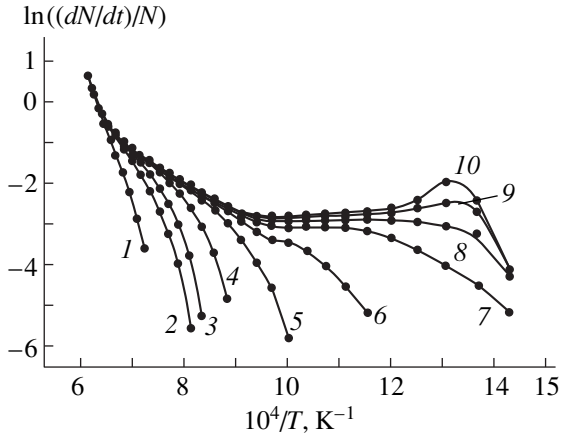

Fig. 3. Dependence of $\ln((dN/dt)/N)$ on T^{-1} for different initial coverages θ_s: (*1*) 0.03, (*2*) 0.1, (*3*) 0.15, (*4*) 0.25, (*5*) 0.4, (*6*) 0.5, (*7*) 0.7, (*8*) 0.82, (*9*) 1.0, and (*10*) 1.1.

For $\theta_s > 0.03$, the plots exhibit a bend, indicating the presence of lateral interactions in the adlayer. For $\theta_s > 0.5$, a linear section parallel to the horizontal axis appears in the graphs, beyond which a maximum is observed for $\theta_s > 1$. The appearance of the maximum is apparently due to the formation of the low-temperature phase.

(b) Thermodesorption of Eu from oxidized tungsten. Figure 4 displays thermodesorption spectra of Eu atoms from the oxygen monolayer–coated W(100) face, which were measured for various initial Eu surface coverages deposited at $T = 300$ K. As the coverage increases, five thermodesorption phases are seen to fill successively, with the high-temperature phase displaced by about 400 K toward higher temperatures compared to the first high-temperature phase of Eu desorption from tungsten, which indicates an increase in the europium binding energy at the monolayer oxygen film on tungsten, W–O. For $\theta_s \leq 0.1$, the activation energy of the Eu desorption from W–O was found to be $E = 4.0 \pm 0.2$ eV, i.e., higher by 1 eV than that from tungsten. The lowest temperature europium desorption phase is actually desorption from the condensed state.

Note that the desorption of europium oxides could be detected only in the case when the sensitivity of the method was increased by raising the heating rate in the flash fivefold. In these conditions, the amount of desorbing EuO was a few percent of that of Eu desorbing in the high-temperature phase from W–O. Note that while before the Eu deposition the heating of a monatomic oxygen film on W resulted in desorption, not just of oxygen, but also of an insignificant amount of tungsten oxides, after Eu was deposited, one observed desorption not of the tungsten oxides, but rather of an approximately equal amount of EuO. The desorption activation energy of EuO, which was derived from the dependence of $\ln((dN/dt)/N)$ on T^{-1}, was found to be $E = 4.1 \pm 0.2$ eV.

Europium deposited on the W ribbon at 300 K undergoes oxidation in an oxygen atmosphere at a pressure of 3×10^{-7} Torr and a temperature of 700 K for a few minutes. This is indicated by the manifestation of EuO molecules in the thermodesorption spectrum, with the EuO peak displaced relative to the high-temperature

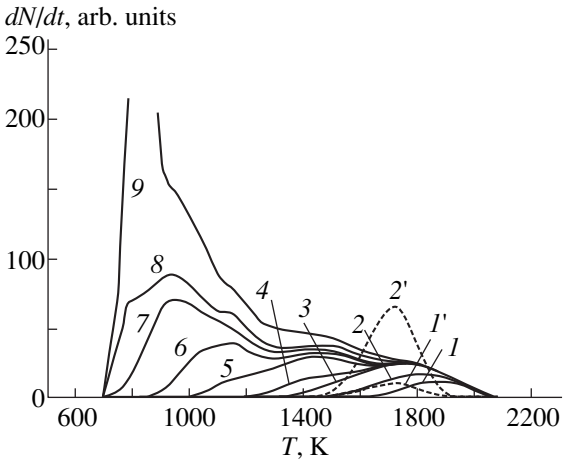

Fig. 4. Thermodesorption spectra of Eu atoms from W coated with a monoatomic oxygen film for different initial coverages θ_s: (*1*) 0.1, (*2*) 0.2, (*3*) 0.4, (*4*) 0.45, (*5*) 0.75, (*6*) 1.05, (*7*) 1.5, (*8*) 1.9, and (*9*) 3.5. $T = 300$ K. Dashed lines show the thermodesorption spectra of EuO after oxidation (at $T = 700$ K for 5 min) of an Eu film deposited preliminarily on W to a concentration θ_s: (*1*') 0.4 and (*2*') 1.05. The heating rate is 200 K s^{-1}.

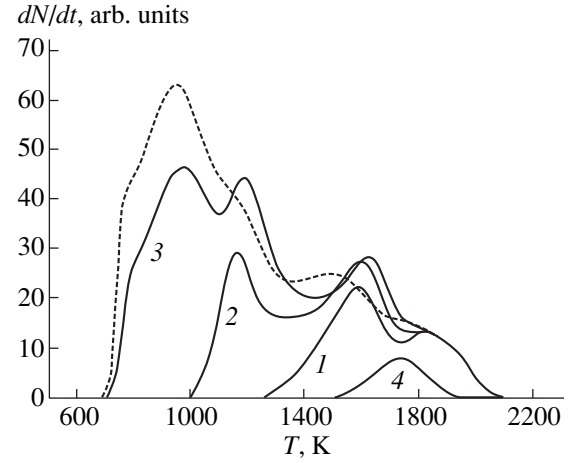

Fig. 5. Thermodesorption spectra of Eu atoms from oxidized W for different europium deposition times (min): (*1*) 6, (*2*) 8, and (*3*) 10. (*4*) Simultaneous desorption of EuO from the film prepared by depositing Eu for 8 min. The dashed line shows the thermodesorption spectrum of Eu atoms from W coated with an oxygen monolayer (europium deposition time $t = 8$ min). The heating rate is 200 K s^{-1}.

desorption peak of Eu atoms from W–O toward lower temperatures by a few tens of degrees Kelvin (Fig. 4).

Figure 5 shows thermodesorption spectra of Eu deposited on a film of bulk tungsten oxides. The spectra are seen to retain the five-phase structure. One observes a slight displacement of the maxima of some phases and a change in their sorption capacity. One also detects a sizable amount of desorbing EuO molecules.

The amount of flash-desorbed Eu atoms decreases with increasing tungsten preoxidation time for the same Eu deposition doses (Fig. 6). This decrease cannot be assigned solely to the simultaneous desorption of EuO, and it does not depend on the substrate temperature within the range $300 < T < 600$ K. This effect is apparently associated with the decrease in the Eu sticking coefficient, which arises after tungsten oxidation. A similar effect of a decreasing adsorption activity of Ir with respect to Yb was observed in [2] after the oxidation of Ir.

(c) Europium adsorption on tungsten and oxidized tungsten. Figure 7 plots the Auger signal intensities of Eu (109 eV) and W (169 eV) as a function of deposited Eu dose expressed in units of θ_s. The deposition was made on clean W (curves *1*, *4*), W–O (curves *2*, *5*), and oxidized tungsten (curves *3*, *6*). The Eu Auger signal increases linearly in all cases up to $\theta_s = 0.75$, which apparently corresponds to the filling of the first layer. Curves *1–3* tend to saturation (or to the region of a slow Auger-signal variation) for different signal amplitudes, depending on the actual substrate oxidation degree. Note that curves *1* and *2* practically coincide up to $\theta_s = 1.5$, whereas curve *3* starts to deviate already at the minimum values of θ_s, with the Auger signal of Eu deposited on clean W first exceeding that of the Eu adsorbed on the oxidized W. Then, one observes the reverse behavior. This disagreement cannot be connected unambiguously with a change in the Eu film growth mechanism, because one has to also take into account such factors as the variation in the Auger line shape of Eu on oxidized tungsten and the decrease in the Eu sticking coefficient with an increase in the degree of W oxidation.

The variation of the W Auger signal intensity with the deposited dose of Eu also argues for the fact that the final state of the Eu film depends on the degree of W oxidation. Total screening of tungsten by a deposited Eu film is attained only when Eu is deposited on oxidized tungsten (curve *6*). When Eu is adsorbed on W or on W coated with an oxygen monolayer, the dependences of the W Auger signal intensity reach saturation, with the saturated amplitude being higher in the case of deposition on clean W. It can be conjectured that, at $T = 300$ K, after a monolayer film with $\theta_s = 0.75$ has formed, three-dimensional Eu crystallites start to grow above this monolayer. When Eu is deposited on clean W, the nonuniformity of the growing film is larger than that in the case of Eu deposited on W–O and the W Auger signal is screened less in this case. Only when deposited on oxidized W, the growing film is close to being uniform and the tungsten is completely screened.

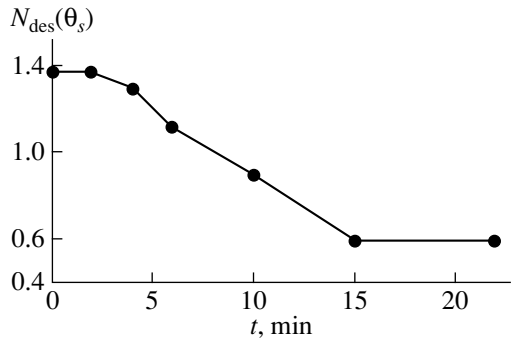

Fig. 6. The amount of Eu desorbing from oxidized W as a function of the preliminary oxidation time for the same initial europium coverage $\theta_s = 1.38$. The oxidation was performed at an oxygen pressure $P = 3 \times 10^{-6}$ Torr and $T = 1000$ K.

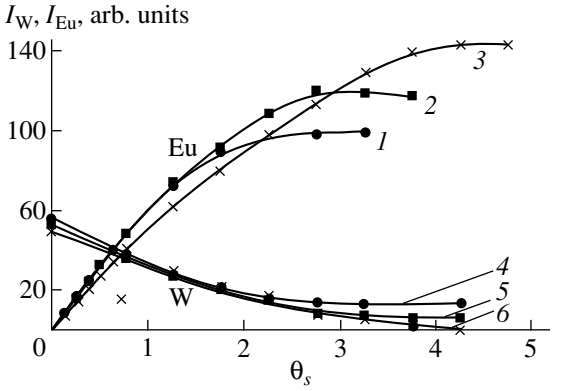

Fig. 7. Auger peak intensity of (*1–3*) Eu and (*4–6*) W as a function of the Eu deposition dose at substrate temperature $T = 300$ K. (*1*, *4*) Deposition on W, (*2*, *5*) deposition on W coated with an oxygen monolayer, and (*3*, *6*) deposition on oxidized W.

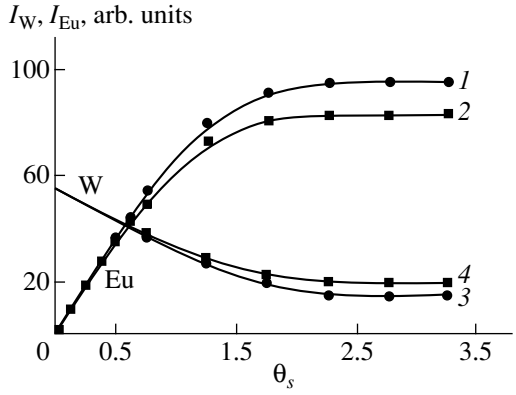

Fig. 8. Auger peak intensity of (*1*, *2*) Eu and (*3*, *4*) W as a function of the Eu deposition dose for various substrate temperatures T (K): (*1*, *3*) 300 and (*2*, *4*) 500.

Figure 8 shows the variation of the Auger signal intensities of Eu and W upon Eu deposition on clean W

at different temperatures (300 and 500 K). One readily sees that up to $\theta_s = 0.5$, the curves measured at different temperatures coincide, after which they deviate from one another and the Auger signals of both Eu and W reach saturation in the final state. The saturated Auger signal intensity of Eu decreases with increasing temperature, while that for W grows with increasing temperature. Because Eu desorption at $T = 500$ K is very low, it can be conjectured that the area occupied by the crystallites diminishes with an increase in T.

The shape of the Auger signal of Eu depends on its chemical state [11]. For Eu_2O_3, one observes an increase in the Auger line intensity due to the direct $4d$–$4f$ recombination compared with that of the $N_{45}O_{23}N_{67}$ Auger line [11]. The intensity ratio of the $N_{45}O_{23}N_{67}$ and $4d$–$4f$ lines reaches a minimum when a monolayer of Eu is deposited on W. However, only when Eu is deposited on oxidized tungsten, this intensity ratio approaches that for the oxide.

4. DISCUSSION

The Auger signal of Eu on tungsten grows linearly with an increase in the coverage up to $\theta_s = 0.75$ (Fig. 7), which corresponds to a europium concentration $N = 7.5 \times 10^{14}$ atoms/cm^2. It can be assumed that up to $\theta_s = 0.75$, the first layer is filling. At $\theta_s = 0.75$, the thermodesorption spectra of Eu atoms from W show the completion of filling of two high-temperature desorption phases. The value $N = 7.5 \times 10^{14}$ atoms/cm^2 is close to the Eu concentration (6.94×10^{14} atoms/cm^2) in the hexagonal close-packed structure with the metallic Eu atomic radius $r = 2.02$ Å. A similar hexagonal structure was observed in the Eu–W(110) system [17]. Hexagonal and pseudohexagonal close-packed structures in a monolayer were detected at $T = 300$ K for a number of rare-earth elements on the faces of differently oriented high-melting transition metals: Gd–W(110), Tb–W(110) [17], Yb–Mo(110), Sm–Mo(110) [18], Sm–W(100) [6], and Yb–Mo(112) [19]. The formation of close-packed structures is usually accompanied by a strong decrease in the heat of adsorption.

It can be assumed that up to the coverages $\theta_s = 0.5$ (which, in the thermodesorption spectra, corresponds to the filling of the high-temperature desorption phase), Eu adsorbs on W(100) by forming simple, substrate-matched structures. (In the case of Sm adsorption on W(100), one observed the $c(2 \times 2)$ structure for $\theta_s \leq 0.5$ [6]). The activation energy of desorption of Eu atoms from W(100) at small coverages ($\theta_s \leq 0.03$) is $E = 3.0 \pm 0.2$ eV. As θ_s increases, the maxima in the thermodesorption spectra shift within the high-temperature phase toward lower temperatures and the dependences of $\ln((dN/dt)/N)$ on T^{-1} cannot be fitted by straight lines. This is a consequence of lateral adatom interactions, specifically of the indirect interaction through the substrate conduction electrons and the dipole–dipole interaction between the electropositive Eu atoms. The formation of the second high-temperature desorption phase is apparently associated with the onset of the formation of a close-packed hexagonal structure in the adlayer. In this stage, compression of the adatom lattice results in a transition from dipole–dipole and indirect interactions between the Eu adatoms to direct exchange coupling. The decrease in the heat of adsorption was assigned in [20] to the electron transition from the localized $4f$ states to the s band.

After a monolayer has been filled, three-dimensional Eu crystallites start to grow already at $T = 300$ K. The area occupied by the crystallites decreases with an increase in the adsorption temperature from 300 to 500 K. The activation energy of desorption from crystallites, $E = 2.1 \pm 0.2$ eV, is close to the heat of Eu sublimation.

The thermodesorption spectrum of Eu atoms from W coated with an oxygen monolayer contains five successively forming desorption phases. The Eu Auger signal varies linearly with coverage up to $\theta_s = 0.75$. This coverage corresponds to the filling of two high-temperature phases of Eu desorption from W–O. As in the case of Eu deposition on W, the deposition of Eu on W–O brings about the formation of a close-packed lattice of Eu atoms in the monolayer, which desorb in two phases. Both desorption phases are displaced toward higher temperatures compared to the Eu–W system. For small coverages, the desorption activation energy is $E = 4.0 \pm 0.2$ eV, which is 1 eV higher than that for Eu adsorbed on clean W. The film growing at $T = 300$ K with Eu concentrations in excess of the monolayer coverage is made up of three-dimensional crystallites, and it is less nonuniform in thickness than the film obtained by Eu deposition on clean W. The Eu deposited on W coated with an oxygen monolayer desorbs in the form of atoms. EuO molecules desorb in the case where W oxides are present on the surface. In thermodesorption of an oxygen monolayer from W (in the absence of Eu), desorption of oxygen is accompanied by that of a small amount of W oxides. After the deposition of Eu, the W oxides no longer desorb and one observes, instead, desorption of a comparable amount of EuO. As the degree of W oxidation increases, the number of desorbing EuO molecules also increases (Fig. 5). EuO oxides desorb by first-order kinetics with an activation energy $E = 4.1 \pm 0.2$ eV. The first order of desorption kinetics implies that the reduction of surface W oxides and the formation of EuO occur before the onset of desorption.

5. CONCLUSION

Thus, the adsorption of Eu on W(100) oxidized to various degrees was studied by AES and TDS methods. It was shown that Eu desorbs from clean W and W coated with an oxygen monolayer in the form of atoms. Desorption from oxidized W takes place in the form of Eu and EuO. The Eu concentration in a monolayer on clean W and on W coated with a monatomic oxygen

film is $N = 7.5 \times 10^{14}$ atoms/cm^2. The monolayer desorbs in two phases. For coverages $\theta_s \le 0.03$, the activation energy of desorption from clean tungsten is $E = 3.0 \pm 0.2$ eV and that from tungsten coated with an oxygen monolayer is $E = 4.0 \pm 0.2$ eV. The Eu concentration in the monolayer is close to that in a hexagonal close-packed lattice. At coverages in excess of a monolayer, three-dimensional crystallites grow at $T = 300$ K on both clean W and W–O. The film growing on W–O is more uniform in thickness (the crystallites are smaller in size). The film growing on oxidized W at $T = 300$ K is continuous, and it completely screens the W Auger signal. The sticking coefficient of Eu atoms decreases with an increase in the degree of W oxidation.

ACKNOWLEDGMENTS

This work was supported by the Russian Foundation for Basic Research (project no. 99-02-17972) and the Russian State Program "Surface Atomic Structures" (project no. 4.5.99).

REFERENCES

1. G. V. Tsyganova, N. Yu. Pasechnik, and N. N. Smirnova, Vysokochist. Veshchestva **2**, 43 (1991).
2. B. K. Medvedev, Candidate's Dissertation (Leningr. Gos. Univ., Leningrad, 1974).
3. M. V. Loginov and M. A. Mittsev, Fiz. Tverd. Tela (Leningrad) **22** (5), 1411 (1980) [Sov. Phys. Solid State **22**, 823 (1980)].
4. M. V. Loginov and M. A. Mittsev, Fiz. Tverd. Tela (Leningrad) **22** (6), 1701 (1980) [Sov. Phys. Solid State **22**, 992 (1980)].
5. M. V. Loginov and M. A. Mittsev, Poverkhnost, No. 5, 37 (1987).
6. A. P. Kazantsev and M. A. Mittsev, Fiz. Tverd. Tela (Leningrad) **33** (7), 1986 (1991) [Sov. Phys. Solid State **33**, 1118 (1991)].
7. M. V. Loginov, M. A. Mittsev, and V. A. Pleshakov, Fiz. Tverd. Tela (St. Petersburg) **34** (10), 3125 (1992) [Sov. Phys. Solid State **34**, 1672 (1992)].
8. V. N. Ageev and Yu. A. Kuznetsov, Pis'ma Zh. Tekh. Fiz. **26** (13), 86 (2000) [Tech. Phys. Lett. **26**, 579 (2000)].
9. V. N. Ageev and E. Yu. Afanas'ev, Poverkhnost, No. 7, 30 (1987).
10. V. N. Ageev and E. Yu. Afanas'ev, Fiz. Tverd. Tela (St. Petersburg) **39** (8), 1484 (1997) [Phys. Solid State **39**, 1318 (1997)].
11. W. H. Hocking and J. A. D. Matthew, J. Phys.: Condens. Matter **2**, 3643 (1990).
12. V. N. Ageev and N. I. Ionov, Fiz. Tverd. Tela (Leningrad) **11** (11), 3200 (1969) [Sov. Phys. Solid State **11**, 2593 (1970)].
13. G. Le Lay, M. Mannerville, and R. Kern, Surf. Sci. **65**, 261 (1977).
14. K. Nagai, Surf. Sci. **176**, 193 (1986).
15. E. M. Savitskiĭ and V. F. Terekhova, *Metal Science of Rare-Earth Metals* (Nauka, Moscow, 1975).
16. V. K. Nikulin and N. D. Potekhina, Fiz. Tverd. Tela (Leningrad) **20**, 3354 (1978) [Sov. Phys. Solid State **20**, 1936 (1978)].
17. J. Kolaczkiewicz and E. Bauer, Surf. Sci. **175**, 487 (1986).
18. A. Stenborg and E. Bauer, Surf. Sci. **189/190**, 570 (1987).
19. I. Ubogyi, S. Stepanovskyi, and J. Kolaczkiewicz, Phys. Rev. B **61** (16), 11097 (2000).
20. S. Yu. Davydov, Fiz. Tverd. Tela (Leningrad) **21**, 1842 (1979) [Sov. Phys. Solid State **21**, 1056 (1979)].

Translated by G. Skrebtsov

Physics of the Solid State, Vol. 43, No. 4, 2001, pp. 778–782. Translated from Fizika Tverdogo Tela, Vol. 43, No. 4, 2001, pp. 745–749.

LOW-DIMENSIONAL SYSTEMS AND SURFACE PHYSICS

Mechanisms of Heteroepitaxial Growth of Cadmium Telluride Thin Films in a Thermal Field of a Temperature Gradient

A. P. Belyaev, V. P. Rubets, M. Yu. Nuzhdin, and I. P. Kalinkin

St. Petersburg Institute of Technology, Zagorodnyĭ pr. 49, St. Petersburg, 198013 Russia

e-mail: belyaev@tu.spb.ru

Received June 6, 2000; in final form, September 7, 2000

Abstract—The processes of forming cadmium telluride films upon vapor-phase deposition onto a substrate in a thermal field of the temperature gradient along the substrate plane are studied. The results of technological, geometric, electron diffraction, and electron microscopic investigations are reported. It is found that the thermal field of temperature gradient leads to a change in the duration of the Ostwald ripening stage and, under certain conditions, enhances the perfection of the formed structure. The mechanism of the influence of a thermal field on the Ostwald ripening is established. The results obtained are in agreement with the current theory of film formation. © *2001 MAIK "Nauka/Interperiodica".*

1. INTRODUCTION

At present, film material science is one of the most important directions of technological progress. This has stimulated theoretical and experimental investigations in this field and motivated the necessity of studying the formation of film systems under nontrivial conditions (at low temperatures, high supersaturations, etc. [1–3]).

The present work is devoted to the features of the CdTe vapor-phase deposition in a thermal field of the temperature gradient.

2. SAMPLE PREPARATION AND EXPERIMENTAL TECHNIQUE

Film formation processes in a thermal field of the temperature gradient were studied using cadmium telluride films synthesized on mica (muscovite) substrates. The film thickness for different samples was no more than 0.7 μm.

The films were synthesized by the quasi-closed (hot-wall epitaxy) method [4], according to which a CdTe powder was placed in a special quartz reactor 30 mm in diameter and heated under a vacuum of $\approx 10^{-3}$ Pa to the sublimation temperature (T_e = 773 K). Then, the reactor was brought into contact with a substrate by a manipulator for a time of synthesis which did not exceed 1 min.

The temperature gradient of a thermal field along substrate *1* was produced by a special metallic ring *4*, which was mounted on the substrate around its periphery, and a metallic substrate holder *5* equipped with a flat heater *7* in the central part (Fig. 1). The relatively high heat capacity of the unheated ring provided the heat outflow from the center to the periphery and, thus, formed the thermal field gradient in the substrate along the *x* coordinate. The substrate temperature was specified and maintained by a temperature controller in the center of the substrate holder. The temperature was controlled by chromel–alumel thermocouples. The geometric measurements (thickness and thickness homogeneity) were carried out on an MII-4 microinterferometer providing measurements with an accuracy of 0.03 μm. Structural investigations were performed with an ÉMR-100 electron diffractometer and a PÉM-100 electron microscope.

3. RESULTS

The study of film formation processes in a thermal field of the temperature gradient involved technological, structural, and geometric investigations. The main experimental results are shown in Figs. 2–4.

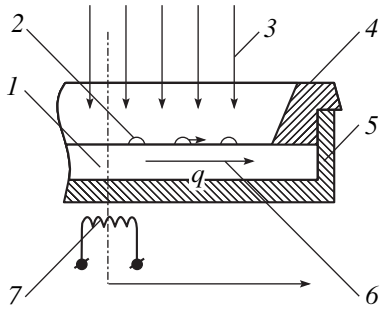

Fig. 1. A scheme of synthesizing cadmium telluride films in a thermal field of the temperature gradient: (*1*) substrate, (*2*) disperse particles of new phase, (*3*) incident flux, (*4*) special metallic ring, (*5*) substrate holder, (*6*) heat flux *q*, and (*7*) heater.

1063-7834/01/4304-0778$21.00

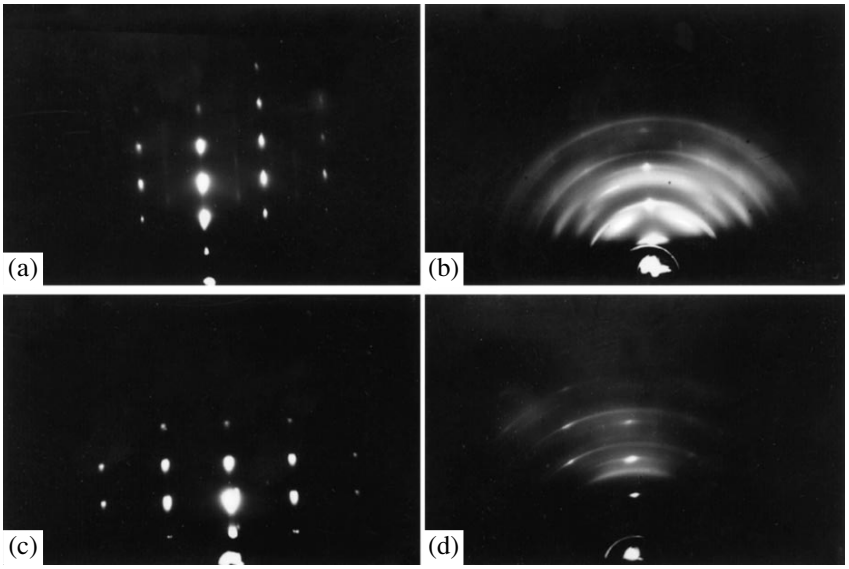

Fig. 2. Electron diffraction patterns of cadmium telluride films synthesized (a, b) under uniform conditions and (c, d) in a thermal field of the temperature gradient at different substrate temperatures T_s (K): (a) 523 and (b–d) 473. (c) Central and (d) peripheral film regions.

The structures of the films grown under different conditions are characterized by the electron diffraction patterns shown in Fig. 2. The electron diffraction patterns that correspond to the typical structures of the films grown in the absence of a thermal field of the temperature gradient at substrate temperatures T_s = 523 and 473 K are displaced in Figs. 2a and 2b, respectively. A comparison of these diffraction patterns demonstrates that a decrease in the substrate temperature to 473 K in the absence of thermal field leads to a substantial deterioration of the perfection of the structure (from epitaxial to polycrystalline).

The electron diffraction patterns of the films synthesized in a thermal field of the temperature gradient at T_s = 473 K are shown in Figs. 2c (the central region of the film) and 2d (the peripheral region of the same film).

A comparison of Figs. 2b–2d demonstrates that the thermal field leads to enhancement of the perfection of the structure formed at the substrate center (from whence the heat outflow comes) and, vice versa, the deterioration of the structure formed at the substrate periphery (the region of the heat inflow).

The degree of uniformity of the film growth rate along the radial coordinate x is illustrated in Fig. 3. Curves *1* and *2* were obtained for the films synthesized under the same conditions (T_s = 473 K) in the presence and in the absence of a thermal field, respectively.

This figure pictorially shows the change in the growth rate in a thermal field of the temperature gradient. The thermal field brings about a decrease in the growth rate at the central region of the substrate and its increase at the substrate periphery.

The influence of the thermal field on the surface morphology of films can be seen in Fig. 4, which displays the electron microscope images of the surface of the films synthesized on the substrates at a temperature T_s = 473 K in the absence (Fig. 4a) and in the presence (Figs. 4b, 4c) of a thermal field. The images that correspond to the central and peripheral regions of the substrate are presented in Figs. 4b and 4c, respectively.

The electron microscopic investigations demonstrate that the thermal field results in an appreciable change in the surface morphology of films. In the presence of the thermal field, the perfection of the surface

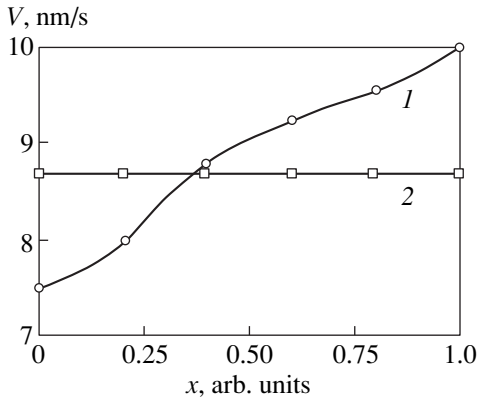

Fig. 3. Dependences of the growth rate on the radial substrate coordinate x for cadmium telluride films synthesized (*1*) in a thermal field of the temperature gradient and (*2*) under uniform conditions.

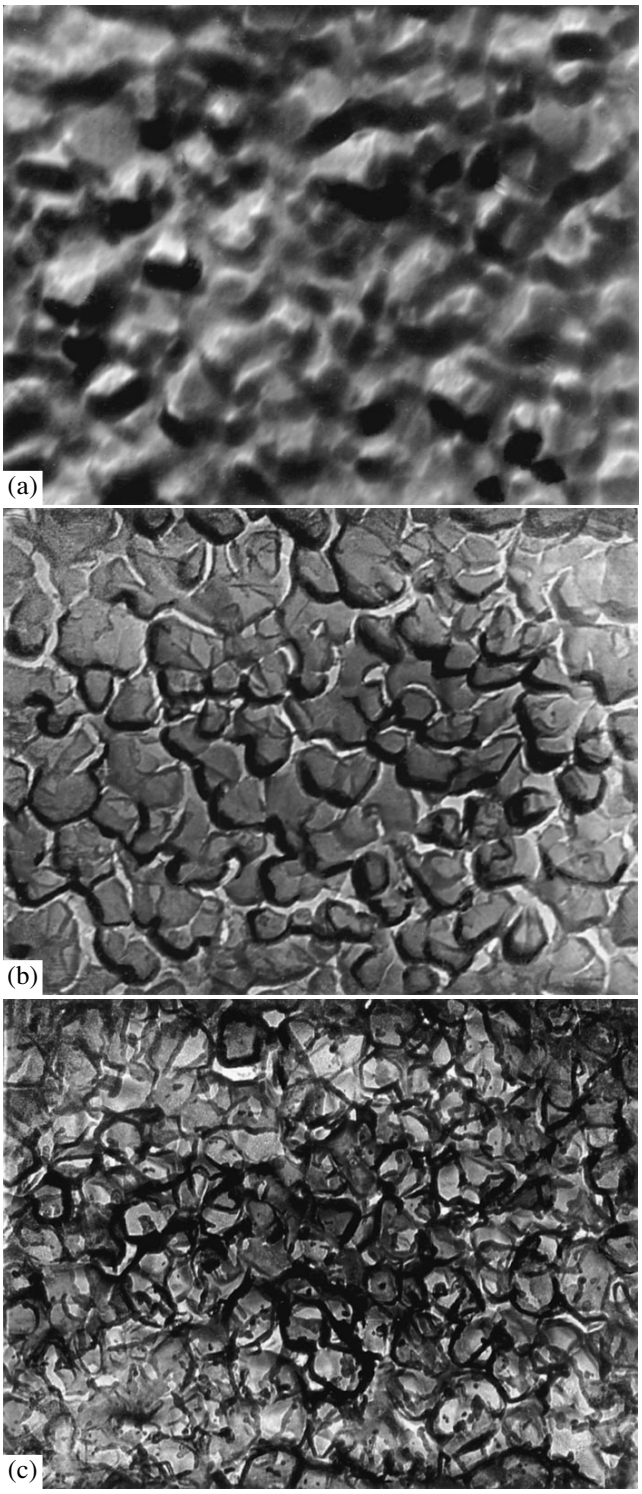

Fig. 4. Surface morphology of cadmium telluride films grown (a) under uniform conditions and (b, c) in a thermal field of the temperature gradient: (b) the central and (c) peripheral film regions (magnification ×40 000).

formed in the central region of films is enhanced and the structure becomes more homogeneous and coarse-grained (Figs. 4a, 4b). By contrast, the structure in the peripheral regions deteriorates and becomes fine-grained and heterogeneous (Figs. 4a, 4c).

No electron diffraction patterns and micrographs are presented for the central and peripheral regions of the films synthesized without a thermal field, because the structural properties of these films are independent of their position on the substrate.

4. DISCUSSION

It is known that the heteroepitaxial growth of cadmium telluride films upon vapor-phase deposition under quasi-equilibrium conditions is observed only at substrate temperatures $T_s \geq 500$ K [5]. At lower temperatures, the structural perfection is disturbed. This is confirmed by typical electron diffraction patterns of CdTe films synthesized at $T_s = 523$ (Fig. 2a) and 473 K (Fig. 2b).

However, as follows from our experiments, in the case when the thermal field of the temperature gradient is produced along the substrate, the heteroepitaxial growth can be observed at considerably lower temperatures. This is evidenced by the electron diffraction pattern of the central region of the film synthesized in a nonuniform thermal field at temperature $T_s = 473$ K (Fig. 2c).

In order to elucidate the mechanism of the effect of the thermal field on the structural perfection, we analyze the rate of film formation. From curves *1* and *2* in Fig. 3 (which correspond to the films with structures shown in Figs. 2b–2d), it can be seen that the film formation process is considerably retarded upon heteroepitaxial growth. Let us consider the possible reasons for this observation. Recall that films of A^2B^6 compounds upon vapor-phase deposition onto a heated substrate are formed through the layer-by-layer normal growth [5]. The formation of each layer involves several stages: a three-dimensional nucleation—the formation of disperse particles, the Ostwald ripening, the coalescence, and the merging into a continuous layer. The growth rate of films is predominantly determined by the first two stages: the nucleation and the Ostwald ripening [6]. The nucleation affects the film growth only at high supersaturations and strong stationary sources of the material. The technological parameters ($T_e = 773$ K and $T_s = 473$ K) used in the experiments cannot be treated as providing such nonequilibrium conditions [4]. Consequently, the Ostwald ripening, rather than the nucleation, is most probably responsible for the retardation of the film formation process. This is all the more probable, because the structural perfection of a layer is usually associated with the Ostwald ripening stage [7]. In the case under consideration, the change in the growth rate of films is attended by the change in their structure [compare the electron diffraction patterns in Figs. 2b and 2c which correspond to the films grown at different growth rates (Fig. 3, curves *1*, *2*)].

An ensemble of disperse particles is formed through the generalized diffusion field at the Ostwald ripening stage. Disperse particles whose sizes are less than the critical size R_c are dissolved, disperse particles with sizes larger than R_c grow, and the disperse particles oriented on a substrate in a nonoptimum manner are arranged in such a way as to provide the minimum energy of the system. New disperse particles virtually are not formed at this stage.

The evolution of disperse particles at the Ostwald ripening stage can be quantitatively evaluated using the distribution function $f(R, t)$ in the size space. In the general case, this function is bell-shaped with a maximum for disperse particles of the critical size R_c. The specific form of $f(R, t)$ is determined by the character of mass transfer upon Ostwald ripening and the source of atoms onto the substrate. However, in any case, the function $f(R, t)$ varies with time so that the ensemble of disperse particles becomes more uniform. For example, in the case of the mass transfer along the substrate surface and in the presence of only nonstationary (dying) sources, the distribution function has the form

$$f(R, t) = \frac{N(t)}{R_c} P(U), \tag{1}$$

where

$$P(U) = \begin{cases} \dfrac{(2e)^{3-2n}(3-2n)U\exp\left(-\dfrac{3-2n}{1-U/2}\right)}{(2-U)^{2+2\left(\frac{3}{2}-n\right)}}, & U < 2, \\ 0, & U \geq 2, \end{cases} \tag{2}$$

$N(t)$ is the two-dimensional density of disperse particles at the substrate surface, n is the exponent of the source dying, and $U = R/R_c$.

As was shown in [8], the distribution function (1) asymptotically tends with time to a form similar to the δ function.

By generalizing all the foregoing about the Ostwald ripening stage, it can be stated that, as its duration increases, the layer homogeneity increases, the film structure becomes coarser-grained and more perfect, and the growth rate of films decreases.

It is easy to see (Fig. 3, curves *1*, *2*; Figs. 2b, 2c, 4a, 4b) that all these features in the experiment under discussion are observed in the central film region in the presence of a thermal field of the temperature gradient. In the peripheral regions of the films, the thermal field produces the opposite effect. The growth rate increases (Fig. 3, curves *1*, *2*), the structural perfection deteriorates (see the electron diffraction patterns in Figs. 2b and 2d), and the structural homogeneity decreases (Figs. 4a, 4c).

Therefore, we can draw the following tentative conclusion: the thermal field of temperature gradient favors a change in the duration of the Ostwald ripening stage in the direction determined by the gradient direction.

In order to elucidate the mechanism of the effect of the thermal field on the Ostwald ripening, we now consider in more detail the initial processes of forming separate layers. According to the classical concepts, the growth of each layer starts with the formation of a "two-dimensional gas" of adatoms upon condensation of atoms and molecules onto a substrate. Three-dimensional nuclei can arise from adatoms when their minimum critical density is reached. A decrease in the density below the critical value results in the completion of the nucleation process and the onset of the Ostwald ripening stage. The density of adatoms on the substrate can be reduced either at the expense of a decrease in the power of the source supplying a material to the substrate or due to the material outflow from the substrate. Evidently, it is unlikely that the thermal field of temperature gradient can substantially change the material source power. However, this field can easily induce a directed outflow of adatoms along the substrate, for example, owing to the different kinetic energies of adatoms in regions with different temperatures. This effect of the thermal field completely correlates with the experimental data. In the central substrate regions with an increased temperature (i.e. the regions of the material outflow), the growth rate decreased, and the Ostwald ripening stage was initiated earlier and was more prolonged. By contrast, at the substrate periphery with a decreased temperature (i.e., the region of the material inflow), the growth rate was higher and the Ostwald ripening stage, most likely, did not occur at all. Therefore, a slowly growing, perfect, and homogeneous structure is formed in the central regions, whereas a rapidly growing and strongly disordered structure is observed in the peripheral region.

The evolution of an ensemble of disperse particles in the presence of different sources was theoretically studied in [8]. The evolution conditions at nonstationary and stationary sources are the closest to those in the case under consideration. The former conditions are similar to those observed at the substrate center, and the latter conditions are similar to the conditions in the peripheral regions, because the thermal field encourages the outflow of atoms from the center and their inflow to the periphery.

In [8], the analytical expression obtained for the distribution function $f(R, t)$, which characterizes the evolution of the system, takes the form of formula (1) for nonstationary sources and is given by the following relationship for stationary sources:

$$f(R, t) \approx N(0)\delta(R - \bar{R}). \tag{3}$$

Here, $\bar{R}$ is the mean size of disperse particles and $N(0)$ is their initial density.

Both functions (1) and (3) were derived under the assumption of the mass transfer along the substrate surface, which is characteristic of the low temperatures used in the present work.

As is seen from these relationships, the theory agrees well with the experiment. The processes of film formation at the center and the periphery of the substrate are qualitatively described by formulas (1) and (3), respectively. The growth patterns are actually coarse at the center of the substrate and fine at its periphery. The scatter in the sizes of film growth patterns at the periphery additionally confirms the presence of a strong source in the system, which, according to the same theory, leads to the secondary nucleation and, as a consequence, the deviation of $f(R, t)$ from the δ function.

5. CONCLUSION

The above results allow us to draw the following inferences.

(1) The thermal field of the temperature gradient along the substrate plane induces the directed flow of a deposited material and, thus, changes the duration of the Ostwald ripening stage in the direction specified by the temperature gradient.

(2) The thermal field of the temperature gradient along the substrate plane favors the perfection of the structure formed upon vapor-phase deposition on the substrate.

ACKNOWLEDGMENTS

The work was supported by the Russian Foundation for Basic Research, project no. 99-03-32676.

REFERENCES

1. A. P. Belyaev, V. P. Rubets, and I. P. Kalinkin, Neorg. Mater. **34** (3), 281 (1998).
2. A. P. Belyaev, V. P. Rubets, and I. P. Kalinkin, Neorg. Mater. **35** (6), 657 (1999).
3. A. P. Belyaev, V. P. Rubets, and I. P. Kalinkin, Fiz. Tverd. Tela (St. Petersburg) **39** (2), 382 (1997) [Phys. Solid State **39**, 333 (1997)].
4. I. P. Kalinkin, V. B. Aleskovskiĭ, and A. V. Simashkevich, *Epitaxial Films of $A^{II}B^{VI}$ Compounds* (Leningr. Gos. Univ., Leningrad, 1978).
5. L. N. Aleksandrov, *Crystallization and Recrystallization Kinetics of Semiconducting Films* (Nauka, Novosibirsk, 1985).
6. S. A. Kukushkin and A. V. Osipov, Usp. Fiz. Nauk **168** (10), 1083 (1998) [Phys. Usp. **41**, 983 (1998)].
7. Ya. E. Geguzin and Yu. S. Kaganovskiĭ, Usp. Fiz. Nauk **125** (3), 489 (1978) [Sov. Phys. Usp. **21**, 611 (1978)].
8. S. A. Kukushkin and V. V. Slezov, *Dispersive Systems on Solid Surfaces (Evolution Approach): Mechanisms of Thin Film Formation* (Nauka, St. Petersburg, 1996).

Translated by O. Borovik-Romanova

Physics of the Solid State, Vol. 43, No. 4, 2001, pp. 783–787. Translated from Fizika Tverdogo Tela, Vol. 43, No. 4, 2001, pp. 750–754.

POLYMERS AND LIQUID CRYSTALS

Effect of the Processes of Orientation of Nonlinear Optical Fragments of a Side Chain in Comb-Shaped Polymers of the Methacrylic Series on the Second-Harmonic Generation in Thin Films

G. K. Lebedeva*, I. M. Sokolova, V. N. Ivanova*, V. A. Lukoshkin***, N. L. Loretsyan*, and V. V. Kudryavtsev***

** Institute of Macromolecular Compounds, Russian Academy of Sciences, Bol'shoĭ proezd 31, St. Petersburg, 199004 Russia*

*** University of Electrical Engineering, St. Petersburg, 197022 Russia*

**** Ioffe Physicotechnical Institute, Russian Academy of Sciences, Politekhnicheskaya ul. 26, St. Petersburg, 194021 Russia*

e-mail: kudryav@hg.macro.ru

e-mail: V.Lukosh@pop.ioffe.rssi.ru

Received August 3, 2000

Abstract—New comblike copolymers of methacrylic acid esters with an optically nonlinear chromophore—a derivative of the 4'-(4-nitrobenzylideneamino)phenol—in a side chain were obtained. Processes of forced orientation of nonlinear optical chromophores covalently bonded with the main chains in an electric field and the effects of the conditions of orientation on the nonlinear second-order optical activity of the polymer films were studied in some detail. The existence of a correlation between the chemical structure and the composition of the copolymers with the magnitude and the stability of the surface electron potential of the corresponding films was shown. It was established that a maximum extent of orientation of chromophores in the bulk of the polymer and, as a consequence, a high intensity of the second-harmonic signal were achieved when the thickness of the region of the uniform electric field maximally approached the thickness of the sample. © *2001 MAIK "Nauka/Interperiodica".*

INTRODUCTION

The investigation of nonlinear optical properties of polymer materials have attracted considerable attention in recent years. The polymers that contain nonlinear optical fragments (chromophores) can exhibit large nonlinear optical coefficients if the organic molecules responsible for the optical nonlinearity are arranged in a certain order. Thin films of polymer materials can easily be obtained by the methods of conventional microelectronics technology, which is especially valuable for applications in optoelectronic devices. In this connection, synthesis of new polymers with nonlinear optical properties and the investigation of conditions under which polymers are capable of revealing maximum nonlinear optical activity (OA) becomes a topical problem.

It is known [1] that for a polymer with noncentrosymmetric optically active groups to be capable of generating second harmonics, oriented molecular structures need to be formed in it. Beginning from the 1980s, processes of poling (polarization under the effect of an applied electric field) at a temperature close to the softening point T_g of the polymer have been widely and successfully applied for orienting dipole molecules of the chromophores in macromolecules. A whole number of works (see, e.g., [2–4]) were devoted to studying the kinetics of decay of the second-harmonic signal intensity after electrization and to revealing relations between the kinetic parameters of the decay of the surface potential and the nonlinear optical susceptibility. The variety of the results obtained and of the models suggested for their explanation is caused by the complexity of relaxation processes that occur in the polymer sample and differently manifest themselves depending on the chemical nature of the polymer studied.

In this work, we performed a complex investigation of the processes of chromophore orientation and second-harmonic generation (SHG) in several new polymers. As the objects of investigation, we chose comb-shaped copolymers of some methacrylic acid esters whose side chains contained alkyl and/or fluoroalkyl radicals along with an optically nonlinear chromophore (the azomethine fragment) that was introduced through a spacer ($–CH_2–$ or $–CF_2–$). The possibility of changing the composition of the copolymers (the number of monomer units with chromophore groups), of the amphiphilic properties (introducing hydrophobic fluoroalkyl and hydrophilic carboxyl groups), and of the free volume of the polymers, as well as the relatively

1063-7834/01/4304-0783$21.00

low values of T_g [5], makes these polymers a suitable material for simulating processes of orientation—of both free orientation (as in Langmuir–Blodgett films) and that which arises under the action of an applied electric field.

1. EXPERIMENTAL

Polymer I and a series of new (not described earlier) polymers II–IV of the general formula shown in Fig. 1 were synthesized by copolymerization of the corresponding comonomers through a free-radical mechanism. Note that the polymers synthesized were capable of forming Langmuir–Blodgett films [6] characterized by a highly ordered structure and optical uniformity, with a thickness that could be controlled to within a bimolecular layer.

The azomethine fragment 4'-(4-nitrobenzylideneamino)phenol, its alkyl (fluoroalkyl) derivatives 6-[4'-(4-nitrobenzylideneamino)phenoxy]hexanol and 6-[4'-(4-nitrobenzylideneamino)phenoxy]decafluorohexanol, and their methacrylic esters 6-[4'-(4-nitrobenzylideneamino)-phenoxy]hexyl methacrylate and 6[4'-(4-nitrobenzylideneamino)-phenoxy]decafluorohexyl methacrylate were synthesized by techniques analogous to [7] and refined by column chromatography using silica gel as the packing material and a mixture of diethyl ether and hexane (1 : 1) as the eluent.

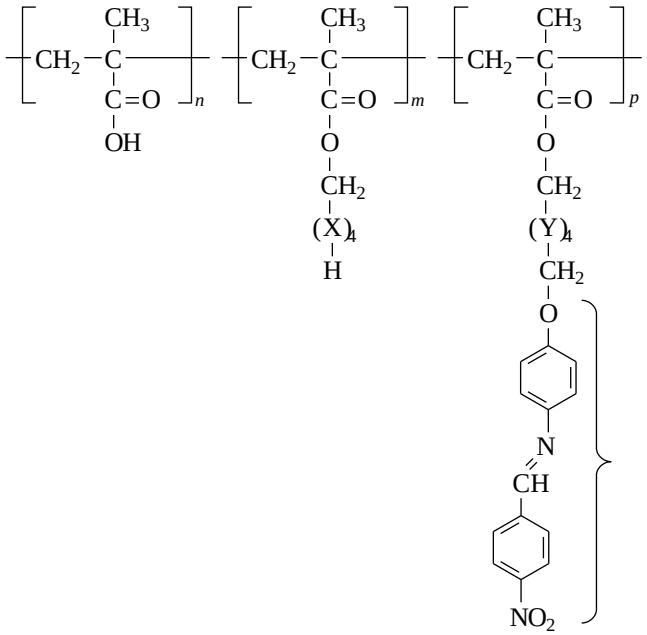

Fig. 1. General formula of copolymers I–IV (the brace bracket indicates the nonlinear optical fragment). Copolymer I: $n : m : p = 60 : 40 : 0$, $X = CF_2$; copolymer II: $n : m : p = 35 : 55 : 10$, $X = CF_2$, $Y = CH_2$; copolymer III: $n : m : p = 0 : 80 : 20$, $X = Y = CH_2$; and homopolymer IV: $n : m : p = 0 : 0 : 100$, $Y = CF_2$; n, m, and p specify the relationship between the initial components (in mol %).

Copolymers I–III were obtained by the free-radical copolymerization of corresponding monomers in solution in *N*,*N*-dimethyl acetamide (30 wt %) with benzoyl peroxide (1 wt %) as the initiation agent at a temperature of 60°C. Homopolymer IV was obtained by bulk thermopolymerization.

The polymers synthesized were refined by reprecipitation from solutions in cyclohexanone to benzene (I, II, and IV) or to methanol (copolymer III) with subsequent drying in a vacuum (10^{-2} Torr) at 50°C. The intrinsic viscosities [η] of copolymers I–III in cyclohexanone were 0.15×10^2 cm^3/g; that of homopolymer IV in acetone was 0.54×10^2 cm^3/g.

The structure and composition of polymers I–IV were confirmed by ^{1}H NMR spectra and UV spectroscopy. The ^{1}H NMR spectra were recorded on a Bruker AC-200 (200.1 MHz) device relative to the signals of the solvent. In this work, we used deuterated chloroform ($(CD_3)_2CO$) and dimethyl sulfoxide (DMSO-d_6) as the solvents. The absorption electron spectra were obtained with a Specord M-40 spectrophotometer.

(1) Polymer I. ^{1}H NMR [$(CD_3)_2CO$], δ = 0.8–1.2 (CH_3), 1.5–2.0 (CH_2), 3.2–3.8 (OCH_2), 4.5–4.9 (CH_2–CF_2), and 6.8 ppm (HCF_2). From the relationships between the signals of protons of specific groups (indicated in parentheses after the magnitude of the signals) in the ^{1}H NMR spectra, we estimated the ratio of repeated units in the copolymer (80 : 20). Hereafter, δ is the chemical shift for protons.

The UV spectrum of the film (λ_{max}): spectrally transparent from 280 nm.

(2) Polymer II. ^{1}H NMR [$(CD_3)_2CO$], δ = 0.88–2.05 (H_{aliph}, i.e., proton contained in the linear chain –CH_2–CH_2–), 3.2–3.8 (CH_2O–benzene ring (Ar.)), 4.00 (CH_2O), 4.5–4.9 (CH_2–CF_2), 6.8 (HCF_2), 7.2–7.8 (H_{arom}, i.e., proton located in the benzene ring), and 8.6 ppm (H located in the N=CH group).

The UV spectrum of the film (λ_{max}) is 265, 300 (low-intensity absorption band with a weak maximum (shoulder)), and 344 nm (shoulder).

(3) Polymer III. ^{1}H NMR [DMSO-d_6], δ = 0.8 (–CH_3), 1.2–1.7 (–CH_2), 3.1–4.0 (CH_2O–Ar.–CH_2O), 7.05–8.4 (H_{arom}), and 8.6 ppm (H in N=CH).

The UV spectrum of the film (λ_{max}) is 265, 300 (shoulder), and 344 nm (shoulder).

(4) Polymer IV. ^{1}H NMR [DMSO-d_6], δ = 1.05–2.2 (H_{aliph}), 3.75–4.5 (CH_2O–Ar., –CH_2O–), 4.9 (CH_2–CF_2), 6.9–7.45 (H_{arom}), 8.2 ppm (H in –N=CH–).

The UV spectrum of the film (λ_{max}) is 328 nm (shoulder).

Using differential scanning calorimetry (DSC), we studied the phase and aggregation state of homopoly-

mer IV (with a maximum content of chromophore groups) in a temperature range of 20–350°C and determined the softening temperature to be T_g = 80°C. The DSC thermogram of homopolymer IV indicates the existence of two transitions: a low-temperature one (at 80°C, with an endothermic effect), caused by the transition of the sample to a softened state; and a high-temperature transition (at 220°C, with an exothermic effect), related to irreversible chemical transformations, since it disappears after repeated scanning. A microscopic investigation in an optical microscope confirmed the DSC results; namely, it showed that at 75–80°C, the polymer begins to spread and at 220°C, the spreading stops.

The calorimetric investigations were performed on a DSM-2M scanning calorimeter at a scanning rate of 16 K/min (samples 20 mg in weight were used; the threshold sensitivity was 10^{-4} W). The optomicroscopic investigations were performed using a Boetius stage in polarized light.

For studying processes of orientation of chromophore groups and the second-harmonic generation, we used polymer films obtained by centrifugation on two types of substrates: silicon substrates for the investigation of the relaxation of charges in the regime of isothermal discharging and a glass slide 180 μm thick for optical measurements. The thickness of the polymer films varied within 0.3–20 μm. The samples were subjected to a heat treatment at 100°C for 3 h and additionally for 1 h immediately before the process of electrization in order to ensure the identical thermal history for all of them. To provide an electric contact during the polarization of polymer films on glass substrates, an electrode in the form of a thin metallic foil was applied onto the back side of the substrate; this electrode was removed before the start of optical measurements. The electrization of the samples was performed in a dc corona discharge (with a current of no more than 3 μA) using a three-electrode scheme. The level of the initial surface potential U_e^0 was specified by a negative potential of the grid electrode and changed from –100 to –600 V. The electrization time t_e varied from 1 to 30 min, and the electrization temperature changed from 14 to 75°C. Upon electrization at enhanced temperatures, the sample was preliminarily heated to a specified temperature; after the termination of the corona discharge, the heating was switched off and the sample was cooled to room temperature under an electric field.

To measure the surface potential of the samples, we used the vibrating-electrode method with an application of a compensating voltage [8]. The use of a grid electrode in the charging device permitted us to control the process of electrization. The efficiency of the process was determined by the ratio of the surface potential to the potential of the control grid (U_e^0/U_g). The falloff of this ratio in time at room temperature was chosen as the characteristic of the process of relaxation in the sample.

Second-harmonic generation in the samples studied was effected using a pulse laser (YAG–Nd^{3+}) operating in the *Q*-switch mode; the radiation wavelength was 1.06 μm, and the pulse duration was 15 ns. The emission energy per pulse was changed in wide limits (up to 30 mJ). The Gaussian shape of the laser-beam profile was ensured by the selection of transverse modes using a diaphragm inside the resonator. Part of the radiation (4%) was split by a beam divider and directed to an FD-24K photodiode to control the energy of the exciting radiation. The major part of the *p* polarized radiation was focused on the sample using a lens with a focus F = 100 mm. The second-harmonic radiation was directed onto an MDR-2 grating monochromator and further onto an FÉU-106 photomultiplier. The electrical signals from both photodetectors were applied to an integrating voltage-to-digital converter and, through a KAMAK interface, to a personal computer to be further processed.

2. DISCUSSION OF RESULTS

First, we studied the electret properties of films of the synthesized polymers I–IV. The results obtained are shown in Figs. 2 and 3. A comparison of the kinetics of the surface-potential falloff for the films of copolymers I–III upon room-temperature electrization (Fig. 2a and curves *1* in Figs. 2b, 2c) suggests that the introduction into the structure of polymer I of units with polar nonliner-optical groups (polymers II and III) leads to a significant decrease in the efficiency of the process of electrization U_e^0/U_g (at t_e = 0) and a decrease in the stability of U_e. Note that the magnitudes of U_e^0/U_g and U_e are smaller for copolymer III, in which the content of chromophore units is greater. However, homopolymer IV is close in the efficiency of electrization and stability of the surface potential to polymer I (Fig. 2a and curve *1* in Fig. 2d).

An increase in the electrization temperature from 14°C to a temperature close to T_g in all polymers containing nonlinear optical groups (II–IV) leads to an increase in the rate of the surface-potential falloff (Figs. 2b–2d); the strongest change is observed for samples of polymer II (curves *1*, *3* in Fig. 2b), which has the smallest content of units with side substituents; i.e., it is characterized by the greatest free volume.

An increase in the initial value of the strength of the internal electric field E_i^0 in the samples immediately after the termination of the polarization procedure virtually does not affect the kinetics of the falloff of the surface potential for polymer II (curves *1*, *2* in Fig. 2b) and strongly affects the kinetics of the process for homopolymer IV (curves *1–3* in Fig. 3). The results obtained indicate that, in the process of U_e relaxation, it

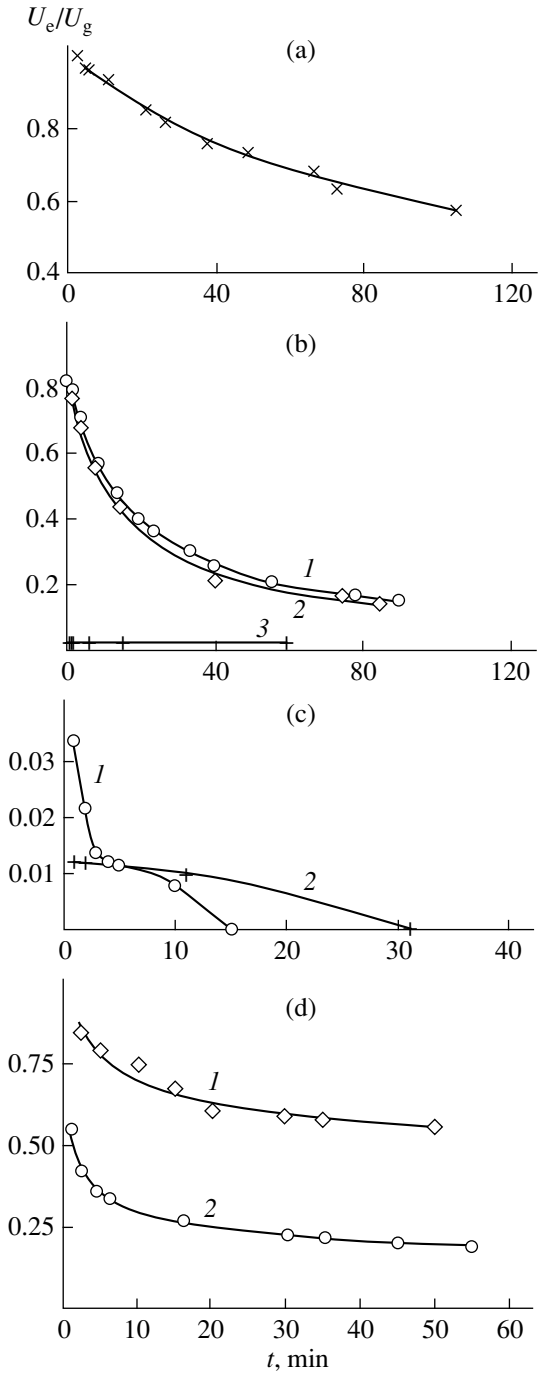

Fig. 2. Kinetics of the falloff of the surface potential U_e/U_g for polymers I–IV at various electrization temperatures T_e and initial values of the strength of the internal electric field E_i^0, respectively: (a) polymer I, 14°C and 0.25×10^7 V/m; (b) polymer II, (*1*) 14°C and 0.25×10^7 V/m, (*2*) 14°C and 1.0×10^7 V/m, and (*3*) 55°C and 0.23×10^7 V/m; (c) polymer III, (*1*) 14°C and 0.25×10^7 V/m and (*2*) 70°C and 0.25×10^7 V/m; and (d) polymer IV, (*1*) 14°C and 0.3×10^7 V/m and (*2*) 60°C and 0.3×10^7 V/m.

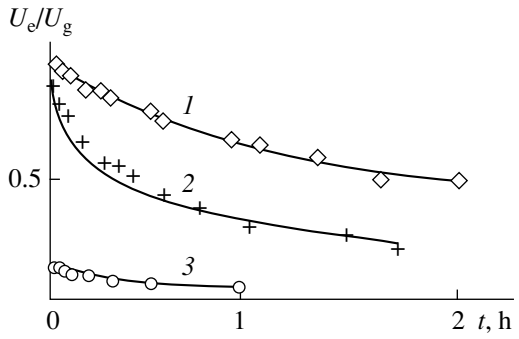

Fig. 3. Kinetics of the falloff of the surface potential depending on the initial value of the strength of the internal electric field E_i^0 in samples of homopolymer IV: E_i^0 = (*1*) 5.7×10^7, (*2*) 12.5×10^7, and (*3*) 66.7×10^7 V/m.

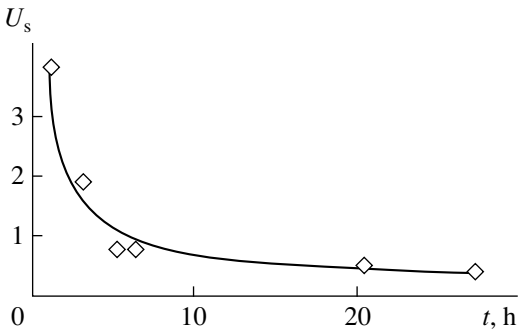

Fig. 4. Kinetics of the falloff of the second-harmonic signal intensity U_s in a film of homopolymer IV 1.6 μm thick at a temperature of 20°C after electrization of the film at T_e = 70°C, U_g = –600 V, and $E_i^0 = 3.3 \times 10^6$ V/m for 10 min.

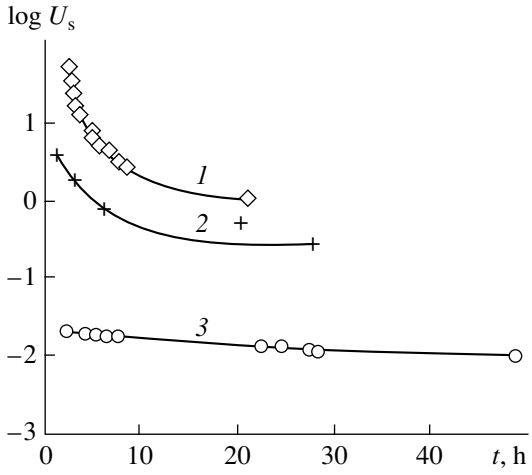

Fig. 5. Kinetics of the falloff of the second-harmonic signal intensity U_s in films of homopolymer IV at 20°C depending on the film thickness d: d = (*1*) 3.5, (*2*) 1.6, and (*3*) 0.3 μm.

is the mechanism of intrinsic conduction that is decisive for polymer II and the drift mechanism of relaxation of the injected discharge for homopolymer IV [9].

Consequently, if we consider polymers I–IV as electrets, then they can be arranged in order of decreasing the electret properties as follows: I–IV–II–III. It is reasonable to assume that an analysis of electret parameters can permit us to preliminarily estimate the efficiency of electrization of the polymers, from the viewpoint of obtaining a maximum extent of orientation of nonlinear optical chromophore groups ensuring the achievement of maximum SHG.

Optical measurements of the intensity of SHG signals from thin films of polymers II–IV confirmed our assumptions. The greatest SHG signal was revealed for films of polymer IV; the intensity of the signal increased by 1.5 orders of magnitude as the electrization temperature increased from 14 to 70°C. Therefore, further investigations of the processes of orientation of nonlinear optical fragments and of second-harmonic generation were performed using homopolymer IV. The time dependence of the intensity of the SHG signal U_s shown in Fig. 4 has two clearly pronounced segments corresponding to fast and slow falloffs, which indicates the existence of fast and slow components of the process of relaxation of the nonlinear optical chromophores. Figure 5 illustrates the effect of the thickness d of a polymer sample on the rate of the falloff of the SHG signal intensity in time for a virtually constant value of E_i^0. The intensity of the signal nonlinearly increases with increasing film thickness. Because of technological difficulties, the measurements of optical characteristics were started 2 h after the termination of the electrization process; therefore, it was difficult to perform an absolute comparison of the time dependences of U_e and U_s, as was done in [10]. However, we were able to reveal the following features: the transition to the region of the slow falloff in the time dependence of U_s occurs later than the analogous transition in the time dependence of U_e/U_g, and in both cases, it occurs later, the greater the thickness of the samples. The combination of the above factors suggests that in the samples of polymer IV that were studied here, a drift of the injected charge to a certain depth inside the sample occurs; this decreases the thickness of the region in which efficient orientation of the chromophore groups can occur in a uniform field. As the sample thickness increases, the effect of this region on the extent of orientation of the chromophores becomes weaker and the intensity of the second-harmonic signal increases. The cause for the falloff of the second-harmonic signal in time is very likely the relaxation of the injected charge due to the drift of the injected charge carriers through the volume of the sample, which leads to a decrease in the field strength operating in the sample and, correspondingly, to a partial misorientation of the chromophore groups. The falloff of the second-harmonic signal intensity occurs with a slight delay with respect to the falloff of U_e, which is caused by the relaxation character of the orientation-related polarization.

3. CONCLUSION

Thus, we established that the maximum extent of orientation of nonlinear optical chromophore units resulting from poling can be obtained in high-resistivity polymers with a high stability of the surface potential in time. The dependence of the stability of the surface potential on the structure and composition of the copolymers studied was established. For comblike copolymers, in which the nonlinear optical fragment is bound with the main chain through an alkyl spacer, the stability of U_e decreases with an increase in the concentration of the chromophores and an increase in the free volume of the polymer upon an increase in the electrization temperature. In the case of a fluorine-containing spacer, even the 100% "loading" with chromophore groups does not lead to degradation of the stability of the electron potential, which is in agreement with the fact of an improvement of dielectric properties of the polymers observed upon substitution of a fluorine-containing spacer for a hydrogen-containing one. The choice of the optimal regime of electrization from the viewpoint of obtaining a maximum magnitude and maximum stability of the second-harmonic signal includes not only the condition that T_e be close to T_g, but also the choice of an optimum thickness of the sample and an optimum electrization potential ensuring the achievement of uniformity of the electric field in a maximally possible volume of the sample.

REFERENCES

1. A. V. Vannikov, A. D. Grishina, R. V. Rikhval'skiĭ, and A. T. Ponomarenko, Usp. Khim. **67** (6), 507 (1998).
2. E. E. Havinga and P. van Peit, Ber. Bunsenges. Phys. Chem. **83**, 816 (1979).
3. G. Meredith, J. van Dusen, and D. Williams, Macromolecules **15**, 1385 (1982).
4. A. Garito and K. Singer, Laser Focus **80**, 59 (1982).
5. T. I. Borisova, L. D. Budovskaya, V. N. Ivanova, *et al.*, Vysokomol. Soedin., Ser. A **12** (12), 2672 (1980).
6. V. Safronov, V. V. Kudriavcev, G. K. Lebedeva, *et al.*, Mater. Sci. Eng., C **5**, 285 (1998).
7. B. K. Mandal, T. Takahashi, M. Maeda, *et al.*, Makromol. Chem. **192**, 1009 (1991).
8. C. W. Reedyk and M. M. Perlman, J. Electrochem. Soc. **15** (1), 49 (1968).
9. J. P. Batra, J. Appl. Phys. **42**, 1124 (1971).
10. L.-Y. Liu, D. Ramkrishna, and H. S. Lackritz, Macromolecules **27**, 5987 (1994).

Translated by S. Gorin

Physics of the Solid State, Vol. 43, No. 4, 2001, pp. 788–791. Translated from Fizika Tverdogo Tela, Vol. 43, No. 4, 2001, pp. 755–758.

FULLERENES AND ATOMIC CLUSTERS

Investigation of Photochromic Cluster Systems Based on Molybdenum Oxides by ESR Spectroscopy

V. N. Andreev*, S. E. Nikitin*, V. A. Klimov*, S. V. Kozyrev, D. V. Leshchev**, and K. F. Shtel'makh*****

** Ioffe Physicotechnical Institute, Russian Academy of Sciences, Politekhnicheskaya ul. 26, St. Petersburg, 194021 Russia*

*** Institute of Highly Efficient Calculations and Databases, St. Petersburg, 198005 Russia*

**** St. Petersburg State Technical University, Politekhnicheskaya ul. 29, St. Petersburg, 195251 Russia*

Received July 18, 2000; in final form, August 17, 2000

Abstract—The electron-spin resonance (ESR) spectra of cluster polyoxometalate systems—a finely dispersed powder of the $(NH_4)_6[Mo_7O_{24}]$–citrie acid complex, molybdic acid, and molybdenum(VI) oxide—are investigated. The initial samples are colored under exposure to ultraviolet (UV) irradiation (photochromic effect) and thermal annealing. The ESR signal ($g_\perp = 1.94$, $g_\parallel = 1.92$) which is observed for the $(NH_4)_6[Mo_7O_{24}]$–citric acid photocolored samples corresponds to an electron of the molybdenum atom. This is in agreement with the data derived from the electronic spectrum. In addition, the $(NH_4)_6[Mo_7O_{24}]$–citric acid colored system exhibits an ESR signal ($g = 2.02$) which corresponds to a hole at the organic ligand. This confirms the previously advanced model of intramolecular electron transfer under UV irradiation. The thermally colored molybdic acid has a similar ESR spectrum ($g = 1.88$, 1.92, 1.93, and 1.98). For the other samples, the ESR signal is not observed. It is demonstrated that an unpaired electron of molybdenum atoms is substantially delocalized over all metal atoms in the cluster. © *2001 MAIK "Nauka/Interperiodica".*

1. INTRODUCTION

It is known that the photochromic effect is observed for solutions and films which contain polyoxomolybdate clusters [1–6]. This effect consists in changing the color under ultraviolet (UV) radiation. In order to explain this effect, a model of coloring polyoxomolybdate cluster systems under UV radiation was advanced in [1–6]. According to the model, the polyoxomolybdate clusters form the complexes through interaction with water, protons, and organic ligands. In this complex, the reaction of intramolecular electron transfer can occur under UV excitation. This reaction results in a change in the oxidation level of the metal in the cluster due to an irreversible change in the organic component. The occurrence of the electron on *d* orbitals of the metal atom leads to the appearance of absorption bands, which are attributed to the *d–d* transitions, in the visible and infrared (IR) ranges.

Investigation of the photochromic effect for a system consisting of a water solution of citric acid $C_6H_8O_7$ and ammonium heptamolybdate $(NH_4)_6[Mo_7O_{24}]$ was carried out in our earlier studies [7, 8]. We revealed the reversibility of the photochromic effect, an absence of the products of oxidation of organic acid, and a decrease in pH. These experimental findings disagree with the theoretical scheme proposed earlier [1–6]. For this reason, we suggested [7, 8] a modified model of coloring cluster systems of molybdenum oxides. A substantial feature of our model is the appearance of unpaired electrons in the course of photocoloring.

In this work, we carried out the ESR investigation of the unpaired electrons generated in polyoxomolybdate clusters under the photochromic effect.

2. EXPERIMENTAL TECHNIQUES

2.1. Sample preparation. The major objects of investigation were finely dispersed powders obtained from solutions of photochromic cluster compounds. This choice of powder sample is explained by the fact that water solutions drastically decrease the potentialities of the experiment. It is our opinion that the processes of interaction of photochromic polyoxomolybdates with UV radiation are similar in solution and finely dispersed powder.

In order to obtain finely dispersed powders, we proposed the following procedure. We prepared two types of water solutions which contained ammonium heptamolybdate $(NH_4)_6[Mo_7O_{24}]$ and citric acid $C_6H_8O_7$. Citric acid (high-purity grade) and ammonium heptamolybdate (Aldrich Chem. Company, USA) were used for preparation of the solutions. Concentrations for the type 1 solution were 0.027 M $(NH_4)_6[Mo_7O_{24}]$ + 0.071 M $C_6H_8O_7$, and concentrations for the type 2 solution were 0.018 M $(NH_4)_6[Mo_7O_{24}]$ + 0.071 M $C_6H_8O_7$. Both solutions were colored under UV irradi-

ation for 85 min. These two solutions had different photochromic properties, i.e., different responses to UV irradiation. The absorption bands of the first solution are observed near 750 nm, while the absorption edge is broadened for the second solution [7, 8]. The irradiated solutions of both types were then dried in an exsiccator in the presence of concentrated sulfuric acid. The powders from unirradiated solutions were also prepared in a similar way. We believe that the ligand environment of the cluster, which plays a dominant role in the photochromic process, was retained in powders obtained through this drying procedure. This approach makes it possible to investigate the properties of the cluster systems for both the ground and excited states.

In addition, we prepared a series of samples of related compounds which included powders of molybdenum oxide (MoO_3) and molybdic acid (H_2MoO_4). It is impossible to color these materials under exposure to UV radiation. However, they can be colored through thermal annealing under vacuum (10^{-5} Torr) or in a hydrogen atmosphere at 773 K. Once annealed, these materials also become blue-colored, which is related to the appearance of an absorption band at approximately 750 nm [9, 10]. The powders obtained were also investigated using the ESR method.

2.2. ESR spectrum. The measurements were carried out on an ER220D (Bruker) ESR spectrometer at room temperature and liquid-nitrogen temperature in the 3-cm range. The microwave power was varied from 75 to 30 mW in the course of measurements. In order to increase the signal, a 100-kHz modulation with an amplitude of 32 G was used. Since cooling to 77 K gave no new results, we analyzed only the spectra measured at room temperature (no annealed samples were investigated at low temperatures).

3. RESULTS AND DISCUSSION

3.1. Experimental results. We compared the ESR spectra of the colored and colorless photochromic polyoxomolybdate compounds. The results of measurements of the ESR signals for various polyoxomolybdate cluster systems are given in the table and in Fig. 1.

The ESR spectrum obtained for colored powders of the ammonium heptamolybdate–citric acid system, which has an absorption band near 750 nm, contains two signals with close g factors (g = 1.92 and 1.94) and a signal with g = 2.02. No hyperfine structure was observed for any of the three signals. The first two signals correspond to an unpaired electron of molybdenum atoms whose g tensor has a weak anisotropy. The g-factor of 2.02 corresponds to an unpaired electron (hole) at the atoms of the organic radical. This interpretation of ESR results is in accordance with conclusions made earlier [5, 11, 12].

The ESR signal was also observed for the samples of molybdic acid annealed under vacuum and in hydrogen. For annealing under vacuum, four signals are observed. Three signals are attributed to the electron of molybdenum atoms (g = 1.88, 1.92, and 1.93), and one signal is caused by the electron of an oxygen atom (g = 1.98) (O^-). Upon annealing in hydrogen, no signal with g = 1.98 is observed, which corresponds to electron detachment from the hydrogen atom.

It is seen from the table that other samples of materials which contained clusters of molybdenum oxide gave no ESR signals.

3.2. Analysis of g tensors. The analysis of g tensors was carried out according to the Bleaney–O'Brien model [13, 14] for the $d^5(d^1)$ configuration of the metal

Values of g factors for cluster systems based on molybdenum oxide

Sample	Effect	Variation	g factors
$(NH_4)_6[Mo_7O_{24}]$–$C_6H_8O_7$(1)	UV	1*	1.92, 1.94, 2.02
$(NH_4)_6[Mo_7O_{24}]$–$C_6H_8O_7$(1)	Not	Not	Not
$(NH_4)_6[Mo_7O_{24}]$–$C_6H_8O_7$(2)	UV	2*	Not
$(NH_4)_6[Mo_7O_{24}]$–$C_6H_8O_7$(2)	Not	Not	Not
H_2MoO_4	Annealing in vacuum	1*	1.88, 1.92, 1.93, 1.98
H_2MoO_4	Annealing in H_2	1*	1.88, 1.93, 1.95
H_2MoO_4	Not	Not	Not
MoO_3	Annealing in vacuum	1*	Not
MoO_3	Annealing in H_2	1*	Not
MoO_3	Not	Not	Not

Note: (1*) Absorption band at 750 nm.
(2*) Absorption edge shift.

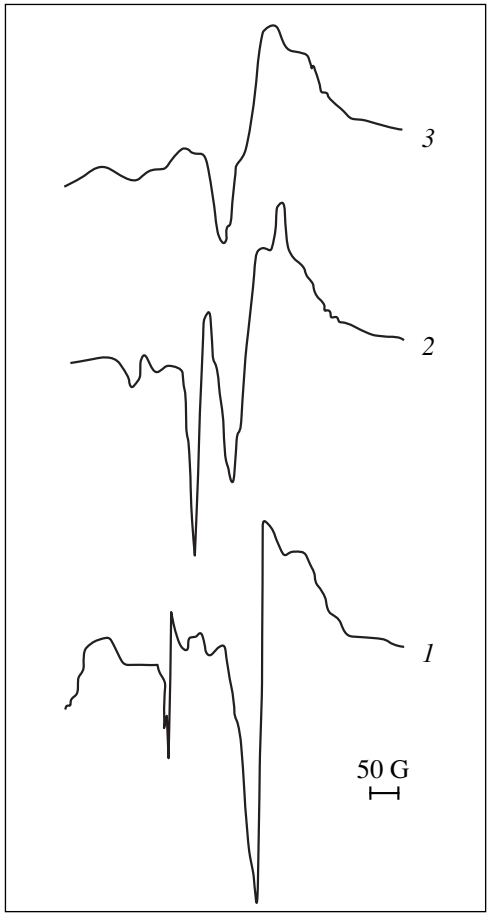

Fig. 1. ESR spectra: (*1*) photocolored ammonium heptamolybdate–citric acid system, (*2*) molybdic acid annealed under vacuum, and (*3*) molybdic acid annealed in air.

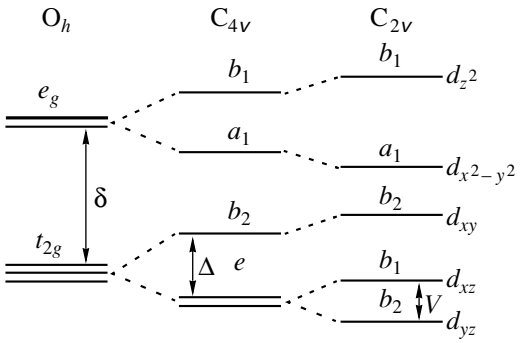

Fig. 2. Scheme of *d* orbital splitting in the ligand field. δ, Δ, and *V* are the energy splitting parameters for *d* orbitals; O_h is the octahedral splitting, C_{4v} is the tetrahedral splitting, and C_{2v} is the orthorhombic splitting.

atom in an octahedral environment:

$$\left.\begin{aligned}\Psi^+ &= a(-id_{yz}\alpha) + b(-d_{xz}\alpha) + c(id_{xy}\beta)\\ \Psi^- &= a(-id_{yz}\beta) + b(d_{xz}\beta) + c(-id_{xy}\alpha)\\ a^2 + b^2 + c^2 &= 1\end{aligned}\right\}\ \text{basis},$$

$$\left.\begin{aligned}(E_{yz} - E)a + (\zeta/2)b + (\zeta/2)c &= 0\\ (\zeta/2)a + (E_{xz} - E)b + (\zeta/2)c &= 0\\ (\zeta/2)a + (\zeta/2)b + (E_{xy} - E)c &= 0\end{aligned}\right\}\ \text{secular equation},$$

$$E_{xz} = -\Delta/3 - V/2,\ E_{yz} = -\Delta/3 + V/2,\ E_{xy} = 2\Delta/3;$$

$$\left.\begin{aligned}g_{xx} &= 2(-a^2 + b^2 + c^2) + 4kbc\\ g_{yy} &= 2(+a^2 - b^2 + c^2) + 4kac\\ g_{zz} &= 2(+a^2 + b^2 - c^2) + 4kab\end{aligned}\right\}\ g\text{-tensor},$$

where ζ is the spin–orbit coupling constant, *k* is the factor of orbital contraction, and *V* and Δ are the energy splitting parameters for *d* orbitals in the ligand field (Fig. 2).

For the *g*-tensor of the ammonium heptamolybdate–citric acid complex (g = 1.92, 1.94), a virtually degenerated solution exists within the error of determination: a = 0.57, b = 0.57, c = 0.58, k = 0.95, V/ζ = 0.00, and Δ/ζ = 0.037. For molybdic acid, the solution has a similar form: a = 0.57, b = 0.58, c = 0.59, k = 0.95, V/ζ = 0.01, and Δ/ζ = 0.037. This solution corresponds to the electron being completely distributed over seven metal atoms and adequately explains the absence of hyperfine structure lines. The presence of three *g* factors for molybdic acid suggests an orthorhombic distortion of the molybdenum atom environment. However, small splitting in the crystal field (V and Δ) allowed us to assume that its magnitude is small. The absence of the third signal for the ammonium heptamolybdate–citric acid complex is indicative of a higher symmetry of the oxygen octahedron (tetrahedral distortion only).

3.3. Photocoloring model. The experiments carried out are in accordance with the model proposed for the photocoloring of a cluster system consisting of ammonium heptamolybdate and citric acid. Assuming that the electronic structures of colored and colorless clusters in the powders obtained according to our procedure are close to those in solutions, we generalized the results of investigations to a unified model of the photochromic effect.

The $(NH_4)_6[Mo_7O_{24}]$–$C_6H_8O_7$ molecular system obtained from type 1 solutions undergoes a transition from ground state I to excited state II (Fig. 3) due to absorption of UV radiation. Then, the system relaxes to state III (blue coloring), in which one electron occurs at the Mo *d* orbitals. This electron is responsible for the appearance of absorption bands near 750 nm. As a result, two unpaired electrons far removed from each

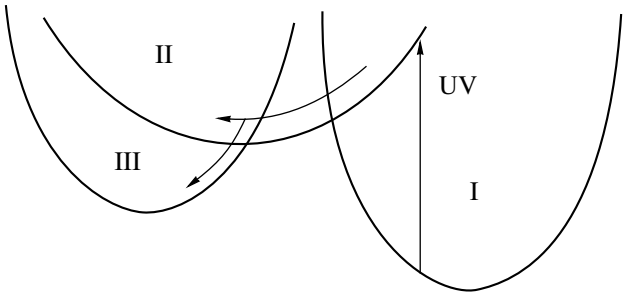

Fig. 3. A model of electron transfer.

other (triplet state) occur in the system: one electron of the molybdenum atoms (with an anisotropic g tensor) and another one at the organic radical ($g = 2.02$). The radiative transition to the ground state (from the triplet to singlet state) is forbidden by the symmetry. The complex can be frozen in this state for an infinite period of time. However, the reverse transfer of the electron from molybdenum to the organic ligand occurs at room temperature and the powder (solution) gradually transforms into the initial state, i.e., becomes decolorized.

For the samples obtained from type 2 solutions, the geometric variations in the complex which are due to the change in the component concentrations suffice to prevent the transition to state III. As a result, the system turns out to be frozen in state II. It is evident that state II is the singlet state (no ESR signal is observed) and that the slow transition to the ground state is determined by kinetic parameters alone.

It is noteworthy that coloring processes in annealed samples of molybdenum oxides and molybdic acid differ from those observed in photochromic cluster systems. The major reason for this difference is the absence of "pliability" of the ligand environment in molybdenum oxide crystals. In other words, the electron transfer proceeds simultaneously with the transformation of the crystal lattice and the electron defect is fixed. These systems do not relax until the "decolorized" state is observed. For this reason, the results of investigations of annealed molybdenum oxides and molybdic acid by the ESR method (for example, [9, 10]) leave the mechanism of the photochromic effect unexplained.

The specific features of the ESR spectrum of molybdic acid can be explained as follows. Upon annealing under vacuum, the electron is detached from the oxygen ion (O^{2-}) and transfers to the molybdenum atom (Mo^{6+}). As a result, two paramagnetic centers are formed: oxygen (O^{-}) and molybdenum (Mo^{+}) ions. The oxygen octahedron in the Mo environment undergoes a weak orthorhombic distortion, and, as a consequence, three ESR signals from the central atom are observed (g_{xx}, g_{yy}, and g_{zz}). Upon annealing in hydrogen, oxidation of free hydrogen and reduction of molybdenum occur. As a result, paramagnetic centers are generated only at molybdenum atoms and no g factor related to the oxygen ion is observed.

The processes occurring during thermal annealing of molybdenum oxide are similar to those described above for molybdic acid. However, after annealing, molybdenum oxide forms rather large clusters in which the interaction of unpaired electrons becomes possible. It seems likely that all electrons in the cluster (at both oxygen and molybdenum) become paired at a high temperature, and the ESR signal is not observed. Here, one more feature of photochromic cluster systems manifests itself, namely, the specificity and individuality of each cluster.

Thus, the experiments performed are in agreement with the model proposed for photocoloring of the ammonium heptamolybdate–citric acid system.

ACKNOWLEDGMENTS

This work was supported by the "Fullerenes and Atomic Clusters" Program of the Russian Federation, assignment 3-1-98.

REFERENCES

1. T. Yamase and K. Tadatoshi, J. Chem. Soc., Dalton Trans. **45**, 2205 (1983).
2. C. Bechinger, G. Oefinger, S. Herminghaus, and P. Leiderer, J. Appl. Phys. **74** (7), 4527 (1993).
3. M. Pope, *Heteropoly and Isopoly Oxometalates* (Springer-Verlag, Berlin, 1983).
4. T. Yamase and T. Ikawa, Inorg. Chim. Acta **37**, L529 (1979).
5. R. I. Bukley and R. J. H. Clark, Coord. Chem. Rev. **65**, 167 (1985).
6. A. Mylonas, A. Hinskia, E. Androulaki, *et al.*, Phys. Chem. Chem. Phys. **1**, 437 (1999).
7. V. N. Andreev, S. E. Nikitin, V. A. Klimov, *et al.*, Fiz. Tverd. Tela (St. Petersburg) **41** (7), 1323 (1999) [Phys. Solid State **41**, 1210 (1999)].
8. V. N. Andreev, F. A. Chudnovskii, S. E. Nikitin, and S. V. Kozyrev, Mol. Mater. **10**, 409 (1998).
9. M. Labanowska, Phys. Chem. Chem. Phys. **1**, 5385 (1999).
10. M. I. Ivanovskaya, A. Ch. Gurlo, E. V. Lyutynskaya, and V. V. Romanovskaya, Zh. Obshch. Khim. **67** (11), 1788 (1997).
11. M. Che, M. Fournier, and J. P. Launay, J. Chem. Phys. **71** (4), 1954 (1979).
12. J. Niu, X. You, C. Duan, *et al.*, Inorg. Chem. **35** (14), 4211 (1996).
13. B. Bleaney and M. C. M. O'Brien, Proc. Phys. Soc. London **69**, 1216 (1956).
14. É. A. Berngardt and P. N. Komozin, Zh. Strukt. Khim. **35** (1), 31 (1994).

Translated by N. Korovin

Physics of the Solid State, Vol. 43, No. 4, 2001, pp. 792–798. Translated from Fizika Tverdogo Tela, Vol. 43, No. 4, 2001, pp. 759–765.

FULLERENES AND ATOMIC CLUSTERS

Static Polarizability of Excited and Charged Alkali Metal Clusters

L. I. Kurkina

Kutateladze Institute of Thermophysics, Siberian Division, Russian Academy of Sciences, pr. Akademika Lavrent'eva 1, Novosibirsk, 630090 Russia

e-mail: kurkina@itp.nsc.ru

Received June 22, 2000

Abstract—The static polarizability of the excited and positively charged (from 1 to 5) sodium, lithium, and potassium clusters containing the "magic" number of valence electrons (from 8 to 198) is calculated by the density-functional method within the "jellium" model. The dependences of the polarizability on the state, size, charge, and composition of clusters are analyzed. © *2001 MAIK "Nauka/Interperiodica".*

1. INTRODUCTION

The static polarizability α_0 is an important parameter that determines the interaction of clusters with each other, external fields, charged particles, and surfaces of solids. In particular, the polarization capture is treated as the main mechanism which is responsible for giant cross sections of inelastic scattering of low-energy electrons by molecular clusters [1–3], fullerenes [4–7], and metallic clusters [8]. The static polarizability of metallic clusters in the ground state has been theoretically studied in sufficient detail (see, for example, reviews [9, 10]). However, experimental data are available only for small-sized sodium [11], potassium [11], and lithium [12] clusters. According to experimental data, the static polarizability of small-sized metallic clusters is several tens of percent higher than that obtained in terms of classical electrostatics for a conducting sphere of the corresponding radius ($\alpha_{cl} = R^3$, where R is the sphere radius). Quantum-mechanical density-functional calculations in the framework of the "jellium" model and different pseudopotential models [13–19] agree much better with experimental data. The main reason for an increase in the polarizability of metallic clusters as compared to its classical value is the penetration of a valence electron cloud outside the positive background boundary of atomic cores (the electron density of a classical conducting sphere has the form of a square step).

In the case when a cluster transforms into an excited or charged state, the charge density distribution and interparticle interaction forces change, and, hence, its response to an external electric field also changes. A number of attendant effects (the Stark effect, a shift in the surface plasma mode, etc.) are directly associated with the cluster polarizability. In the present work, the static polarizability of neutral excited and positively charged (from 1 to 5) lithium, sodium, and potassium clusters was calculated within the nonstationary density-functional theory and the spherical jellium model. In this model, valence electrons are considered in the field of fixed atomic cores whose positive charge is uniformly distributed over the cluster volume. The radius of the positive background $R = N^{1/3}r_s$ is taken as the cluster radius, where N is the number of atoms in the cluster (for alkali atoms, N coincides with the number of valence electrons) and r_s is the Wigner–Seitz atomic radius of the corresponding bulk metal. Since the one-electron potential of a spherical jellium cluster is close to a spherically symmetrical square potential well of a finite depth, stationary electronic states in these systems alternate in a similar way (as roots of a Bessel spherical function with an increase in their magnitude) [20]:

$$1s^2 1p^6 1d^{10} 2s^2 1f^{14} 2p^6 1g^{18} 2d^{10} 1h^{22} 3s^2 2f^{14}$$
$$\times 1i^{26} 3p^6 1j^{30} 2g^{18} 3d^{10} 4s^2 \ldots .$$

As follows from experiments [21, 22], jellium spheres with filled electron shells (clusters with "magic" numbers of atoms) correspond to the most stable structures of clusters of simple metals. The results of calculations of the electronic structure and properties (ionization potentials, electron affinity, polarizability, photoabsorption spectra, etc.) for clusters of simple metals in the framework of the jellium model [9, 10, 13–19, 23] are in good agreement with *ab initio*[italic] calculations and experimental data. This paper reports the results of calculations performed for the jellium clusters of lithium ($r_s = 3.25a_0$, where a_0 is the Bohr radius), sodium ($r_s = 3.98a_0$), and potassium ($r_s = 4.86a_0$) with the magic numbers N = 8, 18, 20, 34, 40, …, 198.

1063-7834/01/4304-0792$21.00 © 2001 MAIK "Nauka/Interperiodica"

2. FORMALISM

The effect of an external electric field $V_{\text{ext}}(\mathbf{r}) = r^l P_l(\cos\vartheta)$ [where $P_l(\cos\vartheta)$ is the Legendre polynomial] on an electronic system leads to a change in the electron density $\delta\rho(\mathbf{r}) = \delta\rho(r)P_l(\cos\vartheta)$. The static polarizability of a spherically symmetrical system is related to $\delta\rho(r)$ by the expression

$$\alpha_0 = -\frac{4\pi}{2l+1}\int_0^\infty \delta\rho(r) r^{2+l} dr. \quad (1)$$

In the framework of the linear-response and nonstationary density-functional theories, the induced electron density $\delta\rho(\mathbf{r})$ is the self-consistent solution of the set of equations [24, 25]

$$\delta\rho(\mathbf{r}) = \int \chi_0(\mathbf{r}, \mathbf{r}')\delta V(\mathbf{r}')d\mathbf{r}', \quad (2)$$

$$\delta V(\mathbf{r}) = V_{\text{ext}}(\mathbf{r}) + \int \frac{\delta\rho(\mathbf{r}')}{|\mathbf{r}-\mathbf{r}'|}d\mathbf{r}' + \frac{\partial V_{xc}(\mathbf{r})}{\partial\rho(\mathbf{r})}\delta\rho(\mathbf{r}), \quad (3)$$

where $\dfrac{\partial V_{xc}(\mathbf{r})}{\partial\rho(\mathbf{r})}$ is the derivative of the exchange–correlation potential with respect to the electron density of the system in the absence of an external field and $\chi_0(\mathbf{r}, \mathbf{r}')$ is the polarization operator in the independent particle approximation, that is,

$$\chi_0(\mathbf{r}, \mathbf{r}') = \sum_i^{occ} \psi_i^*(\mathbf{r})\Psi_i(\mathbf{r}')G(\mathbf{r}, \mathbf{r}', E_i) + \sum_i^{occ} \psi_i(\mathbf{r})\psi_i^*(\mathbf{r}')G^+(\mathbf{r}, \mathbf{r}', E_i). \quad (4)$$

Here, E_i and ψ_i are the eigenvalues and the eigenfunctions of the Kohn–Sham equation

$$\left[-\frac{\nabla^2}{2} + V(\mathbf{r})\right]\psi_i(\mathbf{r}) = E_i\psi_i(\mathbf{r}), \quad (5)$$

which determines the stationary state of the system (in this work, we use the atomic system of units $e = \hbar = m = 1$). For the spherical jellium cluster, the potential $V(\mathbf{r})$ has the form

$$V(\mathbf{r}) = \int \frac{\rho(\mathbf{r}') - \rho^+(\mathbf{r}')}{|\mathbf{r}-\mathbf{r}'|}d\mathbf{r}' + V_{xc}(\mathbf{r}), \quad (6)$$

where

$$\rho(\mathbf{r}) = \sum_i^{occ} |\psi_i(\mathbf{r})|^2$$

is the electron density of the cluster (the summation is performed over all filled states),

$$\rho^+(r) = \frac{3}{4\pi r_s^3}\Theta(R-r)$$

is the density of the positive jellium background (it coincides in magnitude with the mean density of valence electrons in the corresponding bulk metal), $\Theta(R-r)$ is the Heaviside step function, and $V_{xc}(r)$ is the local exchange–correlation potential (in this work, we used the parameterization proposed by Vosko *et al.* [26]).

Relationship (4) for the polarization operator also involves the Green's function $G(\mathbf{r}, \mathbf{r}', E)$, which, for spherically symmetrical systems, is expanded in terms of spherical harmonics:

$$G(\mathbf{r}, \mathbf{r}', E) = \sum_{lm} Y_{lm}(\mathbf{r})G_l(r, r', E)Y_{lm}^*(\mathbf{r}'), \quad (7)$$

where the radial part can be obtained as a combination of the regular $\mathcal{R}_l$ and the singular $\mathcal{N}_l$ (at zero) solutions of the radial part of the Kohn–Sham equation (5):

$$G_l(r, r', E) = \frac{\mathcal{R}_l(r_<, E)\mathcal{N}_l(r_>, E)}{r^2 W_l(E)}.$$

Here, $r_<$ and $r_>$ are the smaller and larger values of r and r', respectively, and $W_l(E)$ is the Wronskian constructed using the $\mathcal{R}_l$ and $\mathcal{N}_l$ functions.

The scheme of calculations is as follows. The self-consistent solution of the Kohn–Sham equation (5) with potential (6) gives the energy spectrum and the wave functions for a specified electronic configuration of the cluster. (The occupation numbers of electron shells are the input parameters, and, hence, this method can be used for both the ground state and excited or charged clusters.) For filled energy states, the radial part of Eq. (5) is integrated from zero and infinity, and the regular and singular solutions obtained are applied to construct the Green's function. The Green's and wave functions for filled states are used for deriving the polarization operator χ_0, which is substituted into Eq. (2). Then, the set of Eqs. (2) and (3) is self-consistently solved by the iteration method (in this case, the convergence is achieved by applying the Aitken δ^2 scheme [27]). The resulting distribution of the induced electron density determines the static polarizability of the cluster.

3. RESULTS

3.1. Excited clusters. Table 1 presents the dipole ($l = 1$) static polarizabilities of excited lithium, sodium, and potassium clusters and the polarizabilities for the ground (nonexcited) state, which were calculated according to the procedure described in the preceding section. The polarizability is normalized to the classical value $\alpha_{\text{cl}} = R^3$. We considered the excited states formed as a result of the dipole transition of an electron from the last filled shell of the cluster to higher-lying levels. The available experimental data on the static polarizability of clusters in the ground state [11, 12] are also listed in the table. As was repeatedly discussed earlier

Table 1. Static polarizabilities of alkali metal clusters in the ground and excited states (the experimental polarizabilities taken from [12] for lithium and from [11] for sodium and potassium are given in parentheses)

N	Electronic configurations of jellium clusters	α_0/R^3		
		Li	Na	K
8	$1s^21p^6$ (ground)	1.56 (2.05)	1.44 (1.77)	1.34 (1.75)
	$1s^21p^52s^1$	2.75	2.20	1.83
	$1s^21p^53s^1$	21.60	17.73	14.86
	$1s^21p^54s^1$	76.66	63.28	47.37
	$1s^21p^51d^1$	1.77	1.55	1.40
	$1s^21p^52d^1$	43.88	27.64	17.71
18	$1s^21p^61d^{10}$ (ground)	1.43 (1.89)	1.33 (1.67)	1.26
	$1s^21p^61d^92p^1$	1.91	1.58	1.39
	$1s^21p^61d^93p^1$	18.90	15.13	11.76
	$1s^21p^61d^94p^1$	52.03	36.34	18.69
	$1s^21p^61d^91f^1$	1.48	1.36	1.27
	$1s^21p^61d^92f^1$	178.98	54.58	17.99
20	$1s^21p^61d^{10}2s^2$ (ground)	1.47 (1.75)	1.37 (1.68)	1.28 (1.63)
	$1s^21p^61d^{10}2s^12p^1$	1.76	1.52	1.36
	$1s^21p^61d^{10}2s^13p^1$	18.53	14.40	10.75
	$1s^21p^61d^{10}2s^14p^1$	47.94	29.85	13.86
34	$1s^21p^61d^{10}2s^21f^{14}$ (ground)	1.34	1.26 (1.63)	1.21
	$1s^21p^61d^{10}2s^21f^{13}2d^1$	1.54	1.36	1.26
	$1s^21p^61d^{10}2s^21f^{13}3d^1$	24.02	17.13	10.47
	$1s^21p^61d^{10}2s^21f^{13}1g^1$	1.35	1.27	1.21
40	$1s^21p^61d^{10}2s^21f^{14}2p^6$ (ground)	1.42	1.32 (1.62)	1.25
	$\ldots2p^53s^1$	1.67	1.45	1.31
	$\ldots2p^54s^1$	13.71	10.81	7.61
	$\ldots2p^55s^1$	30.9	16.56	
	$\ldots2p^52d^1$	1.50	1.36	1.27
	$\ldots2p^53d^1$	18.47	11.17	5.49
58	$1s^21p^61d^{10}2s^21f^{14}2p^61g^{18}$ (ground)	1.28	1.22	1.18
	$\ldots1g^172f^1$	1.36	1.26	1.20
	$\ldots1g^173f^1$	45.90	21.92	5.80
	$\ldots1g^171h^1$	1.28	1.22	1.18
68	$1s^21p^61d^{10}2s^21f^{14}2p^61g^{18}2d^{10}$ (ground)	1.36	1.27	1.21
	$\ldots2d^93p^1$	1.46	1.32	1.23
	$\ldots2d^94p^1$	12.37	8.06	3.82
	$\ldots2d^92f^1$	1.38	1.28	1.22
	$\ldots2d^93f^1$	23.00	7.02	2.29
92	$1s^21p^61d^{10}\ldots1g^{18}2d^{10}1h^{22}3s^2$ (ground)	1.25	1.20	1.16
	$\ldots3s^13p^1$	1.27	1.20	1.16
	$\ldots3s^14p^1$	4.83	2.15	1.37
106	$1s^21p^61d^{10}\ldots2d^{10}1h^{22}3s^22f^{14}$ (ground)	1.30	1.23	1.18
	$\ldots2f^{13}3d^1$	1.36	1.26	1.19
	$\ldots2f^{13}2g^1$	1.31	1.24	1.18
132	$1s^21p^61d^{10}\ldots1h^{22}3s^22f^{14}1i^{26}$ (ground)	1.21	1.17	1.14
	$\ldots1i^{25}2h^1$	1.23	1.18	1.14
	$\ldots1i^{25}1j^1$	1.22	1.17	1.14

Table 1. (Contd.)

N	Electronic configurations of jellium clusters	α_0/R^3		
		Li	Na	K
138	$1s^21p^61d^{10}\ldots3s^22f^{14}1i^{26}3p^6$ (ground)	1.23	1.18	1.14
	$\ldots3p^54s^1$	1.26	1.19	1.15
	$\ldots3p^53d^1$	1.24	1.19	1.14
168	$1s^21p^61d^{10}\ldots2f^{14}1i^{26}3p^61j^{30}$ (ground)	1.19	1.15	1.12
	$\ldots1j^{29}2i^1$	1.20	1.16	1.12
	$\ldots1j^{29}1k^1$	1.19	1.15	1.12
186	$1s^21p^61d^{10}\ldots1i^{26}3p^61j^{30}2g^{18}$ (ground)	1.19	1.15	1.12
	$\ldots2g^{17}3f^1$	1.20	1.16	1.12
	$\ldots2g^{17}2h^1$	1.20	1.15	1.12
	$\ldots2g^{17}3h^1$	1.59	1.21	1.14
196	$1s^21p^61d^{10}\ldots3p^61j^{30}2g^{18}3d^{10}$ (ground)	1.22	1.17	1.13
	$\ldots3d^94p^1$	1.23	1.18	1.13
	$\ldots3d^94f^1$	1.22	1.17	1.13
198	$1s^21p^61d^{10}\ldots1j^{30}2g^{18}3d^{10}4s^2$ (ground)	1.23	1.17	1.13
	$\ldots4s^14p^1$	1.24	1.18	1.14

[9, 10], the jellium model in combination with the local density-functional method more adequately describes the polarizability of clusters of simple metals as compared to the classical theory. However, the theoretical values still remain less than the experimental polarizabilities (in part because of the local approximation for the exchange–correlation potential and owing to ignoring the real geometry of the cluster). Note that the best agreement is achieved for sodium. It is evident that a similar ratio between the calculated and experimental data can also be expected for excited and charged clusters.

As could be expected, the transition of an electron to a higher-lying level leads to an increase in the cluster polarizability. For low-lying excited electronic states, the increase in the static polarizability is relatively small, whereas the polarizability of small-sized clusters in highly excited states increases by a factor of tens and even hundreds. An increase in the polarizability is associated with a decrease in the force of binding the outer shell electron with the cluster upon excitation. The electron cloud of a weakly bound electron is readily deformed in response to an external field, which results in large induced dipole moments. As an illustration, Fig. 1 shows the radial distribution of the electron density $\rho(r)$ in the Na_{58} cluster in the ground $(1s^21p^61d^{10}2s^21f^{14}2p^61g^{18})$ and one of the excited $(1s^21p^61d^{10}2s^21f^{14}2p^61g^{17}3f^1)$ states in the absence of an external field and also the electron density $\delta\rho(r)$ induced by the action of the external potential $V_{ext}(\mathbf{r}) = rP_1(\cos\vartheta)$ on the cluster in the same states. As can be seen from this figure, the electron density induced by the external field in the highly excited cluster extends for distances several times larger than the cluster radius, which, according to formula (1), results in large values of α_0 (in the case depicted in Fig. 1, the static polarizability increases from 1.22 to 21.92).

Table 2 presents the data on the net electron charge outside the boundary of the positive jellium background $Z_{clust} = 4\pi\int_R^\infty \rho(r)r^2dr$ and the contributions of

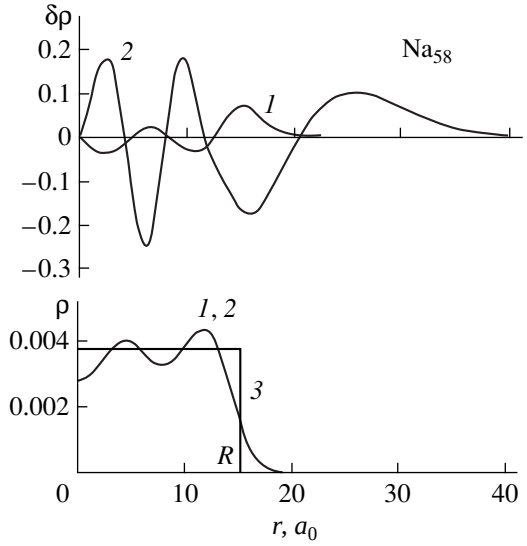

Fig. 1. Electron densities $\rho(r)$ in the absence of an external field and the electron densities $\delta\rho(r)$ induced by the external electrostatic field in the Na_{58} jellium cluster in (*1*) the ground $(1s^21p^61d^{10}2s^21f^{14}2p^61g^{18})$ and (*2*) excited $(1s^21p^61d^{10}2s^21f^{14}2p^61g^{17}3f^1)$ states. (*3*) Radial distribution of the positive jellium background. Curves *1* and *2* for $\rho(r)$ coincide on the given scale.

Table 2. Electron charges outside the positive background boundary of jellium clusters (Z_{clust} is the net charge and Z_{el} is the contribution of the outer shell electron)

N	Electronic configurations of jellium clusters	Li		Na		K	
		Z_{clust}	Z_{el}	Z_{clust}	Z_{el}	Z_{clust}	Z_{el}
18	$1s^21p^61d^{10}$	2.843	0.210	2.575	0.187	1.999	0.144
	$1s^21p^61d^92p^1$	3.135	0.563	2.842	0.476	2.231	0.370
	$1s^21p^61d^93p^1$	3.212	0.918	2.967	0.892	2.456	0.855
	$1s^21p^61d^94p^1$	3.228	0.957	2.989	0.944	2.487	0.928
	$1s^21p^61d^91f^1$	2.921	0.355	2.637	0.302	2.045	0.229
	$1s^21p^61d^92f^1$	3.237	0.960	2.999	0.925	2.487	0.862
58	$1s^21p^61d^{10}\ldots1g^{18}$	6.513	0.165	4.703	0.118	4.170	0.103
	$\ldots1g^{17}2f^1$	6.736	0.418	4.886	0.303	4.317	0.232
	$\ldots1g^{17}3f^1$	6.869	0.933	5.148	0.871	4.616	0.750
	$\ldots1g^{17}1h^1$	6.542	0.237	4.723	0.168	4.185	0.141
196	$1s^21p^61d^{10}\ldots3d^{10}$	13.844	0.162	11.560	0.124	11.425	0.105
	$\ldots3d^94p^1$	13.932	0.294	11.630	0.218	11.479	0.171
	$\ldots3d^93f^1$	13.892	0.245	11.598	0.183	11.453	0.148

the excited electron to this charge for some clusters (the contribution from one electron of the outer filled shell is given for nonexcited clusters) $Z_{el} = 4\pi\int_R^\infty |\psi_{ho}(r)|^2 r^2 dr$, where $\psi_{ho}(r)$ is the wave function of the excited electron or the wave function of the outer filled shell electron in the case of the ground state. The cluster excitation leads to an increase in Z_{clust} and Z_{el}. In this case, there exist highly excited states for which Z_{el} exceeds 0.9 (at $Z_{el} = 1$, the electron becomes free). These weakly bound states provide a high polarizability of clusters. It should be noted that an increase in the net electron charge outside the jellium background boundary upon cluster excitation $\Delta Z_{clust} = Z^e_{clust} - Z^g_{clust}$ (hereafter, the superscripts e and g refer to the excited and ground states, respectively) is less than an increase in the contribution of the excited electron $\Delta Z_{el} = Z^e_{el} - Z^g_{el}$. Therefore, the higher the electronic excitation, the stronger the other electrons are "drawn in" the cluster, which suggests a weakening of the screening of electrons and an increase in their binding in the cluster.

The magnitude of the static polarizability of alkali metal clusters containing the same number of atoms increases with an increase in the atomic number of the substance (note that free atoms Li and Na have close values of polarizabilities $\alpha_0 = 162a_0^3$, whereas the polarizability for K atoms is $\alpha_0 = 286.8a_0^3$ [28]). The normalization of α_0 to R^3 leads to the opposite tendency. This is quite evident, because the larger the atomic number, the lower the density of valence electrons in an alkali metal, the less the electron charge outside the boundary of the positive cluster background, and the closer the electron density distribution at the boundary to the square distribution (i.e., to the classical model). This inference is true for both ground and excited states. The ratio α^e_0/α^g_0 for similar excited states of clusters with identical numbers N decreases when passing from lithium to potassium (a similar tendency is also observed for free atoms [29]). The calculations of the effective orbit radii $r_{ho} = 4\pi\int_0^\infty |\psi_{ho}(r)|^2 r^3 dr$ for outer shell electrons in clusters demonstrate that the relative increase in the electron orbit radius r^e_{ho}/r^g_{ho} upon excitation to the same level decreases from lithium to potassium, which results in the above effect (for example, for clusters consisting of 58 atoms, the transition of an electron from the $1g$ level to the $3f$ level is accompanied by an increase in the effective radius of its orbit by a factor of 2.17 for lithium, 1.8 for sodium, and 1.45 for potassium).

An increase in the cluster size brings about a weakening of the effect of the increase in the static polarizability upon electronic excitation, because the number of free discrete levels in the potential well of the jellium cluster decreases (which results in a decrease in the number of excited states) and the difference between the energies of the ground and excited states is also reduced.

3.2. Charged clusters. From experiments [30, 31], it is known that charged clusters of the $Me^{n\pm}_{N\pm n}$ type (where Me is a metal; $N \pm n$ is the number of atoms in the cluster; and N is the number of valence electrons, which corresponds to the completely filled shells of the jellium sphere), i.e., the clusters that contain the magic

number of valence electrons, often appear to be most stable. In the present work, we calculated the static polarizabilities of the positively charged clusters Li_{N+n}^{n+}, Na_{N+n}^{n+}, and K_{N+n}^{n+} (n = 1–5) with the magic values of N. For these clusters, Fig. 2 depicts the size dependences of α_0/R^3, where $R^3 = (N+n)r_s^3$. The static polarizability decreases with an increase in the size of the neutral cluster. The size dependence of the polarizability for singly charged clusters exhibits a clear maximum near N = 40. This maximum is also observed in the dependences for clusters with larger values of n. However, an increase in n brings about a flattening of the maximum and α_0/R^3 for quintuply charged clusters increases over the entire range. Beginning with N = 58, all the dependences almost monotonically tend to values that exceed α_{cl} by 9–19% for lithium, 7–15% for sodium, and 5–12% for potassium. In order to elucidate the origin of the maximum near N = 40, the dependences of the static polarizability on the cluster charge for lithium clusters of different sizes are plotted in Fig. 3. It can be seen from this figure that an increase in the charge of clusters leads to a decrease in their static polarizability. Moreover, the larger the cluster size, the more flattened the dependence. This results in the intersection of the dependences in the range between n = 0 and n = 4. As a consequence, the dependence of α_0/R^3 on N at fixed n in the range $0 < n < 4$ (Fig. 2) becomes nonmonotonic. Furthermore, it is worth noting that, as the cluster charge increases, the static polarizabilities of clusters which consist of different metals and have the same size approach each other. For example, the values of α_0/R^3 for the Li_8, Na_8, and K_8 neutral clusters are equal to 1.56, 1.44, and 1.34, respectively, whereas the calculated polarizabilities of the Li_{13}^{5+}, Na_{13}^{5+}, and K_{13}^{5+} clusters are 0.65, 0.64, and 0.63, respectively. Thus, it can be concluded that the polarizability (reduced to R^3) of multiply charged clusters of alkali metals only slightly depends on their particular composition.

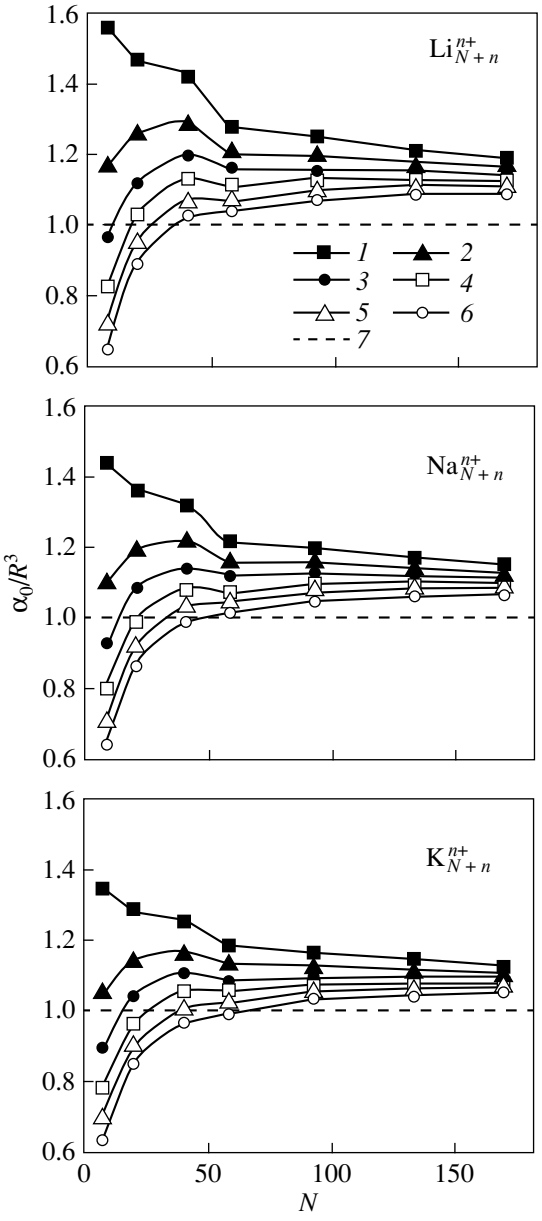

Fig. 2. Dependences of the static polarizability α_0 (normalized to $R^3 = (N+n)r_s^3$) on the number of valence electrons N for Li_{N+n}^{n+}, Na_{N+n}^{n+}, and K_{N+n}^{n+} clusters with different charges n = (*1*) 0, (*2*) 1, (*3*) 2, (*4*) 3, (*5*) 4, and (*6*) 5. (*7*) Static polarizability of the classical conducting sphere.

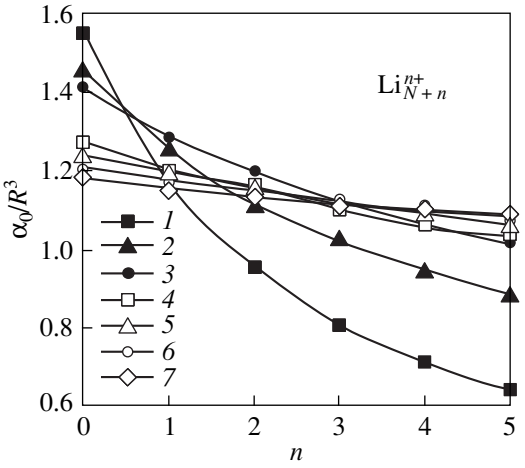

Fig. 3. Dependences of the static polarizability α_0 (normalized to $R^3 = (N+n)r_s^3$) on the cluster charge n for Li_{N+n}^{n+} clusters with different sizes N = (*1*) 8, (*2*) 20, (*3*) 40, (*4*) 58, (*5*) 92, (*6*) 132, and (*7*) 168.

Figure 2 also illustrates how the interparticle interaction in clusters changes with an increase in their size. As is known [28], the static polarizability of positive alkali metal ions in the ^1S state is one or three orders of magnitude smaller than the polarizability of neutral atoms. Therefore, in the absence of interatomic interaction, the polarizability of the Me_{N+n}^{n+} clusters should be virtually independent of n and the dependences shown in Fig. 2 should lie close to each other. As is seen from this figure, a similar tendency is realized only for large-sized clusters, and the polarizability at small N noticeably decreases with an increase in n. This is indirect evidence that interparticle interaction forces in metallic clusters increase with a decrease in their size.

4. CONCLUSION

Thus, in the present work, it was demonstrated that the electronic excitation of metallic clusters leads to an increase in their static polarizability, which is most pronounced for small-sized clusters. As the cluster size increases, the static polarizability nonmonotonically increases for charged clusters and decreases for neutral clusters. An increase in the cluster size is accompanied by a weakening of the dependence of the cluster polarizability on the cluster charge. The polarizability (reduced to R^3) of multiply charged clusters of alkali metals only slightly depends on their specific composition.

ACKNOWLEDGMENTS

This work was supported by the Russian Foundation for Basic Research, project nos. 00-03-33043 and 99-15-96028.

REFERENCES

1. A. A. Vostrikov and I. V. Samoĭlov, Pis'ma Zh. Tekh. Fiz. **18** (7), 58 (1992) [Sov. Tech. Phys. Lett. **18**, 228 (1992)].
2. H. C. Carman, Jr., J. Chem. Phys. **100** (4), 2629 (1994).
3. S. Matejcik, A. Kiendler, P. Stampfli, *et al.*, Z. Phys. D **40** (1–4), 70 (1997).
4. A. A. Vostrikov, D. Yu. Dubov, and A. A. Agarkov, Pis'ma Zh. Tekh. Fiz. **21** (13), 55 (1995) [Tech. Phys. Lett. **21**, 517 (1995)].
5. S. Matejcik, T. D. Märk, P. Spanel, and D. Smith, J. Chem. Phys. **102** (6), 2516 (1995).
6. J. Huang, H. S. Carman, Jr., and R. N. Compton, J. Phys. Chem. **99** (6), 1719 (1995).
7. J. M. Weber, M.-W. Ruf, and H. Hotop, Z. Phys. D **37** (4), 351 (1996).
8. V. Kasperovich, G. Tikhonov, K. Wong, *et al.*, Phys. Rev. A **60** (4), 3071 (1999).
9. M. Brack, Rev. Mod. Phys. **65** (3), 677 (1993).
10. M. Madjet, C. Guet, and W. R. Johnson, Phys. Rev. A **51** (2), 1327 (1995).
11. W. D. Knight, K. Clemenger, W. A. de Heer, and W. A. Saunders, Phys. Rev. B **31** (4), 2539 (1985).
12. E. Benichou, R. Antoine, D. Rayane, *et al.*, Phys. Rev. A **59** (1), R1 (1999).
13. D. E. Beck, Phys. Rev. B **30** (12), 6935 (1984).
14. W. Ekardt, Phys. Rev. B **31** (10), 6360 (1985).
15. M. J. Puska, R. M. Nieminen, and M. Manninen, Phys. Rev. B **31** (6), 3486 (1985).
16. A. Rubio, L. C. Balbas, L. I. Serra, and M. Barranco, Phys. Rev. B **42** (17), 10950 (1990).
17. A. Rubio, L. C. Balbas, and J. A. Alonso, Phys. Rev. B **46** (8), 4891 (1992).
18. L. I. Kurkina and O. V. Farberovich, Z. Phys. D **37** (4), 359 (1996).
19. J. M. Pacheko and J. L. Martins, J. Chem. Phys. **106** (14), 6039 (1997).
20. A. S. Davydov, *Quantum Mechanics* (Nauka, Moscow, 1973; Pergamon, Oxford, 1976).
21. W. D. Knight, K. Clemenger, W. A. de Heer, *et al.*, Phys. Rev. Lett. **52** (24), 2141 (1984).
22. W. D. Knight, K. Clemenger, W. A. de Heer, and W. Saunders, Solid State Commun. **53** (5), 445 (1985).
23. L. I. Kurkina and O. V. Farberovich, Phys. Rev. B **54** (20), 14791 (1996).
24. E. Runge and E. K. U. Gross, Phys. Rev. Lett. **52** (12), 997 (1984).
25. E. K. U. Gross and W. Kohn, Phys. Rev. Lett. **55** (26), 2850 (1985).
26. S. H. Vosko, L. Wilk, and M. Nusair, Can. J. Phys. **58** (8), 1200 (1980).
27. V. L. Zaguskin, *Handbook on Numerical Methods for Solving Algebraic and Transcendental Equations* (Fizmatgiz, Moscow, 1960).
28. A. A. Radtsig and B. M. Smirnov, *Reference Data on Atoms, Molecules, and Ions* (Atomizdat, Moscow, 1980; Springer-Verlag, Berlin, 1985).
29. M. S. Safronova, W. R. Johnson, and A. Derevianko, Phys. Rev. A **60** (6), 4476 (1999).
30. Ch. Schmitt, Ch. Ellert, M. Schmidt, and H. Haberland, Z. Phys. D **42** (2), 145 (1997).
31. K. H. Meiwes-Broer, Appl. Phys. A **A55** (5), 430 (1992).

Translated by O. Borovik-Romanova

Physics of the Solid State, Vol. 43, No. 4, 2001, pp. 799–800. Translated from Fizika Tverdogo Tela, Vol. 43, No. 4, 2001, pp. 766–767.

COMMENTS

Comment on the Paper of A. G. Groshev and S. G. Novokshonov "Negative Magnetoresistance and Hall Coefficient of a Two-Dimensional Disordered System"

I. V. Gornyĭ[1,2], A. G. Groshev[3], and S. G. Novokshonov[3]

[1] *Ioffe Physicotechnical Institute, Russian Academy of Sciences, Politekhnicheskaya ul. 26, St. Petersburg, 194021 Russia*
[2] *Institute of the Nanotechnology, Karlsruhe Research Center, Karlsruhe, 76021 Germany*
[3] *Physicotechnical Institute, Ural Division, Russian Academy of Sciences, ul. Kirova 132, Izhevsk, 426001 Russia*
e-mail: nov@otf.fti.udmurtia.su

Received July 20, 2000

The paper of A.G. Groshev and S.G. Novokshonov [1] was dedicated to the theoretical investigation of the localization corrections to the longitudinal ρ and Hall ρ_H resistivities of a two-dimensional disordered system in a wide range of magnetic fields up to the quantizing fields. In particular, they demonstrated that in the entire range of classically strong magnetic fields in which the mean free path $l = V_F\tau < R_c$ (R_c is the cyclotron radius), the cooperon retains the form of the diffusion propagator and the transition to the ballistic regime in a strong magnetic field when $l > l_B$ ($l_B = \sqrt{c/eB}$ is the magnetic length) manifests itself in the spatial dispersion (nonlocality) of the diffusion process in the Cooper channel.

Employing the definition of the electrical conductivity tensor in the circularly polarized coordinates, the authors of [1] obtained, in a unified form, the expressions for the quantum corrections to the longitudinal and Hall resistivities measured in units of $2\pi^2/e^2$:

$$\begin{Bmatrix}\delta\rho\\ \delta\rho_H\end{Bmatrix} = \begin{Bmatrix}\mathrm{Re}\\ \mathrm{Im}\end{Bmatrix}\frac{1}{(\pi k_F l_B)^2} \times \sum_{n=0}^{\infty}\frac{P_n}{1-P_n}[P_nA_n - B_{n-1}^{(+)^2} - B_n^{(-)^2}], \tag{1}$$

where

$$P_n = 2\pi\int_0^{+\infty}\rho J_{n,n}(\sqrt{2}\rho)P(\rho)d\rho,$$

$$A_n = \frac{2\pi}{m\tau}\int_0^{+\infty}\rho J_{n,n}(\sqrt{2}\rho)K^2(\rho)d\rho, \tag{2}$$

$$B_n^{(\pm)} = \frac{2\pi}{m\tau}\int_0^{+\infty}\rho J_{n,n+1}(\sqrt{2}\rho)G^{\pm}(\rho)K(\rho)d\rho.$$

Here,

$$J_{n,n'}(\rho) = \left(\frac{n_{\min}!}{n_{\max}!}\right)^{1/2}\left(\frac{\rho^2}{2l_B^2}\right)^{|n-n'|/2} \times \exp\left(-\frac{\rho^2}{4l_B^2}\right)L_{n_{\min}}^{|n-n'|}\left(\frac{\rho^2}{2l_B^2}\right), \tag{3}$$

where $L_n^m(x)$ is the associated Laguerre polynomial ($L_n(x) = L_n^0(x)$),

$$P(\rho) = \frac{1}{m\tau}\left|G^{\pm}(\rho)\right|^2 \tag{4}$$

is the probability density of finding an electron at the distance ρ from the point of its last collision, and

$$K(\rho) = \frac{2}{k_F}\frac{\partial}{\partial\rho}\mathrm{Im}G^+(\rho) + i\frac{\rho}{R_c}\mathrm{Re}G^+(\rho), \tag{5}$$

where $G^+(\rho)$ is the translation invariant part of the retarded one-electron Green function in the coordinate representation.

The first term in $\delta\rho(\delta\rho_H)$ in formula (1) is due to coherent backscattering ($\theta \approx \pi$), and the second and third terms are associated with coherent scattering through an arbitrary angle ($0 < \theta < \pi$) [2, 3]. These expressions are valid in a wide range of magnetic fields, including quantizing ones. However, their analysis in [1] contains an error which had a profound effect on the final results. Namely, one term is omitted in the quasiclassical ($n \longrightarrow \infty$) asymptotics of the coefficients $B_n^{(\pm)}$ in formula (2), which determined the contributions of the coherent scattering through an arbitrary angle. As a consequence, the localization corrections that were obtained in [1] to the Hall resistivity are $\delta\rho_H \propto \ln(l_B/l)$ for $B \longrightarrow 0$.

1063-7834/01/4304-0799$21.00

It is well known [2–4] that the processes of coherent scattering through arbitrary angles in classical magnetic fields lead to small corrections to the negative magnetoresistance. However, their consideration in the Hall resistance is of fundamental importance [5, 6], since they guarantee the fulfillment of the Ward identity (the particle conservation law) to the first order in $1/k_F l$.

The correct quasi-classical asymptotics of the integrand in the coefficient $B_n^{(\pm)}$ has the form

$$WG^{\pm}(\rho)K(\rho) \approx \left[1 + i\frac{\rho}{2R_c} \pm i\frac{1}{2k_F}\frac{\partial}{\partial\rho}\right]P(\rho), \qquad (6)$$

where the last term was omitted in [1]. At first sight, these terms cancel out in $\delta\rho_H$ in formula (1) in the limit $B \longrightarrow 0$ ($n \gg 1$). However, already to the first order in $1/n$, they make a nonzero contribution to $\delta\rho_H$, which, in the limit $B \longrightarrow 0$, eliminates the logarithmic singular first term in formula (1). The other terms give the expression for the quantum corrections to the Hall resistivity, which, according to [5, 6], tends to zero when $B \longrightarrow 0$. It should be emphasized that the conclusion concerning the absence of the localization corrections in the Hall resistivity [5, 6] corresponds to the case $B \longrightarrow 0$. Therefore, the question about their behavior in a finite magnetic field remains open. If their absence is due to the particle conservation law, the equality $\delta\rho_H \equiv 0$ (at least in the first order with respect to $1/k_F l$) should hold in the whole range $l < R_c$, where the Landau quantization can be disregarded. The authors of this comment are currently preparing a paper in which the behavior of the localization corrections to the Hall resistivity in both classical and quantizing magnetic fields is analyzed in detail.

REFERENCES

1. A. G. Groshev and S. G. Novokshonov, Fiz. Tverd. Tela (St. Petersburg) **42** (7), 1332 (2000) [Phys. Solid State **42**, 1361 (2000)].
2. A. P. Dmitriev, I. V. Gornyi, and V. Yu. Kachorovskii, Phys. Rev. B **56**, 9910 (1997).
3. I. V. Gornyĭ, Author's Abstracts of Candidate's Dissertation in Mathematica Physics (St. Petersburg, 1998).
4. V. M. Gasparyan and A. Yu. Zyuzin, Fiz. Tverd. Tela (Leningrad) **27**, 1662 (1985) [Sov. Phys. Solid State **27**, 999 (1985)].
5. H. Fukuyama, J. Phys. Soc. Jpn. **49**, 644 (1980).
6. B. L. Altshuler and A. G. Aronov, in *Electron–Electron Interaction in Disordered Systems*, Ed. by A. L. Efros and M. Pollak (North-Holland, Amsterdam, 1985).

Translated by O. Moskalev